Sh. 384

ORNL-5308

Health Physics DIVISION

Annual Progress Report

MASTER

Period Ending June 30, 1977

Reports previously issued in this series are as follows:

ORNL-2384	Period Ending July 31, 1957
ORNL-2590	Period Ending July 31, 1958
ORNL-2806	Period Ending July 31, 1959
ORNL-2994	Period Ending July 31, 1960
ORNL-3189	Period Ending July 31, 1961
ORNL-3347	Period Ending July 31, 1962
ORNL-3492	Period Ending July 31, 1963
ORNL-3697	Period Ending July 31, 1964
ORNL-3849	Period Ending July 31, 1965
ORNL-4007	Period Ending July 31, 1966
ORNL-4168	Period Ending July 31, 1967
ORNL-4316	Period Ending July 31, 1968
ORNL-4446	Period Ending July 31, 1969
ORNL-4584	Period Ending July 31, 1970
ORNL-4720	Period Ending July 31, 1971
ORNL-4811	Period Ending July 31, 1972
ORNL-4903	Period Ending July 31, 1973
ORNL-4979	Period Ending July 31, 1974
ORNL-5046	Period Ending June 30, 1975
ORNL-5171	Period Ending June 30, 1976

Contents

INTRODUCTION xi

SUMMARY xiii

I. Assessment and Technology xiii

II. Biological and Radiation Physics xv

III. Chemical Physics and Spectroscopy xv

IV. Emergency Technology xvi

V. Medical Physics and Internal Dosimetry xvii

VI. Analytic Dosimetry and Education xvii

PART I. ASSESSMENT AND TECHNOLOGY

1. DOSIMETRY FOR NEW ENERGY SYSTEM POLLUTANTS 1

Assessment, Education, and Coordination 1

Instrumental Techniques under Development 2

Second-Derivative UV-Absorption Spectrometry 2

Room-Temperature Phosphorimetry 5

Separation by Differential Sublimation 7

Thermoluminescence Analysis 7

Portable Mass Spectrometer 8

Instrument Testing in Pilot-Plant Environs 8

2. RADIATION DETECTION AND MONITORING PRINCIPLES 9

Dosimetry Intercomparison Studies 9

Third International Intercomparison of Environmental Dosimeters (IIED) Under Field and Laboratory Conditions 9

Bank of Calibrated BeO Ceramic Exoelectron-Thermoluminescence Dosimeters with a Common History 9

Fast-Neutron Personnel Monitoring 10

Detection of Alpha Particles and Low-Level Radon Monitoring 12

Further Development of BeO Ceramic TLD for Low-Level Radiation Measurements 14

3. HEALTH PHYSICS RESEARCH REACTOR 15
Intercomparison Studies and Dosimeter Tests 19
Nuclear Accident Dosimetry Intercomparison 19
Quarterly Accident Readiness Tests 19
Personnel Dosimetry Intercomparison Study 19
Improvements of Safety Block Alignment 21

4. DOSIMETRY FOR HUMAN EXPOSURES 22
Analysis of Leukemic Data from Studies of Atomic-Bomb Survivors Based on Estimates of Absorbed Dose to Active Bone Marrow 23
Neutron Fluence-to-Dose Conversion Factors for Am-B and Am-Be Sources 27
Chord Operators for Insult Assessment to the Radiosensitive Cells of the Tracheobronchial Tree 28
Analog Development for Insult-Specific Risk from Energy Conversion 31

5. RADIATION MEASUREMENTS AND ASSESSMENTS 35
Radiological Surveys at Inactive Uranium Mills 36
Radon and Radon Daughter Sampling 39
^{226}Ra Profiles in Soil 38
Radiological Assessment of Former MED-AEC Facilities 40
Radiological Impact of Uranium Recovery from Wet-Process Phosphoric Acid 49
Instrument Developments 50
Facilities Used in Field Surveys 52
Geographical Distribution of Radiological Survey Sites 55

6. ENVIRONMENTAL HEALTH STUDIES 56
Public Health and Demographic Statistics 56
Health Physics Aspects of Fusion Power 59
Factors Affecting Calculations of Dose Resulting from a Tritium Release into the Atmosphere 59
Conversion of Tritium Gas to Tritiated Water 61
Tritium Conversion Experiments 63

PART II. BIOLOGICAL AND RADIATION PHYSICS

7. PHYSICS OF SOLIDS AND MACROMOLECULES 65
Optical Properties of Arc-Evaporated Carbon Films 66
Convergence of Optical Sum Rules 67
Temperature Dependence of the *K* X-Ray Emission Edge of Lithium 70
Refractive Indices of Transparent Solvents 72
Temperature Dependence of the Pre-Expotential Factor of the Arrhenius Equation 74
High-Temperature Solar Absorbers 76
Plasmon Radiation from Silver 77
Polarization Anomalies from Holographic Gratings 80

Blazed Holographic Gratings Formed with Optical Guided Waves 80
Holographic Zone Plates 81
Increased Sensitivity of Recording Materials when Exposed to Optical Guided Waves 82
Optical Guided Mode Holography Equations 83
Theory of Aberration-Corrected Gratings Using Optical Guided Waves 84

8. TRANSPORT AND SURFACE PHYSICS 87
Pion Beam Dosimetry 88
Estimated *W* Values for Negative Pions in Tissue-Equivalent Gas, CO_2, and N_2 88
Tabulations of Electron Interaction Parameters in Solids 91
Electron Slowing-Down Spectra in Aluminum Metal 91
Influence of Damping on the Mean Free Path of Low-Energy Electrons in an Electron Gas 93
Interaction of Slow Ions with Surfaces 96
Energy and Spatial Dependence of Swift Electrons Transmitted through Thin Solid Films – Effect of Plasmon Interactions 98
Comparison of Vicinage Effects in the Interaction of Ion Clusters with Single Atoms and with Condensed Matter 98
Wake Induced in Condensed Matter by Swift Charged Particles 101
Radiative Capture of Electrons by a Swift Ion in a Thin Foil 103
Velocity Spectra of Convoy Electrons Emerging with Swift Ions from Solids 105

9. ATOMIC AND MOLECULAR PHYSICS, PHYSICOCHEMICAL PROPERTIES OF BIOLOGICALLY IMPORTANT STRUCTURES, AND HIGH-VOLTAGE RESEARCH 108
Systematics of Negative-Ion States of Atoms and Small Molecules 109
Fragmentation of Aliphatic Chlorocarbons under Low-Energy ($\lesssim$10 eV) Electron Impact 109
Absolute Rates and Cross Sections for Electron Attachment to Fluorinated Hydrocarbons 112
Studies of Negative-Ion Resonances Using Electron Transmission Spectroscopy 112
Interaction of Low-Energy Electrons with Fluorine-Substituted Benzenes in Dense Gaseous Environments 113
Long-Lived Parent Negative Ions Formed Via Nuclear Excited Feshbach Resonances: Effective Number of Degrees of Freedom Participating in the Sharing of the Ion's Excess Energy 115
Variation of EA 116
Effective Vibrational Degrees of Freedom Participating in the Sharing of the Ion's Excess Energy 116
Possible Differences Between ν_i' and ν_i 116
Possible Errors in $\sigma(\epsilon_i)$ 117
Conclusion 117
Lifetimes of Metastable Negative Ions 117
Measurement of Electron Mobility in Neopentane at High Gas Pressures and High Temperatures 118
Electron Attachment to CO_2 in Dense Gases 120
High-Resolution Laser Negative-Ion Spectroscopy; Energetics and Kinetics of Charged-Separated States in Liquids 120

Effect of Internal Electric Field on the Recombination of Electron-Hole Pairs in Nonpolar Liquids 123
Photoionization of Molecules in Liquids 125
High-Voltage Research [Breakdown Strengths of Gaseous (and Liquid) Insulators] 125
Apparatus 126
Breakdown Strengths – Unitary Systems 126
Breakdown Strengths of Multicomponent Gaseous Mixtures 126
Discussion 129
International Symposium on Gaseous Dielectrics 130

10. MICRODOSIMETRY, BIOLOGICAL MODELING, AND THEORETICAL BIOPHYSICS 131
Updating of Inverse Mean Free Path (IMFP) Data for Electrons in Liquid Water 131
Low-Energy Elastic Scattering Cross Sections 134
Calculation of Spatial Distributions of Primary Products around a Heavy-Ion Track in Liquid Water 134
Applications of Models for Cell Survival: The Fixation-Time Picture 136
Three-State Model 137
Effect of Growth Medium on Yeast Recovery 138

11. LIQUID AND SUBMICRON PHYSICS 140
Precision Measurements of the Electronic Properties of Liquids and Solutions 141
Submicron Physics 142
Particle Interactions in Holes 143
Electron Scattering on Cylinders 147
Theoretical Calculations of Plasmons and Surface Waves on Cylinders 149
Comparison of Cylinder Theory with Experiments 150

PART III. CHEMICAL PHYSICS AND SPECTROSCOPY

12. ATOMIC PHYSICS AND LASER RESEARCH 153
One-Atom Detection and Resonance Ionization Spectroscopy 153
Demonstration of One-Atom Detection 153
Density Fluctuation Studies Using One-Atom Detection 156
Collisional Line Broadening by Two-Photon Ionization 158
Saturated Photodissociation of Cesium Iodide 160
Sensitive, Absolute, and Time-Resolved Method for the Study of Reactive Atoms 162
Detection of Single Fission-Product Atoms 164
RIS Studies of Proton-Excited Krypton 165
Energy Pathways Research and Its Applications 165
Time-Resolved Quenching of Excited States of Argon 166
Charge Transfer and Penning Ionization of N_2, CO, CO_2, and H_2S in Proton-Excited Helium Mixtures 167
Charge Transfer Studies of Ne-N_2 Mixtures 172
Energy Transfer Processes in Proton-Excited Argon-Xenon and Ar-F_2 Mixtures 174

Energy Pathways for Pollutant Detection 179
Simple Geometry Experiment and Its Supporting Calibration Laboratory 179
Systematics of Compiled Intensity Constants for Diatomic Molecular Electronic Transitions 180
Laser Breakdown and Laser Fluorescence for Pollution Measurements 180
Ultrasensitive Pollutant Analysis by a Laser-Induced Rare-Gas Breakdown Technique 180
Laser-Induced Fluorescence Spectroscopy 183
Theory of Laser Interaction with Matter 183
General Method for Near-Resonance Multiphoton Ionization with Narrow-Bandwidth Lasers 183
Three-Photon Ionization near a Two-Photon Resonance 185
Two-Photon Excitation and Three-Photon Ionization Due to a Narrow-Bandwidth Laser 189
Collision-Induced Resonances in the Two-Photon Ionization of Excited-State Populations 192
Laser-Induced Collisional Excitation Transfer 194
Adiabatic Following in Two-Photon Transition 195
Dynamic Stark Splittings in Two-Photon Processes 196
Conclusion 198

13. CHEMICAL PHYSICS 199
Studies of Molecular Clusters from Supersonic Jet Expansions 199
Two-Photon Ionization of Cesium with Tunable Dye Lasers 200
Multiphoton Ionization of Molecular Species 202
Collisional Ionization between Ground-State Reactants 203
Collisional Ionization Reactions between Alkali Atoms and Some Methane Derivatives 204
Studies of Atomic Polarizability 205
Energy and Angular Distributions of Collisional Ionization Products 206
Collisional Ionization of Cesium by Water 207
Collisional Ionization of Cesium by Oxygen 208
Dissociative Ionization by Electron Impact 208
High Kinetic Energy N^+ Ions from Decay of Doubly Ionized N_2 208
Oscillator Strength Sum Rule for Atomic Isotope Shift 210
Newton's Divided Difference Form of the Schroedinger Equation 211
Angular Momentum in Uniomolecular Kinetics 211
Theoretical Electron Affinities of Polar Molecules 212

PART IV. EMERGENCY TECHNOLOGY

14. CONSEQUENCES OF DISPERSAL OF A RADIOACTIVE SOURCE 215

15. AEROSOL STUDIES 216
Choice of a Simulant 216
Development of Aerosol Generator 216
Sampling Techniques 216

Average Size of Aerosol Particles 217
Calculation of Deposition Velocity 218
Test of Protection Factors Using Vacuum Cleaner 218
Preliminary Field Test 219
Method of Calculating Protection Factor of Closed Houses 219
Definitions 219
Calculation of the Diffusion Protection Factor (P_D) 220
Calculation of the Contamination Protection Factor Due to Filtration 222
Tests on Closed Houses 222
Discussion 223

16. DECONTAMINATION STUDIES 224

17. ELEMENTS OF A WAR-SURVIVAL POLICY FOR THE UNITED STATES 226
Conclusion 230

18. FOREIGN CIVIL DEFENSE STUDIES 231

19. BLAST TESTS OF EXPEDIENT SHELTERS IN THE DICE THROW EVENT 234
Principal Objectives 234
Instrumentation Used and Test Data Recovered 234
Summaries of the Most Significant Tests 235
Small-Pole Shelter at 53 psi 235
Unmodified Russian Pole-Covered Trench Shelters 238
Log-Covered Trench Shelters 241
Door-Covered Earth-Roll Shelters 243
Test Limitations 245
Principal Conclusions and Recommendations 246

20. MANUAL ESTIMATION OF CASUALTIES DUE TO FALLOUT FROM A NUCLEAR ATTACK 248

21. INSTRUMENTATION REQUIREMENTS FOR POPULATION PROTECTION FROM FALLOUT FROM A NUCLEAR WAR 249

22. CLINCH RIVER BREEDER REACTOR PLANT SAFETY DESIGN AND ELECTROMAGNETIC PULSE 250
Safety Considerations 250
EMP Environment 250
CRBRP Design Features 251
EMP Analysis 252
Conclusions and Recommendations 253

23. SOLAR ENERGY DEVELOPMENT PROGRAM 254

PART V. MEDICAL PHYSICS AND INTERNAL DOSIMETRY

24. INTERNAL DOSIMETRY 259

Dose from ^{40}K for the Organs of Reference Man 259

Distribution in the Body 259

Calculation of Dose Rate 260

Calculation of Dose Conversion Factor 262

Discussion 262

Revised Effective Energies for Use In Internal Dose Estimations 263

Radioactive Decay Scheme Data 267

Adjustments of Inhalation Doses to Take Account of Particle Sizes 272

Curve Fitting of Curium Excretion Data 275

Distribution of Dose within the Body from a Photon Emitter Present in an Organ 276

25. EXTERNAL DOSIMETRY 279

Absorbed Dose to Mammary Glands 279

Absorbed Dose During Breast ^{60}Co Therapy 282

Absorbed Doses to the Skin and to a 1.1-cm-Deep Annulus from Broad, Parallel, Monoenergetic X-Ray Beams Incident on the Trunk of the Adult Phantom 283

26. EXPERIMENTAL STUDIES 286

Absorbed Dose from Diagnostic X Rays 286

High-Resolution Ultrasonic Analysis of Burn Damage 286

In-Phantom Spectrometry of Diagnostic Medical X Rays 286

Development of a Mathematical Phantom Representing a Ten-Year-Old Child for Use in Internal Dose Calculations 288

Evaluation of the Distribution of Absorbed Dose in Pediatric Phantoms Exposed to Diagnostic Medical X Rays 289

High-Resolution Ultrasonic Analysis of Burn Damage 291

Instrument System Development 292

Data Analysis of Experimental Burns 292

Linear Scanning Unit 292

Density Studies on Burned Tissue 294

Fourier Spectral Analysis of Attenuation Characteristics 295

27. NUCLEAR MEDICINE IMAGING AND DATA PROCESSING 298

ORIS Components 299

Data Acquisition 299

Data Storage 299

Image Display 299

Image Processing 300

Current Projects 301

Bone Imaging 302

Comparison of Nonlinear Image Processing Techniques 302

Emission Tomography with Small Numbers of Images 303

PART VI. ANALYTIC DOSIMETRY AND EDUCATION

28. ANALYTIC DOSIMETRY 305

29. EDUCATION AND VOCATIONAL TRAINING 307

THESES, PAPERS, PUBLICATIONS AND LECTURES 309

Theses 309

Papers 310

Publications 315

Lectures 329

MISCELLANEOUS STAFF ACTIVITIES 335

Introduction

This annual progress report follows, as in the past, the organizational structure of the Health Physics Division. Each part is a report of work done by a section of the division: Assessment and Technology Section (Part I), headed by H. W. Dickson; Biological and Radiation Physics Section (Part II), H. A. Wright; Chemical Physics and Spectroscopy Section (Part III), W. R. Garrett; Emergency Technology Section (Part IV), C. V. Chester; Medical Physics and Internal Dosimetry Section (Part V), K. E. Cowser; and the Analytic Dosimetry and Education Group (Part VI), J. E. Turner. This year's report covers research activities from July 1, 1976, through June 30, 1977, and will be the last report issued under the name of the Health Physics Division. The division's work in applied health physics and safety is reported by calendar year (see ORNL-5171 for 1976).

In April 1977, the division was reorganized into the Industrial Safety and Applied Health Physics Division and the Health and Safety Research Division. The Industrial Safety and Applied Health Physics Division will be under the direction of J. A. Auxier and will include the Laboratory support functions of the former Health Physics Division. The Health and Safety Research Division will be under the direction of S. V. Kaye and will include the research activities and research organization of the former Health Physics Division, the Analysis and Assessment Section previously in the Environmental Sciences Division, and the Biomedical Radioisotopes group under J. K. Poggenburg, previously in the Operations Division. Organization charts reflecting these changes can be found at the back of this report.

The purposes of the reorganization were to consolidate related functions and to separate the research from the support function.

As in the past, the work of the Health Physics Division was characterized by a strong interaction among the applied, technological, and disciplinary research functions. This report reflects that philosophy. It includes multidisciplinary studies and multidivisional collaboration, all mission-oriented toward the effects of radiation (and in the last few years, other insults) on humans and their environment. An increasing amount of research has been directed recently to other nonnuclear energy problems.

Major support for the work during the year came from a number of federal agencies: U.S. Air Force, U.S. Army, Environmental Protection Agency, Energy Research and Development Administration, Food and Drug Administration, Nuclear Regulatory Commission, and Veterans Hospital at Gainesville, Florida.

Major accomplishments and results of this past year's work are summarized in the following sections.

Summary

PART I. ASSESSMENT AND TECHNOLOGY

The dosimetry for new energy system pollutants has been focused primarily on carcinogenic products of coal conversion processes but has application to other energy systems, such as geothermal. Full characterization of polynuclear aromatic compounds (PNA) in coal conversion products is made with instruments that are sophisticated, time-consuming, and usually expensive. The industrial hygienist uses techniques that are not selective, sensitive, or very accurate. One of our objectives is to provide monitoring instrumentation to bridge this gap.

The compounds to be monitored cover the full range of aromatic compounds from the simplest molecules, such as benzene, to the multiringed, high-boiling PNA compounds. Monitoring capability will be extended to vapors, airborne particulates, and surface contamination, and the data gathered will be in forms suitable for subsequent health studies. Analytical techniques under development for monitoring applications include (1) second-derivative uv-absorption spectrometry, (2) room-temperature phosphorimetry, (3) differential sublimation, (4) thermoluminescence analysis, and (5) portable mass spectrometry.

A major effort in assessment and clarification of monitoring needs continues. To support this effort, a dual workshop (held in conjunction with the Health Division) was held on exposure to PNA in coal conversion processes on medical surveillance and industrial experiences. Contacts have been established with numerous groups interested in promoting occupational health and safety in this fledgling industry.

In spite of diminishing funding, a significant base program is being maintained in radiation detection and monitoring. Fast-neutron dosimetry is recognized as the major unresolved problem in personnel monitoring and an effort to improve this situation is being made the cornerstone of our activity. Using the technique of electrochemical enhancement of neutron-induced recoil tracks, four plastics have been evaluated as potential fast-neutron dosimetry materials. Also, work is proceeding on the detection of alpha particles using track detectors and the application of this technique to low-level radon monitoring. Several projects involving exoelectron dosimeters either have been finished or else scaled down.

In keeping with this section's tradition of conducting dosimetry intercomparisons and standardizations, we are involved in a series of environmental dosimetry intercomparisons at the international level, as well as an international study of calibrated BeO ceramic dosimeters was prepared and calibrated at ORNL and then distributed to research groups in seventeen countries. The Third International Intercomparison of Environmental Dosimeters is being conducted at ORNL, but has been jointly organized by ourselves, the School of Public Health of the University of Texas, and the ERDA Health and Safety Laboratory in New York.

The Health Physics Research Reactor (HPRR) continues to serve as a principal research tool for radiobiological experiments and for dosimeter development. Radiation dosimetry research is accomplished primarily in the Health Physics Division through an active solid-state dosimetry program, and the radiobiology research is accomplished primarily through the Biology Division. Recent controversy over the appropriate relative biological effectiveness of neutrons for radiation protection purposes makes new experiments in this area particularly significant. The HPRR's substantial role in education and training is evidenced by the six major universities that used it during the past year.

The use of the HPRR as an international testing and standardizing facility grows each year. Intercomparison studies of nuclear accident dosimeters and personnel monitoring devices are conducted annually to establish the accuracy and reliability of dosimetry systems in mixed neutron-gamma radiation fields. Additionally, programs have been established for testing criticality alarm systems and accident preparedness.

Two new shields have been fabricated for the intercomparison studies – one of concrete and the other of

steel and concrete. A discrete ordinates transport code has been applied to calculate the neutron spectra transported through the new shields. Also, the initial reference dosimetry has been performed with the shields in place around the HPRR core. As a result, two new spectra will be available for the fourteenth Nuclear Accident Dosimetry Intercomparison Study in July 1977.

To improve the predictability of pulse size in the pulse mode of operation for the HPRR, the safety block has been modified. An antirotation device and a safety block centering device have been fabricated. Currently, the new devices are being tested to determine their effectiveness.

The objective of our studies on the dosimetry of human exposures is to improve techniques for assessing the risk from occupational and environmental exposures to radiation. Inherent in this objective are detailed investigations and predictions of radiation interactions within the body at microscopic and macroscopic levels. An example, which has been used in establishing criteria and standards for exposures to neutrons, is our calculation of depth-dose and linear energy transfer (LET) distributions in a homogeneous tissue-equivalent phantom from plane beams of neutrons. Recently, the Monte Carlo transport codes used in these calculations have been generalized to calculate depth-dose and LET distributions within the body from isotropic and other fields of gamma rays and neutrons encountered in environmental and occupational exposures. Whereas these depth-dose and LET distributions were intended mainly for use in radiation protection and risk analyses, they have application in such other areas as dosimeter design, cancer radiotherapy, and national defense.

During the past year, work in this program has been concentrated on (1) an analysis of leukemia data from studies of atomic-bomb survivors, based on estimates of absorbed dose to active bone marrow, (2) neutron fluence-to-dose conversion factors for isotopic neutron sources, (3) CHORD operators for insult assessment to radiosensitive cells of the tracheobronchial tree, and (4) development of appropriate calculational analogues for insult-specific risk from energy conversion pollutants.

Work in the Offsite Measurements Program was directed toward assessments of the radiological impact of inactive uranium mill sites, radiological surveys of former Manhattan Engineering District/Atomic Energy Commission (MED/AEC) facilities throughout the country, and verification of theoretical source terms for effluent releases from a plant designed to recover uranium from wet-process phosphoric acid. During the year, measurements were completed at 22 inactive uranium mills. Most of the activities in this project were directed toward characterization of the spread of contamination from uranium tailings piles, migration of long-lived radionuclides through airborne, aquatic, and terrestrial pathways, and measurements of radon and radon daughters in structures where tailings had been used in construction. It was shown that in most cases, the highest potential exposure to the general public arises from the diffusion of radon to population centers. Some evidence was found of radium and uranium moving away from a tailings pile where groundwater is active.

Approximately 35 former MED/AEC facilities were visited in order to evaluate the need for a formal survey to document the current radiological condition of the property. Of those visited, it was determined that a survey would be required in 19 cases. Of these, the Offsite Measurements Group was requested to perform 18. During this report period, 15 of these surveys were completed. Careful attention was given to areas at each of these facilities where residues were likely to have been overlooked in previous surveys. Results of the surveys were compared to guidelines used by the United States NRC for the release of property for unrestricted use. Several properties were identified which qualify for an engineering assessment to determine whether remedial action is required prior to release for unrestricted use.

Initial measurements were made to measure the concentration of uranium in the effluent of a central processing plant designed to recover uranium from phosphoric acid. In addition, uranium concentrations in water and soil on the site of this plant were measured. These measurements will be used along with calculated source terms to evaluate exposure to the public as a result of the operations of this plant.

The two major thrusts of the environmental health studies have been in the areas of health physics aspects of fusion power and methodology for assessing health effects related to nuclear facilities.

The methodology assessment has been conducted under the Public Health and Demographic Studies Program, the objective of which is to use and assess the available data sources and the methodology appropriate for use in analytical studies concerning health effects related to nuclear facilities. This program has been concentrated on collecting available mortality statistics for the area surrounding the nuclear facilities at Oak Ridge, which have been in operation for three decades. Data accumulation techniques, the subsequent statistical analyses, and the methodology appropriate to use

in an environmental impact statement for public health assessments are also being developed under this program.

In the past year, three studies in this program have been completed. In the first study, a literature survey, it was found that in the majority of the reported investigations, researchers were unable to discern a dose-response relationship or to find adverse health effects in the local population around nuclear facilities which might be related to radiation exposure. The second study was directed at analyzing the trends in incidence of cancer, congenital malformation, and fetal and infant mortality for Oak Ridge, Anderson County, and Roane County relative to Tennessee. Finally, a more in-depth study on congenital malformations and fetal mortality trends for nine East Tennessee counties surrounding Oak Ridge was completed.

The objective of the Health Physics Aspects of Fusion Power Program is to provide, on a timely basis, scientific information and technical evaluations on the potential impacts of fusion power to occupational workers and to members of the public. Whereas analysis and assessment activities are and will remain a vital part of this program, the work in that area has begun a transition from primarily qualitative assessments to analyses requiring technical accomplishments; this trend is expected to continue since substantive analyses appear to require new technical input. The primary areas of study in this program during the past year have been (1) factors affecting calculations of dose resulting from a release of tritium, (2) an assessment of the potential for reducing occupational risk from exposures to tritium, and (3) experimental studies of tritium conversion from molecular hydrogen to tritiated water.

PART II. BIOLOGICAL AND RADIATION PHYSICS

During the year, research in the Biological and Radiation Physics Section involved a remarkable range of subjects – from the most basic studies of the properties of matter to research having an immediate promise of application. Only a few highlights will be mentioned here. For the first time we made a detailed study of the optical response of a hydrocarbon polymer, polystyrene, over virtually the entire energy range where it has appreciable oscillator strength. This gives important information on the rate of convergence of sum rules for such materials. The temperature dependence of the K x-ray emission edge in lithium was observed for the first time, settling the controversy over the position and width of the Fermi edge. Theoretical calculations which were made of cross sections for electron inelastic interactions, of wake effects in solids due to the passage of ions or ion clusters, and of forces between a slow ion and a solid surface have application not only to radiation physics, but to problems of particle accretion and surface-mediated catalytic reactions. Studies were continued of such physicochemical properties of biologically important molecules as cross sections for electron attachment fragmentation under low-energy electron impact, negative-ion resonances, and electron mobilities. Application of fundamental knowledge on electron-molecule interactions led to the development of many single- and multicomponent gas mixtures which are superior to SF_6 for use as gaseous dielectrics. This has immediate application to high-voltage electrical transmission with a potential for enormous savings in the energy now lost in the distribution system. Monte Carlo calculations were made of the microscopic distribution of energy deposition and of various ionization and excitation products around the track of a heavy ion in liquid water. These results have application to radiation effects models. A method was developed for measuring the reflectance of a liquid surface by using photoionization in the vapor over the surface. This should greatly improve the accuracy of such measurements in the vacuum ultraviolet region. Progress was made in our program to study the properties of submicron structures. As an example, the deflection of a 1-eV electron beam passing through a 3-μm-diam pinhole was measured and used to deduce the potential distribution inside the hole.

PART III. CHEMICAL PHYSICS AND SPECTROSCOPY

Within the period of this report, investigations in the Chemical Physics and Spectroscopy Program have focused on a wide spectrum of problems involving physical or chemical interactions at the molecular and molecular cluster levels. Most of the work has involved studies of various reactive processes between photons, charged particles, ions, and/or neutral particles with other atomic and molecular species. In addition, a new research direction has been the study of the physics of macromolecules (clusters) in the gas phase. Results of these studies have potential applications in radiation and pollutant detection technology, laser development and analytical applications of laser technology, atmospheric physics and chemistry studies, and radiation chemistry and radiation biology. Perhaps the most noteworthy progress in this program over the past year has come in the demonstration of new principles for

ultrasensitive analytical methodology. Specifically, the first successful demonstration was made of one-atom detection and its extension to one-molecule detection by new laser techniques which were developed here over the last two years. Other work supportive of advanced instrumentation development includes multiphoton photoionization studies, laser interaction theory, and line shape and power broadening studies under high-intensity laser fields.

Other new programs which have evolved in the past year include studies of positive and negative ion formation in low-temperature molecular clusters from a supersonic jet expansion, studies of heavy metal polarizabilities, and studies of energy and angular distributions of collisional ionization products in low-energy charge-changing collisions. Results of these studies have potential applications in atmospheric physics and chemistry problems and in radiation chemistry studies. Other ongoing efforts that are relevant to problems in these same areas include electron affinity determinations of highly electronegative molecules and studies of detailed pathways by which energy is transferred from excited states of binary and trinary gaseous mixtures to photons, to bond breakages, and/or to thermal motions.

New programs which are being initiated include studies of one-atom chemistry, laser breakdown and laser fluorescence experiments, and a second-generation molecular clustering experiment for studies of noncondensable gases.

A study has been undertaken to determine whether the consequences of dispersal of radioactive sources not now under safeguards are sufficiently severe to warrant extending safeguards to some of these sources.

The dispersal of sources in large cities is being assumed, and health effects and cleanup costs are being estimated. It appears that cleanup costs predominate and can rival those of a major dam failure.

PART IV. EMERGENCY TECHNOLOGY

As part of the continuing studies of the effects of very severe reactor accidents, an effort was made to develop, test, and improve simple, effective, and inexpensive methods by which the average citizen, using only materials readily available, could protect his residence, himself, and his family from injury by toxic aerosols. The methods for protection against radioactive aerosols should be equally effective against a clandestine biological attack by terrorists.

The results of the tests to date are limited to showing that spores of the harmless bacterium, bacillus globegii (BG), can be used as a simulant for the radioactive aerosols. An aerosol generator of Lauterbach type was developed which will produce an essentially monodisperse aerosol at the rate of 10^9 spores/min. Analytical techniques have been established which give reproducible results. Preliminary field tests have been conducted to check out the components of the system. Preliminary tests of protective devices, such as ordinary vacuum sweepers, have given protection factors of over 1000.

As part of the ongoing research on the effects of very severe reactor accidents, a series of experiments has been designed to provide quantitative information on methods of decontamination of various building materials contaminated by the very finely divided aerosols that might be generated by the accident. Preliminary tests have been made using depleted uranium oxide deposited by the Chemistry Division's reactor safety group's aerosol experiments. The tests show that the Georgia Institute of Technology reactor can be used for activation analysis of the contaminated and decontaminated samples.

The Soviet Union has been vigorously pursuing a war-survival policy for several years, whereas the United States has relied entirely on deterring nuclear war. This has resulted in a situation in which the U.S. population is of the order of ten times more vulnerable to nuclear war than is the Soviet population. Increasingly widespread perception of the disparity in vulnerability could undermine credibility of the U.S. deterrent forces and leave the United States in a very poor bargaining position in a confrontation. A program recommended to reestablish parity in vulnerability consists of the following:

1. make national survival in the event of nuclear war explicit policy,
2. develop crisis relocation plans for the population of all potential target areas,
3. teach a course in nuclear-war survival in high school,
4. assign to Minuteman and/or B-1 the role of preventing the reloading of Soviet "pop-up" silos,
5. reinstitute air defense in the United States if the Soviets continue to deploy the "Backfire" bomber,
6. continue policies encouraging relocation of population and industry outside cities,
7. avoid the development of new target concentrations especially in the new synthetic liquid fuel industry, and
8. develop and encourage integration of blast and fallout protection into new energy-conserving construction.

During the past year, the attitude toward civil preparedness for the American public has been slowly changing. It has become apparent that many nations of the world are actively preparing shelters and underground protection for population and industrial facilities. The Soviets have admitted that they feel that sheltering is absolutely essential (and the "natural, humane" thing to do) when faced with the possibility of war.

Despite the continued resistance of some confirmed non–civil defense people in the United States, the House of Representatives recently voted for approval of an approximate 65% increase in civil defense spending. We feel that efforts by our staff members have contributed a great deal to the current awareness for the need to offer the American public some organized civil preparedness programs which would enable them to obtain knowledgeable assistance in a crisis.

As part of ORNL's continuing development and field testing of expedient shelters and expedient life-support equipment, 18 expedient shelters were blast-tested on October 6, 1976, in the main event of Defense Nuclear Agency's DICE THROW series at White Sands Missile Range, New Mexico. This was a 630-ton ammonium nitrate–fuel oil explosion, producing air-blast effects equivalent to those of a 1-kiloton nuclear detonation.

We list here the most significant test findings and conclusions. (1) Ground-shock effects are much more destructive to expedient shelters than are air overpressure effects; occupants of the unshored ORNL shelters at 53, 31, and 20 psi overpressures would have been injured or killed by the collapsing earth walls of both the closed and open pole-roofed shelters in which effective earth arching prevented roof poles from being even cracked. (2) For unshored shelters built in average earth and subjected to the blast effects of large nuclear weapons, the Soviet judgment of about 7 psi as the outer boundary of the "zone of complete destruction" seems prudent. (3) A small-pole shelter with expedient blast doors can readily be built to withstand the blast effects from a 1-kiloton weapon at 53 psi overpressure. However, due to the manyfold increase in the impulse from a megaton explosion at the same maximum overpressure, the resultant greater earth pressures at depth and the more serious "earth-flow" phenomena, this shelter (even if floored with protective poles) probably would fail at considerably less than 53 psi if subjected to the blast effects of a large nuclear weapon. (4) Shelter damage from parts of buildings, trees, and other heavy objects hurled by blast winds and from the blast-wind scouring of shielding earth would severely limit the practicality of aboveground expedient shelters built in areas subjected to blast overpressures greater than about 5 psi, with accompanying blast winds peaking at about 160 mph from a detonation at optimum burst height. (5) Even the simplest shelters tested, which use only interior doors, sheets, pillowcases, and other common home materials, provide better blast and fire protection than do all but the strongest buildings, and many times the fallout protection. (6) Expedient shelters and their life-support equipment should be tested in blast environments that simulate much more closely those produced by megaton explosions.

Procedures are being developed to enable state and regional civil defense officials to estimate the number of casualties from fallout from a nuclear attack, without requiring the use of computers.

An evaluation of requirements for federally supplied dosimeters and radiation survey meters is being made, based on estimates of the usage of public shelters and home basements in the event of nuclear war.

The design of the Clinch River Breeder Reactor Plant is being examined to determine the probable effects of an intense electromagnetic pulse (EMP) environment. It has been found that the relatively high level of noise and electrical transient protection specified in the design will provide a high level of inherent hardness against an intense EMP environment. Thus, EMP is not considered a serious threat to the safety of the plant. However, as a precautionary measure, additional transient suppressors for some important battery power systems are recommended.

Through the Solar Energy Development Program, ORNL provides technical management assistance to the Solar Energy Division, Agricultural and Process Heat Program, of the Energy Research and Development Administration. During the current fiscal year, monitored programs included the application of solar energy to grain drying (e.g., corn and sorghum); tobacco, forage, and peanut drying; and food processing.

PART V. MEDICAL PHYSICS AND INTERNAL DOSIMETRY

Not submitted.

PART VI. ANALYTIC DOSIMETRY AND EDUCATION

The Analytic Dosimetry Group completed work on the *Guide to Radioactive Waste Management*, which contains an analysis of 1000 selected documents o

various aspects of the subject. Development of a file for health standards for energy production continued. A two-day workshop on dosimetry for radon and radon daughters was held in April and a number of experts from outside ORNL participated. The workshop concentrated on problems associated with the conversion of values measured in air-to-dose estimates and risk assessment. A state-of-the-art summary of the workshop findings is being prepared.

There were ten participants in the third Faculty Institute in Applied Health Physics held during the summer of 1976. The Institute continues to introduce and augment the teaching of health physics to undergraduate science and engineering majors at a number of universities.

Part I. Assessment and Technology

H. W. Dickson

1. Dosimetry for New Energy System Pollutants

R. B. Gammage
D. J. Christian D. J. Simpkin[1]
A. R. Hawthorne J. H. Thorngate
T. Vo-Dinh

Full characterization of polynuclear aromatic compounds (PNA) in coal conversion products is made with instruments that are sophisticated, time-consuming, and usually very expensive. The industrial hygienist uses two "rough-and-ready" techniques to provide a measure of occupational monitoring – irradiation with uv light and the determination of coal tar pitch volatiles. These two techniques are neither selective, sensitive, nor very accurate. Our aim is to provide monitoring instruments suitable for use by the industrial hygienist which will bridge this gap (Table 1.1). The compounds to be monitored cover the full range of aromatic compounds from the simplest molecules, such as benzene and phenol which have established Occupational Safety and Health Administration (OSHA) limits, to the multiringed, high-boiling PNA compounds. Of special interest are compounds that are carcinogens, tumorogens, cocarcinogens, initiators, and promoters. We monitor vapors, airborne particulates, and contaminated surfaces. The data garnered will be in forms suitable for subsequent health studies.

In the last year, the number of people working on this project increased from one to four. There is now the expertise in analytical procedures, spectroscopy, electronics, and microprocessing to lay the foundation for a successful multifaceted program for improved monitoring of synfuel emissions in the work place.

ASSESSMENT, EDUCATION, AND COORDINATION

Assessment and clarification of monitoring needs and of the nature and degree of hazards posed by various forms of synfuel pollution is ongoing; this is a need likely to remain for several years. To illuminate these problems and find directions for further action, we organized a workshop in conjunction with the Health Division on "Exposure to Polynuclear Aromatic Hydrocarbons in Coal Conversion Processes: I. Medical Surveillance, II. Industrial Experiences, Personnel Protection, and Monitoring."

There were 140 participants, representing government [e.g., Energy Research and Development Administration (ERDA), Environmental Protection Agency (EPA), National Aeronautics and Space Administration (NASA), National Institute of Occupational Safety and Health (NIOSH), and Environmental Canada], energy conglomerates (e.g., Exxon, Standard Oil, Gulf Oil, Union Carbide, and U.S. Steel), national laboratories and energy centers, nine universities, and instrument companies such as Barringer Research (Toronto), Wilks Scientific, MDA Scientific, and Lear Siegler. Medical surveillance and instrumental aspects were well-aired, but there was a sparsity of information from pilot-plant operators on their industrial hygiene practices. One notable exception was provided by speakers from Gulf Science and Technology (solvent refined coal). It seems most desirable to improve the level of interaction among plant operators, medical personnel, and the developers of new monitoring devices to minimize the

1. ORAU summer trainee student from the University of Wisconsin at River Falls.

Table 1.1. Techniques and instruments for PNA monitoring by the industrial hygienist

Crude PNA monitoring methods available

1. Benzene solubles within particulate matter (otherwise known as coal tar pitch volatiles)
2. Gross fluorescent emission resulting from uv irradiation of the skin, clothing, or inanimate objects

Highly sensitive and selective research tools for PNA characterization

1. Gas chromatography (or high-pressure liquid chromatography) – mass spectroscopy
2. Matrix isolation, Fourier transform – infrared
3. Chemical separation and gas-liquid chromatography profiling
4. X-ray-excited optical luminescence

Current needs for pilot-plant monitoring to bridge the gap

Techniques and instruments that are:

1. Selective for specific compounds or groups of compounds
2. Sensitive at OSHA concentration limits
3. Real-time or near real-time in producing analytical data
4. Easy to operate using microprocessors
5. Portable or semiportable for personnel monitoring or leak detection
6. Reasonably priced

deleterious effects on workers in the fledgling coal conversion industry.

A portable mass spectrometer will be delivered to us by Analog Technologies of Pasadena, California. Evaluation of this type of instrument and the associated monitoring technique has necessitated visits to the Aberdeen Proving Grounds, Maryland; Langley Research Center, Virginia; Hewlett-Packard and Varian Associates, Palo Alto; and Analog Technologies in Pasadena. A visit was also made to the headquarters of the United Kingdom National Coal Board and the Coal Working Group of the International Energy Agency, both in London, where contacts were established with groups and individuals responsible for worker protection and health. Another important activity involves working with the Life Science Coordinating Committee at the Oak Ridge National Laboratory (ORNL) in promoting interdivisional projects and helping ERDA in overall program planning and the establishment of priorities.

As an aid to the correct assessment of plant safety and chemical monitoring needs, a series of in-house lectures was initiated. Subjects have included basic aspects of coal gasification and liquefaction, processes of cancer initiation, cocarcinogenesis, inhibition, promotion, latency and synergistic effects, luminescence spectroscopy applied to the detection of aromatic carcinogens, and second-derivative techniques in spectroscopy.

INSTRUMENTAL TECHNIQUES UNDER DEVELOPMENT

The analytical techniques described in this section are being studied in terms of their future potential in providing reasonably priced instruments that can measure PNA compounds in real-time, or near real-time, and which are in a form that can be handled by the semiskilled technician or industrial hygienist.

Second-Derivative UV-Absorption Spectrometry

A Lear Siegler SM400 derivative spectrometer (Fig. 1.1) was obtained for assessment and modification. It is a wavelength-modulated, second-derivative uv-absorption spectrometer equipped with a 1-m multipass (up to 32 m path length) sample cell for monitoring vapor-phase pollutants. Primarily sold as a monitor for SO_2 and NO_x, this device holds considerable promise for analysis of the more volatile PNA compounds. It also has the capability for analyzing liquid samples using a 1-cm quartz cell. Initial measurements indicated the desirability of recording and analyzing the spectral data using digital techniques instead of analog signals and a chart recorder. By using digital data storage, the useful dynamic range of a single scan was increased so that both intense and weak peaks would be meaningfully obtained in the same measurement. Data storage also allowed repeated scanning to provide spectrum averaging, which improved the signal-to-noise ratio (S/N) and, in addition, permitted the use of digital data analysis, such as least-squares fitting.[2]

Several instrument modifications were made to improve the sensitivity and reproducibility of the spectrometer.[3] To provide a precise indication of wavelength, a ten-turn potentiometer was coupled to the drive shaft of the monochromator and used as a voltage divider in conjunction with a regulated power supply and a digital voltmeter. This arrangement also improved the reproducibility of monochromator settings. Repro-

2. A. R. Hawthorne and J. H. Thorngate, "Improved Analysis from Second-Derivative Spectrometry," submitted to *Applied Optics.*

3. A. R. Hawthorne and J. H. Thorngate, "Application of Second-Derivative UV-Absorption Spectrometry to PNA Analysis," submitted to *Environmental Science and Technology.*

Fig. 1.1. Measurement of aromatic vapors with the Lear Siegler SM400 derivative spectrometer at the ORNL coal hydrocarbonization unit.

ducible starting points for spectrum scans are important when multiple sweeps of a spectral region are used to integrate the data and improve the S/N. Data were digitized by coupling the analog output of the spectrometer to a voltage-to-frequency converter (V/F) and counting the output of the V/F for fixed time intervals. This also decreased noise by integrating the signals. The digitized signals were recorded on a multichannel analyzer (MCA) operating as a multichannel scaler. Dynamic and wavelength ranges were controlled by choice of the dwell time. Data from the MCA were recorded on a teletype which also provided a punched paper tape for data storage and for input to a time-sharing computer.

A typical calibration curve obtained using the multipass sample cell to measure vapor-phase naphthalene is shown in Fig. 1.2. The desired concentration was generated by using a pump-driven syringe filled with a known concentration of naphthalene in cyclohexane and injecting it at a known rate. The naphthalene was vaporized and diluted to the desired concentration in air by flowing heated air over the end of the syringe.

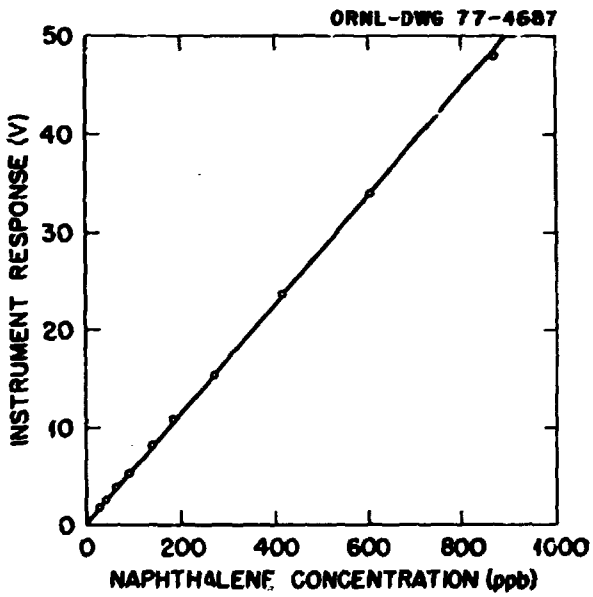

Fig. 1.2. Analytical curve for naphthalene vapor.

As an example of the capabilities of least-squares data analysis using digital spectra, a mixture nominally containing 25 ng/ml of each of the PNA compounds whose spectra are shown in Fig. 1.3 was analyzed using the quartz-cell mode of operation with spectrograde cyclohexane as the solvent. The least-squares fit to the measured spectrum of the mixture is plotted in Fig. 1.4, and the analytical results of the data analysis program are given in Table 1.2. The second-derivative spectrometer shows promise of providing analysis at the low levels of PNA compounds which will be encountered in an occupational monitoring program. Figure 1.5 gives an

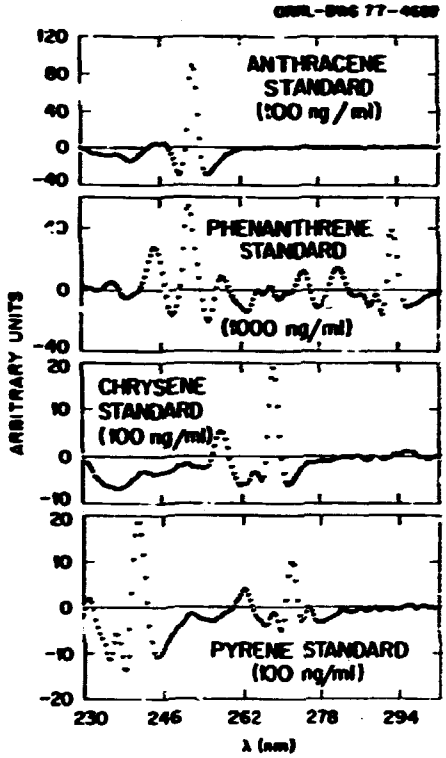

Fig. 1.3. Calibration standards for four PNAs in cyclohexane.

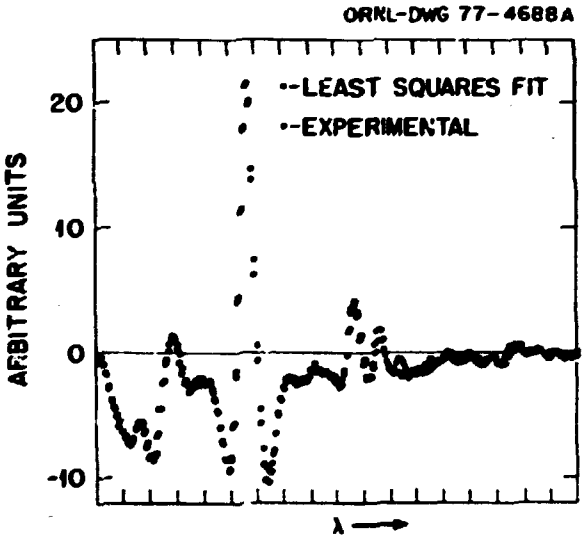

Fig. 1.4. Comparison of least-squares spectral fit to experimental spectrum.

example of the sensitivity for anthracene at 1 ng/ml concentration in cyclohexane. Note that the S/N is still good at this low concentration.

A method was developed to improve the linear response of the spectrometer at high concentrations.[2]

Table 1.2. Least-squares analysis of a mixture of four PNAs

Compound	Nominal concentration (ng/ml)	Least-squares analysis (ng/ml)
Anthracene	25	25.4 ± 0.2
Chrysene	25	25.0 ± 0.7
Phenanthrene	25	18.9 ± 2.6
Pyrene	25	28.2 ± 0.6

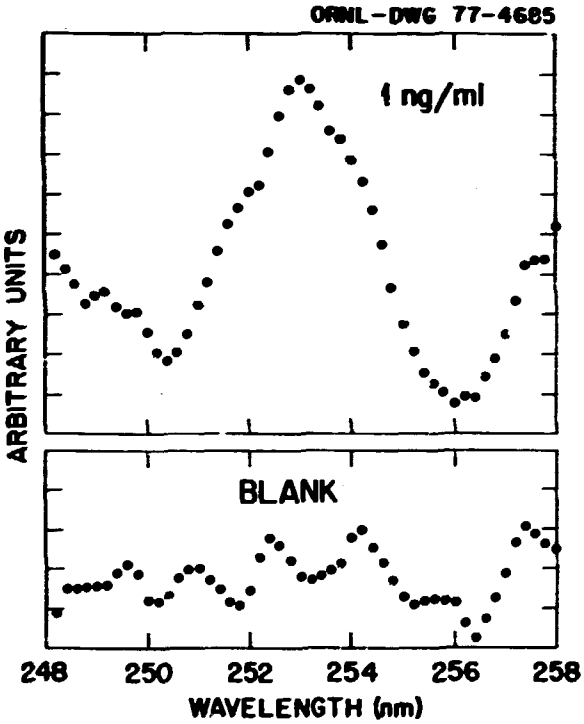

Fig. 1.5. Second-derivative spectrum of anthracene in cyclohexane using a 1-cm cuvette.

This improvement is particularly important for least-squares fitting of the data since that method requires linearity of the response at all wavelengths. Figure 1.6 illustrates the nonlinearity of the the second-derivative response as a function of concentration, $bc\mu_0$, where b is the path length through the sample, c is the concentration, and μ_0 is the absorption coefficient at the peak centroid. Properly combining the first- and second-derivative responses improves the linearity so that the assumption of linearity is satisfied even at high concentrations.

Future modifications of the spectrometer include incorporation of a stepping motor to provide accurate and reproducible positioning of the monochromator under digital control. Plans call for the coupling of a

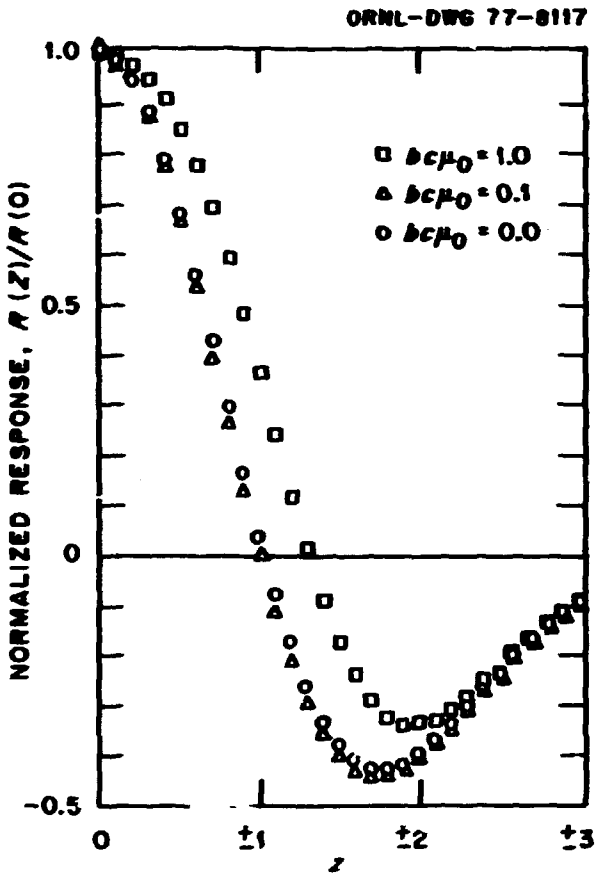

Fig. 1.6. Plot showing the variation in second-derivative peak shape as a function of z [$z = (\lambda - \lambda_0)/\sigma$] for various values of $bc\mu_0$.

minicomputer to the spectrometer to provide both instrument control and data storage and analysis. A portable, microprocessor-based, prototype instrument will be built for field testing in pilot-plant environs.

Room-Temperature Phosphorimetry

Work has begun on the research and development of a new technique of trace analysis based on room-temperature phosphorimetry (RTP) of PNA hydrocarbons (homocyclic and heterocyclic) adsorbed on various surfaces such as asbestos, silica gel, and filter paper. The RTP method (Fig. 1.7) does not require the expensive cryogenic equipment and complex low-temperature technology necessary in conventional luminescent analysis of PNA. Our initial results and our recent progress have been reviewed.[4] Experimental work is being conducted to investigate and extend the use of the external heavy-atom effect. By using heavy-atom solvent perturbers, the phosphorescence quantum yield of nonphosphorescent and weakly phosphorescent

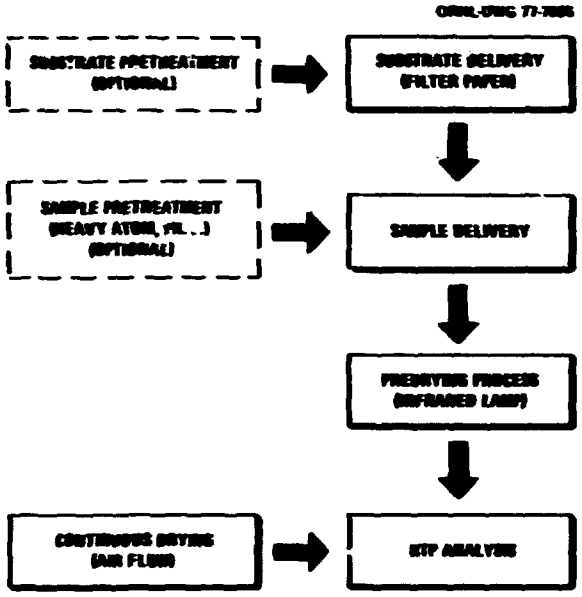

Fig. 1.7. Schematic of the various steps in RTP assay.

compounds can be significantly enhanced. In addition to the commonly used sodium iodide and silver nitrate, other types of heavy atoms have been investigated for the study of a variety of PNAs, such as pyrene phenanthrene, chrysene, fluoranthene, and carbazole (Table 1.3). Adsorption of PNA compounds was achieved by spotting the surface of filter-paper supports with 3-μl sample solutions and allowing the solvent to evaporate under infrared lamps. A new design of the sample holders improved the reproducibility of the measurements and decreased analysis time without affecting sensitivity. The detection limit of many PNAs is in the nanogram or subnanogram range (1.3 ng for chrysene, 60 pg for phenanthrene[5]). Heavy-atom effects using various perturbers which have different interactions with specific types of compounds could be applicable in the analysis of multicomponent mixtures. As the effect of inorganic probes and other perturbers becomes better understood, it should be possible to introduce a metal ion to quench the phosphorescence of one species and another metal ion to enhance the phosphorescence of a second species, thereby picking a specific compound or group of compounds in a mixture for selective phosphorescence emission. The additional technique of selective

4. T. Vo-Dinh and J. D. Winefordner, "Room Temperature Phosphorimetry as a New Spectrochemical Method of Analysis," submitted to *Applied Spectroscopy Review*.

5. T. Vo-Dinh, 2nd ORNL Workshop on Polynuclear Aromatic Hydrocarbons in Coal Conversion Processes, Oak Ridge, Tenn., Mar. 10–11, 1977.

Table 1.3. Limit of detection (L.O.D.) of some PNAs by room-temperature-phosphorescence (RTP)

PNA	$\lambda_{excitation}$ (nm)	$\lambda_{emission}$ (nm)	L.O.D. (ng)	Solvent perturber
Chrysene	305	515	1.3	$AgNO_3$ (0.05 *M*)[a]
Pyrene	330	600	1.3	$AgNO_3$ (0.05 *M*)
Phenanthrene	345	510	0.9	$AgNO_3$ (0.05 *M*)
			31	No heavy atom
			0.06	$AgNO_3$ (0.05 *M*)[a]
Carbazole	323	635	0.7	NaOH:NaI (1 *M*)

[a]With the use of a phosphoroscopic rotating-mirror device.

excitation is being used for multicomponent mixtures, again to enhance compound selectivity. Experiments were performed with different adsorbents, including simple, commercially available filter paper (Whatman, Schleicher and Schuell, etc.), to obtain intense phosphorescence from carcinogenic PNAs found in oils and tars.

In personnel or area sampling procedures, very large numbers of samples may have to be analyzed daily on a routine basis. Such a need has encouraged the development of automated instrumentation for analytical data accumulation. An initial instrumental version for automated RTP, which uses a novel rotating-mirror device to perform the phosphoroscopic time-resolved operation (Fig. 1.8), has been developed.[5,6] The rotating mirror produces a series of periodic, exciting light pulses on the sample paper tape and "optically gates" the detection for a short period at a specific delay after the exciting pulse. Figure 1.9 shows a typical phosphorimetric signal of chrysene obtained with this device. The RTP technique is characterized by simplicity and versatility of sample analysis. The use of filter paper as direct sample support offers an extremely large choice in the types of

6. T. Vo-Dinh, G. Walden, and J. D. Winefordner, "A Simple Instrument for the Facilitation of Room Temperature Phosphorimetry Using a Continuous Filter-Paper Device," submitted to *Analytical Chemistry*.

ORNL-DWG 77-3399

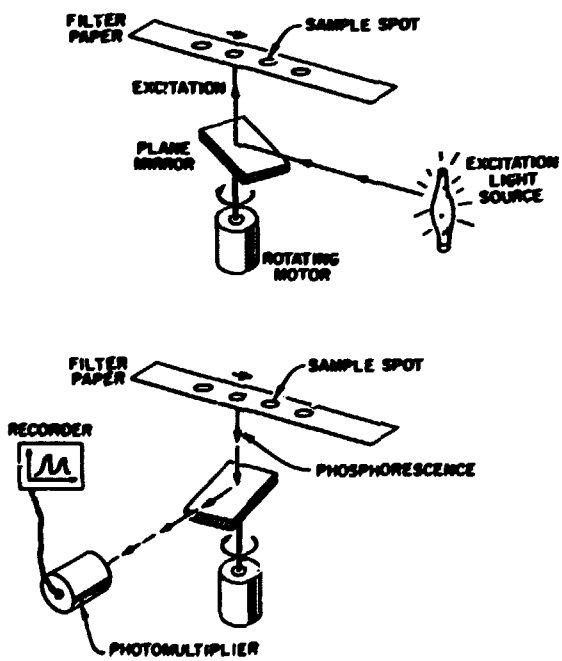

Fig. 1.8. Principle of phosphoroscopic operation for automated RTP.

ORNL-DWG 77-3397

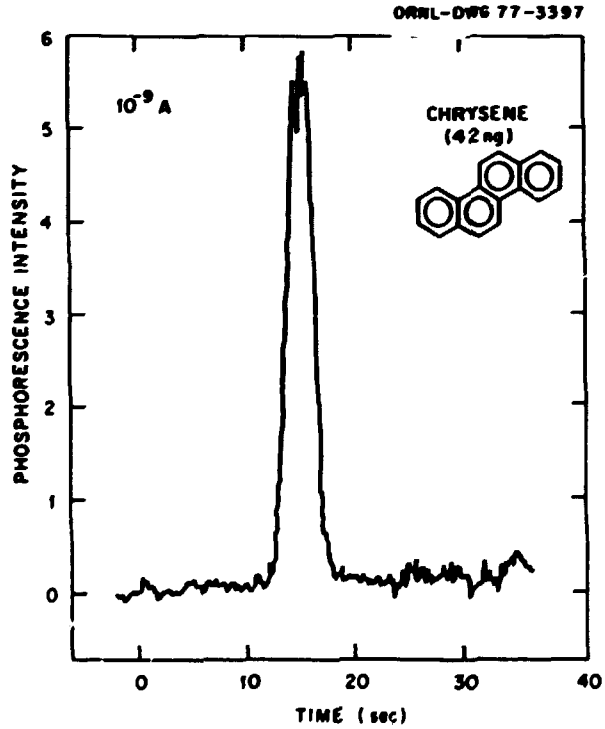

Fig. 1.9. Phosphorimetric peak of chrysene on filter paper.

sample that can be monitored. These include liquid and gas samples collected on filter membranes, as well as swipe samples from contaminated surfaces such as clothing and skin. In such cases, RTP would provide a sensitive analytical method to detect hazardous compounds which are difficult to determine via conventional spectrochemical methods without considerable expense and time delay. In the near future, an effort will be made to develop RTP for greater selectivity in synfuel pollution monitoring by time- and phase-resolved, dual-wavelength scanning and second-derivative spectroscopic techniques.

Separation by Differential Sublimation

Differential sublimation can separate and purify complex mixtures of organic materials. This capability was shown when it was used to purify parasexiphenyl for use as a scintillator.[7] A closely related technique was used elsewhere to separate PNAs for subsequent analysis by fluorescence spectroscopy.[8] A system has been built (Fig. 1.10) to investigate the applicability of this technique to the rapid evaluation of samples taken at coal conversion facilities.

The sample is placed in a furnace in which hot gas flows over and vaporizes it. The apparatus has been designed for maximum flexibility and consists of heaters for the carrier gas and the sample and a furnace designed to provide a linear temperature gradient along the length of a 1-cm-ID quartz tube. The temperatures of the carrier gas, the sample, and the inlet and outlet temperatures of the gradient furnace can all be adjusted independently. Recrystallization occurs in the quartz tube. Using quartz will simplify subsequent analysis of the separated samples by uv absorption spectroscopy. To prevent damage from excessive pressures, an aspirator pumps the carrier gas through the system and disposes of unwanted materials which recrystallize at temperatures below that at which the furnace is set.

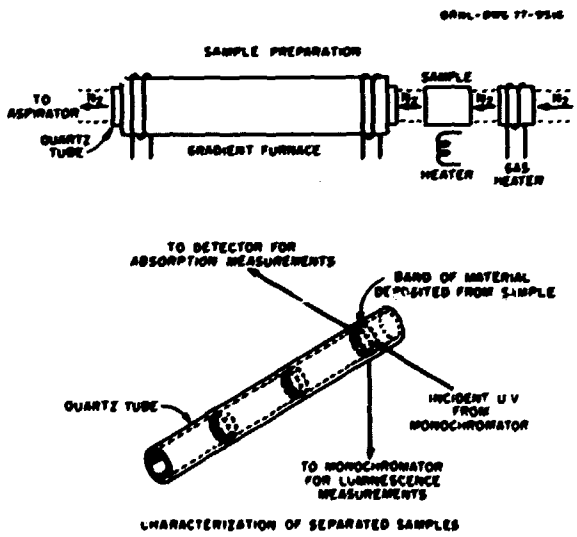

Fig. 1.10. Diagram of differential sublimation apparatus.

It is hoped that this procedure will provide rapid and simple separation of complex samples so that the selectivity required in subsequent analysis by uv absorption or luminescence emission can be decreased. It may also be possible to use an apparatus of this type for continuous air monitoring in work areas. Additional instrumentation could provide for continuous monitoring of several substances in real-time. The apparatus can also purify laboratory samples of the important PNAs to provide better standards for other detection and measurement techniques.

Thermoluminescence Analysis

Many substances emit light by radiothermoluminescence (RTL) if they are exposed to ionizing radiation and then warmed. Most studies of this phenomenon involve inorganic materials, although organic materials also exhibit RTL. In fact, amino acids and enzymes were studied previously by members of this division.[9,10] RTL was observed recently in PNA compounds,[11] which prompted the inclusion of RTL as one of the methods to be investigated for possible use in health protection measurements of the fugitive emissions of coal conversion processes.

The use of RTL as an analytical tool for PNAs differs from its more conventional use in radiation dosimetry: Samples must be exposed to high doses of radiation and the irradiations generally must be made at 80°K, or below. These requirements preclude the use of existing dosimeter readout systems. A new apparatus has been built (Fig. 1.11) for measuring RTL in PNAs, in which a small sample is put into a vacuum chamber and cooled to about 80°K. After cooling, the sample is irradiated with low-energy electrons (<1 keV). Without removing the sample from the chamber, the electron source is replaced with a photomultiplier tube and, as the sample

7. P. T. Perdue and F. T. Arakawa, *Nucl. Instrum. Methods* 128, 201 (1975).

8. J. L. Monkman, L. Dubois, and C. J. Baker, *Pure Appl. Chem.* 24, 731 (1970).

9. J. G. Carter, D. R. Nelson, and L. G. Augenstein, *Arch. Biochem. Biophys.* 111, 270 (1965).

10. D. R. Nelson et al., *Radiat. Res.* 32, 723 (1967).

11. A. P. D'Silva, G. J. Oestreich, and V. A. Fassel, *Anal. Chem.* 48, 915 (1976).

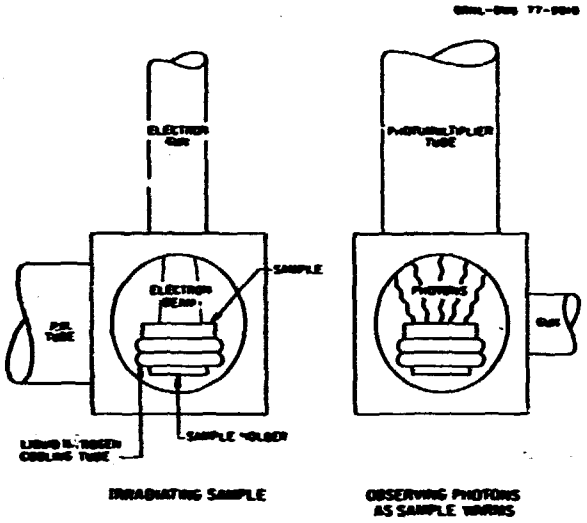

Fig. 1.11. Schematic of operation of radiothermoluminescence unit.

warms to room temperature, the RTL is measured. More detail and possibly greater selectivity could be obtained by measuring the spectrum of the emitted light. There is evidence that the more biologically active PNAs have the largest RTL responses, which would add to the attractiveness of this new analytical method for PNA. The technique also could be valuable for rapid screening of samples from gross measurement of the RTL.

Portable Mass Spectrometer

An informal committee consisting of representatives from three ERDA laboratories [Los Alamos Scientific Laboratory (LASL), Lawrence Livermore Laboratory (LLL), and ORNL] advised the Division of Biomedical and Environmental Research (DBER) to participate in the development of a portable, quadrupole mass spectrometer. ERDA has joined in an interagency agreement with NASA, EPA, Air Force, and Army to provide funds for the research and development. Three of the first units manufactured will be received by ERDA for evaluation by LASL, LLL, and ORNL. Delivery is expected in the late summer of 1977.

The instrument is a computer-based spectrometer with a 2-in. quadrupole mass analyzer with a mass range of 2 to 200 amu. The mass range for the unit to be used in the dosimetry and monitoring program for new energy source pollutants in the Health and Safety Research Division at ORNL is to be extended to a limit of 400 amu to assess the applicability of the instrument to monitoring high-molecular-weight PNA vapors. Also envisioned is the adaptation of a membrane inlet to the spectrometer, which will provide some preconcentration of organic vapors relative to the present gold-foil, molecular leak inlet.

INSTRUMENT TESTING IN PILOT-PLANT ENVIRONS

As part of the dosimetry and monitoring program, we are trying to test and evaluate the performance of possible monitoring instruments in field situations that are as realistic as possible. A bench-scale hydrocarbonization unit, which is operating at ORNL Building 2528, provided us with the means to make such tests. The program was started this year, and only two instruments have been subjected to preliminary field tests. The Lear Siegler SM400 derivative spectrometer was tested, before modifications were made and analytical curves determined, to see if any vapor-phase PNAs could be detected (Fig. 1.1). Compounds that have high vapor pressure, such as naphthalene and phenol, were qualitatively detected, although their concentrations were low relative to the OSHA threshold limit value (TLV) for these materials. A return trip to the hydrocarbonization unit is planned when modifications to the second-derivative spectrometer are completed and quantitative measurements can be made. Also tested at the facility was a Miran IA infrared gas analyzer. Although the sensitivity to PNAs was not sufficient for our purposes, the instrument did detect several low-molecular-weight, aromatic compounds, such as benzene and phenol, for which TLVs are established. Absorption peaks were found at 8.4 μm (phenol) and 3.3 μm (benzene plus other interferences). As other instruments are obtained and further modifications made to improve sensitivity and selectivity for PNA compounds, we will evaluate their performance in as realistic as possible field environs.

2. Radiation Detection and Monitoring Principles

R. B. Gammage
J. Ashraf[1] T. F. Gesell[4]
J. S. Cheka[2] G. de Planque[5]
S. J. Cotter[3] J. H. Thorngate
D. J. Christian

Decreases in personnel and funding have necessitated a reduction in the number of projects under active investigation. Fast-neutron dosimetry is recognized as the major unresolved problem in personnel monitoring. Efforts to improve the situation are being made the keystone of our activities. Additionally, several projects involving exoelectron dosimeters have been finished, or scaled down. In keeping with this section's tradition of conducting dosimetry intercomparisons and standardizations, we are involved in the organization and performance of a series of environmental dosimetry intercomparisons at the international level, as well as an international study of calibrated beryllium oxide (BeO) ceramic dosimeters having a common history.

DOSIMETRY INTERCOMPARISON STUDIES

Third International Intercomparison of Environmental Dosimeters (IIED) Under Field and Laboratory Conditions

The first and second IIED were conducted in low-level, natural-background radiation fields which were spatially isotropic. Most environmental measurements of integrated radiation exposure are concerned with perturbations of the natural radiation environment, such as that caused by radiation leakage from a nuclear facility. To simulate radioisotope spillage, the IIED is conducting its third intercomparison study within the ORNL preserve during July and August 1977. The radiation field to be used is strongly anisotropic and is dominated by radiation from ground-level simulated ^{137}Cs fallout. A trial test was undertaken to ensure the uniformity of the exposure rate along a section of the enclosure fence (Fig. 2.1) from which the dosimeters will be hung. Dosimeters were mailed from Texas and New York for this trial to ensure the occurrence of minimum transit exposures and to check the suitability of a low-background storage shield for the laboratory and control dosimeters. All aspects of this trial produced satisfactory results. The series of IIED are organized jointly by ourselves, the School of Public Health of the University of Texas, and the ERDA Health and Safety Laboratory, New York.

Bank of Calibrated BeO Ceramic Exoelectron-Thermoluminescence Dosimeters with a Common History

An international study of similar exoelectron dosimeters of BeO ceramic (Thermalox 995), which were prepared and calibrated at ORNL and then distributed to groups in 17 countries, is producing results.[6] There is an interlaboratory comparison of readers and a growing awareness of the conditions under which the detectors can be relied on to behave in a reproducible fashion. Those groups with the most sensitive readers are able to measure exposures of the order of 10 μR, which compares with a value of 200 μR in the ORNL gas-flow Geiger counter. Special emphasis is being placed on stability of response under worldwide conditions of laboratory storage. Several investigators have under-

1. Graduate student at The University of Tennessee, on leave from the University of Baluchistan, Quetta, Pakistan.
2. Consultant.
3. Graduate student from Purdue University, Lafayette, Ind.
4. School of Public Health, University of Texas, Houston.
5. ERDA Health and Safety Laboratory, New York, N.Y.
6. R. B. Gammage, "Collaborative Studies with Standardized BeO Ceramic Dosimeters Having a Common History," *Health Physics* (in press).

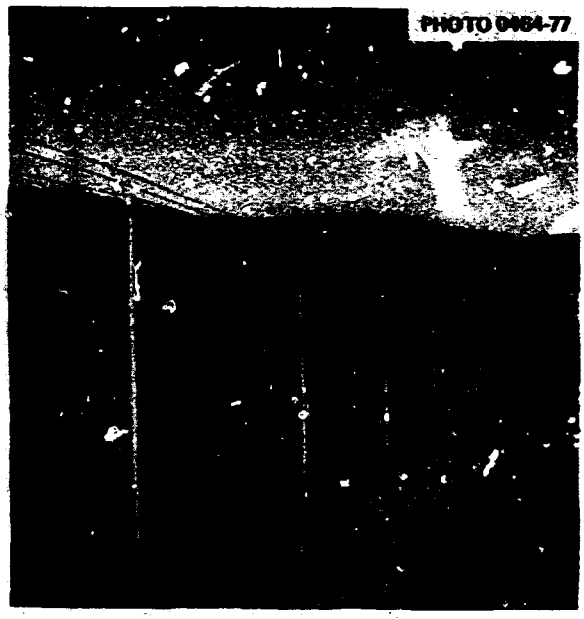

Fig. 2.1. Field site of the Third International Intercomparison of Environmental Dosimeters.

taken long-term testing of this parameter at a standard exposure of 20 mR. Not only will the results better define the stability characteristics of this particular type of exoelectron-thermoluminescence dosimeter, but they will permit a more standardized evaluation of new types of exoelectron phosphor by means of cross calibration.

FAST-NEUTRON PERSONNEL MONITORING

Using the technique of electrochemical enhancement of neutron-induced recoil tracks, four plastics were evaluated as potential fast-neutron dosimetry materials: cellulose acetate (CA), cellulose triacetate (CAT), cellulose acetobutyrate (CAB), and polycarbonate. Polycarbonate was selected by several groups (e.g., Landauer Company, Georgia Institute of Technology, and Lawrence Livermore Laboratory) for more extensive characterization. The threshold energy for neutron-induced track registration is about 1 MeV for this material. Our intention is to study more easily damaged and etched polymers (those having lower volume resistivity and dielectric and tensile strengths) in the hope of effecting a reduction in the threshold energy to below 1 MeV.

For the standardized etching parameters of 1000 V (rms), 1000 Hz, 30 wt % KOH, 4 hr, and 25°C, the following observations were made. Clouding of the surface and development of a spongy texture rendered the CA and CAT polymers unsuitable. A high degree of water absorptivity (2% to 7%) is responsible for the phenomenon that leads to loss of the track identity. Lowering of the voltage and frequency (500 V, 500 Hz) brings about an improvement in contrast between the tracks and the background (less clouding). The CAB plastic, which has the lowest dielectric and tensile strengths of the four, develops fully penetrating cracks which cause shorting of the electrochemical cells containing the KOH. Reduction of the frequency (to 400 Hz) prevents cracking. Fogging by uptake of water is not serious enough to interfere with the visibility of the tracks. Polycarbonate has the highest volume resistivity and dielectric and tensile strengths and the lowest water absorptivity of the four plastics. It produces the most highly contrasted electrochemical etch tracks which can be distinguished from background artifacts, and it does not suffer from stress cracking. It is clearly the best of the four plastics for the general purpose of fast-neutron personnel dosimetry. Nevertheless, polymers such as CA and CAB are known to be chemically more sensitive than polycarbonate for recording damage tracks. By selecting optimum voltages, frequencies, and etching times to avoid the problems of clouding and cracking, one may still provide a sensitive electrochemical track etch detector having a neutron energy threshold of only a few tenths of a mega-electron volt.

In each of the four plastics, the electrochemically etched tracks have roughly the form of an internal cavity with a small entrance hole at a partially collapsed surface. The scanning electron micrographs in Fig. 2.2 reveal the surface structure; the optical micrographs of Fig. 2.3 reveal the larger below-the-surface cavities which are seen visually. At the particular voltage and frequency used for these etchings (1000 V and 1000 Hz), a superior track shape and degree of contrast for the purpose of track counting are evidenced for the Lexan polycarbonate. As yet no mechanism has been advanced to explain satisfactorily the modes of electrochemical etching that lead to these particular structural forms.

Background track density in unirradiated polycarbonate is a particularly important parameter, especially in the measurement of small doses (a few tens of millirads) of fast neutrons. In attempts to reduce the track density by annealing at temperatures between 100° and 140°C (Fig. 2.4), either there is no change in background track density (100°C), or else one obtains the undesirable result of an increase in the number of tracks (120° and 140°C). One presently has to be satisfied with using polycarbonate for fast-neutron dosimetry in the "as-received" state.

Two polycarbonates (Lexan and Transilwrap, thickness 250 μm) were evaluated as neutron dosimeters in

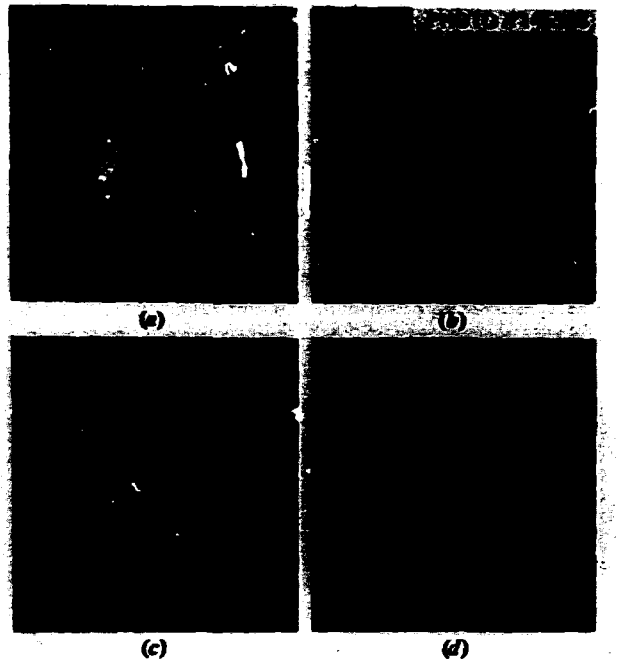

Fig. 2.2. Scanning-electron micrographs of fast-neutron-induced recoil particle tracks etched electrochemically for 4 hr in 30% KOH. (*a*) In cellulose triacetate, 500 V and 500 Hz (1000×); (*b*) in Transilwrap polycarbonate, 1000 V and 1000 Hz (300×); (*c*) in cellulose acetobutyrate, 500 V and 500 Hz (1000×); and (*d*) in cellulose acetate, 1000 V and 1000 Hz (1000×).

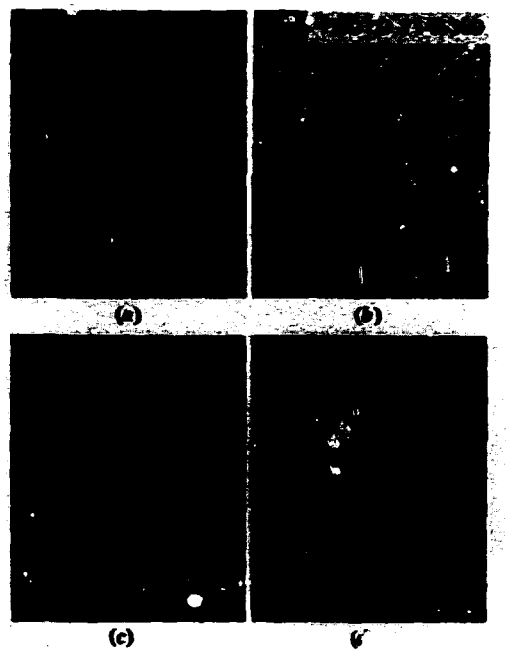

Fig. 2.3. Optical micrographs of fast-neutron-induced recoil particle tracks etched electrochemically for 4 hr in 30% KOH. (*a*) In 250-μm-thick cellulose triacetate, 500 V and 500 Hz (500×); (*b*) in 250-μm-thick Lexan polycarbonate, 1000 V and 1000 Hz (500×); (*c*) in 250-μm-thick cellulose acetobutyrate, 500 V and 500 Hz (500×); (*d*) in 762-μm-thick cellulose acetate, 1000 V and 1000 Hz (500×).

the three well-known standard neutron fields of the Health Physics Research Reactor (HPRR) at doses of 50 or 100 millirads. The background track densities in the as-received Lexan and Transilwrap are 78 ± 14 and 11 ± 2 tracks/cm^2 respectively. Results from the neutron exposures are tabulated in Table 2.1. The Lucite and steel shields, which lower the neutron energies, reduce the etch pit track density as anticipated. Any better quantification is impossible because of the large errors involved in attempting to measure these small doses. Future work will aim at establishing a commercial source of thin polycarbonate foil having a high and reproducible degree of quality control.

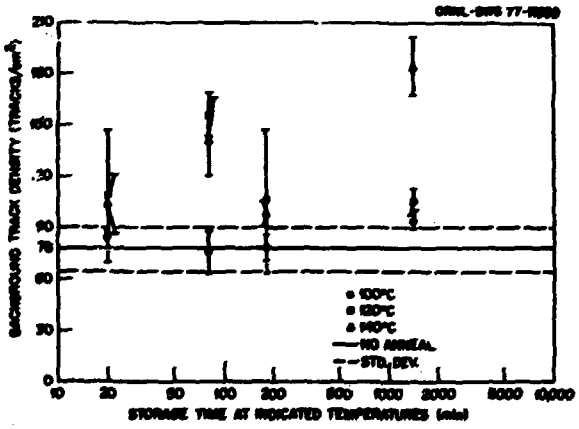

Fig. 2.4. Effect of annealing at different temperatures and times on the background track density of Lexan polycarbonate.

Table 2.1. Results of neutron exposure to polycarbonate foils

Polycarbonate (250 μm)	Background (tracks/cm^2)	Dose (millirads)	Quality factor			Recoil track density (tracks/cm^2)			Response (tracks cm^{-2} millirem^{-1})		
			Bare	Lucite	Steel	Bare	Lucite	Steel	Bare	Lucite	Steel
Lexan	78 ± 14	100	9.4	8.9	9.5	72 ± 37	34 ± 31	21 ±18	0.076	0.038	0.022
Transilwrap	11 ± 2	50	9.4	8.9	9.5	18 ± 8	9 ± 5	17 ±6	0.036[a]	0.022	0.032

[a]Value of 0.054 track cm^{-2} millirem^{-1} obtained for Transilwrap by R. S. Landauer Co.

DETECTION OF ALPHA PARTICLES AND LOW-LEVEL RADON MONITORING

In conventional etching, cellulose nitrate is the preferred plastic detector of alpha particles because of its high sensitivity. Cellulose acetobutyrate (CAB) has better stability against thermal fading and other environmental insults, but it is only 0.64 times as sensitive. To overcome this drawback, one can apply the technique of electrochemical etching to the amplification of alpha-induced etch tracks in CAB foils 360 μm thick. The intention is to produce an environmentally stable detector foil suitable for radon monitoring at activity levels close to natural background.

Alpha particles from ^{239}Pu, lowered in energy by passage through air, were used to evaluate the energy dependence of response for an angle of incidence normal to the surface. Under optimum electrochemical etching conditions (Table 2.2), the registration efficiency (number of visible etch pits per incident alpha particle) varies with energy in the manner shown in Fig. 2.5. At this magnification, an induction time of between 1 and 2 hr is required before the tracks can be visibly resolved in the microscope. (The exact time depends on the frequency used.) The appearance and size of the tracks as a function of etching time (Fig. 2.6) show a dramatic oxygen effect. If the irradiation is conducted in helium rather than air, the tracks remain immune to development.

In a hemispherical chamber for low-level radon gas measurements (Fig. 2.7), radon gas diffuses through the porous shell, and the radon daughter decay products are collected electrostatically on an aluminized Mylar foil lying over the alpha-particle detector. Holders for the detector can be either a CAB foil, a BeO disk, or a silicon diode (Fig. 2.7). The efficiency of collection of the radon daughters, as a function of the potential applied to a metal wire mesh supporting the porous foam shell, was measured between 0 and 5000 V (Fig. 2.8). To lower the energy of the alpha particles and

Table 2.2. Optimized electrochemical etching parameters for various alpha energies etched in 28 wt % KOH at room temperature

Incident alpha energy (MeV)	Applied voltage (V, rms)	Frequency (Hz)	Etching time (hr)	Optimum registration efficiency
0.25	1000	400	3	0.99
1.30	1000	400	3	1.00
2.15	1000	400	3	1.00
3.60	1000	400	3	0.93
4.10	1000	300	5	0.81

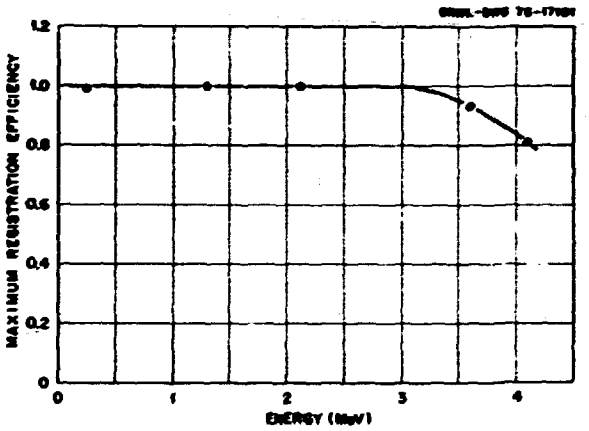

Fig. 2.5. Dependence of registration efficiency on the energy of alpha particles incident normal to the surface.

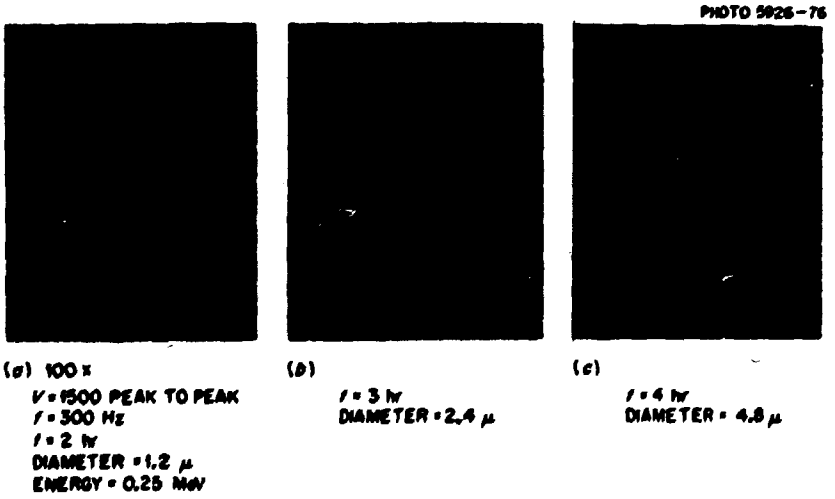

Fig. 2.6. Increase of track diameter with time of electrochemical etching; 1000 V, 300 Hz, 0.25-MeV alpha particles. 100×.

Fig. 2.7. Hemispherical radon monitoring chamber, 21-cm diam, showing holders for the alpha-particle detector which is either a silicon diode, an exoelectron-emitting BeO disk (12.5-cm diam and 1.5-mm thick), or a plastic foil of cellulose acetobutyrate of 2.0-cm² area.

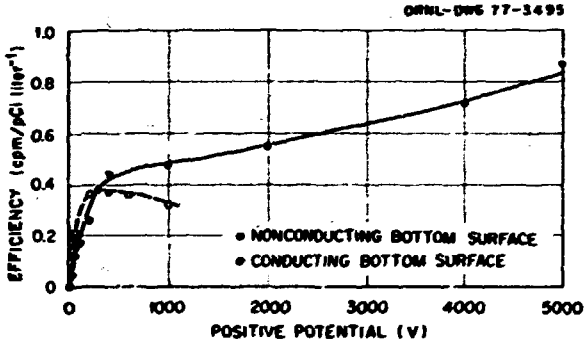

Fig. 2.8. Efficiency of the ORNL hemispherical radon monitor as a function of the positive voltage applied to the wire mesh screen.

obtain etchable tracks in the CAB, thin Mylar absorber foils were interposed between the radon daughter collector and the CAB foil. The sensitivity is maximized when the absorber thickness is ∿22 μm (Fig. 2.9). With this configuration and a collecting voltage of 400 V, one obtains 2 tracks/cm² for each hour's exposure at 1 pCi/liter. Field tests are planned in the near future after a fuller characterization of the exposure response and of the effects of changing humidity.

The BeO ceramic exoelectron dosimeter was also evaluated as a passive environmental radon monitor, using the hemispherical radon chamber.[7] The maximum number of exoelectrons results from the highest-energy alpha particles striking the BeO at near-glancing angles. In contrast, such alpha particles give rise to a minimum number of tracks in CAB. For highest exoelectron sensitivity one needs to place the BeO disk in direct contact with the radon daughter collector (aluminized Mylar foil) without any absorber foil. The net integral exoelectron counts obtained with such an arrangement vary with radon exposure time (Fig. 2.10). The back-

7. R. B. Gammage and T. F. Gesell, "A Passive Environmental Radon Monitor Based on the Exoelectron Dosimeter," submitted to *Nuclear Instrumentation and Methods*.

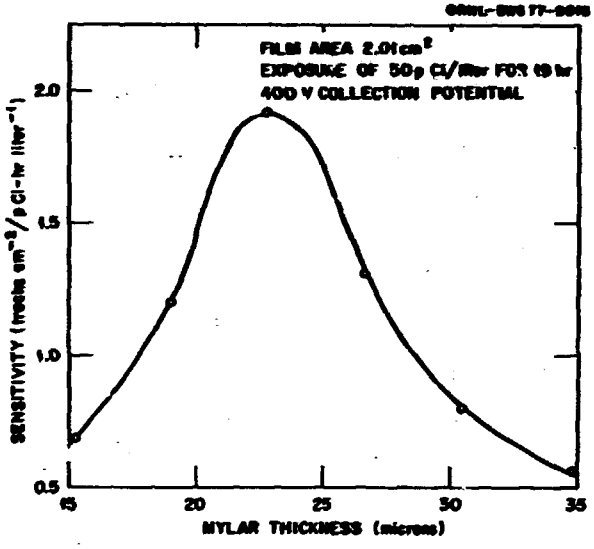

Fig. 2.9. Sensitivity of the passive ORNL radon monitor with cellulose acetobutyrate track etch detector as a function of the thickness of the Mylar absorber.

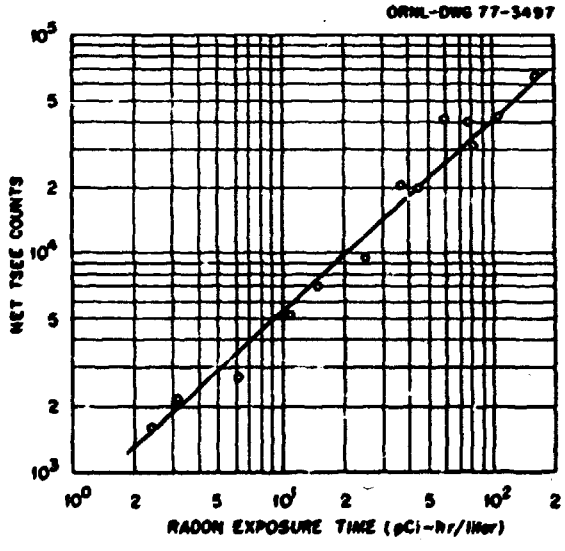

Fig. 2.10. Exoelectron response of thermally stimulated ceramic BeO exposed to radon in a hemispherical chamber at different concentrations and for different times with a collecting potential of +1200 V. The exoelectrons emitted from an unexposed detector number about 200.

ground exoelectron count is about 200; thus, a 10:1 signal-to-noise ratio is obtained for an exposure of 3 pCi-hr/liter. In addition to this satisfactorily high sensitivity, the BeO disk is maintained in a light-tight, dirt-free dosimetry package. These two factors favor maintenance of reliable exoelectron response characteristics. The anticipated use of the radon dosimeter inside dwellings, where excessively high humidities detrimental to exoelectron response are normally avoided, adds a further important attraction. This application of the exoelectron dosimeter is probably the best of the applications studied so far.

FURTHER DEVELOPMENT OF BeO CERAMIC TLD FOR LOW-LEVEL RADIATION MEASUREMENTS

Previous efforts to make thermoluminescent dosimeter (TLD) measurements with BeO ceramic below 20 mR have been marred by too high a background caused by faulty or inappropriate electronic components. Incorporation of state-of-the-art analog and digital integrated circuits into the thermoluminescence (TL) reader brought about a significant improvement. With the addition of an external high-voltage supply, along with a low-noise picoammeter, the noise level has been reduced from 20 to 2 mV peak-to-peak. The picoammeter also provides digital integration of the output from the photomultiplier tube with temperature gating of a thermocouple output. A Triac-controlled heater circuit, incorporating a Sola transformer, provides a constant temperature ramp for the heating.

Pyroelectric incandescence (PI), which is observed only while the temperature of the BeO is changing, is strong enough and close enough in temperature to the temperature of the radiation-induced peak that the TL peak is not completely resolved.[8] This interference limits the minimum detectable radiation exposure. One observes a trough in the glow curve between the TL peak and the continually increasing PI which follows. The peak-to-trough ratio increases between exposures of 0 and 1000 mR (Fig. 2.11). At the higher exposures the magnitude of the trough is controlled by the growth of a second high-temperature TL peak. One must maximize the peak-to-trough ratio to make the most accurate low-exposure measurements. Two techniques proved effective in doing this. The thickness of the uv filter has a pronounced effect, presumably because the radiation-induced TL and the PI have different spectral qualities. An increase in peak-to-trough ratio results from a doubling of the filter thickness in the 0 to 100 mR range of exposure (Fig. 2.12). The most noticeable improvement, however, comes about through better thermal contact between the BeO disk and the

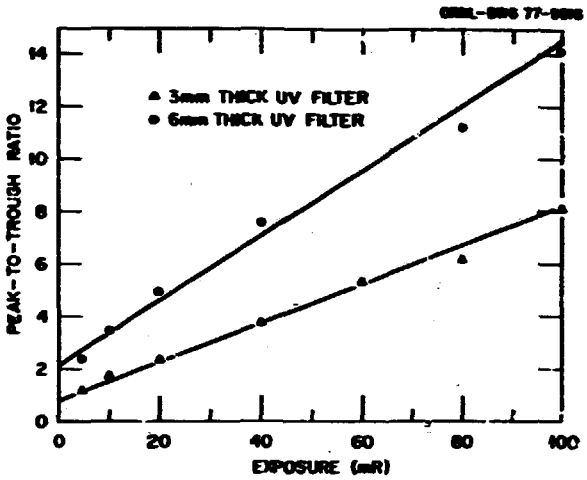

Fig. 2.11. Thermoluminescence peak-to-trough ratio at two different uv filter thicknesses and at low exposures.

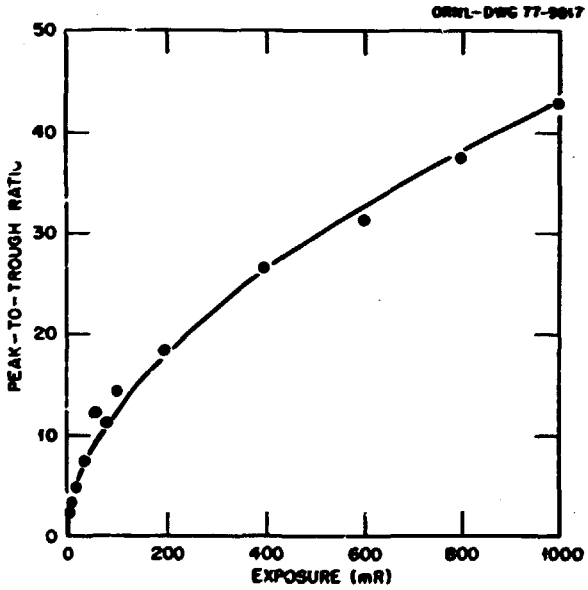

Fig. 2.12. Thermoluminescence peak-to-trough ratio between 1 and 100 mR at a uv filter thickness of 6 mm.

planchet-heater assembly (not shown in Figs. 2.11 and 2.12). The result is a narrower, well-resolved TL peak and a higher peak-to-trough ratio. A thin BeO disk (with high thermal conductivity) between the heater coil and the perfectly flat planchet achieves the desired result: At 20 mR exposure the peak-to-trough ratio has been increased from 5:1 to 18:1. Exposures of 20 and 1 mR can be read repetitively within standard deviations of 1.9% and 30% respectively.

8. R. B. Gammage and J. S. Cheka, "Further Characteristics Important in the Operation of Ceramic BeO TLD," *Health Physics* (in press).

3. Health Physics Research Reactor

H. W. Dickson
L. W. Gilley
D. J. Christian
W. F. Fox
C. P. Littleton[1]
L. B. Holland[2]
D. R. Ward[2]
M. U. Shaikh[3]
F. J. Slagle[4]

The Health Physics Research Reactor (HPRR) is a principal research tool for the Dosimetry Applications Research (DOSAR) Facility. The DOSAR Facility consists of the HPRR housed in the reactor building, the control building with its associated laboratories, and several small support buildings, all located about 3.3 km southeast of ORNL's main research area. The facility is located within a 914-m-radius exclusion fence and is accessible only through a guard post at which each person entering is given a numbered muster badge.

The reactor building is a low-scatter structure 23 m long, 9 m wide, and 15 m high. The reactor is supported in the building by a rather large positioning device mounted on a track that traverses the length of the building and extends 21 m along an exterior concrete pad. The reactor can be positioned remotely to within 0.01 m of any preselected point along the centerline of the track and to a height of up to 5 m.

The control building is located about 274 m from the reactor building behind a ridge which provides shielding for line-of-sight radiation. The roof, exterior walls, and some interior walls are constructed of poured concrete to provide shielding from scattered radiation. The building contains the reactor control room, various laboratories and offices, a counting room, and a fabrication shop.

The HPRR is a small, unshielded and unmoderated, fast reactor suitable for research in health physics, radiobiology, biomedicine, and related fields. The reactor core (Fig. 3.1) is a right circular cylinder (0.20 m diam, 0.23 m high) of enriched uranium (93.14 wt % ^{235}U) alloyed with 10% molybdenum.

The HPRR can be operated in a pulse or steady-state mode. The nominal maximum yield in the pulse mode is 10^{17} fissions, and the maximum power in the steady-state mode is 10 kW. The HPRR is capable of routinely producing neutron doses ranging from a few millirads to thousands of rads, depending on the power level, duration of the exposure, and the location of the experiment relative to the core. Figure 3.2 presents the tissue kerma in air per watt-minute vs distance from the center of the core. Table 3.1 shows the time the reactor can operate at various power levels without exceeding the 588°K operating limit.

To simulate spectra under various criticality accident conditions, Lucite and steel shields were fabricated several years ago for use in nuclear accident dosimetry (NAD) intercomparison studies. To provide additional spectra for these studies, two new spectrum-modifying shields were fabricated. These shields were designed to be placed 1 m from the center of the HPRR core to shield an arc of 135°. One shield consists of a 20-cm-thick concrete annular section 2.1 m high and weighing 3180 kg. The other shield consists of an inner annular section of steel, 5 cm thick, and an outer annular section of concrete, 15 cm thick, both 2.1 m high. The steel portion weighs 2333 kg; the concrete portion, 2475 kg. The shields (Figs. 3.3 and 3.4) are freestanding and can be moved readily into place using the 5-ton-capacity overhead crane in the reactor building.

The new spectrum-modifying shields are being evaluated with regard to the expected neutron spectra and radiation dose through the shields. A discrete ordinates transport (DOT) code used for previous shield evaluations[5] is being used in the ORNL Computer

1. Instrumentation and Controls Division.
2. Operations Division.
3. IAEA Fellow from Pakistan.
4. Graduate student, The University of Tennessee.
5. J. W. Poston, J. R. Knight, and G. E. Whiteside, *Health Phys.* 26, 217 (1974).

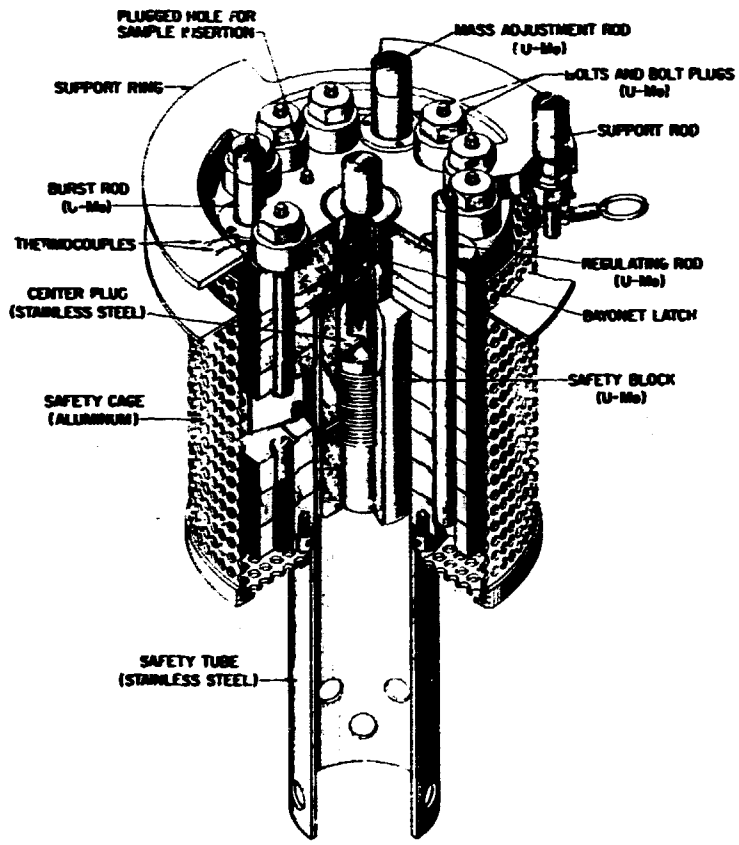

Fig. 3.1. The Health Physics Research Reactor core.

Sciences Division to calculate the neutron distributions transported through the new shields. In addition, both neutron and gamma radiation doses are being measured with the shields in place at the HPRR. Several techniques, including thermoluminescent dosimeters (TLDs), proportional counters, and track etch detectors, are being used to measure the neutron component of the dose. Thermoluminescent dosimeters, Geiger counters, and fluoroglass dosimeters are being used to measure the gamma component of the dose. Preliminary calculations for a pulse of 10^{17} fissions gave the neutron kerma values listed in Table 3.2 at a reactor and detector height of 1.5 m.

A report describing a high-density concrete shield which could be constructed for use around the HPRR core was prepared.[6] This shield would have substantially greater attenuation for both neutrons and gamma rays than the concrete shields recently fabricated. Should it be desirable to have yet another spectrum for intercomparison, the specifications and dose calculations for the high-density concrete shield have been completed.

The major programmatic contributions of the HPRR are in the areas of radiation dosimetry and radiobiological research. Radiation dosimetry research is accomplished primarily in the Health Physics Division; however, several other major ERDA contractors have recently conducted dosimetry research at the HPRR. The HPRR is the single most significant radiation source used in the solid-state dosimetry program. The reactor is also used to verify calculational models of dose to anthropomorphic phantoms and to organs within the phantoms.

6. M. U. Shaikh, H. W. Dickson, and Javaid Ashraf, *Dose Calculations Intercomparison Studies with a Heavy Concrete Shield Around the HPRR Core*, ORNL/TM-5562 (1977).

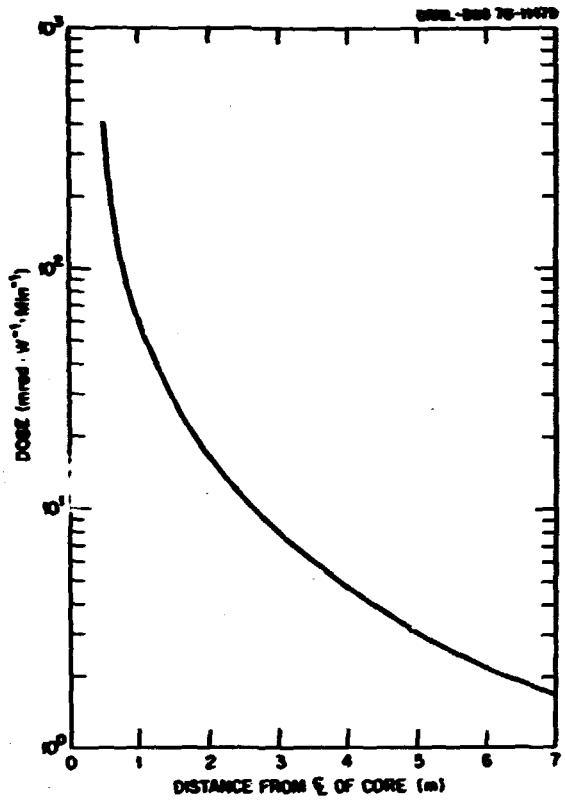

Fig. 3.2. Tissue kerma in air (dose) as a function of distance from the centerline of the HPRR core.

Radiobiological research at the HPRR is accomplished primarily through the Biology Division. The HPRR is used as the radiation source for significant new experiments for determining the relative biological effectiveness (RBE) of neutrons in mice for specific endpoints.

Table 3.1. Maximum integrated power attainable at a given power for the HPRR[a]

Power (kW)	Integrated power (kW-min)	Operating time (min)
1	200	200
2	120	60
5	90	18
10	77	7.7

[a]A maximum permissible pulse is equivalent to 0.9 kWhr of steady-state operation.

Table 3.2. Calculated values of kerma behind concrete and steel-concrete shields

Shield	Kerma (rads)	Distance (m)
20 cm concrete	85	3
5 cm Fe + 15 cm concrete	78	3
None	390	3

ORNL-DWG 77-9402

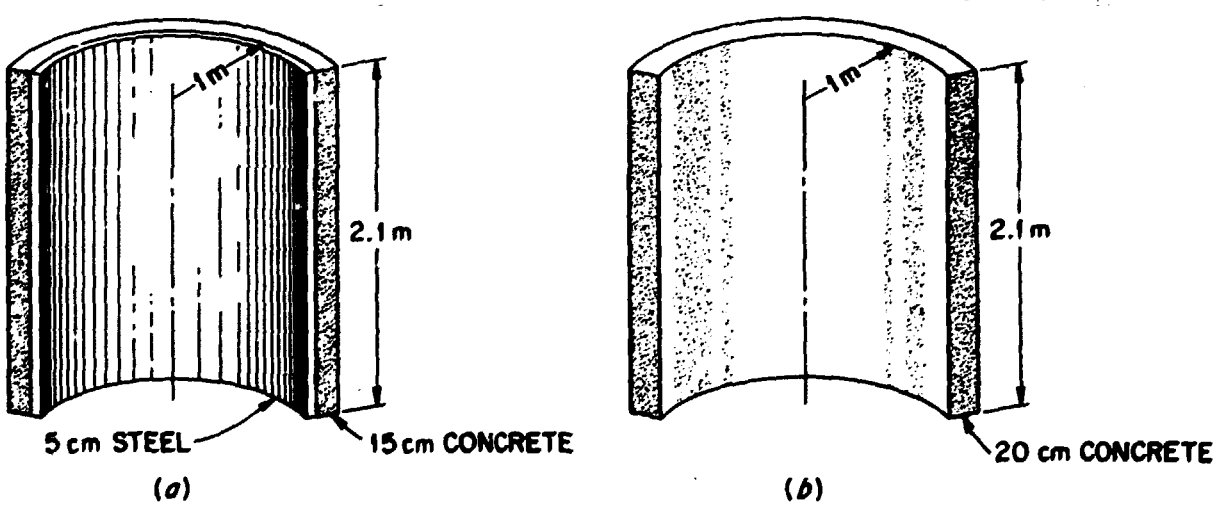

Fig. 3.3. Steel-concrete and concrete shields for modification of HPRR spectrum.

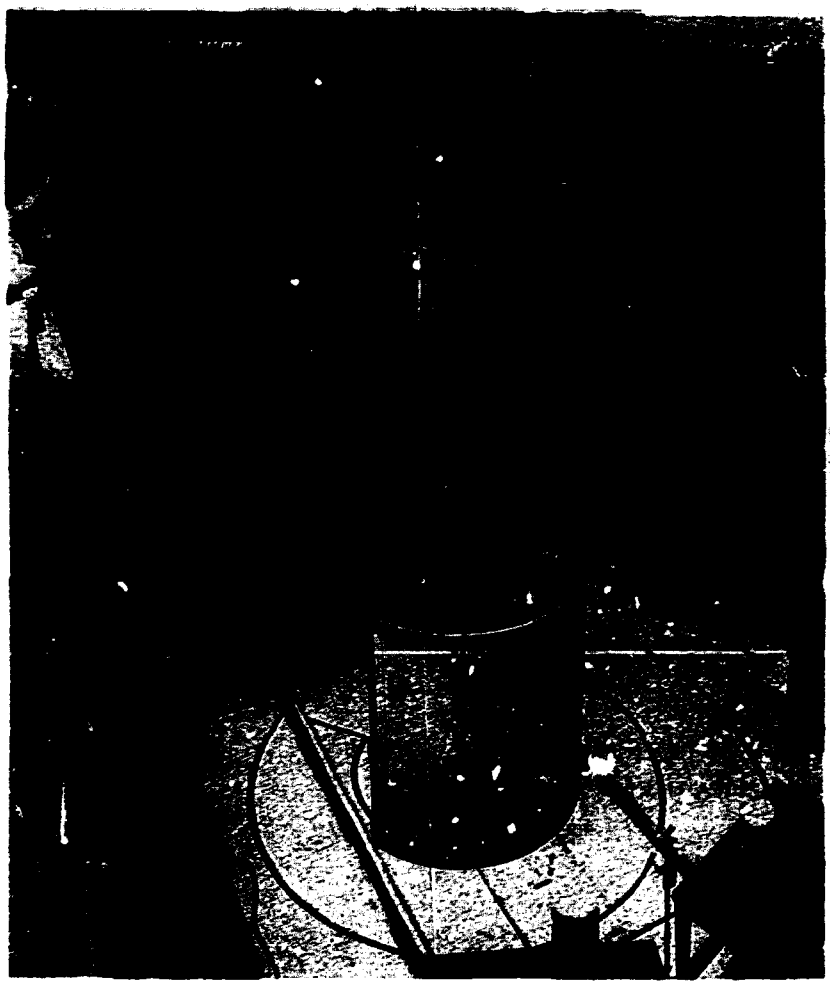

Fig. 3A. Combination steel-concrete shield in place around the HPRR.

Recent controversy over the appropriate RBE of neutrons for radiation protection purposes makes this a particularly significant experiment. The HPRR is also used in radiobiological research programs conducted by other institutions such as the Comparative Animal Research Laboratory in Oak Ridge; The University of Tennessee, Memphis Medical Center; Civil Aeromedical Institute, Oklahoma City, Oklahoma; and the University of Alabama, Birmingham Medical Center.

Use of the HPRR as an international testing and standardizing facility expands each year. Intercomparison studies of nuclear accident dosimeters and personnel monitoring devices are conducted annually to establish the accuracy and reliability of dosimetry systems in mixed neutron-gamma radiation fields. For example, the thirteenth in a series of NAD intercomparisons was held August 16–20, 1976, and the third personnel dosimeter intercomparison study (PDIS) was held March 15–16, 1977.

Additionally, programs have been established for testing criticality alarm systems and accident preparedness. Criticality alarm systems used throughout Union Carbide Nuclear Division facilities are tested at the HPRR. Several other ERDA contractors have recently made use of the HPRR for this purpose, motivated by the proposed ANSI standard[7] for criticality alarm systems.

Finally, the HPRR plays a substantial role in education and training. During the past year, the reactor was used in formal training exercises for nuclear engineering students from The University of Tennessee, Memphis State University, Mississippi State University, Oklahoma

7. ANSI N16.2, "Criticality Accident Alarm Systems," proposed revision, American National Standards Institute, February 1975.

Table 3.3. Principal users of the Health Physics Research Reactor (HPRR)

User group	Percentage of reactor use[a]	
	1975	1976
Universities for training	19.8	32.6
Biology Division (ORNL)	21.6	22.3
DOSAR	30.7	
Dosimetry development		12.8
Criticality alarm tests		6.4
Intercomparisons	2.5	3.8
Civil Aeromedical Institute	6.0	7.3
The University of Tennessee, Memphis Medical Center	7.9	6.0
University of Alabama, Birmingham Medical Center	0.0	1.2
Comparative Animal Research Laboratory	2.5	1.6
Others	9.0	6.0

[a]Use is defined here as operating time for the HPRR.

State University, and Louisiana State University and for health physics trainees from Oak Ridge Associated Universities. Table 3.3 summarizes the use of the HPRR.

The HPRR could play a vital role in new research proposed by the Neutron Physics Division on characterizing fast-fission-product decay heat. This research would effectively remove the existing uncertainty in the current estimates of decay heat release in fast reactors soon after shutdown. It has obvious applications to hypothetical safety-related events of possible importance to fast-reactor design. Secondarily, the work would provide spectra of fission product radiations to update present fission product data files. The HPRR would be virtually an ideal radiation source, and the physical plant could be easily modified to accommodate this experiment.

INTERCOMPARISON STUDIES AND DOSIMETER TESTS

Nuclear Accident Dosimetry Intercomparison

The thirteenth NAD intercomparison study was conducted August 16–20, 1976. Institutions participating in the study included Babcock and Wilcox, from both their Lynchburg, Virginia, and Apollo, Pennsylvania, facilities; Goodyear Atomic Corporation; Lawrence Livermore Laboratory; Mason and Hanger; and Union Carbide Nuclear Division, represented by all three Oak Ridge facilities (ORGDP, ORNL, and Y-12). Preliminary results from this study are presented in Table 3.4.

Quarterly Accident Readiness Tests

Quarterly accident readiness tests (QART) are designed to allow nuclear facilities to test the response of their dosimetry systems and to regularly retrain their dosimetry personnel under simulated accident conditions. The second QART was held July 20–22, 1976, for four participants, and the third QART was held October 19–21, 1976, for five participants. Based upon the small number of participating institutions, it was decided that either this type of test did not meet a need or that most institutions do not have the luxury of time and manpower to devote to this kind of testing. Consequently, the QARTs were discontinued as a regular part of our program. A summary of radiation exposure conditions used for these exercises is given in Table 3.5.

Personnel Dosimetry Intercomparison Study

The third in a series[8,9] of personnel dosimeter intercomparison studies (PDIS) was conducted during the period March 15–16, 1977. The nine participating groups included Brookhaven National Laboratory; Lawrence Livermore Laboratory; ORNL; R. S. Landauer, Jr., and Company; Teledyne Isotopes, Incorporated; U.S. Testing Company; Rockwell International, Rocky Flats Plant; Kernforschungszentrum,

8. H. W. Dickson, W. F. Fox, and F. F. Haywood, *1974 Intercomparison of Personnel Dosimeters*, ORNL/TM-4786 (January 1976).

9. L. W. Gilley, H. W. Dickson, and D. J. Christian, *1976 Intercomparison of Personnel Dosimeters*, ORNL/TM-5672 (December 1976).

Karlsruhe, Germany; and National Tsing Hua University, Taiwan. The exposure conditions for this experiment are given in Table 3.6. Only preliminary and incomplete data from the participants are available at this time; however, the results indicate a continuing trend toward improved neutron dosimetry on the part of the participants. Table 3.7 compares the percent standard deviation of the reported neutron and gamma dose-equivalent values for the first three PDIS intercomparisons.

Table 3.4. Preliminary results of the thirteenth nuclear accident dosimetry (NAD) intercomparison study

Pulse	Shield	Fissions	In-air kerma estimate		Phantom dose estimate	
			Neutron (rads)	Gamma (rads)	Neutron (rads)	Gamma (rads)
1	Lucite	8.6×10^{16}	52	63	92	75
2	Unshielded	9.2×10^{16}	363	46	390	76

Table 3.5. Summary of quarterly accident readiness tests (QART) 2 and 3 exposures

QART No.	Pulse No.	Shield	Fissions	Neutron kerma (rads)
2	1	Lucite	3.6×10^{16}	25
2	2	None	4.4×10^{16}	168
2	3	Steel	5.8×10^{16}	95
3	1	Lucite	5.4×10^{16}	38
3	2	None	8.9×10^{16}	348

Table 3.6. Exposure conditions for the third personnel dosimeter intercomparison study (PDIS)

Run No.	Shield	Fissions	Fluence ($cm^{-2} \times 10^{7}$)	Element 57[a] dose (millirads)	Dose equivalent (millirems)
1	None	1.3×10^{19}	2.6	68	635
2	Steel	3.5×10^{19}	4.2	76	719
3	Lucite	6.4×10^{19}	3.4	50	443

[a]Element 57 is that section of a cylindrical phantom (F. H. Attix and W. C. Roesch, eds., *Radiation Dosimetry*, vol. I, Academic Press, New York, 1968, p. 294) located facing the radiation source, at the vertical center of the phantom, and extending from the surface to a depth of 3 cm.

Table 3.7. Comparison of results of the first three PDIS

Shield	PDIS No.	Standard deviation (%)	
		Neutron	Gamma
None	1	47	24
	2	39	83
	3[a]	12	25
Steel	1	62	24
	2	30	97
	3[a]	15	28
Lucite	1	102	19
	2	29	53
	3[a]	20	34

[a]The results for PDIS 3 are preliminary and represent incomplete returns from all participants.

IMPROVEMENTS OF SAFETY BLOCK ALIGNMENT

One of the main goals in operating a pulse reactor is to be able to produce a pulse of the size specified. Progress has been made at the HPRR toward achieving this goal, and the present two-part change is a continuation of this effort.

In making a pulse with this type of reactor, the safety block (or some other major piece of fuel) is withdrawn from the critical array as one of the final steps in the operation. Later in the sequence the safety block is reinserted; the repositioning must be very accurate or the pulse size will be in error. It has been observed during operation that when the safety block is scrammed out of the core and reinserted, the safety block spring acts as a ratcheting device, that is, it rotates the safety block a slight amount each time. If the insert stop and the top of the safety block are not perfectly aligned, the lower end of the block will be off-center in a different direction each time.

The safety block is supported by a pipe and a collar or disk which travels in a cylinder called a snubber housing. The collar is engaged by the magnet to pick up the safety block. To prevent rotation of the block, the snubber housing has been slotted along one side to accommodate a pin which will be fastened to the collar. As a further refinement of positioning, a many-fingered cup-shaped spring was prepared for attachment to the lower end of the safety block. The spring and the safety block travel in the safety tube with adequate clearance until just before the safety block reaches the inserted limit. At this point the spring fingers will engage a shoulder in the tube and exert a slight force to center the lower end of the safety block in the core. The frictional force from the action of the spring fingers, which opposes the dropout of the safety block during automatic or manual shutdown, will be made less than 5 lb. Adjustment of the amount of frictional force will be made during the final checkout and machining operations. Since the dead weight of the safety block plus the force of the scram-out spring at the inserted position will be greater than this friction force by a factor of 15, the scram capability of the safety block will not be compromised.

The above arrangement has worked satisfactorily at Aberdeen for several years. The HPRR staff believes that this is the next logical step in their efforts to achieve a specified pulse size. The modified parts are shown in Fig. 3.5.

PHOTO 1933-77

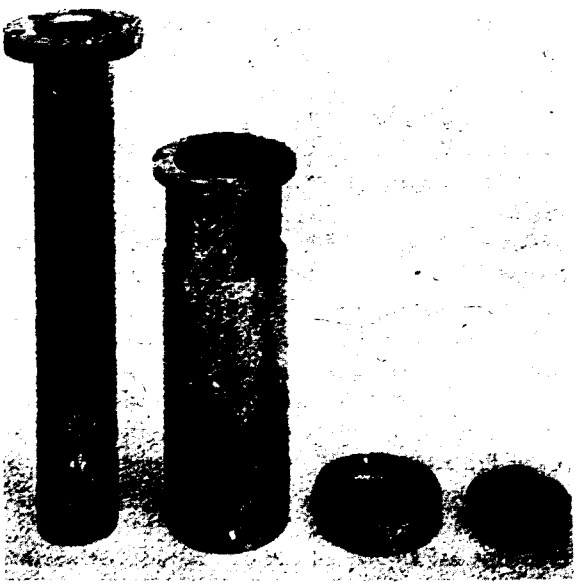

Fig. 3.5. Modified parts for alignment of the safety block, showing, from left to right, the snubber housing, safety tube, end cap, and the many-fingered spring.

4. Dosimetry for Human Exposures

G. D. Kerr T. D. Jones J. M. L. Hwang[1]

The objective of the studies on the dosimetry of human exposures is to improve techniques for assessing the risk from occupational and environmental exposures to radiation. This involves detailed investigations and predictions of radiation interactions within the body at microscopic and macroscopic levels. For example, we have calculated depth-dose and linear energy transfer (LET) distributions in a homogeneous tissue-equivalent phantom from plane beams of neutrons to establish criteria and standards for exposures to neutrons.[2] Recently, the Monte Carlo transport codes used in these calculations were generalized to calculate depth-dose and LET distributions within the body from isotropic and other fields of gamma rays and neutrons encountered in environmental and occupational exposures.[3] Although these depth-dose and LET distributions were intended mainly for use in radiation protection and risk analyses, they have application in other areas such as dosimeter design, cancer radiotherapy, and national defense.

Assessment of risk requires information on the absorbed dose and LET distributions in specific organs and tissues of the body. Due to the large number of neutron scattering and absorption interactions that must be considered in Monte Carlo transport codes, the prediction of dose to specific organs and tissues of the body using an International Commission on Radiological Protection (ICRP) reference man phantom or other mathematical simulation of the body is more difficult and time-consuming for neutrons than for gamma rays. This has stimulated the development of another technique for predicting the dose to critical organs or tissues that receive significant shielding from external fields by the body.[4] This technique assesses body shielding by using an ICRP reference man or other mathematical phantom to calculate a distribution of penetration depths from the irradiated body surface to a critical organ or tissue. The technique is called the critical human organ radiation dosimetry (CHORD) method; for convenience, the penetration depth distributions have been referred to simply as CHORD distributions or operators. By using established depth-dose curves and producing CHORD distributions for an exposure situation and a critical organ of interest, it is possible to save a factor of 5 or more in computer time and a factor of 2 or more in computer logic. It is also possible to obtain reliable results with this method for exposure situations so complex or calculations so lengthy that Monte Carlo transport calculations have not been attempted previously.

The use of CHORD distributions has provided the first method of assessing doses to active bone marrow from anterior-posterior (AP), posterior-anterior (PA), rotational, and isotropic irradiation of the body by neutrons. It has also allowed an extension of bone-marrow dosimetry to x- and gamma-ray energies and exposure situations that were unavailable in the literature.[5] A specific application of this technique has been the estimation of absorbed dose to the active bone marrow of Japanese atomic-bomb survivors.[6] These estimates were used recently in an analysis of the leukemic data on atomic-bomb survivors.[7] This analysis provides important refinements in the estimates of leukemic risk from neutron exposures. It also provides better consistency in the estimation of leukemic risk from x- and gamma-ray

1. Foreign guest, Taiwan.

2. National Committee on Radiation Protection, *Protection Against Neutron Radiation*, Report 38, NCRP Publications, Washington, D.C., 1971.

3. T. D. Jones and J. W. Poston, "Depth Dose from Isotropic and Cloud-Source Irradiation by Gamma-Rays and Neutrons," to be published in *Health Physics*.

4. T. D. Jones, *Radiation Insult to the Active Bone Marrow as Predicted by a Method of CHORDS*, ORNL/TM-5191 (September 1976).

5. T. D. Jones, "CHORD Operators for Cell-Survival Models and Insult Assessment to the Active Bone Marrow," to appear in *Radiation Research* (August 1977).

6. G. D. Kerr, J. M. L. Hwang, and R. M. Jones, *J. Radiat. Res.* 17, 211 (1976).

7. G. D. Kerr et al., "An Analysis of Leukemia Data from Studies of Atomic-Bomb Survivors Based on Estimates of Absorbed Dose to Active Bone Marrow," communication N335 in *Proceedings of the Fourth International Congress of the International Radiation Protection Association*.

exposures derived from data on atomic-bomb survivors and other exposed groups, such as the ankylosing spondylitis patients treated by x-ray therapy.

The CHORD method can also be used in calculating dose to internal organs from inhaled or ingested radionuclides. Work in progress includes calculations of CHORD distributions for the basal cells of the bronchial epithelium, using a mathematical model of the tracheobronchial tree. These CHORD distributions can be used to estimate the dose to basal cells from any inhaled alpha- or beta-particle emitter. The CHORD distributions can be used with dose distributions predicted by methods such as Berger's buildup factor about a point kernel, to estimate the dose to basal cells from beta particles. For alpha particles, the dose is obtained by applying the CHORD distributions to dE/dX data. Because continuous-slowing-down approximations (csda) can be used for alpha particles, it is possible to investigate microdosimetric parameters such as the number and size of energy loss events in basal cells of the bronchial epithelium. Many advantages and refinements are offered by this general approach over other approaches used to investigate doses from inhaled alpha- and beta-particle-emitting radionuclides.

Work of interest to various scientific committees has continued as a supplemental effort.[8] Previous work has been extended to standard neutron fields used for the calibration and development of instruments and dosimeters for the ERDA Division of Safety, Standards, and Compliance and the National Bureau of Standards Center for Radiation Research. Staff members have also worked with an ad hoc committee formed by the National Committee on Radiation Protection, the scientific committees on basic radiation protection criteria and biological aspects of radiation protection criteria. This ad hoc committee has served to review our recent calculations of absorbed dose to active bone marrow. Another supplemental effort has been directed to (1) the development of sequential concepts for assessing risk from radiation and chemicals from energy conversion processes and (2) the application of techniques and methods used in our previous studies in the assessment of risk from occupational and environmental exposures to SO_2, H_2SO_4, benzopyrene, NO_x, CCl_4, PNA, and other chemical pollutants.

ANALYSIS OF LEUKEMIC DATA FROM STUDIES OF ATOMIC-BOMB SURVIVORS BASED ON ESTIMATES OF ABSORBED DOSE TO ACTIVE BONE MARROW

The medical and epidemiological studies of the atomic-bomb survivors are the most extensive source of data on the latent effects of human radiation exposures.[9,10] The atomic-bomb survivors of Hiroshima and Nagasaki – a large group (over 100,000) – have been subjected to a wide range of radiation doses. Estimates of radiation dose are available for most of these survivors and are designated in the literature as T65D estimates. Although the location reported for each survivor and the shielding provided by structures and terrain were taken into account in the T65D estimation of dose, these estimates predict only a survivor's radiation exposure in terms of tissue kerma in air. The estimates neglect body shielding of internal organs.[11]

Self-shielding factors for active bone marrow were calculated recently at ORNL. These calculations show that absorbed doses to active bone marrow of the atomic-bomb survivors vary markedly from the T65D estimates.[4] Three components of absorbed dose to bone marrow were considered: (1) the low-LET absorbed dose for gamma rays incident on the survivor's body from the gamma-ray field about the survivor, (2) the high-LET absorbed dose from neutrons incident on the survivor's body from the neutron field about the survivor, and (3) the low-LET absorbed dose from gamma rays produced within the body by the neutrons incident on the survivor's body from the neutron field about the survivor. For an adult Japanese survivor,[6] the ratio of the low-LET absorbed dose in active bone marrow from gamma rays to the tissue kerma in air from gamma rays was calculated to be 0.56. The self-shielding factors or ratios of high-LET absorbed dose from neutron-produced recoil ions and low-LET absorbed dose from neutron-produced gammas to tissue kerma in air from neutrons were calculated to be 0.28 and 0.067 respectively. These self-shielding factors were used to investigate data on leukemia in atomic-bomb survivors from the life-span studies of the Radiation Effects Research Foundation (RERF), formerly the Atomic Bomb Casualty Commission (ABCC).

Data on the number and the person-years of observations of the survivors and on mortality from leukemia and other causes in survivors are given in the RERF life

8. G. D. Kerr et al., "Dosimetry for Human Exposures," *Health Phys. Div. Annu. Prog. Rep. June 30, 1976*, ORNL-5171 (October 1976), pp. 283–91.

9. Advisory Committee on the Biological Effects of Ionizing Radiation, *The Effects on Populations of Exposure to Low Levels of Ionizing Radiation*, National Academy of Sciences–National Research Council, Washington, D.C., November 1972.

10. United Nations Scientific Committee on the Effects of Atomic Radiation, *Ionizing Radiation: Levels and Effects*, vols. 1 and 2, United Nations, New York, 1972.

11. T. D. Jones et al., *Health Phys.* 28, 367 (1975).

span studies as functions of the radiation exposure received by the survivors.[12,13] That is, the data are grouped into T65D ranges of 0 to 9 rads, 10 to 49 rads, etc., and the mean T65D values of tissue kerma in air from gamma rays and neutrons are given for each of the T65D groupings of survivors. For example, the mean T65D values of tissue kerma in air from gamma rays, K_γ, and neutrons, K_n, are 108.5 and 30.1 rads, respectively, for the 100 to 199 rad grouping of Hiroshima survivors. Using the self-shielding factors for active bone marrow, the mean value of the high-LET absorbed dose, D_n, from neutrons for this T65D group of survivors is calculated to be $0.28K_n$ = 0.28 (30.1 rads) = 8.4 rads. The mean value for the low-LET absorbed dose, D_γ, from gamma rays incident on the survivor's body and neutron capture gamma rays produced within the survivor's body is calculated to be $0.56K_\gamma + 0.067K_n$ = 0.56 (108.5 rads) + 0.067 (30.1 rads) = 62.8 rads. Mean absorbed doses to active bone marrow of other T65D exposure groups of survivors in the two cities, calculated in the same manner, are given in Table 4.1. Also given in this table are incidence rates[14] derived from data in the seventh life-span study report[13] on the number of person-years of observation of survivors and the number of leukemias in survivors in each of the T65D exposure groupings. The data in Table 4.1 were used to investigate the dose response of leukemic incidence as a function of absorbed dose to the active bone marrow of the atomic-bomb survivors.

The Committee on the Biological Effects of Ionizing Radiation (BEIR) of the National Academy of Sciences–National Research Council reviewed the life-span studies and suggested that incidence rates of the 0 to 9 rad groupings of survivors be used as controls. These rates were used to obtain excess incidence rates, Y_e, in the higher T65D exposure groups in each of the two cities. The Y_e values for the two cities were fitted simultaneously by the method of least squares to each of the following dose-response functions:

$$Y_e = A_1 D_n + B_1 D_\gamma \quad (1)$$

$$= A_2 D_n + B_2 D_\gamma + C_2 D_\gamma^2 \quad (2)$$

$$= A_3 D_n + C_3 D_\gamma^2 . \quad (3)$$

Coefficients giving the best fit to the Y_e and the D_γ and D_n values for each exposure group, along with their standard deviations, are: $A_1 = 16 \pm 6$, $B_1 = 3.6 \pm 0.5$; $A_2 = 20 \pm 4$, $B_2 = 0.26 \pm 0.89$, $C_2 = 0.015 \pm 0.004$; and $A_3 = 20 \pm 3$, $C_3 = 0.016 \pm 0.002$. Units of the As and Bs are cases per year per 10^6 person-rads, and the Cs have units of cases per year per 10^6 person-rads^2 of absorbed dose to active bone marrow.

Table 4.1. Incidence rates of leukemia for 1950 to 1972 and mean absorbed doses to active bone marrow for T65D exposure groupings of Hiroshima and Nagasaki atomic-bomb survivors

T65D range (rads)	Mean absorbed dose to active bone marrow (rads)			Cases of leukemia (per 10^6 person-years of observation)
	D_γ	D_n	D_{total}	
		Hiroshima		
0–9	0.5	0.1	0.6	42.8
10–49	10.1	1.2	11.3	80.1
50–99	32.8	3.7	36.5	133.9
100–199	62.8	8.4	71.2	366.2
200–399	122.5	19.2	141.7	832.9
400–599	203.8	33.5	237.3	1277.6
		Nagasaki		
0–9	1.3		1.3	48.2
10–49	11.9		11.9	27.2
50–99	39.4	0.1	39.5	0
100–199	80.9	0.4	81.3	119.6
200–399	148.0	1.1	149.1	403.4
400–599	258.6	2.4	261.0	1243.5

Values of Y_e predicted by fitting an assumed linear gamma-ray dose response [Eq. (1)] simultaneously to the data for the two cities are illustrated by the dashed lines in Figs. 4.1 and 4.2. Values predicted by simultaneously fitting an assumed dose-squared response [Eq. (3)] to the data for the two cities are illustrated by the solid lines in the figures. Figure 4.1 is for Hiroshima, where survivors were exposed to significant levels of both gamma rays and neutrons; Fig. 4.2 is for Nagasaki, where the exposures were due mainly to gamma rays. Bars on the data points in both of these figures are 90% confidence intervals. An important conclusion taken from these investigations is that the magnitude of the risk factor for neutrons is nearly independent of the assumptions regarding the gamma-ray dose response and is within the range of 16 to 20 excess leukemias per year per 10^6 person-rads of high-LET absorbed dose to active bone marrow. Results suggest a curvilinear dose response to the low-LET absorbed dose from gamma rays, but it is impossible to obtain an accurate estimate of the gamma-ray risk factor at low doses by fitting

12. S. Jablon and H. Kato, *Rediat. Res.* 50, 649 (1972).

13. I. M. Moriyama and H. Kato, *Mortality Experience of A-Bomb Survivors 1970-72, 1950-72*, ABCC Report TR 15-73, Atomic Bomb Casualty Commission, 1973.

14. Because leukemia is fatal in all cases, its mortality will equal its incidence over a long period of time.

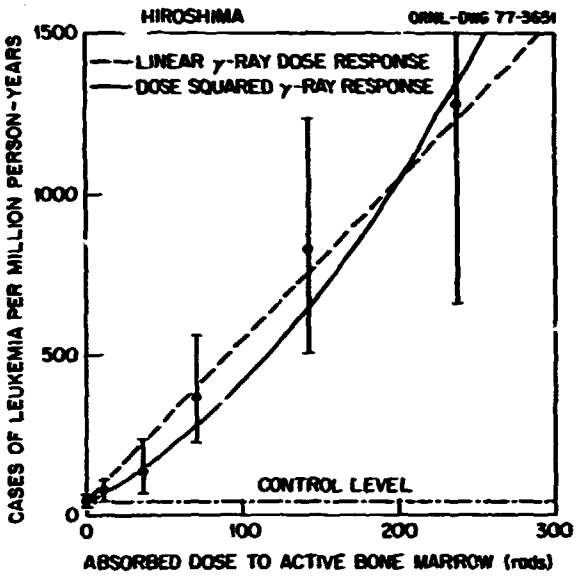

Fig. 4.1. Least-squares fits of excess incidence rates of leukemia in atomic-bomb survivors of Hiroshima to models with a linear neutron dose response and either a linear gamma-ray dose response or a dose-squared response to gamma rays. Bars on the data points are 90% confidence intervals.

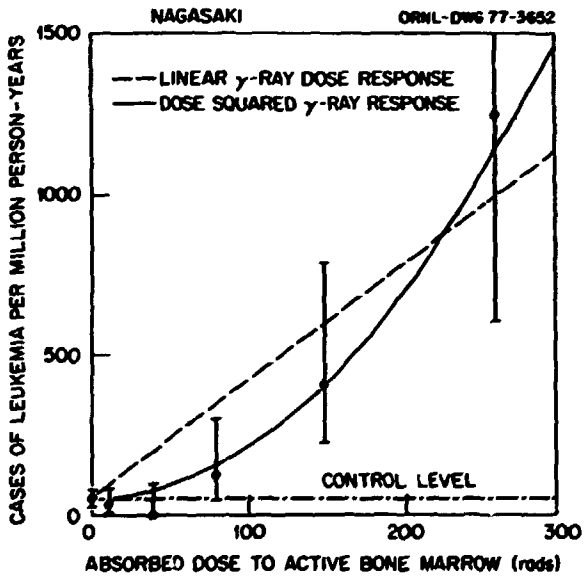

Fig. 4.2. Least-squares fits of excess incidence rates of leukemia in atomic-bomb survivors of Nagasaki to models with a linear neutron dose response and either a linear gamma-ray dose response or a dose-squared response to gamma rays. Bars on the data points are 90% confidence intervals.

dose-response functions to the data. This is illustrated by the large standard deviation in the coefficient, B_2, of the linear dose term for gamma rays in Eq. (2).

The self-shielding factors for active bone marrow were also used to revise the person-rem computations of leukemic risk from data on the atomic-bomb survivors by the BEIR Committee.[9] In these person-rem computations, the excess incidence rate of an observed effect is simply divided by the dose equivalent to the critical organ averaged over all individuals in the exposed group. Dose equivalents for atomic-bomb survivors used in the BEIR report are based, however, on mean T65D values of tissue kerma in air, rather than on mean absorbed doses to critical organs – testes and ovaries for genetic effects, active bone marrow for leukemia, etc. Person-rem estimates of leukemic risk derived in the BEIR report[15] from data on *adult* survivors aged 10 or older at the time of exposure in 1945 were revised by the relationship

$$\text{Risk} = Y_e/(D_\gamma + \text{RBE} \cdot D_n) \ , \qquad (4)$$

where RBE is relative biological effectiveness. These revisions are given in Table 4.2. Groupings of adult survivors with T65D estimates of 0 to 9 rads were used to obtain the excess incidence rates in the 10+ rad groupings of adult survivors. The mean values of tissue kerma in air for these 10+ rad groupings of adult survivors, along with self-shielding factors for active bone marrow, were used to calculate the mean absorbed doses to active marrow. An RBE of 20 to 30 brings the person-rem computations of risk from data on survivors in the two cities into reasonable agreement and predicts risk factors of the order of 18 to 27 excess leukemias per year per 10^6 person-rads of high-LET absorbed dose from neutrons and 0.86 to 1.2 excess leukemias per year per 10^6 person-rads of low-LET absorbed dose from gamma rays.

Although the revised BEIR estimates of risk in Table 4.2 are from data on leukemia in survivors for the period 1950 to 1972 covered in the sixth life-span study report by Jablon and Kato,[12] the results are essentially the same as those obtained from the 1950 to 1972 data on adult survivors in the seventh life-span study report by Moriyama and Kato.[13] Neither do the results in Table 4.2 differ significantly from those obtained using data on survivors of all ages at the time of exposure in 1945. This does not imply that very young survivors are not more radiosensitive than adult survivors. It simply implies that the small number of very young survivors does not have a significant influence on the overall data of mortality from leukemia. The revised values of leuke-

15. Advisory Committee on the Biological Effects of Ionizing Radiation, *The Effects on Populations of Exposure to Low Levels of Ionizing Radiation*, National Academy of Sciences–National Research Council, Washington, D.C., November 1972, Table a-7, p. 117.

Table 4.2. Person-rem estimates of leukemic risk based on 1950–1972 data of mortality from leukemia in atomic-bomb survivors of Hiroshima (H) and Nagasaki (N)

Study group (1945)	Type of radiation	Postexposure follow-up period (years)	Mean bone-marrow dose (rads)	Mean age at exposure (years)	RBE	Cases per year per 10^6 person-rems: Best estimate	Lower 90% confidence interval	Upper 90% confidence interval
H and N	$\gamma + n$	6–25	46	35	1	2.8	2.2	3.5
					5	2.2	1.7	2.7
					10	1.7	1.3	2.1
					20	1.2	0.94	1.5
					30	0.91	0.71	1.1
H	$\gamma + n$	6–25	38	36	1	4.2	3.2	5.0
					5	2.8	2.1	3.3
					10	2.0	1.5	2.4
					20	1.2	0.94	1.5
					30	0.90	0.68	1.1
N	$\gamma + n$	6–25	63	31	1	1.0	0.16	1.8
					5	0.99	0.16	1.8
					10	0.96	0.15	1.7
					20	0.91	0.15	1.6
					30	0.86	0.14	1.5

mic risk of 0.86 to 1.2 excess leukemias per year per 10^6 person-rads of absorbed dose to active marrow for gamma rays from data on atomic-bomb survivors are in good agreement with the values of 0.88 to 1.3 excess leukemias per year per 10^6 person-rads derived by the BEIR Committee from data on x-ray-treated spondylitic and menorrhagic patients.

A recent review by Ichimaru and Ishimaru of leukemia and related disorders in atomic-bomb survivors presents evidence that the leukemic latency period depends, to some extent, on age at the time of exposure.[16] Leukemia in groups under 15 years old and 15 to 29 years old at the time of exposure peaked in the early period (1950 to 1954), then declined rapidly to normal. In groups aged 30 to 44 and 45 or over, leukemia peaked later and remained above normal in recent years. The 1950 to 1972 mortality data do not represent, therefore, the total risk to survivors in the older age groups. Some of the total risk to younger age groups of survivors in the period 1945 to 1950 is also not included in the 1950 to 1972 data. For these reasons, it was assumed that the risk factors for the period 1950 to 1972 were representative of the average annual risk over a 30-year period starting in 1945.

This period, plus the mean age of about 35 for survivors in 1945, is nearly equal to normal lifetime expectancy. A range of lifetime risks of 500 to 800 excess leukemias per 10^6 person-rads of high-LET absorbed dose from neutrons is predicted by our dose-response and person-rem analysis of the leukemic data on the atomic-bomb survivors. From these analyses, the best estimate of the lifetime risk for neutrons appears to be about 600 excess leukemias per 10^6 person-rads based on a 30-year average annual incidence for the atomic-bomb survivors of the order of 20 excess leukemias per year per 10^6 person-rads of high-LET absorbed dose to active bone marrow. The best estimate of the lifetime risk for gamma rays at low dose levels appears to be about 30 excess leukemias per 10^6 person-rads of low-LET absorbed dose to active bone marrow. This lifetime risk for gamma rays is based on a 30-year average annual incidence for the survivors of the order of 1 excess leukemia per year per 10^6 person-rads of low-LET absorbed dose from gamma rays obtained in our person-rem analysis of the leukemic data.

Self-shielding factors are being investigated for other organs and tissues, such as the thyroid, lungs, stomach, and intestines. These self-shielding factors will provide significant refinements in the estimation of neutron risks derived from the medical and epidemiological studies of the atomic-bomb survivors. Both the refined estimates of risks from neutron exposures and the self-shielding factors for neutrons are important in establishing radiation protection criteria and standards. As a

16. M. Ichimaru and T. Ishimaru, *J. Radiat. Res.* (Suppl.) 16, 89 (1975).

supplemental effort, work with scientific committee members and staff members of the RERF is expected to increase.

NEUTRON FLUENCE-TO-DOSE CONVERSION FACTORS FOR Am-B AND Am-Be SOURCES

The most commonly used sources in the calibration of neutron dosimeters are those using the (α, n) reaction in a low-Z material, usually beryllium or boron.[17] Although ^{226}Ra, ^{210}Po, and ^{239}Pu have been used in the fabrication of these sources, the most commonly used alpha emitter at present is ^{241}Am. Some of the advantages offered by ^{241}Am are a lower gamma-ray background than ^{226}Ra, a longer half-life than ^{210}Po (458 years vs 138 days), and a higher radioactive purity and specific activity than ^{239}Pu.[17–19] The 3.2 Ci/g specific activity of ^{241}Am allows fabrication of sources that are physically smaller and more convenient for calibration purposes than those fabricated of ^{239}Pu, which has a specific activity of about 0.61 Ci/g. Also, ^{239}Pu sources may have radioactive impurities and significant yield changes from ^{241}Am ingrowth. The higher radioactive purity of ^{241}Am and the very long-lived ^{237}Np daughter (2.14×10^6 years) of ^{241}Am permit a simple and accurate decay correction for the yield change in neutron emission from the source with time.[18]

Fluence-to-dose conversion factors for Am-Be and Am-B sources are, however, not well known. That is, there are only a few references in the literature on dose conversion factors for such sources.[20,21] Several fluence-to-dose conversion factors of interest in the calibration of neutron dosimeters and dose-rate meters were, therefore, calculated using experimentally measured spectra available in the literature. The neutron spectra used in these calculations are from measurements with Am-Be sources having an activity of 0.7 Ci,[19] 0.1 Ci,[22] and 0.4, 1.5, and 5 Ci (ref. 18) and from Am-B (^{10}B and natural boron, or ^{11}B) sources having an activity of 2 Ci.[18] The cutoff, or lowest, energy of the neutron spectral measurements taken by Werle was about 0.1 MeV.[18] Due to a higher cutoff energy of about 1.5 MeV in the spectral measurements done by Geiger and Hargrove[19] and Thompson and Taylor,[22] it was assumed that 20% of the neutrons emitted by the source had energies below 1.5 MeV and that the mean energies of these neutrons was 0.35 MeV.[19,23]

Several different fluence-to-dose conversion factors are of interest in the calibration of neutron dosimeters and dose-rate meters. These are the average tissue kerma in air, maximum absorbed dose in the body, and maximum dose-equivalence in the body per fluence neutron. The average dose conversion factor of interest, $\bar{F}$, was calculated for each of the neutron spectra by the relation:

$$\bar{F} = \Sigma F(E) N(E) \Delta E / \Sigma N(E) \Delta E , \qquad (5)$$

where $N(E)\ \Delta E$ is the number of neutrons with energies between E and $E + \frac{1}{2}\Delta E$, and $F(E)$ is the value[2] of tissue kerma in air, maximum absorbed dose, or maximum dose-equivalence per fluence neutron of energy E. Results of these dose-conversion calculations for Am-Be sources are given in Table 4.3. Also given in the table

17. R. L. Kathren, *Health Phys.* 29, 143 (1975).
18. H. Werle, *Spectrum Measurements of Radioactive Neutron Sources in the 10 keV–10 MeV Energy Region with Proton-Recoil Proportional Counters*, Karlsruhe Nuclear Research Center External Report INR-4170-25, 1970.
19. K. W. Geiger and C. K. Hargrove, *Nucl. Phys.* 53, 204 (1964).
20. D. R. Johnson, *Health Phys.* 12, 856 (1966).
21. D. Nachtigall, *Health Phys.* 13, 213 (1967).
22. M. N. Thompson and J. M. Taylor, *Nucl. Instrum. Methods* 37, 305 (1965).
23. K. W. Geiger and L. Van der Zwan, *J. Appl. Rad. Isot.* 21, 193 (1970).

Table 4.3. Average energy and fluence-to-dose conversion factors calculated from experimentally measured spectra of Am-Be neutron sources

Am-Be neutron spectrum measurement	Average energy (MeV)	Tissue kerma in air (rads neutron^{-1} cm^2)	Maximum absorbed dose (rads neutron^{-1} cm^2)	Maximum dose equivalent (rems neutron^{-1} cm^2)	Source (Ci)
Geiger and Hargrove[a]	4.26	3.88×10^{-9}	4.54×10^{-9}	3.63×10^{-8}	0.7
Thompson and Taylor[a]	4.30	3.87×10^{-9}	4.53×10^{-9}	3.62×10^{-8}	0.1
Werle	4.24	3.78×10^{-9}	4.46×10^{-9}	3.56×10^{-8}	5
Werle	4.62	3.96×10^{-9}	4.69×10^{-9}	3.68×10^{-8}	0.4
Werle	4.34	3.81×10^{-9}	4.52×10^{-9}	3.60×10^{-8}	1.5

[a]Assumed that 20% of the neutrons emitted by the source had energies less than the 1.5 MeV cutoff of the experimental spectral measurements, and that the average energy of the neutrons with energies less than 1.5 MeV was 0.4 MeV.

are average energies, $\bar{E}$, calculated by the relationship:

$$\bar{E} = \Sigma\, EN(E)\, \Delta E / \Sigma\, N(E)\, \Delta E\,, \qquad (6)$$

where E is the energy of the neutrons and $N(E)\,\Delta E$ is the number of neutrons with energies of $E \pm \frac{1}{2}\Delta E$.

The average energy and fluence-to-dose conversion factors calculated for Am-^{10}B, Am-^{11}B (natural boron), and Am-Be sources are given in Table 4.4. Those for Am-Be are simply the mean of all five corresponding values for Am-Be sources in Table 4.3. The values in Table 4.4 are in very good agreement with the few values previously recommended in the literature for use in the calibration of neutron dosimeters and dose-rate meters. For example, the values in Table 4.4 for Am-Be are within 5% of some earlier values calculated by Nachtigall from experimentally measured spectra of Am-Be sources.[21] The tissue kerma in air per fluence neutron for Am-Be and Am-^{11}B sources in Table 4.4 are also in good agreement with values measured previously at ORNL.[20,24] These measured values were $(4.05 \pm 0.30) \times 10^{-9}$ and $(3.51 \pm 0.26) \times 10^{-9}$ rads neutron^{-1} cm^2 for a 5-Ci Am-Be and a 10-Ci Am-^{11}B source respectively. A recommendation made from these ORNL studies by Johnson[20] and Jones, Johnson, and Thorngate[24] was that an average value for tissue kerma in air (or tissue-absorbed dose in air) per fluence neutron of $(4.0 \pm 0.3) \times 10^{-9}$ rads could be used with either Am-Be, Pu-Be, or Po-Be sources.

CHORD OPERATORS FOR INSULT ASSESSMENT TO THE RADIOSENSITIVE CELLS OF THE TRACHEOBRONCHIAL TREE

Carcinogenesis has usually been considered to exhibit a dose-specific response. This is of special concern in the case of uranium miners, because the absorbed dose to lung tissue is dominated by alpha particles from radium-A and radium-C. These alpha particles are known to produce a high degree of lethality as they pass through cellular nuclei. Neoplastic transformations or precarcinogenic lesions seem to depend on sublethal events, often incurred over a period of several decades. Thus, it seems unlikely that cancer is the result of such injuries. This study provides the dose assessment techniques for an in-depth investigation of insult assessment to the radiosensitive cells of the tracheobronchial tree. CHORD operators[5] permit the detailed description of the absorbed dose, the energy spectrum based on the dE/dX across the site of interest, and the track density probabilities through the cell nucleus for heavy charged particles. For beta particles, which exhibit a great degree of straggling in angle, direction, and energy, CHORD operators are limited to the modification of robust quantities, such as absorbed dose.

According to BEIR,[9] the only common insult to miners who demonstrated an increased risk of lung tumors was inhalation of radon-daughter reaction products. The incidence rate in small laboratory animals seems to be controlled by alpha particles; however, in man, there is some evidence of increased risk from exposure to x and gamma rays. For inhalation, the beta doses from ^{214}Pb and ^{214}Bi greatly exceed the dose from radon-daughter gamma rays and are much more penetrating than the alpha particles from ^{214}Po.

There is little doubt that for inhalation of radon daughter products alpha particles dominate the dose in regions of greatest risk. The specific mechanism in man may be significantly different from that observed in cell colonies and laboratory animals, however, because of the longer latency period for humans and the types of carcinomas involved. There is strong evidence to indicate that dose-like quantities defined according to $\Delta E/\Delta m$ principles are unimportant and misleading for alpha particles in the lung because any direct hit of a cell nucleus results in the reproductive death of that cell.[25] Thus, the excessive insult above that necessary

24. T. D. Jones, D. R. Johnson, and J. H. Thorngate, *Health Phys.* 11, 519 (1965).

25. National Academy of Sciences–National Research Council, *Health Effects of Alpha-Emitting Particles in the Respiratory Tract*, Report of the Ad Hoc Committee on "Hot Particles" of the Advisory Committee on the Biological Effects of Ionizing Radiations, National Academy of Sciences, 1976.

Table 4.4. Average energies and fluence-to-dose conversion factors for Am-B and Am-Be neutron sources

Neutron source	Average energy (MeV)	Tissue kerma in air (rads neutron^{-1} cm^2)	Maximum absorbed dose (rads neutron^{-1} cm^2)	Maximum dose equivalent (rems neutron^{-1} cm^2)
Am-^{10}B	1.90	2.90×10^{-9}	3.37×10^{-9}	3.19×10^{-8}
Am-^{11}B	2.70	3.46×10^{-9}	3.98×10^{-9}	3.56×10^{-8}
Am-Be	4.35	3.86×10^{-9}	4.55×10^{-9}	3.62×10^{-8}

for neoplastic transformations to occur tends to conceal the true neoplastic damage mechanisms.

Bevan and Haque[26] and Smith and Rossi[27] have observed that lethality is usually accompanied by (but is not necessarily caused by) the energy deposition of 1 MeV in the volume of a cell. The BEIR Committee[25] states that alpha traversal through the cytoplasm can damage the cell but leave its reproductive systems unimpaired as long as the nucleus is not hit. It appears that such a cell can pass on to its progeny genetic alterations (precancerous lesions) which may have a bearing on the sequence of events for tumor induction.[28,29] Todd states that human cells irradiated by certain accelerated heavy ions or by alpha particles at the end of their tracks have "strictly exponential survival curves," and that exponential inactivation "is due to single irreparable lethal events and not to a fortuitous summation of survivals of sigmoidally inactivated populations. . . . This corroborates the apparent correspondence of the slopes of exponential survival curves to those predicted on the basis of inactivation due to the passage of a single heavy ion through the cell nucleus."[30]

Todd et al. also estimate that a nucleus insulted by an energy loss of 200 keV/μm results in 50% lethality, and that nuclear insults of 500 keV/μm result in 100% lethality.[31] Inspection of the Bragg-peak region of the *dE/dX* curves indicates that alpha particles deliver less than 250 keV/μm, whereas high-energy recoil nuclei may deliver 1000 keV/μm. For environmental radiation, nuclear recoils are seldom, if ever, expected to possess enough energy to induce lethality even in one cell, whereas most environmentally produced alpha particles attenuate through the Bragg-peak region. It must be remembered that mutagenesis is not a lethal process; it is not even clear whether lethality and mutagenesis depend on the same mechanism. Therefore, the main objective of this work was to estimate the degree of beta insult, that is, sublethal events. The mean linear dimension of the nucleus of a cell is about 10 μm.[31,32] Inspection of the *dE/dX* curve for alpha particles in tissue indicates an energy deposition in excess of 1.6 MeV per cell in the region of the Bragg peak, whereas the region corresponding to the source energy of the alpha particle would result in an energy loss of something less than 1 MeV per cell. Of course, the exact insult would depend on the intercepted length and the *dE/dX* of the alpha particle across the cell.

There are about 10^{11} atoms in a mass of 1 pg, and the path length of radon-daughter alpha particles is less than 71 μm. A csda average-energy-loss model was applied to estimate energy losses.

The insult spectra and track density distributions should be applicable to cell-survival and lesion-prediction models. These distributions should permit statistical estimation of the spatial separation between lesions, for example, the probable number and spacing within DNA molecules. For alpha particles, absorbed dose is a robust concept, in that it is relatively insensitive to most parametric variations. It is also not expected to play a major part in attempts to relate a specific biological response to a specified insult or even in attempts to relate a mean biological response to a specific insult.

To retain generality, it is necessary to construct a calculational analog of the tracheobronchial (TB) tree which produces operators that are not bound closely to geometrical and biological parameters. These parameters include particle attachment, relative concentrations, dichotomy specifications, deposition rate, clearance rate, wall thickness, and areas of metaplasia. The parameters relate in-air concentrations and insults to a specific cell nucleus or estimate dose-specific risk. The analog should be constructed so that additional geometrical or biological refinements do not disrupt the basic application of physics or void all previous specifications. The first step for generality requires that all insult parameters be related directly, according to the theory of probability, to one disintegration of each particular radon daughter somewhere in the bronchial truncation of interest.

A cross-sectional portion of the bronchial epithelium is shown in Fig. 4.3. Cells that interface the basement membrane are subjected to lower insult levels than ciliated and goblet cells in the transbasal layer. It is strange that only the basal cells in the human TB tree have been considered to be important, because the goblet cells are involved in mucus production, as are the Clara cells. Usually, any neoplasm goes undetected until its 30th generation (1 g); and until death occurs (usually

26. J. S. Bevan and A. K. M. M. Haque, *Phys. Med. Biol.* 13(1), 105 (1968).
27. H. H. Smith and H. H. Rossi, *Radiat. Res.* 28, 302 (1966).
28. L. J. Cole and P. C. Nowell, *Science* 150, 1782 (1965).
29. P. C. Nowell, "The Clonal Evaluation of Tumor Cell Populations," in *Report of the Task Group on Reference Man*, ICRP Publication 23, International Commission on Radiological Protection, Pergamon, Oxford, 1975 [*Science* 194 (1976)].
30. Paul Todd, *Radiat. Res.* 34, 378 (1968).
31. P. Todd et al., *Life Sci. Space Res.* 11, 261 (1973).
32. R. M. Gastineau, P. J. Walsh, and N. Underwood, *Health Phys.* 23, 857 (1972).

ORNL-DWG 75-14838

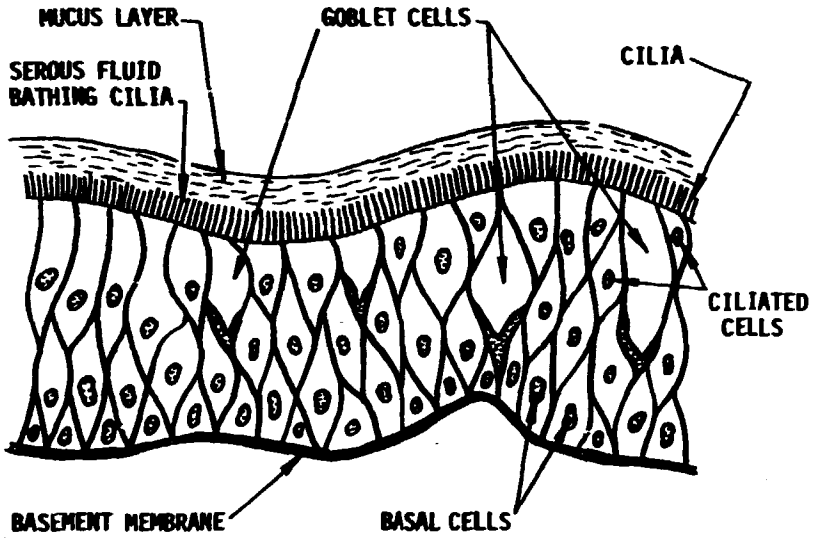

Fig. 4.3. A portion of the bronchial epithelium shown in cross section.

bout the 40th generation), it seems unlikely that pathologists could track its clonal development back to specific cells in a heterogeneous region.

Figure 4.4, based on pathological and modal assumptions,[32,33] estimates normal basal cell depth as a function of bronchial diameter. These estimates include a 14-μm layer (7 μm of mucus plus 7 μm of serous fluid) which insulates the bronchiole from the air in the lumen. Dimensions of the mucus and cilia vary slightly, according to location in the TB tree, age of the person, frequency of tobacco smoking, etc.[32,33] Such dimensions were assumed to remain constant in the calculational analog.

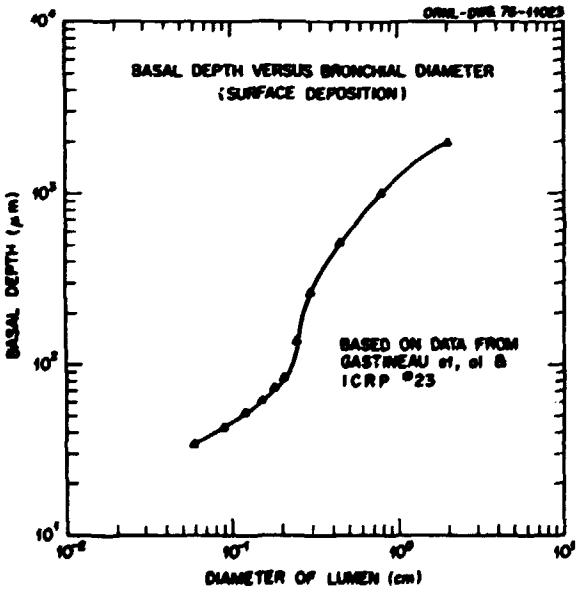

Fig. 4.4. Basal depth vs bronchial diameter (surface deposition).

This treatment assumes that point kernels are deposited randomly and uniformly within the analog truncation of interest, as shown in Fig. 4.5. It is also assumed that the randomly oriented particles are transparent to the reaction products. The location of the point of detection within a specific basal cell will have absolutely no influence on the selection probability of a specific source kernel, because inverse square and attenuation are accurately estimated by the CHORD process. The ^{218}Po, ^{214}Pb, ^{214}Bi, and ^{214}Po are assumed to be deposited on the mucus that insulates the lumen. This provides one model; a second model is obtained by assuming that the kernels are readily and homogeneously absorbed by the mucus and underlying serous fluid which bathes the cilia. The assumptions used should represent both upper and lower bounds for any practical situation. Although the ^{222}Rn is readily absorbed by fluids, and can enter the blood stream in this way, the simulation will assume that all ^{222}Rn nuclear transitions occur in the lumenar volume of the TB system.

33. International Commission on Radiological Protection, *Report of the Task Group on Reference Man*, ICRP Publication 23, Pergamon, Oxford, 1975.

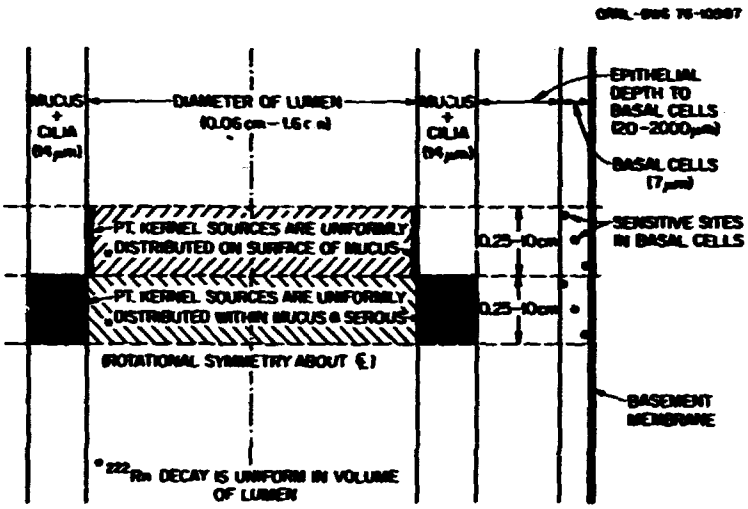

Fig. 4.5. Calculational analog of a tracheobronchial section.

The distribution of an absorbed dose, $D_\beta(l)$, about point isotopic kernels for ^{214}Pb and ^{214}Bi was estimated according to Berger.[34] The distance from the source is designated by l. Beta doses to radiosensitive sites for a given source are then computed according to the equation:

$$\bar{D}_\beta = \pi dh \Sigma D_\beta(l) P\{l\} \Delta l \ (\text{keV cm}^{-2}\ \text{pg}^{-1}), \qquad (7)$$

where d and h are the diameter and height, respectively, of the TB truncation, and $P\{l\}\Delta l$ is the CHORD operator.

Figure 4.6 illustrates the beta dose to a basal cell of the bronchial epithelium as a function of lumen diameter for the analog truncations. The extreme diameters vary by a factor of 27 and the corresponding heights vary by a factor of 40, but the beta dose per disintegration in the lumen varies only by a factor of 2.

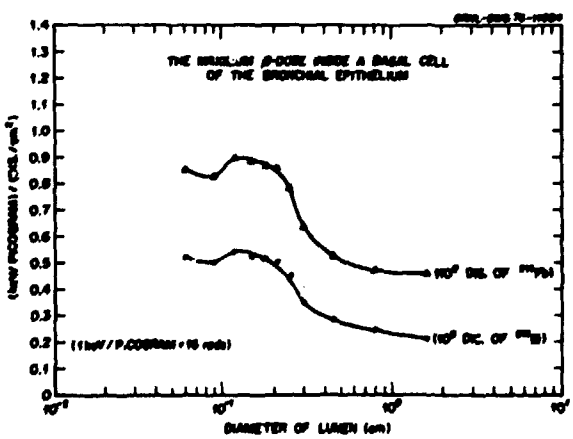

Fig. 4.6. The maximum beta dose inside a basal cell of the bronchial epithelium.

The alpha dose at a detection site such as a basal cell can be expressed as:

$$\bar{D}_\alpha = \frac{\Sigma \Delta E}{\Delta m} =$$

$$\frac{\sum \left(\frac{\pi \epsilon^2}{4\pi l^2} \frac{dE}{dX} \frac{\text{keV}}{\mu\text{m}} \right)_{X=R-l} (4/3\, \epsilon \mu\text{m}) P\{l\} \Delta l \pi dh \ \text{cm}^2}{(4/3\, \pi \epsilon^3 \mu\text{m}^3)\ (1\ \text{pg}/\mu\text{m}^3)}, \qquad (8)$$

where ϵ is the radius of the small spherical detector, and R is the range of the alpha particle corresponding to its source energy. Sample results and comparisons[35,36] are shown in Fig. 4.7.

ANALOG DEVELOPMENT FOR INSULT-SPECIFIC RISK FROM ENERGY CONVERSION

Estimations of morbid and mortal disease rates from specific insult levels for workers and the general public when they have been exposed to chemical releases from coal conversion processes currently depend on underdeveloped methodologies. As a consequence, the few existing protection guidelines for exposure to chemical releases are reminiscent of those based on erythema doses in the early days of ionizing radiations. Chemical releases from coal-powered plants contain many known

34. M. J. Berger, *J. Nucl. Med.* (Suppl. 5) 12, 10 (1971).

35. A. E. Desrosiers, Department of Physiology, School of Public Health, Harvard University, personal communications.

36. N. H. Harley and B. S. Pasternack, *Health Phys.* 23, 771 (1972).

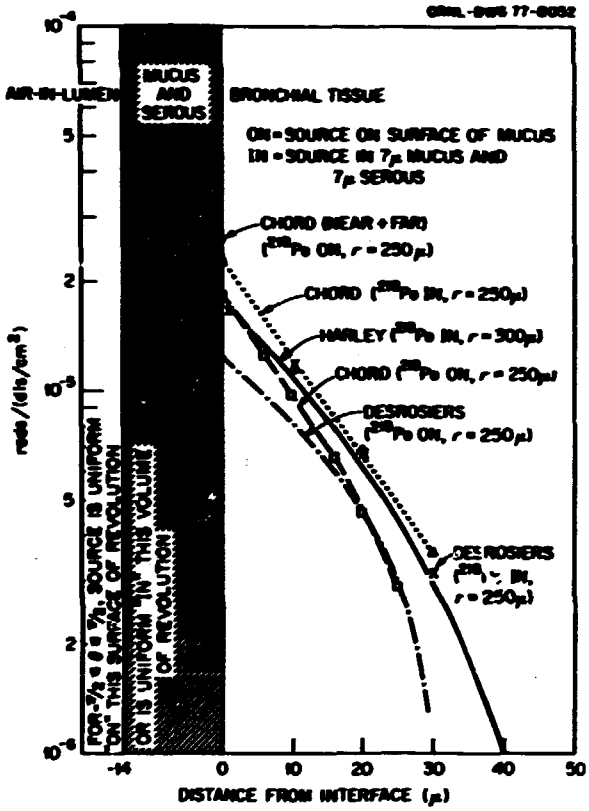

Fig. 4.7. ^{210}Po alpha dose from the near wall per disintegration inside the lumen.

carcinogenic initiators, and existing knowledge is simply inadequate to establish acceptable exposure levels. It is commonly expected that 50% to 90% of all cancers are environmentally produced, and chemical insults need to be investigated with precision enough to determine how to avoid many cancers. Presently, one death in every four is attributed to cancer. Any energy alternative should not increase this risk.

In the attempt to refine techniques used to estimate excess disease rates and appropriate protection guidelines, it is necessary to develop appropriate calculational biophysical analogs in the fashion of those used in Monte Carlo transport calculations of the action of ionizing radiations on biological tissue (e.g., the ICRP lung model and the ICRP reference man analog). Areas of investigation can be broadly grouped into simulation of (1) representative exposure environments, (2) temporal distribution in critical tissues of man from ingestion, inhalation, absorption, and surfactant processes, and (3) associated risk factors for important cancer-initiating agents.

The simulation techniques necessary to assess the increased frequency of morbidity or mortality associated with a specific insult level depend on presently developing technologies involving site releases, chemical attachments, atmospheric transport, in situ air monitoring, aerosol physics, bioassay measurements, observation of health effects through epidemiological-type investigations, neoplastic-damage mechanisms, and cytological observations. The purpose of analog development is to relate biological endpoints, such as cancers and other abnormalities determined by epidemiological investigations, to specific organ insult levels. This is done by observations of laboratory animals (and, in limited cases, men) that have been subjected to inhalation, ingestion, or epidermal absorption of insults of SO_2, H_2SO_4, benzopyrene, NO_x, CCl_4, PNA, etc. It should then be possible to relate these response-specific insult levels to in-air concentration rates and particle-size attachment distributions for occupational and population exposures. In addition, sputum cytology appears to be an excellent indicator of an early adverse biological response to many agents when entry is via inhalation. Investigations of consistent cytogenetic abnormalities through pathology and/or sputum cytology, regressed on basic insult-specific parameters such as chemical form and distribution within body tissues, are expected to help reveal damage mechanisms which should serve as the basis for risk assessment.

Figure 4.8 illustrates the process by which the conversion of basic resources results in some biological insult through modification of the environment. These insults can be broadly grouped into chemical, ionizing, and nonionizing pollutants. The agents are released and then transported through the environment. Chemical and ionizing agents may enter into the biosphere before final entry into the organism of interest. The biosphere is of interest because food supply serves as a vehicle for entry into man, and some agents only become cancer initiators after chemical conversion through metabolic-type processes. In cases where there appears to be no biological modification and latent effects are not expected, more detailed investigations seem unwarranted.

Most insults of a nontrivial level appear to produce many observable biological responses and even cancer; thus it is imperative to investigate macroscopic transport events inside the organism (absorbed dose, in the case of ionizing radiation). The regression of biological response to the frequency of these transport events will permit a gross risk analysis and may help establish protection levels. However, to investigate initiating agents, neoplastic transformations, basic damage mechanisms, promoting agents, inhibiting agents, synergistic effects, cocarcinogenicity, therapy, etc., it is necessary to inves-

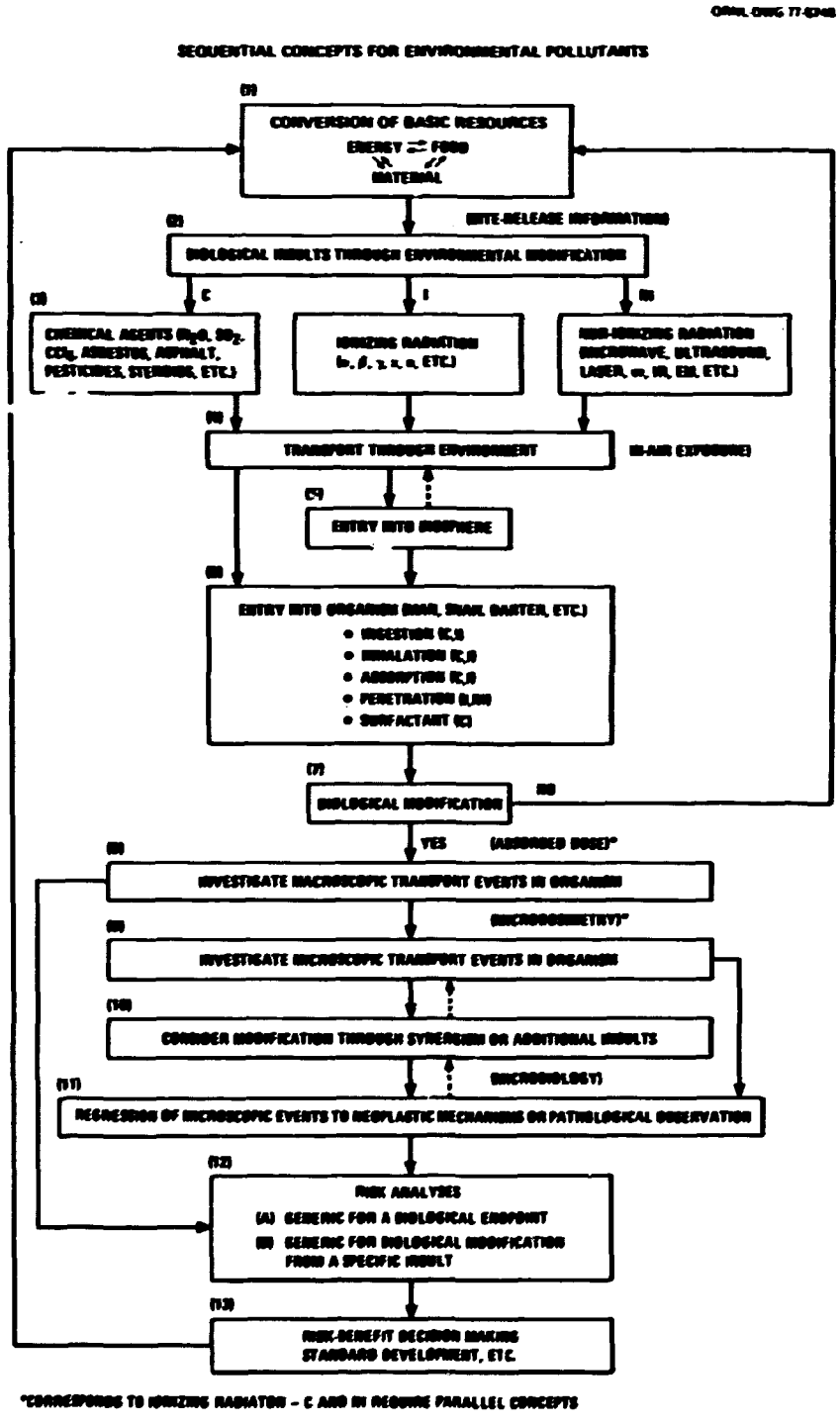

Fig. 4.8. Sequential concepts for environmental pollutants.

tigate microbiological responses to the frequency of basic microscopic chemical and physical changes as estimated from insult assessments. This would mean a study of energy, spatial, and temporal distribution of reaction products for ionizing radiations. As illustrated in Fig. 4.8, various sequential concepts may be bypassed; however, one must then guess at long-term risks and costs.

The basic neoplastic or damage mechanisms for chemical insults are not clearly defined at this time.

Laboratory investigations indicate that carcinogenesis is often observed to be a two-step process – *initiation* of precarcinogenic lesions and *promotion* into a neoplasm. Neither step appears sufficient without the other. Neoplastic transformations are not even consistent relative to chronological sequence or elapsed time between the steps. Man, in contrast to laboratory subjects, does not live in a sterile environment and is subjected to many known and perhaps unknown tumor promoters. These include serum cholesterol, tobacco smoke, alcohol, nutritional factors such as vitamin C, bile acids, etc. Everyone is subjected to tobacco smoke and perhaps many other promoters; therefore, calculational analogs should consider carcinogenesis as a one-step process only – initiation. It is recognized that some initiators applied in a certain fashion do not necessarily result in neoplastic transformations. This has been observed in smoking experiments done with animals, even though tobacco smoke has both initiators and cocarcinogens that are capable of promotion. The level of the biological response often seems to be proportional to the degree of localized insult. For example, insult levels of various degrees seem to produce biological responses which include hypersecretion, removal of cilia from ciliated cells, edema, hyperplasia, bronchoconstriction, laryngeal spasm, and damage and inhibition of mucus and serous secreting cells. Thus, the basic action of noxious or carcinogenic chemicals on biological tissue appears to be irritation. Secreting cells (such as Clara and goblet) and clearance cells (such as ciliated and phagocytic) are expected to be extra-sensitive, as observed in studies involving ionizing radiations.

Squamous cells are expected to suffer a greater risk from localized (nonpenetrating) insults, such as from polynuclear aromatic hydrocarbons (PNA), NO_x, and SO_2, because of their shallow locations and the fact that their nucleus protrudes from the cell. The basal cells of the bronchial epithelium seem quite sensitive to penetrating insults, as found in uranium miners; however, they are at greater depths and should be protected from the direct action of chemical carcinogens by mucus, serous, and other transbasal layers. Basal cells are not expected to be exposed to the direct action of chemical carcinogens, as evidenced by mouse skin papillomas, which are initiated in skin which is normally two cell layers deep. If, however, the degree of insult causes damage to secretory processes and sloughing of these upper layers, then the basal cells must be cause for concern.

Basal cells are of special importance because observations of insulted cells through electron microscopes have indicated that upward migration becomes abnormal, thus resulting in edema, hyperplasia, or even neoplasia. Our initial treatments will concentrate on the upper layer of cells, in the case of the epidermis, and on those cells having direct contact with the mucus, in epithelial tissue.

5. Radiation Measurements and Assessments

F. F. Haywood

D. L. Anderson
J. E. Burden[1]
W. D. Cottrell
H. W. Dickson[2]
R. W. Doane
B. S. Ellis[3]
C. A. Golden[4]
W. A. Goldsmith
R. E. Hamilton
P. M. Lantz
R. W. Leggett
D. K. Lorenzo[5]
P. T. Perdue
M. T. Ryan
W. H. Shinpaugh
S. S. Stockstill
D. R. Stone[1]
E. B. Wagner
W. M. Johnson[4]

In 1975, the Offsite Measurements Group was organized to perform a radiological assessment of the former Vitro Corporation of America Uranium Mill in Salt Lake City, Utah.[6] The work of this group was designed to measure and evaluate radiation-field characteristics and to provide information needed to assess the magnitude of potential radiation hazards to the public and to onsite workers, whether temporary or permanent. These objectives required that we develop improved techniques for measuring components of the natural radiation environment in the presence of man-made radiation through a description of the radionuclides in samples of environmental origin. The capability to make such detailed measurements permits an evaluation of the effectiveness of control measures designed to limit the amount of radioactivity discharged to the environment.

Offsite studies are facilitated by mobile laboratories complete with state-of-the-art equipment. Radiological survey programs include measurements of existing radiation fields; airborne radon, radon daughters, and other radionuclide concentrations; collection of environmental samples and subsequent analysis for specific radionuclides; and characterizations of residual surface contamination inside and outside structures, as well as underground deposits of radioactivity.

After completion of the Vitro survey in Salt Lake City, the group's activities were expanded to include assistance in resurveying facilities formerly controlled by the Manhattan Engineering District (MED) and, later, the Atomic Energy Commission (AEC). Many of these had been relinquished from governmental controls in the absence of adequate radiological survey data. This project received substantial attention after the General Accounting Office released a report identifying specific properties involved and urging ERDA to facilitate resurvey to document current radiological conditions. The ultimate objective of ERDA's resurvey program is to release all properties for unrestricted use so that no continual or periodic surveillance will be required in future years or to ensure control of site use where complete decontamination is impractical by placing the site under appropriate state or federal regulatory control. Based on the results of radiological surveys in this program, remedial action criteria will be developed using an as-low-as-reasonably-achievable (ALARA) approach. It is conceivable that some structures may have to be demolished to minimize exposure hazards and to meet the objectives for unrestricted use. Others will require varying degrees of decontamination, and some facilities will require no action at all. After the completion of remedial measures, follow-up radiological surveys will be needed to certify their effectiveness.

---

1. Consultant.
2. Dual capacity.
3. On loan from Biology Division.
4. Radiation and Safety Survey Section.
5. Georgia Institute of Technology, Atlanta.
6. F. F. Haywood et al., *Assessment of the Radiological Impact on the Inactive Uranium Mill Tailings Pile at Salt Lake City, Utah*, ORNL/TM-5251 (in preparation).

The need for uranium grows continuously; therefore, more and more attention is being focused on ways in which to recover known deposits throughout the country. During the 1950s, some uranium was recovered from wet-process phosphoric acid in pilot operations in central Florida. Plans are now under way for commercial recovery of the uranium in phosphoric acid. Several techniques are being considered. One of these requires that uranium be extracted into solution from the main stream of phosphoric acid, hauled to a central processing plant, stripped, precipitated, calcined, packaged, and shipped to a conversion plant. Such a process would produce several hundred metric tons of uranium per year. The Offsite Measurements Group is engaged in an EPA-sponsored cooperative study with the Chemical Technology and Environmental Sciences Divisions which is designed to determine the radiological impact of the recovery of the uranium from phosphoric acid. The group's specific objective is the verification of source terms in effluent releases as calculated by W. W. Davis of the Chemical Technology Division.[7]

RADIOLOGICAL SURVEYS AT INACTIVE URANIUM MILLS

In the operation to separate uranium from an ore matrix, waste residues (sand and slime tailings) are usually stored on mill property. These mills are frequently vacated with little, if any, attention given to preparation of tailings for long-term storage or disposal. There are 22 such sites in 8 western states. The first of the surveys of these sites was performed in late 1975 in Salt Lake City, Utah. Surveys at the other 21 mill sites were conducted during the period February 23, 1976, to September 24, 1976. Details of the survey schedule are presented in Table 5.1.

The approach used in these studies is that of an evaluation of the various pathways by which man is exposed to radioactivity from the tailings. Pathways considered included (1) radon diffusion from the pile, (2) radioactivity that becomes airborne due to wind, (3) radioactivity that is ingested through the intake of food grown on contaminated land, (4) radioactivity that enters the body directly or indirectly through the aquatic paths, and (5) exposure to direct gamma radiation. Details of these exposure pathways are given in Table 5.2.

7. W. W. Davis, Jr., et al., *Correlation of Radioactive Waste Treatment Costs and the Environmental Impact of Waste Effluents in the Nuclear Fuel Cycle Reprocessing of High Temperature Gas Cooled Reactor Fuel Containing U^{233} and Thorium*, ORNL/NUREG/TM-4 (May 1976).

Table 5.1. List of mill sites surveyed by the Offsite Measurement Group

Inactive mill site	1976 Survey		No. water samples	No. sediment samples	No. surface-soil samples	No. subsurface-soil samples
	Started	Completed				
Shiprock, N.M.	Feb. 23	Feb. 29	2	6	16	64
Monument Valley, Ariz.	Mar. 8	Mar. 10	5	2	22	38
Mexican Hat, Utah	Mar. 11	Mar. 14	5	6	30	19
Tuba City, Ariz.	Mar. 23	Mar. 27	4	3	47	24
Durango, Colo.	Apr. 5	Apr. 8	10	10	32	22
Slick Rock (1), Colo.	Apr. 9	Apr. 10	5	6	14	19
Slick Rock (2), Colo.	Apr. 10	Apr. 11	5	5	16	8
Gunnison, Colo.	May 3	May 7	15	7	25	14
Naturita, Colo.	May 8	May 16	5	5	27	4
Grand Junction, Colo.	May 12	June 3	11	6	28	56
Old Rifle, Colo.	May 18	May 23	[illegible]	5	25	8
New Rifle, Colo.	May 19	June 5	8	6	23	24
Maybell, Colo.	May 22	May 27	6	3	24	13
Ambrosia Lake, N.M.	July 13	July 15	9	3	36	8
Green River, Utah	July 16	July 18	4	4	35	7
Riverton, Wy.	July 25	July 28	9	6	13	30
Converse County, Wy.	July 29	July 31	6	5	25	5
Falls City, Tex.	Aug. 12	Aug. 15	29	9	44	
Ray Point, Tex.	Aug. 16	Aug. 17	7	4	35	
Lake View, Ore.	Sept. 13	Sept. 17	14	14	15	
Lowman, Idaho	Sept. 19	Sept. 24	5	5	16	

Table 5.2. Principal radionuclides involved in pathways from tailings piles to man

Pathway	Radionuclides	Pathway processes	Exposure hazard
Radon diffusion	^{222}Rn	Diffusion to pile surface; atmospheric transport; inhalation	Inhalation of ^{218}Po, ^{214}Pb, ^{214}Bi, ^{214}Po
Airborne activity	^{230}Th	Resuspension from pile surface; atmospheric transport; inhalation; body surface contamination	Inhalation of airborne activity carried by respirable particles
Terrestrial	^{226}Ra	Resuspension from pile surface; atmospheric transport; deposition on soil or foliage; uptake by plants; uptake by animals; consumption of contaminated plants, meat, and milk; consumption of contaminated soil	Ingestion of ^{226}Ra
Aquatic	^{226}Ra	Dissolution of radionuclide in pile; migration through soil to water; migration in water; uptake by aquatic organisms; consumption of aquatic organisms; use of water for irrigation; uptake by plants; consumption of plants; consumption of contaminated drinking water; immersion in contaminated water	Ingestion of ^{226}Ra
External gamma	^{226}Ra daughters	Attenuation by pile material; air-distance attenuation; external exposure	External exposure to gamma radiation produced by the decay of ^{226}Ra and its daughters

For the piles in their present condition, measurements are made to determine the extent to which radioactivity has spread to areas away from the site and to evaluate the exposure conditions that exist. In most cases, radium contamination may be found ranging to a depth of 3 ft below the tailings. However, due to the error associated with sampling techniques and the possibility of some degree of cross-contamination in regions where samples of soil are collected, the actual downward migration of radium and other radionuclides is probably less than that indicated by radioactivity profiles as a function of depth below the surface. Also, the soil base under the tailings changes substantially from site to site. Hard subsurfaces exist in several desert regions such as Ambrosia Lake, New Mexico; Monument Valley, Arizona; and Maybell, Colorado. However, several tailings piles are located on river floodplains. The soil in these areas consists of sand, clay, and river rocks, which created a difficult sampling situation. Often, it was impossible to obtain intact soil samples using available techniques. Therefore, it was necessary to estimate the concentration of ^{226}Ra as a function of depth and confirm the depth of the tailings soil interface, using a collimated gamma-ray detector.

The Offsite Measurements Group and the engineering firm of Ford, Bacon and Davis, Utah, worked jointly to perform the radiological surveys and engineering studies required to evaluate public radiation exposure (both real and potential) attributable to these piles.

Field and laboratory measurements made during the course of this program were designed to determine the exposure associated with each of the pathways mentioned in Table 5.2. The objective of the measurements was to determine the magnitude of source terms both onsite and offsite. Of principal concern were the levels of radon and its daughters in the air in residential and commercial areas and the extent to which particulate contamination had spread to areas surrounding each mill site. These problems were evaluated by making measurements of the radionuclide concentrations in samples of soil underlying the tailings, from surface stream sediments, and from soil on property adjacent to the mill sites. In addition, water samples were obtained from private wells, surface streams, and holes that were drilled or dug on the site.

Gamma-ray measurements as a function of distance from a tailings pile were made to determine the potential hazard due to direct exposure to external

gamma rays at points where the public has access to each site.

Radon and Radon Daughter Sampling

Most of the buildings at the mill sites have been demolished and the materials salvaged. However, a few remain in use. In Shiprock, New Mexico, one building, used as a school for teaching heavy-equipment operating skills, is operated by Navajo Indians. During the course of these studies, radon concentrations were measured by Ford, Bacon and Davis, Utah. Instruments used for this purpose were developed by Wrenn, Spitz, and Cohen.[8] Radon daughter concentrations were measured by the Offsite Measurements Group, using alpha spectroscopy techniques as refined by Kerr.[9] One typical example of the observed concentrations of radon and radon daughters is given in Fig. 5.1. These data were collected over 24 hr in the school mentioned above. It is seen that during the early morning hours when physical activity is at a minimum, the apparent disequilibrium between radon and its daughters widens. This is due to the settling out of condensable nuclei in the air. Most measurements of this type may be used only as an indication of instantaneous concentration of radon and its daughters. To estimate average annual exposure conditions, it is necessary to sample for periods much longer than 24 hr, during periods of representative activity, and during all seasons of the year. It should be pointed out that the alpha spectroscopy technique used to evaluate the air-sample filters in this study is not an automated system. Although it provides badly needed characteristics of the total radon daughter activity, it must be manned during operation. A preliminary concept for an automated version of this instrument has been developed, and it is hoped that a prototype can be fabricated within the next two years.

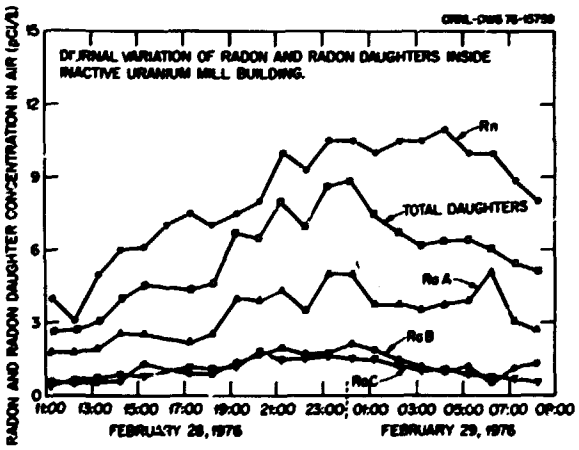

Fig. 5.1. Radon and radon daughter concentration in air (picocuries per liter).

^{226}Ra Profiles in Soil

Many of the tailings piles (especially those in Colorado) have been contoured, covered with a few inches of soil, and planted with vegetation. This minimal action is sufficient only to reduce the amount of material that is resuspended in air and subsequently deposited on the ground in downwind directions. The concentration of radium as a function of depth in soil is determined by collecting samples of soil at known depths and analyzing the samples by gamma-ray spectroscopy. Most samples were obtained using a "split-spoon" sampler; however, at sites situated on hardpan and on floodplains of rivers, it was difficult to drill through the accumulation of riprap. In such cases (Shiprock, New Rifle, Old Rifle, Grand Junction, and Durango), a motorized backhoe was used to excavate a trench from the surface through the tailings-soil interface. Samples were then collected at 1-ft intervals below the surface.

Radium profiles were also determined by logging bore holes with a collimated gamma-ray detector which was calibrated in a test pit in Grand Junction, Colorado. An example of the ^{226}Ra estimates in soil as determined by both gamma-ray "logging" and by gamma-ray analysis of soil samples is presented in Fig. 5.2, which represents the profile in soil along the edge of the large pile at Durango, Colorado. Agreement between these two techniques is good, and results confirm the position of the interface at about 2.5 ft below the surface.

---

8. M. E. Wrenn, H. Spitz, and N. Cohen, *IEEE Trans. Nucl. Sci.* NS-22, 645 (1975).

9. G. D. Kerr, *Measurement of Radon Progeny Concentrations in Air by Alpha-Particle Spectroscopy*, ORNL/TM-4924 (1975).

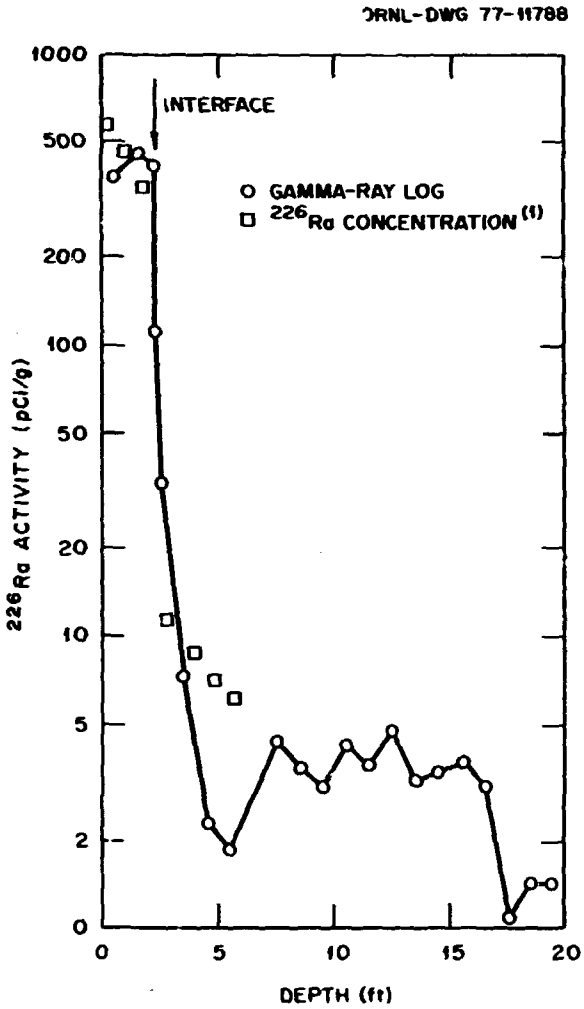

Fig. 5.2. Concentration of ^{226}Ra as a function of depth in soil near the base of the large pile at Durango, Colo.

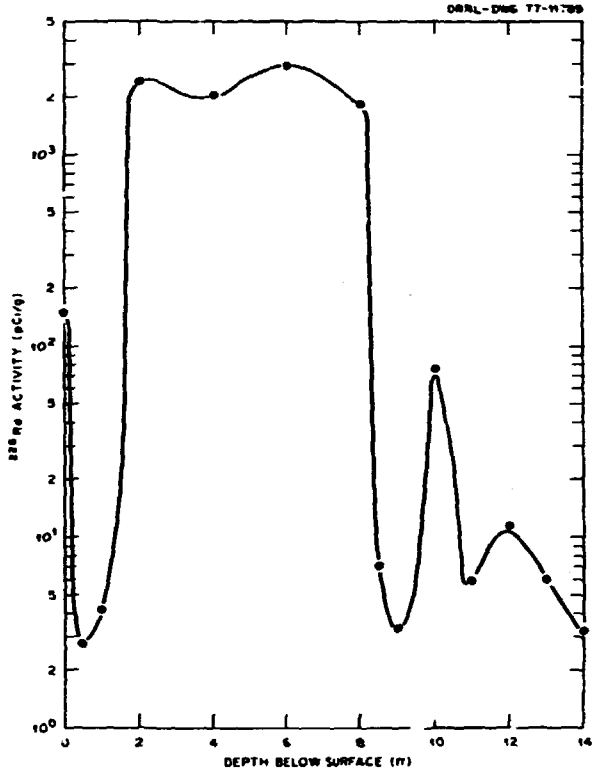

Fig. 5.3. Concentration of ^{226}Ra as a function of depth in test pit on the upper pile at inactive uranium mill in Shiprock, N.M.

The two piles at Shiprock, New Mexico, are situated on very hard soil. Also, considerable debris buried in the upper pile presents a difficult situation for drilling. Therefore, a test pit was dug on each pile. The ^{226}Ra profile in the upper pile is given in Fig. 5.3. In this case, the interface appears to occur at a depth of 8.5 ft, with slight anomalies down to 12 ft.

In Rifle, Colorado, the Union Carbide Corporation operated mills in two locations, both on the Colorado River floodplain. Because the rocky nature of the subsoil at the New Rifle site made drilling difficult, a backhoe was used to dig a test pit about 50 yd from the base of the tailings pile. Results of the samples from this pit are presented in Fig. 5.4.

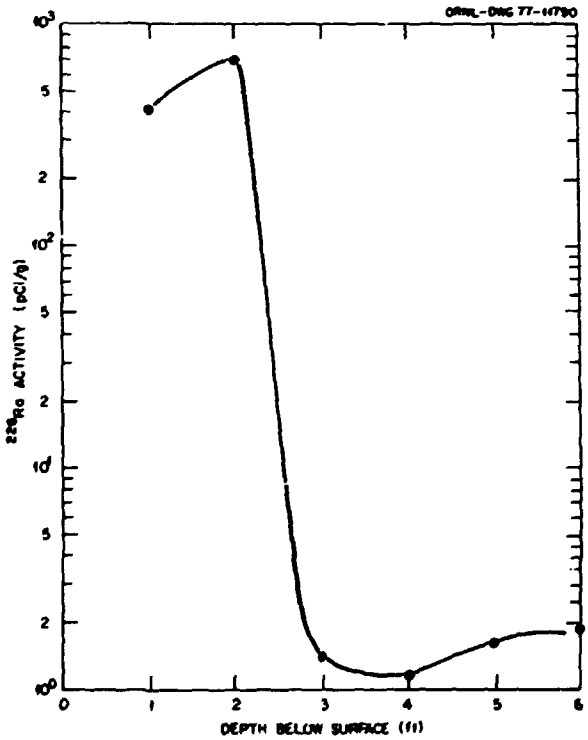

Fig. 5.4. Concentration of ^{226}Ra as a function of depth in soil about 50 m from base of pile at inactive uranium mill at Rifle (New), Colo.

RADIOLOGICAL ASSESSMENT OF FORMER MED-AEC FACILITIES

In 1974, the AEC began a program to document the radiological conditions of several properties which had been used in the early days of the nation's atomic energy program and which had previously been released (as "excess" property) from government control. This survey program was inherited by the Energy Research and Development Administration (ERDA) when it took over many of the AEC's functions in 1975.

Several of the excess sites were used more than 30 years ago in the Manhattan Engineering District's (MED) project which developed the atomic bomb; others were used from the late 1940s through the 1950s or 1960s. For the most part, these sites comprise either undeveloped land where low-level radioactive wastes were stored, or industrial plants where uranium or thorium was extracted from ores and scrap or was made into metal ingots, sheets, or bars. Prior to their release, the sites were decontaminated according to guidelines then in use. However, documentation of residual levels of radioactivity was lacking or inadequate for several sites; in addition, resurveying was necessary in many cases because of the government's adoption of increasingly strict guidelines.

At the request of ERDA, the Assessment and Technology Section undertook the task of characterizing the radiological condition of the thirty-four sites listed in Table 5.3. Between September 1975 and April 1977, brief preliminary surveys were conducted at most of the thirty-four sites; and, at nineteen of these sites, levels of radioactivity approaching guideline limits were discovered, thus warranting formal surveys. The formal surveys began in March 1976, and the field work and final reports for at least seventeen of the sites are scheduled for completion by September 30, 1977. The status of each survey as of May 1, 1977, is described in Table 5.3. Aerial photographs or plan views of some of the sites are shown in Figs. 5.5 through 5.9.

The examples that follow serve to illustrate many of the survey techniques used in the radiological assessments of the excess sites. In the first example, some conclusions drawn from the survey results are also discussed.

The former Haist property (Fig. 5.5) in Tonawanda, New York, is a 10-acre tract which served as a disposal site for refinery residue generated by Linde Air Products (a divison of Union Carbide Corporation) during their period of participation in the refinery operations program of the Manhattan Engineering District. The site, now owned by Ashland Oil, Inc., is used for oil refining. Records indicate that from 1944 to 1946, about 8000 tons of residue comprising essentially low-grade uranium-ore tailings were deposited on the property and were spread out over roughly two-thirds of the site to a depth of 1 to 5 ft. Some of the residue was relocated by earth-moving equipment and by natural runoff, and a large amount of clean fill dirt was placed on the site. In addition, an estimated 30% to 40% of the residue was moved to the Seaway Industrial Park (Fig. 5.6) to prepare the site for construction of two large storage tanks. (It was decided that a separate survey of the Seaway property would be conducted.) The object of the survey performed by ORNL was to characterize the radiological condition of the former Haist property in a manner such that (1) possible health hazards resulting from real and potential uses of the site (and the residue) could be estimated; and (2) radiation levels in excess of the current guidelines could be identified.

To aid in the location and identification of measurement and sampling points, the former Haist property was laid off in a grid (Fig. 5.5). Scintillation survey meters were used for measurement of external gamma-radiation levels at 3 ft above the surface at the grid points and along fences, drainage ditches, and residue piles. Beta-gamma dose rates were measured with Geiger-Muller survey meters at the surface at each of the grid points. At points showing highest external gamma-radiation levels, and at several additional random points, holes were drilled with a motorized drilling rig to depths of 6 to 12 ft. Gamma radiation was measured as a function of depth in the core holes by lowering a scintillation probe inside the auger. This "logging" of the core hole was done as a first step in determining the depth of contamination in the soil. In addition, soil samples were taken from several of the

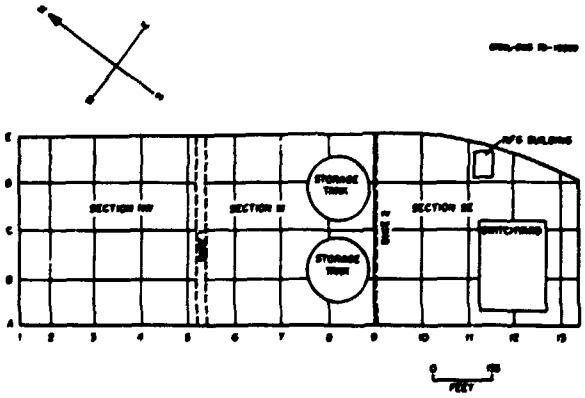

Fig. 5.5. Survey grid used at former Haist property.

Table 5.3. List of excess sites visited or surveyed by the Assessment and Technology Section

Site	Preliminary survey	Required survey	Field work	
			Started	Completed
1. Middlesex Sampling Plant Middlesex, N.J.	9/23/75	Yes	3/29/76	5/21/76
2. Ashland Oil Company Tonawanda, N.Y.	5/17/76	Yes	7/26/76	8/6/76
3. Seaway Industrial Park Tonawanda, N.Y.	7/8/76	Yes	8/9/76	8/13/76
4. Bridgeport Brass Company Adrian, Mich.	8/9/76	Yes	8/17/76	8/19/76
5. Columbia University New York, N.Y.	7/30/76	No		
6. Al-Tech Watervliet, N.Y.	8/19/76	No		
7. Seneca Army Depot Romulus, N.Y.	8/20/76	Yes	9/8/76	9/23/76
8. Hooker Chemical Company Niagara Falls, N.Y.	8/23/76	Yes	10/11/76	10/15/76
9. Electromet Niagara Falls, N.Y.	8/24/76	No		
10. Linde (UCC) Tonawanda, N.Y.	8/25/76	Yes	10/18/76	11/5/76
11. Bethlehem Steel Lackawanna, N.Y.	8/26/76	No		
12. Simonds Steel Lockport, N.Y.	8/26/76	Yes	10/9/76	10/15/76
13. Staten Island Warehouse Staten Island, N.Y.	8/18/76	No		
14. Mallinckrodt St. Louis, Mo.	10/14/76	Yes	7/14/77	9/16/77
15. Vitro Refinery Canonsburg, Pa.	1/12/77	Yes	3/14/77	7/1/77
16. E. I. du Pont Deepwater, N.J.	1/27/77	Yes	3/14/77	3/25/77
17. Joslyn Mfg. Company Ft. Wayne, Ind.	10/23/77	No		
18. Horizons, Inc. Cleveland, Ohio	10/27/77	Yes	2/6/77	2/18/77
19. Metal Hydrides, Inc. Beverly, Mass.	1/25/77	Yes	Deferred until FY 1978	
20. Westinghouse, Inc. Bloomfield, N.J.	10/21/77	Yes	Survey performed by property owner	
21. Bridgeport Brass Bridgeport, Conn.	1/26/77	No		
22. Kellex Corp. Jersey City, N.J.	10/21/76	Yes	3/28/77	3/31/77

Table 5.3 (continued)

Site	Preliminary survey	Required survey	Field work	
			Started	Completed
23. National Lead Company Winchester, Mass.	1/24/77	No		
24. Dow Chemical Company Pittsburgh, Calif.				
25. E. I. du Pont (SOHIO) Cleveland, Ohio	10/28/76	No		
26. Westinghouse, Inc. Pittsburgh, Pa.	10/22/76	No		
27. AEC Airport Storage Site St. Louis, Mo.	10/15/76	Yes	11/15/76	11/19/76
28. Penn. Railroad Blairsville, Pa.	3/16/77	Yes	Deferred until FY 1978	
29. International Minerals Mulberry, Fla.	4/6/77	No		
30. C. F. Industries Bartow, Fla.	4/6/77	No		
31. Conserv, Inc. Nichols, Fla.	4/4/77	Yes	Deferred until FY 1978	
32. Gardinier, Inc. Tampa, Fla.	4/5/77	Yes	Deferred until FY 1978	
33. W. R. Grace Bartow, Fla.	4/6/77	No		
34. U.S.S. Agri-Chemical Bartow, Fla.	4/4/77	No		

core holes and were returned to ORNL for determination of ^{238}U, ^{232}Th, ^{227}Ac, and ^{226}Ra concentrations. Water samples were collected from the drainage areas for determination of ^{238}U and ^{226}Ra concentrations. Finally, radon daughter concentrations in the air were measured in the only building on the site. These radon daughter concentrations were determined in the following way: First, air was flowed through a membrane filter to collect ^{222}Rn daughters attached to airborne dust; then, the filter sample was counted under a silicon surface-barrier detector; finally, quantities of the radon daughters were inferred from the counts measured for specific alpha peaks in the spectrum.

External gamma-radiation levels on the site averaged about three times the natural background level of 8 to 14 μR/hr. An external gamma-radiation profile of the former Haist property and adjacent areas is provided in Fig. 5.7. Continuous exposure to the highest gamma-radiation level measured would result in an integrated dose equivalent of about 1.6 rems/year, which is roughly 10 to 20 times the integrated dose equivalent from natural background radiation. However, it was estimated that onsite workers actually receive an integrated dose equivalent of less than 10% of the dose they receive from natural background radiation. The dose rate attributable to beta radiation appeared to be negligible.

Concentrations of ^{238}U and ^{226}Ra in over 200 soil samples taken on the site ranged from the background level up to about 500 to 1000 times this level, with the highest concentrations being measured in samples taken from covered sludge piles. To assess potential health hazards to the surrounding population from radon gas, a decay product of radium, average radon emanations were estimated from measured radium concentrations. Estimates were based on a differential equation which describes the diffusion of radioactive gases through soils (see, e.g., ref. 10). Estimated emanation rates for various sections of the site are shown in Fig. 5.8, where the numbers in each section represent picocuries per square meter per second. These numbers may be

10. M. V. J. Culot, H. G. Olson, and K. J. Schiager, *Radon Progeny Control in Buildings*, COO-2273-1, Colorado State University, Fort Collins, Colo., May 1973.

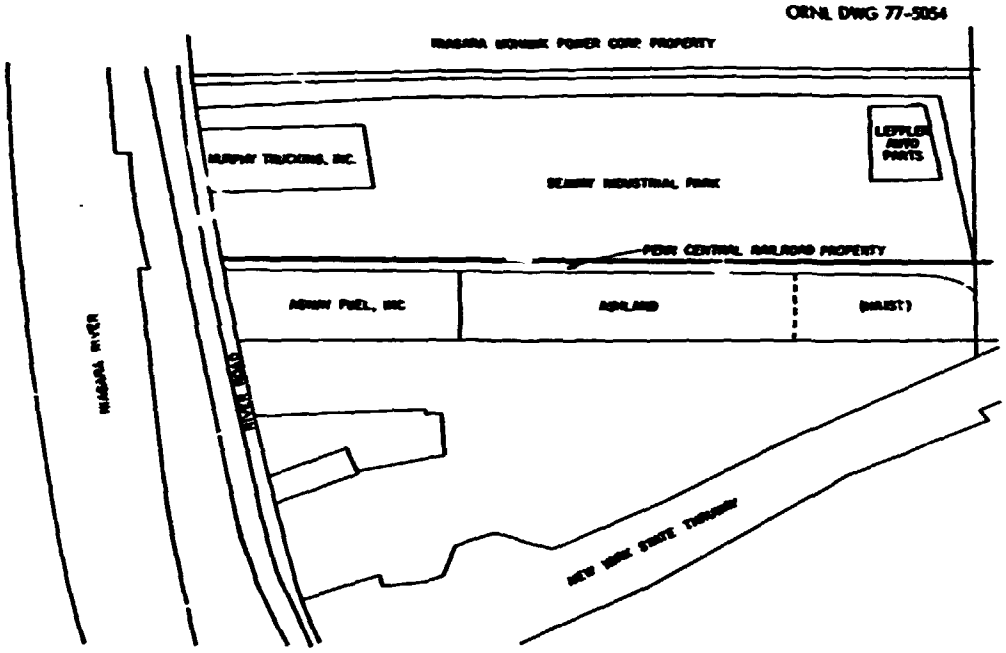

Fig. 5.6. Seaway Industrial Park, Ashland Oil Company, and surrounding area.

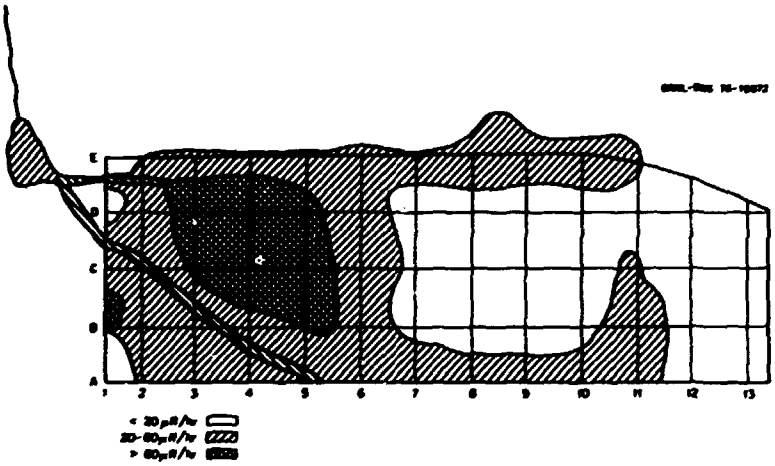

Fig. 5.7. External gamma-radiation profile of former Haist property and adjacent area.

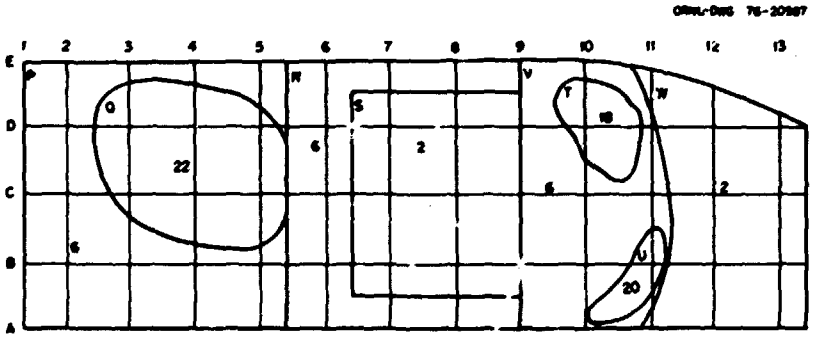

Fig. 5.8. Estimated average radon emanation rates from different sections of former Haist property (numbers in sections are in picocuries per square meter per second).

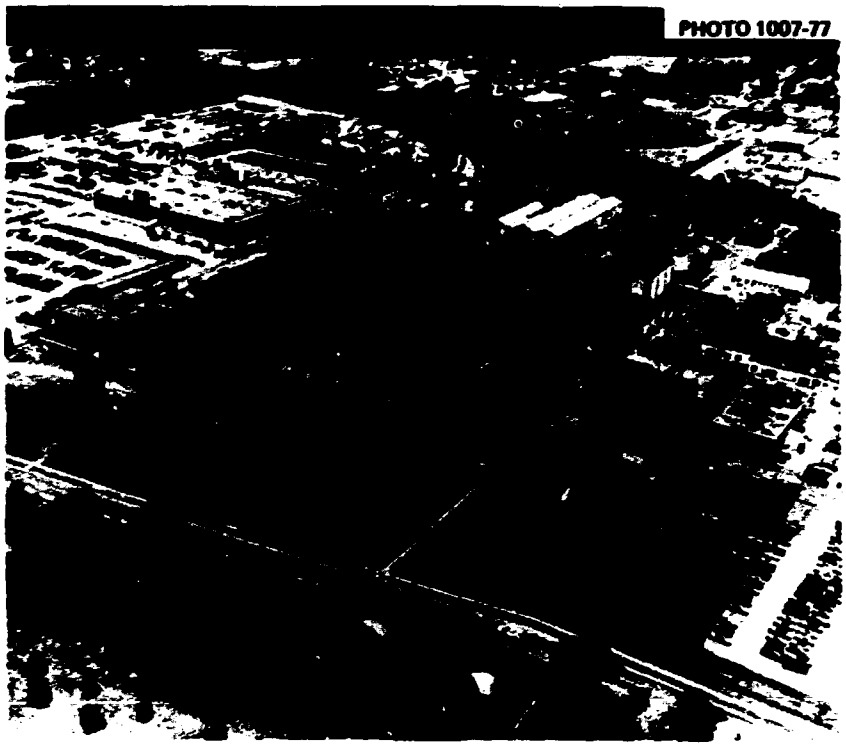

Fig. 5.9. Aerial photograph of Linde Plant site, Tonawanda, N.Y.

compared with the average worldwide background emanation rate of 0.40 to 0.50 pCi m^{-2} sec^{-1}. It was estimated that the total quantity of radon emanating from the former Haist property is roughly equivalent to that emanating from 150 acres of land with natural abundances of radium and that there are no distinct health hazards to the surrounding populations.

Concentrations of radionuclides in water samples taken from the site were several orders of magnitude below the maximum permissible concentrations. Furthermore, radon daughter concentrations in the only building on the site were well within current guidelines.

It was concluded that the residue on the site does not appear to pose any health hazards, assuming that the residue remains in place and that the site continues to be used for oil refining. It was pointed out in a final report, however, that health hazards could result from some uses of the site and the residue. For example, if a building with a basement were built on the site, potentially hazardous radon daughter levels could develop in the building.

To illustrate typical indoor survey procedures, we consider the survey conducted at Linde Air Products in Tonawanda, New York (Fig. 5.9). From 1940 to 194[illegible], this site was used for the conversion of U_3O_8 to UF_4. Five buildings, with a total floor area of more than 3 acres, were involved in these operations. Hence, in addition to an outdoor survey of the type conducted at the former Haist property, it was necessary to make extensive measurements of alpha and beta-gamma contamination levels over the interior surfaces of the buildings.

For the measurement of alpha and beta-gamma contamination levels, separate survey schemes were developed for each building, depending on the extent of contamination as determined in a preliminary survey. For example, the preliminary survey determined that alpha and beta contamination in Building 30 were widespread. The floor area in that building was divided into survey squares of about 5 by 5 m. In each survey square, smear samples were taken and counted to determine removable alpha and beta contamination levels; in addition, all accessible floor space was scanned with alpha scintillation survey meters and with Geiger-Müller survey meters, and average and maximum readings of each type were recorded for that square. The resulting figures (Figs. 5.10 and 5.11) indicate, at a glance, the extent of alpha or beta contamination on the floor in that building. In other buildings, such as Building 14 (Fig. 5.12) and Building 31 (Fig. 5.13),

ORNL DWG 77-6585

	A	B	C	D	E	F	G	H	J	K	L	M
26												
25												
24	0.34	5.14	0.57	1.14	0.29	0.29		0.34	0.34	0.29		0.29
23	0.34	0.57		0.46	0.57			0.57				
22	17.0			1.40	0.46			0.57	0.46			0.46
21				11.00				0.69				0.34
20		23.0		11.00	1.70			0.69	0.23			0.46
19	0.46	0.29	0.57	0.86	0.86			0.46	0.80			0.97
18	0.46	0.29	0.57	0.86	0.46			0.46	0.80			0.86
17	0.46	0.29	0.57	0.86	0.46			0.86	0.86			1.70
16	0.46	0.29	0.57	0.86	0.57			0.29	0.34			1.10
15	1.10	0.57	0.57	0.86	0.57			0.34	0.34			0.34
14	0.46	0.46	0.57	0.86				0.46	0.46			0.46
13	1.10	0.57	0.57	0.86	0.46			0.46	0.57			0.34
12	0.29	0.57	1.10	0.69	0.46			0.57		0.34	0.34	0.46
11	0.46	0.57	0.46	1.70	0.46			0.57	1.10	0.29	0.29	0.46
10	0.29	1.10	0.29	1.40	0.69				0.86	0.57	0.29	0.29
9		0.34	0.57	0.29	0.91			1.00	5.70	0.57	0.46	0.23
8	0.29	0.63	0.20	0.63	0.40	1.70	1.70	1.10	1.70		0.23	0.29
7	1.40	1.70	2.00	0.46	0.86	0.57	2.30	2.30	0.57	0.57	0.57	0.29
6		0.46	0.46	0.34	0.57	0.40		0.23	0.34	0.34	0.29	0.29
5					0.23							
4			0.20	0.20	0.20	0.20		0.20				
3					0.20	0.20		0.26	0.34	1.10	0.51	
2					0.23	0.40	0.63	0.23	1.40	1.10	0.57	0.57
1					0.86	0.57	5.70	1.10	1.10	0.57	0.57	0.29

N

0 40
FEET

Fig. 5.10. Maximum beta-gamma dose rates (exceeding 0.2 millirad/hr) in survey squares in Building 30 at Linde (readings in millirads per hour).

ORNL DWG 77-6583

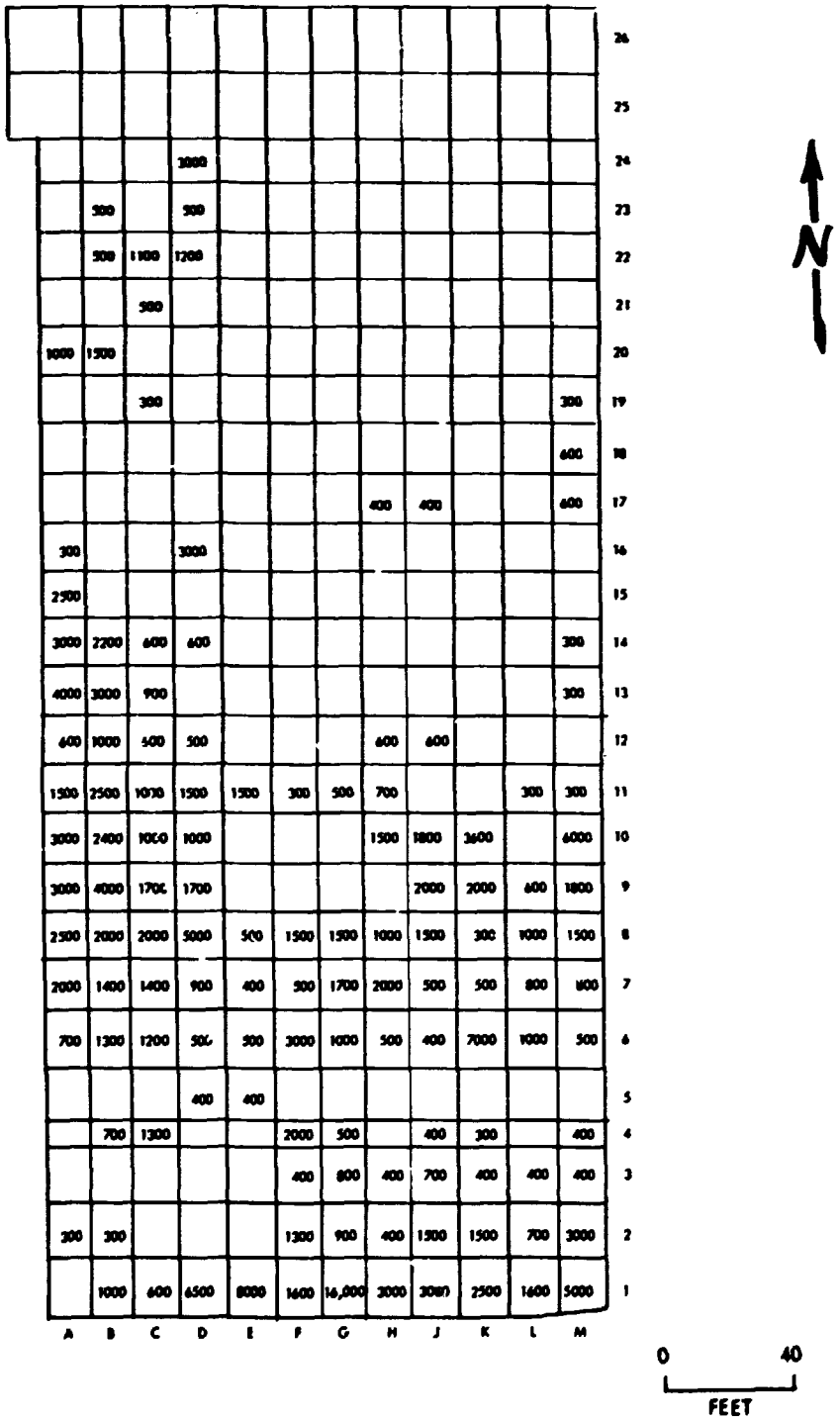

Fig. 5.11. Maximum direct alpha reading [exceeding 300 dis/(min · 100 cm²)] in survey on floor in Building 30 at Linde (readings in disintegrations per minute per 100 cm²).

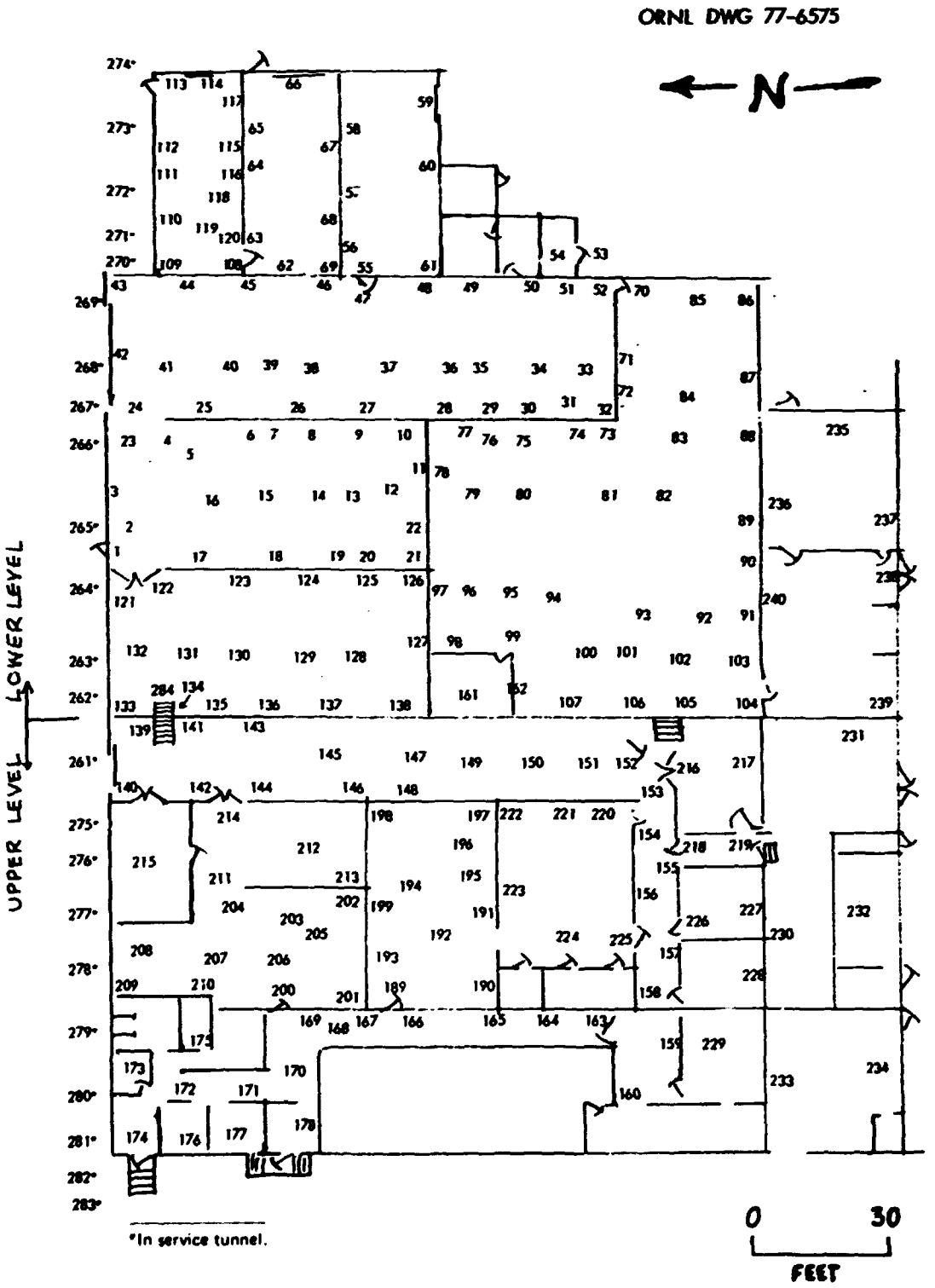

Fig. 5.12. Points of measurement on the floor in Building 14 at Linde.

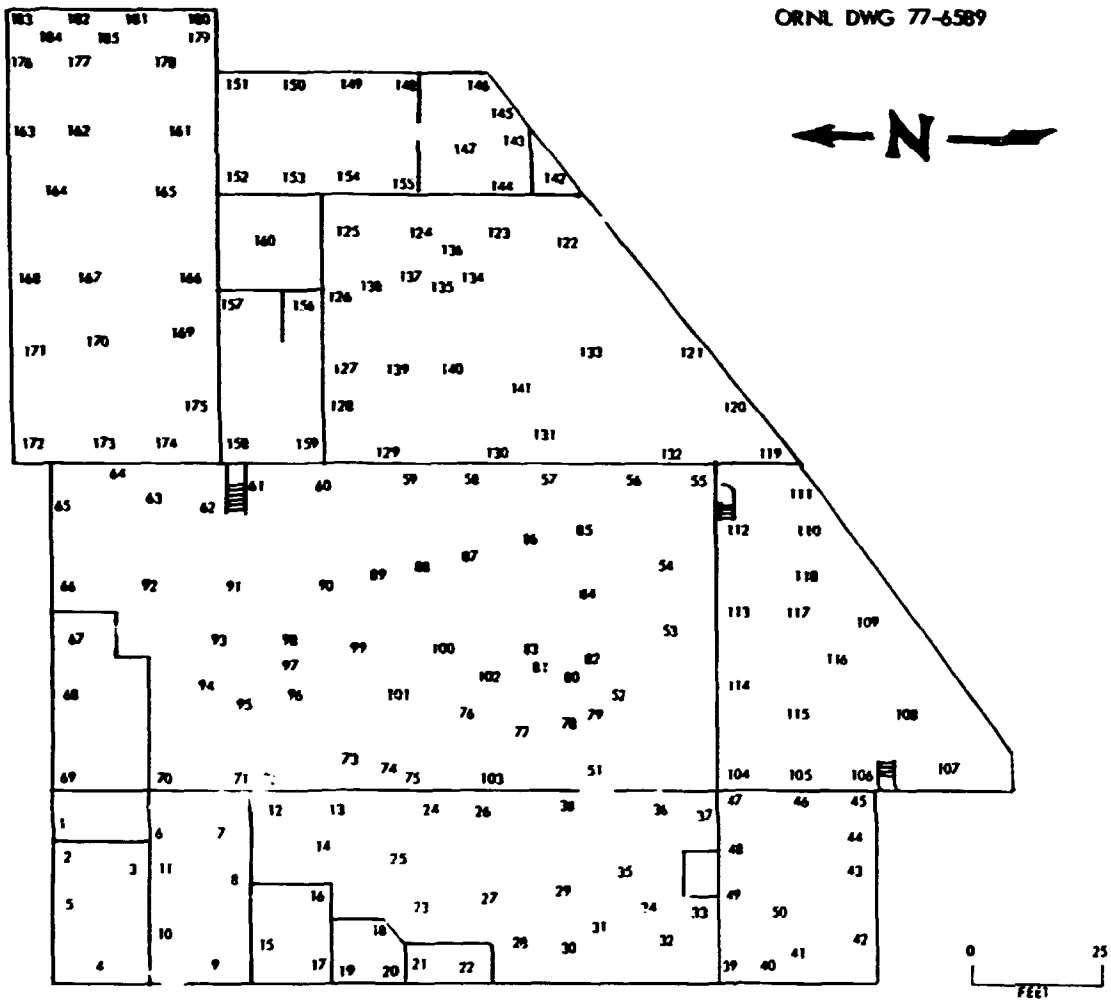

Fig. 5.13. Points of measurement on first floor in Building 31 at Linde.

measurements were made at closely spaced but randomly selected intervals.

Since decisions by ERDA concerning decontamination of surfaces depend, in large part, on whether alpha and beta-gamma contamination levels exceed guidelines[11] provided by the U.S. Nuclear Regulatory Commission (NRC), measurements must be taken so that results may be easily compared with the guidelines. Furthermore, since the NRC limits vary according to the radionuclides present, determination of applicable limits for each site must be made from analyses of samples taken from the site. This is illustrated by the following example.

The Simonds Saw and Steel Company in Lockport, New York, performed rolling mill operations on large quantities of uranium metal and smaller quantities of thorium metal during the period 1948 to 1956. Two large buildings on the site were used during these operations. Most of the elevated levels of radioactivity in these buildings appeared to be near the rolling mill area (Fig. 5.14). This area was divided by a 15-ft grid, and alpha and beta-gamma readings were taken at the grid points. Samples of floor dirt collected from this grid area showed that elevated concentrations of both ^{238}U and ^{232}Th (and associated daughter products of both) were present. Although NRC limits for alpha contamination are 50 times more restrictive for ^{228}Th, a daughter of ^{232}Th, than for ^{238}U, sample analyses indicated that ^{238}U was over 1000 times more abundant in most places than were any daughters of ^{232}Th. Hence, the limits for ^{238}U were applied to the rolling mill area.

11. U.S. Nuclear Regulatory Commission, *Guidelines for Decontamination of Facilities and Equipment Prior to Release for Unrestricted Use or Termination of Licenses for By-product Source, or Special Nuclear Material*, December 1975.

ORNL DWG 77-5063

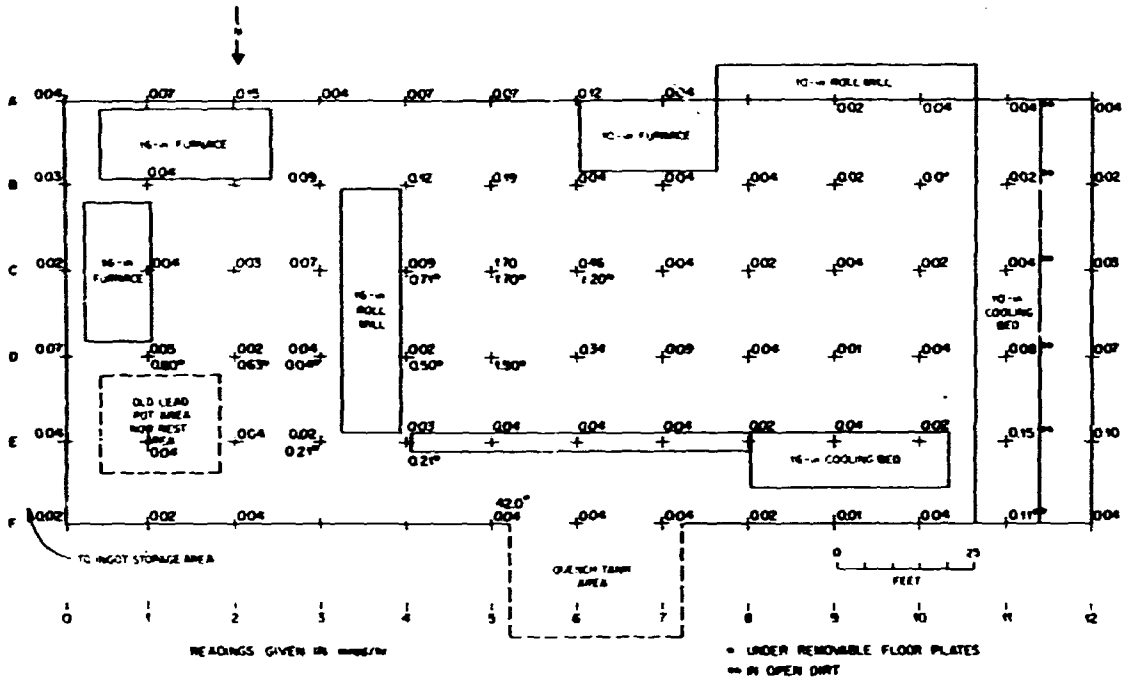

Fig. 5.14. Survey grid used in rolling mill area at Simonds Saw and Steel Company. Direct readings (in millirads per hour) of beta-gamma radiation at 1 cm above floor are given in each grid.

RADIOLOGICAL IMPACT OF URANIUM RECOVERY FROM WET-PROCESS PHOSPHORIC ACID

In August 1976, an interagency agreement was entered between ORNL and the EPA. The stated purpose of the work under this agreement was to evaluate the radiological impact due to the release of radionuclides during the recovery of uranium from wet-process phosphoric acid. This project is a cooperative venture between the Health Physics, Chemical Technology, and Environmental Sciences Divisions.

"Base-case" model plant descriptions were prepared by W. W. Davis of the Chemical Technology Division. Davis also calculated the radionuclide source term per unit of product recovered for each base case (Table 5.4). Measurements will be made by our group in the vicinity of an operational central processing plant near

Table 5.4. Source terms for the model uranium recovery plants immediately after purification

Radionuclide	Radioactivity content (Ci/MTU)	Model 1 (150 MTU/year at wet-process plant)			Model 2 (900 MTU/year at central plant)		
		Available activity (Ci/year)	Activity emitted (Ci/year)		Available activity (Ci/year)	Activity emitted (Ci/year)	
			Case 1[a]	Case 2[b]		Case 1[a]	Case 2[b]
^{234}U	3.34E-1	5.01E1	5.0E-4	2.5E-7	3.01E2	3.0E-3	1.5E-6
^{235}U	1.52E-2	2.28E0	2.3E-5	1.2E-8	1.37E1	1.4E-4	7.0E-8
^{238}U	3.31E-1	4.97E1	5.0E-4	2.5E-7	2.98E2	3.0E-3	1.5E-6
Total	6.80E-1	1.02E2	1.0E-3	5.1E-7	6.12E2	6.1E-3	3.1E-6

[a]Based on air transport of 1% of the available activity and a filter bag efficiency of 99.9%.
[b]Based on the parameters of case 1 and 99.95% efficiency of a HEPA filter.

Mulberry, Florida. The objective of these measurements is to verify Davis's calculated source terms. Specific radiological impact evaluations will be performed by Phil Walsh of the Environmental Sciences Division. His dose calculations will be based on both calculated and measured values of effluent releases.

INSTRUMENT DEVELOPMENTS

For most of the radiological surveys, a full complement of available "off-the-shelf" instruments is used. There are two types of measurements for which most readily available instruments have some drawbacks: low-level alpha surface contamination and low-level radon concentrations in air.

Measurements of residual alpha contamination on surfaces are required in all of the structures in ERDA's resurvey of former MED-AEC facilities. There is, however, a wide range of acceptable values for surface contamination, and these values are dependent on the type of material present. For example, the values recommended by the NRC[11] for uranium are 5000 α dis/min averaged over 100 cm^2. However, for radionuclides such as ^{228}Th and ^{226}Ra, these levels are reduced to 100 α dis/(min·100 cm^2) averaged over 1 m^2 and 300 α dis/min averaged over 100 cm^2. These latter values represent difficult and time-consuming measurements. Alpha survey meters used during this project are portable with a meter (linear and logrithmic scales) readout. To obtain counts of individual events, a small timer scale was designed and fabricated. This unit attaches to the side of the survey meter and receives its signal from the instrument's headphone jack. A timer is provided for taking 15-, 30-, and 60-sec counts. Therefore, it is possible to measure contamination levels less than 50 dis/(min·100 cm^2). The circuit for this scaling unit is shown in Fig. 5.15.

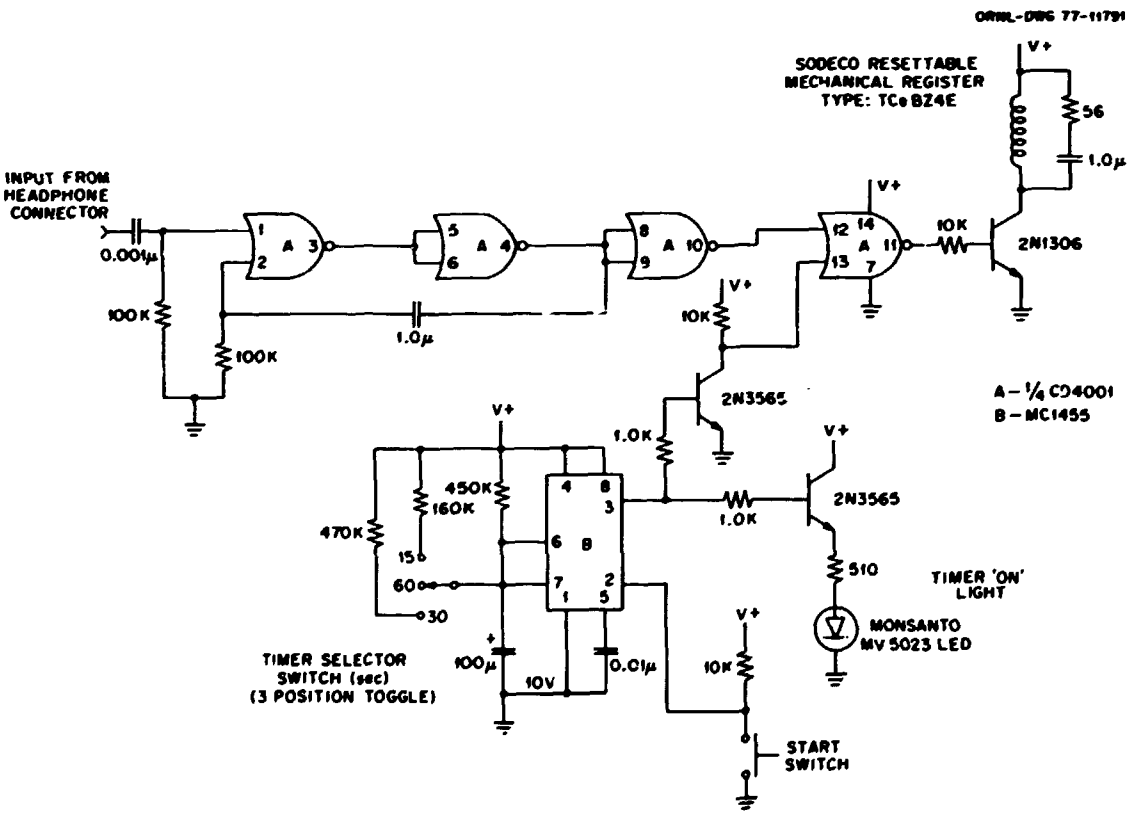

Fig. 5.15. Circuit for portable scaler which attaches to the body of a portable survey meter and receives input signals from headphone jack.

If only uranium was handled in any given facility, regular portable survey meters are adequate for measuring residual contamination levels. However, where radium-bearing ores were handled, deposits of radium are usually found in cracks, drains, and irregular places on the surface. In many cases, a determination of the specific radionuclide is needed in order to apply applicable guidelines. Sample residues and scale may be collected and analyzed for a specific radionuclide. However, often it is not possible to obtain a sample to analyze. To identify alpha-emitting radionuclides, a slight modification was made in the counter used for measuring alpha particles on air filters. A holder was made for the counting head so that the silicon diode could be placed near the surface to be monitored. As with the air samples, helium gas is flowed through the counting chamber to minimize the attenuation of alpha particles between the diode and the surface being monitored. The signals from this detector are routed to a 1024-channel pulse-height analyzer. Tests determined that alpha peaks from the radionuclides of interest can be identified. This technique is, therefore, used to monitor surfaces for which the type of residual contamination is unknown. Figure 5.16 is a cross-sectional diagram of the detector and holder.

Several years ago, a continuous radon monitor was developed by Wrenn, Spitz, and Cohen.[8] This unit uses the concept of radon diffusion into a hemispherical chamber. There, the charged RaA ions are collected electrostatically on a thin Mylar-covered zinc sulfide scintillator and are subsequently counted as the daughters decay. One of the former MED-AEC facilities was used for the recovery of radium. Therefore, a continuous radon monitoring capability was needed. Two units similar to those developed by Wrenn, Spitz, and Cohen were fabricated. In these units, the size of the zinc sulfide detector and phototube assembly was increased in an effort to enhance the sensitivity of the unit. These two detectors and four of the regular Wrenn units were exposed for 24 hr in the lower level of a building at the former Vitro Rare Metals Plant in Canonsburg, Pennsylvania. Results of this test are presented in Fig. 5.17.

ORNL-DWG 77-11792

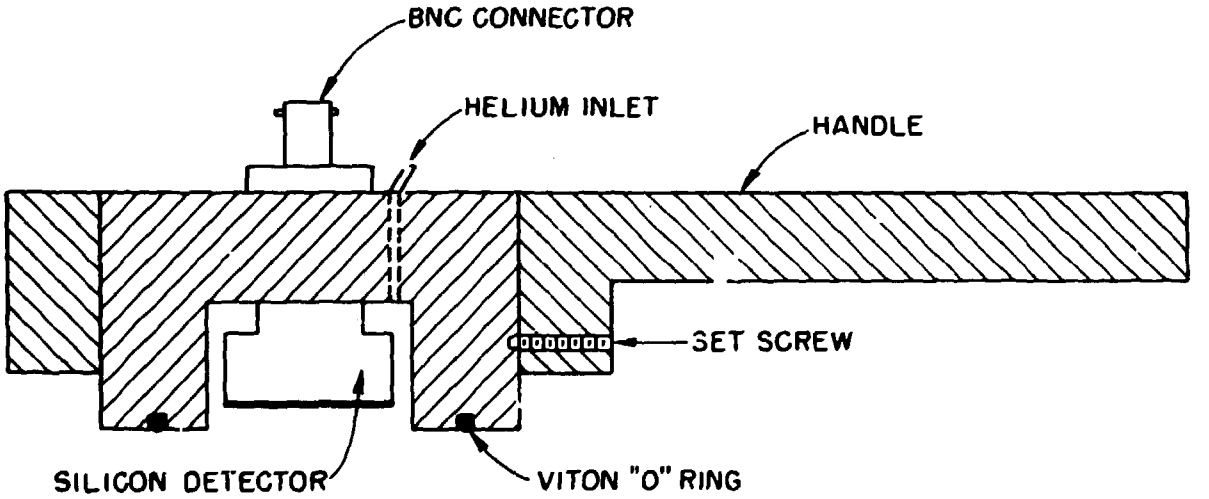

Fig. 5.16. Cross-sectional diagram of detector used on surfaces for the identification of alpha-emitting radionuclides.

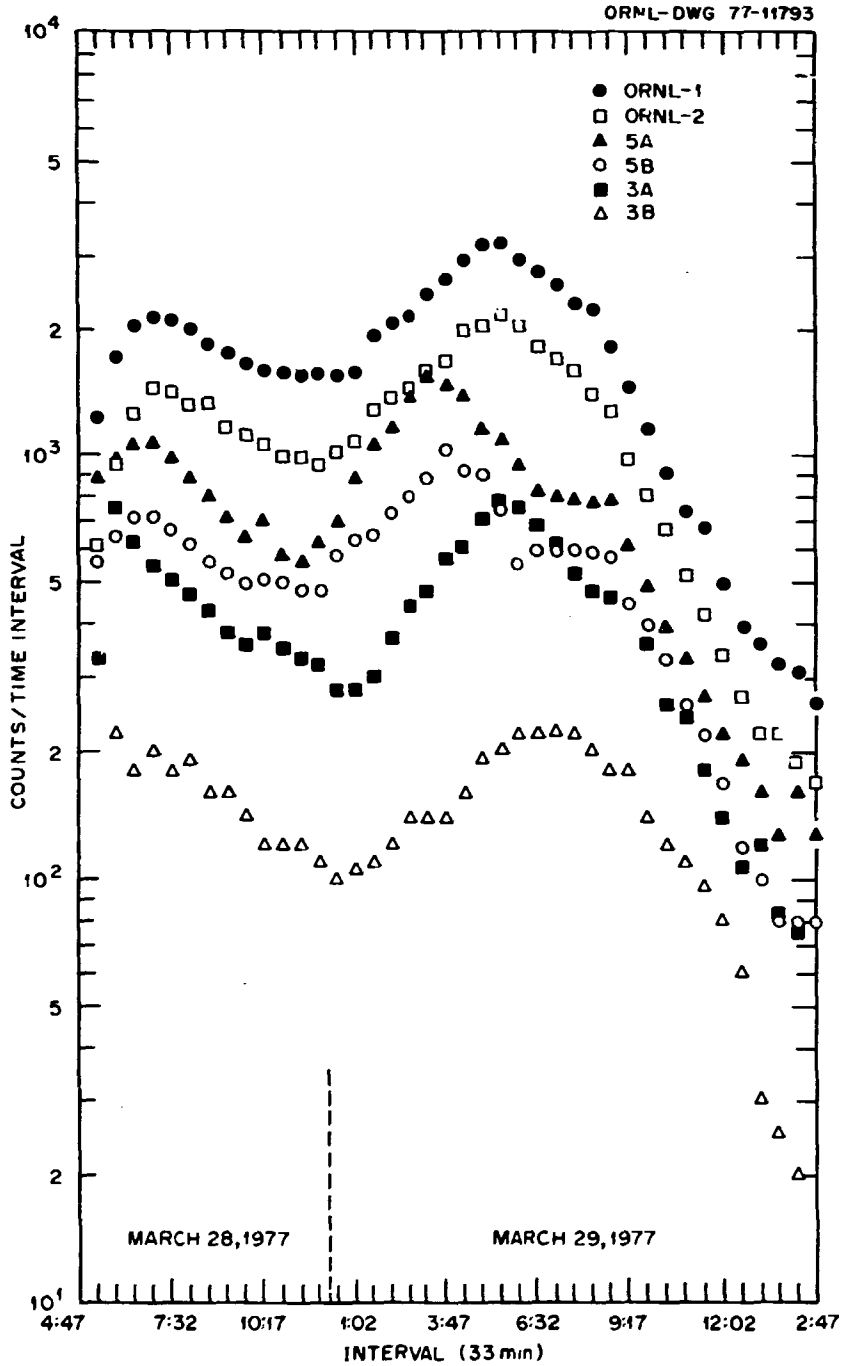

Fig. 5.17. Results of a 24-hr calibration run at Vitro Rare Metals Plant.

FACILITIES USED IN FIELD SURVEYS

Due to the wide variety of radiation measurements that are made in these programs and the remoteness of many locations, it is necessary to use mobile facilities. For this purpose, one panel truck (20 ft) and two motor-home coaches (27 ft) were outfitted with equipment necessary to complete most of the offsite measurements. Electronic instruments such as 1024- or 4096-channel pulse-height analyzers, Ge(Li) detectors,

NaI scintillation detectors, portable alpha, gamma, and beta-gamma survey meters, smear counters, radon and radon daughter counters, gasoline-powered generators for ac power, and other miscellaneous items constitute the typical complement of equipment on each of these mobile units. A view of one of the larger coaches is shown in Fig. 5.18, and a view of the equipment in the small coach is given in Fig. 5.19.

Environmental samples collected from individual survey sites and at background sample locations are returned to ORNL for analysis. Most of the samples are prepared and analyzed in facilities in Buildings 7505 and 7710.

Soil samples are dried for 24 hr at 110°C and then ground to a particle size of 500 μm (Fig. 5.20). The material is then dispensed into 30-ml plastic bottles and labeled. Most of the samples are analyzed for ^{226}Ra, in addition to other radionuclides; therefore, it is necessary for the prepared samples to be stored for a period of about 30 days to allow equilibration of radon daugh-

Fig. 5.18. Mobile laboratory used in Offsite Measurements Program.

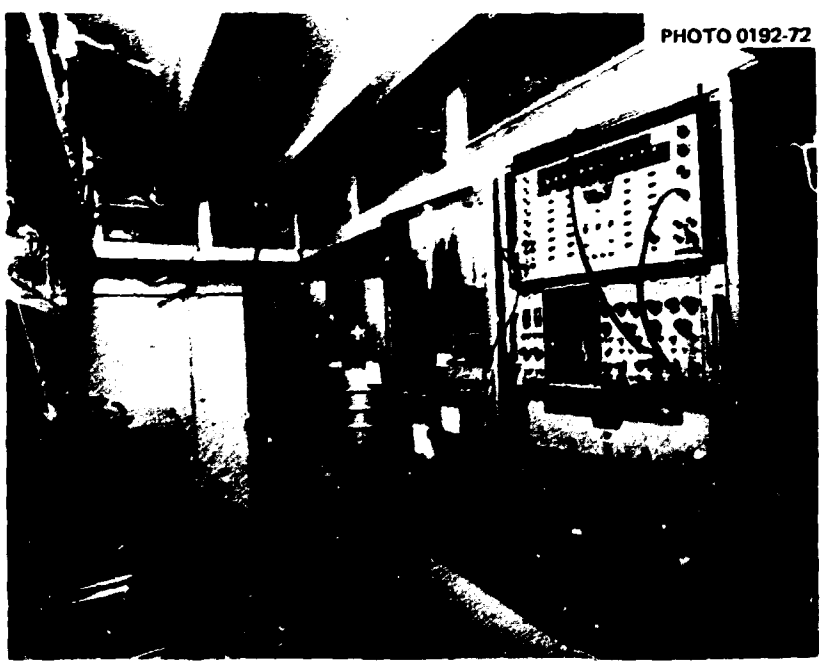

Fig. 5.19. View of interior of van laboratory.

ter activity. A view of the Ge(Li) counting and analyzing facilities is shown in Fig. 5.21.

Each soil sample is counted with a high-resolution Ge(Li) detector for periods ranging from 2000 to 40,000 sec. The pulse-height spectrum is recorded on magnetic tape for permanent storage and analyzed by a computer using sophisticated least-squares techniques. Each photo peak in the spectrum is integrated and compared with a comprehensive library of naturally occurring radionuclides. Results are printed by the computer via teletype. Table 5.5 is a typical list of radionuclides in an analyzed uranium reference standard sample.

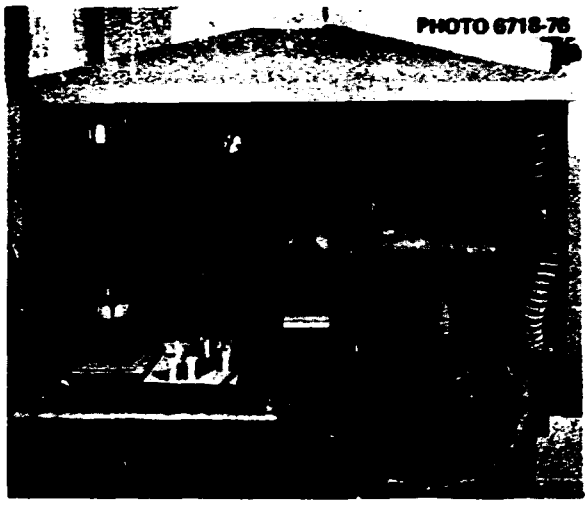

Fig. 5.20. Facility used for grinding and bottling soil samples.

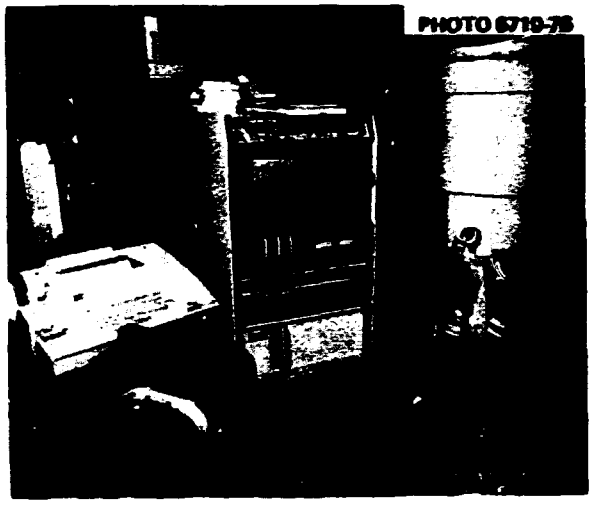

Fig. 5.21. Ge(Li) detector and computer-based pulse-height analysis system.

Table 5.5. Typical computer printout for samples analyzed by computer-based gamma spectroscopy analyzer

SAMPLE ID. – NBØ529
ADC NO. – 1
CALIB. # 1
LIBR. # 227
SAMPLE WT (VOL) = 441.5
DAY = 29 TIME = 11Ø6.46
DECAY TIME = Ø.ØØ

COUNTING TIME = 54ØØ SECONDS (LIVE)

NUCLIDE	NO.	ENERGY	PCI/GM	ERROR%	PCI/GM	2SIGMA
RA-226	2Ø	6Ø9.4	1.71E+Ø2	Ø.7	1.71E+Ø2	2.12E+ØØ
	17	352.Ø	1.73E+Ø2	1.2		
	15	295.2	1.65E+Ø2	1.6		
	28	112Ø.3	1.77E+Ø2	1.8		
	38	1764.6	1.75E+Ø2	3.1		
	21	665.5	1.49E+Ø2	6.8		
TH-234	5	93.Ø	1.57E+Ø2	3.4	1.6ØE+Ø2	1.46E+Ø1
	1	63.Ø	2.1ØE+Ø2	56.4		
AC-227	1Ø	27Ø.Ø	8.68E+ØØ	7.5	8.68E+ØØ	1.3ØE+ØØ

RADIOISOTOPES SOUGHT – NOT FOUND

NUCLIDE	BKGND.	MAX CTS.	MDA PCI/GM
TH-232	2.17E+Ø4	2.Ø8E+Ø2	2.67E–Ø1
CS-137	2.39E+Ø3	6.92E+Ø1	1.3ØE–Ø1
K–4Ø	9.42E+Ø2	4.34E+Ø1	1.43E+ØØ

GEOGRAPHICAL DISTRIBUTION OF RADIOLOGICAL SURVEY SITES

The distribution of survey sites is such that mobile laboratory operations have been carried out in 18 of the contiguous 48 states, from Massachusetts to Oregon. The location of the sites associated with the Offsite Measurements Group's three separate projects is shown in Fig. 5.22. In addition to making a series of measurements at sites in specific states, representative soil samples were collected and gamma-ray measurements made in 35 states.

ORNL-DWG 77-2798

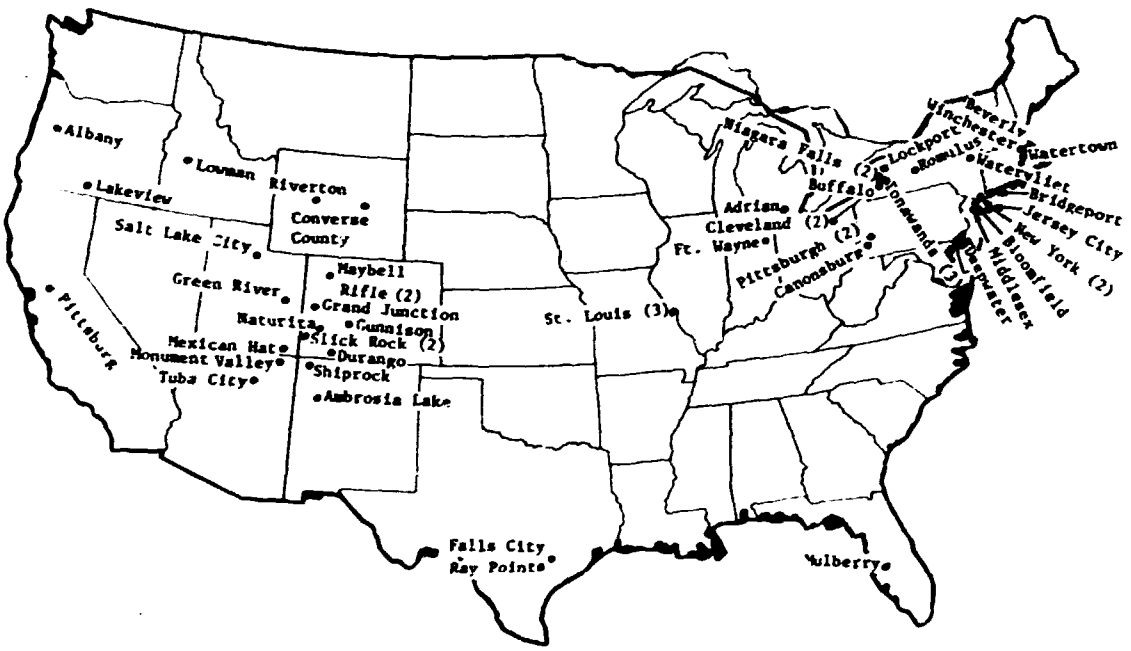

Fig. 5.22. Geographical distribution of radiological survey sites.

6. Environmental Health Studies

C. E. Easterly K. E. Shank
H. M. Butler[1] C. H. Patrick[4]
A. S. Loebl[2] P. J. Papagiannakopoulos[5]
T. W. Oakes J. E. Phillips[6]
P. Otaduy[3] R. L. Shoup[7]
C. E. Wheeler[8]

Environmental health studies at ORNL fall into two categories: retrospective and prospective. The retrospective studies during the past two years have centered on attempting to uncover evidence which can be used to quantify the health effects which the presence of ORNL as a nuclear site has on the general public. To date no effect has been uncovered which can be ascribed to the presence of the nuclear facilities at Oak Ridge. Prospective studies have been undertaken to identify potential health effects associated with future energy sources, particularly fusion reactors. A number of potential areas for study have been identified, and preliminary quantification is under way for several of these.

PUBLIC HEALTH AND DEMOGRAPHIC STATISTICS

The objective of the public health and demographic statistics program is to assess the available data sources and the methodology appropriate for use in analytical studies concerning the health effects related to nuclear facilities. Quantification of health effects on populations in areas surrounding nuclear plants has been a source of constant debate in the past. This program has concentrated on collecting mortality statistics for the area surrounding the nuclear facilities at Oak Ridge, which have been in operation for three decades. The program is also developing the data accumulation techniques, the subsequent statistical analyses, and the methodology appropriate to use in an environmental impact statement for public health assessments. In this aspect of the program, existing data and methods are analyzed to demonstrate the applications of available information on public health.

In the past year, three studies were completed.[9–11] The first study was mainly a literature survey on public health changes in areas surrounding nuclear facilities.[9] It was found that the majority of the reported investigations were unable to discern a dose-response relationship or to find adverse health effects in the local population which might be related to radiation exposure. The investigation[12] that supposedly found an adverse effect has severe methodological limitations which preclude meaningful interpretation of the data.[9] The methodology and data sources used in these investigations are discussed in terms of their usefulness and shortcomings. It was concluded that more research is needed before the effects of low-level radiation exposures can be ascertained, but that existing evidence suggests that nuclear

1. Radiation and Safety Survey Section.
2. Energy Division.
3. Graduate student, University of Florida.
4. On assignment to ERDA, Washington, D.C.
5. Postdoctoral student, The University of Tennessee.
6. Graduate student, University of North Carolina.
7. Medical Physics and Internal Dosimetry Section.
8. Consultant.
9. C. H. Patrick, *Nucl. Saf.* 18(5), 647 (1977).
10. C. H. Patrick, "Mortality Trends in Counties Surrounding the Oak Ridge Nuclear Facilities: A Time Series Analysis," in *Proceedings of the Social Statistics Section*, from the August 1977 meeting of the American Statistical Association, Chicago, Ill.
11. K. E. Shank, C. E. Easterly, and T. W. Oakes, *Congenital Malformations and Fetal Mortality Trends in Counties Surrounding Oak Ridge*, ORNL/TM-5805 (1977).
12. E. J. Sternglass, "Environmental Radiation and Human Health," pp. 145–216 in *Proceedings of the Sixth Berkeley Symposium on Mathematical Statistics and Probability*, vol. 6, J. Neyman, ed., University of California Press, Berkeley, 1970.

power plants will not have a significant impact on public health as a result of normal operations.[9]

The second study was directed at analyzing the trends in incidence of cancer, congenital malformation, and fetal and infant mortality for the city of Oak Ridge and Anderson and Roane counties relative to Tennessee.[10] It was shown in this work that the mortality trends do not show any gradient in time or space which would suggest that the presence of the Oak Ridge nuclear facilities has resulted in adverse impacts to the local population.

A more in-depth study on congenital malformations and fetal mortality trends for nine East Tennessee counties surrounding Oak Ridge was completed.[11] The counties are Anderson, Blount, Campbell, Knox, Loudon, Morgan, Roane, Scott, and Union. Coffee County was also included since it contains the city of Tullahoma, and the socioeconomic structures of the city and county are similar to those of Oak Ridge and Anderson County. (Tullahoma and Oak Ridge were the only two cities analyzed in the study.) The data were obtained from the annual bulletins on vital statistics of the Tennessee Department of Public Health. All the observed values were compared with expected values, which were computed using state rates. Stillbirth data for 1931 to 1971 were obtained. Congenital malformation data were, unfortunately, recorded separately only since 1951; thus, the period of 1951 through 1971 was used. (In the previous study, congenital malformations were combined with other causes of infant mortality.[10]) To analyze the trends before and after the startup of operations at Oak Ridge, the time period was divided into three segments for the stillbirth data – 1930 to 1943, 1944 to 1957, and 1958 to 1971 – and into two segments for the congenital malformation data – 1951 to 1957 and 1958 to 1971. The data and chi-square (χ^2) values are presented in Tables 6.1 to 6.5. There does not appear to be any significant pattern connecting the stillbirth and the congenital malformation mortality rates. Also, the city of Oak Ridge, which is the closest city to the nuclear facilities, had significantly fewer stillbirths and no difference in congenital malformations in comparison with the state as a whole.

Analysis of age- and sex-adjusted cancer mortality trends for these same areas is in progress. This requires a significant effort in format analysis of computer tapes (supplied by the Tennessee Department of Public Health) on individual deaths from 1949 through 1975, since recording techniques have undergone numerous changes over the years. These tapes were read and the records separated into three major categories of death: benign neoplasms, malignant neoplasms, and other causes of death. Each of these categories will later be divided into further subcategories corresponding to the listings of the International Classification of Diseases so that cross-tabulations can be performed on the variables of interest. This type of study is needed since age structure must be considered when analyzing cancer deaths. Further, this new study will consider each type of cancer specifically, such as lymphatic leukemia, malignant neoplasm of the bone, etc.

Table 6.1. Stillbirth data for 1930–1943

County	Values		
	Observed	Expected	χ^{2a}
Anderson	243	238.2	0.10
Blount	411	395.2	0.63
Campbell	292	310.2	1.07
Coffee	114	141.9	5.49[b]
Knox	1268	1275.4	0.04
Loudon	239	192.4	11.3[c]
Morgan	128	136.6	0.54
Roane	227	242.5	0.99
Scott	124	112.2	1.24
Union	74	82.3	0.84

[a] $\chi^2_{df=1,\alpha=0.5}$(one tail) = 2.71.
[b] The observed value was significantly less than expected.
[c] The observed value was significantly greater than expected.

Table 6.2. Stillbirth data for 1944–1957

County	Values		
	Observed	Expected	χ^{2a}
Anderson	352	412.6	8.90[b]
Blount	324	332.1	0.20
Campbell	297	222.5	2.49
Coffee	137	139.2	0.03
Knox	1237	1181.3	2.63
Loudon	142	139.5	0.04
Morgan	94	90.1	0.17
Roane	246	212.1	5.39[c]
Scott	127	113.8	1.53
Union	46	43.2	0.18
City of Oak Ridge (1949–1957)	76	128.0	21.1[b]

[a] $\chi^2_{df=1,\alpha=0.5}$(one tail) = 2.71.
[b] The observed value was significantly less than expected.
[c] The observed value was significantly greater than expected.

Table 6.3. Stillbirth data for 1958–1971

County	Values		
	Observed	Expected	χ^{2a}
Anderson	209	223.4	0.93
Blount	209	209.1	0.0
Campbell	144	113.3	8.32[b]
Coffee	118	118.0	0.0
Knox	931	883.9	2.51
Loudon	107	85.1	5.64[b]
Morgan	57	47.9	1.73
Roane	179	142.4	9.41[b]
Scott	93	71.1	6.75[b]
Union	44	32.5	4.07[b]
City of Oak Ridge (1960–1971)	65	92.2	8.02[c]
City of Tullahoma (1960–1971)	38	43.0	0.58

[a] $\chi^2_{df=1,\alpha=0.5}$(one tail) = 2.71.
[b] The observed value was significantly greater than expected.
[c] The observed value was significantly less than expected.

Table 6.4. Congenital malformation data for 1951–1957

County	Values		
	Observed	Expected	χ^{2a}
Anderson	56	46.3	2.03
Blount	61	46.0	4.89[b]
Campbell	41	28.4	5.59[b]
Coffee	30	19.1	6.22[b]
Knox	190	175.9	1.13
Loudon	23	19.4	0.67
Morgan	10	12.6	0.54
Roane	39	25.5	7.15[b]
Scott	19	14.4	1.47
Union	5	7.0	0.57
City of Oak Ridge	26	23.3	0.31

[a] $\chi^2_{df=1,\alpha=0.5}$(one tail) = 2.71.
[b] The observed value was significantly greater than expected.

A close working relationship has been established with the Environmental Monitoring Group at ORNL by means of dual assignment of personnel. As a cooperative effort, a study on natural background in the area surrounding Oak Ridge is in progress. To study external exposure levels, soil samples from 16 sites in eastern and central Tennessee, at distances of 35 to 210 km from ORNL, were analyzed to determine their radionuclide composition.[13] It was estimated that for 1 m above the ground, the ^{40}K dose varied from 40 to 0.14 millirems per year, with an average value of 13. The range for ^{232}Th (and its daughters) varied from 15 to 1.9 millirems per year, with an average value of 6.9, and the range for ^{238}U (and its daughters) was 8.5 to 3.1 millirems per year, with an average value of 4.5. Authorization to put thermoluminescent dosimeters in selected houses and public facilities was obtained from ERDA. To study internal exposure levels, twenty-one types of fruits and vegetables were collected from local grocery stores and analyzed for their radionuclide and trace-element composition.[14] It is believed that these environmental studies are important to the program in that background information, including a knowledge of the magnitude and fluctuations of radioactivity levels, should be known before effects can be attributed to pollutants from nuclear facilities. Finally, throughout the year, a continuous effort has been under way to collect and analyze literature pertinent to epidemiology, biostatistics, and related disciplines.

Table 6.5. Congenital malformation data for 1958–1971

County	Values		
	Observed	Expected	χ^{2a}
Anderson	113	84.5	9.61[b]
Blount	94	83.1	1.43
Campbell	60	40.4	9.51
Coffee	48	43.2	0.53
Knox	334	347.0	0.49
Loudon	36	34.2	0.09
Morgan	24	20.3	0.67
Roane	45	54.6	1.69
Scott	29	22.6	1.81
Union	11	12.7	0.23
City of Oak Ridge (1960–1971)	45	39.6	0.74
City of Tullahoma (1960–1971)	18	16.4	0.16

[a] $\chi^2_{df=1,\alpha=0.5}$(one tail) = 2.71.
[b] The observed value was significantly greater than expected.

13. T. W. Oakes, K. E. Shank, and C. E. Easterly, "Natural and Man-Made Radionuclide Concentrations in Tennessee Soils," p. 322 in *Proceedings of the Tenth Midyear Topical Symposium of the Health Physics Society, Saratoga Springs, New York, October 11–13, 1976.*

14. T. W. Oakes et al., "Concentrations of Radionuclides and Selected Trace Metals in Fruits and Vegetables," in *Proceedings of the 11th Annual Conference on Trace Substances in Environmental Health, Columbia, Missouri, June 7–9, 1977.*

HEALTH PHYSICS ASPECTS OF FUSION POWER

The goal of the health physics aspects of fusion power program continues unchanged: to provide, on a timely basis, scientific information and technical evaluations of the potential impacts of fusion power to occupational workers and the public. Although analysis and assessment activities are and will remain a vital part of this program, work in that area has begun a transition from primarily qualitative assessments to analyses requiring technical accomplishments; this trend is expected to continue since substantive analyses appear to require new technical input.

The primary areas of study during the past year have been (1) factors affecting calculations of dose resulting from a release of tritium, (2) an assessment of the potential for reducing occupational risk from exposures to tritium, and (3) experimental studies of tritium conversion from molecular hydrogen to tritiated water.

Factors Affecting Calculations of Dose Resulting from a Tritium Release into the Atmosphere

Tritium will likely be the principal source of radiation hazard inside a fusion reactor plant, and it will be the dominant radionuclide of concern in maintaining occupational and public exposures as low as reasonably achievable during normal operations. Large quantities of tritium will be present in various components of the power plant, including the fuel storage and processing system, the fuel injection system, the plasma recovery system, and the breeding blanket and recovery system. Various designs call for 0.4 to 4 kg of tritium in the blanket and coolant and a total tritium inventory in the plant of 2 to 15 kg (1 g = 9600 Ci).[15] It is noted that the tritium inventories may approach 10 kg/1000 MWe due to a potentially low burnup of 1% or less. Jacobs has estimated the worldwide steady-state level of naturally occurring tritium to be 7 to 14 kg;[16] thus, a single fusion power plant may contain as much tritium as the entire natural environment.

During normal operation of a fusion power plant, small amounts of tritium will be lost to the environment due to its diffusion and permeation characteristics. In accident situations, there is a potential for large quantities to be lost to the environment. Prior to the construction of a large tritium-burning experiment or a fusion reactor demonstration plant, it will be necessary to prepare a safety analysis report and an environmental impact statement. These requirements will necessitate compilation of site-specific information and an understanding of the dose implications of the transformation rate of tritium as gas to tritium as water. The latter requirement is due to the fact that tritium as water is several orders of magnitude more hazardous to man than tritium as gas, since the water vapor is more easily absorbed into the body than the gas.

Pinson and Langham report that after inhalation of HT and HTO, equivalent rates of tritium appearance in the body fluids of man occurred when the specific activity of HT (gaseous tritium) in the inhaled air was about 15,000 times greater than that of the HTO (tritiated water vapor).[17] However, the legal concentration guides,[18] which are based on recommendations of the International Commission on Radiological Protection,[19] put tritium as HTO a factor of 200 times more hazardous than tritium as HT, and calculations of dose are usually made according to this recommendation. (In the remaining discussions, this factor will be discussed as the HTO-HT risk factor.)

In performing an assessment of dose from a tritium release, aside from the HTO-HT risk factor, the dominant unknown is the behavior of the tritium in the environment, that is, of the amount released as HT, what fraction is converted to HTO as it is transported through the environment. At this point in the development of the fusion program, it is important to have an understanding of the role that the rate of conversion will have on the dose calculation.

It must be remembered, however, that in the calculation of dose downwind from a tritium release, numerous other variables are imprecisely known. For example, results of transport calculations using the Gaussian plume model developed by Pasquill[20] and Gifford[21] were compared with air concentration measurements, and agreement to within a factor of 2 was generally found for distances up to 15 km.[22,23] Yet, in a com-

15. U.S. AEC, *CTR Engineering Systems Study Meeting*, WASH-1278, 1973.

16. D. G. Jacobs, *Am. Nucl. Soc. Trans.* 14, 160 (1971).

17. E. A. Pinson and W. H. Langham, *J. Appl. Physiol.* 10, 108 (1957).

18. *U.S. Code of Federal Regulations*, Title 10, Part 20.

19. International Commission on Radiological Protection, *Recommendations of the International Commission on Radiological Protection* (Report of Committee 2 on Permissible Dose for Internal Radiation), ICRP Publication 2, Pergamon Press, New York, 1959.

20. F. Pasquill, *Atmospheric Diffusion*, D. Van Nostrand Co., Ltd., London, 1962.

21. F. A. Gifford, Jr., *Nucl. Safety* 4, 47 (1961).

22. F. T. Binford, T. P. Hamrick, and B. H. Cope, *Some Techniques for Estimating the Results of the Emission of Radioactive Effluent from ORNL Stacks*, ORNL/TM-3187 (1970).

23. T. W. Oakes, K. E. Shank, and C. E. Easterly, "Iodine-131 Air Concentrations: A Comparison of Calculated Versus Measured Values," paper presented at ANS/ENS/AIF International Conference, Washington, D.C., Nov. 15–19, 1976.

parison with the measurements taken at the time of the Windscale accident, the calculated air concentration values were greater by a factor of 100 at 100 km.[24] In addition, other factors involved in the calculation of dose are known only to within a factor of 2 or so, and biological variability always will present that much uncertainty. The intent of the present study is to estimate the effect of the conversion of HT to HTO on the calculation of dose, as a release of tritium is transported through the environment.

As described earlier, an atmospheric transport computer code was modified to include the conversion of HT to HTO.[25] In Figs. 6.1 and 6.2 are plotted the relative risk resulting from a release of HT from heights of 0 and 100 m, respectively, where relative risk for the 0%-per-day conversion (HT) is numerically equal to χ/Q (the stack dilution factor) in seconds per cubic meter. (Numerical values of relative risk are related to dose by a constant factor.) The wind speed corresponds to the average wind speed in the United States, 4 mph (1.7 m/sec), and the stability conditions are slightly unstable (Pasquill type C). The hazard from HTO is taken to be a factor of 200 times that of HT, that is, the HTO-HT risk factor is 200. Values along the conversion curves are found by multiplying the HTO concentration by 200 and adding the product to the remaining concentration

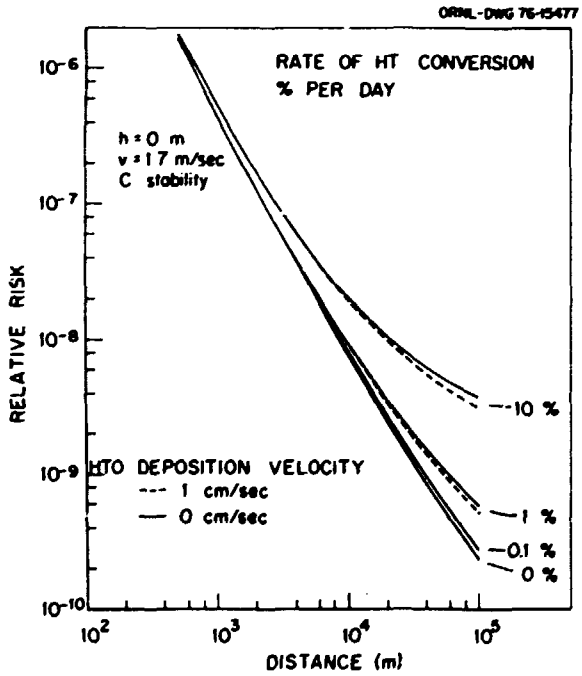

Fig. 6.1. Relative risk for HT and HTO vs distance for varying conversion rates for a release height of 0 m, a wind speed of 1.7 m/sec, and C stability.

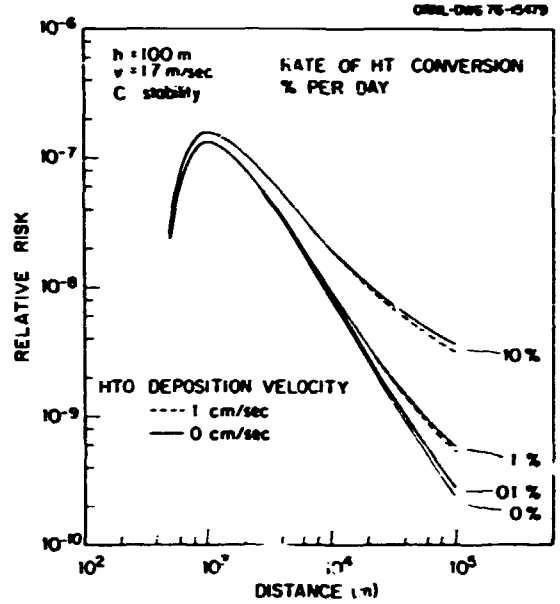

Fig. 6.2. Relative risk for HT and HTO vs distance for varying conversion rates for a release height of 100 m, a wind speed of 1.7 m/sec, and C stability.

of HT. Thus, each curve represents the total risk relative to HT for that conversion rate.

A conversion to dose can be arrived at in the following way: From Fig. 6.1, at 100 km, the relative risk for HT (0% conversion) is 2.4×10^{-10}. This corresponds to a χ/Q of 2.4×10^{-10} sec/m^3. For a release rate of 1 Ci/sec, this χ/Q is converted to a concentration of 2.4×10^{-10} Ci/m^3. If all the HT were HTO, the known conversion factor, F (in rems per curie per second per cubic meter), relating internal dose to time-integrated air concentration could be applied. Since the 0% conversion curve is actually HT, not HTO, the dose conversion factor is reduced by a factor of 200 (the assumed HTO-HT risk factor) and multiplied by the relative risk at 100 km. Thus, the dose at 100 km for 0% conversion is $2.4 \times 10^{-10} \times$ HT release rate $\times F/200 \times$ exposure time. The factor, HT release rate $\times F/200 \times$ exposure time, can now be applied to the ordinate to convert relative risk to dose.

24. P. Cagnetti and M. Pagliari, "Long-Range Transport and Diffusion: An Approach to the Problem from the Health Protection Point of View," *Proceedings of the Third International Radiation Protection Association, Washington, D.C., September 9–14, 1973*, CONF-730907-P1.

25. C. E. Easterly et al., "Health Physics Aspects of Fusion Power," *Health Phys. Div. Annu. Prog. Rep. June 30, 1976*, ORNL-5171 (October 1976), p. 275.

From Figs. 6.1 and 6.2, it is seen that for distances up to 5 km from the point of release, the difference in risk between a 10%-per-day conversion and no conversion is less than a factor of 2; at a distance of 100 km, the difference is a factor of 14. Virtually the same results are seen for both 0 and 100 m release heights, and the variance caused by a deposition velocity of 1 cm/sec compared to 0 cm/sec is at most 15%. This occurs at a distance of 100 km where the initial concentration is reduced by some 9 orders of magnitude.

Calculations of relative risk have been made for varying atmospheric conditions for HTO-HT risk factor values of 200 to 25,000. These are summarized in Fig. 6.3, which can be used to generate curves similar to those shown in Figs. 6.1 and 6.2, by knowing values of χ/Q vs distance (and hence transit time) and by choosing values of conversion rate and risk factor. Figure 6.3 assumes no plume depletion via deposition of the HTO; however, the maximum calculated difference due to this factor (for 100 km and 10%-per-day conversion) is 15%.

An example is taken from Fig. 6.1 at 100 km, choosing a 10%-per-day conversion rate and a risk factor of 200. For this case, the relative risk values are 2.4×10^{-10} and 3.5×10^{-9}, respectively, for no conversion and for 10%-per-day conversion. The solution is arrived at as follows:

Transit Time = 100 km ÷ 1.7 m/sec = 10^3 min
Conversion Rate X Transit Time = 10^4
Fraction of Risk Factor = 0.075 (from Fig. 6.3)
Relative Risk = $2.4 \times 10^{-10} \times 0.075 \times 200 = 3.5 \times 10^{-9}$

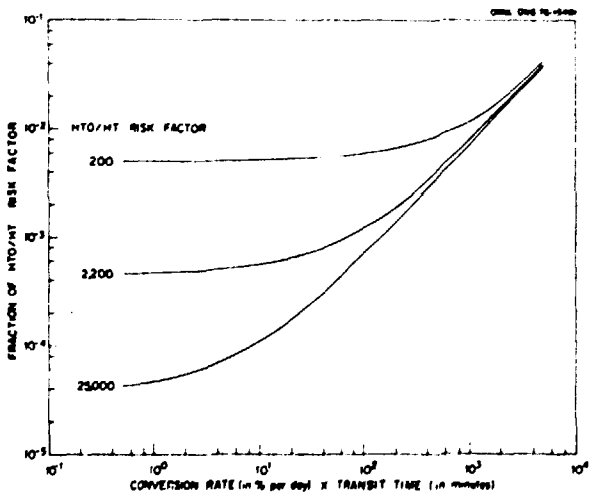

Fig. 6.3. Fraction of HTO-HT risk factor vs quantity of HTO produced for expected range of HTO-HT risk factors.

The difference in dose between the case of no conversion and the case with a 10%-per-day conversion is, for a risk factor of 200, a factor of $3.5 \times 10^{-9} \div 2.4 \times 10^{-10} = 14$, as is seen in Fig. 6.1.

It can be seen in Fig. 6.3 that all the fractions of risk factors approach unity with increasing time and/or conversion rate; hence, the multiplicative factor to the χ/Q value (fraction of risk factor X risk factor) approaches the risk factor.

In summary, a method has been described for calculating the differences in risk for HT and HTO. It appears that for HTO-HT risk factors on the order of 10^2, the knowledge of the conversion rate to within a factor of 10 will result in risk estimates well within the range of uncertainties involved in the other factors relating to dose calculations. Further, the inclusion or neglect of HTO deposition velocity has little bearing on the resultant calculations of dose. The predominant areas of uncertainty in tritium dose calculations are the HTO-HT risk factor, followed by the HT → HTO conversion rate.

Conversion of Tritium Gas to Tritiated Water

During the normal operation of a fusion reactor, small amounts of tritium will be lost to areas occupied by operating personnel and to the external environment. Gaseous tritium (HT) will interact with various atmospheric components and may form tritiated water vapor (HTO), which is substantially more hazardous to man than HT. A knowledge of the formation rate of HTO is important in performing health effect analyses for both occupational personnel and members of the general public. Further, an understanding of the HTO formation mechanism is necessary to assess the potential for reducing the conversion rate of HT to HTO and, hence, to reduce the potential occupational risk within an enclosed area.

The first system considered is similar to atmospheric air except for water vapor. Some experimental data are available since experiments with mixtures of tritium, oxygen, and nitrogen were performed by Casaletto, Gevantman, and Nash.[26] In these experiments, the main component gas was nitrogen and the total pressure of the mixture was 700 mm. Irradiation of such a mixture by the decay of the tritium results in the formation of N_2^+, O_2^+, and T_2^+ positive ions and N_2^*, O_2^*, and T_2^*

26. G. J. Casaletto, L. H. Gevantman, and J. B. Nash, *The Self-Radiation Oxidation of Tritium in Oxygen and Air*, USNRDL-TR-565, Naval Radiological Defense Laboratory, San Francisco, Calif., 1962.

excited molecules. The ionic and excitation processes are:

$$N_2 + e \rightarrow N_2^+ + 2e$$

$$\rightarrow N_2^* + e$$

$$O_2 + e \rightarrow O_2^+ + 2e$$

$$\rightarrow O_2^* + e$$

$$T_2 + e \rightarrow T_2^+ + 2e$$

$$\rightarrow T_2^* + e\,.$$

The N_2^+ ions are the main positive ions in the mixture and probably undergo the reactions[27]

$$N_2^+ + O_2 \xrightarrow{k_1} O_2^+ + N_2$$

$$k_1 = 5 \times 10^{-11}\ \text{cm}^3\ \text{molecule}^{-1}\ \text{sec}^{-1} \quad (1)$$

and

$$N_2^+ + H_2 \xrightarrow{k_2} N_2H^+ + H$$

$$k_2 = 2.1 \times 10^{-9}\ \text{cm}^3\ \text{molecule}^{-1}\ \text{sec}^{-1}\ . \quad (2)$$

In this discussion, H and T are used interchangeably. Although it is recognized that the two isotopes may undergo reactions with somewhat different rate constants, most of these are known only for protium. Reaction (1) is predominant, especially for higher oxygen concentrations. The O_2^+ ions cannot undergo the charge exchange reaction $O_2^+ + T_2 \rightarrow O_2 + T_2^+$; however, a short time after initiating the experiment, many water molecules are available and the O_2^+ and N_2H^+ ions undergo reactions[27,28] which result in the formation of the hydronium ion H_3O^+.

The T(H) atoms induce a number of free radical reactions, the most important of which are given for the protium isotope:[27]

$$H + O_2 + N_2 \rightarrow HO_2 + N_2$$

$$k_3 = 5.5 \times 10^{-32}\ \text{cm}^6\ \text{molecule}^{-2}\ \text{sec}^{-1} \quad (3)$$

$$H + HO_2 \rightarrow H_2 + O_2$$

$$k_4 = 1.3 \times 10^{-11}\ \text{cm}^3\ \text{molecule}^{-1}\ \text{sec}^{-1} \quad (4)$$

$$\rightarrow OH + OH$$

$$k_5 = 1.7 \times 10^{-11}\ \text{cm}^3\ \text{molecule}^{-1}\ \text{sec}^{-1} \quad (5)$$

$$\rightarrow H_2O + O$$

$$k_6 = 1.6 \times 10^{-11}\ \text{cm}^3\ \text{molecule}^{-1}\ \text{sec}^{-1} \quad (6)$$

$$OH + H_2 \rightarrow H_2O + H$$

$$k_7 = 6.4 \times 10^{-15}\ \text{cm}^3\ \text{molecule}^{-1}\ \text{sec}^{-1} \quad (7)$$

$$O + HO_2 \rightarrow OH + O_2$$

$$k_8 = 1 \times 10^{-11}\ \text{cm}^3\ \text{molecule}^{-1}\ \text{sec}^{-1} \quad (8)$$

$$OH + HO_2 \rightarrow H_2O + O_2$$

$$k_9 = 2 \times 10^{-10}\ \text{cm}^3\ \text{molecule}^{-1}\ \text{sec}^{-1} \quad (9)$$

$$OH + OH \rightarrow H_2O + O$$

$$k_{10} = 1.6 \times 10^{-12}\ \text{cm}^3\ \text{molecule}^{-1}\ \text{sec}^{-1}\ . \quad (10)$$

The above sequence is characterized by the presence of the radicals HO_2, OH, and H, and water is produced via reactions (6), (7), (9), and (10). A small number of hydrogen atoms are removed through reactions with an inert gas M – $H + H + M \rightarrow H_2 + M$ – which is a much slower process than reaction (3).

The rate of H_2O formation can be given by the equation:

$$\frac{d[H_2O]}{dt} = k_6[H][HO_2] + k_7[OH][H_2] + k_9[OH][HO_2] + k_{10}[OH]^2\ . \quad (11)$$

It is assumed that the free radicals H, O, OH, and HO_2 are in steady state, and the following equations are obtained:

$$\frac{d[H]}{dt} = k_2[N_2^+][H_2] - k_3[N_2][O_2][H] - (k_4 + k_5 + k_6)[H][HO_2] + k_7[OH][H_2] = 0 \quad (12)$$

27. M. J. McEwan and L. F. Phillips, "Chemistry of the Atmosphere," John Wiley & Sons, New York, 1975.
28. C. J. Howard et al., *J. Chem. Phys.* 57, 3491 (1972).

$$\frac{d[OH]}{dt} = 2k_5[H][HO_2] - k_7[OH][H_2] + k_8[O][HO_2] - k_9[OH][HO_2] - 2k_{10}[OH]^2 = 0 \quad (13)$$

$$\frac{d[HO_2]}{dt} = k_3[H][O_2][N_2] - (k_4 + k_5 + k_6)[H][HO_2] - k_8[O][HO_2] - k_9[OH][HO_2] = 0 \quad (14)$$

$$\frac{d[O]}{dt} = k_6[H][HO_2] - k_8[O][HO_2] + k_{10}[OH]^2 = 0. \quad (15)$$

Using the above equations, the rate of H_2O formation in Eq. (11) becomes

$$\frac{d[H_2O]}{dt} \propto [N_2^+][H_2] \quad (16)$$

This relationship has a hidden dependence on $[O_2]$ tied to the production of N_2^+ ions. Over the normal (atmospheric) range of O_2 concentrations, the calculated production rate for HTO remains fairly constant and in order-of-magnitude agreement with the results of Casaletto, Gevantman, and Nash.[26] Agreement is less good when the O_2 fraction is on the order of 50% or greater as in the experiments of Dorfman and Hemmer,[29] who used a hydrogen-oxygen mixture. To solve for an equivalent Eq. (16), the reactions of Eqs. (1), (2), and (3) must be rewritten for H_2^+ instead of N_2^+. The resulting rate of water formation then has an explicit dependence on $[O_2]$; however, this relationship predicts values an order of magnitude lower than those observed under the high $[O_2]$ conditions.[29] It is clear that the preliminary model deviates from experimental results for some experimental conditions; however, for typical atmospheric conditions, agreement is quite satisfactory.

In conclusion, for typical atmospheric conditions, the formation of tritium atoms through ion-molecule reactions appears to be a very important process for the final formation of HTO. Further, the tritium atoms initiate the radical reactions that result in the formation of HTO. Both of these mechanisms could be hindered by introducing gaseous components which (1) compete favorably with the ion-molecule reactions and (2) reduce the number of tritium atoms before they initiate the water-forming radical reactions. Therefore, it appears reasonable to pursue the concept of reduction in risk to the occupational worker via a physical understanding of the conversion mechanisms.

Tritium Conversion Experiments

Initial experiments were performed by allowing HT to react to form HTO in the presence of dry air, dry air and soil, and moist air. The experimental apparatus consists of a pumping and backfilling manifold and a tritium recovery system. The pumping and backfilling manifold consists of an oil diffusion pumping system, a uranium trap (for the tritium), pressure sensors, and a manifold for expanding tritium and other gases into 1-liter reaction flasks. At discrete time intervals, approximately 1 cm^3 of volume is removed from the reaction flasks and passed through the recovery system, which consists of a set of water bubblers to collect the HTO, a copper oxide furnace to convert the unreacted HT to HTO, and a second set of bubblers. Liquid scintillation counting of the bubbler water is used to provide a measurement of the reacted and unreacted tritium.

Initial tritium concentrations were somewhat lower than those of the previous work. This was done specifically in an attempt to determine the reaction rates for tritium concentrations more like expected potential occupational levels than those reported for earlier works.[26,29–31] The data were analyzed by assuming that the relationships

$$R_0 = \left(\frac{-d[T_2]}{dt}\right)_0 = k_2[T_2]_0^2 \quad (17)$$

and

$$R_t = \left(\frac{-d[T_2]}{dt}\right) = k_2[T_2]_0[T_2] \quad (18)$$

are valid over the range of initial tritium concentrations. In these equations, R is the reaction rate, $[T_2]$ is the concentration of tritium in the gaseous form, k_2 is the second-order reaction rate, t is the time, and "0" indicates initial conditions. Equation (17) has been established experimentally for initial tritium concentrations

29. L. M. Dorfman and B. A. Hemmer, *J. Chem. Phys.* 22, 1555 (1954).
30. L. F. Belovodskii et al., *At. Energ.* 38, 379 (1975).
31. J. Yang and L. H. Gevantman, *J. Phys. Chem.* 68, 3115 (1964).

between 100 and 1 mCi/ml;[26] Eq. (18) has not been verified. However, Eq. (18) should be a good approximation for the small reaction yields observed in the experiment since $[T_2]$ is nearly constant and equal to $[T_2]_0$. The value of k_2 can be found from $k_2 = m/[T_2]_0$, where m is the slope of the plot vs time of the logarithm of the initial concentration minus the HTO.

For the dry-air atmosphere, initial concentrations from two data sets were very similar so the data were combined for analysis. This gave a k_2 value of 9.5×10^{-2} ml mCi^{-1} hr^{-1}, which is somewhat higher than the 6.2×10^{-4} ml mCi^{-1} hr^{-1} determined by Casaletto, Gevantman, and Nash.[26] However, in the present experiment, the initial tritium concentration of 0.22 μCi/ml is significantly lower than the 0.10 to 3.0 mCi/ml range investigated by Casaletto, Gevantman, and Nash.[26] Analysis of the data collected for dry air and sterilized soil with an initial concentration of 0.45 μCi/ml yielded a k_2 value of 5×10^{-2} ml mCi^{-1} hr^{-1}, which is slightly lower than that found for dry air alone. However, no significance is attached to the difference at this time.

The second-order rate constant for the moist-air reaction was found by combining both data sets taken. For an initial concentration of 42.8 μCi/ml, which is within the range investigated by Casaletto, Gevantman, and Nash[26] (oxidation) and Yang and Gevantman[31] (isotopic exchange), the second-order rate was found to be 1.8×10^{-4} ml mCi^{-1} hr^{-1}. It might be expected that the reaction rate for the conversion of tritium to tritium oxide in moist air is equal to the sum of the rates of tritium oxidation in dry air[26] and of tritium isotopic exchange,[31] which were found to be 6.2×10^{-4} and 1.5×10^{-3} ml mCi^{-1} hr^{-1} respectively. This is certainly not true of the present data. Belovodskii et al.[30] compared the conversion rate of tritium in moist air (50% relative humidity) with the conversion rate in an argon-oxygen mixture (20% oxygen) and found that the rates are approximately equal for equivalent tritium concentrations. They also found the conversion rate to vary with the $^5/_3$ power of the initial tritium concentration, whereas other investigators have found a first- or second-order dependence. The initial reaction rate of the present experiment with moist air agrees quite well (within 15%) with the data of Belovodskii et al.[30]

For comparative purposes, previous and present data were used to extract first-order rate constants for the initial reactions. These are presented in Fig. 6.4. It is seen that the present data at the lowest tritium concentrations give a higher constant than one might expect based on the extrapolation of the data of Dorfman and Hemmer,[29] Casaletto, Gevantman, and Nash,[26] and Yang and Gevantman.[31] Thus, based on these preliminary results, it would appear unwise to extrapolate conversion rates at high concentrations to those at low concentrations for radiation protection planning.

Work on tritium concentrations down to $(MPC)_a$ levels for breathing-type environments is planned. For this work, a new system is being fabricated to allow greater precision of measurements.

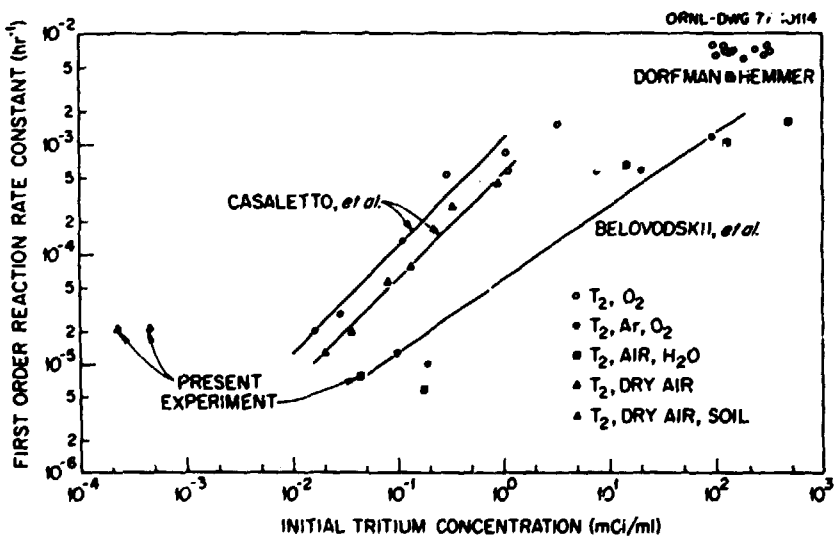

Fig. 6.4. First-order reaction rate constant as a function of the initial tritium concentration.

Part II. Biological and Radiation Physics

H. A. Wright

7. Physics of Solids and Macromolecules

E. T. Arakawa

J. K. Baird
H. L. Barnawell[1]
R. D. Birkhoff
A. J. Braundmeier[2]
T. A. Callcott[3]
M. S. Chung[4]
J. J. Cowan[5]
J. T. Cox
T. L. Haltom[6]
R. N. Hamm
T. Inagaki[7]
R. A. MacRae[2]
L. R. Painter[2]
H. R. Petty[2]

M. W. Williams

Much of our experimental and theoretical work concerning the optical properties of materials developed over the past decade culminated this year in a detailed study of the response of the electrons in a simple hydrocarbon polymer to electromagnetic radiation covering essentially the whole energy range. This was achieved through an examination and testing of various sum rules. In the past, such calculations and their interpretation suffered to a greater or lesser extent because the experimental data were generally unavailable over a wide enough energy range to give the desired certainty in the required extrapolations to infinite energy. Once it can be shown that sum rules can be applied to a set of data such that all information, both input and derived, is consistent, then a wealth of information can be obtained about the material. Polystyrene was chosen because optical data, both ours obtained previously and literature values, were available spanning a wide energy range. Also, polystyrene is a simple hydrocarbon polymer and is hence of basic biological interest. It was found for all the sum rules studied that the convergence was slow, with saturation not occurring until the kiloelectron-volt region. Thus, meaningful conclusions can only be deduced for a hydrocarbon material from sum rule calculations when they are applied to data covering all the electronic excitations, including the innermost core excitations. This situation arises because of coupling between the inner- and outer-shell electrons. In fact, a redistribution of the oscillator strength corresponding to 2.7% of the total electrons was found between the valence and core excitations of the carbon in polystyrene. Studies of this sort are of use in understanding the basic interactions of ionizing radiations with hydrocarbon molecules and hence with molecules of biological interest. They will also be of use to others who are trying to understand the behavior of forces in biological systems. Our measurements this year of the optical properties of arc-evaporated carbon from 0.6 to 3.8 eV, using ellipsometric techniques, fit into this same overall program, providing an addition to composite data on carbon already in the literature.

Using our previously developed semicylinder technique, we measured the refractive indices of some

1. Instrumentation and Controls Division.
2. Consultant.
3. On sabbatical from The University of Tennessee, Knoxville.
4. Graduate student.
5. Physics Division.
6. Southern College University Union participant from Millsaps College, Jackson, Miss.
7. Osaka Kyoiku University, Osaka, Japan.

common solvents over their energy range of transparency from the near infrared up to the region of the absorption edge. These data, required in the proper interpretation of fluorescence spectra, for example, have not been available in the literature over as wide an energy range and/or with the necessary accuracy. We also made a study of the methods used to obtain the kinetic parameters associated with chemical reactions in the liquid and solid states at elevated temperatures. We suggested extensions of three of the methods to take into account the temperature dependence of the pre-exponential factor of the Arrhenius equation; that is, we suggested a modification of the form of the assumed dependence of the rate constant on the temperature at which the reaction is taking place.

The temperature dependence of the *K* x-ray emission edge of lithium was observed for the first time. Lithium films were illuminated with 2-keV electrons and the soft x rays emitted normal to the surface were recorded by a grazing-incidence monochromator, accurately calibrated to at least ±0.03 eV. These measurements allow an interpretation of the shape of the *K* x-ray edge of lithium. More importantly, they settle the long-standing controversy as to the position and width of the Fermi edge. Preliminary data obtained by us at NBS showed a separation of ~0.06 eV between the Fermi edges associated with the soft x-ray absorption and emission spectra of lithium.

Studies initiated last year on multilayer systems for use as solar energy collectors were extended to elevated temperatures. Our copper oxide–silver–glass system, promising at room temperature, deteriorated at elevated temperatures because of interdiffusion of the components. An antidiffusion barrier is being investigated because it is felt that if diffusion problems can be solved, a copper oxide–silver–glass system can be developed into an efficient solar absorber.

Volume and surface plasmons, excited by high-energy (50 to 80 keV) electrons, were studied previously by observation of their radiative decay. Of basic interest is the possibility of a change in volume-plasmon excitation parameters with incident electron energy as that energy becomes small. We studied the radiative decay of volume and surface plasmons excited in silver by low-energy (10 to 2000 eV) electrons. It was found that at low electron energies, surface-plasmon effects dominate the radiative decay spectrum except for spectra from very smooth thin films. Since the spectra are closely related to the surface roughness characteristics, they could be used to obtain information about the sample roughness. On the other hand, it will be more difficult to obtain the information of interest about the volume-plasmon radiation at low excitation energies because it is obscured by surface effects.

We continued last year's work on the fabrication of gratings with specified characteristics using interferometric techniques developed in the field of holography and the study of the characteristics actually obtained. More detailed studies were made of grating efficiencies as well as grating anomalies. The study of optical guided waves continued, including the enhancement of the sensitivity of recording material exposed to guided waves and the production of holograms using these waves. The possibilities of blazing gratings by surface and optical guided waves and also of making zone plates by similar techniques are being investigated. Finally, detailed calculations were initiated for the correction of aberrations in gratings, using both ordinary and optical guided waves.

OPTICAL PROPERTIES OF ARC-EVAPORATED CARBON FILMS

The optical constants of thick arc-evaporated carbon films were determined between 0.6 and 3.8 eV by ellipsometry. Carbon films prepared in this way have many applications, including their use as substrates in both electron microscopy and optical spectroscopy. In some of these cases, a complete analysis of the experimental results requires a knowledge of the thickness and optical properties of the substrate. Although there is voluminous literature on the properties of other types of carbon, we found only fragmentary data on the optical properties of arc-evaporated carbon films.

Bulk carbon was arc-evaporated in vacuum, and a thick carbon film formed by sublimation onto a substrate at room temperature. The optical properties of this film were then determined by analysis of ellipsometric measurements. The experimental techniques used and the method of analysis of the ellipsometric measurements have been described previously.[8] Since carbon does not oxidize at room temperature it was possible to make the measurements at atmospheric pressure. The quartz windows of the ellipsometer were removed and the sample positioned so that reflectance took place at a 70° angle of incidence at the carbon-air interface. Ellipsometric measurements were obtained over the range of photon energies from 0.6 to 3.8 eV. The values derived from these measurements for the real and imaginary parts n and k, respectively, of the com-

8. T. Inagaki et al., *Phys. Rev. B* 13, 2305 (1976).

plex refractive index as a function of photon energy are presented in Fig. 7.1.

Examination of unannealed arc-evaporated carbon films by electron microscopy and electron diffraction techniques and interpretation of their electrical properties led to the suggestion that unannealed arc-evaporated carbon is "more truly amorphous in structure than any other form of carbon yet obtained."[9] However, the electrical and optical properties of unannealed arc-evaporated carbon films do depend on the conditions under which the films are prepared, and annealing then produces irreversible changes in these properties. Hence the paucity of data which might be directly compared with those presented in Fig. 7.1. It is of interest, however, to compare the present data for arc-evaporated carbon with those for glassy carbon.[10] The results obtained previously for n and k of glassy carbon over the energy range of the present study are reproduced in Fig. 7.1. Also presented are values of n and k obtained from analysis of ellipsometric measurements on the same sample as was used in ref. 10. Values of the optical properties are similar for the two types of carbon except at the lowest energies measured. In fact, it is most likely that differences in optical properties due to structural differences would occur at low energies where excitations are associated with the bonding electrons. Thus, it is felt that where the optical properties of arc-evaporated carbon are required over a more extended energy range than those presented in Fig. 7.1, the results for glassy carbon above 3.8 eV may be used. In fact, a composite set of data published for evaporated carbon[11] uses the data for k for glassy carbon[10] from 0.5 to 80 eV, together with data for graphite below 0.5 eV and data for arc-evaporated carbon above 80 eV The present data is a useful addition to this compilation in the low-energy region, where differences are likely to be most significant. If more exact optical properties are required for evaporated carbon for a particular application, the optical properties of the actual sample, or samples prepared under identical conditions, should be measured.

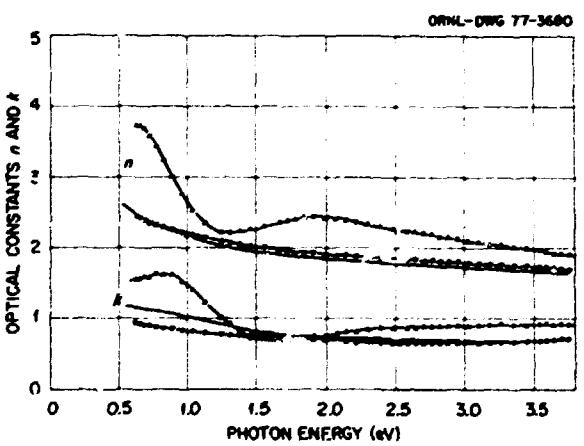

Fig. 7.1. Optical properties of arc-evaporated carbon (▲) and of glassy carbon (○) from ellipsometric measurements vs incident photon energy. Also shown are the optical properties of glassy carbon obtained from reflectance measurements (—) and reproduced from ref. 10.

CONVERGENCE OF OPTICAL SUM RULES

We examined in detail the response of the electrons in polystyrene to electromagnetic radiation covering essentially the whole energy range.[12] This was achieved through sum rule calculations which have been employed to determine the way in which the oscillator strength converges. In the past, such calculations and their interpretation suffered to a greater or lesser extent because the experimental data were generally unavailable over a wide enough energy range to give the desired certainty in the required extrapolations to infinite energy. Polystyrene was chosen for this study because it is one of the simplest hydrocarbon polymers and measurements of the extinction coefficient k were already available over a wide energy range. The data for k are reproduced in Fig. 7.2. From 0.6 to 82 eV the values of k were obtained in our laboratory;[12,13] those from 30 to 1550 eV were taken from Lukirskii, Fomichev, and Brytov[14] and those from 1490 to 8050 eV from Nordfors.[15] The combined spectrum of k covers substantially all the electronic excitations (>99.9% of the total oscillator strength), including the carbon core excitations starting at ~282 eV. The best fit of the data between 20 and 60 eV is given by the expression

$$k(E) = 7.81 \times 10^3 E^{-3.23} , \qquad (1)$$

where E is the photon energy in electron volts, and the extrapolation of this to higher energies is shown as the

9. M. D. Blue and G. C. Danielson, *J. Appl. Phys.* **28**, 583 (1957).
10. M. W. Williams and E. T. Arakawa, *J. Appl. Phys.* **43**, 3460 (1972).
11. H. J. Hagemann, W. Gudat, and C. Kunz, *Optical Constants from the Far Infrared to the X-ray Region: Mg, Al, Cu, Ag, Au, Bi, C, and Al_2O_3*, report DESY SR-74/7, May 1974.
12. T. Inagaki et al., *Phys. Rev. B* **15**, 3243 (1977).
13. E. T. Arakawa et al., *Health Phys. Div. Annu. Prog. Rep. June 30, 1975*, ORNL-5046 (September 1975), pp. 131–32.
14. A. P. Lukirskii, V. A. Fomichev, and I. A. Brytov, *Opt. Spectros. USSR* **20**, 202 (1966).
15. B. Nordfors, *Ark. Fys.* **11**, 587 (1957).

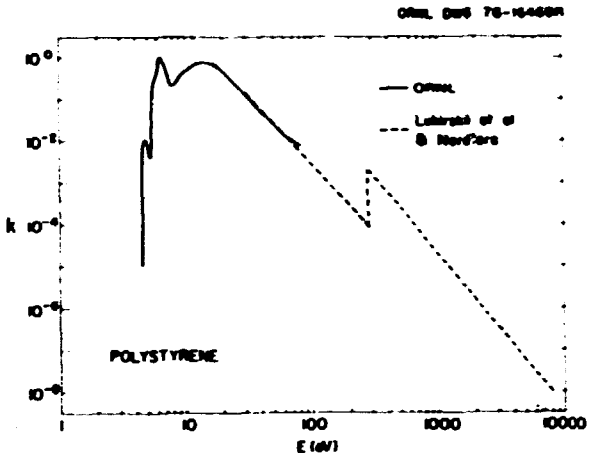

Fig. 7.2. The extinction coefficient k for polystyrene as a function of photon energy E. Dotted line is extrapolation of the data between 20 and 60 eV.

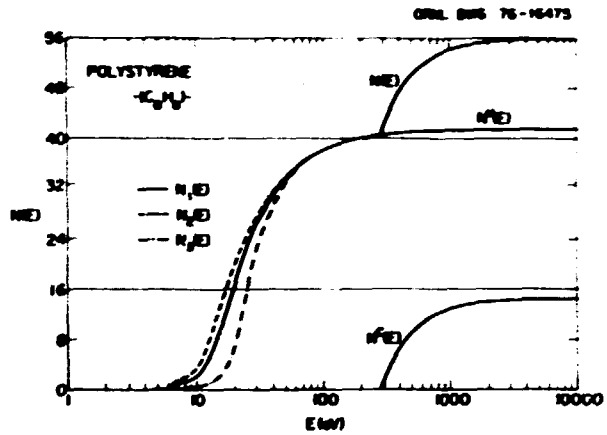

Fig. 7.3. Effective number of electrons $N_1(E)$, $N_2(E)$, and $N_3(E)$ per monomeric unit of polystyrene obtained from the extinction coefficient k, the imaginary part of the complex dielectric function $\epsilon(=\epsilon_1 + i\epsilon_2)$, and the energy loss function $\mathrm{Im}(-1/\epsilon)$, respectively, as functions of photon energy E. $N^v(E)$ and $N^c(E)$ represent the contributions from the valence and core electron excitations respectively.

dotted line in Fig. 7.2. The jump in the experimental data at 282 eV is due to the carbon K-shell absorption edge.

The validity and internal consistency of the combined experimental k data presented in Fig. 7.2 over such an unusually wide energy range were first checked by evaluating the sum rule

$$N_1(E) = (4/\pi)(m/4\pi n_0 e^2 \hbar^2) \times \int_0^E E' k(E')\, dE' \to N;\ E \to \infty, \qquad (2)$$

where m is the free electron mass, $\hbar$ is Planck's constant divided by 2π, n_0 is the molecular density, and N is the total number of electrons in a molecule. Taking a monomeric unit $-(C_8H_8)-$ of polystyrene as a molecular unit, N is 56. In carrying out the integration in Eq. (2), the k values above 8050 eV were assumed to be represented by $k(E) = 2.21 \times 10^6\, E^{-3.68}$ to an infinite photon energy;[12] in the region below 0.6 eV the k values were assumed to be so small that the contribution of $E'k(E')$ to $N_1(E)$ could be neglected. The results of calculations of $N_1(E)$ are plotted in Fig. 7.3 as a function of E. Since in this study it was difficult to determine experimentally the density of the polystyrene film ρ with an uncertainty less than ±2%, the molecular density n_0 $(= L\rho/M)$ was adjusted so that the value of $N_1(E)$ became equal to N in the limit of $E \to \infty$. (L is Avogadro's number, and M is the molecular weight.) This adjustment gave a film density of 1.040 g/cm^3, in excellent agreement with the measured value of (1.05 ± 0.02) g/cm^3. Thus, in this check, the overall validity of the k values was confirmed with an uncertainty of ±1%.

Further evaluations of $N_1(E)$ were made separately on the k values due to the valence and core excitations. The sawtooth shape of the k spectrum in the logarithmic plot at ~282 eV allows us to separate the absorption due to the core excitations from the total absorption. The separation was made by assuming Eq. (1) to hold for the valence electrons for all energies above 20 eV. The results of $N_1^v(E)$ and $N_1^c(E)$, the contributions to $N_1(E)$ from the valence and core excitations, respectively, are given in Fig. 7.3. A redistribution of electron numbers corresponding to 1.51 electrons is found between the valence and core excitations. $N_1^v(E)$ and $N_1^c(E)$ should tend to 40 and 16, the numbers of valence and core electrons, respectively, in the limit $E \to \infty$, if there is no oscillator strength coupling between them. Also, the effective numbers of electrons (plotted in Fig. 7.3 as functions of photon energy E) do not saturate until a few thousand electron volts. This applies even to the valence electrons, showing that even at these high energies the contribution of valence excitations to the oscillator strength is not negligible.

The refractive index $n(E)$ at a photon energy E was then determined from the k spectrum using the Kramers-Kronig relation

$$n(E) - 1 = \frac{2}{\pi} \int_0^\infty \frac{E' k(E')}{E'^2 - E^2}\, dE'. \qquad (3)$$

It can be shown[12] that if the $k(E)$ values can be expressed for $E \geq E_1$ in the form

$$k(E) = \alpha E^{-\beta}, \tag{4}$$

then for $\beta > 2$, $n(E) - 1$ goes asymptotically to

$$n(E) - 1 = -\frac{E_p^2}{2E^2} \tag{5}$$

at high energies, where E_p^2 is a constant defined by $E_p^2 = (4/\pi) \int_0^\infty E'k(E')\,dE'$. Then, from Eq. (2), $E_p^2 = (4\pi n_0 e^2 \hbar^2/m)N_1(\infty)$. Equation (5) is the form of $n(E) - 1$ representing the behavior of a free-electron gas in the high-energy limit. Since the data for polystyrene can be represented by a relationship of the form of Eq. (4) for $E_1 = 20$ eV and since $\beta > 2$, polystyrene should behave as a free-electron gas at high energies. It was found that $n(E) - 1$, $n^v(E) - 1$, and $n^c(E) - 1$, calculated from Eq. (3) where $n^v(E) - 1$ and $n^c(E) - 1$ are the contributions to $n(E) - 1$ from the valence and core excitations, respectively, do tend to zero at high energies. The monotonic convergences of $n^v(E) - 1$ and $n^c(E) - 1$ to the respective free-electron values were found to start at ~100 and 900 eV respectively.

Analyses were then performed for several sum rules, using the optical functions $n(E)$ and $k(E)$ obtained over essentially the whole energy spectrum. These included the well-known f-sum rules[16] for $N_2(E)$ and $N_3(E)$ involving the imaginary part ϵ_2 of the complex dielectric function $\epsilon[\epsilon = \epsilon_1 + i\epsilon_2 = (n + ik)^2]$ and the energy loss function $\mathrm{Im}(-1/\epsilon)$ respectively. These sum rules are given by the expressions

$$N_2(E) = \frac{2}{\pi}(m/4\pi n_0 e^2 \hbar^2) \times \int_0^E E'\epsilon_2(E')\,dE' \to N;\ E \to \infty$$

and

$$N_3(E) = \frac{2}{\pi}(m/4\pi n_0 e^2 \hbar^2) \times \int_0^E E'\,\mathrm{Im}\left[\frac{-1}{\epsilon(E')}\right] dE' \to N;\ E \to \infty .$$

The calculated values of $N_2(E)$ and $N_3(E)$, obtained from the values of $n(E)$ and $k(E)$ and the same value of n_0 as was used in the calculation of $N_1(E)$, are also plotted in Fig. 7.3. All these numbers of effective electrons converge, as expected, to the same value in the high-energy limit.

The average photoexcitation energy $\bar{E}_2(E_0)$, averaged over the spectral region from E_0 to infinity, was obtained from

$$\bar{E}_2(E_0) = \int_{E_0}^{\infty} E\epsilon_2(E)\,dE \Big/ \int_{E_0}^{\infty} \epsilon_2(E)\,dE .$$

Similarly, the average energy loss suffered by fast charged particles interacting with the medium was calculated from

$$\bar{E}_3(E_0) = \int_{E_0}^{\infty} E\,\mathrm{Im}\left[\frac{-1}{\epsilon(E)}\right] dE \Big/ \int_{E_0}^{\infty} \mathrm{Im}\left[\frac{-1}{\epsilon(E)}\right] dE .$$

Plots of $\bar{E}_2(E_0)$ and $\bar{E}_3(E_0)$ as functions of E_0 are of help in evaluating the contribution of excitations in a particular energy range to the average excitation energy and energy loss. These quantities are of key importance in radiation physics, which deals with the interaction of high-energy ionizing radiations with matter. Since, in the present results, the onset of valence absorption was found at 4.5 eV, the values of $\bar{E}_2(E_0)$ and $\bar{E}_3(E_0)$ at $E_0 = 4.5$ eV give the average excitation energy and energy loss, respectively, over the entire oscillator strength distribution. $\bar{E}_2$ and $\bar{E}_3$ at $E_0 = 4.5$ eV were found to be 25.1 and 36.8 eV respectively. The difference in these quantities can be attributed to an energy loss associated with the creation of collective oscillations due to the interaction of fast charged particles with matter, since photons generally do not excite collective oscillations in experimental systems designed for the measurement of k.

A simple and interesting sum rule,

$$S(E) = \int_0^E \{n(E') - 1\}\,dE' \to 0;\ E \to \infty , \tag{6}$$

was derived recently by Altarelli et al.[17] for the refractive index $n(E)$ of isotropic media, including conductors. This sum rule asserts that the average value of the refractive index over the whole spectral range is equal to unity, the only assumption being that in the high-energy limit the medium responds like a free-electron gas. Values for $S(E)$ evaluated from $n^v(E) - 1$ and $n^c(E) - 1$

16. P. Nozières and D. Pines, *Phys. Rev.* 113, 1254 (1959).
17. M. Altarelli et al., *Phys. Rev. B* 6, 4502 (1972).

are given in Fig. 7.4 as functions of photon energy E up to 10^4 eV. Both $S^v(E)$ and $S^c(E)$ converge slowly to zero at high energies. For a high energy E, above which the behavior of $n(E) - 1$ can be represented by the free-electron expression [Eq. (5)], $S(E)$ may be approximated by

$$S_F(E) = \int_E^{\infty} [n(E') - 1]\, dE' \simeq E_p^2/2E . \qquad (7)$$

This form describes the asymptotic behavior of $S(E)$ in the high-energy limit. $S_F(E)$ from the valence and core contributions are presented in Fig. 7.4 and compared with the results for $S(E)$. Over a wide range in the high-energy region, $S(E)$ is described well by $S_F(E)$. Relative deviations between $S(E)$ and $S_F(E)$ are, however, about the same as those found in similar plots for the other sum rules.

In conclusion, the convergence of all sum rules associated with the optical constants of polystyrene is quite slow, and the almost perfect saturations do not occur until the kiloelectron-volt region. This is for a material having one of the simplest of all electronic configurations. Experimentally, the f-sum rules have provided useful criteria for consistency checks of the optical constants. However, f-sum rules are applicable only when the experimental data cover all electronic excitations, including the innermost core excitations. In addition to the slow convergences, difficulties arise in applying the f-sum rules for a particular shell because a nonnegligible amount of oscillator strength coupling always occurs between the inner- and outer-shell electrons. If experimental data cover only a part of the total oscillator strength distribution, as is so in most cases, the oscillator strength for a particular shell, to which the f-sum rules should converge, cannot be known a priori without knowing those for the remaining shells. It has been proposed recently by Altarelli et al.[17] that the $S(E)$ sum rule for the refractive index given by Eq. (6) may be used as a saturation criterion and/or as a consistency check for the optical constants obtained experimentally. The present results for $S(E)$ (Fig. 7.4) indeed converge to the free-electron values $S_F(E)$ given by Eq. (7) much faster than the f-sum rules converge. Differences between $S(E)$ and $S_F(E)$, however, are not negligibly small up to quite high energies. Further, E_p^2 for a particular shell in the expression for $S_F(E)$, which is proportional to the oscillator strength, cannot be known until the convergence of the f-sum rule is attained. Practically, the new sum rule for $S(E)$, if applied to a particular shell, is subject to the same uncertainty as the f-sum rules.

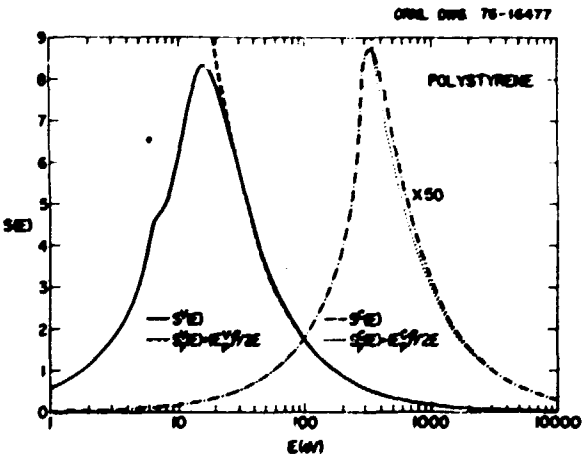

Fig. 7.4. The sum rule $S(E)$ for the refractive index n of polystyrene as a function of photon energy E. $S^v(E)$ and $S^c(E)$ represent the contributions from the valence and core electron excitations respectively. $S_F^v(E)$ and $S_F^c(E)$ represent the corresponding free-electron values.

TEMPERATURE DEPENDENCE OF THE K X-RAY EMISSION EDGE OF LITHIUM

The interpretation of the shape of the K x-ray edge of lithium has long been a source of controversy. The soft x-ray emission spectrum has been studied by several different workers, but in each case the spectrum was only recorded at essentially a single temperature. Since these data can be described by several different theories, additional information is necessary to choose the correct interpretation from among them. Recently, some additional related information has been reported in the form of measurements[18] on the temperature dependence of the K x-ray absorption edge of lithium. These measurements were made from 4°K to above the melting point of lithium with a resolution of 0.11 eV. We have performed complementary experiments[19] by measuring the soft x-ray emission spectra of lithium with a resolution of 0.1 eV at a number of temperatures between 85° and 490°K. These two experiments, performed over a large range of temperatures, have resolved much of the controversy concerning the K x-ray edge of lithium.

18. H. Petersen, *Phys. Rev. Lett.* **35**, 1363 (1975); E. E. Koch, C. Kunz, and B. Sonntag, *Electronic States in Solids Investigated by Means of Synchrotron Radiation*, DESY internal report F41-75/03, May 1976; H. Petersen and C. Kunz, to be published.

19. T. A. Callcott and E. T. Arakawa, *Phys. Rev. Lett.* **38**, 442 (1977).

Our soft x-ray emission measurements were made on thick lithium films (~10,000 Å) evaporated on a polished copper block in an ion-pumped ultrahigh vacuum chamber. The block was cooled by circulating liquid and heated by electron bombardment. Its temperature was monitored by a thermocouple clamped under a screw on the face of the block. The system operated at a base pressure of 2×10^{-9} torr after a mild bakeout and at 1×10^{-8} torr when connected to the monochromator used in the experiments, but pressure bursts to $\sim 2 \times 10^{-7}$ torr were observed during evaporation of the lithium films. For the measurements reported here, the lithium films were illuminated by a 3- to 4-mA beam of 2-keV electrons incident at an angle of 45° to the film surface. Soft x rays emitted normally from the sample surface were analyzed by a MacPherson 247 grazing incidence monochromator equipped with a 1200 lines/mm gold-coated grating and a Spiraltron detector. A careful calibration of the monochromator was made immediately before the experiment at a resolution of 0.07 eV using a spark spectrum of air, which produces a multitude of sharp lines in the energy range of interest. The lithium experiments were performed with slit widths of 50 μm and a resolution of 0.1 eV as determined directly from the half-widths of the line spectra at this slit setting. We believe that our energy scale is accurate to at least 0.03 eV. In temperature cycling experiments, a reduction in peak amplitude of about 15% occurred between 200° and 440°K. This change was reversible so long as the sample did not melt. A further irreversible reduction of about 20% was observed when the sample melted. After storage in a 10^{-8}-torr vacuum for six days, the lithium peak level decreased to 35% of its original value, and a lithium oxide peak was observed with a magnitude $1/10$ as large as the reduced lithium peak. No significant change in the overall shape of the lithium peak was observed as a function of time.

To obtain high-resolution results, we digitized and added repeated spectral curves at approximately 0.025-eV intervals. Figure 7.5 shows the averaged results of 15 measurements of the high-energy edge of the soft x-ray emission spectrum made at 85° ± 5°K shortly after a fresh evaporation of lithium onto the liquid-nitrogen-cooled substrate. Figure 7.6 shows similar data for measurements made at six temperatures between 85° and 490°K; the curve at 435°K gives data taken just below the melting point of lithium. The different curves were normalized to the same height for clarity in comparing structural changes with increasing temperature.

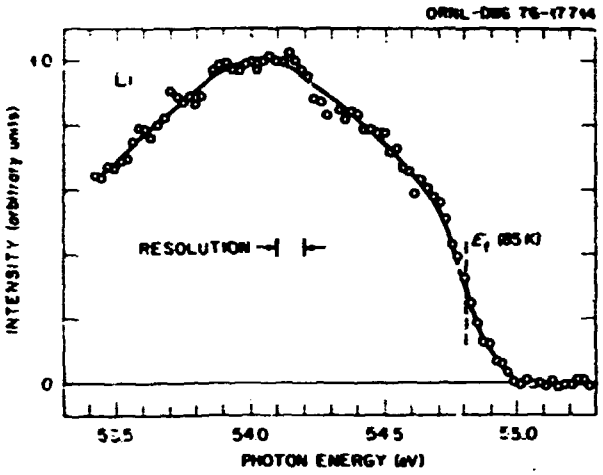

Fig. 7.5. The x-ray emission spectrum of lithium at 85°K. The points are the average of fifteen measurements of the spectrum, and the line is a smooth curve drawn through the points.

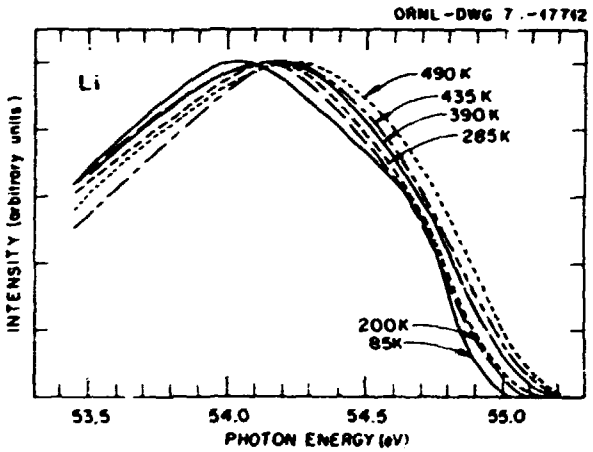

Fig. 7.6. Emission spectra of lithium at six temperatures from 85° to 490°K. The curves represent smooth fits to digital data (Fig. 7.5).

The most striking feature of the spectrum at 85°K (Fig. 7.5) is the well-developed shoulder at 54.7 eV. Low-temperature data obtained previously by various workers had indicated this structure in the emission spectrum, but it was completely absent in data obtained on targets which, because of electron heating, were above room temperature. Because data were not obtained on a single sample over an extensive range of temperatures, there was uncertainty as to the reliability of the spectra and their interpretation. In particular, the width of the true emission edge, and hence where to locate the Fermi edge, was widely debated. Our data (Fig. 7.6) is consistent with the previously published data in that the structure seen at 85°K is progressively

broadened as the temperature is increased and is no longer visible above room temperature except as a gradual change in slope. We have interpreted the steeply falling region above the shoulder in energy as the true Fermi edge.[19] We can then locate the edge at the center of the steeply falling portion of the curve (54.8 eV at 85°K). The width of the edge is ~0.2 eV as measured between the 10% and 90% points of the steep portion above the shoulder. The maximum in the emission spectrum is located ~0.7 eV below the Fermi edge and a full 0.6 eV below the shoulder. This interpretation is in complete accord with that given for the absorption spectrum.[18] In that case, the Fermi edge at 80°K was located at ~54.9 eV and was assigned a width of ~0.2 eV. The maximum in the absorption spectrum occurred ~0.5 eV above the Fermi edge. It should be possible through band structure calculations to explain the peaks in the emission and absorption spectra at 0.7 and 0.5 eV, respectively, away from the Fermi edges in terms of one-electron transition probabilities associated with structure in the density of states. Different theoretical approaches predict either the observed structure in the absorption or in the emission spectra, but no single theory predicts both structures. We find, in fact, that no combination of currently available one-electron calculations, in which are included any of the various broadening processes, can give a satisfactory account of both the soft x-ray emission and absorption spectra of lithium, but such an explanation may well be possible.

In Fig. 7.7, we display two of our soft x-ray emission curves along with the absorption curves of Petersen et al.[18] All curves are normalized to the same maximum height, and the symmetry of the emission and absorption curves is quite striking. The steeply rising Fermi edges of both curves have about the same width. Moreover, both curves shift to higher energy and broaden by comparable amounts with changes of temperature. A separation of about 0.07 eV is observed between the Fermi edges of the soft x-ray emission and absorption curves, and this separation is maintained as the curves shift and broaden with increasing temperature. This apparent gap between the edges was questionable, however, since the curves were made with separately calibrated instruments and calibration uncertainties are comparable in magnitude to the measured separation. Recently we have recorded both the soft x-ray absorption and emission spectra of lithium on the same sample using the same spectrometer. This experiment, performed in collaboration with NBS using synchrotron radiation for the absorption spectrum, showed a separation of ~0.06 eV between the Fermi edges and hence confirmed the general validity of the data presented in Fig. 7.7. The complete analysis of these data and their theoretical significance will be presented in next year's annual report.

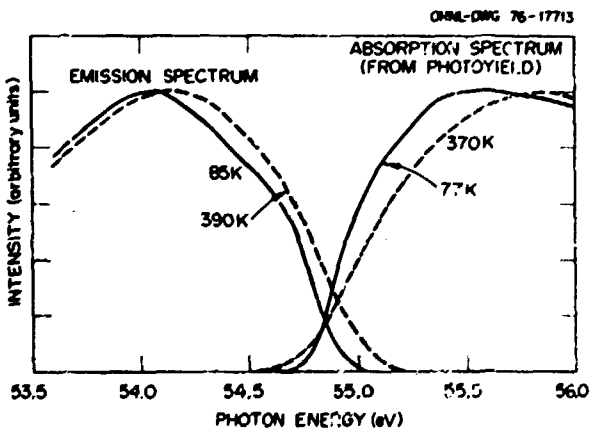

Fig. 7.7. Comparison of absorption and emission edges of lithium. Absorption curves are taken from ref. 18.

We conclude this account with a few comments on possible self-absorption effects, since it has been suggested that the steep edge might be an experimental artifact resulting from self-absorption.[20] Our experiments were performed with excitation conditions that rough calculations indicate should give negligible self-absorption (2-keV electrons incident at 45° and normally emitted photons). Internal evidence in the data confirms the calculations. If self-absorption were important, the steep upper edge should persist to higher temperatures since emission and absorption probabilities do not change much with temperature and since the overlap is greater at higher temperatures. Additional experimental checks were made by measuring the edge with excitations between 1 and 3 keV with the 45° gun and by using a different gun which produced 1-keV electrons incident at 75° from the sample normal. In all cases the shape of the edge was unchanged from that observed with 2-keV electrons.

REFRACTIVE INDICES OF TRANSPARENT SOLVENTS

We measured the refractive indices of some common solvents over their energy range of transparency from the near infrared up to the region of the absorption edge. These data, required in the proper interpretation of fluorescence spectra, for example, have not been available in the literature over as wide an energy range

20. A. J. McAlister, *Phys. Rev.* **186**, 595 (1969).

and/or with the necessary accuracy. The only comprehensive study of refractive indices of liquids over an extended energy range already reported was performed by Voellmy[21] in 1927. The highest photon energy to which Voellmy made measurements was 5.77 eV (2150 Å), although for some liquids measurements were only made up to 3.87 eV (3200 Å). Our method of obtaining refractive indices involves critical angle measurements using a liquid cell with a semicylindrical window. Since this method does not depend on proper normalization techniques, in most cases it is possible to obtain the refractive indices of transparent solvents to higher energies than were reported by Voellmy.

Details of the experimental technique have been described previously.[22,23] The solvents were reagent grade and were used without further purification. Each liquid under investigation was contained in a closed cell, one side of which consisted of a transparent semicylinder. Light entered the semicylinder along a radius and hence normal to the curved surface, was reflected at the plane semicylinder-liquid interface, and exited from the semicylinder along a radius. If the refractive index of the material of the semicylinder, n_s, is greater than that of the liquid, n, for a given photon energy, then $n/n_s = \sin\theta_c$ where the critical angle θ_c is defined as the angle which marks the onset of total reflection. Thus, if n_s is known and θ_c is measured, n can be calculated. In practice, n_s was measured for the material of the semicylinder with the cell empty.

For the observations reported here, a quartz (Suprasil) semicylinder was used. This was cleaned initially with soap and water, then dipped in concentrated solutions of chromic acid and sodium hydroxide to remove any soap or oil films. It was then rinsed thoroughly with distilled water and flushed with isopropyl alcohol. Finally, the crystal was flushed with freshly distilled Freon 113 from a vapor degreasing bath. This cleaning procedure was used before measuring the refractive index of the semicylinder and also before the measurement of the refractive indices of each of the solvents. Scans of reflectance as a function of angle of incidence at the plane semicylinder-air and semicylinder-liquid interfaces were recorded for selected wavelengths over the range of 2000 to 5900 Å. When the solvent is completely transparent, as in the present case, its extinction coefficient k is zero, and ideally the critical angle should be sharply defined. However, the observed reflectance vs angle of incidence curves did not show a perfectly defined critical angle as predicted by Fresnel's equations due to the limitations of instrumental resolution. This effect was taken into account when estimating values of θ_c from our experimental reflectance vs angle of incidence curves. The refractive indices obtained for the quartz semicylinder and the four solvents, *n*-hexane and methyl, ethyl, and isopropyl alcohol, are given in Table 7.1 as functions of incident photon wavelength.

21. H. Voellmy, *Z. Phys. Chem. Stoechiom. Verwandschaftsl.* **127**, 305 (1927).
22. L. R. Painter, R. D. Birkhoff, and E. T. Arakawa, *J. Chem. Phys.* **51**, 243 (1969).
23. R. A. MacRae, M. W. Williams, and E. T. Arakawa, *J. Chem. Phys.* **61**, 861 (1974).

Table 7.1. Refractive index *n* as a function of photon wavelength λ

λ (Å)	*n*				
	Quartz (Suprasil)	*n*-Hexane	Methyl alcohol	Ethyl alcohol	Isopropyl alcohol
2000	1.551	1.482	1.423	1.467	1.482
2100	1.535	1.464	1.405	1.450	1.464
2200	1.525	1.452	1.392	1.435	1.451
2300	1.518	1.441	1.383	1.423	1.441
2400	1.512	1.433	1.377	1.415	1.433
2600	1.502	1.421	1.367	1.404	1.421
2800	1.493	1.411	1.359	1.396	1.413
3000	1.487	1.405	1.353	1.390	1.406
3200	1.482	1.399	1.348	1.385	1.401
3400	1.478	1.395	1.344	1.381	1.397
3600	1.475	1.392	1.342	1.378	1.393
3800	1.472	1.389	1.339	1.375	1.390
4000	1.469	1.386	1.337	1.373	1.388
4500	1.465	1.382	1.333	1.368	1.383
5000	1.461	1.378	1.331	1.365	1.380
5500	1.459	1.376	1.329	1.363	1.378
5900	1.458	1.375	1.329	1.362	1.377

Use of a semicylindrical window enables a direct observation of θ_c, since light enters and leaves the semicylinder normal to the curved surface and hence is not refracted at these interfaces. Since the location of θ_c does not depend on a proper normalization of the variation of reflectance with angle of incidence, reflections at the curved surfaces do not affect the location of θ_c. For the same reason, our technique can be used even when the solvent is fluorescent. In Voellmy's work,[21] absorption by low-lying singlet π states apparently limited some of his results; for example, for benzene his observations cut off at 4.59 eV (2700 Å), whereas our technique using a suitable semicylinder can yield the refractive index of benzene up to the absorption edge at 5.64 eV (2200 Å). Furthermore, the observed location of θ_c is relatively insensitive to surface imperfections at the semicylinder-liquid interface. The uncertainty in the absolute refractive index values obtained by this method are estimated to be ±0.001 over the whole wavelength range studied. This uncertainty arises mainly in the treatment of the instrumental resolution in estimating θ_c from the experimental reflectance vs angle of incidence scans. All observations were made at a room temperature of 22° ± 1°C. Where values of n are available in the literature, they agree with those in Table 7.1 within the stated experimental accuracies.

The solvents studied this year all have relatively low refractive indices, enabling a quartz semicylinder to be used. For solvents with relatively large refractive indices, such as benzene and toluene, a semicylinder of some material having a larger refractive index, such as sapphire, will have to be used.

TEMPERATURE DEPENDENCE OF THE PRE-EXPONENTIAL FACTOR OF THE ARRHENIUS EQUATION

Three widely used methods make use of thermogravimetric data to evaluate the kinetic parameters of chemical reactions in the liquid and solid states at elevated temperatures. The most frequently used method, developed by Freeman and Carroll,[24] is a difference-differential method involving differences in rate which attempts to determine both the order of the reaction and the activation energy. The approach taken by Coats and Redfern[25] involves an "integral" method which utilizes weight loss vs temperature data directly. This method assumes that the correct choice of the order of the reaction yields the best linear plot from which the activation energy is determined. Achar, Brindley, and Sharp[26] developed a differential method, using the rate of weight loss in a reaction, which has the advantage of applying even if an order cannot be assigned to the reaction. Sharp and Wentworth[27] compared these methods and concluded that Freeman and Carroll's method is less satisfactory than the other two, both of which can lead to satisfactory kinetic analyses if the experimental conditions minimize temperature gradients within the reactant. In all three methods it was assumed that the pre-exponential factor of the Arrhenius equation for the rate constant is temperature independent. It has been shown experimentally, however, for a number of gas- and solution-phase reactions that a more general form of the Arrhenius equation is necessary to explain the kinetic data. We have proposed extensions of these three methods which take into account the temperature dependence of the pre-exponential factor of the Arrhenius equation.[28]

Consider a liquid or solid reactant which decomposes into two substances, one of which is in a condensed state and the other volatile. The rate of disappearance of the reactant from the mixture can be expressed, for a constant temperature T, by

$$\frac{d\alpha}{dt} = k(1-\alpha)^n , \tag{8}$$

where α is the fraction of the reactant decomposed at time t, k is the rate constant, and n is the order of the reaction. The Arrhenius equation represents as closely as possible the experimentally observed dependence of k on the temperature at which the reaction is taking place. We have assumed the Arrhenius equation to be of the form

$$k = ZT^b \exp(-E/RT) , \tag{9}$$

where Z and b are constants, R is the gas constant, and E is the activation energy. We also assume a linear heating rate given by

$$a = dT/dt , \tag{10}$$

which conforms to previously used experimental techniques and theoretical assumptions. The difference between this and all previous analyses lies in the possi-

24. F. S. Freeman and B. Carroll, *J. Phys. Chem.* **62**, 394 (1958).
25. A. W. Coats and J. P. Redfern, *Nature* **201**, 68 (1964).
26. B. N. N. Achar, G. W. Brindley, and J. H. Sharp, *Proc. Int. Clay Conf., Jerusalem* **1**, 67 (1966).
27. J. H. Sharp and S. A. Wentworth, *Anal. Chem.* **41**, 2060 (1969).
28. H. R. Petty, E. T. Arakawa, and J. K. Baird, to be published in *Journal of Thermal Analysis.*

bility of nonzero values of b in Eq. (9). The way in which a nonzero b appears in each of the established methods will now be demonstrated.

Freeman and Carroll's method is known to possess several difficulties but is still frequently used and hence needs to be considered here. It has been used successfully in solution studies and is unique in that it allows for the direct determination of the order of the reaction. Combining Eqs. (8) and (9) to eliminate k and differentiating the logarithmic form of the resulting equation with respect to T gives

$$d\ln(d\alpha/dt) = \frac{E\,dT}{RT^2} + \frac{b\,dT}{T} + n\,d\ln(1-\alpha)\,. \qquad (11)$$

The values of E, b, and n may be obtained from a least-squares fit of the data to Eq. (11). Alternatively, if b is chosen to have a specific value, a plot of

$$\frac{d\ln(d\alpha/dt) - b(dT/T)}{d\ln(1-\alpha)} = n + \frac{E}{R}\left[\frac{dT}{T^2\,d\ln(1-\alpha)}\right]$$

will yield a straight line with a slope of E/R and an intercept of n. Several values of b should be used to find the best fit of the data. The factor Z may also be obtained from the original equation once E, b, and n have been determined.

The method devised by Coats and Redfern[25] is an integral method; hence, derivative thermogravimetric data are unnecessary. Since there is theoretical justification for orders of reaction of 0, ½, ⅔, and 1, these are the values of n generally assumed. The most nearly linear Coats and Redfern plot is then chosen to correspond to the correct values of n, E, and Z. Combining Eqs. (8), (9), and (10) and integrating gives

$$\int_0^{\alpha} \frac{d\alpha'}{(1-\alpha')^n} = \frac{Z}{a}\int_0^{T} T'^b \exp(-E/RT')\,dT'\,. \qquad (12)$$

The left-hand integral may be treated by standard techniques, but that on the right is more complicated. It can be shown[28] that the right-hand side $J(T)$ of Eq. (12) is given by

$$J(T) = \frac{Z}{a}\left(\frac{R}{E}\right)T^{b+2}\left[1 - \frac{b+2}{(E/RT)} + \frac{(b+2)(b+3)}{(E/RT)^2}\cdots\right] \times \exp(-E/RT)\,. \qquad (13)$$

Equation (13) is an asymptotic (semiconvergent) series. The series is finite and exact, however, when b is a negative integer less than -2. When $b = -2$, Eq. (13) is a simple exponential function. When $b = 0$, Eq. (13) corresponds to the result found by Coats and Redfern. It is noteworthy that n and b are not restricted to the integers but may be allowed to take on any real values. If we include only the first two terms in Eq. (13), then Eq. (12) becomes

$$\frac{1-(1-\alpha)^{1-n}}{1-n} = \frac{ZRT^{b+2}}{aE}\left[1 - \frac{RT(b+2)}{E}\right] \times \exp(-E/RT)\,. \qquad (14)$$

Thermogravimetric data may be analyzed according to Eq. (14) in a number of ways.

Of these, we consider two. First, we follow Coats and Redfern and write Eq. (14) in the form

$$\ln\left\{\frac{1-(1-\alpha)^{1-n}}{(1-n)T^{b+2}}\;\frac{aE}{R\left[1 - \frac{(b+2)RT}{E}\right]}\right\} = \ln Z - \frac{E}{RT}\,.$$

If n and b are given assumed values, the quantities E and Z may be obtained by the method of least squares by iterating on E. Secondly, Eq. (14) may be written in the form

$$\ln\left\{\frac{1-(1-\alpha)^{1-n}}{1-n}\;\frac{aE}{R\left[1 - \frac{(b+2)RT}{E}\right]}\right\} = \ln Z + (b+2)\ln T - \frac{E}{RT}\,.$$

If n is given an assumed value, then E, Z, and $b + 2$ may be determined by the method of least squares by iterating on E and b. The success of this method will depend on whether $\ln T$ varies enough so that the value of the determinant of the least-squares matrix is not dominated by random errors in the measurements of α and T.

The method of Achar, Brindley, and Sharp[26] is a differential method involving the rate of weight loss in a reaction. From Eqs. (8), (9), and (10), after rearranging and taking logarithms, we find

$$\ln\{(a\,d\alpha)/[T^b(1-\alpha)^n\,dT]\} = \ln Z - (E/RT)\,. \qquad (15)$$

A plot of $\ln\{a\,d\alpha/[T^b(1-\alpha)^n\,dT]\}$ as a function of $1/T$ results in a straight line from which the values of E and Z can be determined. Values of n and b may be obtained from iterative calculations. Clearly, it is also possible to expand Eq. (15) and employ b as a least-squares parameter.

Even though thermogravimetric and derivative thermogravimetric data often span wide temperature ranges, there has as yet been no quantitative test of the temperature dependence of the pre-exponential factor. In some cases where the activation energy is small, this temperature dependence may be observable. It is hoped that this theoretical study will prompt a more exact analysis of the kinetic parameters associated with condensed-phase reactions.

HIGH-TEMPERATURE SOLAR ABSORBERS

Last year we initiated a program designed to investigate the various factors influencing the suitability of multilayer systems for use as solar energy collectors.[29] Of the systems measured experimentally, copper oxide on silver appeared promising, with specular reflectances of less than 10% in the visible and 95% or more over parts of the infrared spectrum. These observations were obtained at room temperature on systems that had not been exposed to high temperatures except those involved in their fabrication. This year we investigated the high-temperature characteristics of copper oxide on silver systems. Obviously, for a system to be suitable for use as a solar energy collector, its mechanical and optical properties must remain stable under both prolonged operation at elevated temperatures and repeated thermal cycling.

Copper oxide on silver is an example of the absorber-reflector tandem[30] approach to solar energy collectors, in which a thick metal film with high infrared reflectance is overlaid with a thick semiconductor film having an absorption edge in the region of 1 to 2 μm. Photons in the visible are highly absorbed by the semiconductor, which is, however, transparent to photons in the infrared. This property permits the high reflectance (low thermal emittance) of the underlying metal film to dominate in the infrared. Thus the basic characteristics of this solar energy collector depend on the intrinsic optical properties of the copper oxide.

Samples were made by vacuum evaporation of about 5000 Å of silver onto a glass microscope slide. A film of copper was then vacuum-evaporated over the silver, and this system was then heated in air at 150°C for 12 hr and at 380°C for 17 hr. This process produced complete oxidation of the copper. An x-ray analysis[31] showed the copper oxide films produced in this way to contain more than 90% CuO, the remaining component being Cu_2O. The optical characteristics of these systems were obtained using Perkin Elmer spectrophotometers, model 4000 in the 0.4- to 2.7-μ region and model 621 in the 2.5- to 15-μ region. All reflectances were measured relative to a fresh aluminum film and corrected for the reflectance of the aluminum, using handbook values.

Figure 7.8 shows the reflectance of one of our samples as a function of time at a temperature of 400°C. The general trend is quite clear. Even short times at 400°C degrade the performance of a copper oxide–silver absorber. Apparently the materials diffused into each other. An Auger depth profile[32] of this sample, obtained after the termination of the heat treatment and reflectance measurements, showed that silicon had outdiffused to the surface and that oxygen was abundant throughout the interior of the sample. At this stage in its deterioration no sharp interfaces were seen in this sample. A depth profile is obtained by analyzing the energy of the Auger electrons released during electron and argon ion bombardment. The sample surface is sputtered away so that the chemical analysis is obtained as a function of sample depth. Hence the sample is

29. E. T. Arakawa et al., *Health Phys. Div. Annu. Prog. Rep. June 30, 1976*, ORNL-5171 (October 1976), p. 165.

30. R. E. Hahn and B. O. Seraphin, *J. Vac. Sci. Technol.* 12, 905 (1975).

31. X-ray analysis performed by O. B. Cavin of the Metals and Ceramics Division at ORNL.

32. Auger depth profiling studies were done at the Materials Research Laboratory of the University of Illinois.

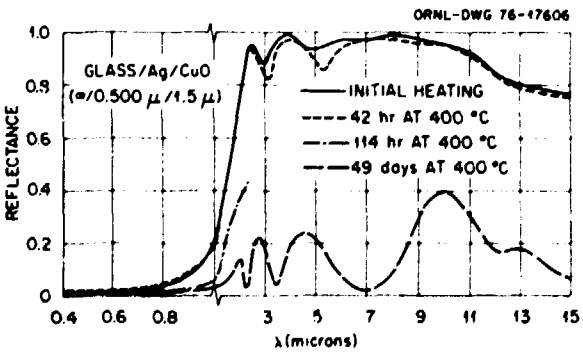

Fig. 7.8. Reflectance of a copper oxide–silver–glass system as a function of time since fabrication at a temperature of 400°C.

destroyed in the process. Figure 7.9 shows an Auger depth profile of one of our copper oxide–silver–glass samples which had been held at 380°C for one weekend after the initial oxidation of the copper. At this stage, moderate deterioration had occurred. This sample shows that copper and oxygen are the majority elements in the outer bulk of the sample, but surprisingly there is also a detectable amount of sulfur. As the silver layer is approached, we find that there is a fairly sharp interface, but the second interface between the silver and glass is washed out. Also there is considerable oxygen throughout the silver. Apparently the heat treatment has provided the energy for oxygen to diffuse into the silver and silver to diffuse into the glass. We believe that this interdiffusion is the primary reason for failure of our samples as solar absorbers at sustained high temperature.

Hahn and Seraphin[30] found that Cr_2O_3 can form an efficient diffusion barrier between the metal and semiconductor layers, in their case silver and silicon, respectively, up to temperatures of at least 540°C. We initiated a search for suitable antidiffusion barriers between copper oxide and silver and between silver and glass. We tried using a CaF_2 antidiffusion barrier between the silver and copper oxide but found that this layer does not prevent oxygen from reaching the silver even when the sample is maintained at temperatures as low as 300°C. We also attempted to put a Cr_2O_3 layer between the copper oxide and silver and between the silver and glass. We observed that at temperatures near 400°C this barrier protects the silver from oxidation, but at temperatures near 500°C even this barrier does not inhibit oxygen diffusion into the silver. We believe this is most likely due to our not having deposited Cr_2O_3 directly onto the silver; instead we evaporated chromium and tried to oxidize it. This process most likely resulted in a lower oxide than Cr_2O_3 as the barrier.

We feel that we need to investigate antidiffusion barriers more thoroughly. Figure 7.10 shows the reason that this investigation could be so important. It presents the optical characteristics of one of our copper oxide–silver–glass systems before heat treatment compared with the optical characteristics of one of the systems constructed by Hahn and Seraphin.[30] These systems incorporate antidiffusion barriers and an antireflection coating operating over the solar emission band to reduce the high reflectance of the semiconductor in the visible spectrum and to maximize the fraction of the solar energy that enters the absorber. The characteristics of our system compare favorably with those of Hahn and Seraphin. Thus, if the diffusion problems can be solved,

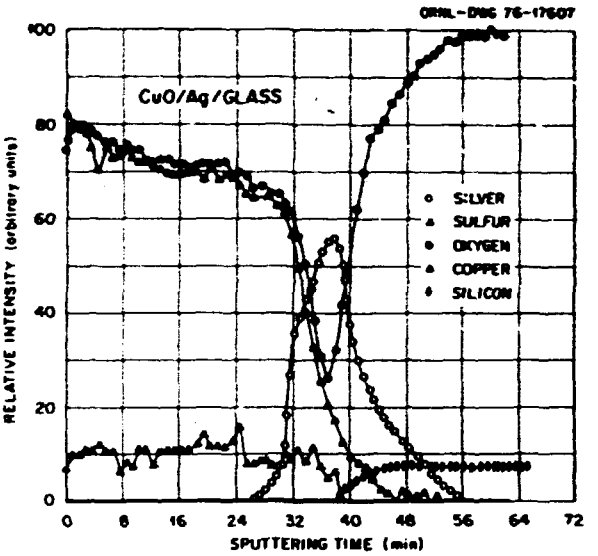

Fig. 7.9. Auger depth profile of a copper oxide–silver–glass sample which had been held at 380°C for one weekend after fabrication.

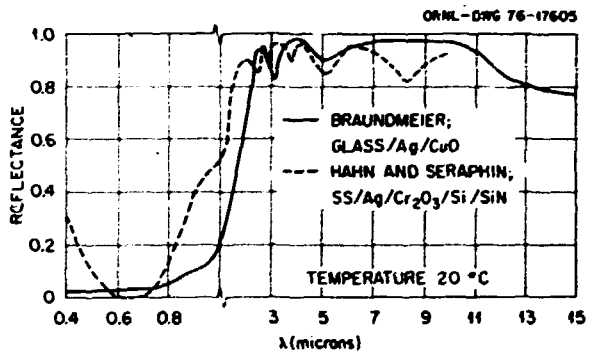

Fig. 7.10. Optical characteristics of a copper oxide–silver–glass absorber compared with those for an absorber developed by Hahn and Seraphin (ref. 30).

it appears that a copper oxide–silver–glass system can be developed into an efficient solar absorber.

PLASMON RADIATION FROM SILVER

Charged particle irradiation of a conductor produces collective excitations of the conduction electrons both in the bulk (volume plasmons) and at the surface (surface plasmons). These excitations have frequently been studied using electron energy loss spectroscopy, which measures the spectra of discrete losses suffered by an incident beam of monochromatic electrons. They may also be studied by measuring the optical radiation produced when the plasmons decay and emit their energy as photons of equal energy.

Ferrell[33] showed that plasma oscillations induced by charged particles incident on a smooth ideal metal may decay by the emission of photons at the bulk plasma frequency. This so-called transition radiation was studied in silver by several workers using high-energy electrons (~50 keV) normally incident on thin metal films. For normally incident electrons they generally found radiation whose photon energy, polarization, and angular distribution are characteristic of the transition radiation produced by the decay of volume plasmons. It is of interest to investigate whether this radiation, characteristic of the bulk material, depends in any way on the energy of the incident electrons. On the other hand, "nonradiative" surface plasmons produced by charged particles cannot radiate at an ideally smooth surface but can couple to an external radiation field if the surface is rough.[34] The spectral characteristics of the emitted radiation in this case depend on surface roughness parameters which are characteristic of each individual interface. Any dependence of the surface-plasmon radiative decay on electron energy would hence be complicated by surface roughness effects. We previously studied the radiative decay of both volume and surface plasmons excited in aluminum by high-energy (80 keV) electrons.[35] This year we made similar observations on silver, but we used low-energy (10 to 2000 eV) electrons. For "smooth" films two peaks were resolved. One, at 3.73 eV, the bulk plasmon energy, is thought to result from ordinary transition radiation. The second, at about 3.60 eV, is very sensitive to surface roughness in both position and magnitude and is produced by roughness-coupled radiation from nonradiative surface plasmons. For rough films, this surface plasmon peak dominates the emission and persists to electron energies at least as low as 10 eV.

The experimental apparatus has been described previously.[36] Silver films were prepared in situ by evaporating silver onto various substrates. Film thickness was monitored by a quartz-crystal thickness monitor. Light emitted by the films was analyzed in the wavelength range between 3000 and 4500 Å, using a grating monochromator and photomultiplier detection. The experiments were performed in an unbaked ion-pumped vacuum system operated with a base pressure of about 5 $\times 10^{-7}$ torr, which rose to the 10^{-6}-torr range during evaporation. Film preparation and treatment had a very strong effect on the radiation produced by the electrons. Substantially different results were obtained for silver films deposited on shiny silver sheet, molybdenum plate with a matte finish, and glass slides. The rate of silver deposition and local heating of the electron beam also affected the radiation observed. However, the general conclusions reached here could be applied to all the data.

Figure 7.11 shows the spectral distribution of light emitted from a specularly reflecting silver plate irradiated with electrons of 500 and 1000 eV both before and after the rapid (~1000 Å/min) evaporation of a 2000-Å silver overlayer. A double-peaked spectrum is observed with peaks located at about 3320 Å (3.73 eV) and 3440 Å (3.60 eV). Note that the magnitude of the 3440-Å peak is enhanced for the evaporated film. Figure 7.12 shows the polarization of the radiation emitted from a rapidly evaporated silver overlayer for 500-, 1000-, and 1500-eV incident electrons. The predominance of *p*-polarized radiation at 3300 Å demonstrates

33. R. A. Ferrell, *Phys. Rev.* **111**, 1214 (1958).
34. J. M. Elson and R. H. Ritchie, *Phys. Rev. B* **4**, 4129 (1971); also *Phys. Status Solidi B* **62**, 461 (1974).
35. A. J. Braundmeier et al., *Phys. Rev. B* **5**, 2754 (1972).
36. E. T. Arakawa et al., *J. Phys. Radium* **25**, 129 (1964).

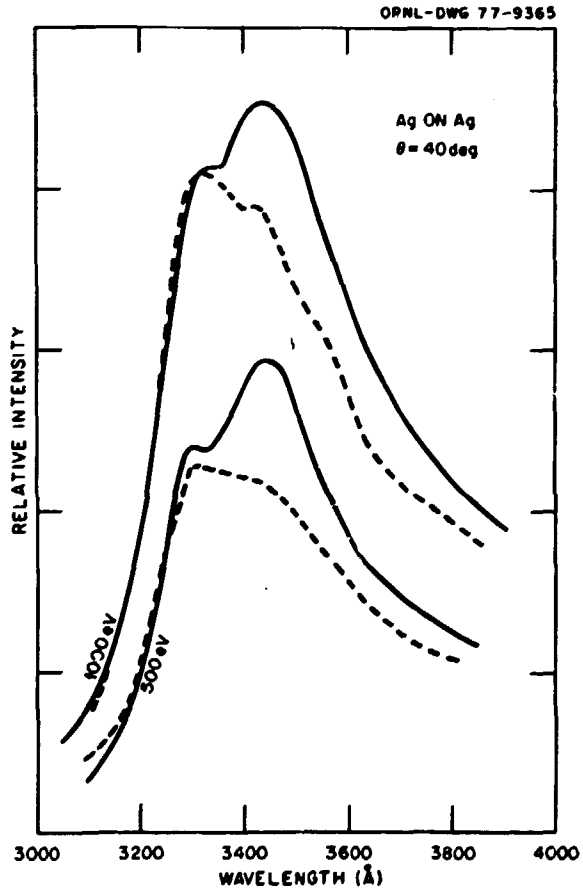

Fig. 7.11. Emission spectrum of evaporated silver (–) and bulk silver (—) showing both surface- and volume-plasmon peaks.

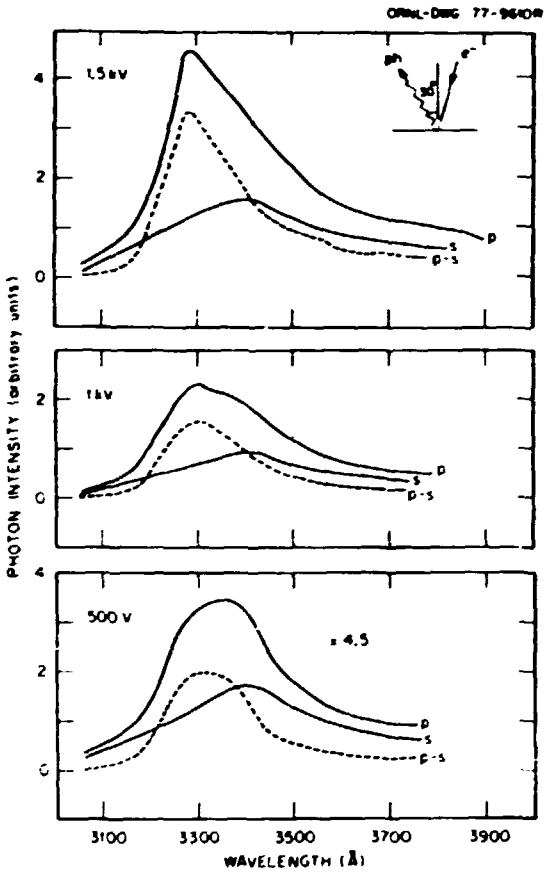

Fig. 7.12. Emission spectra as a function of polarization for 0.5-, 1.0-, and 1.5-keV incident electrons.

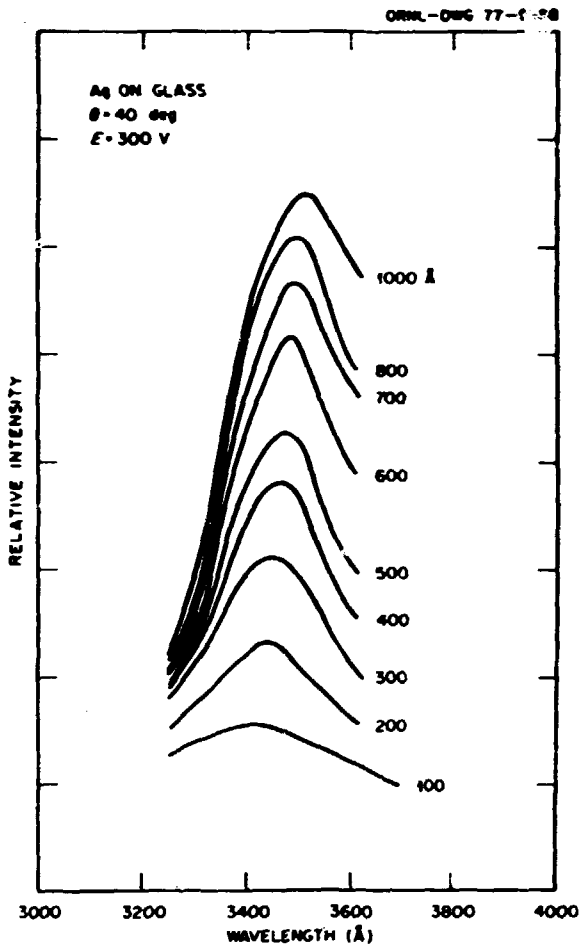

Fig. 7.13. Emission spectra for different thicknesses of silver on glass.

that low-energy electrons can still excite bulk or volume plasmons, that is, that transition radiation is still seen for low-energy electrons. The intensity of this radiation decreases with decreasing electron energy and, in our experiments, was unresolved for electrons with energies below ~500 eV. In contrast to the component at 3300 Å, the component of the radiation in the vicinity of 3400 to 3500 Å is not associated with any pronounced polarization. Subsequent experiments have shown that this component is associated with surface-plasmon radiative decay influenced by the surface roughness coupling in each case and is seen for electron energies as low as 10 eV on silver.

Figure 7.13 shows the emission from silver on glass for films of increasing thickness. A rather broad peak centered at 3400 Å grows in magnitude and shifts to longer wavelengths with increasing film thickness. In these curves the only evidence for the volume-plasmon peak is a small shoulder on the thicker distributions at about 3320 Å. These curves can be explained if successive evaporations of silver produce increased surface roughness. Such an increase in roughness with film thickness has been observed by many workers (e.g., see ref. 35).

If excessive electron beam power was dissipated in the silver on glass films, the appearance of the films changed with time from shiny to frosty as a result of film damage by local heating. The frosty spots on such films were rough when viewed through an optical microscope. Figure 7.14 shows the accompanying change in the emission as a silver film was subjected to a high-intensity electron beam. The peak is strongly shifted to longer wavelengths as film roughening proceeds. A fresh evaporation of silver on such a damaged region does not move the emission peak back to its original position as would be the case if the shift were due to the formation of an oxide or other contamination layer on the surface.

Thus, at low electron energies, surface-plasmon effects dominate the radiative decay spectrum except for spectra from very smooth surfaces obtained with high resolution (Fig. 7.11). Since they are closely related to

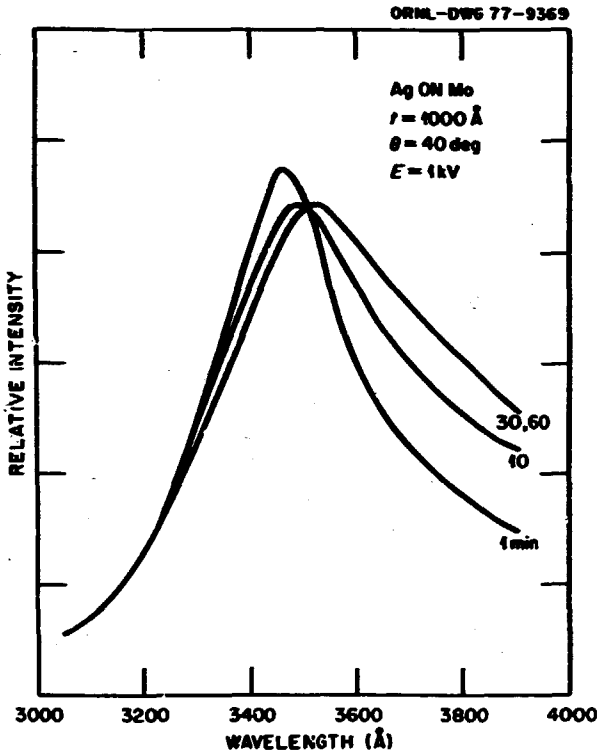

Fig. 7.14. Shift of emission peak as the roughness of a silver film is increased by electron beam heating.

the surface roughness characteristics, the spectra could be used to obtain information about the sample roughness. On the other hand, information about the volume-plasmon radiation at low excitation energies will be very difficult to obtain because it is obscured by surface effects.

POLARIZATION ANOMALIES FROM HOLOGRAPHIC GRATINGS

The study, initiated last year,[37] of the polarization anomalies that result when a grating is overcoated with a layer of a dielectric was completed.[38] For a metallized grating without a dielectric overcoating, grating anomalies result from surface-plasmon excitation. With a dielectric overlayer, additional anomalies are observed which are due to resonances in a waveguiding structure, that is, in the dielectric layer. These resonances can be referred to as optical guided modes.

Last year we made an aluminized grating, overcoated it with a layer of photoresist, and then fitted data obtained on this grating to the theoretical dispersion curves given by Otto and Sohler.[39] First-order diffraction spectra only were studied at that time. Measurements have since been extended on the same grating to include the reflected, or zero-order, beam. Several spectra were obtained where, in each case, the angle of incidence was held fixed (20° to 65°) and the wavelength was varied. In addition, measurements were extended to longer wavelengths by the use of infrared-sensitive phototubes.

Figure 7.15 shows the theoretical dispersion curves obtained from ref. 39 for the visible spectral region. The points are the experimental data obtained from the reflectance measurements (uncircled) and from the diffraction measurements (circled). This can be compared with our preliminary data presented last year (ref. 37, Fig. 29.11). Determination of the theoretical curves depended on knowing accurate values of the index of refraction of the photoresist over the spectral range considered. In a series of reflection measurements conducted on photoresist, the index was found to vary from 1.62 at 689 nm to 1.70 at 413 nm.

The good agreement between theory and experiment shows that the interpretation of the additional anomalies in terms of optical guided modes in a waveguiding structure is probably a valid one.

BLAZED HOLOGRAPHIC GRATINGS FORMED WITH OPTICAL GUIDED WAVES

Experimental work was continued on the formation of blazed holographic gratings using optical guided modes. Whereas our previous work was concerned

37. E. T. Arakawa et al., *Health Phys. Div. Annu. Prog. Rep. June 30, 1976*, ORNL-5171 (October 1976), pp. 165–72.
38. J. J. Cowan and E. T. Arakawa, *Opt. Commun.* 21, 428 (1977).
39. A. Otto and W. Sohler, *Opt. Commun.* 3, 254 (1971).

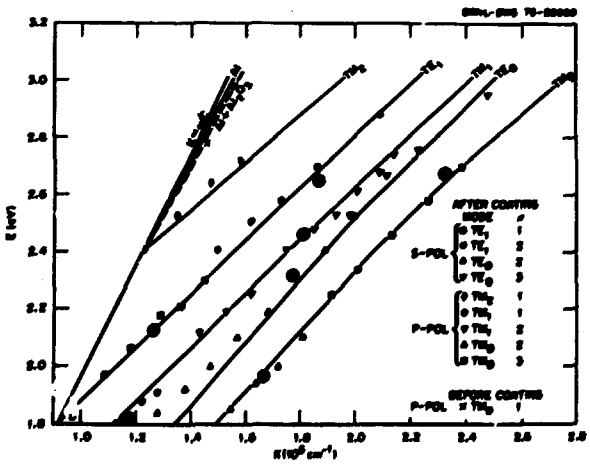

Fig. 7.15. Dispersion relations for surface plasmons and for optical guided waves on an aluminized grating without and with a photoresist overlayer respectively.

mainly with feasibility studies on the new technique,[37,40] the present work has been involved with detailed studies on efficiencies, exposure techniques, and determination of the groove shape by means of scanning-electron-microscope (SEM) photographs.

Some technical improvements were made in the production of the blazed gratings. To obtain efficient coupling of incident beam energy over a large area, we coupled the glass prism optically to a 2- by 2-in. glass slide or plate with an index-matching fluid (xylene, index = 1.496). In this case the slide or plate instead of the prism face is overcoated, first with silver and then with photoresist. The spin-coated photoresist layer was found to be especially uniform in thickness over the center of the slide where the optical contact is made with the prism over a square area 28 mm on each side. A finished grating 28 X 28 mm^2 could thus be produced in this manner on a flat glass blank. This technique was also useful in obtaining SEM photographs of the groove profile because a slide could be made with a grating on it, then broken perpendicular to the groove direction. When mounted in the SEM it was thus possible to view the profile from the edge. Figure 7.16 is a photograph obtained in this way of a grating made with a groove spacing of 748 nm and blaze angle of 22.2°. The blaze wavelength is calculated from $\lambda_b = 2d \sin \gamma$, where γ is the blaze angle and d is the grating spacing. Hence, λ_b = 565 nm. Efficiency measurements were

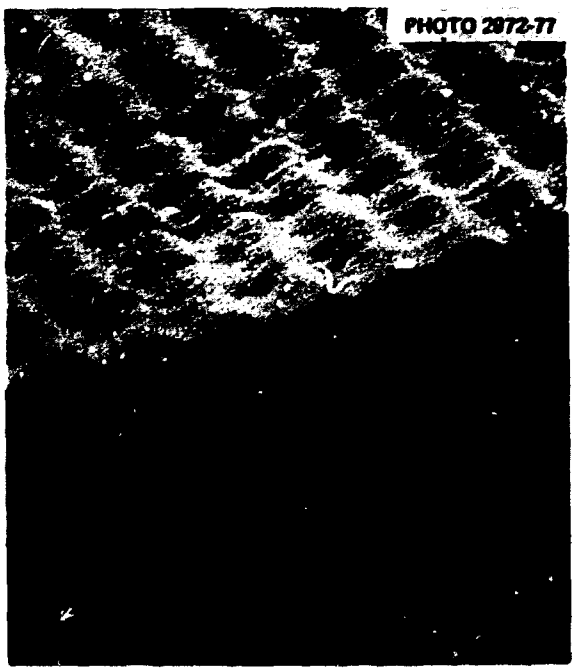

Fig. 7.16. Scanning electron micrograph of blazed grating groove profile.

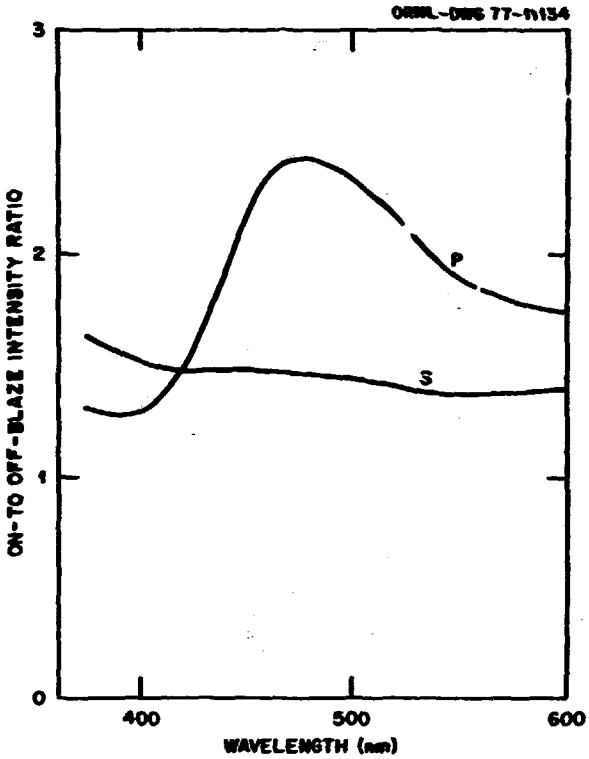

Fig. 7.17. Ratio of on- to off-blaze first-order intensities at normal incidence for both p and s polarizations for a blazed holographic grating.

made on this grating to determine the effectiveness of the blaze. Figure 7.17 shows the ratio of the on- to off-blaze first-order intensities at normal incidence for both p and s polarizations. The intensity ratio is about 2:1 over the visible region with a peak for p polarization at about 480 nm. This peak may be related to a polarization anomaly. The slight roundness of the groove profile, evident in Fig. 7.16, may be responsible for the fairly flat efficiency response. A more peaked response near the blaze wavelength would be expected if the profile were an ideal sawtooth.

HOLOGRAPHIC ZONE PLATES

A zone plate is an optic element that consists of a number of opaque concentric rings, each of the same area, with clear spaces in between. Because of the concentric geometry and the ring spacing, incident light interferes constructively and destructively in such a way that it can be focused; thus the zone plate has lenslike properties. But since the zone plate also has gratinglike properties, due to the periodic ring structure, it exhibits

40. J. J. Cowan, *J. Opt. Soc. Am.* 66, 1114 (1976).

pronounced chromatic dispersion. A zone plate and a lens can be interchanged in many situations: both can be used in some spectral ranges, such as the infrared and visible. In the uv and soft x-ray regions, however, the zone plate is particularly useful because conventional lenses are not available at these wavelengths. The only other optic elements that can be used for focusing are reflection optics like spherical mirrors at grazing incidence, but the aberrations are usually too severe to make them effective for imaging purposes. Thus the zone plate, which operates in transmission and is relatively free from aberrations, affords practically the only means of imaging in the soft x-ray and far uv regions. There would be obvious applications for biological purposes if, for example, the zone plate could be used as the objective lens in an x-ray microscope. Both the magnifying power and the resolution increase with the number of rings, or zones, that exist for a given diameter zone plate, and in a recent study it was shown that for a wavelength of 4.6 nm (carbon *K*-alpha x rays), resolutions of 0.5 μm were achieved.[41] This was for a zone plate of 1-mm diameter, 850 zones, and a focal length of 6.45 cm. In vivo imaging has not yet been achieved, but it is possible in principle.

The holographic technique affords a particularly simple and useful method for making zone plates having the high line densities and short focal lengths desired for imaging. The method consists of allowing a plane wave to interfere with a spherically diverging wave in a suitable photosensitive medium. We have initiated a series of experiments to make zone plates in this fashion, using the geometry shown in Fig. 7.18. A beam of laser light (488 nm) is divided by a beam splitter; one of the beams is spatially filtered, expanded, and collimated while the second beam is spatially filtered and expanded but not collimated. A photoresist-coated glass blank is positioned where these two beams overlap. After exposure and development, a number of concentric rings of photoresist remain on the glass blank. The rings are sufficiently opaque so that without further processing

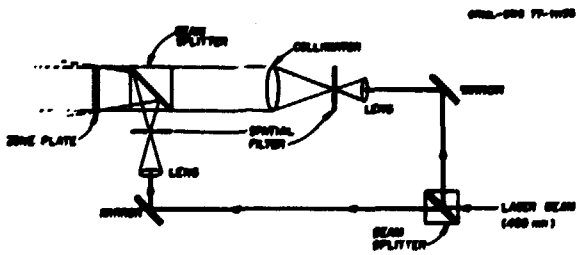

Fig. 7.18. Experimental arrangement for the production of zone plates by holographic techniques.

they can be used for imaging at visible wavelengths. However, for use in the soft x ray region, the glass blank will first be coated with a thin carbon film before overcoating with photoresist. The carbon film can be separated from the glass so that it is self-supporting, and for small thicknesses ($t \simeq 30$ nm) it will be transparent to many of the soft x rays of interest. Prior to separation, the photoresist zone plate will be replaced by a complementary gold zone plate by evaporating gold so that it overcoats both the clear carbon and the tops of the photoresist rings, then dissolving away the remaining photoresist. These experiments are continuing at the present time. A related experiment has been initiated to make, with the holographic technique, a new type of optic element: a reflection zone plate. A glass tube is coated on the inside with photoresist and exposed to two intersecting, spherically expanding laser beams. An interference pattern is thus formed on the inside of the tube. After the photoresist is developed and overcoated with a reflecting metal like aluminum, the tube can be used as an imaging element in reflection for grazing incidence. Because of the circular geometry, aberrations would be expected to be less severe than for the usual grazing incidence optics. Also, the complications involved with preparing a suitably transparent substrate as in the transmission mode are avoided. Furthermore, the collection area can be made larger than that of the conventional zone plate. The reflection zone plates that we made in this fashion were tested in the visible region. We plan to continue these experiments and extend the region of investigation into the soft x-ray region.

INCREASED SENSITIVITY OF RECORDING MATERIALS WHEN EXPOSED TO OPTICAL GUIDED WAVES

Theoretical considerations have led us to believe that the high field strengths that result from coupling into optical guided waves should require shorter exposure times than do the more conventional interference methods. In fact, it has already been observed that gratings made using optical coupling required less exposure than those made by ordinary interference techniques for a photoresist recording medium.[37]

Preliminary experiments were conducted to measure the sensitivity of recording materials using different recording techniques. A direct measurement of sensitivity was made by spin-coating liquid photographic

41. B. Niemann, D. Rudolph, and G. Schmahl, *Appl. Opt.* 15, 1883 (1976).

emulsion (Kodak Nuclear Track Emulsion) onto half-silvered glass slides. These slides, when optically contacted to a glass prism by an index-matching fluid (xylene) were illuminated through the prism[37] in such a way that an optical guided mode was stimulated in the thin emulsion layer, acting as a waveguide. This emulsion had a thickness of about 500 nm. Part of the slide that was not silvered was also in optical contact with the prism, and in this part an evanescent surface wave was stimulated rather than the guided mode. The rest of the slide that was not in contact at all with the prism was subjected to simple transmission of the incident beam. Thus, it was possible, for incident light of the same intensity, to compare the optical densities of the emulsion after exposure, using three different techniques: transmission, surface wave, and optical guided mode. The optical density, O.D., is given by O.D. = $\log(1/T)$, where $T = I/I_0$ and I_0 is the intensity transmitted through the emulsion before exposure and I that transmitted after exposure. The values of the optical density obtained for two typical exposures at 488 nm are shown in Table 7.2. For the low exposure, the O.D. resulting from the transmitted beam and the evanescent wave differed by a factor of 4; that resulting from the transmitted beam and the guided mode differed by over an order of magnitude. For the larger exposure, where saturation effects are beginning to be noticeable, there is still a difference of a factor of 2 between the optical densities due to the optical guided mode and the other two cases. Other results showed that the optical density of the evanescent wave case lies consistently between that for the transmitted beam and the guided mode.

OPTICAL GUIDED MODE HOLOGRAPHY EQUATIONS

Our previous work[37,42] has shown that if two optical guided modes, each moving in the same direction, are excited simultaneously in a photosensitive medium, it is possible to record the interference that occurs between them. On developing the photoresist layer, the vacuum-photoresist interface takes on a sinusoidal variation in the direction of the interfering waves. The height of this surface variation depends on the length of time the exposed layer is allowed to develop, or etch. When either of the guided modes is subsequently excited, light is coupled into the other mode because of the grating perturbation; in other words, the developed layer exhibits properties like an ordinary hologram. The equations describing this phenomenon have been worked out for the TE (s-polarized) case and are given below.

Table 7.2. Optical densities of emulsion after exposure to both low and high incident photon intensities for different coupling techniques

Technique	Exposure	
	96 mJ/cm²	600 mJ/cm²
Transmitted beam	0.009	0.081
Evanescent wave	0.036	0.097
Optical guided mode	0.125	0.174

A transverse electromagnetic wave propagating in the positive x direction with electric field E in the y direction can be expressed by[39]

$$\mathbf{E} = e^{i(Kx-\omega t)}(0, E_A e^{iK_\perp z} + E_B e^{-iK_\perp z}, 0) \ , \qquad (16)$$

where K is the propagation wave number in the x direction,

$$K_\perp = \left(\frac{n_s^2\omega^2}{c^2} - K^2\right)^{1/2} ,$$

and n_s is the complex refractive index of the propagating medium. Figure 7.19 shows the geometry to be considered, with medium 1 representing vacuum, medium 2 the photoresist layer of thickness d, and medium 3 the metal. The wave, represented by Eq. (16), is shown propagating in the photoresist. It may be considered to be composed of two separate plane waves, with amplitudes E_A and E_B, which are reflected at the

42. J. J. Cowan, *J. Opt. Soc. Am.* 66, 1062 (1975).

ORNL-DWG 77-11135

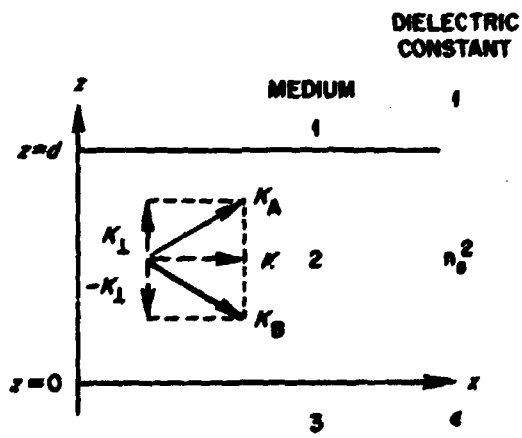

Fig. 7.19. Optical guided mode geometry.

boundaries $z = 0$ and $z = d$ and interfere constructively. E_A is the amplitude of the wave moving in the positive z direction and E_B that of the wave moving in the negative z direction. These amplitudes are connected by

$$E_B e^{-iK_\perp d} = e^{i\phi_{21}} E_A e^{iK_\perp d}$$

and

$$E_A = e^{i\phi_{23}} E_B ,$$

where the ϕs represent the phase changes at each reflection and are given by

$$\phi_{21} = -2 \tan^{-1}(K_1/K_\perp)$$

and

$$\phi_{23} = -2 \tan^{-1}(K_3/K_\perp) ,$$

where $K_1 = [K^2 - (\omega^2/c^2)]^{1/2}$, $K_3 = [K^2 - \epsilon(\omega^2/c^2)]^{1/2}$, and ϵ = the complex dielectric function for the metal. The guided modes obey the mode equation

$$2K_\perp d + \phi_{21} + \phi_{23} = 2\pi m$$

or (17)

$$K_\perp d + \Phi_{21} + \Phi_{23} = \pi m ,$$

where m = the mode number, $\Phi_{21} = \phi_{21}/2$, and $\Phi_{23} = \phi_{23}/2$. Equation (16) can thus be rewritten as

$$\mathbf{E} = Ae^{i(Kx-\omega t)} e^{i\Phi_{23}} (0, \cos\beta, 0) , \qquad (18)$$

where $\cos\beta = (1/2)(e^{i\beta} + e^{-i\beta})$, $\beta = \Phi_{23} + K_\perp z$, and $A = 2E_B$. Consider now the interference between two low-order TE modes: TE_0 and TE_1. Equation (17) for $m = 0$ is

$$(\Phi_{23})_a = -K_\perp d - (\phi_{21}/2) = \Phi_a ,$$

and for $m = 1$, it is

$$(\Phi_{23})_b = \pi - K_\perp d - (\phi_{21}/2) = \Phi_b .$$

Equation (18) for the TE_0 mode is

$$\mathbf{E}_a = Ae^{i(K_a x-\omega t)} e^{i\Phi_a} (0, \cos\beta_a, 0) ,$$

and for the TE_1 mode, it is

$$\mathbf{E}_b = Ae^{i(K_b x-\omega t)} e^{i\Phi_b} (0, \cos\beta_b, 0) .$$

The interference intensity within the photoresist layer is thus given by

$$I = |\mathbf{E}_a \cdot \mathbf{E}_b|^2 = |\mathbf{E}_a|^2 + |\mathbf{E}_b|^2 + \mathbf{E}_a \cdot \mathbf{E}_b^* + \mathbf{E}_a^* \cdot \mathbf{E}_b$$

$$= A^2 \{\cos^2\beta_a + \cos^2\beta_b + 2\cos\beta_a \cos\beta_b$$

$$\times \cos[(K_a - K_b)x + (\Phi_a - \Phi_b)]\} . \qquad (19)$$

The treatment given above assumes equal intensities for each of the two waves. The first two terms in Eq. (19) represent the intensity due to each of the waves considered alone. The third term represents the interference between the two waves and is responsible for the grating that is formed. The grating periodicity is represented by the first term in brackets; the second term is a constant phase shift that depends on the properties of the media involved. The equation is identical to that for ordinary holography except that the usual constant density terms have been replaced here with sinusoidally varying ones, because the guided modes are actually standing waves in the transverse (z) direction.

THEORY OF ABERRATION-CORRECTED GRATINGS USING OPTICAL GUIDED WAVES

Aberration-corrected gratings can be made holographically by recording the interference pattern of two coherent, spherically diverging waves that originate from point sources placed at appropriate distances from the grating blank. The potential advantages of these gratings over ruled gratings include higher resolution, large apertures, low stray light, and greater ease in producing aberration-free, or nearly aberration-free, systems while still achieving moderate efficiencies.

Namioka, Noda, and Seya[43,44] have presented generalized equations for producing aberration-corrected holographic gratings using two coherent sources having the same wavelength. The problem is complex, and, generally, the grooves are neither straight nor equally spaced. However, the proper recording parameters for producing a grating with a specified groove geometry which, in use, minimizes certain aberrations such as astigmatism and coma have been worked out mathematically. The type of mounting and/or mechanism of wavelength scanning, as well as the type of aberration and the wavelength at which one wishes to minimize the

43. T. Namioka, H. Noda, and M. Seya, *Sci. Light* **22**, 77 (1973).

44. H. Noda, T. Namioka, and M. Seya, *J. Opt. Soc. Am.* **64**, 1031 (1974).

aberration, must all be specified before a detailed calculation is carried out. The generalized equations were applied by us[37] and by Namioka, Noda, and Seya[43,44] to the calculation of the recording parameters for gratings to be used at normal incidence and also in the Eagle and Seya-Namioka geometries. Holographic gratings were fabricated according to these parameters and then tested against predictions and against comparable ruled gratings for performance. For these geometries, the positions of the recording sources are at accessible points on the Rowland circle. In addition, the aberrations to be corrected are not very severe.

In the extreme uv and soft x-ray regions, grazing incidence monochromators have to be used. In these cases, both astigmatism and coma are severe in an uncorrected grating. In addition, one of the recording sources for construction of a holographic grating for use at grazing incidence needs to be virtually in the grating surface. This can, in theory, be achieved by introducing this source in the form of an optical guided wave in the recording medium. The advantages of this are high recording intensity and the ease with which the wave can be coupled in at the desired geometry. However, since the recording wavelength of this source is changed, the generalized equations presented by Namioka, Noda, and Seya[43,44] have to be modified to allow for the two recording sources to have different wavelengths. We made the necessary modifications and performed calculations to compare the recording parameters and characteristics of astigmatism-corrected holographic gratings made using two ordinary waves with those made using an ordinary and an optical guided wave.

When using a concave grating which has been fabricated using two recording sources of the same wavelength λ_0, each on the Rowland circle, the light path function F for a wavelength λ can be written according to Namioka, Noda, and Seya[43,44] as

$$F_{ijk} = M_{ijk} + \frac{m\lambda}{\lambda_0} H_{ijk} , \tag{20}$$

where M_{ijk}'s are terms characteristic of mechanically ruled gratings with straight, equally spaced grooves, H_{ijk}'s are terms peculiar to holographic gratings or to ruled gratings with unequally spaced and/or curved grooves, and m is the order of the diffracted light. To minimize a specific aberration at the wavelength λ, integrals involving F_{ijk} are minimized. This imposes restrictions on the coefficients H_{ijk}, which are expressed in terms of R, the radius of curvature of the grating blank, and the recording parameters (γ, r_C, z_C, δ, r_D, z_D, λ_0) using the notation of refs. 43 and 44. The parameters are γ, the angle of incidence of recording source C; r_C, the distance from the center of the grating to recording source C; and δ and r_D, the corresponding quantities for source D. For the recording sources in the plane of incidence, $z_C = z_D = 0$. Explicit expressions for M_{ijk} and H_{ijk} are given in refs. 43 and 44. For the special case that $z_C = z_D = 0$, the effective grating constant σ at the center of the grating is given by

$$\sigma = \frac{\lambda_0}{\sin\delta - \sin\gamma} . \tag{21}$$

When the two recording sources have different wavelengths, the $(m\lambda/\lambda_0)H_{ijk}$ terms in Eq. (20) which involve the source C with recording parameters γ, r_C, λ_{01} become $(m\lambda/\lambda_{01})(H_{ijk})_{eff}$, and terms involving source D with parameters δ, r_D, λ_{02} become $(m\lambda/\lambda_{02}) \times (H_{ijk})_{eff}$. Expressions for $(H_{ijk})_{eff}$ are obtained by multiplying each term in H_{ijk} which contains δ or r_D by $P = \lambda_{01}/\lambda_{02}$. In this case Eq. (21) becomes

$$\sigma = \frac{\lambda_{01}}{P\sin\delta - \sin\gamma} .$$

When a common source λ_{01} is used to provide the two coherent sources, one of which, λ_{02}, is an optical guided wave, then $P > 1$.

Table 7.3 illustrates the use of the equations in refs. 43 and 44 (i.e., $P = 1$) for the correction of astigmatism in the grazing incidence geometry. These results suggest that a grating could be optimized simultaneously for several wavelength ranges. In Table 7.3 the parameter that varies the most is r_D; the other parameters hardly

Table 7.3. Recording parameters required for fabrication of a grazing incidence (α = 86°) holographic grating

R = 2.2 m and $1/\sigma$ = 2400 lines/mm, using recording sources of the same wavelength λ_0 = 457.9 nm, i.e., P = 1. This grating would be corrected for astigmatism over the wavelength correction range shown

γ (°)	δ (°)	r_C (mm)	r_D (mm)	Correction range (nm)
−5.73	87.78	2189.54	85.9	300–400
−5.68	89.71	2189.55	11.4	100–200
−5.68	89.9	2189.51	2.57	50–100

change at all. Thus, for different center positions on the fabricated grating satisfying the different values of r_D, astigmatism will be approximately minimized for the corresponding wavelength ranges shown in the table. When in actual use in a spectrometer, the grating could be moved during a spectral scan so that its center would be at the same distances r_D from the point source D as given in Table 7.3. The position of source C given by (λ, r_C) can be achieved with ease by using the collimator lens, if this is adjusted to be slightly divergent.

One observes that the incidence angle of the other source, D, is almost 90° and the distances r_D are small. This would be a difficult recording geometry by the usual methods but could be realized by the use of a guided mode. Since the guided mode propagates parallel to the surface, the angle of incidence is automatically 90°. A mode that originated from a point source in the photoresist layer would satisfy the distance requirement. An effective point source geometry could be achieved by focusing collimated light through a cylindrical lens, then coupling the resultant image into the mode in the usual way by means of a prism.

Experimental work is currently under way to construct a grating in this fashion.

Table 7.4 shows the need for using our modified equations when fabricating a grazing incidence holographic grating using an optical guided wave for which $\lambda_{02} \neq \lambda_{01}$.

Table 7.4. Recording parameters required for fabrication of a grazing incidence (α = 86°) holographic grating

R = 2.2 m, $1/\sigma$ = 3600 lines/mm, corrected for astigmatism over the wavelength range 50 to 100 nm. For P = 1, both sources are λ_{01} = 488 nm. For P = 1.5, one source λ_{01} = 488 nm; the other source, an optical guided wave, has a wavelength λ_{02} = 375 nm

P	γ (°)	δ (°)	r_C (nm)	r_D (nm)
1	−49.18	89.91	1438.24	3.79
1.5	−14.88	89.90	2128.16	5.70

8. Transport and Surface Physics

R. H. Ritchie

V. E. Anderson[1] T. L. Ferrell[2]
J. C. Ashley R. N. Hamm
G. Basbas[2] F. Hecker, Jr.[5]
J. J. Cowan[3] J. Neufeld[2]
P. M. Echenique[4] C. J. Tung[6]
J. M. Elson[2] J. E. Turner
H. A. Wright

The role of the Transport and Surface Physics Group is to study the interaction of particles with matter and to use the results to explain existing experimental data or to propose new experiments. Our work usually considers matter in its condensed state, with particular emphasis on phenomena associated with the presence of surfaces. Within this quite general framework, a wide variety of problems were studied last year.

The computer program PION has undergone further improvements and forms the basis for calculations of dose at muscle-bone interfaces, average path lengths in detectors, and fluxes in tissue-equivalent (TE) chamber cavities and chamber walls. New estimates have been made of W values for negative pions in TE gas, CO_2, and N_2. This work is important in our collaborative efforts with other research centers on the use of pion beams in cancer radiotherapy.

Because of their fundamental role in many physical and biological processes, electron inelastic interactions have been a subject of continuing interest. Cross sections for such interactions have been derived from several models to form the basis for extensive tabulations of energy loss and mean free paths for swift electrons in several materials and for a description of the energy spectrum of electrons slowing down in aluminum metal. The excitation of plasmonlike modes by electrons has been shown to be important in a theoretical interpretation of experimental data on straggling of electrons transmitted through thin carbon foils. Dissipative processes in solids can produce significant changes in interaction probabilities for low-energy electrons. This effect is illustrated by new calculations of the mean free path for electrons interacting with an electron gas when damping is included.

Phenomena associated with the passage of ions through solids are the subjects of widespread theoretical and experimental study. A fast ion moving in a solid sets up a trailing wake of electron density fluctuations. The potential thus generated may trap electrons which then accompany the ion as it exits from the solid. The spectrum of such convoy electrons has been calculated and comparisons made with experimental results and with charge transfer to the continuum theory. For an ion cluster moving through a solid, the wakes set up in the medium can lead to vicinage, or spatial correlation, to effects such as alignment of the cluster fragments along the direction of motion, and to changes in the forces acting on one part of the cluster due to the proximity of other parts. Comparisons of these results with those for the interaction of an ion cluster with a single atom indicate that some vicinage effects are unique to condensed matter.

The forces between a particle and a nearby solid or liquid surface are important in studies of particle accretion and adhesion and of surface-mediated catalytic

1. Computer Sciences Division.
2. Consultant.
3. Physics Division.
4. Present address: Institute of Theoretical Physics, University of Lund, Lund, Sweden, and NORDITA, Copenhagen, Denmark.
5. SCUU/NSF student
6. Postdoctoral fellow.

reactions. We have considered a slow ion moving adjacent to a metal surface as a model system. The energy loss calculated for the slow ion is found to be due to excitation of electron-hole pairs in the metal and surface plasmons. Such model calculations are quite useful in providing insight into the origin of dispersion forces between particles and surfaces. A process proposed by others to provide information on surface properties of solids is that of radiative electron capture, in which an ion moving through a solid captures an electron and emits a photon. On the contrary, our calculations indicate that the process is determined largely by the bulk properties of the material and thus will provide little information on surface effects for foil thicknesses of practical importance.

PION BEAM DOSIMETRY

We are collaborating with the University of New Mexico Cancer Research and Treatment Center and the Los Alamos Scientific Laboratory to utilize our pion calculational capabilities toward preclinical and early clinical applications of the biomedical pion beam at the Los Alamos Meson Physics Facility (LAMPF) for cancer radiotherapy. We are performing support calculations to provide information on problems of dosimetry at muscle-bone interfaces, average path lengths in various detectors, and details of charged-particle fluxes in TE chamber cavities and chamber walls.

We also began collaboration with the Swiss Institute for Nuclear Research (SIN) (Zurich, Switzerland) on dosimetry for the biomedical pion beam that is being constructed near Zurich. Dr. Werner Hett of the SIN staff spent two months at ORNL this year, and it is planned that an ORNL staff member will spend some time in Zurich. Initial calculations were made for the specific configuration of the SIN pion beam and the results were in good agreement with the measurements made at SIN.

We continued to improve our computer code, PION-1, for the transport of pions, muons, electrons, and all secondary products produced by interaction of pions with nuclei. We reviewed our cross-section data for in-flight interactions of pions with atomic nuclei. We have now included provision for elastic scattering of pions from both hydrogen and nonhydrogen nuclei. We developed a new method of simulating the transport of neutrons that are produced following the absorption of negative pions by nuclei. This new method will permit a significant reduction in running time for computer calculations and also the core size required. It will, however, still give the details of the neutron dose needed from the Monte Carlo calculations. The new method is presently being tested and will be incorporated into our computer calculations.

ESTIMATED *W* VALUES FOR NEGATIVE PIONS IN TISSUE-EQUIVALENT GAS, CO_2, AND N_2

In a previous report[7] we presented estimates of *W*, the average energy needed to produce an ion pair (eV/*ip*), for negative pions in nitrogen and argon. Measured values of *W* were plotted as functions of energy for a number of light ions in these gases.[8] These data were folded into the number-energy spectra calculated by Guthrie, Alsmiller, and Bertini[9] for the fragments produced by capture of stopped negative pions by nuclei of carbon, nitrogen, and oxygen. Except for the neglect of neutrons, the values thus obtained correspond to the average energy per ion pair that would be measured in a small cavity of the gas, if surrounded by material in which all the radiation was produced by capture of stopped negative pions. A weighted average was also computed for *W* when the absorbing material is soft tissue with relative atomic densities of 0.2593 for C, 0.0370 for N, and 0.7036 for O.

Neutrons could be included in the calculations, as we have done in previous computations of depth-dose curves and isodose contours. However, in the region of a target where pions stop, the particular flux density of neutrons depends strongly on the spatial and momentum distributions of the incident pions. In contrast, the charged-particle spectrum resulting from pion capture in the stopping region will not change greatly when the beam parameters are altered. As in the previous report,[7] we treat neutrons for the particular beam discussed in an approximate fashion here.

Dennis[10] has published empirical formulas that give *W* as a function of the atomic number *Z*, mass *M*, and energy *E* of various ions in hydrocarbon gases, including TE gas. The formulas can also be used for CO_2 and N_2. For energies below 1000 keV per atomic mass unit (amu), Dennis's formula is

$$W(E) = W_\beta[1.035 + A(Z)(E/M)^{-n(Z)}] \ . \qquad (1)$$

7. J. E. Turner, H. A. Wright, and R. N. Hamm, *Health Phys.* 29, 792 (1975).
8. J. A. Dennis, *Radiat. Eff.* 8, 87 (1971).
9. M. P. Guthrie, R. G. Alsmiller, Jr., and H. W. Bertini, *Nucl. Instrum. Methods* 66, 29 (1968); erratum, *Nucl. Instrum. Methods* 91, 669 (1971).
10. J. A. Dennis, *Phys. Med. Biol.* 18, 379 (1973).

Here, W_β is the appropriate value for fast electrons, E/M is expressed in keV/amu, and $A(Z)$ and $n(Z)$ are empirical constants given by Dennis for each ion. For energies above 1000 keV/amu Dennis gives

$$W(E) = W_\beta(E/M)[(E/M) - C(Z)]^{-1} , \qquad (2)$$

where $C(Z)$ is the constant obtained for each ion by fitting $W(E)$ by both formulas at 1000 keV/amu. In the present work, we combine the empirical formulas given by Dennis[10] for W as a function of E with the number-energy spectra of Guthrie, Alsmiller, and Bertini[9] to estimate W for pions in CO_2, N_2, and a TE gas.

Some of the numerical data given by Dennis are shown in Table 8.1. The values of A and n can be used generally for hydrocarbon gases with the appropriate value of W_β. Equations (1) and (2) can also be used for CO_2 and N_2 if the coefficients $A(Z)$ are multiplied by 0.626. Dennis gives the values W_β = 29.2 eV/*ip* for the TE gas mixture (64.4% CH_4, 32.4% CO_2, and 3.2% N_2) and W_β = 32.9 eV/*ip* for CO_2. We have also assumed the value W_β = 34.6 eV/*ip* for N_2 from Dennis's earlier paper.[8] The constants $C(Z)$, which we have calculated from Dennis's work, are given in Table 8.2 for the TE gas and for CO_2 and N_2. Some numerical results for protons, alpha particles, and nitrogen ions are shown in Table 8.3, together with values for N_2 found in our earlier work.[7]

Values of W were computed as functions of energy for the charged particles produced by capture of a stopped negative pion by nuclei of C, N, and O. These values were combined with the number-energy spectra of Guthrie, Alsmiller, and Bertini[9] to estimate the average value of W for charged particles resulting from pion capture by these nuclei. In folding in these spectra, we assumed that W for deuterons and tritons is the same, as a function of E/M, as for protons and that W for ^{3}He nuclei is the same function of E/M as that for alpha particles. Guthrie, Alsmiller, and Bertini[9] present the number and total-energy distributions for each of the products heavier than the alpha particle, but not the individual-particle energy spectra. They give only the energy spectrum of the "heavy recoils" lumped together for each type of capturing nucleus. We have assumed that each of the products heavier than the alpha particle has this spectrum. The error thus intro-

Table 8.1. Data from Dennis[10] used in present calculations

Ion	$A(Z)$	$n(Z)$
Proton	0.1301	0.04902
Helium	1.810	0.5360
Lithium	3.219	0.7630
Beryllium	2.240	0.8208
Boron	1.903	0.7226
Carbon	1.909	0.6337
Nitrogen	1.907	0.5828

Table 8.2. Calculated values of $C(Z)$ for ions in TE gas, CO_2, and N_2

Ion	$C(Z)$	
	TE gas	CO_2 and N_2
Proton	113.3	85.13
Helium	73.76	59.21
Lithium	49.02	43.39
Beryllium	40.97	38.31
Boron	45.74	41.31
Carbon	55.69	47.62
Nitrogen	64.58	53.31

Table 8.3. Estimated W (eV/*ip*) for protons (P), alpha particles (α), and nitrogen ions (N) in TE gas, CO_2, and N_2

E (MeV)	W (eV/*ip*)											
	TE gas			CO_2			N_2 (present work)			N_2 (previous work[7])		
	P	α	N	P	α	N	P	α	N	P	α	N
0.4	33.1	34.7	38.1	36.0	37.2	39.6	37.9	39.1	41.7	36.8	38.9	42.1
0.6	33.0	33.8	36.5	36.0	36.6	38.4	37.9	38.5	40.4	36.7	38.2	40.7
1.0	32.9	33.0	34.8	36.0	36.0	37.3	37.8	37.8	39.2	36.6	37.7	39.8
2.0	31.0	32.1	33.3	34.4	35.4	36.2	36.2	37.2	38.1	36.5	36.9	38.9
5.0	29.9	31.0	32.0	33.5	34.5	35.3	35.2	36.3	37.2	36.4	36.5	38.6
10.0	29.5	30.1	31.4	33.2	33.7	34.9	34.9	35.4	36.7	36.3	36.4	38.5

duced in the W estimate is probably not large compared with other uncertainties in this work.

Our computed results for capture by C, N, and O are given in Table 8.4. In addition, an average was taken to estimate W for pion capture in soft tissue. We weighted the atomic densities, given above, of C, N, and O in tissue by their atomic number Z, in accordance with the Fermi-Teller[11] capture law. The resulting relative capture probabilities for these three nuclei in tissue are then 0.2091 for C, 0.0348 for N, and 0.7561 for O. The numerical estimates of W thus obtained for TE gas, CO_2, and N_2 are shown, together with the values for N_2 found in our earlier work.[7] In addition to the differences in the W values used for different ions, as discussed above, use of the number-energy spectra of Guthrie, Alsmiller, and Bertini[9] based on statistical models for light nuclei introduces uncertainties of an unknown nature.

Finally, we compare the values of W estimated in the region of the maximum dose in a tissue target, irradiated by a parallel beam of negative pions, with W near the surface of the target – in the "peak" and "plateau" regions. We performed depth-dose calculations for a uniform circular beam of 3-cm radius. The pions had a Gaussian distribution of momentum with a mean of 153.4 MeV/c (mean range in tissue = 15.0 cm) and a spread such that 50% of the particles had momenta within ±3% of the mean. The relative contributions of different particles to the total dose in the plateau and peak regions are given in Table 8.5, together with the resulting computed W values for TE gas, CO_2, and N_2. For the direct ionization by pions in flight and by protons, we used the value of W for 10-MeV protons given in Table 8.3 for each gas, the newer value being used for N_2. For other charged particles and for neutrons, we used the average of those values in Table 8.3 for α and N at 2 MeV, as indicated in Table 8.5. The numerical results indicate that the value of W increased by 0.6 to 0.7 eV, or 2% to 3%, in going from the plateau to the

11. E. Fermi and E. Teller, *Phys. Rev.* 72, 399 (1947).

Table 8.4. Estimated W (eV/ip) for TE gas, CO_2, and N_2 for capture of negative pions by elements in soft tissue and W averaged over tissue elements

	TE gas	CO_2	N_2 (present work)	N_2 (previous work[7])
W_C	29.62	33.28	35.00	36.40
W_N	29.68	33.33	35.05	36.42
W_O	29.75	33.39	35.12	36.44
W_{tissue}	29.72	33.36	35.09	36.43

Table 8.5. Estimated W for TE gas, CO_2, and N_2 in plateau- and peak-dose regions of target irradiated by pion beam

Particle type	Relative dose (%)		W (eV/ip)		
	Plateau	Peak	TE gas	CO_2	N_2
Pions (ionization only)	89	42	29.5	33.2	34.9
Protons (including deuterons, tritons)	3	25			
Heavy particles (^{3}He, α, particles with $A > 4$)	6	28	32.7	35.8	37.7
Neutrons	2	5			
Average W (eV/ip)					
Plateau			29.8	33.4	35.1
Peak			30.6	34.1	35.8

peak region in a tissue target irradiated by a beam of negative pions. In our earlier work, a difference of the order of 1% was reported for N_2. The larger difference found here is due to (1) the lower value of W used here for 10-MeV protons (cf. Table 8.3) and (2) the use of W at 2 MeV for heavy particles and neutrons, rather than 10 MeV. Although considerable uncertainty exists in some of the numbers used in making these estimates, the indicated increase of several percent in the value of W in going from the plateau to the peak region is probably real.

TABULATIONS OF ELECTRON INTERACTION PARAMETERS IN SOLIDS[12]

We continued our program of theoretical calculations of inelastic mean free path, stopping power, and range (in the continuous slowing-down approximation) of electrons in a variety of solids for electron energies of ~10 eV to 10 keV. We compiled tables of these interaction parameters which should prove useful to workers in many areas. The determination of these parameters is based on currently available theoretical cross sections for the various mechanisms involved in the interaction of electrons with matter. Much of this work relies on theoretical models developed and tested in our group over a period of years.

For the electron energy range of interest here, the principal mechanisms determining the interaction parameters are (1) the interaction of electrons with the conduction band or valence band electrons and (2) the excitation of electrons into the continuum from the inner shells of the constituent atoms of the solid. Mechanism (2) as applied to the solids aluminum and aluminum oxide was discussed in some detail in a previous annual report[13] and elsewhere.[14] For the extended electron states of the solid [mechanism (1)], several models have been used to obtain a linear dielectric response function which describes the response of this group of electrons to a given energy and momentum transfer. The insulator model and the electron gas model have been described in detail previously.[15,16] For the case of a semiconductor, our calculations rely on a model based on the Callaway-Tosatti model of a semiconductor.[17,18] This model treats an amorphous material with a single isotropic energy gap introduced into an electron gas and has been discussed in some detail in a study of the electron slowing-down spectrum in silicon.[19] In this model, as in the electron gas model, the energy losses of an incident electron due to excitation of valence band electrons divide naturally into (1) losses resulting from excitation of single electrons out of the Fermi sea, and (2) losses to collective oscillations of the valence band electrons (plasmon excitation).

During the past year, two sets of tabulations were produced. The tabulation for germanium and gallium arsenide[20] uses the model insulator theory for the valence band electrons and inner-shell ionization derived from classical binary-collision cross sections. The second tabulation, for the solids nickel, copper, silver, and gold,[21] uses a statistical model described in previously published work.[22,23] Tabulations such as these have proved valuable for both theoretical and applied calculations in the little-studied energy range below 10 keV.

ELECTRON SLOWING-DOWN SPECTRA IN ALUMINUM METAL[12]

The study of the distribution in energy of electrons as they lose energy in interactions with a medium is an important step in providing a better understanding of, and the possibility of predicting, the physical or biological damage to a medium due to a radiation insult. In a previous report,[24] we described, in detail, theoretical calculations of such electron slowing-down spectra in aluminum metal due to monoenergetic sources of elec-

---

12. Research sponsored in part by the Deputy for Electronic Technology (DET), Air Force Systems Command, under Contract Y77-6, but this report does not necessarily reflect endorsement by DET.

13. R. H. Ritchie et al., *Health Phys. Div. Annu. Prog. Rep. June 30, 1975*, ORNL-5046 (September 1975), pp. 154–55.

14. J. C. Ashley, C. J. Tung, and R. H. Ritchie, *IEEE Trans. Nucl. Sci.* NS-22, 2533 (1975).

15. R. H. Ritchie et al., *Health Phys. Div. Annu. Prog. Rep. June 30, 1975*, ORNL-5046 (September 1975), pp. 144–48.

16. R. H. Ritchie et al., *Radiat. Res.* 64, 181 (1975) and references contained therein.

17. J. Callaway, *Phys. Rev.* 116, 1368 (1959).

18. E. Tosatti and G. P. Parravicini, *J. Phys. Chem. Solids* 32, 623 (1971).

19. L. C. Emerson et al., *Phys. Rev. B* 7, 1798 (1973).

20. J. C. Ashley et al., *Inverse Mean Free Path, Stopping Power, CSDA Range, and Straggling in Ge and GaAs for Electrons of Energy <10 keV*, RADC-TR-76-350, Rome Air Development Center, New York, November 1976.

21. J. C. Ashley et al., *Inverse Mean Free Path, Stopping Power, CSDA Range, and Straggling in Ni, Cu, Ag, and Au for Electrons of Energy <10 keV Calculated from a Statistical Model*, RADC-TR-76-220, Rome Air Development Center, New York, June 1976.

22. R. H. Ritchie et al., *Health Phys. Div. Annu. Prog. Rep. June 30, 1976*, ORNL-5171 (October 1976), pp. 177–79.

23. J. C. Ashley et al., *IEEE Trans. Nucl. Sci.* NS-23, 1833 (1976).

24. R. H. Ritchie et al., *Health Phys. Div. Annu. Prog. Rep. June 30, 1976*, ORNL-5171 (October 1976), pp. 179–83.

trons. The fundamental theoretical quantity required in studies of electron energy loss is the probability per unit path length, or differential inverse mean free path (DIMFP), for an electron of a given energy to participate in any of the various inelastic processes that may occur in the medium. For the very low energy electron sources considered previously, the energy losses of the source electrons were due to interaction with the conduction band electrons of the solid. The DIMFPs for the three dominant inelastic processes, that is, the creation of plasmons, electron-hole pairs, and secondary electrons, were described in detail based on the Lindhard form[25] of the dielectric response function for an electron gas.

For a comparison of our theoretical calculations with measurements of electron slowing-down spectra from Keplertron studies which cover the energy range from a few electron volts to 10^5 to 10^6 eV, we must include the contributions to the electron flux from inner-shell ionizations and Auger electrons. Theoretical calculations of the cross sections for excitation of electrons from the inner shells of atoms in a solid are based on two assumptions: (1) that the binding energies of the tightly bound inner shells are not changed appreciably from the values appropriate for isolated atoms and (2) that widths of the energy bands corresponding to inner shells are narrow enough to be neglected. With these assumptions, a theoretical determination of the cross sections for the excitation and ionization of inner shells may be obtained in the first Born approximation, using atomic generalized oscillator strength functions for such inner shells. The details of our calculations of DIMFPs for inner-shell excitation have been published and need not be repeated here.[14]

The equation describing the electron flux takes a relatively simple form for a uniform isotropic medium with source electrons born at a constant rate throughout, as in the experimental arrangement. In this case, attention may be focused on the energy dependence of the slowing-down spectrum. Suppose there are $N(E)\,dE$ electrons born per unit volume in the medium in the infinitesimal energy range between E and $E + dE$. The equation that expresses the statistical balance between electrons produced in this range and electrons scattered out through inelastic collision processes is:

$$\phi(E)\,dE \int_0^\infty dE'\tau(E,E') = N(E)\,dE$$

$$+ \int_E^\infty dE'\phi(E')[\tau(E',E'-E) + \tau_s(E',E)]\,dE\,, \quad (3)$$

where $\phi(E)\,dE$ represents the electron flux in the energy range between E and $E + dE$. $\tau(E, E')$, the DIMFP, describes the probability per unit path length for an electron with energy E to lose energy E' per unit energy through the collision with the medium. $\tau_s(E', E)$ is the DIMFP for an electron with energy E' to generate a secondary electron with energy E per unit energy interval about E.

To illustrate the effect of including inner-shell contributions, we show in Fig. 8.1 the calculated slowing-down flux $\phi(\epsilon)$ vs $\epsilon \equiv E/E_F$, where E_F is the Fermi energy, for a monoenergetic electron source with energy $\epsilon_0 = 40$ in aluminum metal. The flux represented by curve A results from interactions of the source electrons with the conduction band electrons only, whereas that represented by curve B also includes contributions from inner-shell ionization. For high energies, the slowing-down flux $\phi(\epsilon)$ is actually smaller when the contribution from inner shells is included than when it is neglected, whereas at the lower energies this situation is reversed. The peaks just below the source energy correspond to electrons that have generated one, two, three, etc., plasmons in succession. After several fluctuations as ϵ decreases, the flux becomes fairly smooth.

To complete the flux calculations, we must include the Auger electrons generated in the material. When an inner-shell electron is removed from an ion core, the vacancy it leaves is filled within 10^{-7} to 10^{-12} sec by an electron from an outer shell. The energy liberated in this transition may be taken up by the radiation field, or it may be absorbed in the creation of an Auger elec-

25. J. Lindhard, *K. Dan. Vidensk. Selsk. Mat.-Fys. Medd.* 28(8) (1954).

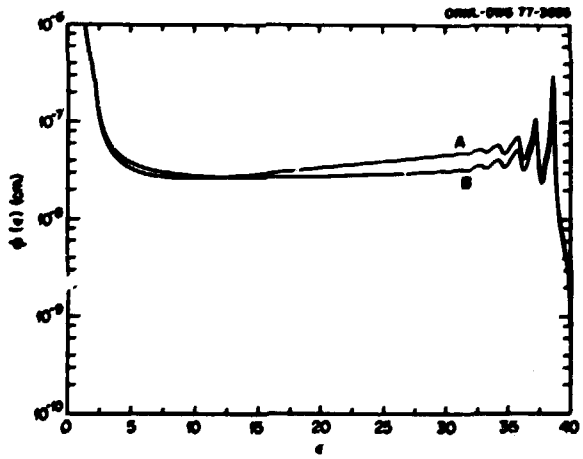

Fig. 8.1. Electron slowing-down flux in aluminum metal due to a monoenergetic electron source with energy $\epsilon_0 = 40$. Curves B and A represent, respectively, results calculated with and without the contribution from inner shells.

tron or in the generation of intershell Auger cascades. For low-Z materials, the emission of Auger electrons is more likely than photon emission. We neglect details of the Auger processes and assume that Auger electrons are produced by filling of a hole in a given shell by an electron from the adjacent shell with smaller binding energy. The contribution to the electron slowing-down spectrum from Auger electrons is thus obtained by adding monoenergetic electron sources, $M(E_i)\,\delta(E - E_i)$, at various characteristic Auger energies, E_i, to Eq. (3). Here the Auger source density at energy E_i is given by

$$M(E_i) = \sum_j M_{ij} \int_0^{\infty} \mu_j(E)\phi(E)\,dE\,, \qquad (4)$$

where M_{ij} is the number of Auger electrons produced with energy E_i following the creation of a vacancy in the jth shell, and $\mu_j(E)$ is the electron inverse mean free path at energy E for ionization of the jth shell. The matrix M_{ij} is determined as follows. Consider the filling of a vacancy in the aluminum K shell from an electron in the aluminum $L_{2,3}$ subshell. The filling will create an Auger electron having energy $E_K \simeq \hbar\omega_B^K - 2\hbar\omega_B^{L_{2,3}}$ and will give rise to two holes in the aluminum $L_{2,3}$ subshell. Then, each of the aluminum $L_{2,3}$ subshell vacancies will give rise to two holes in the conduction band and an Auger electron with energy $E_{L_{2,3}} \simeq \hbar\omega_B^{L_{2,3}} - E_F$. Therefore, $M_{K,K} = M_{L_{2,3},L_{2,3}} = 1$ and $M_{L_{2,3},K} = 2$. We thus account for intershell Auger cascades in a schematic way which is accurate enough for our purposes.

To find electron slowing-down spectra accurately and efficiently over the wide energy range covered by the Keplertron measurements, modifications of Eq. (3) and the numerical procedure are both necessary. First, electron slowing-down spectra obtained by Spencer and Fano,[26,27] who used the continuous slowing-down approximation and the Møller scattering cross section, are valid for energies greater than several times the binding energy of the most tightly bound inner shell. For aluminum, the binding energy of the K shell is ∿1550 eV. Thus, we have assumed that electron slowing-down spectra obtained by the Spencer-Fano method were correct for energies above $E_0 = 10$ keV. To solve for the electron flux at energies below 10 keV, one adds to the source flux $N(E)$ in Eq. (3) an equivalent source flux, $S_{SF}(E)$, obtained from the calculation of the integral on the right-hand side of this equation integrated between E_0 and infinity. Electron flux at energies below E_0 may then be calculated from Eq. (3), starting with a solution at E_0, according to the distribution of the new source flux $S(E) = N(E) + S_{SF}(E)$. Figure 8.2 shows a plot of the function $S_{SF}(E)$ vs E computed from the Spencer-Attix equation,[27] assuming an allowed beta spectrum. At high energies, most of the contribution to the flux is from degraded "Spencer-Fano" flux electrons above E_0. As the electron energy decreases immediately below E_0, the flux also decreases and reaches a minimum value. It then rises steeply as energy further decreases. A detailed plot of the source flux for energies close to E_0, shown at the bottom left corner of Fig. 8.2, is needed for close examination because the plasmon contribution only extends over a limited energy region below E_0.

The resulting electron slowing-down spectrum is shown in Fig. 8.3, together with the theoretical result from a Monte Carlo calculation (histogram) and experimental data on the slowing-down flux of electrons from ^{198}Au beta rays in aluminum metal. The first Auger electron contribution to the theoretical curve at ∿1380 eV can be seen just barely from the figure. Other Auger electrons contribute to the flux at ∿100 and ∿65 eV. The two theoretical curves agree better with each other than with the experiment. The small differences between the theoretical results for energies between 10^3 and 10^4 eV are due to different models and methods of solution employed. Agreement between our model calculations and experimental measurements using the Keplertron is fairly good, especially with respect to the magnitudes of these two in the high-energy region. Discrepancies between theory and experiment in the low and intermediate energy regions require further study.

A detailed account of this work was submitted for publication in *Physical Review*.[28]

INFLUENCE OF DAMPING ON THE MEAN FREE PATH OF LOW-ENERGY ELECTRONS IN AN ELECTRON GAS[12]

Undamped plasmons cannot be excited by electrons having energy less than the plasmon energy. However, in any real system, the plasmon state is damped, and an electron with arbitrarily small energy above the Fermi level can deliver its energy to the plasmon field. In a recent paper,[29] we estimated the mean free path against

26. L. V. Spencer and U. Fano, *Phys. Rev.* 93, 1172 (1954).
27. L. V. Spencer and F. H. Attix, *Radiat. Res.* 3, 239 (1955); see, also, R. T. McGinnies, National Bureau of Standards Circular 597 (February 1959).
28. C. J. Tung and R. H. Ritchie, to be published in *Physical Review Section B*.
29. J. C. Ashley and R. H. Ritchie, *Phys. Status Solidi B* 62, 253 (1974).

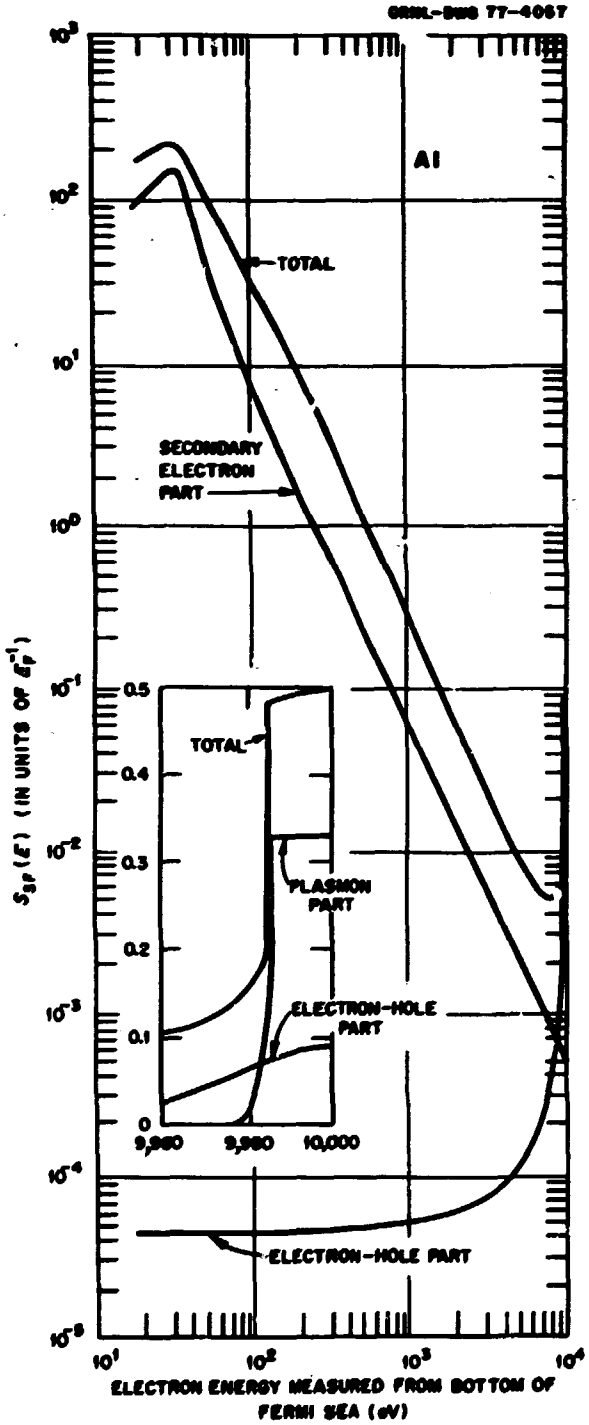

Fig. 8.2. First collision electron source density, $S_{SF}(E)$, in aluminum, calculated from differential inverse mean free path functions and from Spencer-Fano flux for electron energies above 10 keV.

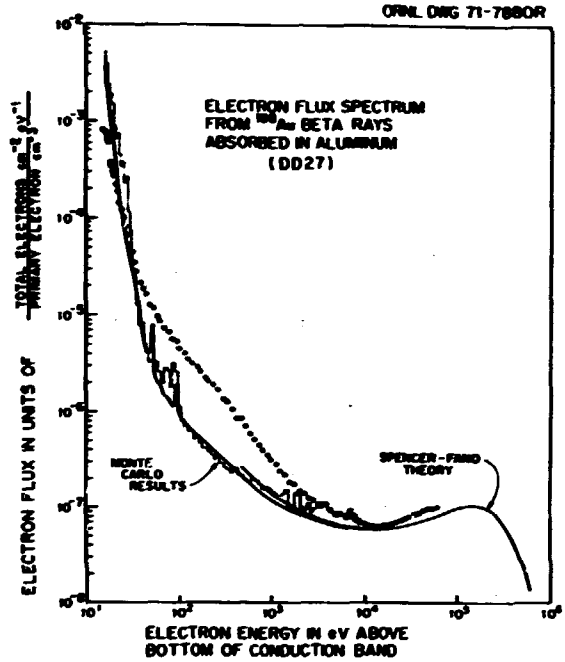

Fig. 8.3. Electron slowing-down spectrum in aluminum metal due to ^{198}Au beta rays. The solid curve is the result of the present calculations. The histogram is the spectrum calculated from a Monte Carlo code. Experimental values are shown as open circles. The Spencer-Fano flux at higher energies is shown as a solid line.

plasmon creation by very low energy electrons in aluminum metal, including damping explicitly. We present here some further results from that work as well as new calculations based on the Mermin-Kliewer-Fuchs form of the dielectric function of a damped electron gas to compare with results based on our earlier approach.

In ref. 29, a many-body theory approach was used to calculate the mean free path of an electron for plasmon excitation in an electron gas. The plasmon resonance line and the cutoff wave vector for plasmon excitations were determined from the Lindhard dielectric function in the no-damping limit,[25] while dissipative processes leading to decay of the plasmon states were included in a plasmon propagator. The inclusion of dissipative processes in this fashion ensured consistency with the overall response of the electron gas through a built-in sum rule constraint. The quantity $\overline{\omega}_z$, which enters in the plasmon propagator, is a measure of the dissipative processes leading to decay of plasmon states and can be connected with measurements of the width of the plasmon loss from characteristic energy loss experi-

ments. Using the data of Ninham, Powell, and Swanson[30] and Festenberg[31] for aluminum, we find

$$\omega_z]_{\exp} = [x_z(0.0858 + 0.592z^2 + 10.5z^4)]^{1/2}, \qquad (5)$$

where z is the momentum transfer in units of twice the Fermi momentum, and x_z is the position (in energy) of the plasmon loss peak in units of the Fermi energy. The results for the inverse mean free path for plasmon excitation, λ_p^{-1}, calculated from the theory of ref. 29, are shown in Fig. 8.4. The quantity $\alpha^2 - 1$ is the energy of the incident electron measured from the Fermi level in units of the Fermi energy. The curve labeled $\bar{\omega}_z = 0$ is calculated assuming no damping of the plasmon states and exhibits a threshold at ~23 eV. The curve $\bar{\omega}_z]_{\exp}$ indicates that plasmon excitation contributes substantially to the mean free paths of electrons with energies below the "no-damping" threshold when damping of the plasmon states is included. Also shown in Fig. 8.4 is λ_p^{-1} calculated assuming the width of the plasmon loss peak is 0.5 eV independent of z, indicated by $\bar{\omega}_z = (0.0429x_z)^{1/2}$, and the electron-electron inverse mean free path, λ_{ee}^{-1}, as calculated by Kleinman.[32]

An alternative approach to calculations of mean free paths is to allow for the effect of dissipative processes occurring in a real metal in an approximate way by including a damping coefficient in the Lindhard dielectric function $\epsilon_L(k, \omega)$, as was done by Lindhard.[25] Kliewer and Fuchs[33] later proposed a modification of this function to overcome the defect that, for the dissipative case, Lindhard's function is equivalent to treating collisions in a relaxation-time approximation which does not conserve electron number. Mermin[34] subsequently obtained an analytical form, differing from the Kliewer-Fuchs expression, in an approximation that conserves electron number and in which collisions relax the electron density matrix to a local equilibrium density matrix. In addition, the Mermin form exhibits limiting properties which yield correct expressions for quantities such as the dc conductivity and the Thomas-Fermi screening.[34] Recent experimental measurements of the (k, ω) dependence of the energy loss function $\mathrm{Im}[-1/\epsilon(k, \omega)]$ for aluminum metal by Gibbons et al.[35] and Batson and Silcox[36] were fitted by both groups using the Mermin formula with an empirical correction for exchange and correlation effects.

In calculating mean free paths, we have used the Mermin form of the dielectric response function[34]

$$\epsilon_M(z, x, \Gamma) = 1 + \frac{(x + i\Gamma)F(z, x + i\Gamma)}{x + i\Gamma[F(z, x + i\Gamma)/F(z, 0)]}, \qquad (6)$$

where x is energy transfer in units of the Fermi energy, E_F, and Γ is related to the phenomenological damping rate γ by $\Gamma \equiv \hbar\gamma/E_F$. The function $F(z, x + i\Gamma) + 1 \equiv \epsilon_L(z, x + i\Gamma)$ is the Lindhard longitudinal dielectric function.[25] The total inverse mean free path was calculated from

$$\lambda^{-1}(\alpha^2) = \frac{1}{\pi a_0 \alpha^2} \times \int_0^{\alpha} \frac{dz}{z} \int_0^{4z(\alpha - z)} dx\, \mathrm{Im}(-1/\epsilon_M)\theta(\alpha^2 - 1 - x), \qquad (7)$$

where the step function θ prohibits transitions into the filled levels of the Fermi sea. Here $a_0 \equiv \hbar^2/me^2$ is the Bohr radius. In Fig. 8.5 are plotted values of λ

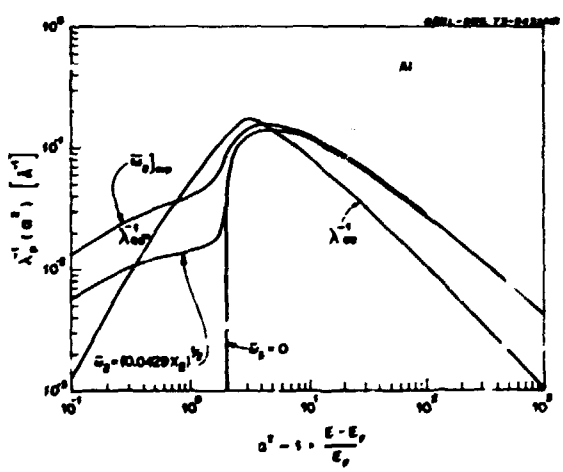

Fig. 8.4. The curve denoted by $\bar{\omega}_z]_{\exp}$ shows the inverse mean free path (in units of Å^{-1}) for excitation of a plasmon by an electron of energy $\alpha^2 - 1$ (energy measured from the Fermi level in units of E_F) in a free-electron gas with $r_s = 2.074$, using experimentally derived values for the damping of plasmons in aluminum. The curve indicated by $\bar{\omega}_z = 0$ represents the inverse mean free path in the absence of damping of the plasmon states; the curve designated $\bar{\omega}_z = (0.0429x_z)^{1/2}$ corresponds to a constant value of the width of the plasmon loss of 0.5 eV. The additional curve designated λ_{ee}^{-1} shows, for comparison, the electron-electron inverse mean free path as calculated by Kleinman.[32]

30. B. W. Ninham, C. J. Powell, and N. Swanson, *Phys. Rev.* 145, 209 (1966).
31. C. von Festenberg, *Phys. Lett.* 23, 293 (1966).
32. L. Kleinman, *Phys. Rev. B* 3, 2982 (1971).
33. K. L. Kliewer and R. Fuchs, *Phys. Rev.* 118, 552 (1969).
34. N. D. Mermin, *Phys. Rev. B* 1, 2362 (1970).
35. P. C. Gibbons et al., *Phys. Rev. B* 13, 2451 (1976).
36. P. E. Batson and J. Silcox, to be published.

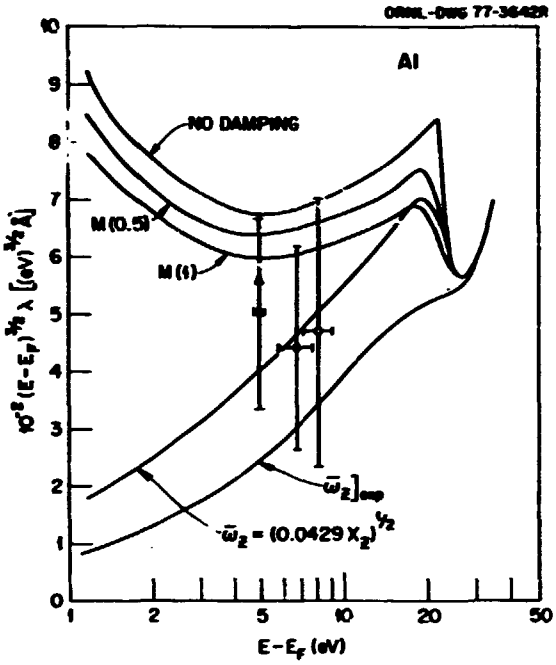

Fig. 8.5. The mean free path, λ, in units of Å, of low-energy electrons in an electron gas (r_s = 2.074), plotted as $10^{-2}(E - E_F)^{3/2}\lambda$ vs electron energy measured from the Fermi level. The various curves are described in detail in the text. The ^ experimental values are from Kanter[37] and ○ from Callcott and Arakawa.[38]

computed from this equation for an electron gas with the same density as that of the conduction band in aluminum, plotted in the form $10^{-2}(E - E_F)^{3/2}\lambda$ as a function of electron energy above the Fermi energy. The curve labeled "no damping" corresponds to $\Gamma = 0$, and the curves $M(1)$ and $M(0.5)$ correspond to values of $\hbar\gamma$ of 1 and 0.5 eV respectively. Values of $\hbar\gamma$ in the range of 0.5 to 1 eV appear to be the smallest values obtained for this quantity in experimental work.[30,31,35,36] In the electron energy range 1.5 eV $\lesssim E - E_F \lesssim$ 20 eV, the values of λ predicted by the curve $M(0.5)$ [$M(1)$] are ∼7% [∼13%] smaller than values of λ for no damping. Note that the no-damping curve in this energy range corresponds to the mean free path for electron-hole pair excitation only, since in the absence of damping the threshold for plasmon excitation in aluminum occurs at ∼23 eV.

Also shown in Fig. 8.5 are the results from our many-body theory calculations as obtained from Fig. 8.4 through $\lambda = (\lambda_{ee}^{-1} + \lambda_p^{-1})^{-1}$. We find, with this calculation, values of mean free path, λ, which vary from ∼1/4 to ∼1/8 of λ_{ee} at 1.5 eV and 15% to 37% lower than λ_{ee} at 20 eV for the range of $\bar{\omega}_z$ values indicated. The points in Fig. 8.5 show measurements of attenuation lengths in aluminum metal.[37,38] The error bars indicate the large uncertainties associated with measurements of electron mean free paths in this low-energy region.

Widely different values of λ for low-energy electrons are found using these two different approaches. However, the measurements of the energy loss function in aluminum and comparisons made with the predictions of the Mermin form of the dielectric response function[35,36] indicate that the use of a constant value of Γ not only underestimates the width, but also fails to reproduce the asymmetry of the plasmon resonance for $z > 0$. Hence, the results presented here based on the Mermin form probably underestimate the influence of damping on electron mean free paths. A detailed treatment which includes the change in width of the plasmon loss peak with z should thus tend to produce better agreement with the results predicted for λ from the many-body theory calculations.

INTERACTION OF SLOW IONS WITH SURFACES

The forces on a molecule located near a solid or liquid surface are of crucial importance in the processes of particle accretion and adhesion of particulate matter to macroscopic bodies and in catalytic reactions among molecules at gas–condensed matter interfaces. A model worthy of study in this connection involves the motion of an ion or a neutral molecule moving in vacuo in the vicinity of a metal surface. If the velocity, v, of this particle is small compared with $v_0 = e^2/\hbar$, and if the surface plasmon (SP) state on the metal is completely undamped, the particle can be expected to excite only electron-hole pairs. However, the SP state is never completely sharp in any real metal. In this case, SP excitation may contribute significantly to the force fields.

We have studied the dissipative component of the "dispersion" force acting on a point particle of charge Ze moving in the vicinity of a plane-bounded, semi-infinite electron gas. A solution was found using a specular reflection model of the bounded metal. We used this model earlier to study properties of the surface plasmon.[39] More recent comparison with detailed many-body theory predictions indicates that the model can describe the collective and single-particle responses of such a system with surprisingly good accuracy.[40]

37. H. Kanter, *Phys. Rev. B* 1, 522 (1970).
38. T. A. Callcott and E. T. Arakawa, *Phys. Rev. B* 11, 2750 (1975).
39. R. H. Ritchie and A. L. Marusak, *Surf. Sci.* 4, 234 (1968).
40. V. Celli, p. 393 in *Surface Physics*, IAEA, Vienna, 1974.

We find that the energy loss per unit path length, dW/dx, by the charge moving parallel to and at distance z_0 from a metal surface may be written

$$\frac{dW}{dx} = \frac{(Ze)^2}{\pi v^2} \int_{-\infty}^{\infty} dk_y \int_0^{\infty} \frac{\omega d\omega}{\kappa} \operatorname{Im}\left(\frac{\kappa I - \pi}{\kappa I + \pi}\right) e^{-2\kappa z_0} . \quad (8)$$

The quantities in the integrand are defined by

$$I = \int_{-\infty}^{\infty} \frac{dk_z}{k^2 \epsilon_{k,\omega}} , \quad (9)$$

where $k^2 = \kappa^2 + k_z^2$, $\kappa^2 = k_y^2 + \omega^2/v^2$, and $\epsilon_{k,\omega}$ is the linear dielectric response function of the metal.

A very slow particle, $v \ll v_0$, may lose energy to electron-hole pair excitations in the metal. These contributions are best evaluated in this limit by using the form of the dielectric constant of an electron gas appropriate when $\hbar\omega$ is small compared with the Hartree energy, that is, $\omega \ll me^4/\hbar^3$. We find, for $v \ll v_0$,

$$\left(\frac{dW}{dx}\right)_{eh} = \frac{3}{4}\left(\frac{Ze\omega_p}{v_F}\right)^2 \left(\frac{v}{v_F}\right) \int_0^{2k_F/k_D} du \frac{u^3 s}{(u+s)^2}$$

$$\times \left[\frac{u^2+2}{s^2} \ln\left(\frac{s+1}{s-1}\right) - \frac{2}{s}\right] e^{-2k_D z_0 u} , \quad (10)$$

where $s = \sqrt{1+u^2}$, $k_D = 3\omega_p/v_F$, ω_p is the plasma frequency of electrons in the metal, and v_F is the Fermi velocity. For $k_D z_0 \gg 1$, this expression reduces to

$$\frac{dW}{dx} \sim \frac{24 Z^2 \hbar v}{\pi a_0^2 (2k_D z_0)^4} \ln\left(\frac{k_D z_0}{1.4475}\right) , \quad (11)$$

where $a_0 = \hbar^2/me^2$ is the first Bohr radius. A plot of numerical values of a constant times $(1/v)(dW/dx)$ vs $2k_D z_0$ obtained by evaluating the integral of Eq. (10) is displayed in Fig. 8.6 (solid curve).

Even when the ion has kinetic energy much smaller than the nominal energy of the surface plasmon, when the latter is damped there is a nonvanishing probability that the ion can deliver energy to the surface plasmon field.

The contribution to dW/dx corresponding to the excitation of collective modes at the surface may be obtained by using the Mermin[34] form of the dielectric constant of a damped free electron gas. In the limit of small k, the Mermin form reduces to $\epsilon_{k,\omega} \sim 1 - \omega_p^2/[\omega(\omega + i\Gamma)]$, where Γ is the damping frequency of electronic excitations in the metal. Using this result in Eq. (8), one finds

$$\frac{dW}{dx} \sim \frac{Z^2 e^2 \Gamma v}{4\omega^2 z_0^3} , \quad (12)$$

in the limit $v \ll v_0$ and $z_0 a_0 \gg 1$. Figure 8.6 shows a plot of the contribution to $(1/v)(dW/dx)$ from plasmon excitation for the case of aluminum metal, where $\hbar\omega_p = 15.4$ eV and $\hbar\Gamma \simeq 1$ eV. This is shown as a dashed curve and is also displayed as a function of $2k_D z_0$. Although the SP contribution must dominate for very large z_0, the two contributions are comparable over the range $0 < 2k_D z_0 < 10$. A complete description of these theoretical results will be given elsewhere.

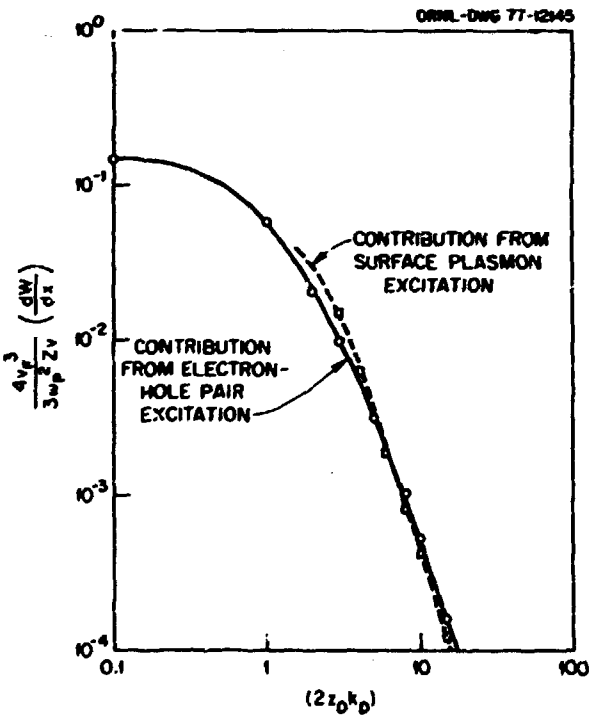

Fig. 8.6. Energy loss per unit path length by a slow ion moving in vacuo parallel to a metal surface. The quantity $(4v_F^3/3\omega_p^2 vZ)dW/dx$ is plotted as a function of $2k_D z_0$, where k_D is the Debye wave vector and z_0 is the distance of the ion from the surface. The solid curve shows the contribution of electron-hole excitations; the dashed curve shows the energy loss to plasma excitations.

ENERGY AND SPATIAL DEPENDENCE OF SWIFT ELECTRONS TRANSMITTED THROUGH THIN SOLID FILMS – EFFECT OF PLASMON INTERACTIONS

Our previous work with electron transmission in thin foils[41,42] showed that the asymmetric energy distributions obtained experimentally could be reasonably well explained using the straggling theory of Landau.[43] For the foil thickness ($t \sim 100$ Å of carbon) and primary energies ($E_p \sim 1000$ eV) of the experiments, a good approximation to a realistic type of interaction can be made by assuming single-particle collisions of the bombarding electrons with those of the foil medium. The distribution of energy losses, using the Landau method, was a set of universal asymmetric curves whose widths and peak energies matched closely those curves obtained experimentally, but the intensities remained arbitrary. The best agreement was for large primary energies and low foil thickness, where one would expect the above assumption to be valid. In the present work an energy loss mechanism has been considered which includes not only the single-particle interaction but the collective plasmon interaction as well, and this has been incorporated into an energy distribution function using a convolution method instead of the Laplace transform technique of the Landau method.

The differential inverse mean free path is written (in atomic units) as

$$\frac{d\Lambda^{-1}}{d\omega} = \frac{2}{\pi v^2} \int_{q_-}^{q_+} \frac{dq}{q} \mathrm{Im}(-\epsilon^{-1}) , \qquad (13)$$

where v is the incident electron velocity, ω is the energy transfer, and q is the momentum transfer. In Eq. (13), $q_\pm \equiv v \pm \sqrt{v^2 - 2\omega}$ are the limits on the momentum transfer from energy-momentum conservation. The energy loss function, $\mathrm{Im}(-\epsilon^{-1})$, of the medium is written as a dispersed Lorentzian as follows:

$$\mathrm{Im}(-\epsilon^{-1}) = \frac{A\Gamma\omega}{\Gamma^2\omega^2 + [(\omega_0 + q^2/2)^2 - \omega^2]^2} , \qquad (14)$$

where ω_0 is the plasma energy of the medium, Γ is the damping constant, and A is an amplitude factor, all of which are obtained from experiment.

The energy distribution function, f, is obtained from the convolution method of Bichsel and Saxon[44] as

$$f_{2x}(\Delta) = \int_0^\Delta f_x(\Delta - \omega) f_x(\omega)\, d\omega , \qquad (15)$$

where x is the foil thickness and Δ is the maximum energy loss at thickness x.

We take as a boundary condition $f_0(\Delta) = \delta(\Delta)$ and write the distribution function for small thickness dx as

$$f_{dx}(\Delta) = (1 - \Lambda^{-1}\, dx)\, \delta(\Delta) + dx \frac{d\Lambda^{-1}}{d\omega} ; \qquad (16)$$

then, from Eq. (15), at arbitrary x we may write

$$f_x(\Delta) = A_x \delta(\Delta) + g_x(\Delta) , \qquad (17)$$

where $A_x = 1 - \Lambda^{-1}\, dx$ and $g_x(\Delta) = dx(d\Lambda^{-1}/d\omega)$. From Eqs. (17) and (15) we obtain

$$g_{2x}(\Delta) = 2A_x g_x(\Delta) + \int_0^\Delta d\omega g_x(\omega) g_x(\Delta - \omega) . \qquad (18)$$

Thus, by starting with a distribution at a small thickness x, the energy distribution at multiples of this thickness can be found by successive iterations.

A numerical scheme was worked out for evaluation of these equations. Specifically, the integral in Eq. (18), $I_{2x}(\Delta) = \int_0^\Delta d\omega g_x(\omega) g_x(\Delta - \omega)$, was replaced by the sum $I_n = \sum_{k=2}^{n} W_k g_k g_{n+1-k}$, where n is proportional to the mesh size and W_k is the weighting function which depends on the type of numerical integration used.

The energy distributions were obtained for carbon films of varying thicknesses, using parameters obtained from the optical data of Williams and Arakawa[45] for $\mathrm{Im}(-\epsilon^{-1})$ for amorphous carbon.

Distribution curves are shown in Fig. 8.7 for thicknesses of 5, 20, 80, and 160 Å and a primary electron energy (E_p) of 1000 eV. The results show pronounced peaks at the plasma energy and weaker peaks at multiples of this energy. The broad asymmetrical straggling distribution becomes apparent as the thickness increases. Also apparent is the shift in the peak of this distribution to larger energy loss values as the thickness increases.

COMPARISON OF VICINAGE EFFECTS IN THE INTERACTION OF ION CLUSTERS WITH SINGLE ATOMS AND WITH CONDENSED MATTER

When a swift molecular ion impinges on a target, only a few collisions may be needed to strip all valence elec-

41. R. H. Ritchie et al., *Health Phys. Div. Annu. Prog. Rep. June 30, 1976*, ORNL-5171 (October 1976), pp. 196–98.
42. J. Cowan and J. Hoelzl, *Thin Solid Films* 32, 355 (1976).
43. L. Landau, *J. Phys. (Moscow)* 8, 20 (1944).
44. H. Bichsel and R. P. Saxon, *Phys. Rev. A* 11, 1286 (1975).
45. M. W. Williams and E. T. Arakawa, *J. Appl. Phys.* 43, 3460 (1972).

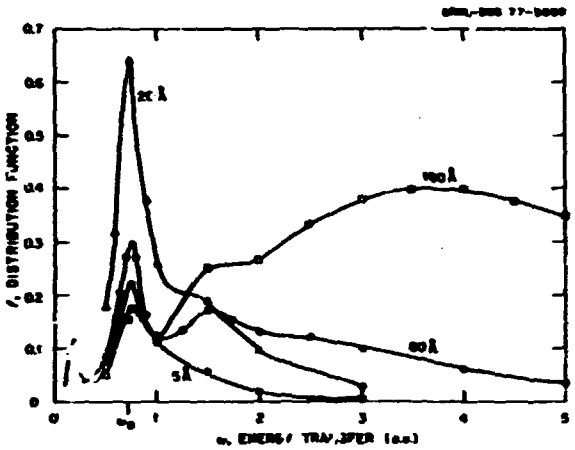

Fig. 8.7. Energy distribution functions for various carbon foil thicknesses at a primary electron energy E_p = 1000 eV. Vertical scale for 160 A has been expanded by a factor of 10 for clarity.

trons from the projectile. The residual ionic fragments then begin to recede from each other under the influence of interionic Coulomb forces.[46] When the fragments are traveling in close proximity, there may be substantial vicinage,[46] or spatial correlation, effects on electronic transitions induced in the target. For example, the retarding force on one ion (and hence its energy loss) may be influenced by the presence of other ions in the cluster.

We have studied vicinage effects associated with the penetration of clusters in solids and in collision with atomic systems. For purposes of comparison, we use idealized models. Vicinage terms in the energy loss of a dicluster are studied using (1) a quantum dielectric model of condensed matter, (2) a classical harmonic oscillator model of electronic excitation in a single molecule, and (3) a quantum mechanical description of the excitation of an atomic system.

Let two point charges, z_1e and z_2e, proceed with velocity $\mathbf{v}$ in a medium characterized by the dielectric function $\varepsilon(k, \omega)$. The particle separation is specified by the vector $\mathbf{R}$ with components $\mathbf{D}$ and $\mathbf{B}$ in directions parallel with, and perpendicular to, $\mathbf{v}$ respectively. In linear response theory and in the first Born approximation, S_c, the energy loss of the cluster per unit path length to electronic excitation, may be written

$$S_c = (z_1^2 + z_2^2)S_p(\mathbf{v}) + 2z_1z_2S_v(\mathbf{v}, B, D) . \qquad (19)$$

Here $S_p(\mathbf{v})$ is the energy loss per unit path length by a single proton with the same velocity as the cluster. The vicinage stopping power $S_v(\mathbf{v}, B, D)$ becomes equal to $S_p(\mathbf{v})$ as $\mathbf{R} \to 0$ and goes to zero as $\mathbf{R} \to \infty$. Using a simplified form of the response function of an electron gas, one finds

$$g_v(\mathbf{v}, B, D) \equiv \frac{S_v(\mathbf{v}, B, D)}{S_p(\mathbf{v})}$$

$$\approx k_p^2 \left[\cos(Dk_p) \int_0^{\kappa_c} \frac{\kappa d\kappa}{\kappa^2 + k_D^2} J_0(\kappa B) \right.$$

$$\left. + \int_{k_1}^{k_2} \frac{dk}{k} \cos(\hbar k^2 D/2mv) J_0(\kappa B) \right] / S_p(\mathbf{v}) ; \qquad (20)$$

where $k_p = \omega_p/v$, $k_1 = (2m\omega_p/\hbar)^{1/2}$, $k_2 = 2mv/\hbar$, $\kappa_c^2 = k_1^2 - k_p^2$, and ω_p is the plasma frequency of the electron gas. Figure 8.8 is a plot of $g_v(\mathbf{v}, B, 0)$ and $g_v(\mathbf{v}, 0, D)$ for v = 3 atomic units and $\hbar\omega_p$ = 15 eV. The independent variables are $\omega_p B/v$ and $\omega_p D/v$ respectively.

In many experimental situations, clusters are formed with random orientation of $\mathbf{R}$, the interionic axis. A vicinage stopping power $\langle S_v(\mathbf{v}, R)\rangle$ appropriate to this

46. W. Brandt, A. Ratkowski, and R. H. Ritchie, *Phys. Rev. Lett.* 33, 1325 (1974).

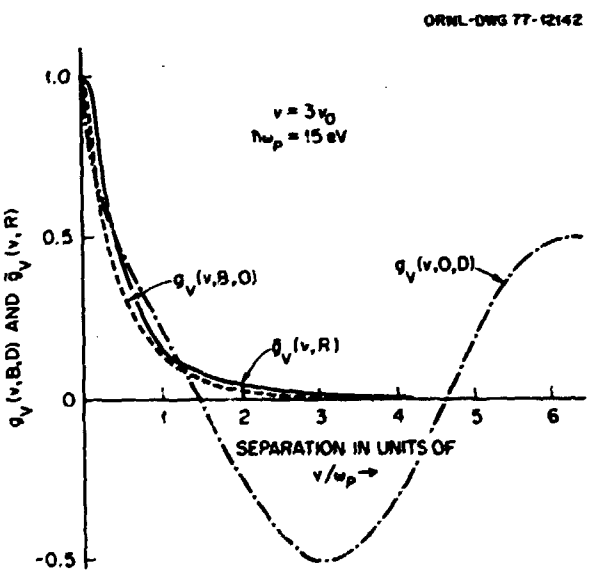

Fig. 8.8. Ratio of vicinage stopping power of the medium for a cluster to the stopping power of an electron gas for a proton with the same velocity. The function g_v is appropriate to an oriented cluster, whereas $\bar{g}_v$ is computed for randomly directed cluster axes.

situation may be obtained by performing a spherical average over the direction of $\mathbf{R}$. In the same approximation as above,

$$\bar{g}_v(v, R) \equiv \langle S_v(v, R)\rangle / S_p(v) = [si_2(k_p R) - si_2(2mvR/\hbar)] / \ln(2mv^2/\hbar\omega_p), \quad (21)$$

where $si_2(x) = \int_x^\infty \sin u du/u^2$. Figure 8.8 shows a plot of g_v (v, R) vs $R\omega_p/v$ for v = 3 atomic units and for $\hbar\omega_p = 15$ eV.

To compare the vicinage function found above with that for collision with a molecular target we use a harmonic oscillator model for electronic excitation of the latter. The energy transfer cross section corresponding to a dicluster–bound electron collision may be written

$$S = \int \Delta E \, d\sigma \equiv (z_1^2 + z_2^2) S_p(v) + 2z_1 z_2 S_v(v, \mathbf{R}), \quad (22)$$

where ΔE is the energy transfer and $d\sigma$ is the differential cross section, S_p is the stopping cross section for a single proton with velocity v in collision with the electron, and the vicinage stopping cross section S_v(v, B, D) is to be compared with S_v(v, $\mathbf{R}$) above. The Bohr harmonic oscillator model, extended to account for large momentum transfer collisions in an approximate way, yields

$$S_v(v, B, D) = \frac{4\pi e^4}{mv^2} \cos\left(\frac{\omega_0 D}{v}\right) \times \int_0^{Q_M} \frac{Q dQ}{Q^2 + \omega_0^2/v^2} J_0(BQ), \quad (23)$$

where ω_0 is the resonant frequency of the electron and $Q_M = [(2m\omega_0/\hbar) - \omega_0^2/v^2]^{1/2}$. If $BQ_M \gg 1$, we may write

$$S_v(v, B, D) = \frac{4\pi e^4}{mv^2} \cos\left(\frac{\omega_0 D}{v}\right) K_0\left(\frac{\omega_0 D}{v}\right), \quad (24)$$

where $K_0(x)$ is the modified Bessel function of the second kind. If $B \to 0$, we have

$$S_v(v, 0, D) = \frac{4\pi e^4}{mv^2} \cos\left(\frac{\omega_0 D}{v}\right) \ln\left(\frac{vQ_M}{\omega_0}\right). \quad (25)$$

For the case of random incidence we may again perform an average over directions of $\mathbf{R}$, obtaining

$$\langle S_v(v, R)\rangle = \frac{4\pi e^4}{mv^2} [si_2(\omega_0 R/v) - si_2(2mR/\hbar)]. \quad (26)$$

A quantum treatment of the collision between a cluster and an atomic system is straightforward. One finds for randomly oriented diclusters,

$$\langle S_v(v, R)\rangle = 2\pi\left(\frac{2e^2}{\hbar v}\right)^2 \sum_f E_f \times \int_{q_0}^{\infty} q dq \left(\frac{\sin qR}{qR}\right) \frac{|F_{f0}(q)|^2}{q^4}, \quad (27)$$

where $F_{f0}(q) = \langle f|\Sigma_{j=1}^{z} e^{i\mathbf{q}\cdot\mathbf{r}_j}|0\rangle$ is the matrix element of the density operator between the ground state $|0\rangle$ and a given final state $|f\rangle$ of the atomic system, $\mathbf{r}_j$ is the coordinate of the jth electron in the atom, and E_f is the energy of the state $|f\rangle$ measured from the ground-state energy. It may be shown that for v large compared with ground-state atomic velocities, the dipole approximation to F_{f0} (q) is useful and that, in this case, Eq. (27) is approximated well by Eq. (26).

The similarity between Eqs. (20) and (23) and between Eqs. (21) and (26) is striking. It seems clear that an interesting correspondence exists between the response of a dielectric medium characterized by a single well-defined plasmon state and the response of a single harmonic oscillator. It appears that in summing over impact parameters to obtain an energy transfer cross section from the harmonic oscillator model, one, in effect, builds up a continuous medium of noninteracting atoms, each with resonant frequency ω_0. The net vicinage response of this fictitious medium is quite comparable with the response of an electron gas with plasma frequency $\omega_p = \omega_0$. It is clear, however, that a real wake of electron density fluctuations extending behind each ion in a cluster can exist only when the cluster penetrates condensed matter. Thus, the tendency of an ion to align itself behind another which leads it, as observed by Gemmell and coworkers[47] in condensed matter, generally will not be found in collisions of clusters with single atoms. Similarly, wake-bound electron states are conceptually possible only in condensed matter.

Numerical work is being carried out to evaluate Eq. (27) for single-electron excitation from the $2p$ shell of aluminum for comparison with results of the cluster experiments of Lurio, Andersen, and Feldman.[48] This

47. D. S. Gemmell et al., *Nucl. Instrum. Methods* 132, 61 (1976).

48. A. Lurio, H. H. Andersen, and L. C. Feldman, "Search for Cluster Effects in X-ray Production by Fast Hydrogen Molecules," to be published.

work is being carried out in collaboration with Dr. G. Busbas (Physics Department, North Texas State University).

WAKE INDUCED IN CONDENSED MATTER BY SWIFT CHARGED PARTICLES

Gemmell and coworkers[47,49,50] performed an elegant set of experiments on the angular and energy distributions of channeled protons emerging from single crystals of silicon bombarded by swift $(HeH)^+$ ions. They show that it is necessary to take into account the influence of the wake of electronic density fluctuations trailing the leading ion[51–53] on the motion of the following proton. Subsequently, they introduced an expression for the wake potential[54] which differs from that given earlier[55] in that the wake properties of the struck electron are accounted for in an approximate way.

We wish to point out that an alternative representation for the wake follows from a well-studied approximation to the wave vector- and frequency-dependent dielectric function of the medium in which the ions travel. This representation includes collective and single-particle effects and may be generalized to include the effects of damping in an approximate way.

Vager and Gemmell[54] considered a local dielectric function $\epsilon(\omega)$ for the medium and concluded that, in this approximation, the density of electron polarization induced by a swift classical point charged particle moving with constant velocity is simply a line of charge stretching behind the particle. To obtain a more realistic representation of the response of the medium, they introduced in a phenomenological way the quantity $\hbar/mv$ (the wavelength of a stationary electron as viewed from the frame of the moving ion) into an expression for $\phi(R, z - vt)$, the scalar electric potential in the medium. They compared their experimental measurements of the joint distribution in energy and angle of protons emerging from a carbon foil bombarded by $(HeH)^+$ ions with calculations of this same distribution function, employing an expression for the electric force on a trailing ion derived from their phenomenological potential function. They found very good agreement, probably because their experiment sampled a fairly small region of ionic separation.

We feel that the straightforward procedure we used to describe the wake potential and the associated density fluctuation function should represent these quantities well over the whole of space. Our approach begins with the standard expression for the scalar electric potential:

$$\phi(\rho, \tilde{z}) = \frac{Z}{\pi v} \int_0^\infty \kappa d\kappa J_0(\kappa\rho) \times \int_{-\infty}^{\infty} d\omega \exp(i\omega\tilde{z}/v)[k^2\epsilon(k, \omega)]^{-1}, \qquad (28)$$

where the cylindrical coordinates $\rho = (x^2 + y^2)^{1/2}$ and $\tilde{z} = z - vt$ are defined relative to the position of the charge, $(0, 0, vt)$, at time t. The wave number $k = (\kappa^2 + \omega^2/v^2)^{1/2}$, $\epsilon(k, \omega)$ is the dielectric function of the medium and v is the particle velocity. If we take the following expression:

$$\epsilon = 1 + \frac{\omega_p^2}{\omega_0^2 + \beta^2 k^2 + k^4/4 - \omega(\omega + i\gamma)}, \qquad (29)$$

we may obtain a reasonable representation of the response of a metal or a semiconductor. This representation takes into account plasmon dispersion through the presence of the term containing β^2, single-particle effects through the term $k^4/4$, and broadening through the presence of the damping frequency γ. Also, ω_0 may be considered to represent the gap energy in the case of a semiconductor.

When the form for ϵ given in Eq. (29) is substituted in Eq. (28), one finds that ϕ may be expressed finally in terms of a single integral of an analytic function. The integral over ω in Eq. (28) may be evaluated by the calculus of residues and has interesting features. Figure 8.9 indicates schematically the locus of poles of the ω integrand in the complex ω plane as κ increases from zero to infinity. There are four poles occurring in pairs. The pair of poles $\omega_-^\pm$, which lie below the real axis when $0 < \kappa < \kappa_c$, correspond primarily to the existence of long-wavelength collective motion in the medium. Here $\kappa_c = [(v^2 - \beta^2)^2 - \omega_p^2 - \omega_0^2]^{1/2}/v$. The poles move away from the origin rather slowly with increasing

49. D. S. Gemmell et al., *Phys. Rev. Lett.* 34, 1420 (1975).
50. Z. Vager, D. S. Gemmell, and S. J. Zabransky, *Phys. Rev. A* 14, 638 (1976).
51. J. Neufeld and R. H. Ritchie, *Phys. Rev.* 98, 1632 (1955).
52. J. Neufeld and R. H. Ritchie, *Phys. Rev.* 99, 1125 (1955).
53. R. H. Ritchie, Ph.D. dissertation, The University of Tennessee, Knoxville (1959), unpublished.
54. Z. Vager and D. S. Gemmell, *Phys. Rev. Lett.* 37, 1352 (1976).
55. R. H. Ritchie, W. Brandt, and P. M. Echenique, *Phys. Rev. B* 14, 4808 (1976).

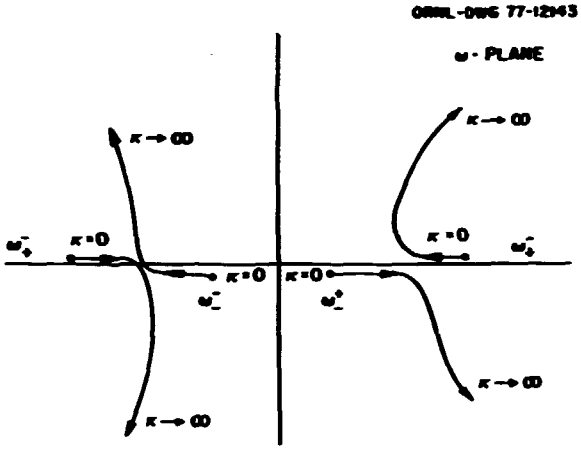

Fig. 8.9. Schematic representation of the variation in position of the four poles of the ω integrand in Eq. (28) with κ, as κ increases from zero to infinity.

κ, then acquire sizable imaginary parts for $\kappa \gg \kappa_c$. The pole ω_-^- crosses the real axis and moves to infinity in the second quadrant as $\kappa \to \infty$, while ω_-^+ remains in the fourth quadrant, also moving to infinity as $\kappa \to \infty$. The pair of poles $\omega_+^\pm$ lie above the real axis when $0 < \kappa < \kappa_c$ and have vanishingly small imaginary components in the limit $\gamma \to 0$. At first glance this may be quite surprising since the presence of such poles seems to signal the breakdown of causality; that is, the effect of the moving ion appears to precede it in time. In reality, since we assume in obtaining Eq. (28) that the charged particle has been in uniform rectilinear motion long enough for transient effects to have subsided, there are precursor, or bow, waves of electron density fluctuation preceding the particle. These waves are associated primarily (but not completely) with "knock-on" electrons, or electrons that are ejected from the medium with energies $\gtrsim 10$ eV in the forward hemisphere of directions.

The poles at $\omega = \omega_+^\pm$ are primarily associated with the bow waves. The scale of length of variations in ϕ originating from these poles is $\sim 1/v$ ($\hbar/mv$ in ordinary units), the de Broglie wavelength of an electron that has acquired momentum v (mv in regular units) from the ion. By way of comparison we note that the scale of length associated with collective motion in the wake is $\sim v/\omega_p$, and that fluctuations on this scale of distance originate primarily from the poles at $\omega = \omega_-^\pm$.

A closed expression for ϕ for the case $\gamma \to 0$ is given by:

$$\phi(\rho, \tilde{z}) = \phi_1(\rho, \tilde{z}) + \phi_2(\rho, \tilde{z}) + \phi_3(\rho, \tilde{z}) , \qquad (30)$$

where

$$\phi_1(\rho, \tilde{z}) = \sqrt{2} Z \omega_p \times \int_0^{Q_c} Q J_0(\sqrt{2}\rho Q) \frac{\sin(\sqrt{2} z \tilde{\xi}_+)}{\beta \xi_+ (Q^2 + \xi_+^2)} dQ . \qquad (31)$$

Here $\xi_\pm = (\alpha \pm \beta)^{1/2}$, $\alpha = v^2 - \beta^2 - Q^2$, $\beta = [(v^2 - \beta^2)^2 - 2v^2 Q^2 - \tilde{\omega}_p^2]^{1/2}$, and $\tilde{\omega}_p^2 = \omega_p^2 + \omega_0^2$. Also,

$$\phi_2(\rho, \tilde{z}) = -\frac{Z\omega_p^2}{\sqrt{2}} \times \int_{Q_c}^{\infty} Q J_0(\sqrt{2}\rho Q) \frac{\exp(-\sqrt{2}\gamma_- |\tilde{z}|)}{\gamma_+ \gamma_- (\gamma_+^2 + \gamma_-^2)} \frac{N}{D} dQ , \qquad (32)$$

where

$$N = (Q^2 + \gamma_+^2 - \gamma_-^2)[\gamma_+ \cos(\sqrt{2}\gamma_+ \tilde{z}) + \gamma_- \sin(\sqrt{2}\gamma_+ \tilde{z})] + 2\gamma_+ \gamma_- [\gamma_+ \sin(\sqrt{2}\gamma_+ \tilde{z}) - \gamma_- \cos(\sqrt{2}\gamma_+ \tilde{z})] ;$$

$$D = (Q^2 + \gamma_+^2 - \gamma_-^2)^2 + 4\gamma_+^2 \gamma_-^2 ;$$

$$\gamma_\pm = \frac{1}{\sqrt{2}} [(Q^4 + 2\beta^2 Q^2 + \tilde{\omega}_p^2)^{1/2} \pm (v^2 - \beta^2 - Q^2)]^{1/2} .$$

The function

$$\phi_3(\rho, \tilde{z}) = Z \left[\frac{1}{(\rho^2 + \tilde{z}^2)^{1/2}} - \frac{\omega_p}{v} \times \int_0^{\infty} \exp(-\kappa |\tilde{z}|) \frac{J_0(\kappa\rho)\, d\kappa}{(\kappa^2 + \omega_p^2/v^2)} \right] \qquad (33)$$

describes the bare potential of the ion plus a nonoscillatory screening function. Corresponding expressions for $\delta n(\rho, \tilde{z})$, the electron density associated with the wake, may be found but are omitted because of their length.

Figure 8.10 shows a plot of the surface $(1/Z)[\phi_1(\rho, \tilde{z}) + \phi_2(\rho, \tilde{z})]$ in the $(\rho, \tilde{z})$ plane. One sees the distinctive oscillation of the potential in the region behind the particle, characterized by the wavelength $2\pi v/\omega_p$, and the bow wave preceding the particle, distinguished by

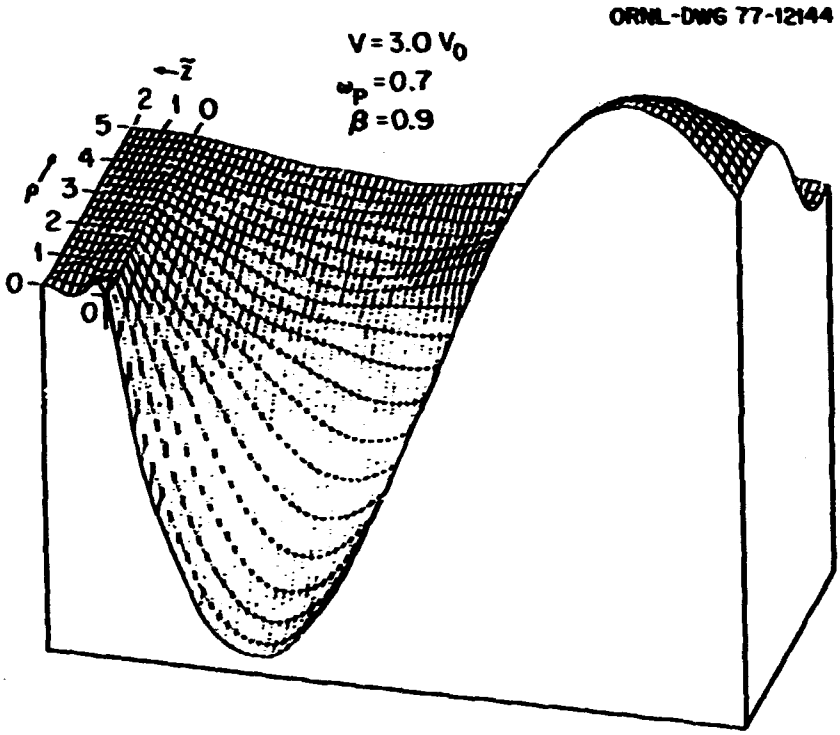

Fig. 8.10. Plot of the scalar electric potential, $(1/Z)\phi(\rho, \tilde{z})$, vs ρ and $\tilde{z}$ for $v = 3$, $\tilde{\omega}_p = 0.7$, $\beta = 0.9$, and $\gamma = 0$.

short-wavelength ($\sim\hbar/mv$) and amplitude. Also easily discerned is a conical disturbance with apex at the particle and extending behind it with half-angle $\sim\sin^{-1}(\beta/v)$. This corresponds to a Cerenkov-type emission of plasmons by the charged particle.

The surface of Fig. 8.10 is quite different from that inferred by Vager and Gemmell[54] from their approximate theoretical inclusion of recoil effects into the classical expression for ϕ. The retarding force acting at the particle, inferred from Eqs. (30) and (32), gives the correct stopping power of the medium for the particle, whereas that found in ref. 54 does not.

Figure 8.11 shows a plot of the surface $(1/Z)\,\delta n(\rho, \tilde{z})$ in the $(\rho, \tilde{z})$ plane. One sees again a long-wavelength disturbance behind the particle and a very intricate pattern of fluctuations in the vicinity of the ion. The Cerenkov-type cone is clearly seen.

These results indicate that the spatial pattern of density fluctuations created in condensed matter by swift charged particles has a rich, intriguing structure. Highly interesting physical manifestations of this structure have already been seen in experiment, and others are expected to emerge with further research.

RADIATIVE CAPTURE OF ELECTRONS BY A SWIFT ION IN A THIN FOIL

The phenomenon of radiative electron capture (REC), wherein a stripped ion captures an electron into one of its shells and emits a photon in the process, has been known for some time from studies in astrophysics and laboratory plasma physics. The first observation of REC by heavy ions in solids was reported only recently[56] but has been followed by numerous experimental and theoretical studies,[57,58] resulting in a significant increase in understanding of general phenomena associated with the generation of photons by swift ions.

One of the most promising aspects of the REC phenomenon is the possibility that REC line widths may be interpreted in terms of velocity distributions in solids of electrons undergoing capture.[58] Practical complications render such interpretations rather difficult. Comparison of experiment with predictions from theoretical models of the capture process, however, is encouraging.[58,59]

More recently, Koyama and Ohtsuki[60] developed a theory of the REC process which emphasizes the role of the surface of a solid in determining the yield of REC

56. H. W. Schnopper et al., *Phys. Rev. Lett.* 29, 898 (1972).
57. See, for example, *Atomic Collisions in Solids*, vol. 2, S. Datz, B. R. Appleton, and C. D. Moak, eds., Plenum Press, New York, 1975, pp. 481ff and references therein.
58. B. R. Appleton et al., *Journal of Nuclear Materials* (in press).
59. R. H. Ritchie et al., *Health Phys. Div. Annu. Prog. Rep. July 31, 1974*, ORNL-4979 (September 1974), pp. 183–86.
60. K. Koyama and Y. H. Ohtsuki, *Phys. Rev. B* 15, 61 (1977).

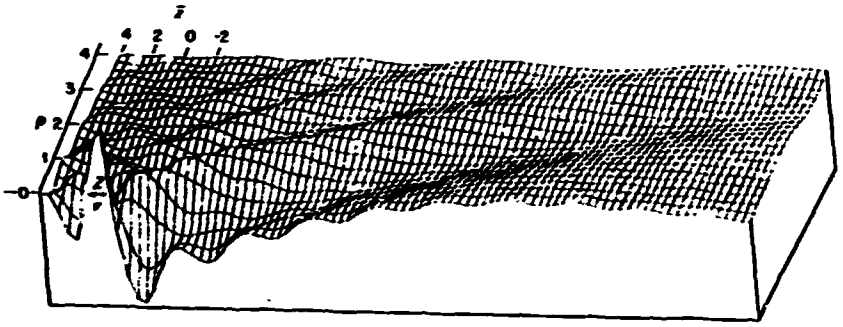

Fig. 8.11. Plot of the electron density fluctuation function $(1/Z)\delta n(\rho, \tilde{z})$ vs ρ and $\tilde{z}$ for $v = 3$, $\tilde{\omega}_p = 0.7$, $\beta = 0.9$, and $\gamma = 0$.

photons. Their final result is found by assuming (1) that the ion is stationary at the surface and (2) that all electrons in a solid are describable in terms of valence electron wave functions. Both these assumptions seem questionable. Since their numerical results for the total REC cross section seem to have a dependence on v (the speed of the ion) which resembles that determined experimentally by Appleton et al.,[58] considerable interest has been generated by their work. In light of their paper, there seems to be some hope that REC experiments may be useful in studying surface properties of solids.

However, we reexamined the problem studied by Koyama and Ohtsuki[60] and found little justification for their simplifying assumptions. We used an approach conceptually more straightforward than theirs, employing wave functions for the ion-electron system which describe the ion in quantum terms.

We neglect coupling between ionic motion and the radiation field. The transition rate, γ, for photon emission accompanying transition of an ion-electron pair from a state described by energy E_i and state vector $|i\rangle$ to a final state corresponding to the energy E_f and state vector $|f\rangle$, may be computed from Golden Rule perturbation theory. One finds

$$\gamma = \frac{(2\pi)^2}{\Omega} \sum_i \sum_f \sum_{\mathbf{k}\lambda} \frac{1}{\omega k} \langle f|\hat{e}_{\mathbf{k}\lambda} \cdot \nabla_r|i\rangle|^2 \, \delta(E_i - E_f - \omega_k) , \quad (34)$$

where $\Omega = L^3$ = normalization volume, $\hat{e}_{\mathbf{k}\lambda}$ = polarization vector of a photon with energy ω_k and polarization index λ, and ∇_r = gradient operator in relative coordinate of the ion-electron pair. Atomic units are used throughout. Then we may take

$$\langle \mathbf{R}, \mathbf{r}|i\rangle = \frac{1}{\sqrt{\Omega}} \exp(i\mathbf{P}_0 \cdot \mathbf{R}) u_0(\mathbf{r}) \quad (35)$$

and

$$\langle \mathbf{R}, \mathbf{r}|f\rangle = \frac{1}{\sqrt{\Omega}} \exp(i\mathbf{P} \cdot \mathbf{R}) u_f(\mathbf{r}) , \quad (36)$$

corresponding to plane-wave center-of-mass momentum, where $\mathbf{R} = (M\mathbf{r}_i + \mathbf{r}_e)/(1 + M)$, $\mathbf{r} = \mathbf{r}_e - \mathbf{r}_i$, and $(\mathbf{r}_e, \mathbf{r}_i)$ is the position vector of the (electron, ion).

If we take the ion to be described in terms of momentum eigenfunctions in both initial and final states, and if the electron is initially in a state appropriate to the assumption of translational invariance parallel with the foil surface,[60] then

$$\langle \mathbf{R}, \mathbf{r}|i\rangle = L^{-5/2} \exp\{i\mathbf{P}_{0i} \cdot [\mathbf{R} - \mathbf{r}/(1 + M)] + i\kappa_0 \cdot [\mathbf{R} + M\mathbf{r}/(1 + M)]\} \, u^i[X + Mx/(1 + M)] . \quad (37)$$

In this equation, κ_0 is the initial momentum of the electron parallel with the surface, $\mathbf{P}_{0i} = M\mathbf{v}$ is the initial ion momentum, $\mathbf{R} = (X, Y, Z)$, $\mathbf{r} = (x, y, z)$, and the foil normal is taken parallel with the x coordinate axis. For simplicity, we take $\mathbf{v} = (v, 0, 0)$. The function $u^i(x)$ is an eigenfunction describing motion in the direction normal to the solid foil surface. The final state wave function in relative motion may be written

$$u^f(\mathbf{R}) = \left(\frac{Z_1}{\pi}\right)^{1/2} e^{-Z_1 r} , \quad (38)$$

representing a K-shell orbital on the ion, which has charge Z_1. The matrix element appearing in Eq. (34) may be written

$$\langle f|\hat{e}_{\mathbf{k}\lambda} \cdot \nabla_r|i\rangle = iL^{-2} \, \delta_{\mathbf{k}_\rho, \mathbf{P}_\rho} \{\hat{e}_{\mathbf{k}\lambda} \cdot [\mathbf{P}/(1 + M) - \mathbf{v}]M\} \, u^i_{M\mathbf{v} - P_x} u^{f*}_{M\mathbf{v} - M\mathbf{P}/[1 + M]} , \quad (39)$$

where $\mathbf{P} = (P_x, \mathbf{P}_p)$, $u_q = \int_{-\infty}^{\infty} u(x)\exp(-iqx)\,dx$ is the Fourier transform of $u(x)$, and $\delta_{A,B}$ is a Kronecker delta in momentum parallel with the surface. Repeated integrations by parts have been carried out in obtaining Eq. (39). Substituting Eq. (39) into Eq. (34), we find

$$\gamma = (2\pi)^2 L^{-1} \sum_{\mathbf{P}} \sum_{k_0} \sum_{\mathbf{k}\lambda} \sum_{i} \frac{1}{\omega_k} f \delta^2(\kappa_0 - \mathbf{P}_p) \times \delta(\epsilon_i + E_B - \omega_k + E_e), \quad (40)$$

where

$$E_e = \frac{1}{2}[Mv^2 + \kappa_0^2 - P^2/(1+M)]$$

and

$$f = \left| \hat{e}_{\mathbf{k}\lambda} \cdot \left(\frac{\mathbf{P}}{1+M} - \mathbf{v} \right) \times M u^i_{Mv - P_x} u^f_{Mv - MP/(1+M)} \right|^2$$

Here ϵ_i is the energy of x motion in the initial state and $E_B = Z_1^2/2$ is the binding energy of the K electron. Carrying out the sum over $\mathbf{k}$ and λ and dividing by v/L, the rate at which ions strike the surface, one obtains an expression for P, the probability of photon emission accompanying capture from all possible initial conduction electron states to the specified final state. One finds

$$P = \frac{32 Z_1^5}{3\pi^2 v c^3} \times \int d^2\kappa_0 \sum_i \int_{-\infty}^{\infty} dP_x\, \omega_k |u^i_{Mv - P_x}|^2 \frac{g^2}{Z_1^2 + g^2}, \quad (41)$$

where $\omega_k = E_e + \epsilon_i + E_B$ and $g^2 = \{\kappa_0^2 + [Mv - MP_x/(1+M)]^2\}$.

One may show that for initial states u^i lying close enough together in energy, that is, for the foil thickness, d, much greater than a_0 (the Bohr radius), this expression reduces to

$$P \to \frac{16 d Z_1^5}{3\pi^2 v c^3} \int \frac{d^3k (\mathbf{v} - \mathbf{k})^2}{[Z_1^2 + (\mathbf{v} - \mathbf{k})^2]^3}, \quad (42)$$

where the integral runs over the Fermi sphere of allowed states in the conduction band. This result agrees exactly with that obtained neglecting surface effects.[58,59] We seem to find little resemblance to the results of Koyama and Ohtsuki[60] in Eq. (41).

VELOCITY SPECTRA OF CONVOY ELECTRONS EMERGING WITH SWIFT IONS FROM SOLIDS

Ions emerging from gases[61] or solids[62] are accompanied by electrons with distributions in velocity, $\mathbf{v}_e$, which have a well-defined cusp in $|\mathbf{v}_e - \mathbf{v}_1|$ centered at the ion velocity, $\mathbf{v}_1$, and a pronounced forward peaking in the angle θ relative to the ion beam direction. Such electron convoys have been discussed in terms of charge transfer to the continuum (CTC).[63-65] The CTC velocity distributions are taken to be unaffected by the collisions within the target leading to the ejection of electrons, which then make transitions into continuum states associated with the Coulomb potentials of the ions moving in vacuo.

Recent work[55,66,67] has pointed to the possibility of bound electron states in the wake of coherent density fluctuations trailing swift ions inside solids at velocities $v_1 \gg v_0 = e^2/\hbar$, when well-developed wakes can exist and the electrons can cross the surface of the medium without significant distortions of the momentum distribution. We have considered typical velocity distributions expected for convoy electrons that were wake-riding (WR) behind ions before emerging from the solid. They differ significantly from CTC distributions. The characteristics of WR distributions should not appear at low velocities, nor after penetration of media where coherent wakes do not form.

61. G. B. Crooks and M. E. Rudd, *Phys. Rev. Lett.* 25, 1599 (1970).

62. H. K. G. Harrison and M. W. Lucas, *Phys. Lett.* 33A, 142 (1970).

63. J. Macek, *Phys. Rev. A* 1, 235 (1970).

64. K. Dettmann, p. 81 in *Interaction of Energetic Charged Particles with Solids*, Istanbul, 1972, BNL 50336, Brookhaven National Laboratory, Upton, N.Y., February 1973.

65. K. Dettmann, H. K. G. Harrison, and M. W. Lucas, *J. Phys. B* 7, 269 (1974); see, also, K. Dettmann, M. N. Kahn, and M. W. Lucas, *J. Phys. C* 9, 1879 (1976).

66. V. N. Neelavathi, R. H. Ritchie, and W. Brandt, *Phys. Rev. Lett.* 33, 302 (1974).

67. V. N. Neelavathi and R. H. Ritchie, p. 289 in *Atomic Collisions in Solids*, S. Datz, B. R. Appleton, and C. D. Moak, eds., Plenum Press, New York, 1975.

The absolute square of the Fourier transform of the variational wave function of a wake-bound electron in the ground state at the first wake-potential trough is:[67]

$$f(\mathbf{v}_e, \mathbf{v}_1, \theta) = N \exp[-v_e^2 \sin^2\theta/2\beta - (v_e \cos\theta - v_1)^2/2\alpha] \ . \quad (43)$$

Atomic units are used throughout. The electron velocity $\mathbf{v}_e$ and the ion velocity $\mathbf{v}_1$ form the angle θ; N is a normalization constant. The parameters

$$\alpha = \frac{k^2}{4}\left[\sqrt{2}W \ln\left(\frac{W}{\sqrt{2}\Gamma}\right)\right]^{1/2} , \qquad \beta = k^2 W/4\sqrt{2} \quad (44)$$

depend on the wave number, k, of the wake and on the effective charge number $Z_1^{\mathrm{eff}}(v_1)$ of the ion through $W = 8Z_1^{\mathrm{eff}}C\eta/k$, where the constant C accounts for the damping of the wake in the region of the first trough. The wave number $k = \Omega_{\mathrm{res}}/v_1$ is proportional to the collective resonance (plasma) frequency, Ω_{res}, of the medium, and $\Gamma = 1.781$. The correlation between the wake and the wave function of the wake-bound electron is incorporated in an average manner in the constant η, which has values between 1 and 2.

The analytical form of Eq. (43) reflects the trial function chosen for the wake-bound state. Still, the trends of f with material and ion properties should be realistic. It peaks strongly at $\theta \simeq 0$ for $v_e = v_1$ and decreases rapidly with increasing θ. It has fallen off to $f = 1/2$ when

$$\theta = \theta_{1/2}^{\mathrm{WR}} = \left[\frac{4Z_1^{\mathrm{eff}}C\Omega_{\mathrm{res}}(\ln 2)}{\sqrt{2}v_1^3}\right]^{1/2} \ (\mathrm{rad}) \ . \quad (45)$$

The curve in Fig. 8.12 displays Eq. (45) for an electron convoy emerging from carbon, $\Omega_{\mathrm{res}} = 20$ eV, $\eta = 1$, and $C = 0.1$, with protons, $Z_1^{\mathrm{eff}} = 1$, of peak velocity equal to the proton velocity v_1. The data[68] follow the curve.

The WR velocity distribution f has a pronounced maximum at $v_e = v_1$ and diminishes as $|v_e - v_1|$ increases. The full width at half maximum in electron kinetic energy, $\Delta E_e^{\mathrm{FWHM}}$, relative to the peak energy, E_e, becomes

$$\left(\frac{\Delta E_e^{\mathrm{FWHM}}}{E_e}\right)^{\mathrm{WR}} = \frac{4\sqrt{2\alpha \ln 2}}{v_1} , \quad (46)$$

essentially independent of the angle $\theta \ll 1$ (rad). By comparison, the relative CTC width is[64]

$$\left(\frac{\Delta E_e^{\mathrm{FWHM}}}{E_e}\right)^{\mathrm{CTC}} = 3\theta \ . \quad (47)$$

Equation (46) is shown as a solid line in Fig. 8.13. Allowing for the conditions of the experiment, the

68. M. M. Duncan and M. G. Menendez, *Phys. Rev. A* 13, 566 (1976).

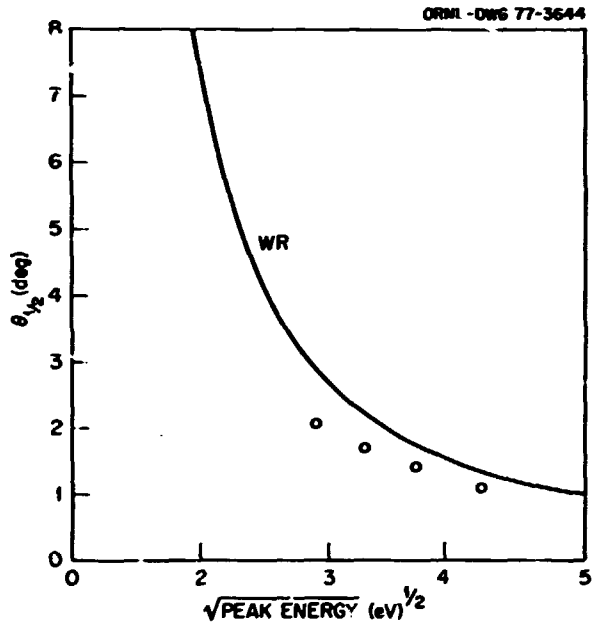

Fig. 8.12. Angles $\theta_{1/2}$, where $f = ½$ when $v_e = v_1$, for electron convoys of protons emerging from carbon. Curve depicts Eq. (45). Data are from ref. 68.

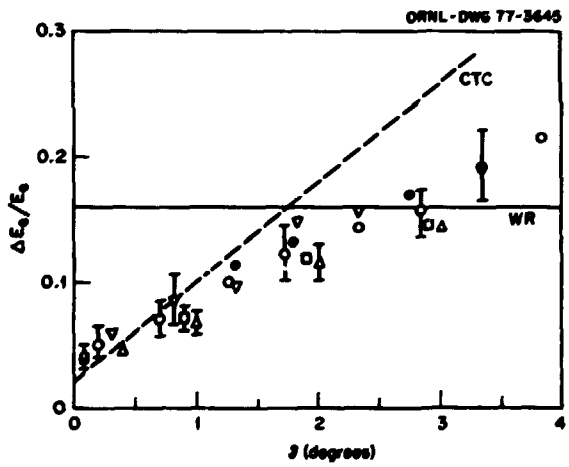

Fig. 8.13. Angle dependence of $\Delta E_e^{\mathrm{FWHM}}/E_e$ for $v_e = v_1$. Dashed CTC curve is from ref. 69. The solid WR curve was calculated from Eq. (46) for electron convoys of 0.5-MeV protons emerging from carbon. Data were measured with 0.35-, 0.5-, 0.7-, and 1.0-MeV protons.

dashed line was computed[68] for CTC given in simple theory by Eq. (47). The calculations were for convoys accompanying 0.5-MeV protons emerging from carbon foils. The data[68] measured with 0.35-, 0.5-, 0.7-, and 1.0-MeV protons initially follow Eq. (47) but may tend toward Eq. (46) at large θ. Convoys emerging with 2-MeV helium ions from argon gas[69] follow Eq. (47) for angles $<2.5°$.

The FWHM of the forward ($\theta = 0$) velocity distribution, $F = 2w_e - v_1|^{FWHM}$, is given by $F = \Delta E_e^{FWHM}/2E_e^{1/2}$ so that

$$F^{WR}(\text{eV})^{1/2} = 2^{3/2}\,(\alpha \ln 2)^{1/2}(13.6\ \text{eV})^{1/2}\ , \qquad (48)$$

essentially independent of the detector acceptance angle θ_0(rad). By comparison,[64]

$$F^{CTC}(\text{eV})^{1/2} = \tfrac{3}{2}\theta_0\,[E_e(\text{eV})]^{1/2}\ . \qquad (49)$$

Figure 8.14 displays data[61,65,70] measured under various conditions and adjusted approximately to equal θ_0. The dashed line, representing Eq. (49), predicts the solid-target data[65] closely for $v_1 < 2v_0$ and the gas-target data[61] at all velocities. The data form a broad maximum near $v_1 \sim 3v_0$ and appear to decline at the largest velocities measured. The solid curve shows that this trend agrees with Eq. (48).

In conclusion, low-velocity and small-angle solid-target data follow the CTC predictions. At velocities greater than $2v_0$ and angles greater than 2°, new trends appear. They signify momentum distributions in the electron convoys of ions emerging from solids that resemble those predicted for wake-bound electrons trailing swift ions inside the solids. The convoy electron yield should depend on the properties of the surface domain.[55] Comparative measurements ceteris paribus of the velocity distributions of electrons emerging with ions from gases and solids would be important in revealing the effects of collective motion in solids on the properties of electron convoys.

69. M. G. Menendez et al., *Phys. Rev. A* 15, 80 (1977).
70. W. Mechbach et al., to be published in *Journal of Physics B: Atomic and Molecular Physics.*

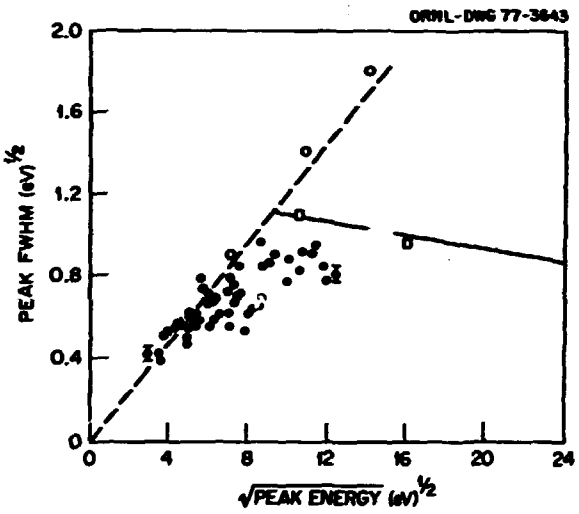

Fig. 8.14. The FWHM peak width in forward direction versus peak position. Dashed CTC curve depicts Eq. (49); solid WR curve depicts Eq. (48). Gas-target data (open symbols) are from ref. 61. (For the solid-target data (closed symbols), the points are from ref. 65; the squares are from ref. 70.

9. Atomic and Molecular Physics, Physicochemical Properties of Biologically Important Structures, and High-Voltage Research

L. G. Christophorou

J. D. Allen[1]
V. E. Anderson[2]
J. K. Baird
J. B. Birks[1]
D. W. Bouldin[1]
J. G. Carter
C. E. Easterly[3]
J. R. Frazier[4]
K. S. Gant[4]
M. W. Grant[5]
D. R. James
J. P. Johnson[4]
E. T. Loy
J. L. Malone
R. A. Mathis
D. V. Maxey
D. L. McCorkle
C. Metcalfe[4]
M. O. Pace[6]
R. Y. Pai
K. Siomos
C. M. Tung[1]
H.-t. Wang[5]
K. L. Webster[4]

A unified semiempirical scheme allowing correlation of negative-ion states of atoms and small molecules in both their ground and excited parent states has been developed. The fragmentation of ten aliphatic chlorocarbons of physical and environmental significance under low-energy ($\lesssim$10 eV) electron impact has been investigated. Absolute rates and cross sections for electron attachment to fluorinated hydrocarbons of environmental significance and of direct interest to gaseous dielectrics have been measured.

Studies of negative-ion resonances of molecules using electron transmission spectroscopy have been initiated, with emphasis on fluorobenzenes. The results of these investigations are related to concurrent molecular orbital calculations and to low-energy electron attachment studies of fluorine-substituted benzenes in dense gaseous environments.

The theoretical dependence of the autodetachment lifetime of $C_6F_6^{-*}$ on electron energy, molecular electron affinity, and number of vibrational degrees of freedom participating in the sharing of the ion's excess energy has been investigated. It was concluded that only about 30% of the possible vibrational modes are involved in sharing the energy of the $C_6F_6^{-*}$ negative ion in the lowest π-state configuration. Recent work on the lifetimes of metastable atomic and molecular negative ions has been synthesized, previous discussions extended, and a wider understanding attempted.

Electron mobilities in neopentane have been measured as a function of pressure and temperature. The observed temperature dependence of the electron mobility has been used to determine the position of the Ramsauer-Townsend minimum for this molecule at $\sim$0.15 eV. Determining Ramsauer-Townsend minima this way is a novel method uniquely suited for low-lying minima (close to $\frac{3}{2}kT$) which cannot be determined accurately by electron beam methods.

Our work on electron attachment to molecules in dense gases continued, and our preliminary findings on electron attachment to CO_2 in N_2 are outlined.

A new approach to the study of the energetics and kinetics of charge-separated states in the liquid phase

1. Consultant.
2. Computer Sciences Division.
3. Assessment and Technology Section.
4. Graduate student.
5. Postdoctoral fellow.
6. Part time, Electrical Engineering Department, The University of Tennessee, Knoxville.

and the spectroscopy of negative ions in liquid media has been developed and is described. An apparatus has been designed and built for the measurement of the minimum energy required to ionize a molecule in a liquid for fluorescent pure liquids or for fluorescent organic molecules (solutes) dissolved in minute amounts in various liquids (solvents). A theoretical study has been made of the probability of escaping neutralization when the electron mobility is field-dependent.

Highlights of our progress in high-voltage research [Breakdown Strengths of Gaseous (and Liquid) Dielectrics] are described. The design of improved gaseous dielectrics has been pursued by developing an understanding of how to control both the number density and energy of free electrons in the gaseous dielectric through application of fundamental, detailed knowledge on electron-molecule interaction processes underlying the breakdown process. Many new unitary (single-component) and multicomponent gas mixtures superior to SF_6 are listed.

SYSTEMATICS OF NEGATIVE-ION STATES OF ATOMS AND SMALL MOLECULES[7]

A unified semiempirical scheme allowing correlation of negative-ion states of atoms and small molecules in both their ground and excited parent states was developed. This scheme, although similar in many respects to that of Read,[8] is more general and detailed. In our approach, the electron affinity (EA) of an atom or a molecule in its ground or excited state is proportional to the electron binding energy, $T^{*}_{n_f l}$, of the neutral state, namely, $EA = (\alpha - 1)T^{*}_{n_f l}$. For configurations such as $[\text{core}]n_f l^2$, $\alpha = 2(Z_c - 1)\sigma$, where Z_c is the charge of the core and σ is the screening constant. For a nonpenetrating $n_f l$ orbital, $\sigma = \sigma'$, where σ' is the "pure" screening constant. In the presence of precursor of the same l in the core, the interaction between the $n_f l$ electrons and the core needs to be considered. This leads to the definition of Δn^{*}_{fl}, the change in the effective quantum number of the parent state due to the addition of the second $n_f l$ electron. The quantity σ' is a function of n^{*}_{fl} (i.e., of the size of the neutral state), Z_c, and configuration. The behavior of σ (or σ', or Δn^{*}_{fl}) manifests itself in the changes of the electron affinities of atoms in the same group of the periodic table. Conversely, it enables predictions of the electron affinity of atoms and also of small molecules. We estimated this way the electron affinities of gallium, indium, thallium, germanium, tin, lead, tellurium hydride, and methyl radical (CH_3) to be 0.46, 0.43, 0.42, 1.36, 1.26, 1.22, 2.18, and 0.59 eV respectively.

FRAGMENTATION OF ALIPHATIC CHLOROCARBONS UNDER LOW-ENERGY ($\lesssim$10 eV) ELECTRON IMPACT[9]

Despite recent advances in our understanding of the negative ions of polyatomic molecules, much knowledge is still needed concerning the multiple fragmentation of molecular negative-ion states and its relation to molecular structure. Studies of structurally similar compounds differing only slightly (say, in terms of the numbers and relative positions of certain atoms) and observation of how such small changes in structure affect the nature, magnitude, and energy dependences of fragment ions are of both intrinsic and practical value. They help relate the details of molecular structure to electron-molecule interaction processes and also establish modes of molecular fragmentation (i.e., patterns of molecular "explosion" at the very presence of an electron of suitable energy) common to bigger structures. Such fragmentation patterns for certain groups of molecules of atmospheric and environmental significance aid in the identification of precursors of atmospheric products and elucidate their reaction pathways in the atmosphere.

In line with our aforementioned dual goal, we investigated the negative ions formed when slow electrons (0 to 10 eV) collide with each of the following ten chlorinated hydrocarbons: chloroform, 1,1,1-trichloroethane, 1,1,2-trichloroethane, 1,1-dichloroethane, 1,2-dichloroethane, tetrachloroethylene, trichloroethylene, 1,1-dichloroethylene, cis-dichloroethylene, and trans-dichloroethylene. A number of these compounds received attention recently in atmospheric research because of the possible effects of chlorinated and fluorinated hydrocarbons on the stratosphere.

Three types of fragment negative ions were observed: Cl^-, Cl_2^-, and $(M-Cl)^-$ (parent molecule, M, less one Cl atom)$^-$; for C_2Cl_4, the parent ion, $C_2Cl_4^{-*}$, was also observed at $\sim$0.0 eV (Fig. 9.1) and found to be metastable with an autodetachment lifetime of 14 ± 3 μsec. The Cl^- ion was by far the most abundant. The intensities of Cl_2^- and $(M-Cl)^-$ with respect to Cl^- depended very strongly on the number and relative positions of the Cl atoms in the molecule. The yield of Cl_2^- was, as a rule, very much lower when the two Cl atoms in the Cl_2^- ion originated from the same C atom. The mea-

7. H.-L. Wang and L. G. Christophorou, submitted to *Journal of Physics B: Atomic and Molecular Physics.*

8. F. H. Read, *J. Phys. B* 10, 449 (1977).

9. J. P. Johnson, L. G. Christophorou, and J. G. Carter, *J. Chem. Phys.* 67, 2196 (1977).

ORNL-DWG 77-3776

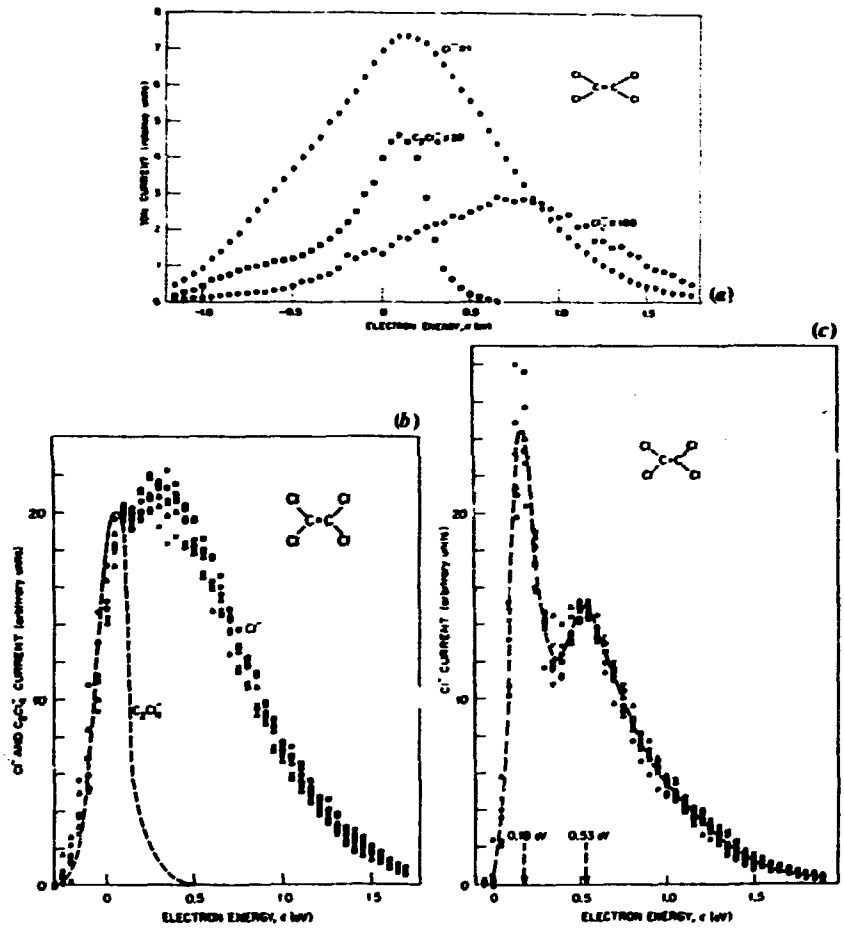

Fig. 9.1. Negative ions in tetrachloroethylene. (*a*) Ion current (without RPD) as a function of ϵ for Cl^-, Cl_2^-, and $C_2Cl_4^-$. The relative intensities of Cl_2^- and $C_2Cl_4^-$ were multiplied by a factor of 100 and 20, respectively, in order to be on the same scale as Cl^-. (*b*) Cl^- ion current (with RPD) as a function of ϵ (six sets of data normalized at 0.1 eV). The parent ion $C_2Cl_4^{-*}$ taken with the RPD is also shown for comparison. (*c*) Unfolded Cl^- current as a function of ϵ using the corresponding Cl^- (same symbol) data sets in Fig. 9.1*b*. The functions were normalized at their respective second peaks.

sured Cl^- currents as a function of electron energy were corrected for the finite width of the electron pulse, and the resultant unfolded functions exhibited distinct resonances whose relative intensity depended strongly on the molecular structure (Figs. 9.2 and 9.3). They indicated the existence of at least five such resonances below ∿2 eV for both the chloroethanes (Fig. 9.2) and the chloroethylenes (Fig. 9.3) studied. The average positions of the observed resonances were 0.18, 0.54, 0.8, 1.06, and ∿1.45(?) eV for the chloroethanes and 0.19, 0.53, 0.75, 0.95, and ∿1.35 eV for the chloroethylenes. The spacings and energy dependences of the intensities of the observed resonances seem to preclude the involvement of vibrational levels, and the similarity in their positions for the two groups of molecules (chloroethanes and chloroethylenes) seems to suggest that they are associated with orbitals dominated by the *p* orbitals of the Cl atoms. The C=C π orbital is clearly involved in the formation of the long-lived $C_2Cl_4^{-*}$ ion. The relative magnitudes and energy dependences of the Cl^-, Cl_2^-, and $(M-Cl)^-$ have been partially rationalized on the basis of the energetics involved in the production of the respective ions. Comparison of the present results with electron-swarm data (Fig. 9.4) is very satisfactory; based on the swarm data, absolute cross-section values for the Cl^- ions of some of the compounds studied were obtained.

The observed resonances in the Cl^- cross-section functions have been associated with the Cl-atom-dominated molecular characteristics. For this reason the observed fragmentation patterns for the chlorinated hydrocarbons investigated should be common to similar big-

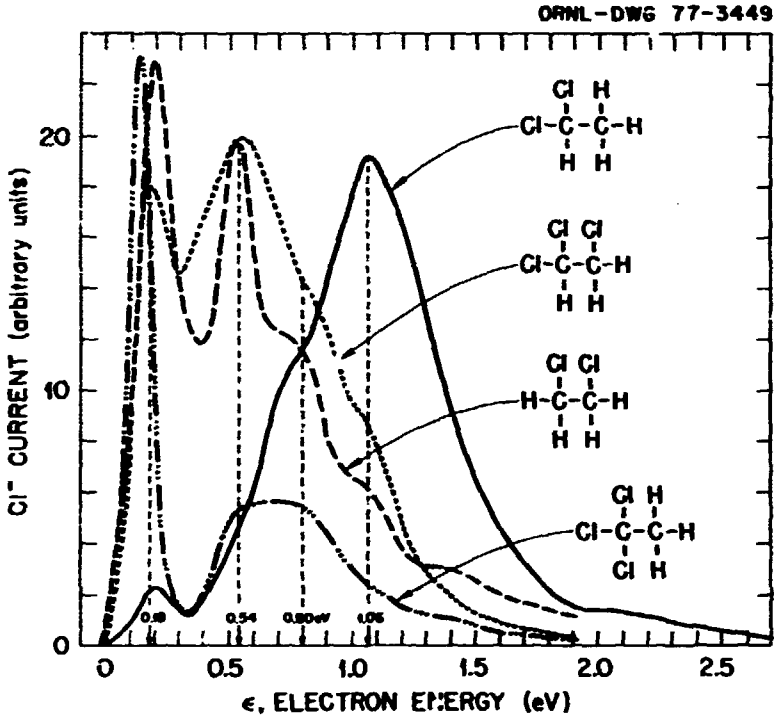

Fig. 9.2. Comparison of the unfolded Cl^- currents as a function of ϵ for chloroethanes.

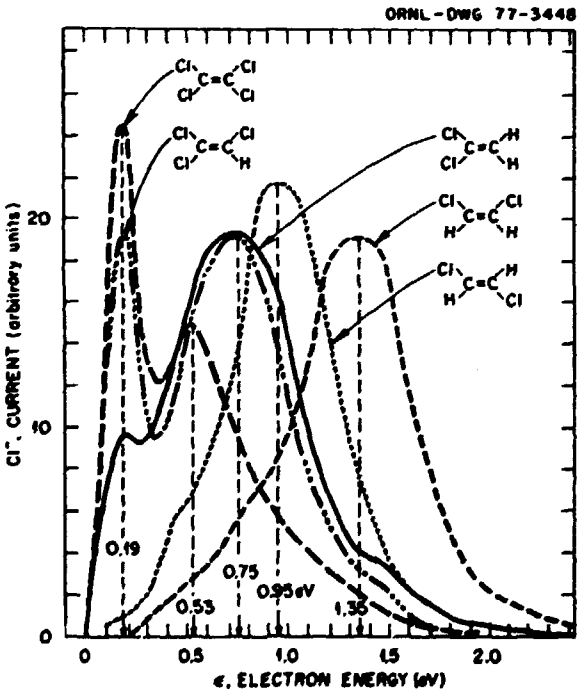

Fig. 9.3. Comparison of the unfolded Cl^- currents as a function of ϵ for chloroethylenes.

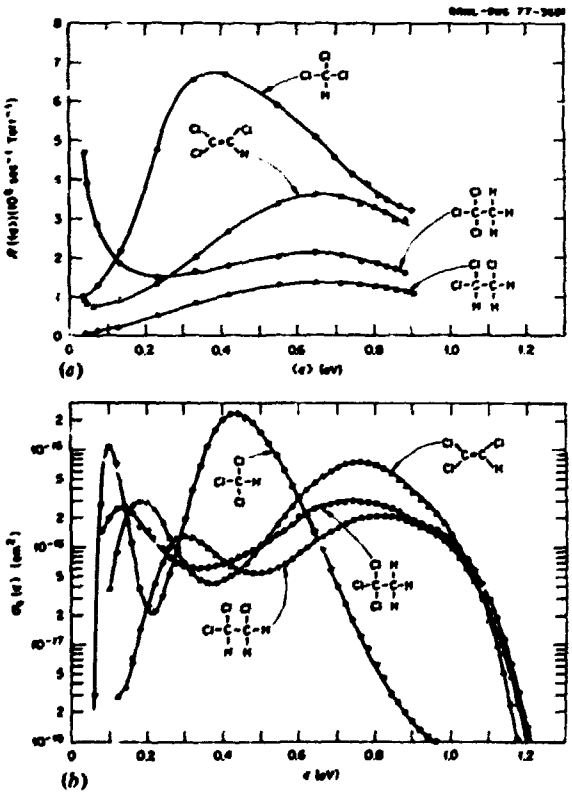

Fig. 9.4. Electron-swarm data for chloroform, trichloroethylene, 1,1,1-trichloroethane, and 1,1,2-trichloroethane. (a) Attachment rate $R(\langle\epsilon\rangle)$ as a function of mean electron energy $\langle\epsilon\rangle$. (b) Swarm-unfolded electron attachment cross section as a function of electron energy.

ger structures. Furthermore, the multiplicity of ions produced and their high yields of production clearly show that slow electrons are far more disruptive in their impacts with molecules than are low-energy photons.

ABSOLUTE RATES AND CROSS SECTIONS FOR ELECTRON ATTACHMENT TO FLUORINATED HYDROCARBONS

Our measurements of absolute rates and cross sections of electron attachment to halogenated hydrocarbons of environmental significance continued. The following fluorocarbons have been studied: C_3F_8, C_4F_6, iso-C_4F_8, C_5F_{10}, and C_6F_{12}. For some of these (e.g., C_6F_{10}; see Fig. 9.5) the attachment cross section is exceptionally high, extending to 1 to 2 eV. Such systems are ideal for use as additives in multicomponent gaseous insulators (see later in this chapter). The data in Fig. 9.5 for C_6F_{10} (perfluorocyclohexene) were chosen to illustrate the very large magnitude of the attachment rate (and cross section) for this molecule. At each value of the mean electron energy $\langle\epsilon\rangle$, the distribution of electron energies $f(\epsilon, \langle\epsilon\rangle)$ is known because these studies were conducted in N_2 containing less than one part per million of C_6F_{10}. The maximum attachment rate was determined as a function of $\langle\epsilon\rangle$ from

$$[\alpha w(\langle\epsilon\rangle)]_{max} = N_{torr}\left(\frac{\pi^2\hbar^4}{2m^3}\right)^{1/2} \times \int_0^\infty \epsilon^{-1/2} f_{N_2}(\epsilon, \langle\epsilon\rangle)\, d\epsilon \ , \quad (1)$$

using the known distributions,[10] f_{N_2}, in N_2 (N_{torr} is the number of attaching gas molecules per cubic centimeter per torr at $T = 298°K$). The swarm-unfolded electron attachment cross section is shown in the inset of Fig. 9.5, where it is compared with the maximum ($\pi\lambda\!\!\!^{-2}$) s-wave capture cross section over a range of electron energies. If these experimental cross sections are used to determine the thermal attachment rate via

$$(\alpha w)_{thermal} \equiv N_{torr}\left(\frac{2}{m}\right)^{1/2} \times \int_0^\infty \epsilon^{1/2} f_M(\epsilon)\sigma_a(\epsilon)\, d\epsilon \ , \quad (2)$$

where $f_M(\epsilon)$ is a Maxwellian function ($T = 298°K$), it is found that $(\alpha w)_{thermal} = 1.13 \times 10^{10}$ sec^{-1} torr^{-1},

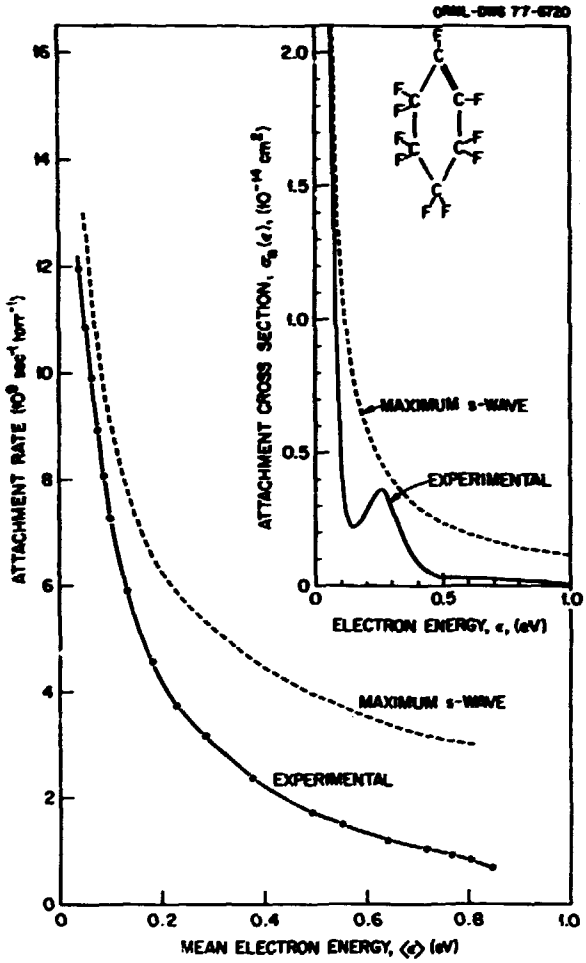

Fig. 9.5. Electron attachment rate as a function of mean electron energy $\langle\epsilon\rangle$ and swarm-unfolded electron attachment cross section as a function of electron energy ϵ for C_6F_{10} (perfluorocyclohexene), compared with the maximum s-wave capture rate and cross section (see text).

which is, to our knowledge, the largest attachment rate measured to date. The lifetime of $C_6F_{10}^{-*}$ at thermal energies is $\sim 1.1 \times 10^{-4}$ sec.

STUDIES OF NEGATIVE-ION RESONANCES USING ELECTRON TRANSMISSION SPECTROSCOPY

Electron transmission techniques have replaced the trapped-electron method previously used in our investigation of negative-ion resonances of polyatomic molecules. The trochoidal electron monochromator that we designed and fabricated has been extensively tested and

10. L. G. Christophorou, *Atomic and Molecular Radiation Physics*, Wiley-Interscience, New York, 1971.

improved. The magnetic field (up to 400 G) for the collimation of the electron beam and for energy selection is provided by a long (70 cm) solenoid. An electron beam (full width at half-height, $\simeq$25 meV) is produced by the monochromator, passed through the collision chamber, and collected by a Faraday cup at the end of the collision chamber. Typical electron transmitted currents are of the order of 5×10^{-9} A.

The electron beam energy is modulated by a sine-wave voltage (10 to 50 mV) applied to the chamber walls. This modulation, accompanied by current collection at the same frequency and phase, produces a signal which corresponds to the derivative, $dI/d\epsilon$, of the transmitted current. Since

$$\frac{dI}{d\epsilon} \propto \frac{d\sigma_t}{dt}, \tag{3}$$

the measured signal is directly proportional to changes in the total electron scattering cross section σ_t.

We initially restricted our investigation to low energies ($\lesssim$5 eV) and to the negative-ion resonances of multiply fluorinated benzene derivatives. Typical data are shown in Fig. 9.6 for N_2, C_6H_6, and C_6HF_5. These studies are part of our effort to measure the positions, cross sections, and lifetimes of negative-ion states of fluorinated benzene derivatives and to relate them to concurrent predictions of molecular orbital theory and the results obtained from a sister program on electron attachment to the same molecules in dense gases.

INTERACTION OF LOW-ENERGY ELECTRONS WITH FLUORINE-SUBSTITUTED BENZENES IN DENSE GASEOUS ENVIRONMENTS

Benzene and its derivatives remain the common building blocks of and are related to many biomolecules. A better understanding of these organic molecules and their interactions with slow electrons can, therefore, serve as a basis for understanding larger biostructures. We continued our theoretical, electron transmission, and high-pressure swarm studies of these systems. In connection with the latter studies, we focused our attention on fluorinated benzenes, since these constitute a uniquely suitable group of molecules in which to study the effect of structure on the positions, lifetimes, and cross sections of the negative-ion resonance states.

Having completed a study of hexafluorobenzene (C_6F_6),[11] we began investigating electron attachment to pentafluorobenzene (C_6HF_5) in dense gases, especially high-pressure N_2. These experiments proved to be difficult because C_6HF_5 is adsorbed onto the inner surfaces of the drift chamber and because, unlike any pre-

11. K. S. Gant and L. G. Christophorou, *J. Chem. Phys.* 65, 2977 (1976).

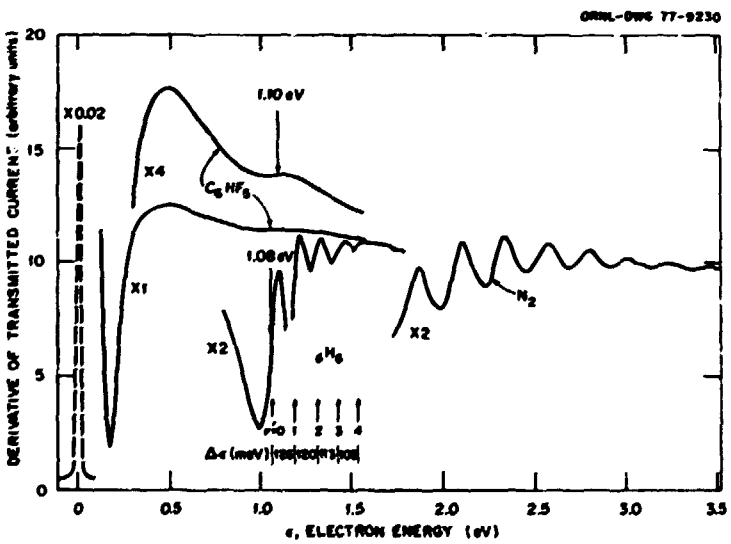

Fig. 9.6. Derivative of transmitted electron current vs electron energy for C_6HF_5, N_2, and C_6H_6. Vibrational structure is clearly visible on the broad shape resonances of the N_2 and the C_6H_6 spectra. The C_6H_6 spectrum agrees very well with that of Sanche and Schulz [*J. Chem. Phys.* 58, 479 (1973)]. Note the anharmonicity of the $C_6H_6^-$ vibrations. The C_6HF_5 spectrum reveals the symmetric peak (at $\sim$1.10 eV) characteristic of a shape resonance of higher angular momentum states. Since the electron affinity of C_6HF_5 is positive ($\sim$0.6 eV), only the upper portion of the lower-lying negative-ion resonance is seen. The sharp peak at $\sim$0.0 eV is the derivative of the transmitted current with no gas in the collision chamber.

viously studied compound, the attachment rate for C_6HF_5 depends strongly on its pressure, $P_{C_6HF_5}$. For a fixed pressure-reduced electric field, E/P, and nitrogen pressure, P_{N_2}, the attachment rate increases with increasing $P_{C_6HF_5}$ and then levels off at high $P_{C_6HF_5}$. The general features of this behavior can be seen from the preliminary results shown in Fig. 9.7.

Although the mathematical details of the $P_{C_6HF_5}$ dependence of the attachment rate are not yet distinct, the qualitative outlines seem apparent. An electron collides with a C_6HF_5 molecule and forms an excited $C_6HF_5^{-*}$ ion. The $C_6HF_5^{-*}$ ion possesses considerable internal energy which, if not removed, will induce autoionization. This energy is most efficiently removed through collision with another body. The available bodies are N_2 and C_6HF_5 molecules. The inclusion of C_6HF_5 as a possible collision partner for $C_6HF_5^{-*}$ may seem pointless, for C_6HF_5 is present only to the extent of a few to a few thousand parts per million of N_2. If we compute the classical Langevin collision rate constant k_L for the N_2–$C_6HF_5^{-*}$ system from the expression

$$k_L = 2\pi e\left(\frac{\alpha}{M_r}\right)^{1/2} , \tag{4}$$

where α is the electric polarizability of N_2 and M_r is the reduced mass of the N_2–$C_6HF_5^{-*}$ system, we obtain $k_L = 6.45 \times 10^{-10}$ cm³/sec. If we now consider a collision between a dipolar molecule and an ion, we may write, for the potential energy V of the system,

$$V = -\frac{\alpha e^2}{2r^4} - \frac{\mu e}{r^2}\cos\theta , \tag{5}$$

where α is the electric polarizability and μ is the permanent electric dipole moment of the dipolar molecule, r is the separation distance of the centers of the ion and the dipolar molecule, and θ is the angle between the line of centers and the dipole moment. If we take $\theta = 0$, we have, as an upper limit for the ion–dipolar molecule collision rate constant k_c, the expression[12]

$$k_c = 2\pi e\left(\frac{\alpha}{M_r}\right)^{1/2} + 2\mu e\left(\frac{2\pi}{kTM_r}\right)^{1/2} . \tag{6}$$

For the $C_6HF_5^{-*}$–C_6HF_5 system, we obtain for k_c a value equal to 2.53×10^{-9} cm³/sec, which is roughly four times the value of k_L for the $C_6HF_5^{-*}$–N_2 system. If by k_A we designate the rate constant for stabilization of $C_6HF_5^{-*}$ in a collision with the body A, and by p_A we designate the probability of stabilization of $C_6HF_5^{-*}$ in each $C_6HF_5^{-*}$–A collision, then

$$k_A = p_A k_c . \tag{7}$$

From data such as in Fig. 9.7, we obtained values of $P_{C_6HF_5}$ which are (depending on E/P) as much as 10^4 times larger than P_{N_2}. It is thus seen that C_6HF_5 is far more efficient in stabilizing $C_6HF_5^{-*}$ than is N_2. This can be attributed to the much larger density of vibrational states of C_6HF_5, compared with N_2, to the existence of nearly degenerate vibrational states in $C_6HF_5^{-*}$ and C_6HF_5, and to the large (~1.6 D) permanent electric dipole moment of C_6HF_5 which makes possible a strong long-range interaction between C_6HF_5 and $C_6HF_5^{-*}$.

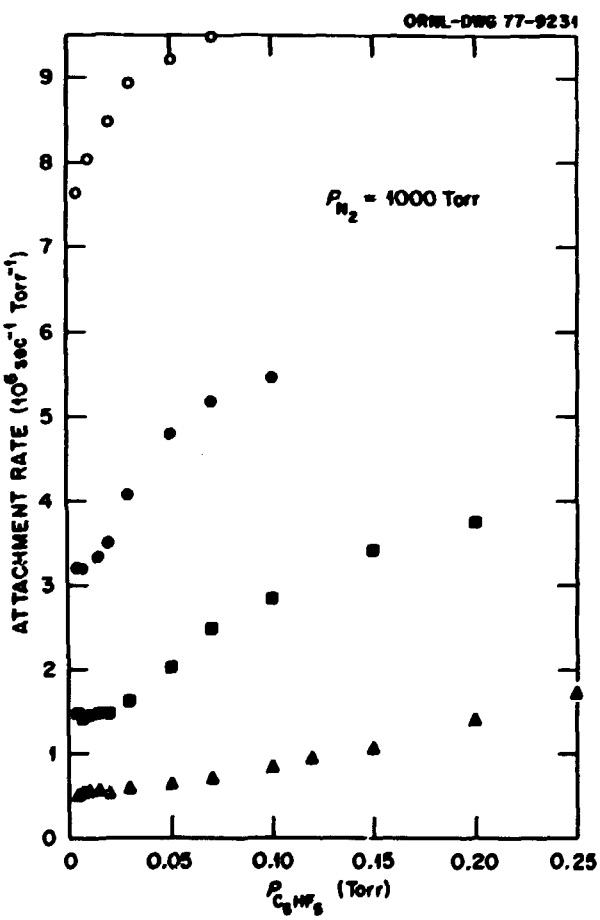

Fig. 9.7. Attachment rate vs $P_{C_6HF_5}$ for E/P values equal to 0.15 (○), 0.30 (●), 0.50 (■), and 1.0 (▲) V cm⁻¹ torr⁻¹.

12. T. Su and M. T. Bowers, *J. Chem. Phys.* 58, 3027 (1973).

Experiments that will elucidate the details of the dependence of the attachment rate on the C_6HF_5 and N_2 pressures are in progress. These data will enable the determination of the autoionization lifetime of $C_6HF_5^{-*}$. The effect of T on the attachment rate is also under investigation.

LONG-LIVED PARENT NEGATIVE IONS FORMED VIA NUCLEAR EXCITED FESHBACH RESONANCES: EFFECTIVE NUMBER OF DEGREES OF FREEDOM PARTICIPATING IN THE SHARING OF THE ION'S EXCESS ENERGY[13]

The variation of the autodetachment lifetime of long-lived parent negative ions with incident electron energy and a theoretical model to explain this lifetime variation were reported earlier.[14] The following reaction scheme was then considered:

$$e(\epsilon_i) + AX(\epsilon_t + \epsilon_z) \quad (a)$$

$$\xrightarrow{\sigma(\epsilon_i)} AX^{-*}(\epsilon_t + \epsilon_z' + \epsilon_i + \mathrm{EA}) \quad (b)$$

$$\underset{\sigma^{(*)}(\epsilon_f)}{\overset{1/\tau}{\rightleftharpoons}} AX^{(*)}[\epsilon_t + \epsilon_z + (\epsilon_i - \epsilon_f)] + e(\epsilon_f)\,, \quad (c) \qquad (8)$$

where ϵ_t is the translational energy (assumed here to be zero), EA is the adiabatic electron affinity of the molecule, and ϵ_i and ϵ_f are the energies of the incident and autodetached electrons respectively. The zero-point energies of the neutral molecule and the negative ion are

$$\epsilon_z\left(= \tfrac{1}{2}\sum_{i=1}^{N} h\nu_i\right) \quad \text{and} \quad \epsilon_z'\left(= \tfrac{1}{2}\sum_{i=1}^{N} h\nu_i'\right),$$

respectively, where ν_i and ν_i' are the respective fundamental vibrational frequencies, and $N(= 3n - 6$, for a nonlinear molecule with n atoms) is the number of vibrational degrees of freedom; τ is the autodetachment lifetime of AX^{-*}. The attachment cross section for $a \to b$ is $\sigma(\epsilon_i)$, and the attachment cross section for $c \to b$ is $\sigma^{(*)}(\epsilon_f)$.

The principle of detailed balance was used to relate the transitions between b and c:

$$\tau^{-1} = \frac{\rho_0}{\rho_-} v_f \sigma^{(*)}(v_f)\,, \qquad (9)$$

where ρ_0 is the number of states per unit energy per unit volume for the final products $AX^{(*)}$ and $e(\epsilon_f)$, and ρ_- is the number of states per unit energy for the negative ion AX^{-*}.

In ref. 14, it was assumed that $v_f\sigma^{(*)}(v_f) = v_i\sigma(v_i)$ and $\nu_i' = \nu_i$. Removing these assumptions, but using the same expressions for ρ_0 and ρ_- as in ref. 14, Eq. (9) becomes

$$\tau^{-1} = \frac{\Gamma(N)\prod_{i=1}^{N} h\nu_i'}{[\epsilon_i + \mathrm{EA} + \epsilon_z'(1-\beta\omega')]^{N-1}}\,\frac{m}{\pi^2\hbar^3}$$

$$\times \int_0^{\epsilon_i} \frac{[\epsilon_i - \epsilon_f + \epsilon_z(1-\beta\omega'')]^{N-1}}{\Gamma(N)\prod_{i=1}^{N} h\nu_i}$$

$$\times\ \epsilon_f\sigma^{(*)}(\epsilon_f)\,d\epsilon_f\,, \qquad (10)$$

where m is the electron mass, $2\pi\hbar$ is Planck's constant, $1-\beta\omega'$ and $1-\beta\omega''$ are known correction factors,[15,16] ω' and ω'' are, respectively, functions of $(\epsilon_i + \mathrm{EA})/\epsilon_z'$ and $(\epsilon_i - \epsilon_f)/\epsilon_z$, and β is a frequency dispersion parameter given by

$$\beta = \left(\frac{N-1}{N}\right)\frac{\langle\omega^2\rangle}{\langle\omega\rangle^2}\,. \qquad (11)$$

In deriving Eq. (10), we assumed that the density of states of the neutral molecule (following electron detachment) and the negative ion can be represented by similar expressions and that the excess energy in both the negative ion and the neutral molecule is shared equally among the available vibrational degrees of freedom. This last assumption was tested by applying Eq. (10) to the case of $C_6F_6^{-*}$.

Hexafluorobenzene (C_6F_6) has 30 vibrational degrees of freedom. The electron affinity of C_6F_6 has been reported to be +1.8 eV,[17] the attachment cross section

13. L. G. Christophorou, K. S. Gant, and V. E. Anderson, *Journal of the Chemical Society, Faraday Transactions 2* (in press).
14. L. G. Christophorou, A. A. Hadjiantoniou, and J. G. Carter, *J.C.S. Faraday Trans. 2* **69**, 1713 (1973).
15. B. S. Rabinovitch and R. W. Diesen, *J. Chem. Phys.* **30**, 735 (1959).
16. G. Z. Whitten and B. S. Rabinovitch, *J. Chem. Phys.* **38**, 2466 (1963).
17. C. Lifshitz, T. O. Tiernan, and B. M. Hughes, *J. Chem. Phys.* **59**, 3182 (1973).

$\sigma(\epsilon_i)$ has been determined,[11] and the autodetachment lifetime τ of $C_6F_6^{-*}$ at thermal energies has been measured using time-of-flight (TOF) mass spectrometers.[18,19] The 20 fundamental frequencies[20] of C_6F_6 were used to calculate β and ϵ_z, with the ten degenerate levels assigned to those degenerate in benzene.

Using the aforementioned values of $\sigma(\epsilon_i)$, N, $h\nu_i$, and EA, we first calculated the negative-ion lifetime, $\tau_{cal}(\epsilon_i)$, under the assumption that $\nu_i' = \nu_i$ and $\sigma^{(*)}(\epsilon_f) = \sigma(\epsilon_i)$. The results of this calculation are shown in Fig. 9.8 by the broken curve. The value of $\tau_{cal}(\epsilon_i)$ at thermal energies is seen to be several orders of magnitude larger than the 12 μsec measured in TOF mass spectrometric experiments at thermal electron energies.[18,19] In search of possible reasons for this apparent discrepancy, we repeated our calculation of $\tau_{cal}(\epsilon_i)$ by varying the values of several of the basic quantities in Eq. (10).

Variation of EA

We have repeated the calculation of $\tau_{cal}(\epsilon_i)$, again taking $N = 30$, $\nu_i' = \nu_i$, and $\sigma^{(*)}(\epsilon_f) = \sigma(\epsilon_i)$, but varying

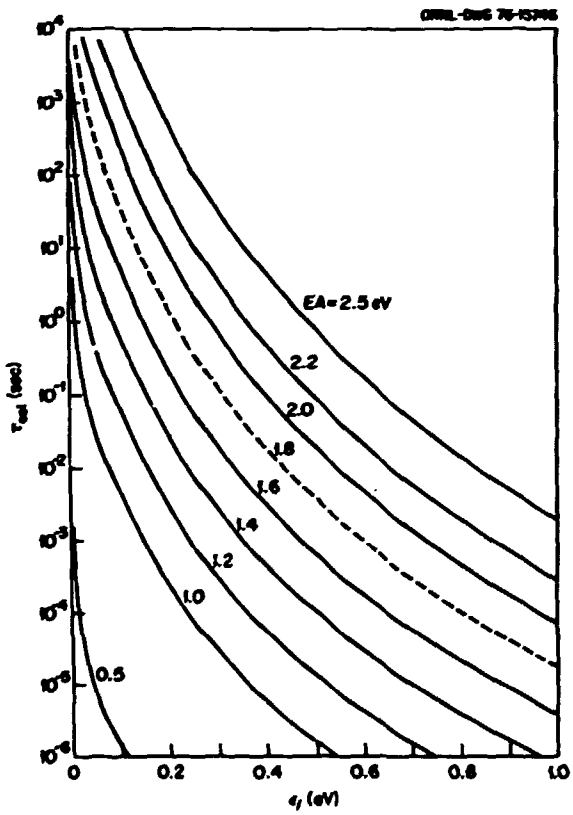

Fig. 9.8. Negative-ion lifetime, τ_{cal}, for $C_6F_6^{-*}$ as a function of incident electron energy, ϵ_i, for several values of the electron affinity.

EA from 0.5 to 2.5 eV. The results of these calculations are presented in Fig. 9.8. A reduction in EA lowers the lifetime, but only for EA = 0.5 eV is the value of $\tau_{cal}(\epsilon_i)$ comparable to the experimentally measured value, τ_{exp}. Since this degree of error in EA seems highly improbable, the source of the discrepancy between the measured and the calculated values of the lifetime must be sought elsewhere.

Effective Vibrational Degrees of Freedom Participating in the Sharing of the Ion's Excess Energy

We next examined the possibility that not all the vibrational modes of $C_6F_6^{-*}$ participate in the sharing of its excess energy. Thus, we took EA = 1.8 eV, $\nu_i' = \nu_i$, and $\sigma^{(*)}(\epsilon_f) = \sigma(\epsilon_i)$ and replaced N by N' in Eq. (10), where $N = 30$ and N' is an effective number of degrees of freedom (<30) sharing the ion's excess energy. The negative ion's zero-point energy ϵ_z' was multiplied by N'/N; β was as given in Eq. (11), with $\langle\nu^2\rangle/\langle\nu\rangle^2$ remaining the same. The calculated negative-ion lifetimes for different values of N' are shown in Fig. 9.9. A decrease in N' results in a shorter $\tau_{cal}(\epsilon_i)$. It is seen that at thermal energy ($\sim$0.04 eV) $\tau_{cal} \simeq \tau_{exp}$ when $N' \cong 9$. This conclusion is unchanged if $\tau_{cal}(\epsilon_i)$ is averaged over $\sigma(\epsilon_i)F(\epsilon_i)$, where $\sigma(\epsilon_i)$ is the electron attachment cross section, and $F(\epsilon_i)$ is an electron energy distribution function characteristic of the TOF mass spectrometer electron beam at thermal energies.[13]

Possible Differences Between ν_i' and ν_i

For a large molecule such as C_6F_6, the vibrational frequencies of the negative ion, ν_i', are not expected to differ appreciably from those, ν_i, of the neutral molecule. To investigate, however, the effect of any such possible differences between ν_i' and ν_i on the value of N' determined in the preceding section, we took $\nu_i' = f\nu_i$, where f is a constant. We then repeated the lifetime calculations as in the preceding section, giving f a number of values between 0.5 and 1.1. The results of these calculations are shown in Fig. 9.10. It is seen that differences between ν_i' and ν_i of as high as 20% do not

18. W. T. Naff, C. D. Cooper, and R. N. Compton, *J. Chem. Phys.* 49, 2784 (1968).
19. J. P. Johnson and L. G. Christophorou, 1976, unpublished results.
20. D. Steele and D. H. Whiffen, *Trans. Faraday Soc.* 55, 369 (1959).

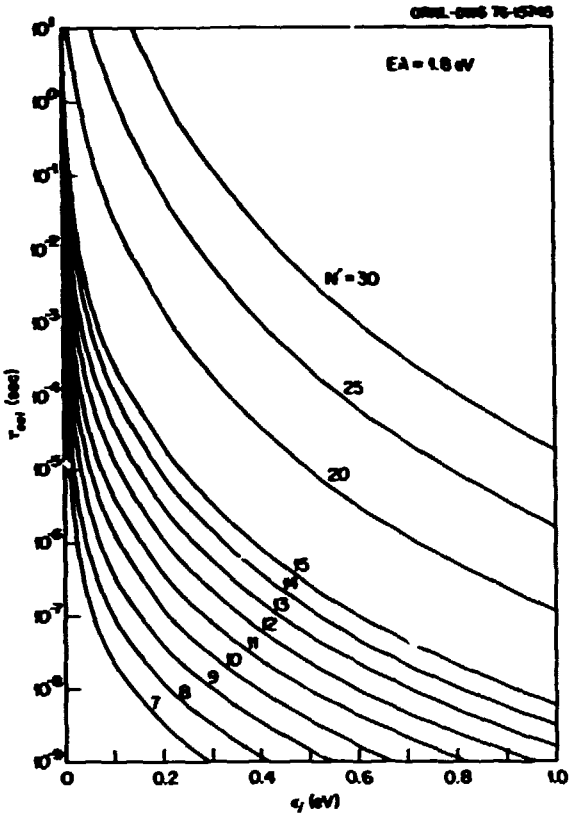

Fig. 9.9. Negative-ion lifetime, τ_{cal}, for $C_6F_6^{-*}$ as a function of incident electron energy, ϵ_i, for different numbers of effective degrees of freedom N'.

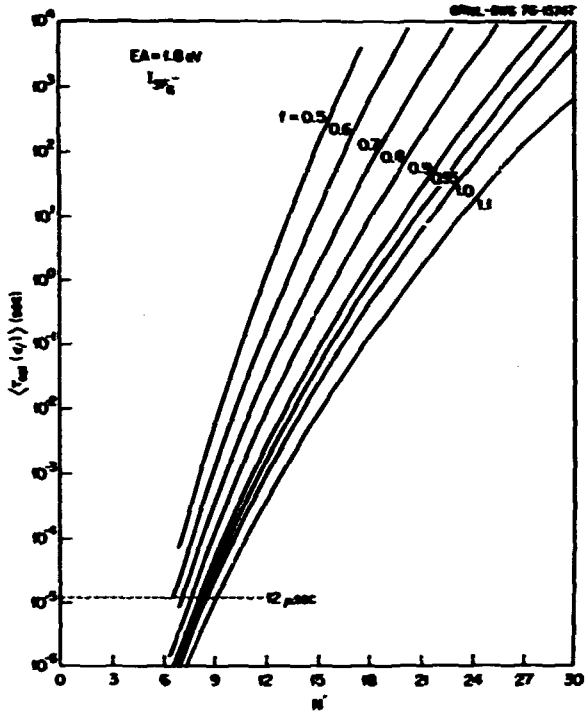

Fig. 9.10. Calculated lifetime averaged over $\sigma(\epsilon_i)F(\epsilon_i)$, $\langle \tau_{cal}(\epsilon_i) \rangle$, for $C_6F_6^{-*}$ as a function of the effective number of degrees of freedom, N', when the fundamental frequencies of the negative ion are a fraction, f, of those of the neutral molecule. $\sigma(\epsilon_i)$ is the electron attachment cross section for C_6F_6 and $F(\epsilon_i)$ is an electron energy distribution function characteristic of the TOF mass spectrometer electron beam at thermal energies. The horizontal broken line is the value of τ_{exp}.

affect the optimum value (8 to 9) of N' determined for $f = 1$ in the previous section.

Possible Errors in $\sigma(\epsilon_i)$

If the shape of the attachment cross section $\sigma(\epsilon_i)$ were incorrect and the true attachment cross section continued to rise as ϵ_i approached 0.0 eV,[11,13] the calculated lifetimes would be shorter. We thus calculated $\tau_{cal}(\epsilon_i)$ under the same assumptions as in "Effective Vibrational Degrees of Freedom Participating in the Sharing of the Ion's Excess Energy," but employed an attachment cross section that rose to $\epsilon_i \approx 0.01$ eV. The lifetimes calculated in this case were only slightly lower, and the optimal value of N' was, again, between 8 and 9.

Conclusion

It would seem from the preceding analyses that an agreement between the calculated and the measured lifetimes can reasonably be achieved by a considerable reduction in the effective number of degrees of freedom which share the ion's excess energy. The consistent optimal value of 8 to 9 for N' leads to the conclusion that only about 30% of the possible vibrational modes are involved in sharing the energy of the $C_6F_6^{-*}$ negative ion in the lowest π-state configuration. A combination of factors such as a slight reduction in EA and in ν_i' would change the best value of N', but not enough to alter this conclusion (see further discussion in ref. 13).

LIFETIMES OF METASTABLE NEGATIVE IONS

Recent work on the lifetimes of metastable atomic and molecular negative ions was synthesized in a coherent way, previous discussions were extended, and a wider understanding was attempted. Special emphasis was accorded the lifetimes of long-lived parent negative ions and their relation to molecular structure and to extending the existing understanding in this area from small molecules to complex polyatomic structures. The

use of the observed extreme dependence of the lifetime of metastable negative ions on structure (the lifetime of metastable negative ions has been found to vary by more than 14 orders of magnitude, from one compound to another, from 10^{-16} to $>10^{-2}$ sec) as a probe for the study of intramolecular charge distribution, intramolecular complexing, and as a means of identification of functional groups which constitute the electrophilic sites of complex biostructures has been indicated. This comprehensive piece of work, consisting of about 140 pages of text, 32 figures, and 200 references, is being prepared for publication.

MEASUREMENT OF ELECTRON MOBILITY IN NEOPENTANE AT HIGH GAS PRESSURES AND HIGH TEMPERATURES

We have placed considerable emphasis recently on understanding how basic physical properties of molecules change in going from the gaseous to the liquid state. A very direct way to investigate this problem is to measure a molecular property as a function of gas density (or pressure), increasing the density as high as possible. Since the energy of the conduction state for quasi-free electrons, V_0, is <0 eV for neopentane and $\mu_L/\mu_G \simeq 12$, where μ_L is the electron mobility in the liquid and μ_G is the gaseous mobility, one might expect a similar behavior of the mean cross section for electron scattering, $\langle\sigma_m\rangle$, to that exhibited by CH_4 and the heavier rare gases to account for the increase in mobility for the liquid relative to that in the gas.[21,22] We have thus undertaken a study of electron mobility in gaseous neopentane at high pressure and high temperature, using our newly constructed apparatus designed and built for such studies. The pressure chamber is designed to operate at a maximum pressure of 750 psi at 450°C.

Electron mobilities were determined by measuring the voltage rise time across a parallel plate capacitor. Electrons, produced photoelectrically at the cathode, were drifted through the neopentane gas and produced a linear voltage rise in an external circuit. This voltage is amplified and oscilloscope photographs at various values of E/P'_{298} yield the drift times directly, where E is the applied electric field in volts per centimeter:

$$P'_{298} = \frac{P}{z}\frac{298}{T} ;$$

P is the measured gas pressure, T is the temperature of the measurement, and z is the compressibility of the gas at P and T.

To investigate the effect of gas temperature on the electron mobility, we measured electron drift velocities in neopentane as a function of E/P'_{298} at constant P'_{298} (constant density, N) and temperatures in the range $27.5° < T < 350°C$. Shown in Fig. 9.11 are drift velocities plotted at 27.5°, 150°, and 300°C. In the thermal region ($E/P'_{298} \lesssim 0.1$ V cm^{-1} torr^{-1}), w varies linearly with E/P'_{298}, and the slope yields the thermal value of μ_{torr}, which is the electron mobility normalized to 1 torr pressure. From the inset in Fig. 9.11, we see that μ_{torr} increases with increasing temperature. At higher E/P'_{298}, w increases more rapidly and maximizes at $E/P'_{298} \simeq 5.5$ V cm^{-1} torr^{-1}. However, at $1 < E/P'_{298} < 2$ V cm^{-1} torr^{-1} the curves cross and above this E/P'_{298} range w actually decreases with increasing temperature.

Electron drift velocities were also measured in neopentane as a function of E/P'_{298} at 27.5°C for several values of P'_{298} (10 torr $< P'_{298} <$ 1500 torr) and at 200°C for 10 torr $< P'_{298} <$ 18,000 torr. From these measurements we conclude that either there is not a pressure dependence of w for neopentane for $0.01 < E/P'_{298} < 15$ V cm^{-1} torr^{-1} at 27.5°C and for $0.01 < E/P'_{298} < 4$ V cm^{-1} torr^{-1} at 200°C, or it is within our experimental error. These results do not show an increase in w with density as might have been expected since $\mu_L > \mu_G$, but neither do they show a decrease with density, which is the case for helium, neon, and a number of hydrocarbons for which $\mu_L/\mu_G < 1$.[23] Possibly, higher densities than we were able to obtain are necessary to observe a pressure dependence.

Momentum transfer cross sections for electrons in neopentane were deduced from the temperature dependence of w at constant P'_{298} = 100 torr and various values of E/P'_{298}. Data used are such as those shown in Fig. 9.11. Actually, at each E/P'_{298}, measurements at w were made at nine temperatures from 27.5° to 350°C.

The momentum transfer cross section is related to w by[24]

$$w = -\frac{4\pi}{3}\frac{e}{mN}\frac{E}{P'_{298}}\int_0^\infty \frac{v^2}{\sigma_m(v)}\frac{df_0}{dv}\,dv , \qquad (12)$$

where $f_0(v) = (m/2\pi kT)^{3/2} \exp(-mv^2/2kT)$ for a Maxwellian velocity distribution. Here, e, m, and v are

21. L. G. Christophorou and D. L. McCorkle, *Chem. Phys. Lett.* 42, 533 (1976).

22. L. G. Christophorou and D. L. McCorkle, *Canadian Journal of Chemistry* (in press).

23. L. G. Christophorou, *Int. J. Radiat. Phys. Chem.* 7, 205 (1975).

24. W. P. Allis, p. 413 in *Handbuch der Physik*, S. Flügge, ed., vol. 21, Springer-Verlag, Berlin, 1951.

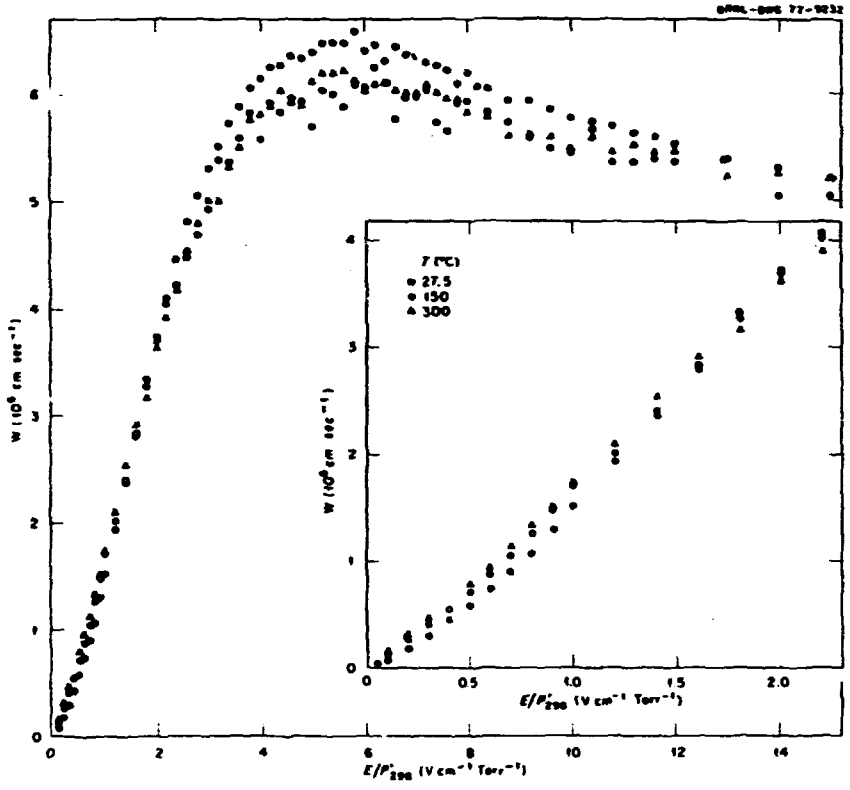

Fig. 9.11. w vs E/P'_{298} for neopentane at three different temperatures.

the electron's charge, mass, and velocity respectively. We assumed that σ_m may be expanded in powers of v as

$$\sigma_m(v) = \frac{A_\alpha}{v^\alpha}, \tag{13}$$

where A_α is a constant. It may be shown that[25]

$$w = \frac{4}{3(2\pi)^{1/2}} \frac{e}{mN} \frac{E}{P'_{298}} \frac{2^{\alpha/2}}{A_\alpha} \times \Gamma(\tfrac{1}{2}\alpha + 2)\left(\frac{m}{kT}\right)^{1/2(1-\alpha)}, \tag{14}$$

where $\Gamma(x)$ is a gamma function of x. Since Eq. (14) was derived assuming a Maxwellian velocity distribution, it is strictly correct only in the thermal region. The velocity distribution f_0 is not known for neopentane at energies higher than thermal. However, from measurements[26] of electron diffusion coefficient to mobility ratio, D/μ, we may determine a mean electron energy as a function of E/P'_{298} as

$$\langle\epsilon\rangle = \tfrac{3}{2}(eD/\mu). \tag{15}$$

Therefore, we assumed that at each E/P'_{298} the electron energy distribution is Maxwellian, and $\langle\epsilon\rangle$ is made up of two contributions, one from the temperature at which w is measured, T_1, and another from the field E. Then, at a particular E/P'_{298} and T_1, we have for the mean energy

$$\langle\epsilon\rangle = \tfrac{3}{2}kT_1 + (\tfrac{3}{2}eD/\mu - \tfrac{3}{2}kT_2), \tag{16}$$

where $T_2 = 294°K$. Thus, the temperature, T_3, used in Eq. (14) to deduce α and A_α is given by

$$T_3 = \tfrac{2}{3}\langle\epsilon\rangle/k. \tag{17}$$

Table 9.1 gives α as determined from least-squares fitting of w and T_3 to Eq. (14). Also given are mean energies for neopentane, using Eq. (15) and the D/μ data of Walker.[26] Such analyses show that α decreases from ~3 at the lowest E/P to 0 at $E/P \cong 2.5$ V cm^{-1} torr^{-1}. Above this E/P value, α becomes negative. This behavior suggests the existence of a minimum in σ_m for

25. L. G. Christophorou, G. S. Hurst, and W. G. Hendrick, *J. Chem. Phys.* 45, 1081 (1966).

26. I. C. Walker, private communication.

Table 9.1. Values of E/P, $\langle\epsilon\rangle$, and α for neopentane

E/P ($V\,cm^{-1}\,torr^{-1}$)	$\langle\epsilon\rangle$ (eV)	α	A_α [$cm^2 - (cm/sec)^\alpha$]
0.05	0.038	2.812	6.28×10^5
0.1	0.039	2.664	5.18×10^4
0.2	0.041	2.650	4.07×10^4
0.3	0.044	2.424	9.05×10^2
0.4	0.047	2.271	7.04×10
0.5	0.051	2.109	4.68
0.6	0.056	2.000	7.48×10^{-1}
0.7	0.060	1.906	1.51×10^{-1}
0.8	0.066	1.800	2.57×10^{-2}
0.9	0.071	1.693	4.11×10^{-3}
1.0	0.077	1.571	5.15×10^{-4}
1.2	0.090	1.290	4.45×10^{-6}
1.4	0.104	1.317	6.82×10^{-6}
1.6	0.12	0.693	1.62×10^{-10}
1.8	0.135	0.614	4.09×10^{-11}
2.0	0.15	0.523	8.49×10^{-12}
2.2	0.165	0.476	3.67×10^{-12}
2.4	0.18	0.332	3.04×10^{-13}
2.6	0.195	−0.018	7.55×10^{-16}
2.8	0.218	−0.077	2.66×10^{-16}
3.0	0.233	−0.179	4.55×10^{-17}

neopentane at $\langle\epsilon\rangle \simeq 0.15$ eV similar to that in CH_4 and argon. The use of the temperature dependence of the drift velocity to determine the position of the Ramsauer-Townsend minima lying close to $\frac{3}{2}kT$ is a novel method uniquely suited for low-lying minima which cannot be detected by electron beam methods.

ELECTRON ATTACHMENT TO CO_2 IN DENSE GASES

In collaboration with the Physics Department of The University of Tennessee and as part of our program to study electron interactions with molecules of environmental interest, we began an investigation of electron attachment to CO_2 in mixtures with nitrogen at high gas pressures. The high pressures are necessary to stabilize the CO_2 negative ion and thus detect it before autoionization occurs (other investigators have unsuccessfully tried to measure electron attachment to CO_2 at low pressure). This molecule is of particular significance because of its abundance in the atmosphere. It is known that CO_2 undergoes profound geometric changes when capturing an electron. Thus, an understanding of the effects of the nature and density of the medium on the interactions of CO_2 with slow electrons will aid in the elucidation of basic electron-molecule interaction processes.

We measured the rate of electron attachment to CO_2 at several total pressures (N_2 and CO_2) up to 20,000 torr as a function of CO_2 pressure. Since CO_2 attaches electrons very weakly – $\sim 10^3$ sec^{-1} $torr^{-1}$ ($\sim 10^{-13}$ cm^3/sec) – it was necessary to mix CO_2 with N_2 in a percentage of up to $\sim 1\%$ CO_2. It was found that such a high percentage of CO_2 changes appreciably the electron drift velocity and the electron energy distribution functions in the mixture with respect to those in pure N_2. To correct the measured attachment rates for this effect, we measured electron drift velocities in CO_2-N_2 mixtures at the same pressures and concentrations as the attachment studies. Moreover, since CO_2 is a strong thermalizing agent for electrons in N_2, electron energy distribution functions which are known for N_2 change dramatically when CO_2 is added to N_2. To correct for this effect, we have begun implementation of a digital computer program (similar to the one developed by A. V. Phelps and colleagues) for calculating distribution functions for electrons in N_2-CO_2 mixtures.

HIGH-RESOLUTION LASER NEGATIVE-ION SPECTROSCOPY; ENERGETICS AND KINETICS OF CHARGE-SEPARATED STATES IN LIQUIDS

We have developed a new approach to the study of the energetics and kinetics of charge-separated states in the liquid phase and the spectroscopy of negative ions in liquid media. Charge-separated states are the ones most affected by the density and the nature of the medium. Presently, both experimental and theoretical understanding of these states is lacking, despite their enormous importance in any serious effort to understand the effects, reaction mechanisms, and biological action of biologically active molecules. In pursuit of this key knowledge, we designed and built an elaborate system encompassing three types of spectroscopy (photon, electron, and ion) suitable for liquid-phase studies.

We are now able to pursue knowledge on (1) the mobility of charge carriers in liquids, (2) the rates of electron attachment to molecules in liquid media, (3) the electron affinities of molecules embedded in liquids, (4) the mechanisms and energetics of electron–neutral molecule attachment-detachment-recapture processes in liquid media ($M^0 + e^- \rightarrow M^- \xrightarrow{h\nu} M^0 + e^- \rightarrow M^-$), and (5) the spectroscopy of negative-ion states in liquid environments.

Special sophisticated instrumentation, electronics, optics, and purification systems, as well as an N_2-laser pumped dye laser, were installed. Figure 9.12 is a block diagram of the overall apparatus.

The emitted wavelength of the coherent light source can be tuned continuously from 3600 Å (3.44 eV) to

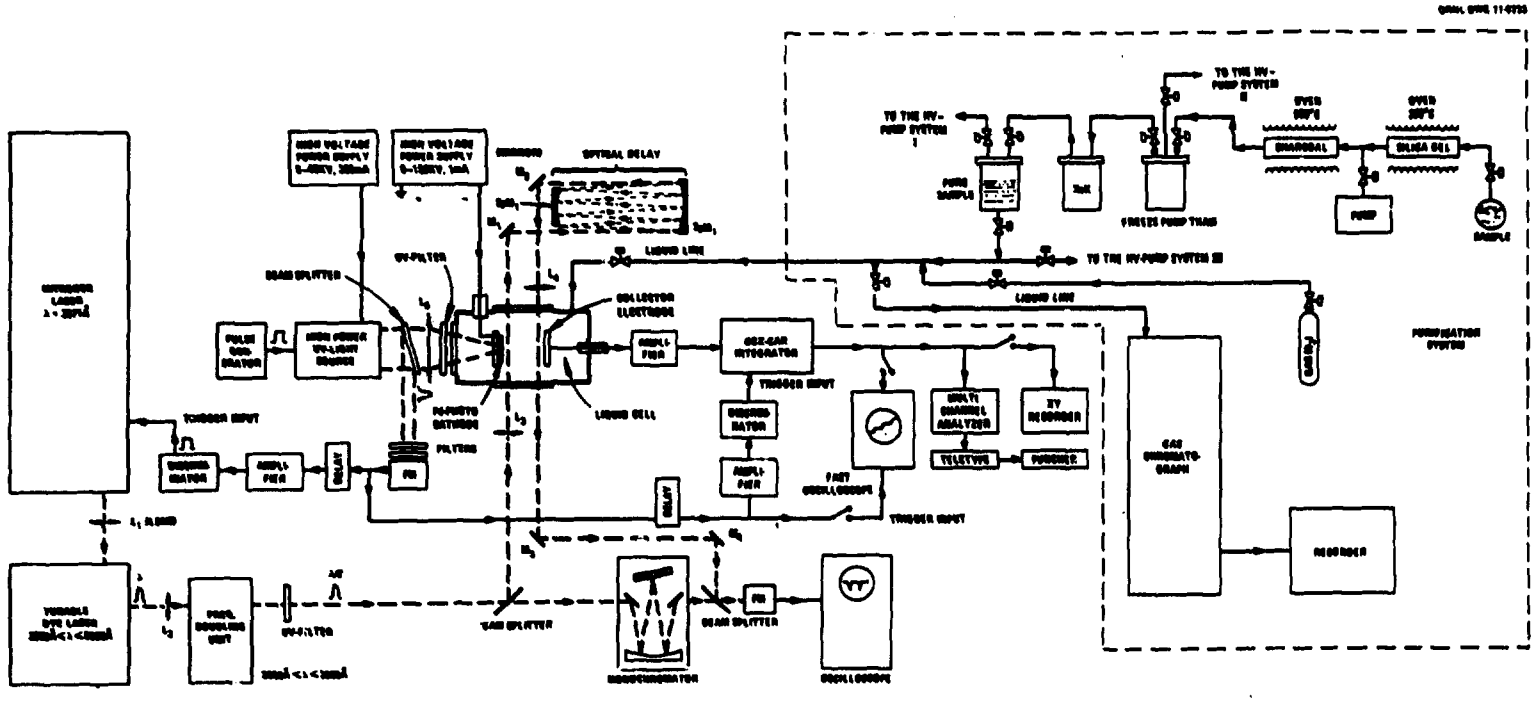

Fig. 9.12. Layout of apparatus for high-resolution laser negative-ion spectroscopy in liquids.

8500 Å (1.46 eV). Frequency doubling further expands the short wavelength of this spectral region down to 2175 Å (5.7 eV). By mixing the output frequencies of two dye lasers in a nonlinear crystal, for example, $LiIO_3$, down-converted infrared radiation to ∿5 μm (0.25 eV) could be achieved.[27] The dye laser spectral linewidth is 0.01 Å, and the laser light pulse duration is 5 nsec. The laser light can be focused very precisely on the liquid cell by Suprasil quartz lenses and can be optically delayed by a confocal ($R_1 = R_2 = L$) spherical mirror system. Its output wavelength can be controlled by using a monochromator. Pulse duration and delay time can be measured with a fast oscilloscope (Tektronix model 7904).

The incoherent light source consists of a special electronic and high-voltage device and a commercial high-pressure xenon flashlamp. This device, constructed in our laboratory, can increase the lifetime of the flashlamp by a factor of more than a thousand. The flashlamp light output energy is ∿10 J and has a pulse duration of 0.4 μsec. Its spectral distribution has a bandwidth of 420 Å at 2000 Å, achieved by using a narrow-band uv filter (Actor Research Company). The uv light is focused by means of a Suprasil quartz lens system on the photoelectrode of the liquid cell for creation of electrons.

The liquid photocell was designed and constructed at our laboratory. It is made of stainless steel and constitutes one of the most important parts of the experimental apparatus. Figure 9.13 shows schematically its principal parts. The cell is divided into two parts which

27. H. Gerlach, *Opt. Commun.* 12, 405 (1974).

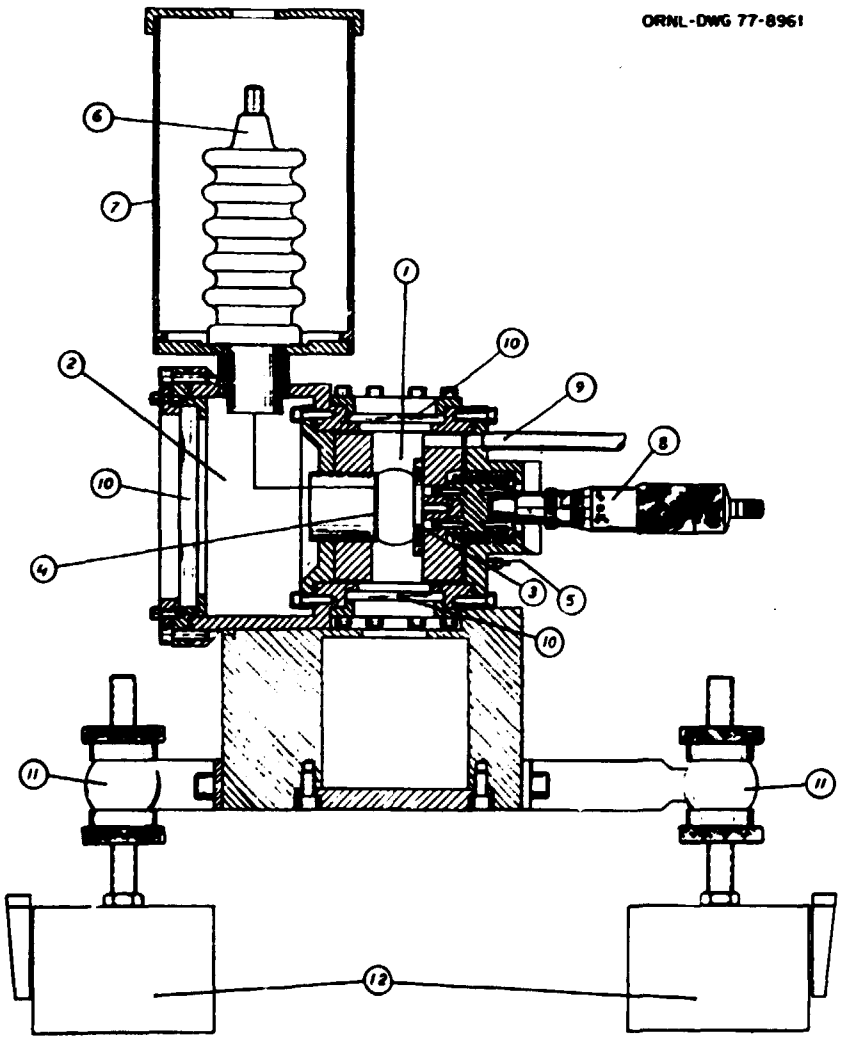

Fig. 9.13. Cross-sectional view of the liquid photocell: (1) liquid chamber, (2) high-voltage chamber, (3) adjustable collector electrode, (4) palladium photocathode, (5) signal output feedthrough, (6) high-voltage connector, (7) high-voltage oil container, (8) micrometer, (9) liquid inlet, (10) quartz windows, (11) three-point kinematic holder, (12) magnetic bases.

can be evacuated independently. The first part (high-voltage chamber, see 2 in Fig. 9.13) allows for the connection of the high-voltage source (0 to 100 kV) to the palladium photocathode (4 in Fig. 9.13). It comprises a ceramic high-voltage feedthrough (6 in Fig. 9.13), which is enclosed in a container of transformer oil (7 in Fig. 9.13), to avoid corona, and a Suprasil quartz window (10 in Fig. 9.13) to allow uv light irradiation of the photocathode. The chamber can be evacuated up to 10^{-7} torr or filled with SF_6 to avoid breakdown inside the chamber.

The second part of the cell (the liquid chamber, see 1 in Fig. 9.13) consists of four Suprasil quartz windows (10 in Fig. 9.13) mounted in cross symmetry and two electrodes. The photocathode (4 in Fig. 9.13) consists of a 1-in.-diam Suprasil quartz plate with a thin palladium layer, and the collector electrode (3 in Fig. 9.13) consists of a 1-in.-diam stainless steel plate which is connected to the signal output feedthrough (5 in Fig. 9.13). They are mounted in such a way that their separation can be changed continuously from 0 to 15 mm to an accuracy of 0.02 mm by means of a micrometer (8 in Fig. 9.13). The liquid chamber provides connections to the high-vacuum pump system, the purification system (9 in Fig. 9.13), and the gas chromatograph. The whole cell is mounted on a three-point kinematic holder (11 in Fig. 9.13) fixed on a vibration-free metallic table by means of magnetic bases (12 in Fig. 9.13).

The charge carrier detection system (Fig. 9.12) consists of a very fast preamplifier-amplifier unit, a boxcar integrator, multichannel analyzer, teletype, and paper-tape punch. Connections to a fast oscilloscope and an x-y recorder are available. The voltage-sensitive amplifier unit has a rise time of <20 μsec and an amplification factor of 300.[28-30] The boxcar integrator (Princeton Appl. Res. model 160) is used as a narrow-band filter.

The purification system is a combination of three high-vacuum pump systems with different distillation steps and molecular filters. A gas chromatograph is used to control the purity level of the liquid and to determine the concentration of solutes.

The first experiments are under way.

EFFECT OF INTERNAL ELECTRIC FIELD ON THE RECOMBINATION OF ELECTRON-HOLE PAIRS IN NONPOLAR LIQUIDS

Mozumder recently made a novel suggestion concerning the theory of the geminate ion dissociation in a dielectric liquid.[31] The basis for his suggestion is the observation that the mobility of the electron depends on the value of the electric field of the ion. He incorporates this effect into Onsager's calculation of the probability that the electron will escape from the field of the ion.[32,33] Mozumder makes two basic assumptions concerning the electron transport coefficients: (1) The electron diffusion coefficient D is independent of the field of the ion. (2) The drift mobility $\mu(r)$ is related to D through the generalized Nernst-Einstein relation $\mu(r)/D = (e/kT)g(r)$, where r is the distance between the monovalent ion and the electron of charge e, k is Boltzmann's constant, and T is the absolute temperature. Letting ϵ be the dielectric constant of the liquid so that the electric field is given by $E = e/\epsilon r^2$, he evaluates $g(r)$ from the relation $\mu(E) = \mu(0)g(E)$, which is well known from experiment.[34-40] Here, $\mu(0)$ is the electron mobility in zero electric field.

Mozumder's calculation of the escape probability can be improved by replacing his two assumptions with the better-established relation[41,42]

$$D(E)/\mu(E) = (kT/e)[1 + \partial \ln \mu(E)/\partial \ln E] \quad . \qquad (18)$$

Specifically, one notes in Eq. (18) that the diffusion coefficient is also field-dependent. For ion transport in neutral gases, this fact was first predicted from an analysis of the Boltzmann transport equation.[43] In situations involving electron transport, theory indicated that the

28. M. K. Kopp, *Rev. Sci. Instrum.* 42, 714 (1971).
29. M. K. Kopp, *Rev. Sci. Instrum.* 46, 1120 (1975).
30. M. K. Kopp and J. A. Williams, *Rev. Sci. Instrum.* 48, 69 (1977).
31. A. Mozumder, *J. Chem. Phys.* 65, 3798 (1976).
32. L. Onsager, *Phys. Rev.* 54, 554 (1938).
33. A. Mozumder, *Adv. Radiat. Chem.* 1, 1 (1970).
34. W. F. Schmidt and G. Bakale, *Chem. Phys. Lett.* 17, 617 (1972).
35. G. Bakale and W. F. Schmidt, *Z. Naturforsch. Teil A* 28, 511 (1973).
36. G. Bakale and W. F. Schmidt, *Chem. Phys. Lett.* 22, 164 (1973).
37. G. Bakale, U. Sowada, and W. F. Schmidt, p. 41 in *Proceedings of the 43rd Annual Conference on Electrical Insulation and Dielectric Phenomena*, 1974.
38. W. F. Schmidt, G. Bakale, and U. Sowada, *J. Chem. Phys.* 61, 5275 (1974).
39. L. S. Miller, S. Howe, and W. E. Spear, *Phys. Rev.* 166, 871 (1968).
40. M. G. Robinson and G. R. Freeman, *Can. J. Chem.* 51, 641 (1973).
41. C. E. Klots and D. R. Nelson, *Bull. Am. Phys. Soc.* 15, 424 (1970).
42. R. E. Robson, *Aust. J. Phys.* 25, 585 (1972).
43. G. H. Wannier, *Bell Syst. Tech. J.* 32, 170 (1953).

relevant temperature for use in Eq. (18) was that of the neutrals, whereas in the case of ion transport, a higher temperature had to be used.[42] Since then, most work has continued to concentrate on charged-particle motion in gases. For example, Eq. (18) has received experimental confirmation for ion motion in low external fields and has been extensively studied from the point of view of kinetic theory for electrons and for ions.[44–53] In solid-state physics, its applicability to electrons in semiconductors has been suggested.[54] A derivation based on nonequilibrium thermodynamics, however, suggests that Eq. (18) may be extended to any state of matter, so long as conditions do not depart too far from equilibrium.[42]

In the case of dielectric liquids, although the field dependence of the electron mobility is well established, there are no measurements known to us which give the field dependence of the diffusion coefficient. Hence, at present, the application of Eq. (18) to the liquid phase must be regarded as a postulate. Nevertheless, with this proviso we proceeded to calculate the probability P that an electron originally located at a distance r_0 from a positive ion will escape to infinity. The electron density $n(r)$ satisfies the equation

$$\frac{I}{4\pi r^2} = -D\left[\frac{dn}{dr} + \frac{\mu}{D}\frac{dV}{dr}n\right], \tag{19}$$

where I is the electron particle current, and $V(r) = -e/\epsilon r$ is the electric potential experienced by the electron.[32,33] If we use Eq. (18) for μ/D with

$$G(r) = \{1 + \partial \ln[\mu(E(r))]/\partial \ln[E(r)]\}^{-1}, \tag{20}$$

then Eq. (19) takes the form

$$\frac{I}{4\pi r^2} = -D(r)\left[\frac{dn}{dr} + n\frac{r_c}{r^2}G(r)\right], \tag{21}$$

where $r_c = e^2/\epsilon kT$. Letting r_1 be the ion radius, we divide the domain $r_1 \leq r < \infty$ into two subregions, $r_1 \leq r \leq r_0$ and $r_0 \leq r < \infty$, in which electron densities and currents are defined as $n_<(r)$, $I_<$ and $n_>(r)$, $I_>$ respectively. If we make the variable substitution $x = r^{-1}$, Eq. (21) has the solutions

$$n_<(x) = (4\pi)^{-1} I_< \exp[\Psi(x)] \times \int_{x_1}^{x} dx' \exp[-\Psi(x')]/D(x') \tag{22}$$

and

$$n_>(x) = (4\pi)^{-1} I_> \exp[\Psi(x)] \times \int_0^{x} dx' \exp[-\Psi(x')]/D(x'), \tag{23}$$

where we have applied boundary conditions $n_<(x_1) = 0$ and $n_>(0) = 0$ and made the definition

$$\Psi(x) = r_c \int_0^{x} G(x')\, dx'. \tag{24}$$

We note that $P = I_>$. By joining Eqs. (22) and (23) according to the relations $n_<(x_0) = n_>(x_0)$ and $I_> - I_< = 1$, one obtains

$$P = \left[\int_{x_0}^{x_1} dx' \exp(-\Psi(x'))/D(x')\right] \Big/ \left[\int_0^{x_1} dx' \exp(-\Psi(x'))/D(x')\right]. \tag{25}$$

Equation (25) differs from its counterpart in the original work [Eq. (5) of ref. 31] in two important respects: (1) There is now an explicit dependence on the diffusion coefficient $D(x)$ which did not appear earlier. (2) Capitalized functions $\Psi(x)$ and $G(x)$ replace the lowercase $\psi(x)$ and $g(x)$ which appeared formerly; whereas Eq. (24) is a definition linking either of a pair [$\Psi(x)$ with $G(x)$ or $\psi(x)$ with $g(x)$], $G(r)$ defined by Eq. (20) is very different from the former $g(r) = \mu(E(r))/\mu(0)$.

44. J. H. Whealton and E. A. Mason, *Ann. Phys.* **84**, 8 (1974).
45. L. A. Viehland and E. A. Mason, *Ann. Phys.* **91**, 499 (1975).
46. R. Y. Pai et al., *Phys. Rev.* **A12**, 1781 (1975).
47. L. A. Viehland and E. A. Mason, *J. Chem. Phys.* **63**, 2913 (1975).
48. R. Y. Pai et al., *J. Chem. Phys.* **63**, 2916 (1975).
49. K. Kumar and R. E. Robson, *Aust. J. Phys.* **26**, 157 (1973).
50. G. H. Wannier, *Aust. J. Phys.* **26**, 897 (1973).
51. J. H. Whealton, E. A. Mason, and R. E. Robson, *Phys. Rev.* **A9**, 1017 (1974).
52. H. R. Skullerud, *J. Phys. B* **9**, 535 (1976).
53. R. E. Robson, *J. Phys. B* **9**, L337 (1976).
54. R. E. Robson, *Phys. Rev. Lett.* **31**, 825 (1973).

To illustrate the contrast, we choose a case (e.g., liquid ethane[38]) for which the electron-drift mobility is given by the relation

$$\mu(E) = (2\lambda\nu/E)\exp(-\Delta G/kT)\sinh(\lambda eE/2kT)\,,$$

where ΔG is the free-energy barrier, ν the attempt frequency, and λ the electron mean free path.[55] To evaluate Eq. (25) in the present formulation, we would use Eqs. (18) and (20) to find $G(x) = (r_c\lambda x^2/2)^{-1}\tanh(r_c\lambda x^2/2)$ and $D(x) = \lambda^2\nu \times \exp(-\Delta G/kT)\cosh(r_c\lambda x^2/2)$. In the earlier formulation, we would have evaluated Eq. (25) using $g(x) = (\lambda r_c x^2/2)^{-1}\sinh(r_c\lambda x^2/2)$ and $D(x) = 1$. Consequently, for fixed x_1, we see that the new formulation differs most strongly from the earlier one in the limit of large values of the product λr_c.

PHOTOIONIZATION OF MOLECULES IN LIQUIDS

The need for accurate knowledge of the minimum energy, I_L, required to ionize a molecule embedded in a liquid is overwhelmingly pressing. A program has been initiated to acquire such knowledge. An apparatus was designed and built for the measurement of I_L for fluorescent pure liquids or for fluorescent organic molecules (solutes) dissolved in minute amounts in various liquids (solvents). Our method establishes the threshold for solute ionization by monitoring its fluorescence quantum yield as a function of excitation photon wavelength. Preliminary results are shown in Fig. 9.14 for 2-ethyl naphthalene, a fluorescing substance which is liquid at room temperature. The onset for the decline in the fluorescence quantum yield at 6.84 eV is tentatively identified as the value of I_L for liquid 2-ethyl naphthalene at room temperature. This value is ~1.2 eV lower than the gaseous value of the first ionization potential (~8.0 eV) of 2-ethyl naphthalene.

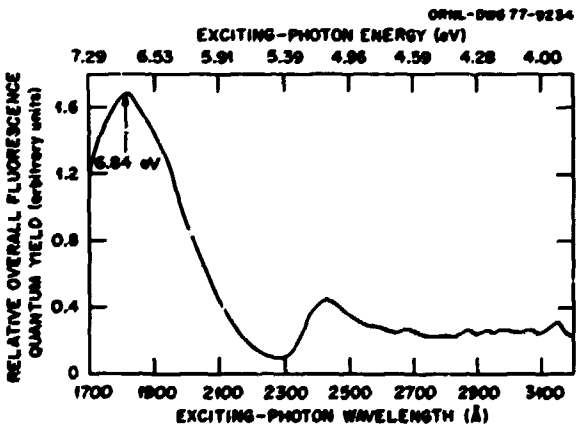

Fig. 9.14. Relative overall fluorescence quantum yield vs wavelength of exciting light (from H_2 continuum) for liquid 2-ethyl naphthalene at room temperature.

HIGH-VOLTAGE RESEARCH [BREAKDOWN STRENGTHS OF GASEOUS (AND LIQUID) INSULATORS]

A detailed account of our progress in this area can be found in refs. 56 through 59. The design of improved gaseous dielectrics is being pursued by building an understanding of how to control both the number density and energy distribution of free electrons in the gaseous dielectric through application of fundamental detailed knowledge of electron-molecule interactions underlying the breakdown process. It is the thesis of this work that breakdown can be inhibited by reducing the number of free electrons and by reducing the energies of those electrons remaining free. The number of electrons is to be reduced by using gas molecules which attach electrons to themselves, thus tying up free electrons in negative ions which are too large and too slow to participate in breakdown formation. Since different molecules possess different abilities to attach electrons at different energies, the best dielectrics should be *multicomponent gas mixtures* designed systematically according to fundamental knowledge so that the attachment cross sections are as large as possible over as wide an energy range as possible. In an insulator, certain molecules should also be used to reduce the energies of free electrons, not only because this will directly help inhibit ionization but also because basic physics dictates that electron attachment can be effected well only at lower energies ($\lesssim 1$ eV), and the attachment process is thus enhanced by helping to confine free electrons to these lower energies where they are subject to effective capture.

55. B. G. Bagley, *Solid State Commun.* 8, 345 (1970).
56. L. G. Christophorou et al., *High Voltage Research (Breakdown Strengths of Gaseous and Liquid Insulators)*, ORNL/TM-5604 (1976).
57. L. G. Christophorou et al., *High Voltage Research (Breakdown Strengths of Gaseous and Liquid Insulators)*, 2nd quarterly report (for period ending Sept. 30, 1976), ORNL/TM-5713 (1976).
58. L. G. Christophorou et al., *High Voltage Research (Breakdown Strengths of Gaseous and Liquid Insulators)*, 3rd quarterly report (for period ending Dec. 31, 1976), ORNL/TM-5806 (1977).
59. M. O. Pace et al., paper to be presented at the 1977 *Electrical/Electronics Insulation Conference*, Chicago, Illinois, Sept. 26–29, 1977; to be published in *IEEE Transactions on Insulation*.

On the basis of the above philosophy we undertook a program of studying breakdown strengths of gases/mixtures, first in dc uniform fields. Simultaneously, fundamental data are being compiled, and new data are being obtained on electron attachment and electron slowing-down cross sections as functions of electron energy and on negative-ion resonances, electron affinities, and electron impact ionization cross sections. The breakdown and fundamental data are correlated in the design of gaseous dielectrics. Chemical and physical properties, the effects of nonuniform fields, rough surfaces, and particles, as well as ac and impulse tests, etc., are considered and so are numerous practical "spin-offs" from this research, such as the detection and prevention or diversion of incipient breakdown. Presently, however, the emphasis is on the question, "What is it that makes a good gaseous dielectric?"

Apparatus

Two fully automated breakdown apparatuses are now in operation. A versatile third apparatus allowing high-voltage (to $\gtrsim$300 kV), high-pressure (to $\sim$10 atm), and variable-temperature (−40° to +120°C) measurements is under construction. A fourth "applied-testing facility" nears completion.

Breakdown Strengths – Unitary Systems

We continued our investigation of the dc breakdown strength of unitary (single-component) systems and found numerous gases which have dielectric strengths higher than SF_6. Some of these are listed in Table 9.2 and are shown in Figs. 9.15 and 9.16.

Especially significant is our discovery of the new system C_4F_6 (hexafluorobutyne). This compound was found to have a dielectric strength of 2.1 to 2.2 relative to the 1.0 of SF_6. Unlike many of the fluorocarbons with good dielectric strengths, C_4F_6 has a high vapor pressure (at least 6 atm) at room temperature. Its high dielectric strength is associated with the details of its structure and the magnitude as well as the energy dependence of its electron attachment cross section (Fig. 9.17). C_4F_6 is an example of a compound with a triple bond. We have found that the presence of double and triple bonds in the molecule has a dramatic effect on the breakdown voltage. This has been attributed to the increase in the inelastic scattering cross sections with increasing number of double or triple bonds found earlier.[60]

The superior dielectric strengths of C_6F_{10} and C_6F_{12} are also worth noting. These two compounds have relatively low vapor pressures at room temperature, but they can be used as additives to multicomponent mixtures. Their electron attachment cross sections are substantial (see Fig. 9.5 for data on C_6F_{10}).

Breakdown Strengths of Multicomponent Gaseous Mixtures

With the fluorocarbons we found to be better dielectrics than SF_6, we have undertaken to develop mixtures

60. L. G. Christophorou, R. P. Blaunstein, and D. Pittman, *Chem. Phys. Lett.* 22, 41 (1973).

Table 9.2. Relative breakdown strengths of some unitary gases

Gas	Relative strength
High pressure; uniform field (plane-plane electrode geometry)	
C_4F_6 (hexafluorobutyne)	2.1 to 2.2
iso-C_4F_8 (perfluorobutene-2)	1.7 to 1.8
c-C_4F_8 (perfluorocyclobutane)	1.3
SF_6 (sulfur hexafluoride)	1.0
Low pressure; nonuniform field (sphere-plane electrode geometry)	
C_6F_{12} (mixture of 1,2- and 1,3-perfluorodimethylcyclobutane)	2.3 to 2.4
C_6F_{10} (perfluorocyclohexene)	1.9 to 2.2
C_7F_{14} (perfluoromethylcyclohexane)	2.1
C_4F_6 (hexafluorobutyne)	1.7 to 1.9
C_7F_{14} (perfluoroheptene-1)	1.2
SF_6 (sulfur hexafluoride)	1.0

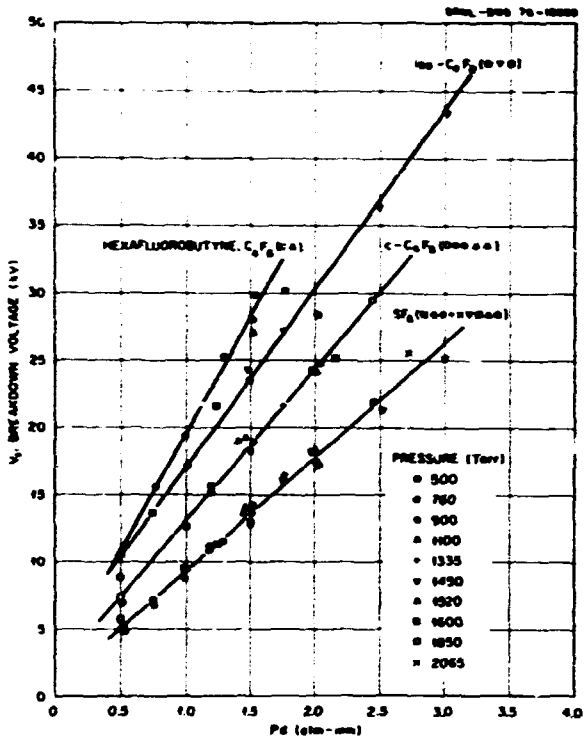

Fig. 9.15. Breakdown strengths of single gases (unitary systems).

with N_2 (a very efficient electron thermalizer) with a twofold thrust: (1) to develop a better basic understanding of the interaction processes that control breakdown in gaseous mixtures and (2) to develop mixtures that are superior dielectrics. Thus, the breakdown strengths of various mixtures of fluorocarbons, SF_6, and N_2 were systematically measured to construct an experimentally based picture of the effectiveness of these gases as additives to N_2 and to correlate their effectiveness with their cross sections for electron attachment and electron slowing-down as functions of electron energy, as well as their individual breakdown strengths. Table 9.3 shows relative breakdown strengths obtained for C_4F_6-SF_6-N_2 mixtures; three of these mixtures proved better as dielectrics than SF_6 and cheaper than SF_6 (based on cost estimates of \$0.001/ft^3 for N_2, \$0.83/ft^3 for SF_6, and \$2.50/ft^3 for C_4F_6).[58] The results in Table 9.3 indicate that C_4F_6 is extremely effective as an additive to N_2. It should be noted that a mixture containing N_2 is expected to be better in comparison with SF_6 under nonuniform fields and impulse voltages than under dc uniform fields.

Table 9.4 shows measurements made on three- and four-component mixtures in which N_2 was the primary gas. The effect of removing any one additive (and replacing it by N_2) was investigated. C_4F_6 was found to be the most effective additive to the 10% level, fol-

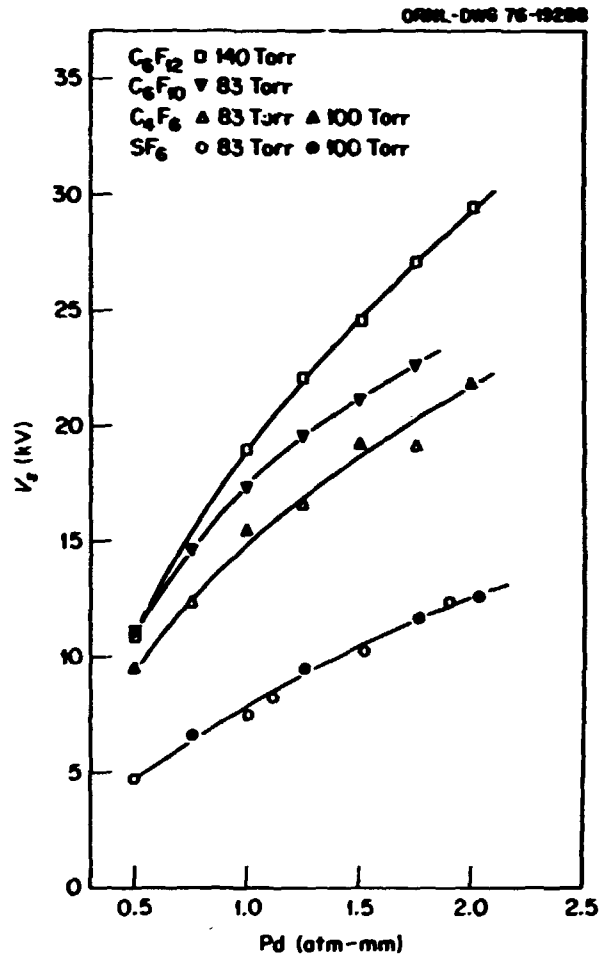

Fig. 9.16. Breakdown voltages vs *Pd* measured for C_6F_{12}, C_6F_{10}, C_4F_6, and SF_6 at the indicated pressures (sphere-plane electrodes).

Table 9.3. Relative breakdown strengths[a] of some two- and three-component gaseous mixtures

Gaseous mixture (%)			$\frac{\Delta V_s}{\Delta(Pd)}\left(\frac{kV}{atm\text{-}mm}\right)$
N_2	C_4F_6	SF_6	
100			2.98
		100	8.65
	100		19.76
90	10		6.77
80	20		8.71
70	30		10.18
80		20	6.53
80	10	10	7.60
60	20	20	9.51
50	30	20	11.51

[a]Plane-plane, uniform-field geometry; total pressure was 500 torr.

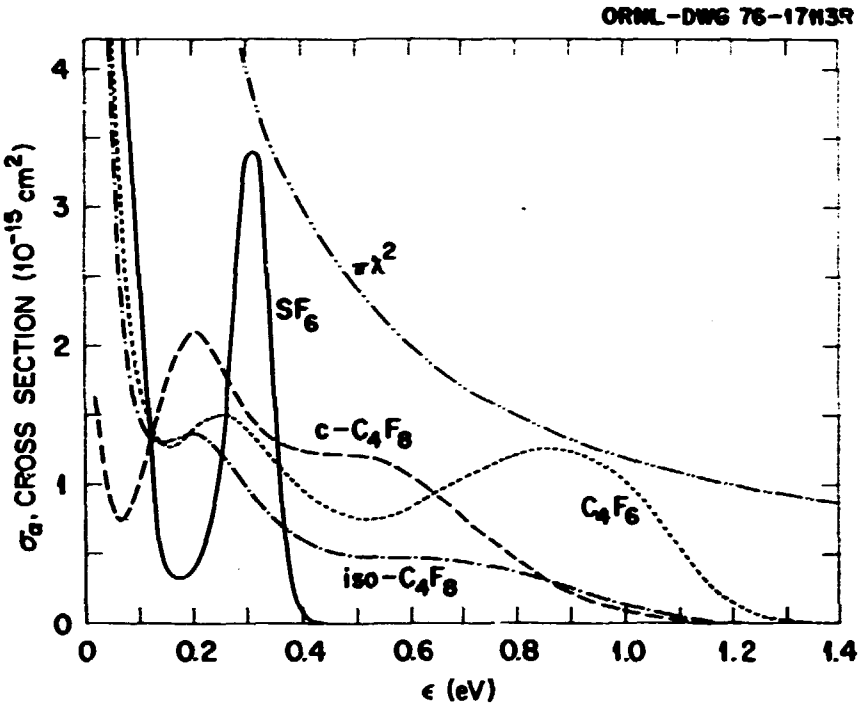

Fig. 9.17. Electron attachment cross section vs electron energy. $\pi\lambda^2$ is the maximum s-wave capture ($\lambda = 2\pi\lambda$ is the electron de Broglie wavelength).

Table 9.4. Relative breakdown strengths[a] of some four-component gaseous mixtures

Gaseous mixture (%)					$\frac{\Delta V_s}{\Delta(Pd)}\left(\frac{\text{kV}}{\text{atm-mm}}\right)$	Relative $\frac{\Delta V_s}{\Delta(Pd)}$ (%)
N_2	C_4F_6	SF_6	c-C_4F_8	C_3F_8		
60	10	10	10	10	8.42	100
70	10	10		10	8.28	98.3
70	10		10	10	7.94	94.3
70	10	10	10		8.11	96.3
70		10	10	10	6.88	81.7

[a]Plane-plane, uniform-field geometry; total pressure was 500 torr.

lowed, in decreasing order of effectiveness, by C_3F_8, SF_6, and c-C_4F_8.

Breakdown strengths measured for single additives (C_4F_6, iso-C_4F_8, c-C_4F_8, SF_6) to N_2 are shown in Fig. 9.18. Although for each case the dielectric strength of the mixture increases more rapidly with increase in additive at small quantities of the additive, the others do not suffer from the marked saturation effect evident for the SF_6 additive. C_4F_6 is the best additive for any proportion, whereas SF_6 is only better than iso-C_4F_8 and c-C_4F_8 at low proportions of additive. Preliminary results on mixtures of these gases with a buffer gas com-

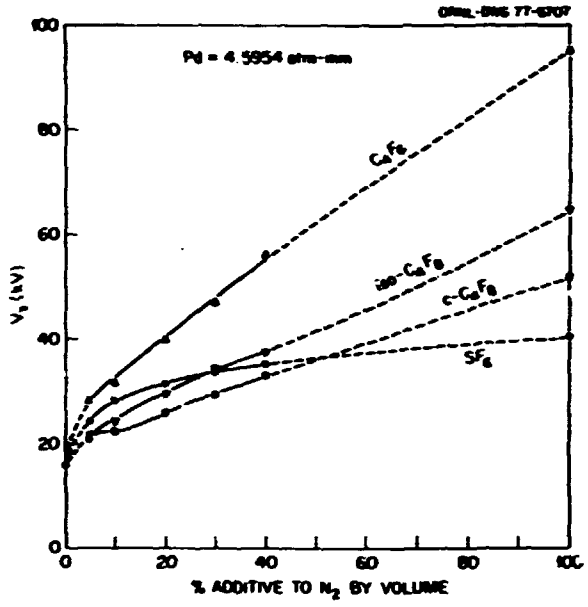

Fig. 9.18. Breakdown strengths for N_2–single-additive mixtures.

posed of equal quantities of N_2 and CO_2 led to similar conclusions.

Discussion

The electron attachment cross sections for SF_6, c-C_4F_8, C_4F_6, and iso-C_4F_8 for electron energies up to 1.4 eV are shown in Fig. 9.17 (see, also, Fig. 9.5 for similar data on C_6F_{10}), along with the calculated maximum cross section for *s*-wave capture. As exemplified by this maximum value as a function of energy, basic physics limits attachment cross sections to smaller values at higher energies; therefore, if breakdown is to be controlled by electron attachment, either the electrons must be captured before the electric field accelerates them above the energy range 0.0 to ∿2 eV, or gases must be added to slow down effectively electrons that reach higher energies, thus returning them to the energy range where they are likely to be captured. It is noted that although N_2 does not capture electrons itself, it is, nevertheless, a good buffer gas because it possesses a negative-ion resonance at ∿2.3 eV, which is very effective in slowing down electrons around this energy.[10]

The attachment cross sections in Fig. 9.17 begin to reveal a picture of effective breakdown control, although further details, both on electron attachment and on the inelastic processes that slow down electrons, must still be obtained. Figure 9.17 suggests that all four molecules are good dielectrics because of their high electron attachment cross sections. It also indicates that C_4F_6 has the best dielectric strength of the four by virtue of its large cross section to substantially higher energies compared with SF_6, c-C_4F_8, and iso-C_4F_8. The better dielectric strength properties of the two C_4F_8 forms compared with SF_6 may similarly be due to the fact that they can attach electrons over a wider range than can SF_6. It would appear from the data in Fig. 9.17 that effective electron attachment in the energy range ∿0.5 to ∿1.5 eV is very significant in controlling breakdown. It is not yet clear why iso-C_4F_8 is a better dielectric than c-C_4F_8, although the latter has a larger cross section in the 0.2 to 1.0 eV range than the former. However, it should be noted that the iso-C_4F_8 has a much larger attachment cross section *below* 0.2 eV than does the c-C_4F_8, and it contains a double bond which is likely to provide inelastic interactions with free electrons to slow down to energies where capture is more efficient.[6]

One striking feature of the SF_6 scattering cross section in Fig. 9.17 is that its value is relatively quite small above ∿0.4 eV, whereas those for the fluorocarbons are substantial up to ∿1.2 eV. This may suggest that SF_6 is a poorer dielectric compared with these fluorocarbons because it loses control of free electrons once they attain an energy of $\gtrsim$0.4 eV, and they continue accelerating in the applied electric field.

The breakdown strengths of mixtures of SF_6 and the above-mentioned fluorocarbons, each with N_2, are shown in Fig. 9.18. The better dielectric each fluorocarbon is in its pure form, the better it is as an additive to N_2 (Figs. 9.15, 9.16, and 9.18). There is relatively little departure from linearity for the mixture breakdown strength versus proportion of each additive. SF_6 in *small* amounts appears to be as good an additive to N_2 as the fluorocarbons and even better than the two C_4F_8 forms. However, increasing the proportion of SF_6 additive provides relatively little gain; that is, the benefit of adding SF_6 seems to "saturate." This point is still under investigation, but it appears that this behavior may be due to the fact that a modest amount of SF_6 could attach almost all electrons at low energies (0 to ∿0.4 eV; see Fig. 9.17) so that additional amounts of SF_6 serve little purpose. On the other hand, the fluorocarbons attach electrons over a wider part of the free electron energy distribution and increasing their proportions provides additional attachment. It is stressed that it is important to attach electrons over a fairly wide energy range and that it would be advantageous to use (in addition to electron-attaching molecules) molecules that can slow down electrons which

have attained enough energy to escape the effective attachment energy range, thus returning them to the energy range where they are more readily attached.

INTERNATIONAL SYMPOSIUM ON GASEOUS DIELECTRICS

Preparations are in progress for an international symposium on gaseous dielectrics to be held at the Hyatt Regency Hotel in Knoxville, Tennessee, on March 6–8, 1978, for the purpose of bringing together key individuals from leading research centers, industrial laboratories, and funding agencies to review and to discuss the progress and the problems of current interest in gaseous dielectrics and to seek solutions to the latter. The conference, to be hosted by ORNL, will provide a forum to coordinate present and future efforts in this most important area of endeavor. The conference proceedings will be published. The conference sponsors are ERDA and the Electric Power Research Institute.

10. Microdosimetry, Biological Modeling, and Theoretical Biophysics

H. A. Wright

W. R. Garrett — M. G. Payne
R. N. Hamm — R. H. Ritchie
F. W. Hecker, Jr.[1] — P. W. Todd[2]
J. Neufeld[2] — J. E. Turner

UPDATING OF INVERSE MEAN FREE PATH (IMFP) DATA FOR ELECTRONS IN LIQUID WATER

Our electron Monte Carlo code for computing the transport of electrons in liquid water has proved extremely versatile.[3] The inelastic IMFP values used in this program are directly appropriate to liquid water, the main constituent of biological media, and are unique in this respect at the present time.

Our data are based on the work of Heller et al.,[4] who used optical methods to study the dielectric response function of liquid water over an energy range of 5 to 26 eV. Their work showed evidence of a collective electron resonance at an energy of ∿23 eV. Currently, long-range, intermolecular electronic resonances such as this are not, in any practical sense, obtainable from data relating to properties of the isolated molecule. Hence, we decided to base our electron inelastic IMFP values on the data of Heller et al.,[4] extrapolated to nonzero momentum transfer to the water medium. Although approximate, this procedure[3] is based on experiment and on general sum rule constraints, together with a knowledge of the asymptotic behavior of $\mathrm{Im}[-1/\epsilon(q,\omega)]$, the energy (and momentum) loss function. Here, $\epsilon(q,\omega)$ is the dielectric function of the medium as it depends on momentum transfer $\hbar q$ and energy transfer $\hbar\omega$.

We recently revised both the inelastic and elastic IMFP values used in our Monte Carlo code, making allowance for exchange and relativistic effects. Figure 10.1 shows a check of the sum rule applied to the energy loss function. The "Bethe" sum rule states that $\int_0^\infty \omega\,\mathrm{Im}[-1/\epsilon(q,\omega)]\,d\omega = \pi\omega_p^2/2$, where $\omega_p^2 = 4\pi ne^2/m$, n being the mean density of electrons in the medium. Note that this result is independent of q. Plotted in Fig. 10.1 is the cumulant $(2/\pi\omega_p^2) \times \int_0^\Omega \omega\,\mathrm{Im}[-1/\epsilon(q,\omega)]\,d\omega$ vs Ω for two different values of q. One sees that at the maximum value of Ω, the sum rule is satisfied to within 2% for both values of q.

Figure 10.2 shows a plot of $E\omega^2(d\mu/d\omega)$ vs ω. Here, $d\mu/d\omega$ is the IMFP for inelastic interaction, differential in $\hbar\omega$, the energy loss, for a swift electron with an energy of 100 keV. This is computed from the energy loss function according to

$$\frac{d\mu}{d\omega} = \frac{1}{\pi E}\frac{(1+E/c^2)^2}{(1+E/2c^2)}\int_{q_-}^{q_+}\frac{dq}{q}\,\mathrm{Im}\left[\frac{-1}{\epsilon(q,\omega)}\right], \qquad (1)$$

where E is the electron kinetic energy in atomic units (27.2 eV) and

$$q_\pm = [2E(1+E/2c^2)]^{1/2} \pm [2E(1+E/2c^2) - 2\omega(1+E/c^2)+\omega^2/c^2]^{1/2} .$$

Atomic units are used for all quantities appearing in Eq. (1), with $c = 137$. The quantity $E\omega^2(d\mu/d\omega)$ is displayed in Fig. 10.2 to emphasize the free-electronlike behavior of the differential IMFP (DIMFP) at large ω. Note that in these units, one expects this quantity to be asymptotic to πn, since for large enough energy and

1. Student, Southern Colleges and Universities Union.
2. Consultant.
3. See, for example, R. N. Hamm et al., p. 1037 in *Proc. 5th Symp. on Microdosimetry, Verbania Pallanza, Italy, Sept. 22–26, 1975*, EUR-5452 d-e-f, Commission of the European Communities, 1976; see also, *Health Phys. Div. Annu. Prog. Rep. June 30, 1976*, ORNL-5171 (October 1976), p. 229.
4. J. M. Heller et al., *J. Chem. Phys.* 60, 3483 (1974).

ORNL-DWG 77-12151

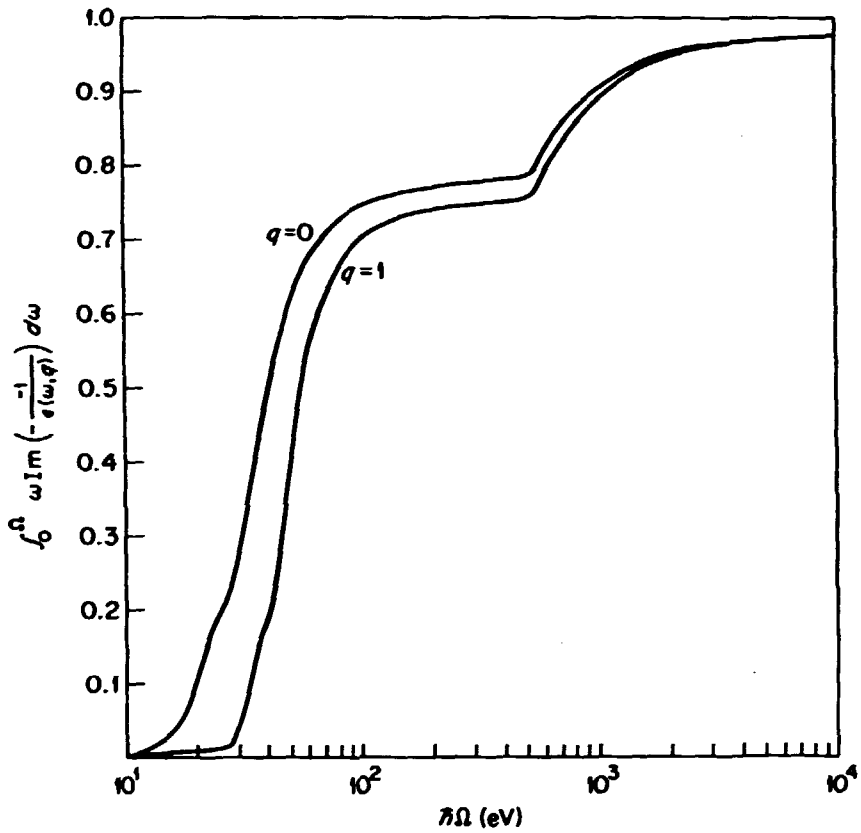

Fig. 10.1. Cumulative integral over energy transfer $\hbar\omega$ of the energy loss function $\omega \mathrm{Im}[-1/\epsilon(q, \omega)]$ for liquid water plotted as a function of the upper limit of the integral Ω. The two curves are for different values of momentum transfer $\hbar q$.

momentum imparted to struck electrons, binding effects will be unimportant and the DIMFP should be closely given by the Møller formula. Figure 10.2 also shows an abrupt discontinuity at the K-shell edge in oxygen at ∿500 eV.

Figure 10.3 shows a plot of the stopping power, $(-dE/dx)$, computed from our DIMFP values and corrected for exchange, as a function of electron energy E. Also shown are values inferred from the experimental work of Cole.[5] Note that the experimental uncertainties attending Cole's data are comparable to the differences between our results and his.

Our elastic DIMFP values for liquid water were revised recently. For electron energies higher than 1 keV, we use the Born approximation to represent elastic scattering from the medium, which, for these purposes, we assume to consist of an uncorrelated assembly of hydrogen and oxygen atoms at the density of liquid water. At lower energies, we have carried out a phase-shift analysis using Hartree-Slater-Fock potentials for individual hydrogen and oxygen atoms (Fig. 10.4). The uppermost solid curve in Fig. 10.4 is $\mu^e(E)$, the total elastic IMFP vs electron energy, E, computed as described. The lower curve shows $\mu_t^e(E)$, the transport IMFP, vs E. The quantity $\mu_t^e(E)$ is a measure of the effectiveness of the elastic scattering processes in causing substantial deflection of an electron; $\mu_t^e(E) = \int(d\mu^e/d\Omega)(1 - \cos\theta)\, d\Omega$, where $d\mu^e/d\Omega$ is the elastic IMFP differential in scattering into an interval of solid angle $d\Omega$ at polar angle θ measured from the original direction. Thus, one sees that at low energies there is comparatively little difference between $\mu(E)$ and $\mu_t(E)$ at a given value of E. However, at energies $\gtrsim 1$ keV, scattering is predominantly in the forward direction so that μ_t^e is appreciably smaller than μ^e. For comparison, we also display $\mu^i(E)$ (dashed curve in Fig. 10.4), the total inelastic IMFP, as a function of E.

5. See W. K. Sinclair et al., *Linear Energy Transfer*, ICRU report 16, International Commission on Radiation Units and Measurements, Washington, D.C., 1970.

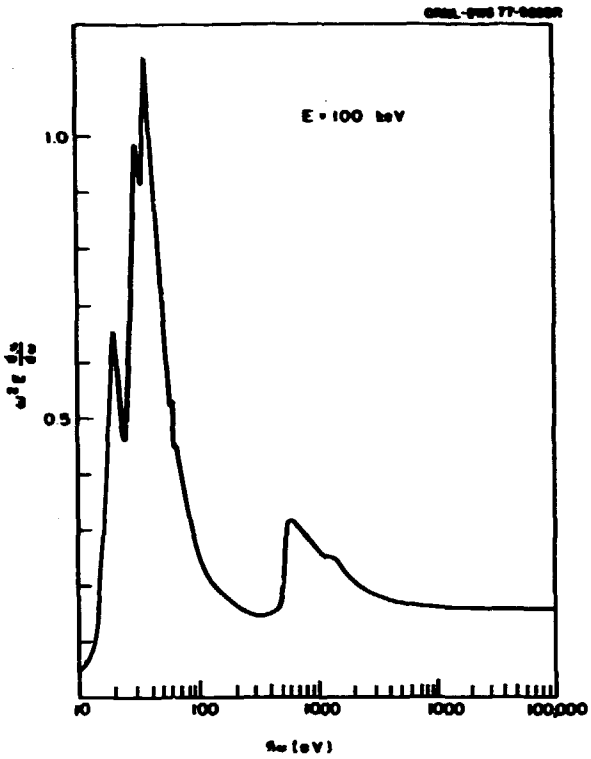

Fig. 10.2. A plot of $\omega^2 E(d\mu/d\omega)$, the DIMFP for energy transfer $\hbar\omega$ to liquid water for an electron with energy $E = 100$ keV vs $\hbar\omega$. Atomic units are used.

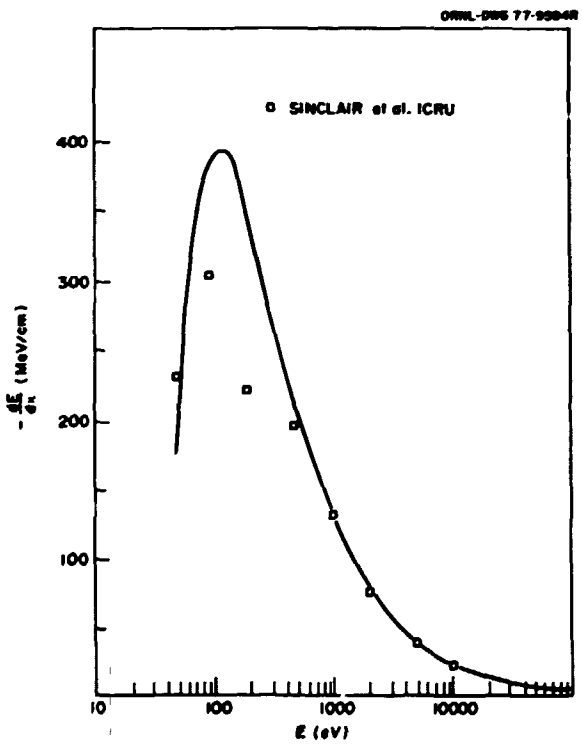

Fig. 10.3. A plot of the stopping power $(-dE/dx)$ of liquid water for electrons with energy E plotted vs E. The solid curve was obtained using our IMFP data; the points were taken from the data of Cole.[5]

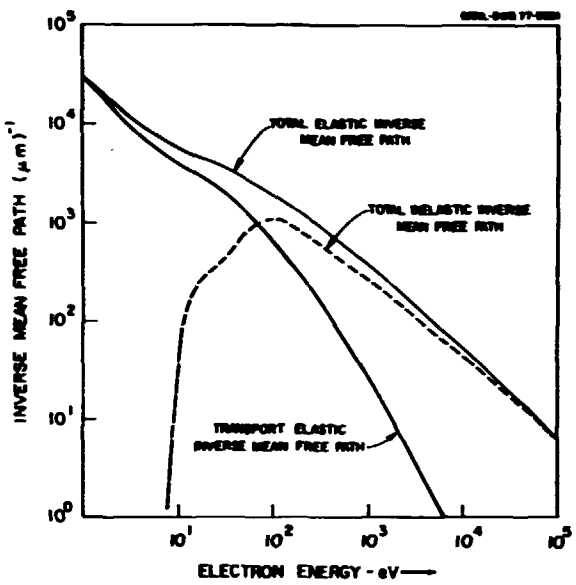

Fig. 10.4. Elastic, elastic transport, and inelastic IMFP data for electrons with energy E in liquid water.

Using the updated IMFP values, we obtained preliminary results on the penetration of monoenergetic electrons in water. Figure 10.5 shows the quantity $2\pi\rho f(\theta, \rho)$ vs ρ for $\theta = 30°$ and for 5-keV electrons as computed from our Monte Carlo code (histogram) and as taken from the work of Berger[6] (solid curve). $f(\theta, \rho)$ is the

6. M. J. Berger, p. 157 in *Proc. 3rd Symposium on Microdosimetry, Stresa, Italy, Oct. 18–22, 1971*, EUR-4810 d-f-e, Commission of the European Communities, 1972.

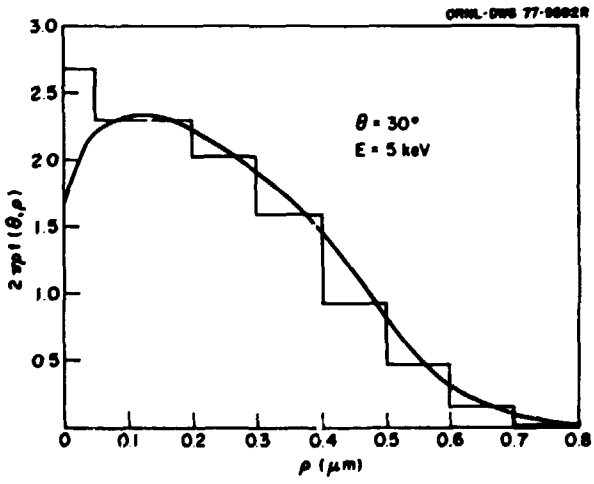

Fig. 10.5. Differential fractional dose $f(\theta, \rho)$ deposited at distance ρ vs ρ from a line source of 5-keV electrons emitted at angle $\theta = 30°$ relative to the line source in liquid water. The solid curve is from Berger;[6] the histogram is computed from our Monte Carlo code.

relative dose at distance ρ from a line source of monoenergetic electrons emitted at the angle θ relative to the source line; the integral of $2\pi\rho f(\theta, \rho)$ over all ρ is unity. Figure 10.6 shows a similar comparison for $\theta = 90°$. It is seen that our results compare quite closely with Berger's, considering the differences in IMFP data used in the calculations.

Work on elastic and inelastic IMFP data for our electron Monte Carlo code is continuing. We are making critical comparisons with input data of other workers who have developed codes for calculating electron penetration with microdosimetric applications.

LOW-ENERGY ELASTIC SCATTERING CROSS SECTIONS

In the energy region below 1 keV, the Born approximation for electron scattering cross section becomes doubtful. We have used partial-wave analysis to determine differential and total elastic scattering cross sections of water for electrons of 1 keV to 10 eV. The water molecule was treated as an oxygen atom plus two hydrogen atoms, with independent electron scattering amplitudes for the two species. In this approximation, details of the molecular charge distribution and the resultant effect on differential cross sections were ignored, as were vibrational and rotational excitations of water. Up to seventeen elastic scattering phase shifts were determined by solving the appropriate radial equations for electrons moving in the potential fields of oxygen and hydrogen. The distortion of the atomic system by the scattered electrons was included by using a polarized orbital dipole polarization potential,[7] but exchange effects between target and projectile were ignored. These results should give an adequate representation of elastic scattering events in the energy region below 1 keV.

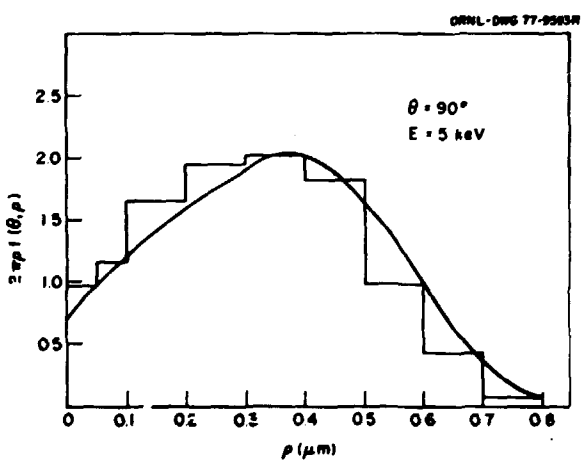

Fig. 10.6. Differential fractional dose $f(\theta, \rho)$ deposited at distance ρ vs ρ from a line source of 5-keV electrons emitted at angle $\theta = 90°$ relative to the line source in liquid water. The solid curve is from Berger;[6] the histogram is computed from our Monte Carlo code.

CALCULATION OF SPATIAL DISTRIBUTIONS OF PRIMARY PRODUCTS AROUND A HEAVY-ION TRACK IN LIQUID WATER

The Monte Carlo calculations reported last year[8] for electrons in liquid water were extended to heavy charged particles by using the appropriate limits of integration for momentum transfer. We performed detailed studies of the products formed around a short segment of a heavy-particle track, over which the total inverse mean free paths (IMFPs) were assumed to be constant. The calculated mean rate of energy loss gave the correct stopping power. All secondary and subsequent electrons and the events they undergo were computed by Monte Carlo procedures, and the physical data were compiled in volumes surrounding the track. As with the work reported last year, a total of 22 specific events could occur. Delta rays and other secondary electrons were followed in the code down to an arbitrary cutoff value of 10 eV.

Figure 10.7 shows the average dose computed as a function of distance from the track of a proton with speed $\beta = 0.05$ ($E = 1.2$ MeV) compared with the velocity of light in vacuum and an alpha particle with $\beta = 0.15$ ($E = 43.2$ MeV). These doses were obtained by averaging the secondary-electron histories calculated for a large number of protons and alpha particles with the specified values of β. The delta rays produced by the heavy particles were assumed to originate at points right along the track, where $t = 0$, with the angular distributions obtained as though the electrons were initially free. The curves show expected trends. The relative number of delta rays per unit path length depends on the square of the charge, whereas the spectrum depends on β. The curve for the alpha particle is less steep than that for the proton, reflecting the broader spectrum of delta rays.

Figure 10.8 shows a comparison of our calculated radial distributions of dose divided by the square of the

7. W. R. Garrett and H. T. Jackson, *Phys. Rev.* 153, 28 (1967).

8. *Health Phys. Div. Annu. Prog. Rep. June 30, 1976*, ORNL-5171 (October 1976), p. 229.

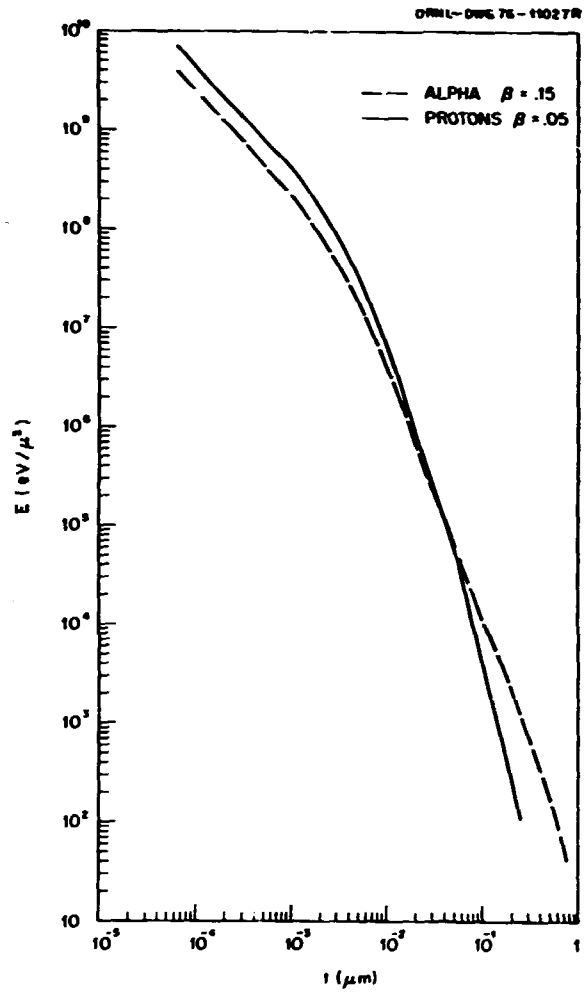

Fig. 10.7. Distribution of average dose (eV/μ^3) as a function of the radial distance t (μm) from the tract of an alpha particle with speed β = 0.15 (compared with the speed of light) and from the track of a proton with β = 0.05.

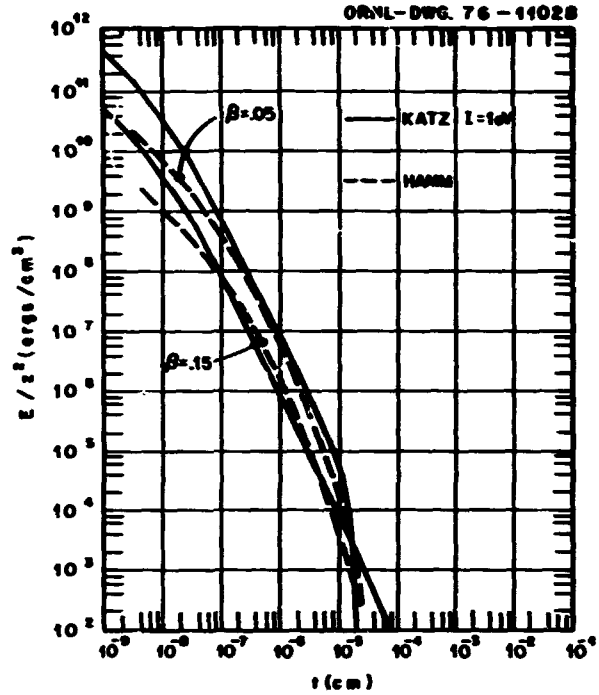

Fig. 10.8. Radial dose distributions divided by the square of the particle's charge (ergs/cm³) calculated by Katz et al.[9] and by us for β = 0.05 and β = 0.15 as functions of distance t (cm) from the particle track.

particle's charge z with those of Katz et al.[9] for β = 0.05 and β = 0.15. In the figure, t is the distance from the particle track. Katz et al.[9] assumed I = 1 eV for the mean excitation energy of water. (Although this value is unrealistic, Katz et al. obtained essentially the same curves for other choices of I.) They also tried various ways of calculating the delta-ray spectrum and concluded that these curves were not particularly sensitive to the detailed assumptions made. Katz et al. did not, of course, explicitly treat the secondary electrons produced by delta rays, as we have done in these detailed computations. In view of the many assumptions that were made in both sets of calculations, it is gratifying that the curves lie close together over several decades of distance from the track. The curves have no physical meaning at very small distances, where t is less than several angstroms. Our values appear to be considerably below those of Katz et al. when $t \lesssim 10$ Å.

Figure 10.9 shows another comparison with Katz et al.[9] In many of their analyses, Katz et al. calculated the average dose distributions in right circular cylinders of radius a_0 with axes parallel to the particle track at a distance t from the track. They then multiplied these distributions by β^2/z^2 to obtain universal curves. We used our code to calculate this quantity for β = 0.05 and for a range of values of a_0. Some results are presented in Fig. 10.9, where the solid curves are those of Katz et al. and the points show our values. Again, the agreement is good, considering the vastly differing points of departure. Our values seem to be consistently smaller for the smaller a_0 and do not yield as abrupt a shoulder. We obtain almost identical curves for protons and alpha particles, as predicted by Katz et al.[9]

Finally, in Fig. 10.10 we present the raw data for the average spatial distributions of initial products calculated as a function of the radial distance t (μm) from the track of a proton with β = 0.05. One striking result

9. R. Katz et al., *Radiat. Res.* 47, 402 (1971).

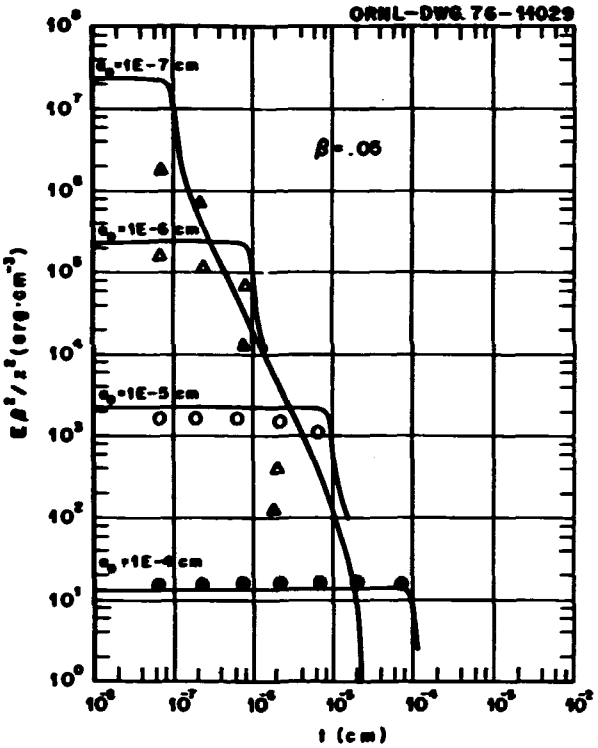

Fig. 10.9. Comparison of $E\beta^2/z^2$ (ergs/cm³) calculated by Katz et al.[9] (solid curves) and by us (points), averaged over circular cylinders of radius a_0 with parallel axes at distances t (cm) from track.

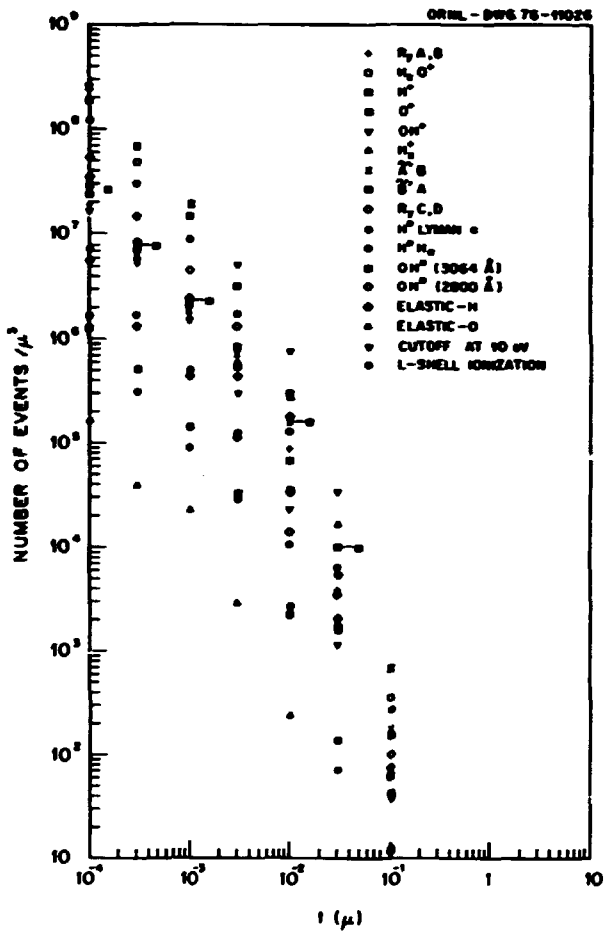

Fig. 10.10. Average spatial distributions of initial products as functions of distance t (μ) from track of a proton with $\beta = 0.05$ in liquid water.

is that the most abundant species produced everywhere is the subexcitation electron, that is, an electron whose energy falls below the 10-eV cutoff and is no longer followed in the program. The next most abundant product is H_2O^+. As expected, L-shell ionization of oxygen occurs frequently near the track. The abundances of the species calculated span about three decades at any given distance.

APPLICATIONS OF MODELS FOR CELL SURVIVAL: THE FIXATION-TIME PICTURE

In a recent paper,[10] a rather general statistical problem was solved and the solutions discussed in the context of various cell-survival models. Within the previous formalism it was shown that the probability of survival could be predicted under a wide variety of assumptions.[11] Under fairly realistic assumptions about the physical parameters in the problem, we obtained analytical solutions which allowed for arbitary time dependences of the radiation field and concentrations of repair enzymes or other chemical components.

It was also shown that several earlier models, including those considered by Lea,[12] Dienes,[13] and Kappos and Pohlit,[14] were contained as special cases of the more general three-state model. In a later publication,[15] we showed some relations between two different survival models in which different assumptions were made about the production of lesions and prelesions. The

10. M. G. Payne and W. R. Garrett, *Radiat. Res.* 62, 169 (1975).

11. *Health Phys. Div. Annu. Prog. Rep. July 31, 1974*, ORNL-4979 (September 1974), p. 235.

12. D. E. Lea, *Actions of Radiations on Living Cells*, Cambridge University Press, London, 1956.

13. G. J. Dienes, *Radiat. Res.* 28, 183 (1966).

14. A. Kappos and W. Pohlit, *Int. J. Radiat. Biol.* 22, 51 (1972).

15. M. G. Payne and W. R. Garrett, *Radiat. Res.* 62, 388 (1975).

relation of special cases of these models to an earlier model by Roesch[16] was also demonstrated.

We have made some further applications of modeling to a rather unique set of cell-survival experiments. In particular we examined studies which were designed to maximize repair effects on survival of various cell types. Two- and three-state models were found to provide satisfactory agreement with experiments when accompanied by the "fixation-time" pictures for causing nonlethal lesions to result in lethality if not repaired within a given time interval.

Three-State Model

We follow the previous notation wherein we take our picture of a cell to be an enclosure with N_0 "sensitive sites" distributed in an arbitrary way within the interior. Each site is assumed to exist in one of three states – A, B, or C – where A is undamaged, B is damaged but repairable, and C is irreparably damaged. Through direct and indirect effects, the radiation is allowed to induce transitions between states A and B, B and C, and A and C (Fig. 10.11).

Here we will consider the special case in which N_0 is taken to be very large. Thus the number of sites in state A remains essentially unchanged, even under high doses of radiation. We then solve the statistical problem of determining $P(N_B, N_C, t)$ = the probability of a cell (or of a DNA molecule if one prefers) having N_B sites in state B and N_C in state C at time t.

We define a transition probability such that the combination of direct and indirect radiation damage in a cell will cause a site to make a transition from condition A to B between t and $t + dt$ with a probability $\gamma_{AB}(t)\,dt$. Likewise, $\gamma_{BC}(t)\,dt$ and $\gamma_{AC}(t)\,dt$ represent the probabilities that a transition from B to C or A to C, respectively, will occur between t and $t + dt$. Further, we assume that repair of radiation damage takes place through the induction of transitions from B back to state A. However, we allow for the additional possibility of an abortive step in this enzyme-mediated reaction in which a certain fraction of the repair reactions leads to lethality, that is, the transition is from B to C rather than the normal B to A repair step. Thus, we let $R(t)(1 - k)\,dt$ be the probability that a site in state B will be repaired between t and $t + dt$ and thereby restored to A. The fraction k is, however, promoted to state C.

Following the same reasoning as before,[10] and with the added proviso that N_0 is very large, we get the following differential equation for (N_B, N_C, t).

$$\begin{aligned}\frac{d}{dt}P(N_B,N_C,t) &= (N_B+1)\,R(t)\,(1-k)\,P(N_B+1,N_C,t)\\ &\quad + N_0\gamma_{AC}(t)\,P(N_B,N_C-1,t)\\ &\quad + N_0\gamma_{AB}(t)P(N_B-1,N_C,t)\\ &\quad + (N_B+1)\,[kR(t)+\gamma_{BC}(t)]\\ &\quad \times P(N_B+1,N_C-1,t) - [N_0\gamma_{AB}(t)+N_B\gamma_{BC}(t)\\ &\quad + N_0\gamma_{AC}(t)+N_BR(t)]\,P(N_B,N_C,t)\,. \qquad (2)\end{aligned}$$

It is easy to verify that the solution to this equation corresponding to no damaged cells at $t = 0$ is

$$P(N_B,N_C,t) = \frac{\left[N_0P_B(t)\right]^{N_B}\left[N_0P_C(t)\right]^{N_C}}{N_B!N_C!} \times \exp[-N_0(P_B(t)+P_C(t))]\,, \qquad (3)$$

ORNL-DWG 74-6853

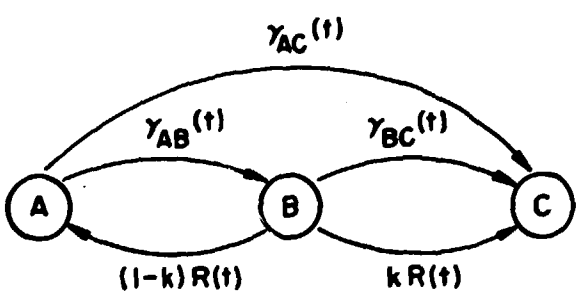

Fig. 10.11. Schematic representation of transitions between the three possible states of a critical site.

16. W. C. Roesch, *Hit Theory for Low LET Radiation*, BNWL-SA-4172, Battelle Northwest, Richland, Wash., 1972.

where $P_B(t) = P_C(t) = 0$ at $t = 0$. $P_B(t)$ and $P_C(t)$, which are the probabilities of being in states B and C, respectively, are given by

$$P_B(t) = \int_0^t dt' \gamma_{AB}(t') \exp\,[\Gamma_{BC}(t') + \rho(t') - \Gamma_{BC}(t) - \rho(t)] \quad (4a)$$

and

$$P_C(t) = \int_0^t dt'\,[\gamma_{BC}(t') + kR(t')] \int_0^{t'} dt'' \gamma_{AB}(t'') \times \exp[\Gamma_{BC}(t'') + \rho(t'') - \Gamma_{BC}(t') - \rho(t')] + \Gamma_{AC}(t)\,, \quad (4b)$$

where

$$\Gamma_{AC}(t) = \int_0^t \gamma_{AC}(t')\,dt'; \quad \Gamma_{BC}(t) = \int \gamma_{BC}(t')\,dt'$$

and

$$\rho(t) = \int_0^t R(t')\,dt'\,.$$

With these analytical solutions, a specific cell-survival model can be formulated by making choices for $R(t)$, $\gamma_{AB}(t)$, $\gamma_{AC}(t)$, and $\gamma_{BC}(t)$ with a further specification of the recipe by which the probability of survival is determined from a knowledge of $P(N_B, N_C, t)$. Here we examine further the utility of the "fixation-time picture" for specifying the conditions for lethality in cell-survival studies. In this picture, all repairable lesions, state B, are converted into irreparable lesions, state C, if not repaired within a certain specified time interval, t_f, called the fixation time.[11,15]

Effect of Growth Medium on Yeast Recovery

Here we consider a set of experiments on survival of irradiated yeast[17] in which the effects of cell-replication rates, as produced by growth on media of different nutritive values, affected survival. In the experiments, diploid yeast cells were irradiated with 110 kR of gamma rays and immediately inoculated on growth medium. Two different media, designated I and II, were used: I was richer in nutrient than II. Under these conditions, the survival on medium I (6.5%) was less than that for cells grown on medium II (4.0%). These results are shown as S_I (survival on medium I) and S_{II} (survival on medium II) in Fig. 10.12.

The multiplication rates for cells on media I and II are shown in the top curves of Fig. 10.13. We note that the

17. V. J. Korogodin, M. N. Meissel, and T. S. Remesove, pp. 538–57 in *Proc. Third International Congress on Radiation Research*, North Holland Publishing Co., Amsterdam, 1967.

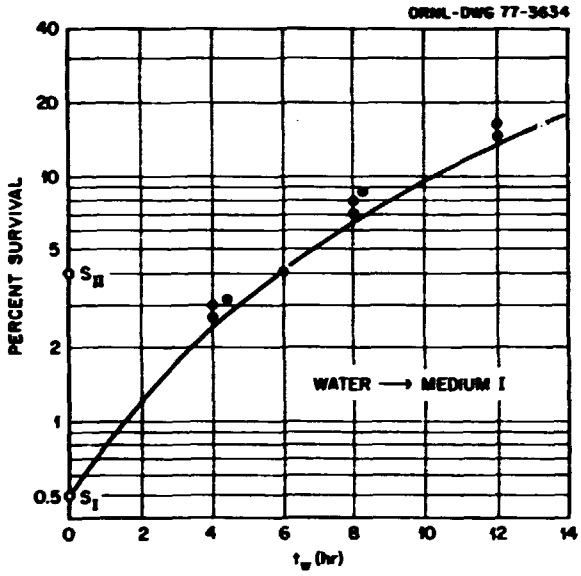

Fig. 10.12. Survival curve for yeast cells irradiated with 110 kR of gamma rays and held in water for time t_w before transfer to medium I. The points marked S_I and S_{II} are survival fractions for cells that are inoculated immediately on media I and II respectively.

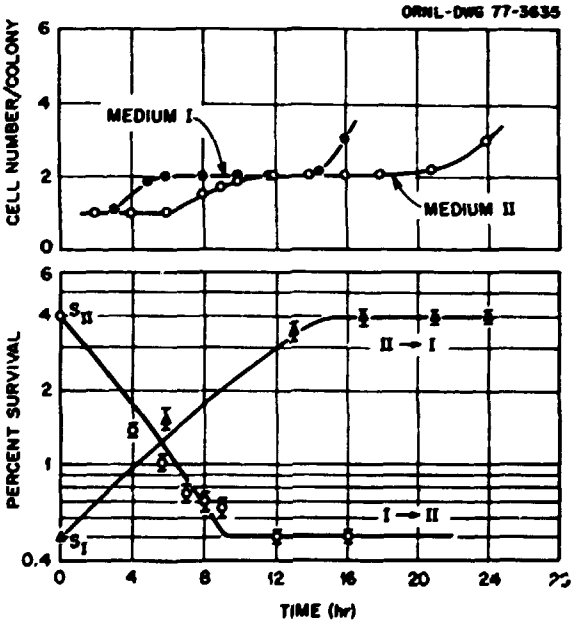

Fig. 10.13. Upper curve: multiplication rates for cells grown on media I and II; lower curves: survival curves for cells transferred from medium I to medium II after time t and for the reverse transfer from medium II to medium I.

doubling time on medium II was about 6 hr longer than that on I. Cells held in water for a "recovery" period before being transferred onto growth medium experienced enhanced survival as shown in the data points of Fig. 10.12, and holding the cells in water for about 6 hr before inoculation on I yielded approximately the same survival as growth on II.

Finally, cells originally inoculated on I were transferred to medium II after time t and, conversely, cells were grown on II for time t and transferred to medium I. The results of these experiments are shown by the data points in Fig. 10.13.

These experiments on yeast cell survival are readily described by the present formalism and the fixation-time model. We assume that all cells that retain one or more unrepaired lesions (state B) at the time the cells reach a certain point in their cell cycle will undergo reproductive death. These times, τ, are proportional to the replication times which are, in turn, determined by the residence times on the two growth media.

We adopt the simplest possible physical description of the cells' progression from the initial radiation exposure to the final point in time, τ, at which radiation damage becomes fixed, that is, irreparable. Namely, we assume a linear progression in time at a rate ν_{I} for cells on medium I, ν_{II} for these on medium II, and a zero progression rate when the cells are held in water.

With this picture, the surviving fractions, F_s, in the growth media studies can be obtained from Eq. (4). We have taken the simplest case, $N = 1$, and since the experiments were performed at a single dose, the fraction k, which undergoes disruptive repair, is not revealed. Thus, we take $k = 0$, $R(t) = R_0$, $\gamma_{AC} = 0$, and $\Gamma_{AB}(t) = \alpha D(t)$ in Eq. (4). When the cells reach the fixation point in their cycle, all sites in state B are converted to state C. Thus, from Eq. (3), the probability that a cell will have N sensitive sites in C after fixation is

$$P_s(N, t) = \sum_{N_B=0}^{N} P(N_B, N - N_B, t)$$

$$= \frac{1}{N}(\mu D e^{-R_0 t})^N \exp(-\mu D e^{-R_0 t})$$

and

$$F_s = \exp(-\mu D e^{-R_0 t}), \tag{5}$$

where the fixation time, τ, as determined by the present model is easily seen to be

$$\tau = (\tau_{\mathrm{I}} + 6\ \mathrm{hr}) - t_{\mathrm{I}}\left(\frac{6\ \mathrm{hr}}{\tau_{\mathrm{I}}}\right) \tag{6}$$

for the experiments in which the transfer from I to II was carried out after time t_{I} on medium I;

$$\tau = \tau_{\mathrm{I}} + t_{\mathrm{II}}\left(\frac{6\ \mathrm{hr}}{\tau_{\mathrm{I}} + 6\ \mathrm{hr}}\right) \tag{7}$$

for the experiments in which a transfer from II to I was made after time t_{II} on medium II; and

$$\tau = \tau_{\mathrm{I}} + t_w \tag{8}$$

for the experiments in which the cells were held in water for time t_w and then inoculated on medium I. τ_{I} is the fixation time on medium I alone. Thus, μ, R_0, and τ_{I} are parameters which must be fixed by the experiments.

Note that τ in Eq. (6) is less than or equal to τ_{I} since any delay longer than τ_{I} in transferring to medium II will incur fixation before the transfer. Thus, any delay past τ_{I} should show no change in survival. Likewise, in Eq. (7) we have $\tau < \tau_{\mathrm{II}}$ since residence on medium II incurs fixation of lesions at τ_{II} and further delay in transfer to I will have no effect. From the data points on Fig. 10.13 we note that the expected break in the I → II experiment occurs at about 9 hr, and the break in the II → I experiment occurs 6 hr later at $t = 15$ hr. Thus, we choose $\tau_{\mathrm{I}} = 9$ hr and $\tau_{\mathrm{II}} = 15$ hr by simply noting the expected behavior of the data. We found identical survival for cells grown on medium II and those held in water for 6 hr and then grown on medium I. With this, one easily obtains $R_0 = 0.083\ \mathrm{hr}^{-1}$ and $\mu D = 11.19\ \mathrm{hr}^{-1}$.

The agreement of the present model with the experimental data is shown in Figs. 10.12 and 10.13. The solid lines are the theoretical survival curves, which seem to agree rather well with the series of experiments.

II. Liquid and Submicron Physics

R. D. Birkhoff
J. D. Allen[1] R. A. MacRae[1]
R. N. Hamm L. R. Painter[1]
J. M. Heller, Jr.[1] D. P. Spears[2]
H. H. Hubbell, Jr.[1] C. S. Hesemann[3]
R. Zauper[4]

The attempt to develop a more accurate method of determining the optical and dielectric properties of liquids and solutions continued. In this method, the ionization in the vapor adjacent to the liquid is used to monitor the photon beam strength before and after reflection. The ratio of ion currents is simply related to the reflectance, which can, in turn, be analyzed to yield the electronic properties of the liquid. The fifth design, tried this year, eliminated all problems found previously and gave highly accurate values for the reflectance of a well-known sample, gold. A system for monitoring the height of the liquid sample (necessary to obtain the highest precision with this technique) was found to be adequate for the low-vapor-pressure liquids, but to be insensitive for water samples because of vapor ionization collected by the monitoring probe. Preliminary data on reflectances of liquids show an order-of-magnitude improvement in accuracy over data taken previously.

A pinhole electron gun was used to measure the deflection of low-energy (1 to 70 eV) electrons passing near surfaces. Deflection of a 1-eV beam passing through a 3-μ pinhole in a 2000-Å-thick gold film was noted and data were evaluated to obtain the potential distribution inside the hole. The potential declined smoothly from 750 Å (near the edge) to 15,000 Å (the axis) but failed to discriminate between classical, quantum, and van der Waals theories of image potentials. Slits were used instead of pinholes and seem to offer advantages of higher count rate and somewhat simpler analysis of data. The experiment is in its infancy and should show much-improved accuracy next year.

An ultrahigh-vacuum facility was designed and construction is almost complete. The vacuum chamber will have the pinhole experiment described above, a determination of the surface potentials of submicron fibers by electron deflection, an experiment on the generation of surface waves on submicron cylinders by laser excitations, and a vacuum evaporator. The vacuum chamber was received and tested, and the various experimental components will be added to it as time and money permit.

Work continued on the generation of surface waves on submicron cylinders by laser excitation. The newly acquired nitrogen and dye lasers were used to explore the reflectance of aluminum- and/or silver-coated fibers. So far we have found no evidence for surface wave excitation as suggested by Miziumski[5] and Pfeiffer and Economou.[6] Our companion theoretical effort also failed to predict their existence. The causes for the discrepancies between our experiments and theories and those of others are being explored.

Two spin-off developments should be noted. Tests were completed on an electrometer-ratiometer developed in cooperation with F. M. Glass of the ORNL Instrumentation and Controls Division. No ratiometer suitable for very small currents is commercially available, and our model should be useful in many health physics and other applications. The other development was an electron gun filament circuit, which in a simple, inexpensive way eliminates the magnetic field from and the voltage drop along the filament.

---

1. Consultant.
2. Postdoctoral fellow.
3. SCUU/NSF student.
4. ORAU student.
5. C. Miziumski, *Phys. Lett. A* 40, 187 (1972).
6. C. A. Pfeiffer, E. N. Economou, and K. L. Ngai, *Phys. Rev. B* 10, 3038 (1974).

PRECISION MEASUREMENTS OF THE ELECTRONIC PROPERTIES OF LIQUIDS AND SOLUTIONS

Over the last several years, the optical and dielectric properties of a dozen liquids have been determined for photon energies of 3 to 26 eV, using the reflectance technique. In all liquids, a collective electron resonance was found, as predicted by Platzman[7] for water. The chemical and biological consequences of this energy absorption mechanism are under study at several laboratories throughout the world. The difficulties of making reflectance measurements to high accuracy (less than 1% uncertainty) are increased for liquid surfaces because of the presence of vapor in the optical path. To improve the accuracy of the reflectance measurements and hence the derived dielectric functions (where the reflectance uncertainty is amplified by an order of magnitude), we attempted to introduce a new measurement technique which avoids one of the principal causes of uncertainty – the gold reference mirror – and takes advantage of the presence of vapor. In this method, the ionization of the vapor along the optical path, both before and after reflection at the liquid, is measured with a double ion chamber. The instantaneous ratio of these ion currents is the required reflectance independent of fluctuations in the light source.

In the past year we designed and built two additional ion chamber systems (for a total of five) in a cooperative program with Professor Linda R. Painter at The University of Tennessee. The final design (Fig. 11.1) has achieved adequate control of photoemission from the liquid, electrical leakage, and extraneous currents. The outer metal box is kept at ground potential and serves as a mount for the insulated inner metal box held at a positive voltage which supplies the ion chamber field. The Teflon standoff insulators (not shown) supporting the collector wires in each chamber (which are near ground potential) are also mounted on the grounded outer box. Thus, the outer box serves as a guard electrode, and no leakage currents ($<10^{-14}$ A) are found on collector wires even at collector voltages of up to 100 V. The design in general is complicated by the small sizes involved which are, in turn, dictated by photon mean free paths in the pressure regions used. That is, larger sizes with longer paths would have resulted in unsuitably large photon beam attenuations.

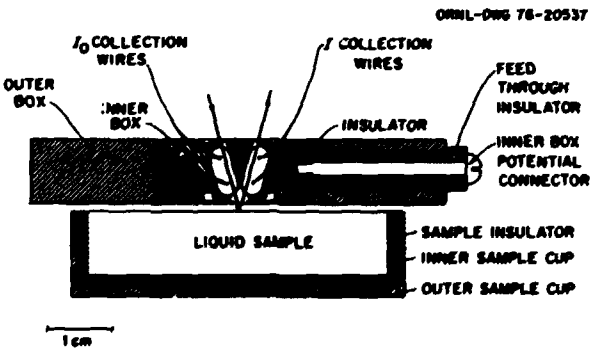

Fig. 11.1. Cross-sectional view of ion chambers and sample. *Light enters left chamber producing ion current I_0. After reflection, light enters and exits right chamber, producing ion current I. Collection wires and outer box are at ground potential, whereas inner box has a positive potential applied to produce the collecting field. Sample also has a positive potential to suppress photoemission from it.*

The grounded outer box faces the sample, which is maintained at a high enough positive voltage to suppress photoemission from it (~20 V). Ionization of gas molecules in the region between the box and sample creates electrons and ions which are attracted to and collected by the sample and box respectively. Little collecting field leaks through the entrance and exit slits in the monochromator, and hence ions formed before or after beam passage through the two chambers are collected by the slits or recombined with their geminate electrons. Attention to these currents is necessary if ion chamber saturation is to be achieved. We varied the sample potential V_c and the collection potential V_p to ensure that the reflectance of a gold reference was independent of them. In Fig. 11.2, the ion current ratio is plotted as a function of V_c, the sample potential, for a box potential V_p of 30 V and a pressure of 1000 μ of air. It can be seen that the current ratio is independent of sample voltage for $V_c \geq 20$ V, a not surprising observation for photoelectron energies of a maximum of ~15 eV resulting from 841-Å photons.

With the sample held at 30 V, the ratio was measured as a function of box potential V_p; these data are also shown in Fig. 11.2. Here, a saturation of the ion chamber is found between 15 and 35 V, with a slight increase in ratio above this latter potential.

The third parameter that could be varied was the pressure (Fig. 11.3). The exponential behavior predicted by theory is clearly seen; that is, theory[8] predicts that the

7. R. L. Platzman, p. 20 in *Radiation Research*, G. Silini, ed., North-Holland, Amsterdam, 1967.

8. R. D. Birkhoff, L. R. Painter, and J. M. Heller, Jr., "Measurements of Reflectance by Gas Ionization," accepted for publication in *Journal of the Optical Society of America*.

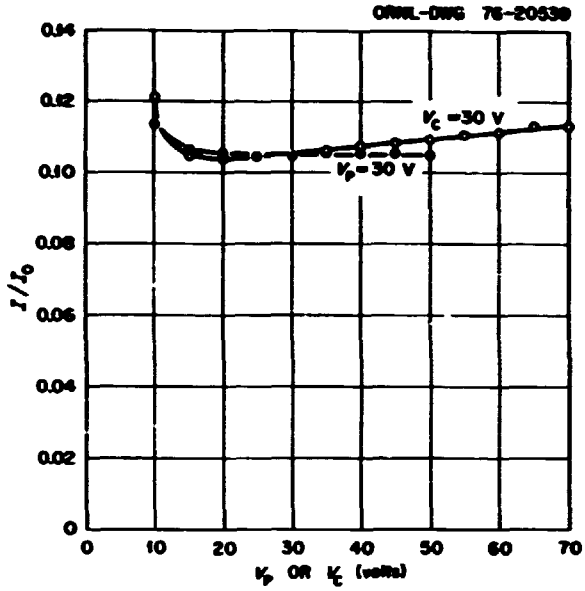

Fig. 11.2. Current ratios as a function of applied potentials. Sample is a gold film, and gas is air at a 1-torr pressure. Ratios independent of sample potential (V_c) and chamber potential (V_p) are found if these voltages are between 15 and 35 V.

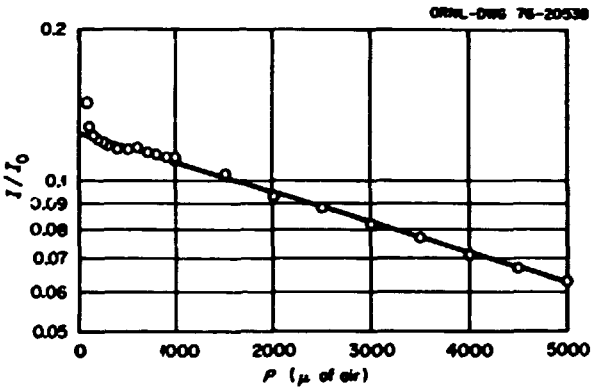

Fig. 11.3. Current ratio as a function of pressure (air). Experimental behavior predicted by theory is found above 100 μm (0.1 torr). Reflectance of sample surface is found by extrapolating to zero pressure. Least-squares fit to data gives a reflectance of 0.1247 in good agreement with data of Canfield, Hass, and Hunter.[9]

current ratio should decline with pressure exponentially:

$$I/I_0 = Re^{-\gamma P}, \qquad (1)$$

where R is the reflectance of the surface and γ is a constant at each wavelength which involves the dimensions of the chambers and the ionization and excitation cross sections of the gas. An overall decrease in ratio of about a factor of 2 is seen out to 5000 μ. This is a typical decrease to be expected if studies are made on aqueous solutions, because the vapor pressure of water is 4579 μ at 0°C. The data extrapolates to a value of R = 0.1247 at P = 0 for a gold surface. The 95% confidence limits are 0.1255 and 0.1240, and the value of 0.1247 agrees with the value of 0.125 given by Canfield, Hass, and Hunter.[9]

One of the problems that has not been solved satisfactorily is the determination of the height of the liquid surface. If the liquid level drops due to evaporation, the reflected beam will move to the right (Fig. 11.1) and may strike the walls of the ion chambers. This will cause an error in the ion current in the right chamber. A solution[10] to this problem was suggested by Dr. H. H. Hubbell, Jr.: Place an electrode in the reflected photon beam after it exits from the second chamber. Then, motion of the beam due to change in liquid level will shift the beam off the electrode, resulting in a change in the current of the photoelectrons emitted from it. Thus, a measuring of this current would monitor the liquid level. Unfortunately, the photon beam will also ionize the gas in the vicinity of the electrode, and positive ions will be collected which will look like photoelectrons emitted. That is, there will be a "background" ion current which would tend to mask the photoelectron current. A calculation of the total current as a function of pressure is plotted in Fig. 11.4 for two values of photoelectron yield – 0.01 and 0.001. At low pressures, the ion current is a small proportion of the total, and the latter is sensitive to liquid level. This is not true at higher pressures, so the method would not be useful.

The ion chamber was outfitted with this electrode, but results were inconclusive due to other problems. Apparently, the idea would be useful with low-vapor-pressure liquids but not with water or water solutions.

SUBMICRON PHYSICS

Physical studies of objects of sizes between 1 μ (10,000 Å) and molecular dimensions are exceedingly rare. This size range is interesting and important because here the concepts of solid-state physics metamorphose into those of molecular physics. Yet, the difficulty of dealing experimentally with holes, slits, cracks, cylin-

9. L. G. Canfield, G. Hass, and W. R. Hunter, *J. Phys. (Paris)* 25, 124 (1964).

10. H. H. Hubbell, Jr., private communication.

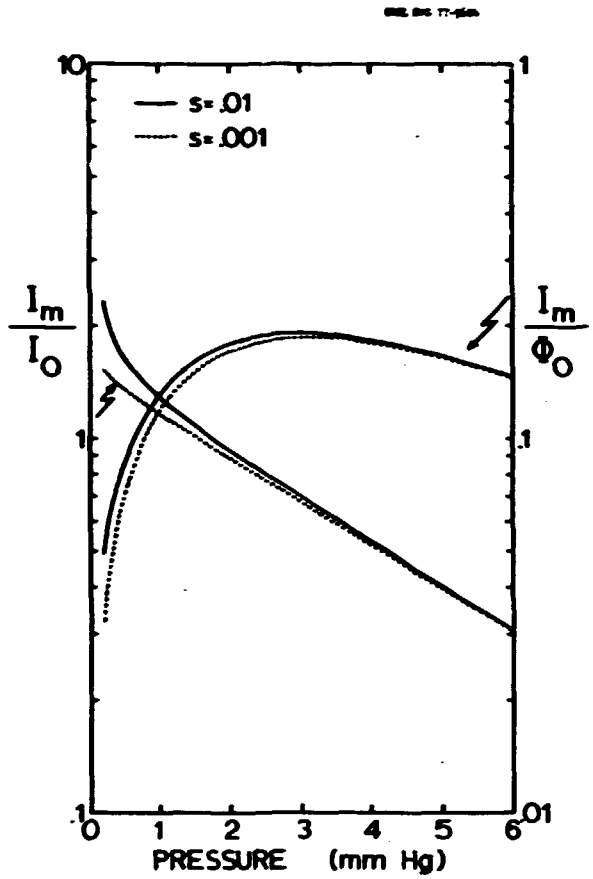

Fig. 11.4. Current to monitoring electrode as a function of pressure for photoyields of 0.01 and 0.001. Left scale measures ratio of monitor current to ion current I_o. Differences between dotted and solid curves show sensitivity of ratio to monitor current, and hence to cup position. Differences are measurable only for pressures $\lesssim 1$ torr. Right scale measures ratio of monitor current to light flux and is interpreted similarly.

ders, spheres, and fibers, which are usually visible only under the electron microscope, has evidently deterred experimenters almost completely. Nature and man furnish many examples of submicron objects, including interstellar dust, polar ice clouds, asbestos fibers, nuclear particle tracks, fiber-reinforced materials, nuclear dosimeters, antibody carriers, air and liquid micropore filters, information storage systems, nerve fibers, cracks, and macromolecules. The dimensions of these objects and their surfaces are equivalent to or less than photon wavelengths and absorption lengths, electron mean free paths, and surface wave attenuation lengths. Thus, submicron objects may possess unusual and unsuspected properties.

At ORNL, we are using nitrogen and dye lasers of high power (necessary because of the small target size) to study quantized electron energy states on metal cylinders of micron size. Also, we designed a low-divergence ($\sim 10^{-5}$ radian), low-energy (~ 1 eV) electron gun which we are using to study image potentials on these cylinders. In another part of the program we are studying electron transport through <1-μ holes and slits in thin films. A large submicron facility has been designed to incorporate all present experiments and some new ones in an ultrahigh-vacuum enclosure.

In what follows we will describe (1) experiments on electron transmission through pinholes, (2) determination of surface potentials on cylinders by electron scattering, and (3) generation of surface waves on cylinders by laser excitation.

Particle Interactions in Holes

One of the submicron structures accessible to physical investigation is the hole (micron-hole, pinhole, pore). Such features are found in biological systems, in membrane (micropore) filters, and in nuclear dosimeters. The mechanisms whereby these holes pass or collect aerosols, bacteria, viruses, and charged particles can only be speculated about at this time. We found we were able to produce holes and slits in any medium by using high-power lasers focused on targets by optical microscope objectives. A 500-kW N_2 laser, a 50-kW dye laser, and a 500-mW argon ion laser were used successively as we learned to produce smooth round holes of sizes down to 1 μ in thin films. An electron microphotograph of a typical hole is shown in Fig. 11.5. The hole is

PHOTO 0435-77

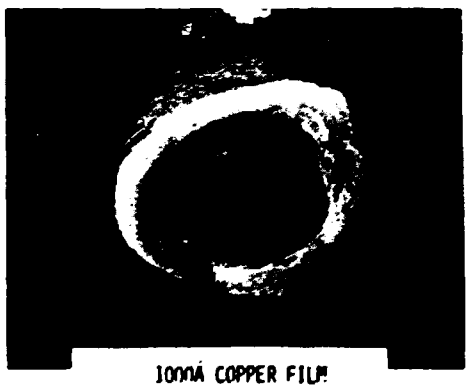

100Å COPPER FILM
SCANNING ELECTRON MICROSCOPE
MAGNIFICATION 5750X
HOLE DIAMETER 5μ

Fig. 11.5. Electron microphotograph of laser-drilled pinhole. Pinholes and slits as small as 1 μ can be drilled in any solid with either nitrogen, dye, or argon ion lasers.

about 5 μ in diameter and was drilled with an argon ion laser focused with a microscope objective. The film material is copper, about 1000 Å thick. From elementary optics, it can be shown that the diameter of the hole is the order of the product of lens focal length and angular divergence of the beam. Thus, the hole shown is of a size expected for a 5-mm focal length lens and a beam divergence of 1 milliradian. Further reduction in diameter is accomplished by using a shorter focal length lens and/or by vacuum evaporating film material into the hole-containing film.

To study electron deflection from fields in holes and near cylinders it was necessary to develop an electron gun which contained beam-defining apertures of micron size mounted 10 cm (10^5 μ) apart. These defined a beam monodirectional to about 0.05 milliradian or about twenty times more stringently collimated than the best laser. One can speculate on uses for such a narrowly collimated beam in the detection of weak electric and magnetic fields, in seismology and elsewhere. Beam energy can be varied from ~0.1 to 70 eV.

A special filament heating circuit (Fig. 11.6) was developed which produced zero magnetic field. Any residual field would have caused electron beam deflection which would have masked deflection due to fields within the holes. Power is derived from the ac line for both the filament current (right-hand circuit) and accelerating potential (left-hand circuit). The filament voltage is adjusted by a Variac in the primary of a 10-V filament transformer. Current for the filament is half-wave-rectified by the 6-A diode (IN1344) which heats the filament during the negative half ac cycle.

The line also supplies power to a step-up transformer (230 V rms) whose secondary is connected to a series array composed of a diode, a 7000-Ω current-limiting resistor, and a pair of 27-V Zener diodes in series. The voltage appearing across the diodes is impressed across a Helipot which provides an adjustable accelerating potential. A single power transformer may be used to supply both filament and accelerating potentials rather than the two transformers shown.

During the filament heating half cycle, the diode in the accelerating potential circuit is reverse-biased – that is, one side of the filament is at ground potential. If the accelerating circuit is connected to the proper side of the filament, the central, emitting part of the filament will be self-biased above ground by the heating current, thus suppressing emission.

When the ac line polarity changes, the heating current is cut off by the diode in the filament circuit. The voltage in the accelerating circuit now appears in part across the Zeners and Helipot. Thus the filament circuit is biased below ground, and electrons are accelerated toward the grounded electrode and its pinhole. Because the 325-V peak voltage developed by the transformer secondary is clipped to 54 V by the Zeners, the resulting pulse is very nearly rectangular in shape. The current emitted by the filament may be determined by monitoring the voltage appearing across the 100-Ω resistor in the ground return. Since the capacitance of the supplies to ground causes them to draw current through this resistor, it is important to keep its value small to minimize the resulting interfering signal. We have used a simple operational amplifier to amplify this signal,

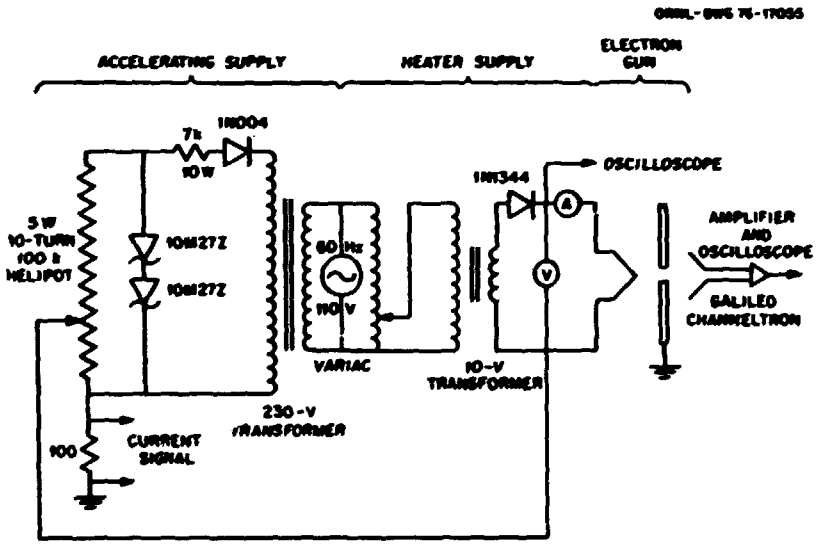

Fig. 11.6. Accelerating supply and heater supply. Signals derived from the line alternately heat the filament and extract electrons from it. Thus, there is no IR drop or magnetic field to cause energy spread in or deflection of the electron beam.

ORNL-DWG 76-17054

Fig. 11.7. Voltage waveform applied to filament (lower trace) and Channeltron pulses from emitted electrons (upper trace). Filament is alternately heated (rounded part of "square" wave) or has electrons extracted (negative square wave). Channeltron pulses show that electron emission occurs only during negative cycle.

which is then measured by a high-input impedance electrometer.

A photograph of an oscilloscope display of the filament voltage is shown in the lower half of Fig. 11.7. The negative-bias pulses are shown with the half-sine-wave heating pulses impressed between them. The upper curve is the output of a Galileo Channeltron which detects the electrons that have passed through the small pinhole adjacent to the filament. It is seen that electrons are transmitted only during the biased condition, not during heating.

We believe that the above simple circuit produces a filament with no magnetic field and no voltage drop and at little more cost or complexity than a conventional filament supply.

Successful operation of the electron gun meant that we could examine the angular distribution of electrons emerging from the second aperture. A Channeltron electron multiplier was again used as a detector. To increase the signal-to-noise ratio, the electron detector was mounted in an aluminum box having an entrance slit of adjustable width. The high-voltage feedthroughs were made of nonmagnetic materials with the complete unit being compatible with an ultrahigh-vacuum system for eventual inclusion in the ultrahigh-vacuum facility. It was necessary to build a metal screen to shield the electron beam from the high voltages on the Channeltron. The electron gun and the front of the Channeltron holder were gold-plated for more uniform surface potentials in the area of the electron beam. To study the scattering distribution of the electrons passing through the final pinhole of the electron gun, a system was designed to allow sweeping of the entrance slit across the electron beam in a uniform motion. The angular distribution of the scattered electron was measured for small pinholes in gold for electron energies between 0.5 and 20 eV.

Some sample data are shown in Fig. 11.8. The scattering is from a 3-μ-diam hole in a gold film. The ordinate $M(y, w)$ is the measured count rate for a slit located y(cm) above the center of the axially symmetric distri-

ORNL-DWG 77-10025

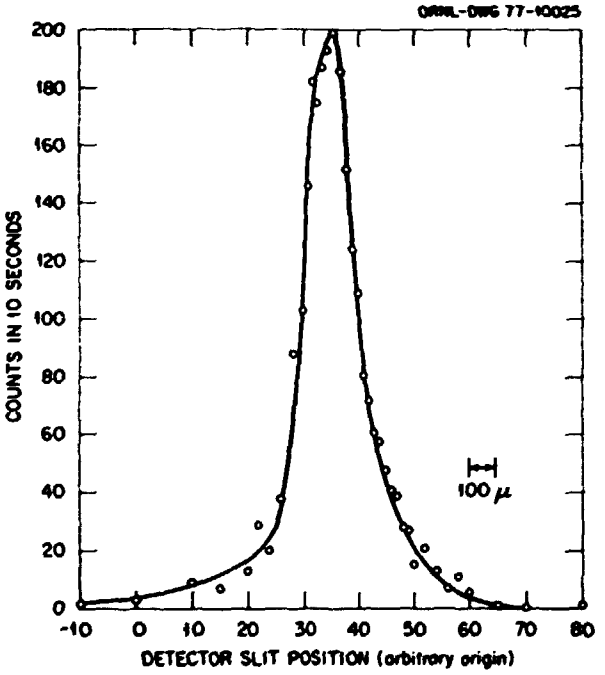

Fig. 11.8. Angular distribution of electrons scattered by pinhole. Ordinate is measured count rate of Channeltron located behind slit y centimeters off pinhole axis. Pinhole is 5 μ in diameter in 0.3-μ gold film and electron energy is 2.0 eV.

bution and of width $w = 69\ \mu$. The slit takes a horizontal cut through the distribution $N(\theta)$ of electrons incident on the plane of the slit. The derivation of the potential function $\Phi(\rho)$ within the pinhole from the observed count rate $M(y, w)$ is rather involved. From $M(y, w)$ we calculate the density of electrons (number per cm^2) incident on the detector plane, $I(r)$. This density is simply related to the angular distribution of electrons emerging from the pinhole and incident on the detector plane, namely, the function $N(\theta)$. When the latter is calculated, it is used to get the potential within the pinhole $\Phi(\rho)$.

The $I(r)$ distribution is related to the measured distribution $M(y, w)$ as follows. Consider an opaque straight edge that blocks all electrons from entering the detector between the axis ($y = 0$) and y as shown in Fig. 11.9. Then the number of electrons that strike the detector above y is:

$$\int_y^\infty 2 \int_0^{\cos^{-1}(y/r)} I(r)\, dr\, r d\phi$$

$$= 2 \int_y^\infty I(r) r \cos^{-1}(y/r)\, dr\,. \quad (2)$$

If another edge, extending from $(y + w)$ to ∞, is introduced, then the number of electrons that enter this slit so formed of width w is:

$$M(y, w) = 2 \int_y^\infty I(r) r \cos^{-1}(y/r)\, dr$$

$$- 2 \int_{y+w}^\infty I(r) r \cos^{-1}(y + w/r)\, dr\,. \quad (3)$$

The data of Fig. 11.8 were used in an iterative procedure to calculate $I(r)$ as above.

Note that the angular distribution $N(\theta)$ from the pinhole is related to the density distribution $I(r)$ at the detector plane:

$$N(\theta)\, d\theta = I(r)\, dr\,. \quad (4)$$

Since $r = B \tan\theta$, $N(\theta) = I(r)(dr/d\theta) = B \sec^2\theta I(r)$, where B is the distance between pinhole and detector plane. Thus, $N(\theta)$ may be quickly obtained from $I(r)$ just found.

In the pinhole we can equate the number of electrons in the cylindrical shell of radius ρ and thickness $d\rho$ with the number falling between the conical sheets defined by θ and $\theta + d\theta$. Thus,

$$N'(\rho)\, d\rho = N(\theta)\, d\theta\,. \quad (5)$$

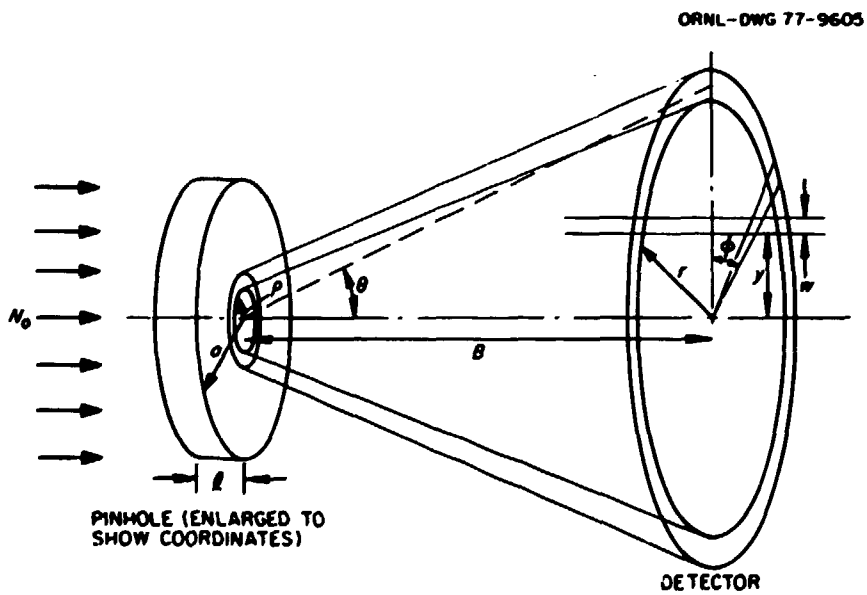

Fig. 11.9. Geometrical arrangement of pinhole (at left) and detector slit (at right). Electrostatic potential in pinhole is calculated from count rate of electrons passing through slit.

Noting that $N'(\rho)$ is given by

$$N'(\rho) = N_0 \frac{2\rho}{a^2} , \tag{6}$$

we can write

$$\frac{N_0}{a^2} \int_0^{\rho} 2\rho \, d\rho = \int_0^{\theta(\rho)} N(\theta) \, d\theta ,$$

or

$$N_0 \frac{\rho^2}{a^2} = \int_0^{\theta(\rho)} N(\theta) \, d\theta , \tag{7}$$

where N_0 is the electron current (assumed uniform) incident on the pinhole. Equation (7) can be solved for the $\theta(\rho)$ for any ρ.

We can relate this association between ρ and $\theta(\rho)$ to the potential $\Phi(\rho)$ in the following way. Let us assume that the equipotentials are coaxial cylinders lying completely within the pinhole and thus that there is no force on the electron when it is outside the pinhole. We assume that the electron will experience no radial displacement as it passes through the pinhole, confining its motion to one equipotential but receiving a radial impulse Δp. This impulse results in a change in electron direction θ. In the pinhole,

$$F = (-e)\left(-\frac{d\Phi}{d\rho}\right) = \frac{\Delta p}{\Delta t} = \frac{m(v \tan \theta)}{l/v} ,$$

where Δp is the radial momentum imparted to the electron, Δt is the transit time through the hole, v is the axial velocity, and l is the length of the pinhole. Thus,

$$d\Phi = \frac{mv^2}{el} \tan \theta \, d\rho . \tag{8}$$

Integrating between $\rho = 0$, where $\theta = 0$, and $\rho = \rho$, where $\theta = \theta(\rho)$, we have

$$\int_0^{\rho} d\Phi = \frac{mv^2}{el} \int_0^{\theta(\rho)} \tan \theta \frac{N(\theta)}{N'(\rho)} d\theta , \tag{9}$$

in which use has been made of the defining relation between incident and scattered distributions [Eq. (5)].

We have, finally,

$$\Phi(\rho) = \Phi(0) + \frac{Ea^2}{elN_0\rho} \int_0^{\theta(\rho)} \tan \theta \, N(\theta) \, d\theta , \tag{10}$$

where $\theta(\rho)$ is obtained from Eq. (7) and E is the kinetic energy of the electron.

The resulting potential is shown in Fig. 11.10, with the ordinate given in arbitrary units and the abscissa (the impact parameter measured from the edge of the pinhole) given in angstroms. The data should not be taken seriously because of uncertainties in pinhole shape and because of the approximate methods used to obtain the potential from the count rate. Nonetheless, the data represent a milestone in this research, demonstrating feasibility and indicating the kind of information we can obtain from this and similar experiments.

It is interesting to note that our data span all the functional forms of behavior for image potentials currently being advanced by theorists. The rounding off of the potential at distances close to the surface has been predicted by Ray and Mahan[11] and others. For greater distances, the classical r^{-1} behavior gives way to an r^{-2} dependence according to Ritchie[12] and Tomas and Sunjic[13] using a quantum approach. Still higher dependences are found from the analogy with the van der Waals interaction between a neutral atom and a dielectric surface.

Electron Scattering on Cylinders

Many of the submicron objects mentioned in the introduction to this section possess cylindrical symmetry. The physical and biological properties of such objects depend, in part, on the potential each exhibits: tendency to clump, to adhere to surfaces, or to collect other particles. Thus, a part of our program consists in measuring the electrostatic potentials of cylinders by scattering electrons off them.

Last year, we reported general calculations for the deflection of low-energy electrons by the cylindrical potential.[14] This year, in a feasibility study, we calcu-

11. R. Ray and G. D. Mahan, *Phys. Lett. A* 42, 301 (1972).
12. R. H. Ritchie, *Phys. Lett. A* 38, 189 (1972).
13. M. S. Tomas and M. M. Sunjic, *Phys. Rev. B* 12, 5363 (1975).
14. *Health Physics Div. Annu. Prog. Rep. June 30, 1976*, ORNL-5171, pp. 143–151.

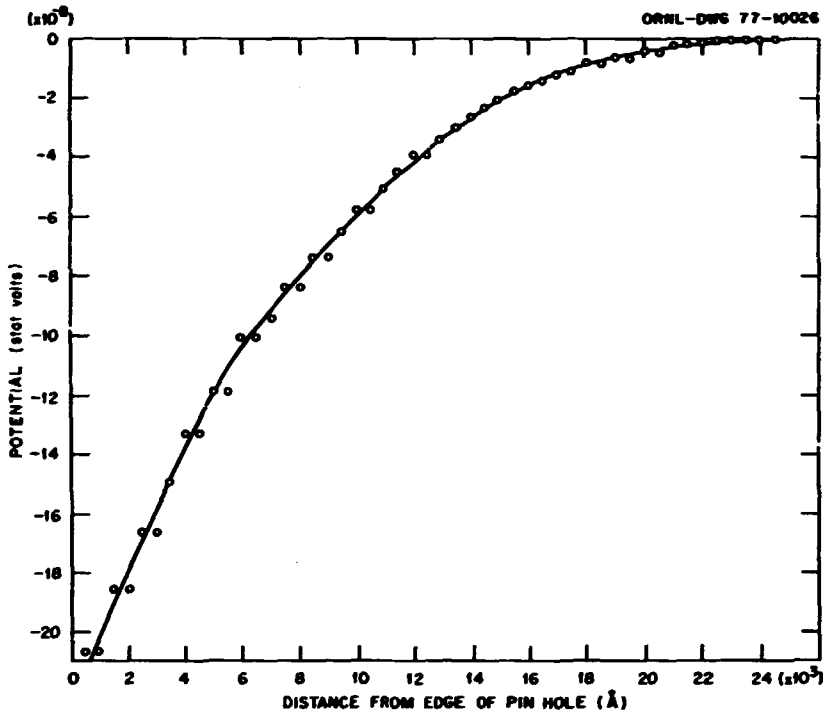

Fig. 11.10. Electrostatic potential within pinhole. From the early data we are unable to decide among various theoretical models for image potentials.

lated the deflection by the induced field due to the image charge set up by an electron passing near the cylinder. The geometry is shown in Fig. 11.11, and the dependence of deflection angle on impact parameter for a 1-μ fiber is shown in Fig. 11.12. It is clear that substantial angular deflection will be anticipated for impact parameters of a few microns. It is also clear that the incident electron beam will have to be collimated and positioned to submicron accuracy – hence the work in progress on a suitable electron gun.

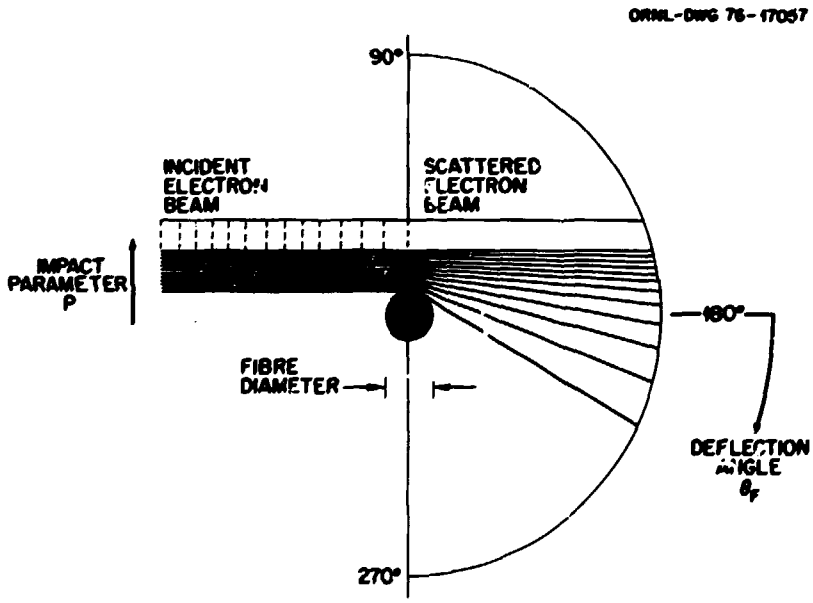

Fig. 11.11. Schematic of fiber-scattering experiment. 1-μ bundle of electrons is deflected by potential adjacent to fiber.

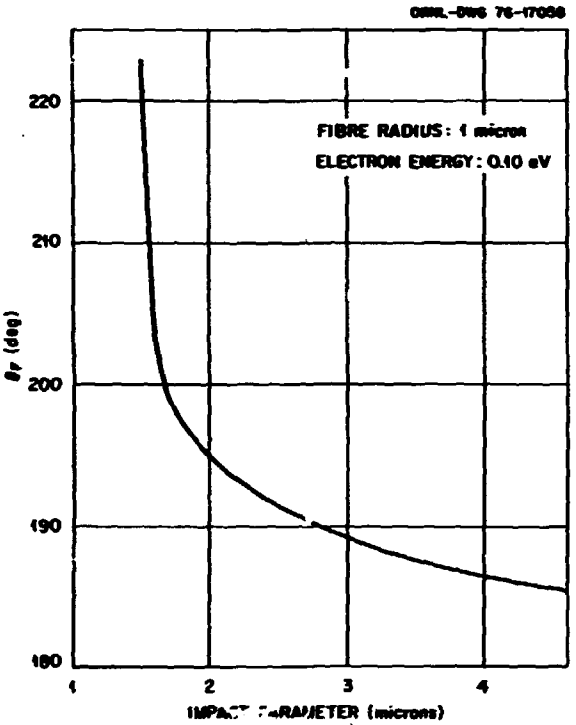

Fig. 11.12. Theoretical deflection of an electron beam by the image potential induced in a 1-μ fiber.

Work continued on developing a suitable vacuum facility to house the fiber and pinhole work. Delays in delivery severely slowed progress in the construction of this new ultrahigh-vacuum submicron research facility. The current status of each of the major subsystems and an estimate of the time required to complete construction and testing are: (1) The coater which will be used for in-situ deposition of various materials (metals, semiconductors, insulators) on single fibers and small apertures exists in a crude form in a bell jar coater and can be transferred to the new system when needed. (2) The altazimuth detector positioning system is complete and ready to mount in the system. (3) The cylindrical condenser scattering chamber has not been constructed. It should be ready for use in not more than nine months. (4) The electron gun–monochromator exists as a pinhole gun and is being tested. It can be installed in the new system on short notice. We are investigating two other sources of reasonably monoenergetic electrons for this application, the tunnel diode emitter and the laser-excited photocathode. (5) A cylindrical-sector electron energy analyzer has been acquired for the energy-loss measurements. This will be mounted on a rotary motion feedthrough and used with the pinhole gun for small-aperture scattering experiments even before the scattering chamber is complete. (6) The translatable carriage-mounted yoke and the associated guide-support rails are complete and will be mounted in the new system as time permits. (7) The pumping system for the new chamber is installed and the chamber is undergoing leak testing. (8) The Helmholtz coils are in place and in routine service for our preliminary experiments.

THEORETICAL CALCULATIONS OF PLASMONS AND SURFACE WAVES ON CYLINDERS

Our study of the theory and experiments on the scattering of light from small, metal-coated cylindrical fibers (0.1- to 10-μm radius) continued. Efforts were concentrated on extending the ranges of the variables for which the computer program could calculate the expected intensity of the scattered light and the relation of the scattering to plasmon effects in metals. The basic theory of the scattering of obliquely incident light by dielectric or metallic cylinders was developed by Wait[15] and considerably extended by Birkhoff et al.[16] The detailed equations are given in ref. 16 and in previous progress reports[17–19] and will not be repeated here. It is sufficient to point out that the various expressions for the scattering, absorption, and extinction of the light contain infinite sums of coefficients A_n and B_n. Each of these coefficients is a function of Bessel functions of order n, their arguments, and the angles of observation. The arguments, in turn, depend on the angles and on the optical constants of the cylinder and the surrounding medium. The computer program previously developed and discussed in refs. 16 through 19 was only satisfactory for low-order Bessel functions, for a small range of fiber radii around 1 μ, and for one experimentally usable material – aluminum – because aluminum has a single plasma resonance controlling the dielectric constants. The original program was written in straightforward fashion, following exactly the steps of the equations. In computer use, however, several problems arose which severely restricted its range of validity and its usefulness. The program was also very inefficient in its use of computer time since the same numbers were computed many times in the course of one run.

15. J. R. Wait, *Scattering from Cylindrical Structures*, Pergamon Press, New York, 1959.
16. R. D. Birkhoff et al., *J. Opt. Soc. Am.* 67, 564 (1977).
17. R. D. Birkhoff et al., *Health Phys. Div. Annu. Prog. Rep. July 31*, 1974, ORNL-4979, p. 137.
18. R. D. Birkhoff et al., *Health Phys. Div. Annu. Prog. Rep. June 30*, 1975, ORNL-5046, p. 148.
19. R. D. Birkhoff et al., *Health Phys. Div. Annu. Prog. Rep. June 30*, 1976, ORNL-5171, p. 153.

This greatly increased the cost and slowed the turnaround time.

Therefore, the program was extensively rewritten. First, a subroutine to permit the use of any pair of the optical constants n and k, ϵ_1 and ϵ_2, or plasma frequency and damping was developed and inserted. Previously, only the free electron gas-plasmon model was used, but there are relatively few materials for which this is even approximately correct. The new routine permits the use of experimentally derived optical constants, or the plasmon model, or any other values desired.

Next, it was discovered that only a very narrow range of fiber radii could be used in the program, because, outside this range, either the values of the Bessel functions exceeded the capacity of the computer ($\sim 10^{74}$) or their products used in the equations got too large.

Further, it was found that the recursion formula used to obtain higher-order Bessel functions determined them as small differences between large numbers so that successive steps gave errors increasing exponentially with each increase in order. Beyond about order 4 or 5, the Bessel functions J_n were meaningless. This phenomenon is well known among those familiar with both Bessel functions and computers, but became known to us only after consultation with various ORNL staff members.

To circumvent the second problem, many unsuccessful attempts were made to write programs to calculate the Bessel functions of all orders up to about 60 and large, real arguments up to about 300. Finally, a program by Gautschi was found in the literature[20] and another in the computer library[21] which gave all desired orders of the J_n functions for the range of real arguments wanted, producing values agreeing with existing tables in the limited range where tables exist. Therefore, we must assume that the values beyond the range of the tables are correct.

The two programs agreed with each other in all aspects. At the suggestion of J. H. Marable (ORNL) a different system was used for Bessel functions of complex arguments. Ashley's equations, as given by Birkhoff et al.,[16] for the coefficients involve ratios of Bessel functions such as $J_n'(u)/[uJ_n(u)]$, where u is a complex number derived from the complex dielectric constant and the angles used, and the prime means the derivative with respect to the argument. The properties of Bessel functions enable one to express this ratio in terms of the ratio $J_{n+1}(u)/J_n(u)$. The recursion relations permit one to write this as a convergent continued fraction, which one iterates until it converges. This ratio is then the ratio sought for the highest-order n needed, and the lower orders can be calculated correctly by backward recursion. The values were checked for the lowest orders from tabulated values; they agreed to 10 significant figures, the limit of the tables. The ratios also were calculated directly from the Bessel J_ns derived from the Gautschi program, and the values agreed. But Marable's technique was much simpler and faster. We now feel that these numbers are correct.

To remove the problem of overflow of too-large numbers, the equations for the coefficients were rewritten in terms of ratios of the Bessel functions $J_n(v)/Y_n(v)$. Since it is the Bessel function of the second kind, $Y_n(v)$, that becomes very large for small v, this procedure made the ratios go to zero so the term in question would vanish. Care had to be taken to be sure the zeros never appeared in the denominator of any term.

Comparison of Cylinder Theory with Experiments

The complete program is now running and we are beginning to get results to compare with other theories in the literature, with our earlier calculations, and with our experimental data. Our usual method of determining fiber radii has been to obtain the Fraunhofer diffraction pattern from the fiber placed perpendicular to the laser beam. Simple wave theory then gives the radius for an opaque cylindrical obstacle as $R = \lambda/(2 \sin \theta)$, where λ is the wavelength and θ is the angle from the direct beam to the first diffraction minimum. For values such as λ = 6328 Å and R = 0.54 μm, the angle θ = 35.90°.

For a silver-coated cylinder, our calculation gives the angle at the first minimum as 24° (Fig. 11.13) and for an aluminum-coated cylinder, 23° (Fig. 11.14). These values are only two-thirds of those the simple equation predicts and hence our approximate radii were too large. This correction in radius will be quite important in future calculations.

We also ran the calculation for the experimental parameters used by Miziumski,[22] namely, an aluminum-coated fiber of 29-μm radius irradiated with a helium-neon laser at 6328 Å. None of the intensity minima reported by Miziumski showed up on the calculated plot. The program was run using the measured optical constants reported by Hagemann, Gudat, and

20. W. Gautschi, *Commun. ACM* 7, 479 (1964).
21. Argonne National Laboratory, Applied Math Division, Program Library, ANL C370S Program BESJY.
22. C. Miziumski, *Phys. Lett. A* 40, 187 (1972).

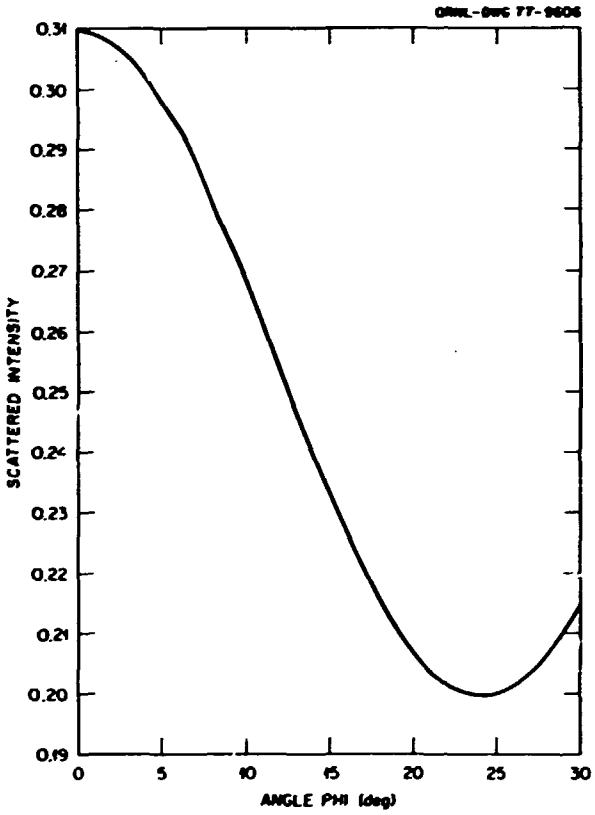

Fig. 11.13. Calculated diffraction pattern for silver-coated fiber. *Red light (6328 A) is incident perpendicular to a silver-coated quartz fiber of 0.54-μm radius. Light is polarized perpendicular to the fiber axis. The pattern resembles Fraunhofer diffraction, but the minimum is at a smaller angle.*

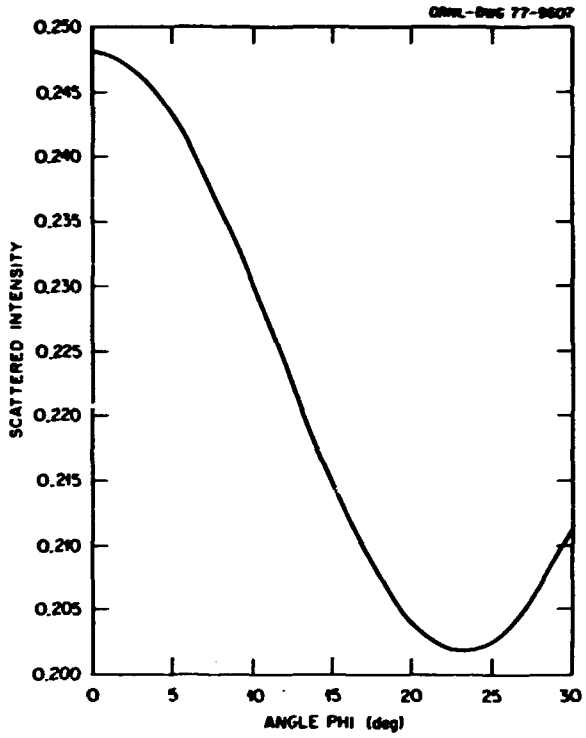

Fig. 11.14. Calculated diffraction pattern for an aluminum fiber. Red light (6328 A) is incident perpendicular to the fiber. The minimum is at a different angle from that for silver (Fig. 11.13) or the Fraunhofer pattern minimum.

Kunz[23] and also with the optical data Miziumski used, namely, a plasma resonance wavelength of 828 Å and no damping. In our calculation with no damping, the detailed figures for the denominator factor in the equation for the scattering-term coefficients show slight evidence of minima for orders 41 to 53, but the total sum of all the coefficients for all orders up to 60 shows only a smooth variation. Miziumski reported small, sharp minima for orders 55 to 59, but we feel there is an error in his calculation. In any case, a calculation with no damping is quite unrealistic.

Other preliminary calculations indicate only a smooth variation of the integrated scattered radiation intensity, in agreement with our recent observations which show no significant structure in the integrated light-scattering curves as a function of the angle of incidence between the laser beam and the fiber axis. This result is in marked contrast to our earlier observations[16–19] of strong maxima and minima in the differential scattered intensity at the point 180° from the undeviated laser beam. This structure in the differential curves checked very well with the older calculated values for low-order Bessel functions.

Since our dye laser now permits taking scattering data as a function of wavelength, the calculation was run over the range of wavelengths covering the apparent plasma resonance in silver (Fig. 11.15). The curve closely resembles the usual reflectance curve for silver for a plane surface as given by Hagemann, Gudat, and Kunz.[23]

Extensive further calculations and experiments are in progress in our continuing effort to understand plasmon and other solid-state effects by the use of light scattering from metals.

23. H.-J. Hagemann, W. Gudat, and C. Kunz, *Optical Constants from the Far Infrared to the X-Ray Region: Mg, Al, Cu, Ag, Au, Bi, C, and Al_2O_3*, DESY SR-74/7, May 1974.

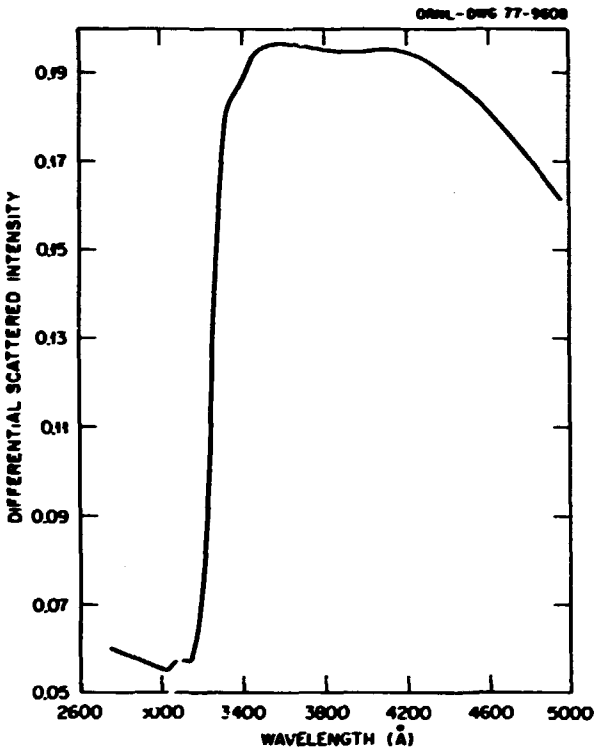

Fig. 11.15. Calculated intensity of light scattered from a silver fiber. Light is polarized parallel to the axis of the 0.54-μm-radius fiber at a point opposite to the undeflected light spot on the ring of scattered light. Light was incident at 11° to the fiber axis. Pattern resembles the usual reflectance curve for silver.

Part III. Chemical Physics and Spectroscopy

W. R. Garrett

12. Atomic Physics and Laser Research

G. S. Hurst
M. G. Payne
S. L. Allman
C. H. Chen
C. W. Choi[1]
L. W. Grossman[1]
Ray Hefferlin[2]
J. P. Judish
S. D. Kramer
T. G. Miller[3]
M. H. Nayfeh
J. E. Parks[2]
M. G. Payne
J. P. Young[4]

During the past year, the Atomic Physics and Laser Research Program was highlighted by several important developments. The accelerator program continued to be productive in the areas of energy pathways and their applications for the detection of low levels of pollution and for applications to excimer lasers (ArF, KrF, and XeF). New theories on multiphoton ionization were widely accepted and resulted in several invited papers. Finally, we were pleased that one-atom detection reached maturity, and even one-molecule detection was shown to be feasible.

ONE-ATOM DETECTION AND RESONANCE IONIZATION SPECTROSCOPY

Demonstration of One-Atom Detection

Resonance ionization spectroscopy (RIS), a photoionization method in which all of a given quantum-selected species is converted to ion pairs, was used to develop a detector for a single atom. We demonstrated the detection of one atom by using a pulsed dye laser to photoionize cesium to saturation and a proportional counter for the detection of single electrons. Some current applications, for example, the slow transport and chemical reactions of atoms, are briefly discussed.

A technique for identifying and counting small numbers of atoms would have far-reaching applications in nearly all the sciences. Although the need predates Democritus (400 BC), only in recent years was it possible to detect as low as 100 atoms/cm^3, and this by cw resonance fluorescence[5] requiring a steady-state concentration of atoms. We report here a time-resolved method for detecting one atom of a specified type in a defined volume of space. Our development of one-atom detection coincides with the current importance of detecting rare events, for example, quarks,[5] solar neutrinos,[6] and superheavy elements.[7]

Previously we developed[8,9] a photoionization method [resonance ionization spectroscopy (RIS)] for the complete conversion of a quantum-selected excited population to ionization, making possible sensitive and

1. Graduate student, University of Kentucky, Lexington.
2. Consultant.
3. On assignment from Redstone Arsenal, Huntsville, Ala.
4. Part time, Analytical Chemistry Division.
5. W. M. Fairbank, Jr., T. W. Hänsch, and A. L. Schawlow, *J. Opt. Soc. Am.* 65, 199 (1975) and references therein.
6. M. S. Freedman et al., *Science* 193, 1117 (1976).
7. R. V. Gentry et al., *Phys. Rev. Lett.* 37, 11 (1976).
8. G. S. Hurst et al., *Phys. Rev. Lett.* 35, 82 (1975).
9. M. G. Payne et al., *Phys. Rev. Lett.* 35, 1154 (1975).

absolute measurement of the selected population in a gas. Laser pulses of about 1 J/cm^2 of beam area were shown to saturate.[8,9] To detect atoms in their ground states, it is often advantageous to use two lasers; photons of energy $h\nu_1$ promote from a ground state to a low-lying excited state, then photons of energy $h\nu_2$ promote to a higher-lying bound state. In the RIS technique, at least one of the photons must ionize the higher excited state. Gas proportional counters or evacuated electron multipliers will detect one electron; thus, in principle, RIS can be extended to one-atom detection.

In cesium, the transition $6^2S_{1/2} \rightarrow 7^2P_{3/2}$ (4555 Å) can be excited with pulsed dye lasers. Since these photons will also ionize the $7P$ level, only one laser is required for photoionizing cesium from the ground state. The photon fluence (ϕ) required for saturation can be calculated from measured[10] photoionization cross sections (σ): 8.8×10^{-18} cm^2 for the above transition. At 4555 Å, 1 J = 2.4×10^{18} photons; to make $\sigma\phi = 2.4$ (i.e., 90% ionization) requires 100 mJ/cm^2. The light source used in this work is a flashlamp-pumped dye laser.[11] It has a beam divergence of 1 milliradian, a diameter of 3 mm, a linewidth (FWHM) of about 0.7 Å, and a pulse width (FWHM) of 2 μsec. About 1-mJ pulses are obtained at 4555 Å (15 mJ/cm^2); therefore, 100 mJ/cm^2 requires modest focusing.

Since we anticipated certain applications, we elected to carry out the demonstration of one-atom detection with a proportional counter (Fig. 12.1). It was made of brass and gold plated; field tubes defined a wire length of 12 cm. With P-10 gas (90% Ar + 10% CH_4) at 100 torr, the gas amplification was about 10^4 when the wire (2 mil in diameter) was at +1000 V. To prevent capture of the free electrons to electronegative molecules such as O_2, the P-10 gas was pumped through the counter. Arbitrarily low concentrations of cesium in the laser beam can be prepared in the following way. A cesium source is situated as shown in Fig. 12.1 so that the distance from source to beam can be adjusted. Whenever highly reactive atoms, such as cesium, are at very low concentrations in a counting gas, the steady-state concentration may be determined by a transport process rather than by thermodynamic equilibrium. In the transport process, the diffusion time for cesium is about 0.5 sec/cm of distance when the counting gas pressure is 200 torr. In 0.5 sec most of the cesium atoms react with traces of impurity molecules, even if the concentration of the latter is less than 10^{-7} in the counting gas. We take advantage of these transport properties to control the concentration of cesium atoms in the beam simply by changing the counting gas pressure or the source-to-beam distance.

To obtain sufficient fluence (ϕ) to saturate, the 3-mm-diam laser beam was focused below the center of the counter wire by using a lens of 25-cm focal length. With 1-milliradian divergence, the beam focused to 0.025 cm in diameter and was about 0.10 cm in diam-

10. H. D. Zeman, pp. 581–94 in *International Symposium on Electron and Photon Interactions with Atoms*, H. Kleinpoppen and M. R. C. McDowell, eds., Plenum Press, New York, 1974.

11. We used a linear flashlamp-pumped dye laser, model CMX-4, Chromatix Corp., Mountain View, Calif.

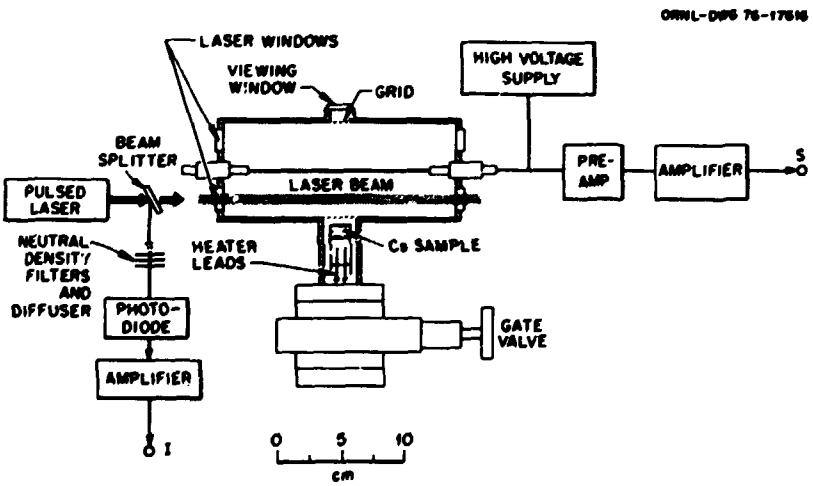

Fig. 12.1. Schematic of the experimental arrangement. The function $S(I)$ was plotted directly with a two-parameter MCA, and the pulse-height distribution $N(S)$ was plotted with a one-parameter MCA gated with the condition $I > I_{min}$.

eter under both ends of the counter wire, creating a volume of about 5×10^{-2} cm^3. Under these conditions and with the field tubes decoupled from the wire to suppress photoelectrons from the quartz windows, there was no measurable photoelectron background. Backgrounds due to external radiations, such as cosmic rays, were eliminated by using electronic time-gating techniques.

The data in Fig. 12.2 (100 torr) show the function $S(I)$, that is, the proportional counter pulse height S as a function of laser energy per pulse I. Its asymptotic behavior at large I indicates saturation. Moreover, extensive studies demonstrating saturation were made in the proportional counter and in a parallel-plate ionization chamber filled to 1 atm of argon. In Fig. 12.3 we plot a pulse-height distribution for a large number of cesium atoms with the condition that the laser always saturated the ionization. From the known fact that each 6.4-keV x ray produces 250 electrons in P-10 gas, we find that the cesium peak in Fig. 12.3 corresponds to 1.4×10^4 cesium atoms. Similar distributions were measured for populations of 10^2 to 10^6 atoms. One electron in a proportional counter produces an exponentiallike pulse-height distribution (e.g., ref. 12). Figure 12.4 was obtained by using a mercury lamp to release single photoelectrons from the inner walls of the counter at a low rate. With the cesium sample in its lowest position and a gas pressure of 200 torr, we obtain a nearly identical distribution due to the ionization of a cesium atom. In Fig. 12.4 the fluctuations in the distributions are due

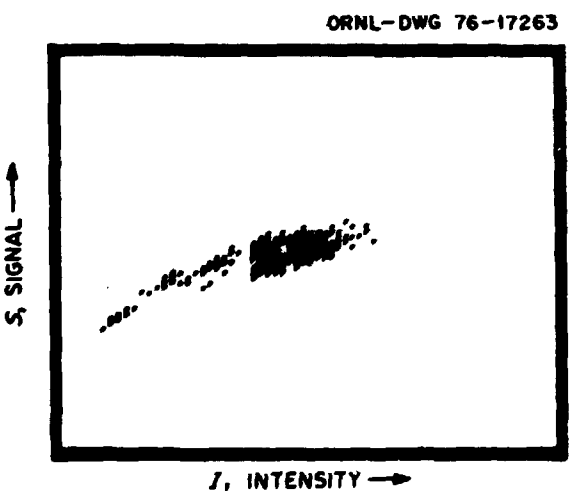

Fig. 12.2. Two-parameter plot of the pulse height from the proportional counter vs laser intensity. Saturated signal corresponded to about 1.4×10^4 atoms. At the higher intensity, additional counts were acquired to obtain the pulse-height distribution shown in Fig. 12.3.

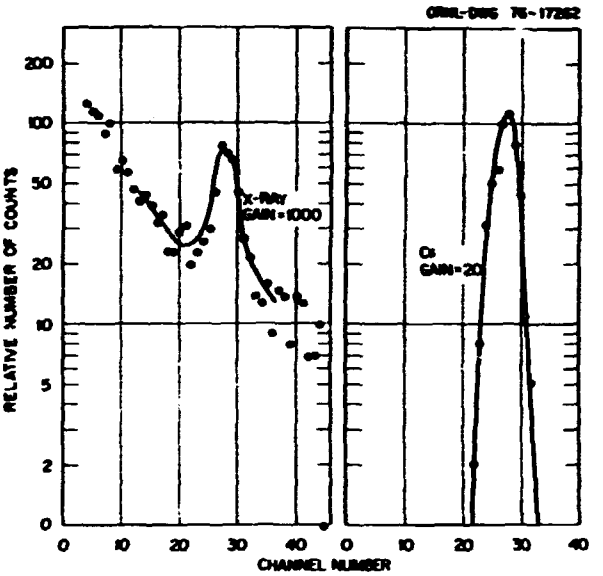

Fig. 12.3. Pulse-height distribution of signals corresponding to Fig. 12.2. Only the high-intensity part of the distribution, where the ionization was saturated, could gate the MCA. Comparison of the cesium atom peak is made with a 6.4-keV x-ray peak (^{57}Co).

to counting statistics, which do not reflect uncertainty in the total number of atoms counted. By integrating the total number of pulses produced above the normal electronic and laser transient noise, we find that it is not difficult to count directly 95% of the one-atom pulses. At all population levels, including one atom, we observed that the signals vanished when the laser was detuned from the cesium transition.

Our demonstrated method of one-atom detection can be extended to a variety of atoms in a variety of instrument configurations, including the use of more than one laser. The method is extremely selective. We have shown that one atom in an environment of 10^{19} atoms or molecules of another kind can be measured, and we do not believe this to be a limit. Pulsed lasers can be triggered in some known time relationship with either periodic or random external events; thus, one-atom detection can incorporate time resolution. Applications may include the detection of daughter atoms from radioactive decay, characterizations of a few atoms of the higher actinides, the discovery of new elements, slow evaporation of atoms from surfaces, slow transport processes, and the rate of reaction of the elements in various chemical environments. Analytical applications can be made even with molecular substances, for

12. H. Genz, *Nucl. Instrum. Methods* 112, 83 (1973).

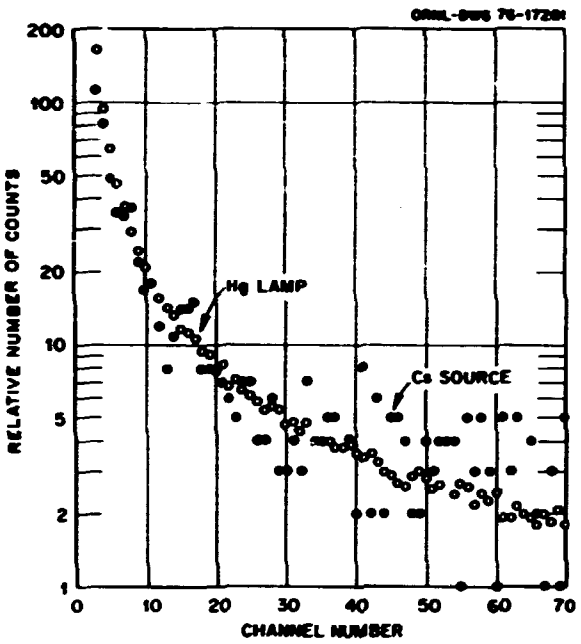

Fig. 12.4. Pulse-height distribution for the case where one cesium atom was counted per 20 laser pulses, compared with a one-electron distribution produced by an incoherent light source. Sensitive volume was 0.05 cm³ per laser pulse. With available lasers, the volume per pulse could be greater than 100 cm³.

example, the classification of a compound by dissociation and subsequent identification of resultant atoms. We are now pursuing several of these applications.

We are pleased to acknowledge the expert work of R. E. Zedler, ORNL Instrumentation and Controls Division, on many aspects of our one-atom detection program.

Density Fluctuation Studies Using One-Atom Detection

A new measuring technique which can detect a single atom of a given kind, even in the presence of 10^{19} or more atoms of another kind, with good space and time resolution, was used to study the density fluctuation of less than 100 cesium atoms in a small volume of space filled with inert gases. Repeated measurements of the absolute number of atoms in a defined volume at an arbitrary time were recorded for the first time in order to obtain a statistical distribution giving the fluctuation of the number of atoms around the mean value.

A method for selective counting of free atoms down to the one-atom level has been an outstanding need in all of modern science. Recently, we briefly reported on such a method;[13] here we show one interesting application: a direct measurement of the density fluctuation of free atoms.

In our method, a laser is pulsed into a defined volume of space at any arbitrary time. All atoms within the volume at that time are ionized and recorded. Thus, time-resolved one-atom detection requires pulsed lasers; on the other hand, cw lasers would most appropriately be used to sample a steady-state concentration of atoms. To illustrate this fundamental nature of the new method, we report the first direct study made on the fluctuation of free atoms in a small volume of space. Previously, density fluctuations could only be deduced from such phenomena as Brownian motion or Rayleigh scattering.[14]

Because we are interested in a direct study of the fluctuation of a few atoms and, in particular, the detection of a single atom, it is necessary to understand how to control the population of the atoms to be detected as they diffuse through a gas containing a much larger number of inert atoms or molecules. Interesting questions arise as a consequence of the present technique in which a ground-state population of atoms in a laser beam is totally removed during a short laser pulse. For instance, do atoms diffuse into the laser beam (radius r) during the pulse? We take for D_1 (the diffusion coefficient at 1 atm), 0.25 cm²/sec, which is the measured value[15] at low concentrations of rubidium in argon, as representative of an alkali atom in an inert gas, since data for cesium-argon are not available. The mean spread, x, of atoms due to diffusion in an infinite space is given by

$$x^2 = 4D_1(760/P)t \ , \qquad (1)$$

where x is in cm, t is in seconds, and P is the pressure in torr. Let us put $x = r/20$, to get a 10% effect, and take $r = 0.1$ cm. For a pulse duration of 10^{-6} sec, $P = 30$ torr; thus, only below this pressure would atoms diffusing into the beam contribute more than 10% to a signal during a laser pulse. A related question is: At what pressure would diffusion be too low to refill the laser volume between pulses? With t in Eq. (1) equal to the period between pulses, for example, 10^{-1} sec and $x = 2r$, then $P = 1900$ torr. Therefore, to avoid this effect, the gas pressure should be kept below 1 atm.

13. G. S. Hurst, M. H. Nayfeh, and J. P. Young, *Appl. Phys. Lett.* 30, 229 (1977).

14. R. D. Present, *Kinetic Theory of Gases*, McGraw-Hill, New York, 1958, pp. 157–77.

15. W. F. Franzen, *Phys. Rev.* 115, 850 (1959).

The slow rate of diffusion of an alkali atom in an inert gas can cause enormous ground-state chemistry effects during the transport of the alkali atom from the source to a laser beam. Consider the transport of atoms evaporated from a small source at a rate of S_0 atoms per second which leak into an infinite hemisphere filled with an inert gas. At a distance R much greater than the source dimensions, one finds for the concentration of atoms,

$$\rho_0 = \frac{S_0}{4R^2\bar{v}}, \tag{2}$$

where $\bar{v}$ is the speed of the alkali atom. One can calculate S_0 per unit source area from vapor pressure data;[16] for cesium, we find 5×10^{14} atoms cm^{-2} sec^{-1} at 300°K. When $R = 2$ cm, one finds $\rho_0 = 4 \times 10^8$ atoms/cm^3 above a source 1 cm^2 in area. If cesium reacts chemically, the concentration is reduced to ρ, where

$$\rho = \rho_0 e^{-\sigma_i \rho_i \bar{v} t}, \tag{3}$$

and where σ_i is the cross section for cesium to react chemically with an "impurity" at concentration ρ_i; t is the time for cesium to diffuse from the source to the laser beam. From Eq. (1) we find t to be about 4 sec for a distance of 2 cm and for the inert gas pressure equal to 760 torr. To ensure that the exponential argument is no more than 1 requires that ρ_i be less than 3×10^{11} cm^{-3} (for $\sigma_i = 5 \times 10^{-17}$ cm^2), which is an impurity level less than 1 part in 10^8 at 1 atm. In normal circumstances, when one must have large concentrations, the above discussion points out the necessity for ultraclean systems. However, here we take advantage of the process as a means of preparing a very small concentration of atoms for one-atom demonstrations and for fluctuation studies.

To demonstrate one-atom detection and to provide a method for observing density fluctuations, a proportional counter (see above) was used as the electron detector.

Calibration of the proportional counter was done at the one-electron level by illuminating the walls with a mercury pen lamp, thus releasing single electrons from the walls at a very low rate. Calibration at the 250-electron level[17] was achieved by placing a weak ^{57}Co source [giving Fe($K\alpha_1$) x rays at 6.4 keV] just inside the window. The argon escape peak at 3.44 keV provides another calibration at the 130-electron level.

In the proportional-counter experiments, we focused the laser beam below the center of the wire and directly above the cesium source with a lens of 25-cm focal length. With 1-milliradian divergence, the beam focused to a 0.025-cm diam and was about 0.10 cm in diameter under both ends of the counter wire, creating a volume of about 0.05 cm^3.

A particularly interesting pulse-height distribution is shown in Fig. 12.5. We recall that the laser samples a small volume of space (0.05 cm^3), and from every atom therein an electron is ejected and counted. Furthermore, for a range of counting gas pressures, the time for diffusion of cesium atoms into the sensitive gas volume is much greater than the time width of the laser pulses and is much less than the time between laser pulses. With these conditions, one may visualize the process of sampling as the successive emptying and refilling of a small volume surrounded by an infinite source of free atoms. By x-ray calibration we find that the distribution in Fig. 12.5 peaks at 67 atoms and that the fluctuation is considerable. We conclude, therefore, that in Fig. 12.5 we see the fluctuation of atoms in a fixed volume of space. These fluctuations were not previously observable but were deduced from such experimental observations as Brownian motion and the scattering of light.[14]

To analyze the fluctuations in Fig. 12.5 quantitatively, we turn to the proportional-counter literature

16. Saul Dushman, *Scientific Foundations of Vacuum Techniques*, Wiley, New York, 1949, p. 20.

17. The mean number of electrons produced in the x-ray peaks is found by using a "W value," that is, mean energy to form an ion pair, equal to 26 eV. See C. E. Melton, G. S. Hurst, and T. E. Bortner, *Phys. Rev.* 96, 643 (1954).

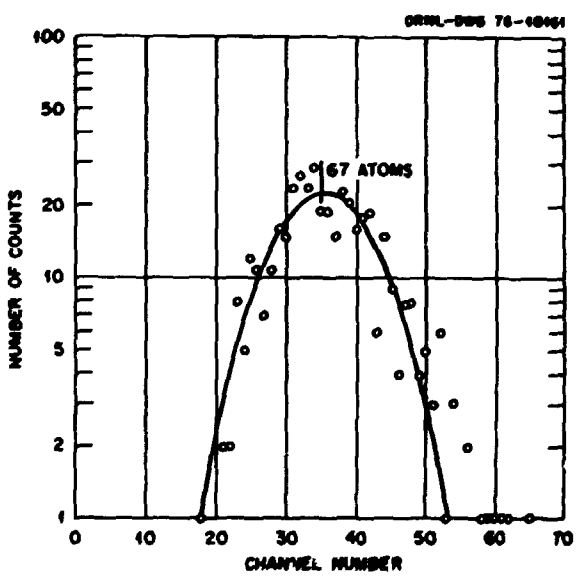

Fig. 12.5. Pulse-height distribution when most probable number of cesium atoms is 67.

involving the Fano factor.[18] The mean number of initial ion pairs produced, $\bar{N}$, is related to the mean pulse height, $\bar{P}$, and the mean gas amplification, $\bar{A}$, by the following:[18]

$$(\sigma_P/\bar{P})^2 = (\sigma_N/\bar{N})^2 + 1/\bar{N}(\sigma_A/\bar{A})^2 \ , \qquad (4)$$

where $\bar{P} = \bar{N}\bar{A}$ and σ_N, σ_P, and σ_A are the standard deviations of the indicated quantities. Normally, Eq. (4) is used to evaluate fluctuation of ionization for fixed energy losses in a proportional counter, in which case the σ_N is smaller than that due to random events,[19] a fact that leads to the Fano factor. Here we have a rather different point of view; namely, we assume that σ_N is the standard deviation for the spatial fluctuation of the free atoms of cesium, and for a measured $\sigma_P/\bar{P}$ we can calculate $\sigma_A/\bar{A}$. A Gaussian function was fitted to the data in Fig. 12.5 for which $\sigma_P/\bar{P}$ is 0.209. Assuming that the free atoms in space obey binomial statistics for random events, $(\sigma_N/\bar{N})^2$ is just $1/\bar{N}$ and $\sigma_A/\bar{A} = 1.39$. By comparison, the most elementary theory of the gas amplification process predicts that $\sigma_A/\bar{A} = 1$, whereas deductions[20] from experimental data suggest values somewhat less than 1. From the analysis we conclude that the fluctuation of the number of atoms in a specified volume of space is consistent with a random distribution described by Poisson statistics. Furthermore, we believe that the method described here can help to obtain improved experimental estimates of the Fano factor, because $\sigma_A/\bar{A}$ can be determined quite directly from the laser ionization measurements.

Collisional Line Broadening by Two-Photon Ionization

We report on a photoionization method which allows (with extreme sensitivity and simplicity) measurements of line broadening on the very far wing where absorption and fluorescense become extremely small. The method involves the conversion of essentially every absorption event of a colliding system to an ion pair in a two-photon ionization process. Thus, we avoid measurements of small numbers of absorbed or emitted photons in favor of the much more sensitive detection of free electrons. Previously, we have used this scheme, which we call resonance ionization spectroscopy (RIS), in measuring absolute populations and lifetimes of excited states[8,9] following charged-particle excitation of helium gas. Moreover, we recently used the RIS method in achieving detection and identification of single atoms[13,21] by using the two-photon ionization process in a proportional counter. The sensitivity and convenience[22,23] of the ionization channel have also been realized in studies of high Rydberg states and quadrupole transitions.[24]

Previously, line broadening by foreign gases was studied by absorption[25] and fluorescence.[26–28] In these studies, high-temperature absorption tubes are required to induce appreciable absorption or fluorescence. Dense samples not only introduce self-broadening but also dimer absorption. Moreover, high-pressure buffer gases can make three-body collisions wash out the satellite structure otherwise observable in the two-body collisions. The extra sensitivity achieved in the ionization method, however, will allow measurements at the very far wing of optically thin samples where the higher density problems are eliminated; this promises complete resolution of the satellites.

The present studies are also of particular interest to single-atom detection in gas proportional counters since noble gases are frequently used in the counting gas mixtures.[13,21] Specifically, the broadening and shift of the atomic line by the foreign gas will reduce the selectivity due to overlap of nearby levels of some other atomic species. Line broadening work is even more important to studies of low-level analysis where isotope discrimination is required.

In this experiment, we studied the two-photon ionization of cesium-argon mixtures with the broadened Cs(7*p*) as an intermediate state. Since Cs(7*p*) lies more than halfway to the ionization limit, two photons at 455 nm can photoionize the cesium ground states. To eliminate the effects of dense samples and high-pressure buffer gases, we studied the process with cesium densities of the order of 10^9 per cm^3 at 760-torr buffer gas pressure. The two-photon ionization line shapes and thus the absorption line shapes were measured as a func-

18. J. L. Campbell and K. W. D. Ledingham, *Brit. J. Appl. Phys.* 17, 769 (1966).
19. U. Fano, *Phys. Rev.* 72, 26 (1947).
20. G. D. Alkhazov, *Nucl. Instrum. Methods* 89, 155 (1970).
21. G. S. Hurst, M. H. Nayfeh, and J. P. Young, *Phys. Rev. A* 15, 2283 (1977).
22. S. M. Curry et al., *Opt. Commun.* 16, 251 (1976).
23. M. G. Littman et al., *Phys. Rev. Lett.* 36, 788 (1976).
24. M. Lambropoulos et al., *Phys. Rev. Lett.* 35, 159 (1975).
25. D. G. McCartau and J. M. Farr, *J. Phys. B* 9, 985 (1976) and references therein.
26. R. E. M. Hedges, D. L. Drummond, and A. Gallagher, *Phys. Rev. A* 6, 1519 (1972).
27. F. H. Mies, *J. Chem. Phys.* 48, 482 (1968).
28. J. M. Farr and W. R. Hindmarsh, *Phys. Lett.* 27A, 512 (1968).

tion of laser field intensity. From the absorption line profile, the form and coefficient of the interaction forces between the colliding atoms were found.

A theoretical model for the two-photon ionization process based on the rate equations was developed. The model involves the ground state 6s, excited state 7p, and the radiatively populated 5D state. Figure 12.6 shows the power dependence of the ionization yield at line center and at 29, 46, and 77 Å detunings from the isolated atom line. The power dependence predicted by the above theoretical model is also shown in Fig. 12.6. Figure 12.7 shows the two-photon ionization line shape at 2.5×10^{18} photons/cm^2 power level along with the theoretical fit. Both Figs. 12.6 and 12.7 show good agreement with the theoretical model. The analysis yields a value for the photoionization cross sections of 5D and gives new information on the interaction potentials of colliding cesium-argon atoms.

In conclusion, we have shown that in studies of line broadening, the ionization channel provides an extremely sensitive and simple way to monitor absorption. Even on the far wing where absorption or fluorescence becomes vanishingly small, the ionization method can be used because single absorption events are detectable in proportional counters.[13,21] Therefore, dense and high-pressure samples are not a requirement, thus allowing the possibility of complete resolution of satellite structure on the far wing. These studies also provide accurate measurement of the potential parameters as we discussed above.

The above study indicates that, in some cases, selectivity in single-atom detection is reduced by pressure broadening. However, low-pressure proportional counters, or even Channeltrons working in a vacuum, can be used where extreme selectivity is essential. Pressure broadening can be put to advantage in studies of rare events where there is a lack of accuracy on the energy levels. Such a case arises in searches for free quarks attached to a nucleus.

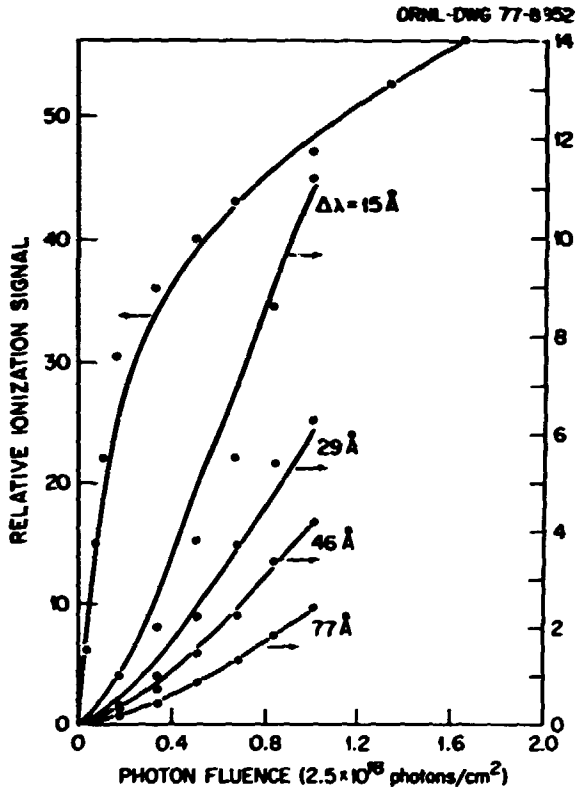

Fig. 12.6. Ionization signal as a function of photon fluence for the indicated detuning in argon gas at 760 torr.

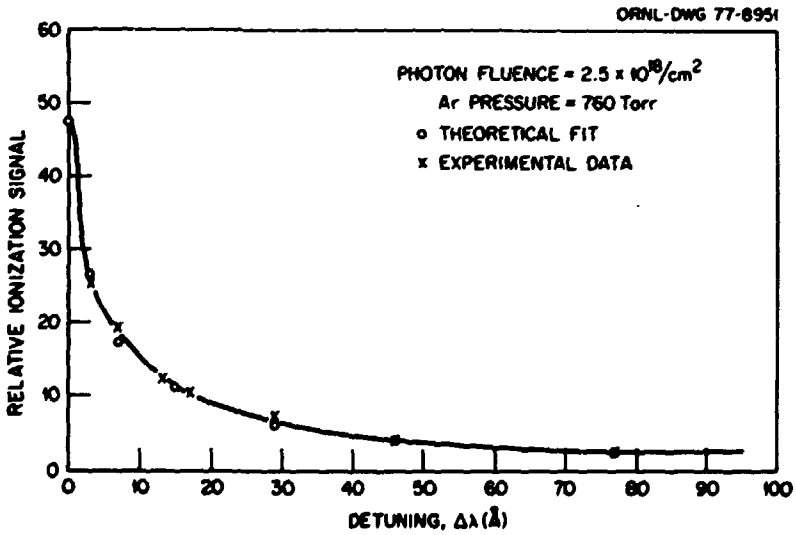

Fig. 12.7. Ionization signal as a function of detuning at a fixed photon fluence (2.5×10^{18} cm^2) for argon gas at 760 torr.

Saturated Photodissociation of Cesium Iodide

In the present work we show that molecular (e.g., cesium iodide) photodissociation can be used to produce a spatially defined population of atoms in their ground states at a well-defined time. Such sources of atoms can be combined with time- and space-resolved one-atom detectors in a number of novel experimental arrangements. In the course of the present studies we showed that all of the cesium iodide molecules in the central portion of a laser beam could be dissociated to neutral cesium atoms in their ground states. This, along with the previous demonstrations that each cesium atom can be ionized with another pulsed laser, proves that single molecules of cesium iodide can be detected. We also obtained new information on the photodissociation of cesium iodide, including the absolute cross section as a function of wavelength.

The experimental arrangement (Fig. 12.8) uses a parallel-plate ionization chamber mounted inside a vacuum system. Even when the cesium iodide sample is heated to 700°K, the concentration of cesium iodide molecules between the parallel plates is quite low; nevertheless, it is more than adequate for our method of detection. A pulsed laser[29] using Kiton red dye pumped with a linear flashlamp is used to dissociate cesium iodide. The narrow beam is about 0.5 mm in diameter when focused and is ideal for defining the initial location of free cesium atoms at time $t = 0$. A second pulsed laser[30] having a much larger beam, about 7 mm in diameter, is coaxial with the first narrow beam. In this way the second pulsed laser can be used to detect those free atoms which were liberated on the axis of the detector beam at time $t = 0$ and which are still contained in the detector cylinder at the arbitrary time $t > 0$. It will be shown below that the photon fluence (ϕ_S) associated with the source beam is large enough to dissociate all of the cesium iodide molecules contained in the volume swept by the source beam, and the photon fluence (ϕ_D) associated with the detector beam is large enough to remove one electron from each of the liberated atoms in the detector volume.

ORNL DWG 76-15852R

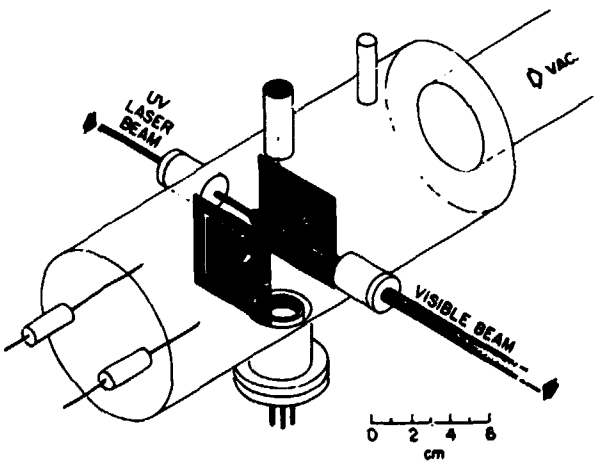

Fig. 12.8. Experimental arrangement for the study of saturated photodissociation of alkali-halide molecules. The pulsed uv laser is used to dissociate cesium iodide molecules at time $t = 0$, and the pulsed visible laser is used to detect cesium atoms at $t > 0$.

The electronics logic and data acquisition are quite conventional and will not be discussed. Each pulse of the detector laser is fired manually when a condition is met – namely, that it is preceded with a pulse from the source laser at a prescribed time. For each event, three quantities are recorded: (1) the relative energy per pulse of the source laser, (2) the relative energy per pulse of the detector laser, and (3) a signal proportional to the amount of ionization (i.e., number of free electrons) produced in the guarded region of the parallel-plate ionization chamber.

In the initial experiments, the wavelength of the source laser was set at 3175 Å near the dissociation peak.[31] To detect the neutral cesium, the detector laser was set to produce photons at 4593 Å, which promotes $Cs(6^2S_{1/2})$ to $Cs(7^2P_{1/2})$; and, as appropriate for two-photon RIS, a second photon of the same wavelength will photoionize $Cs(7^2P_{1/2})$. When a buffer gas such as argon is used at moderate pressure (e.g., 100 torr), several desirable effects occur. First, the cesium iodide molecules will be in thermal equilibrium near 300°K due to argon collisions. Also, photoionization will occur from the degenerate magnetic levels. Finally, with a buffer gas, cesium-atom diffusion is of no consequence during the lifetime (FWHM) of the laser pulse, that is, 1.5 μsec for the source laser and 0.5 μsec for the detector laser. For these reasons, most of the studies were made with a buffer gas. Ionization signals were studied as a function of the detector laser fluence ϕ_D. We found that as ϕ_D increased, the ionization signal

29. For the dissociation of CsI molecules we used a linear flashlamp-pulsed dye laser, model CMX-4, Chromatix Corp., Mountain View, Calif.

30. For the detection of Cs atoms we used a coaxial lamp dye laser, model 2 00C, Phase-R Co., New Durham, N.H.

31. P. Davidovits and D. C. Brodhead, *J. Chem. Phys.* 46, 2968 (1967).

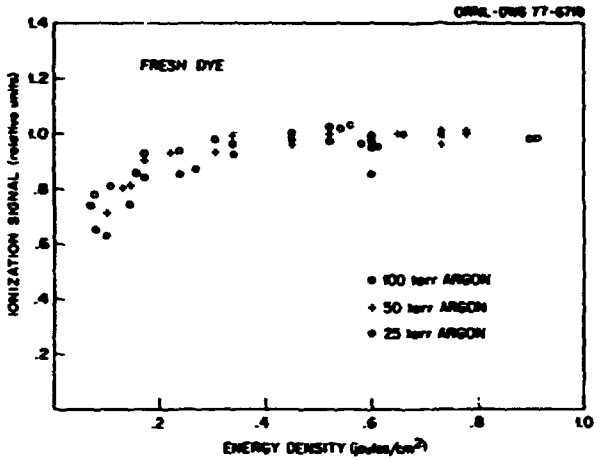

Fig. 12.9. Measured signals due to cesium atoms as a function of the energy density of the detector laser.

climbed gradually to a saturated value, consistent with earlier work[13] (Fig. 12.9).

With sufficient fluence ϕ_D to saturate the ionization, that is, to detect each free atom in the laser beam, studies were then made of the photodissociation process. Several significant observations were made on the production of neutrals. For instance, there was a gradual decline in the number of free atoms as the time between the source and detector lasers was increased; but this variation was expected based on calculations of the rate of diffusion of the atoms out of the detection region. Special tests were made with very short time delays between the source and detector lasers; all the atoms were dissociated in less than 0.5 μsec after the source-laser pulse. No ionization signals due to the source laser alone were observed. Berkowitz[32] observed ionization with a photoionization mass spectrometer only when the photon energy exceeded 7 eV.

Figure 12.10 shows the ionization signal as a function of the number of photons in a single pulse of the source laser, both for an unfocused beam and for a beam which was focused with a 50-cm focal length lens. The focused beam signals continue to rise gradually because of a nonuniform source beam. To obtain the cesium photoproduction cross section, σ, the following analysis was made. Assuming a Gaussian beam profile, we write

$$\phi(\rho) = \phi_0 e^{-\rho^2/R^2}, \tag{5}$$

where ϕ_0 is the fluence when the radius $\rho = 0$, and R is a constant. Since each atom is detected, the measured signal is proportional to

$$n_l = N \int_0^\infty 2\pi\rho \, d\rho \, | 1 - \exp(-\sigma\phi_0 e^{-\rho^2/R^2}) | , \tag{6}$$

where n_l is the number of atoms dissociated per unit of length and N is number density of the cesium iodide molecules. It can be shown that

$$F(\sigma\phi_0) \equiv \frac{n_l}{N\pi R^2} = \gamma + \ln \sigma\phi_0 + E_1(\sigma\phi_0) , \tag{7}$$

where E_1 is the exponential integral and γ is Euler's constant (0.577 . . .). The ratio of the focused beam signal to the unfocused beam signal (Fig. 12.10) is just $F(\sigma\phi_0)/\sigma\phi_0$, since in the limit $\sigma\phi_0 \to 0$, $F(\sigma\phi_0) = \sigma\phi_0$. For a given total number of photons (e.g., 2.5×10^{14}), we find the $\sigma\phi_0$ which makes $F(\sigma\phi_0)/\sigma\phi_0$ equal to the experimental ratio (0.41). The fluence ϕ_0 was determined experimentally by measuring the energy transmitted through a small aperture with a joule meter. In this way, we found at 3175 Å a value of 2.9×10^{-17} cm² for the cesium photoproduction cross section.

Figure 12.11 shows the cross section for the production of cesium neutral from cesium iodide as a function of wavelength. The present results have a functional form similar to that for photoabsorption,[31] and our cross sections at the peak agree to within a few percent with those of ref. 31. The present measurements were made at 320°K, whereas the photoabsorption data were taken at about 1000°K; this temperature difference could account for the difference in widths. A knowledge of the vapor pressure of cesium iodide was not

32. J. Berkowitz, *J. Chem. Phys.* **50**, 3503 (1969).

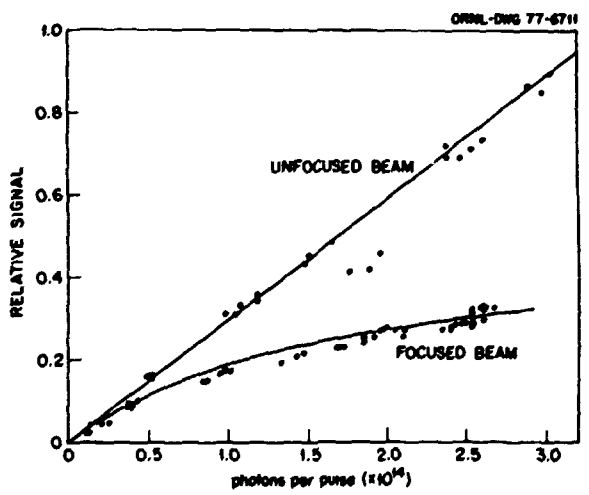

Fig. 12.10. Signals due to cesium atoms as a function of the number of photons in a single pulse of the source laser. Each atom produced was detected with the RIS process. Data are shown for unfocused and focused beams. The function $F(\sigma\phi_0)$ [Eq. (7)] is fitted to the experimental data and is the curve drawn through the focused data points.

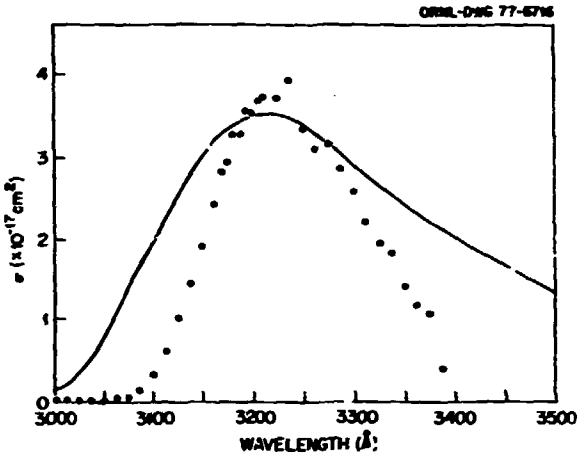

Fig. 12.11. Cross section for the photoproduction of cesium from cesium iodide as a function of wavelength.

required to obtain our photodissociation cross sections. In the present technique, the number density of cesium iodide molecules is obtained directly from the saturated curve obtained by plotting the number of cesium atoms per pulse against the laser energy per pulse, or it is obtained through fitting to Eq. (7).

We have shown that all cesium iodide molecules in a volume can be dissociated by using a photon fluence exceeding 3×10^{17} cm^{-2} in a single laser pulse of microsecond duration. When this fact is combined with the demonstrated fact that one atom can be detected when using an RIS scheme and a proportional counter,[13] one-molecule detection is obvious.

Some clarifications of the photodissociation process in cesium iodide can be deduced from the present studies. Berry[33] showed that in the alkali halide molecules, one may expect to observe in some cases a band system and in other cases a smooth continuum in the photoabsorption spectrum. Here we observe a smooth continuum in the actual appearance of neutral atoms; furthermore, these neutrals appear in a short time, that is, in less than 0.5 μsec after excitation. Presumably, then, we are observing a simple process in which photoabsorption occurs from an ionic ground state to a nonionic predissociation state, which dissociates into the neutral continuum state in a short time, perhaps much less than our measured upper limit of 0.5 μsec. Because the predissociation state changes from a nonionic to an ionic state at a rather large internuclear distance (about 20 Å), nuclear motion can no longer be considered adiabatic with respect to electronic motion; hence, an otherwise valid noncrossing rule is violated. Our direct observations of prompt neutral atoms produced in a smooth photon energy continuum, as well as our observation that no Cs^+ or I^- ions are formed, are consistent with the simple and vivid picture of the alkali halide photodissociation process painted by Berry.[33]

Sensitive, Absolute, and Time-Resolved Method for the Study of Reactive Atoms

A dual-laser technique for the production of free atoms at time $t = 0$ and their detection at $t > 0$ has been used to measure the diffusion of cesium atoms in argon and the reaction of cesium with oxygen.

Resonance ionization spectroscopy (RIS) was developed initially for the absolute measurement of the number of excited atoms.[8,9] More recently, RIS was used for the detection of a single atom of cesium in its ground state[13,21] and for the detection of each cesium atom released from cesium iodide molecules when they were photodissociated to saturation.[34] In the course of these developments it became obvious that studies were needed on the reaction of alkali metal atoms with traces of impurities as the alkali atoms slowly diffuse through a noble gas. Fortunately, our methods contain some features that make possible the study of these problems in a unique way.

Specifically, the method introduced for the study of alkali halide photodissociation is well suited to rather direct measurements of the diffusion of small numbers of alkali atoms in various gases and to a remarkably simple determination of the rate of reaction of free atoms with various other atoms or molecules.[34] Here we present a new method for the study of diffusion and chemical reaction kinetics. Results for the diffusion coefficient of cesium in argon gas, as well as the cross section for cesium reactions with oxygen, are discussed.

A schematic diagram of the method is shown in Fig. 12.8. A pulsed laser (FWHM = 1.5 μsec), called a source laser,[34] produces a spatially defined (e.g., on a narrow, straight line) group of atoms at time $t = 0$. At time $t > 0$, a second pulsed laser (FWHM = 0.5 μsec), called a detector laser, sweeps a cylindrical volume of space coaxially with the line source in such a way that every atom in the cylinder is selectively detected. By repeating the source and detector laser pulses at various time delays, the number of atoms which have not escaped the cylinder by diffusion and which have not reacted chemically within the volume of the cylinder can be

33. R. Stephen Berry, *J. Chem. Phys.* 27, 1288 (1957).

34. L. W. Grossman, G. S. Hurst, and S. L. Allman, "Saturation Photodissociation of CsI," *Chemical Physics Letters* (in press).

measured quite directly as a function of time. The measured fraction of surviving atoms, $\gamma(t)$, contains both the diffusion coefficient and the cross section for chemical reaction, as we now show.

Suppose a line source of atoms, λ, per unit length is created along an infinitely long line at time $t = 0$. When $t > 0$, the line source spreads by diffusion through a gas while reacting chemically at rate β. Here $\beta = \sigma N_c \bar{v}$, where σ is the reaction cross section, N_c is the number density of a chemical species that can react with the alkali atom, and $\bar{v}$ is the mean relative velocity of the alkali atom and the other reactive species. We further stipulate that $N_c \ll N_I$, the number density of an inert gas which determines the diffusion coefficient, D, for the alkali atom. In other words, if n is the number density of the alkali atom,

$$\frac{\partial n}{\partial t} = D\nabla^2 n - \beta n \,. \tag{8}$$

The solution for an unbounded medium is

$$n(\rho, t) = \frac{\lambda}{4\pi Dt} \exp[-\rho^2/4Dt]\, e^{-\beta t} \,, \tag{9}$$

where ρ is the radial distance from the line source.

If we define $\gamma(t)$ as the fraction of the number of ions contained in the cylinder of radius R, then

$$\gamma(t) = \frac{1}{\lambda} \int_0^R 2\pi\rho \, d\rho \, n(\rho, t)$$

$$= \left[1 - \exp\left(-\frac{R^2}{4Dt}\right)\right] e^{-\beta t} \,. \tag{10}$$

Expression (10) is a slowly varying function of time with $\beta = 0$; for example, if $D = 2.5$ cm^2/sec and $R = 1.0$ cm, $\gamma(t) = 0.63$ when $t = 0.1$ sec. Thus, atoms can be "contained" for relatively long times so that a chemical reaction can be measured even when β is relatively small. Examples of fitting to Eq. (10) to obtain both D and β are given below.

The above idealization is essentially met in practice. Both production of atoms and their detection occur far from all walls since the parallel-plate ionization chamber collects electrons only from those atoms that were in a volume defined by the area of the detector laser beam and the length of the guarded collector plate. Thus the assumption of an unbounded medium is a good one.

The initial experiments were performed on the diffusion of cesium atoms in argon. The cesium iodide sample was heated to 620°K, producing about 3×10^8 cesium iodide molecules per cubic centimeter in the region of the laser beams. The source laser photodissociated all the molecules in a small volume of 10^{-2} cm^3 (area = 2.5×10^{-3} cm^2, length = 4 cm) – thus about 3×10^6 cesium atoms. The detector laser, operated at 4593 Å, ionized all the cesium atoms by first exciting to the Cs($7^2P_{1/2}$) level. With argon pressure at 100 torr and below, we found that the fraction $\gamma(t)$ was diffusion controlled; that is, reactive gas impurities were at sufficiently low concentration that $e^{-\beta t}$ was close to unity. At higher argon pressures, we found it difficult to keep impurity levels low enough that the diffusion process would control the loss of atoms. We show in Fig. 12.12 a fit of Eq. (10) to the data where $\beta = 0$ and $D = 2.9$ cm^2/sec at 50 torr – thus 0.19 cm^2/sec at 1 atm compared with 0.25 cm^2/sec for rubidium in argon at 1 atm.[15] We do not know of comparable data for cesium in argon, although mutual diffusion coefficients are a subject of current interest.[35]

Figure 12.13 shows the effect of adding small concentrations of oxygen. The functions $\gamma(t)$ are controlled almost entirely by the exponential term $e^{-\beta t}$; that is, over the range of t in Fig. 12.13, losses due to diffusion are negligible. From the slopes in Fig. 12.13, we find β directly for each oxygen pressure. These results at 100 torr of argon and at several other argon pressures all fit to a simple three-body reaction rate, $\beta = 7 \times 10^3 P_{O_2} P_{Ar}$. The large three-body coefficient is surprising and needs theoretical interpretation. We have not found comparable results in the literature for this reaction, although several recent studies were made on alkali-metal atom reactions with halogen molecules.[36,37]

In conclusion, we believe that we have a useful method for the study of reactive atoms. The ability to produce free atoms in a well-defined region of space and the ability to detect them in a selective fashion in another well-defined region of space are salient features of the new method. Time resolution of both the atomic source and the atomic detector, as well as the ability to detect all the surviving atoms, makes possible the sensitive measurements of chemical kinetics and chemical transport processes in general in a very direct and simple way.

---

35. T. N. Bell, I. R. Shankland, and P. J. Dunlop, *Chem. Phys. Lett.* **45**, 445 (1977).

36. S. A. Edelstein and P. Davidovits, *J. Chem. Phys.* **55**, 5164 (1971).

37. J. Maya and P. Davidovits, *J. Chem. Phys.* **59**, 3143 (1973).

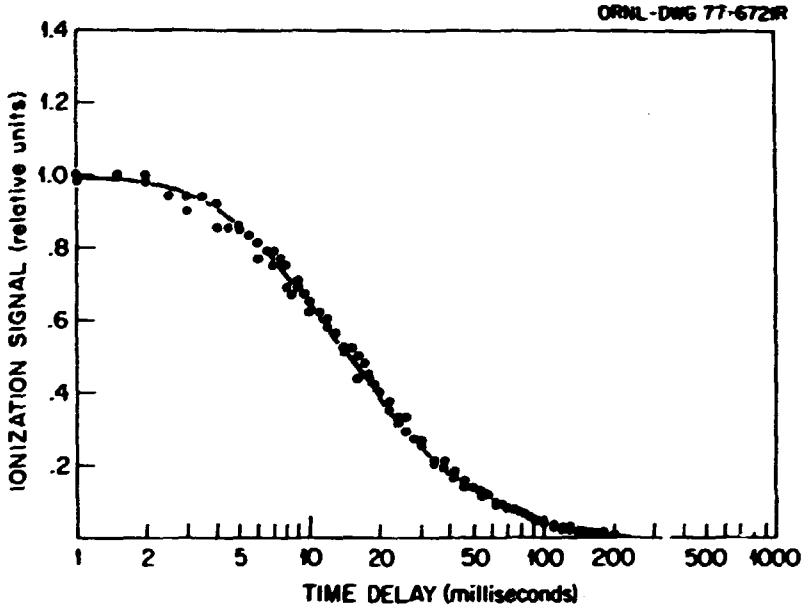

Fig. 12.12. Relative cesium atom signal as a function of time in pure argon. A comparison of experimental data is made with diffusion theory.

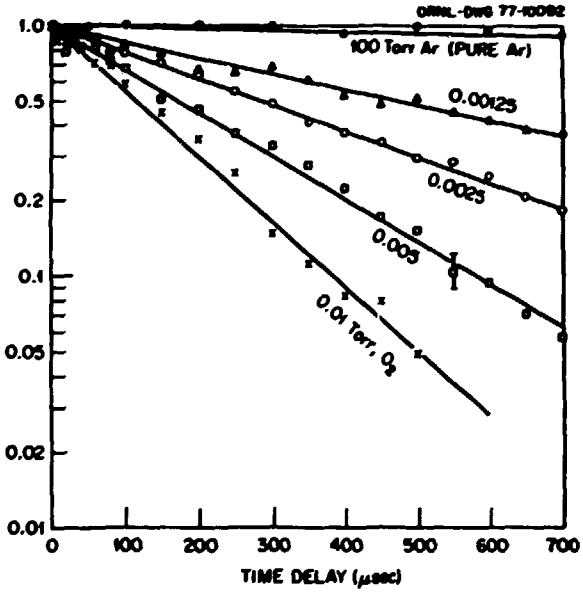

Fig. 12.13. Relative cesium atom signal as a function of time for various partial pressures of oxygen in 100 torr of argon.

Detection of Single Fission-Product Atoms

The RIS technique has particular applicability to studies of the fission process and the interaction and thermalization of fission fragments in gases. The total fission yield of cesium from the spontaneous fission of ^{252}Cf is about 8%. One-atom detection techniques are being applied to determine what fraction of cesium fission products are neutral atoms at thermalization. Previously, it was not possible to obtain experimental data of this kind. The experiment will be performed using a cell shown schematically in Fig. 12.14. The cell consists of two large-diameter parallel plates to which a potential can be applied. A proportional counter, housed in a rectangular box, is located behind one of

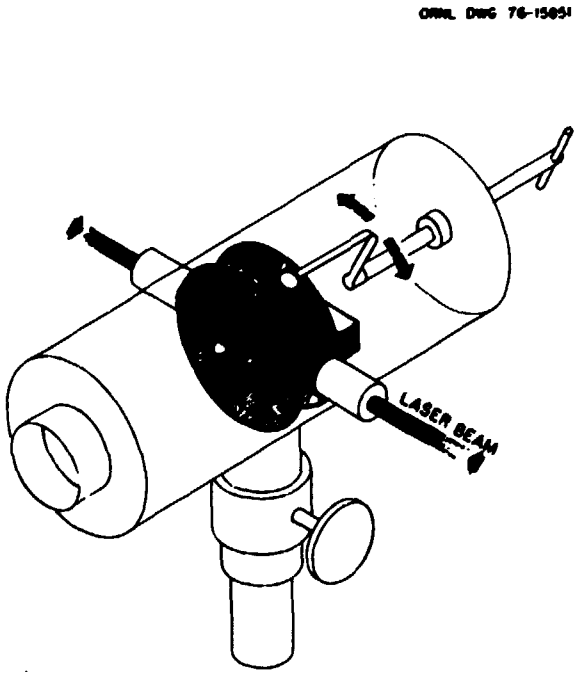

Fig. 12.14. Schematic diagram of a one-atom experiment for the detection of single fission daughters.

the plates. The edge of this box can be seen in the figure; a grid covers the portion of the plate that is one side of the proportional counter.

A ^{252}Cf source ion implanted on 0.9-mg/cm^2 nickel foil is located in front of a surface-barrier particle detector. The source and detector are separated by collimators to limit the angular divergence. This assembly is on a rotatable arm and is positioned between the parallel plates. The occurrence of a fission event is signaled by the surface-barrier detector and, together with appropriate energy gating to select the light-mass fragment, ensures that the complementary heavy-mass fragment is directed toward the center of the chamber. After a suitable delay period, a dye laser tuned to 4555 Å is triggered to selectively excite and ionize the resultant thermalized cesium atom. By controlling gas pressure within the apparatus, this heavy-mass complementary fission fragment can be thermalized within the effective laser beam volume. During travel of this fission fragment, the potential on the parallel plates is such that the large number of electrons formed are drifted to the plate away from the counter. After thermalization and collection of the directly produced electrons, the electric field between the plates is reversed; then the pulsed laser is fired. Single electrons thus formed as individual cesium atoms are photoionized and will drift into the proportional counter to be detected.

This experiment is a precursor of many planned experiments with radioactive atoms. Besides gaining information concerning fission fragments, the technique can be used to study the interaction of these fragments with gases, that is, time-resolved chemistry at the one-atom level. Another such experiment will involve the direct detection and characterization of nuclear fission isomers as they are synthesized in accelerator experiments.

RIS Studies on Proton-Excited Krypton

In previous annual reports we described an experimental technique that uses a tunable dye laser fired in conjunction with a pulsed proton beam from the ORNL 3-MV Van de Graaff accelerator (Fig. 12.15). The method provides a means for the determination of the absolute number of ion pairs and absolute number of selected excited states created per unit of energy deposited in a gas target by the proton beam burst. The number of ion pairs created by the proton beam burst is found from a measurement of the voltage change that occurs when the ion pairs are collected on the plates of an ionization cell which encloses the gas target. The number of atoms in a selected excited state at any chosen time after their creation is measured by collecting the ion pairs that are produced when only the states of interest are ionized by firing (at a chosen time) an energetic photon pulse from a dye laser tuned to the proper wavelength. We continued to refine our technique and extend it to other systems. In previous measurements, the cylindrical volume swept out by the photon beam burst from the laser was made to completely overlap the smaller-diameter cylindrical volume of ion pairs and excited states produced by the proton beam burst. In more recent investigations of the $^1P_1$ and $^3P_1$ resonance states of krypton, we not only overlapped the cylindrical regions traversed by the proton and laser beams but, in other measurements, also spatially displaced the laser beam parallel to, but away from, the proton beam. For instance, by positioning the laser beam over the path of the drifting electrons being collected in the ionization chamber, we observed the number of atoms (in the $^1P_1$ and $^3P_1$ states) which we presume were created when the drift electrons collided with neutral krypton atoms. By positioning the laser beam away from the paths of both the proton beam and the drifting electrons, we observed excited krypton atoms which we presume became excited in the process of trapping the radiation which was propagating away from the excited atoms produced initially by the proton beam burst. Our investigation of these processes, as a function of E/P, is continuing.

ORNL DWG 78-13040

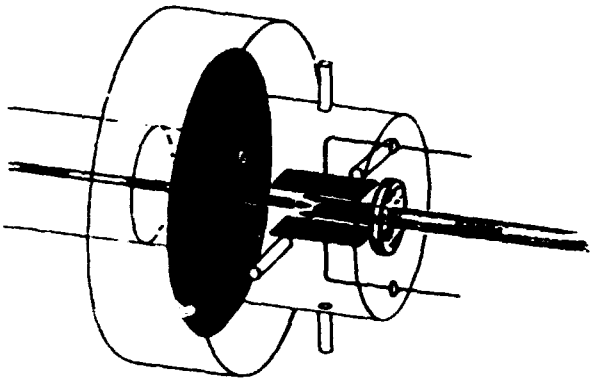

Fig. 12.15. Illustration of the use of RIS to study excited states produced by charged particles.

ENERGY PATHWAYS RESEARCH AND ITS APPLICATIONS

The demand for ultrasensitive detection of air pollutants (radioactive and nonradioactive pollutants) is very high. During the past year, our energy pathways

research was extended to the study of air pollutants such as NO, NO_2, and N_2O and radioactive pollutants such as HTO. On the other hand, the development of high-power uv gas lasers for isotope separation and laser-induced fusion plays an important role in the development of nuclear energy. The study of energy pathways in various gases or gas mixtures provides key information for new laser developments or for improvement of existing lasers.

A multipurpose reaction cell was built to study the detailed kinetics of pure gases or gas mixtures. The ion-pair collection plates are set up to collect all the ion pairs produced by a proton beam. Thus the Jesse effect can be studied. Time-resolved spectroscopies in the vacuum uv and in the uv and visible regions were obtained to determine the reaction rate constants of energy transfer and charge transfer, the precursors of excited atoms or molecules, natural lifetimes of excited molecules, and the mechanism of dissociative recombination as well as ion-ion recombination. We also set up a new facility for measuring absolute fluorescence efficiencies of various gas mixtures.

Time-Resolved Quenching of Excited States of Argon

Detailed knowledge of energy transfer processes in noble gases is in strong demand because of its application to gas lasers, radiation chemistry,[38] and atmospheric pollution research.[39,40]

It is well known that the effective lifetimes of resonance states can be even longer than those of metastable states at high pressure because of radiation trapping.

The destruction of metastable states has been investigated using absorption techniques.[41,42] Piper, Velazco, and Setser[43] made measurements of the quenching of metastable states by a flow afterglow method. Bourene and LeCalve[44] also measured the quenching cross section of $Ar(^3P_{2,0})$ by small molecules by monitoring the emission of $N_2(C^3\Pi_u)_{v=0} \rightarrow N_2(B^3\Pi_g)$.

Clark, Masson, and Wayne[45] studied the quenching of $Ar(^3P_1)$ by O_2 and NO. Klots and Anderson[46] measured some Penning ionization processes and found the results in agreement with theoretical calculations by Watanabe and Katsuura.[47] Hurst, Wagner, and Payne[48] and McNeely et al.[49] used time-resolved emission spectral features to measure the quenching rates of $Ar(^1P_1)$ and $Ar(^3P_1)$ by C_2H_4, NO, N_2, and H_2. Recently, Bourene, Dutuit, and LeCalve,[50] using an absorption technique, obtained the quenching cross sections of $Ar(^3P_2)$, $Ar(^3P_1)$, and $Ar(^1P_1)$ quenched by CO and H_2.

It has been reported that $Ar(^3P_2)$ can form $Ar_2^*(1_u)$ by three-body collisions ($\sim 10P^2$). Chen and Payne[51,52] measured the quenching rates of $Ar_2^*(1_u)$ by H_2O and Cl_2. Since for high-pressure gas lasers most of the excited argon atoms eventually appear in $Ar_2^*(1_u)$, such quenching rates are of extreme importance. We measured additional rates and determined the quenching rates of $Ar(^3P_1)$ and $Ar(^1P_1)$ by CH_4, O_2, N_2O, CO_2, HI, CF_4, and CH_3F.

The experimental quenching frequencies of $Ar(^1P_1)$ and $Ar(^3P_1)$ for various gases such as Cl_2 and CO are plotted and fitted with straight lines in Fig. 12.16. The overall quenching rates of $Ar(^3P_1)$ and $Ar(^1P_1)$ by CO are 5.2×10^{-11} and 9.2×10^{-11} cm^3/sec respectively. All the numerical values of quenching constants of $Ar(^3P_1)$ and $Ar(^1P_1)$ by Cl_2, CO, CO_2, N_2O, HI, HBr, CH_3F, O_2, CF_4, CH_4, and H_2O are tabulated in Table 12.1. The accuracy of our results is believed to be 25%.

It has been demonstrated previously that $Ar(^3P_2)$ can be converted to $Ar_2^*(1_u)$ by three-body collisions. The conversion rates were obtained as $9P^2$, $13.5P^2$, and $11.26P^2$. Thus, for high argon partial pressure and low quenching gas pressure, $Ar(^3P_2)$ can be efficiently converted to $Ar_2^*(1_u)$, which gives the second continuum around 1250 Å. The lifetime of $Ar_2^*(1_u)$ has been measured as 3.5 μsec and is independent of argon pressure.

38. G. S. Hurst and C. E. Klots, pp. 1–96 in *Advances in Radiation Chemistry*, vol. 5, M. Burton and J. L. Magee, eds., Wiley-Interscience, New York, 1976.

39. A. P. D'Silva and V. A. Fassal, *Anal. Chem.* 44, 2115 (1972)

40. C. C. Wang et al. *Appl. Phys. Lett.* 28, 14 (1976).

41. A. V. Phelps and J. P. Molnar, *Phys. Rev.* 89, 1202 (1953).

42. A. H. Futch and F. A. Grant, *Phys. Rev.* 104, 356 (1956).

43. L. G. Piper, J. E. Velazco, and D. W. Setser, *J. Chem. Phys.* 59, 3323 (1973).

44. M. Bourene and J. LeCalve, *J. Chem. Phys.* 58, 1452 (1973).

45. I. D. Clark, A. J. Masson, and R. P. Wayne, *Mol. Phys.* 23, 985 (1972)

46. C. E. Klots and V. E. Anderson, *J. Chem. Phys.* 56, 120 (1972).

47. T. Watanabe and K. Katsuura, *J. Chem. Phys.* 47, 800 (1967).

48. G. S. Hurst, E. B. Wagner, and M. G. Payne, *J. Chem. Phys.* 61, 3680 (1974).

49. J. R. McNeely et al., *J. Chem. Phys.* 63, 2717 (1975).

50. M. Bourene, O. Dutuit, and J. LeCalve, *J. Chem. Phys.* 63, 1668 (1975).

51. C. H. Chen and M. G. Payne, *Appl. Phys. Lett.* 28, 219 (1976).

52. C. H. Chen and M. G. Payne, *Opt. Commun.* 18, 476 (1976).

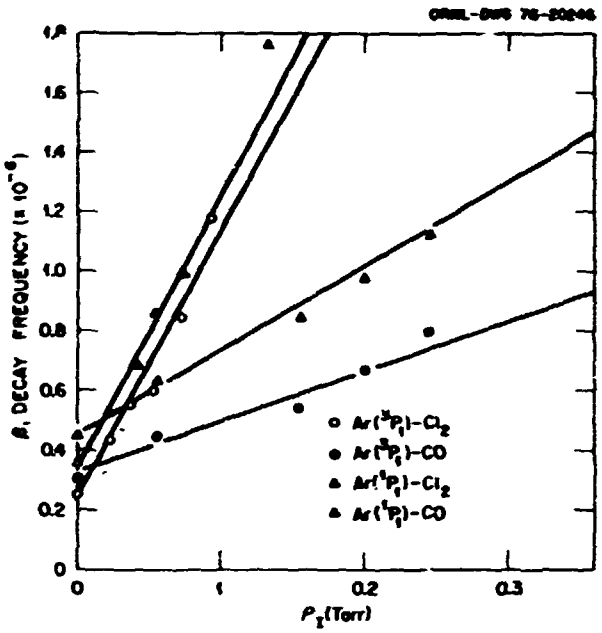

Fig. 12.16. Decay frequency of $Ar(^1P_1)$ and $Ar(^3P_1)$ against various pressures P_I of quenching gases Cl_2 and CO. P_{Ar} = 60 torr.

For high argon partial pressure with a quenching gas added, the kinetics can be described with the following equations:

$$Ar(^3P_2) + 2Ar \xrightarrow{b} Ar_2^*(1_u) + Ar \ . \tag{11}$$

$$Ar(^3P_2) + Ar \xrightarrow{a} \text{to other states} \ , \tag{12}$$

$$Ar(^3P_2) + Q \xrightarrow{\beta'_Q} Q^* + Ar \ , \tag{13}$$

$$Ar_2^*(1_u) + Q \xrightarrow{\beta''_Q} Q^* + 2Ar \ . \tag{14}$$

$$Ar_2^*(1_u) \xrightarrow{1/\tau} 2Ar + h\nu \ , \tag{15}$$

where a and b are the two three-body conversion rates, β'_Q and β''_Q are the quenching frequencies for $Ar(^3P_2)$ and $Ar_2^*(1_u)$, respectively, and τ is the lifetime of $Ar_2^*(1_u)$. From the above equations, the populations of $Ar(^3P_2)$ and $Ar_2^*(1_u)$ can be seen described by two differential equations:

$$\frac{d[Ar(^3P_2)]}{dt} = -(aP_{Ar} + bP_{Ar}^2 + \beta_Q P_Q)[Ar(^3P_2)] \ , \tag{16}$$

$$\frac{d[Ar_2^*(1_u)]}{dt} = bP_{Ar}^2[Ar(^3P_2)] - \tfrac{1}{2}[Ar_2^*(1_u)] - \beta'' P_Q[Ar_2^*(1_u)] \ . \tag{17}$$

The solutions of (16) and (17) are

$$[Ar(^3P_2)] = [Ar(^3P_2)]_0 \times e^{-(aP_{Ar} + bP_{Ar}^2 + \beta'_Q P_Q)t} \ , \tag{18}$$

$$[Ar_2^*(1_u)] = [Ar_2^*(1_u)]_0 [e^{-(aP_{Ar} + bP_{Ar}^2 + \beta'_Q P_Q)t} - e^{-[(1/\tau) + \beta''_Q P_Q]t}] \ . \tag{19}$$

For high argon pressures, the quantity bP_{Ar}^2 will cause a fast rise time. Thus the decay part of the emission of $Ar_2^*(1_u)$ should have a destruction frequency $(1/\tau) + \beta''_Q P_Q$. Therefore, from time-resolved emission spectra, the quenching rate constants β''_Q of various molecules can be obtained.

The experimental data of $Ar_2^*(1_u)$ quenched by various amounts of CO_2 are shown in Fig. 12.17 for an argon partial pressure of 500 torr. The decay frequencies are plotted against various amounts of CO, CO_2, HI, and O_2 and fitted by straight lines in Fig. 12.18. Numerical values are tabulated in Table 12.1. The quenching rate constants and quenching cross sections of $Ar(^3P_2)$ and $Ar(^3P_0)$ are also given in Table 12.1 for easy comparison.

The quenching rate ratio for $Ar(^1P_1)$ to $Ar(^3P_1)$ is close to 1.7 in most cases. Quenching cross sections for metastable states are not much smaller than those of resonance states. A more accurate theory than presently available is needed to calculate all these quenching rate constants, especially for discrete-discrete energy transfer processes.

Charge Transfer and Penning Ionization of N_2, CO, CO_2, and H_2S in Proton-Excited Helium Mixtures

In the past few years, the resonant charge transfer process has been considered an important process in atmospheric chemistry and also an ideal mechanism for providing a high-power gas laser for laser isotope separation and laser-induced fusion. Stimulated emission for the transition of $N_2^+(B^2\Sigma_u^+ \rightarrow X^2\Sigma_g^+)$ from He-N_2 mixtures excited by an intense pulsed electron beam has already been observed. Intense laser emission at 4278 Å ($v' = 0$, $v'' = 1$) was reported with an efficiency of 1.9% relative to the energy lost by the electron beam.

Table 12.1. Quenching rate constants and quenching cross sections of $Ar(^1P_1)$, $Ar(^3P_2)$, $Ar(^3P_1)$, $Ar(^3P_0)$, and $Ar_2^*(1_u)$ by various molecules

	$Ar(^1P_1)$		$Ar(^3P_2)$		$Ar(^3P_1)$		$Ar(^3P_0)$		$Ar_2^*(1_u)$		I.P.
	k^a	$\sigma(A)^{2\,b}$	k^a	$\sigma(A)^{2\,b}$	k^a	$\sigma(A)^{2\,b}$	k^a	$\sigma(A)^{2\,b}$	k^a	$\sigma(A)^{2\,b}$	(eV)
C_2H_4	*10.3*[c]	*161*	6.4[d]	100[d]	*5.6*	*87.5*					10.45
H_2	*2.2*	*12*	0.66,[e] 1.1[d]	3.6,[e] 6[d]	*2.1*	*11.5*	0.78	4.3			15.43
N_2	*0.54*	*8.7*	0.36,[e] 0.3[d]	5.8,[e] 5.0[d]	*0.08*	*1.9*	0.16	3.8			15.58
NO	*5.4*	*88*	2.2,[e] 1.7[d]	36,[e] 29[d]	*3.2*	*52*	2.5	41			12.06
CH_4	*5.7*	*78*	3.3,[e] 6[d]	45,[e] 81[d]	*4.5*	*62*	5.5	74	*2.4*	*35*	12.7
Cl_2	*2.8*	*57*	7.5,[f] 4.7[e]	153,[f] 96[e]	*2.7*	*55*			*6.3*	*153*	13.7
O_2	*3.1*	*52*	2.1,[e] 1.8[d]	35,[e] 29[d]	*2.5*	*42*	2.4	41	*1.6*	*30*	12.04
N_2O	*5.8*	*107*	4.4,[e] 4.3[d]	81,[e] 80[d]	*4.2*	*77*	4.8	87	*2.3*	*48*	12.89
CO_2	*7.4*	*132*	5.3,[e] 5.6[d]	97,[e] 100[d]	*5.0*	*89*	5.9	108	*3.9*	*81*	13.77
HI	*1.2*	*27*	7[e]	155[e]	*1.4*	*32*			*0.8*	*22*	12.8
HBr	*1.4*	*29*	7.2[e]	150[e]	*1.8*	*38*					
CF_4	*1.3*	*26*	0.4[e]	8[e]	*1.0*	*20*	0.4	8	*0.38*	*9.8*	13.2
CH_3F	*8.0*	*139*	6.9[d]	120[d]	*5.2*	*90*			*7.9*	*153*	12.85
H_2O	*13.5*	*206*	4[d]	61[d]	*13*	*198*			*10*	*152*	12.61
Xe	*3.3*	*73*	1.8,[e] 2.1[d]	40,[e] 47[d]	*2.2*	*49*	3	67	*2.4*	*67*	12.13
CO	*0.92*, 0.85[g]	*15*, 14[g]	0.14,[e] 0.55,[d] 0.185[g]	2.3,[e] 9,[d] 3.0[g]	*0.52*	*119*	1.3	21	*0.5*	9	14.01
SF_6	*7.9*	*178*	1.6,[e] 0.4[d]	36,[e] 90[d]	*6.3*	*142*	1.7	38	*3.4*	97	16.2
F_2	*12.9*	*260*	7.5,[f] *9.4*	151,[f] *189*	*8.9*	*179*			*5.2*	*105*	17.8

[a] k is in units of 10^{-10} cm^3/sec.
[b] $\sigma = k/v = k/[8k'T/\pi\mu]^{1/2}$, where μ is reduced mass and k' is Boltzmann's constant.
[c] Numbers in italic are the results of work at ORNL.
[d] Ref. 44.
[e] Ref. 43.
[f] Ref. 63.
[g] Ref. 50.

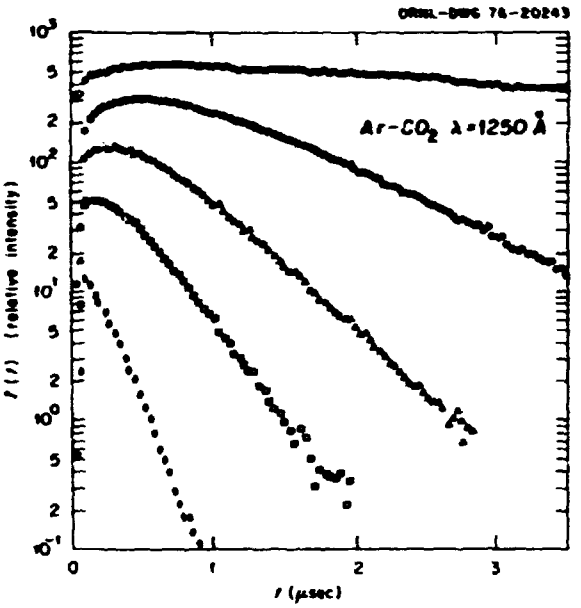

Fig. 12.17. Experimental data for the emission of 1250 Å from Ar^* (1_u) for Ar-CO_2 mixtures. $P_{Ar} \sim 500$ torr. ○, ●, △, □, and ● represent CO_2 partial pressures of 0, 0.0703, 0.1761, 0.2896, and 0.5301 torr respectively.

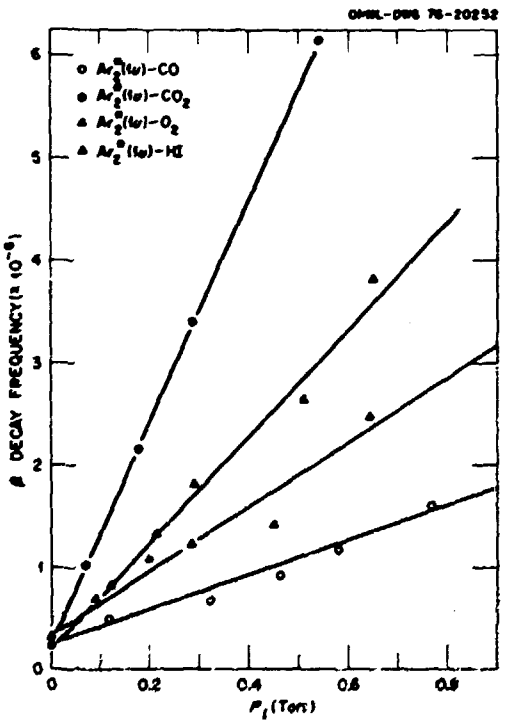

Fig. 12.18. Decay frequency of Ar_2^* (1_u) for various partial pressures P_f of CO_2, O_2, CO, and HI.

The process in which charge is transferred from He^+, He_2^+, and He_3^+ to nitrogen molecules to populate $N_2^+(B^2\Sigma_u^+)_{v=0}$ with the extraction of stimulated emission in the transition of $N_2^+(B^2\Sigma_u^+ \rightarrow X^2\Sigma_g^+)$ is a potential pumping mechanism for lasers.

Ion-molecule reactions, which are important in the development of gas lasers and in studies of planetary atmosphere, have aroused much interest. Charge transfer reactions

$$He^+ + N_2 \begin{cases} \nearrow He + N_2^+ \\ \searrow He + N^+ + N \end{cases}$$

have been investigated by using a photoionization technique. The overall rate (k_1) of both reactions was obtained as 1.5×10^{-9} cm^3/sec. The ratio of the N^+ ion to the N_2^+ ion produced was observed as 48:52. Since a large amount of energy (~9 eV) is released in forming $N_2^+(X^2\Sigma_g^+)$, its production might not be very significant compared to the production of $N_2^+(B)$.

Recently, Lee, Collins, and Waller[53] measured the bimolecular and termolecular charge transfer rates of $He_2^+ + N_2$ by monitoring the emission of $N_2^+(B^2\Sigma_u^+)$ from intense electron beam pumping for high helium pressure. Thus, $N_2^+(B^2\Sigma_u^+)$ should be produced through charge transfer from He^+ when the helium partial pressure is kept low. On the other hand, He^+ can be converted to He_2^+ when the helium partial pressure is high. Patterson[54] reported the first experimental evidence of the existence of He_3^+, for which he determined a dissociation energy of 0.17 eV. Lee, Collins, and Waller[53] showed that He_3^+ is formed according to

$$He_2^+ + 2He \rightleftarrows He_3^+ + He$$

in the pressure range of 300 to 1500 torr. Since He_3^+ has an even closer resonance to the energy level of $N_2^+(B^2\Sigma_u^+)$, one can expect the rate coefficient of the termolecular reaction

$$He_2^+ + N_2 + He \rightarrow N_2^+(B^2\Sigma_u^+) + 3He \qquad (20)$$

to be large. The rate coefficient of this termolecular reaction (K_2) has been obtained as 16×10^{-30}

53. F. W. Lee, C. B. Collins, and R. A. Waller, *J. Chem. Phys.* 65, 1605 (1976).
54. P. L. Patterson, *J. Chem. Phys.* 48, 3625 (1968).

cm^6/sec,[53] which is competitive with the charge transfer process of $He_2^+ + N_2$ even if the helium partial pressure is only a few hundred torr.

In this work, a low-intensity proton beam was used to excite He-N_2 mixtures to prevent any dissociative recombination. The partial pressure of He and N_2 can be sufficiently controlled that the charge transfer rates for He^+ and He_2^+ to N_2 can be measured. The existence of He_3^+ is also observed, and the rate coefficient of the termolecular reaction of Eq. (20) is obtained. From time-resolved emission spectra of $N_2^+(B^2\Sigma_u^+)$, the conversion rate of He^+ to He_2^+ is also observed. In addition to the charge transfer mechanism for populating $N_2^+(B^2\Sigma_u^+)$, the Penning ionization process might be an important mechanism for producing $N_2^+(B^2\Sigma_u^+)$ when an He-N_2 laser is produced by an intense electron beam.

The charge transfer processes of He-N_2 mixtures were also studied by time-resolved emission of the transition of $N_2^+(B^2\Sigma_u^+)_{v=0} \rightarrow N_2^+(X^2\Sigma_g^+)_{v=0,1}$ at low helium pressures. In this case ($P_{He} < 50$ torr), the decay of $N_2^+(B)$ can be written as

$$[N_2^+(B^2\Sigma_u^+)_{v=0}] = [N_2^+(B^2\Sigma_u^+)_{v=0}]_0 e^{-(k_1 P_{N_2} + K_1 P_{He}^2)t} , \quad (21)$$

where k_1 is the quenching rate of He^+ by N_2, K_1 is the three-body conversion rate to form He_2^+, and the destruction frequency of He^+ is

$$\nu_{He^+} = k_1 P_{N_2} + K_1 P_{He}^2 . \quad (22)$$

The charge transfer rate constant for He^+ to N_2 is obtained as 1.44×10^{-9} cm^3/sec.

For high helium pressure ($P_{He} \geqslant 200$ torr), the destruction frequency of He^+ corresponds to the rise time of the formation of $N_2^+(B^2\Sigma_u^+)$. Experimental data are shown in Fig. 12.19. The conversion rate (k_1) of the He^+ into He_2^+ by helium is obtained as 8.1×10^{-32} cm^6/sec.

In the pressure regions $P_{He} \geqslant 200$ torr and $P_{N_2} < 0.05$ torr the decay of $N_2^+(B^2\Sigma_u^+)_{v=0}$ corresponds to the destruction of He_2^+. Thus the destruction frequency is

$$\nu_{He^+} = k_2 P_{N_2} + K_2 P_{N_2} P_{He} , \quad (23)$$

where k_2 and K_2 represent the quenching of He_2^+ and termolecular rate constant for charge transfer of He_2^+. The destruction frequency of He_2^+ vs pressure is plotted in Fig. 12.20. From Eq. (23), k_2 can be obtained as

$$k_2 \equiv \frac{\nu(0, P'_{N_2}) - \nu(0, P''_{N_2})}{P'_{N_2} - P''_{N_2}} , \quad (24)$$

where $\nu(0, P'_{N_2})$ and $\nu(0, P''_{N_2})$ represent the decay frequency of $N_2^+(B^2\Sigma_u^+)_{v=0}$ for $P_{He} = 0$ torr and for nitrogen pressure at P'_{N_2} and P''_{N_2} respectively. For a fixed N_2 partial pressure, the destruction frequency is plotted against helium pressure. Then, from extrapo-

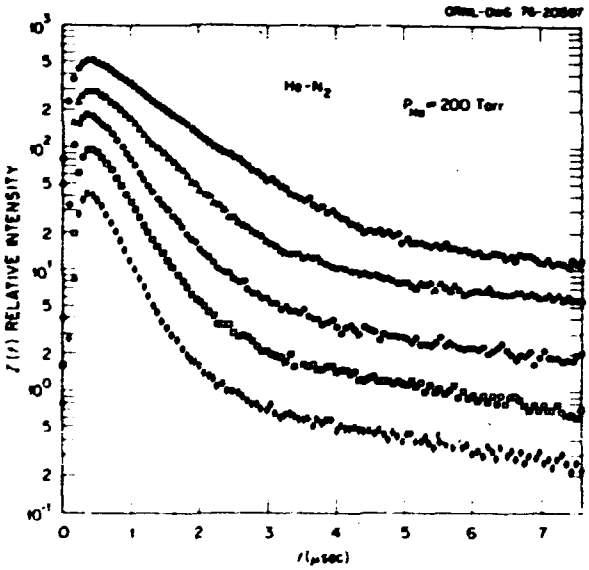

Fig. 12.19. Time histories of $N_2^+(B^2\Sigma_u^+)_{v=0}$ for $P_{He} = 200$ torr. ●, ▲, ○, □, and ◇ represent P_{N_2} at 0.0065, 0.015, 0.024, 0.034, and 0.047 torr respectively. Note the three regions: rise, fast decay, slow decay.

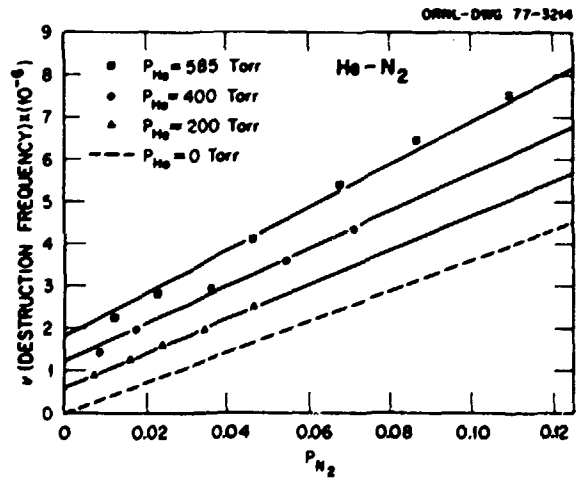

Fig. 12.20. Decay frequency of $N_2^+(B^2\Sigma_u^+)_{v=0}$ vs nitrogen partial pressure.

lation to $P_{He} = 0$ torr, the destruction frequency for various N_2 pressures is plotted. From this line, k_2 is obtained as 1.1×10^{-9} cm^3/sec, which also agrees with the results of Lee, Collins, and Waller[53] and Bohme et al.[55] In Fig. 12.21, $d\nu/dP_{N_2}$ is plotted for the three observed helium pressures. K_2 is obtained as 18×10^{-30} cm^6/sec, which agrees, within experimental error, with the results of Lee, Collins, and Waller.[53] Since the maximum helium pressure in this work was only 600 torr, the accuracy of K_2 is considered to be within 50%.

In Fig. 12.19, the slow-decay parts come from the Penning ionization of N_2 due to metastable helium atoms or molecules. When decay frequency is plotted for various N_2 partial pressures, the destruction rate constant is obtained as 1.1×10^{-10} cm^3/sec. The emission intensity of $N_2^+(B^2\Sigma_u^+)_{v=0}$ due to Penning ionization is estimated to be 10% of the intensity from the charge transfer process for $P_{He} < 200$ torr. The ratio of the total emission intensity from Penning ionization to the emission from the charge transfer process decreases when helium partial pressure increases and nitrogen partial pressure is kept relatively low.

The destruction rate of He_2^+ by charge transfer ($k_2 = 1.1 \times 10^{-9}$ cm^3/sec) differs by a factor of 10 from the rate by Penning ionization (1.1×10^{-10} cm^3/sec). The ratio of emission intensity due to the charge transfer process to that due to Penning ionization is also a factor of 10.

Since the emissions of $N_2^+(B^2\Sigma_u^+)_{v=0}$ are mainly due to charge transfer processes involving atomic and molecular helium ions, the destruction rate constants for atomic and molecular helium ions due to other molecules can be measured by time-resolved emission of $N_2^+(B^2\Sigma_u^+)_{v=0} \rightarrow N_2^+(X^2\Sigma_g^+)_{v=0}$ if this emission is not overlapped with the spectra of other molecules. Results for $P_{He} = 32$ torr and $P_{N_2} = 0.014$ torr (shown in Fig. 12.22) lead to destruction rate constants k_1 of He^+ by CO, CO_2, and H_2S as 1.9×10^{-9}, 1.3×10^{-9}, and 6×10^{-10} cm^3/sec respectively. The results for He^+-CO and He^+-CO_2 agree, within experimental error, with the previous results.

The destruction frequency of $N_2^+(B^2\Sigma_u^+)_{v=0}$ by CO_2 at $P_{He} = 400$ torr for various CO_2 pressures was also determined. The total quenching rate constant was obtained as 2.6×10^{-9} cm^3/sec. The termolecular rate constant K_2 for He-CO_2 was measured as 67×10^{-30} cm^6/sec by Lee, Collins, and Waller.[53] Thus the charge transfer rate of He_2^+ to CO_2 is obtained as 1.7×10^{-9}

55. D. K. Bohme et al., *J. Chem. Phys.* 52, 5094 (1970).

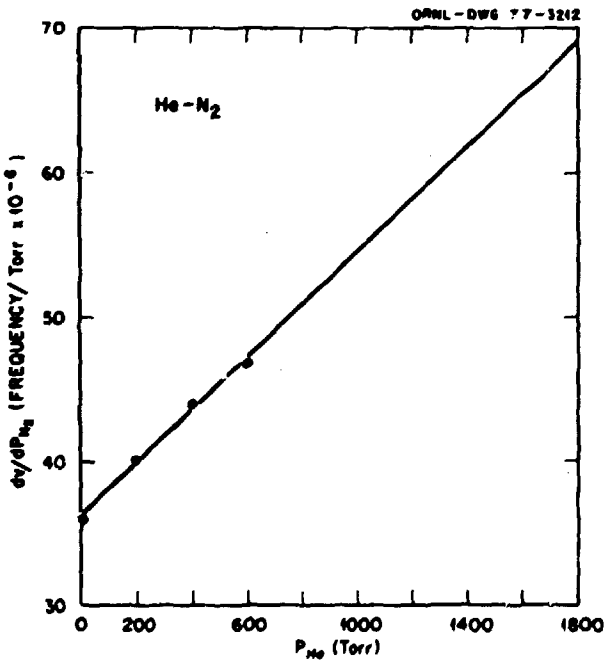

Fig. 12.21. The slope of the decay frequency vs nitrogen pressure (from Fig. 12.20), plotted against helium partial pressure.

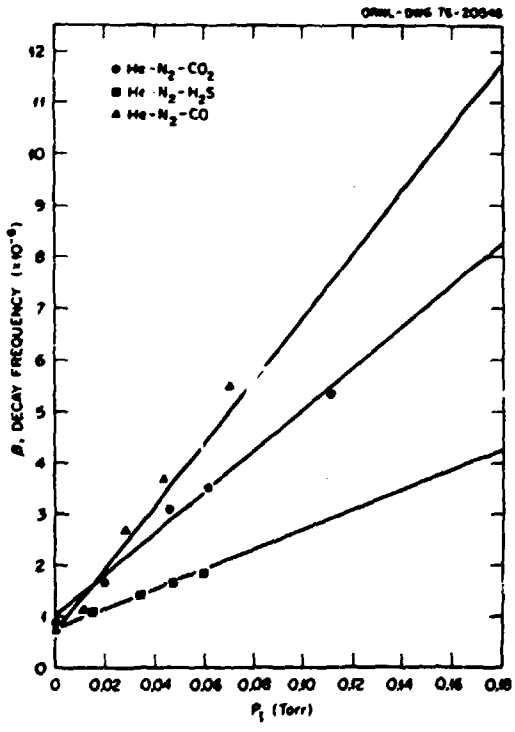

Fig. 12.22. Decay frequency of $N_2^+(B^2\Sigma_u^+)_{v=0}$ plotted for various pressures of H_2S, CO, and CO_2. $P_{He} = 32$ torr; $P_{N_2} = 0.014$ torr.

cm^3/sec. The accuracy of the atomic and molecular helium ion quenching rate constants in this work is believed to be within 25%.

Collins, Cunningham, and Stockton[56] demonstrated the laser action of He-N_2 mixtures excited by an electron beam. A peak laser power was obtained for helium pressure at 7 atm with P_{N_2} between 5 and 10 torr. The pulse width was obtained as 15 nsec. The termolecular charge transfer process is a factor of 3 greater than the bimolecular charge transfer rate for P_{He} at 7 atm. If the branching ratio for producing $N_2^+(B^2\Sigma_u^+)_{v=0}$ compared with the overall rate for both charge transfer processes is about the same, the termolecular process will populate about 70% of $N_2^+(B^2\Sigma_u^+)_{v=0}$. From the Penning ionization rate to form $N_2^+(B^2\Sigma_u^+)_{v=0}$ and from the ratio of the emission intensity by the Penning ionization process to the emission by the charge transfer process, we estimate that the contribution of the He-N_2 level by Penning ionization is only 6%.

Charge Transfer Studies of Ne-N_2 Mixtures

Since the energy levels of Ne_2^+ are so close to $N_2^+(B^2\Sigma_u)_{v=0}$, the charge transfer rate from Ne_2^+ to N_2 is expected to be large. The conversion rate for the reaction

$$Ne^+ + 2Ne \rightarrow Ne_2^+ + Ne$$

has previously been determined to be 7×10^{-32}, 7.9×10^{-32}, and 5.8×10^{-32} cm^6/sec by afterglow and drift tube methods. Thus, for Ne-N_2 mixtures excited by fast charged particles, $N_2^+(B^2\Sigma_u^+)$ should be produced through charge transfer from Ne^+ when the neon partial pressure is kept low. On the other hand, most Ne^+ can be converted to Ne_2^+ when the neon partial pressure is high. Since the energy level $N_2^+(B^2\Sigma_u^+)_{v=0}$ is close to the energy of Ne_2^+, the efficiency to produce $N_2^+(B^2\Sigma_u^+)_{v=0}$ by charge transfer from Ne_2^+ should be high.

The charge transfer mechanisms of atomic and molecular neon ions to N_2 are studied by time-resolving the fluorescence emission from $N_2^+(B^2\Sigma_u)_{v=0}$. Our experimental data also give indirect evidence for the existence of Ne_3^+.

The lifetime of $N_2^+(B^2\Sigma_u)_{v=0}$ and the quenching rate of $N_2^+(B^2\Sigma_u^+)_{v=0}$ by N_2 are 62 nsec and 3.44×10^{-10} cm^3/sec respectively. In this work, the nitrogen partial pressure is always kept so low that the rate of destruction of $N_2^+(B^2\Sigma_u)_{v=0}$ is much faster than the charge transfer rate. The destruction frequency of Ne^+ is

$$\nu_{Ne^+} = k_1 P_{N_2} + K_1 P_{Ne}^2 .$$

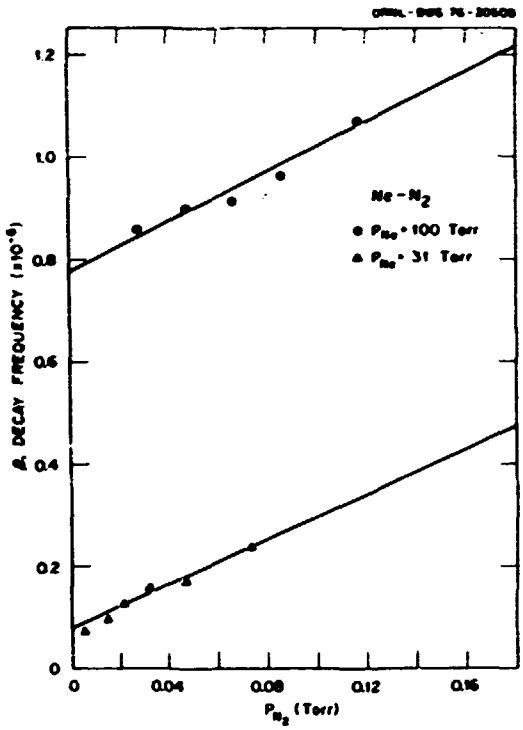

Fig. 12.23. Decay frequency is plotted against various nitrogen partial pressures for P_{Ne} at 100 and 31 torr.

The destruction frequency of Ne^+ for various nitrogen pressures is shown in Fig. 12.23. The overall quenching rate (k_1) of Ne^+ by N_2 is obtained as 7.2×10^{-11} cm^3/sec. The three-body conversion rate (K_1) to form Ne_2^+ is obtained as 7.6×10^{-32} cm^6/sec. When the neon partial pressure is sufficiently high so that $K_1 P_{Ne}^2 \gg k_2 P_{N_2}$, the decay part of time-resolved emission spectra of $N_2^+(B^2\Sigma_u)_{v=0}$ corresponds to the destruction of Ne_2^+. In Fig. 12.24, experimental data of time-resolved spectra for neon pressure at 600 torr are plotted. The destruction frequencies of Ne_2^+ by N_2 for neon pressure at 300 and 600 torr are plotted in Fig. 12.25. The discrepancy in the intercepts for neon pressures of 300 and 600 torr is quite significant. Thus, the experimental data give indirect evidence of the existence of Ne_3^+. The destruction frequency of Ne_2^+ is similar to He_2^+ by N_2. The overall quenching rate of Ne_2^+ by N_2 is obtained as 5.3×10^{-10} cm^3/sec. The termolecular rate of charge transfer (K_2) can be obtained as 23×10^{-30} cm^6/sec.

The fluorescence spectrum of Ne-N_2 mixtures excited by a proton beam is shown in Fig. 12.26. Emission lines

56. C. B. Collins, A. J. Cunningham, and M. Stockton, *Appl. Phys. Lett.* **25**, 344 (1974).

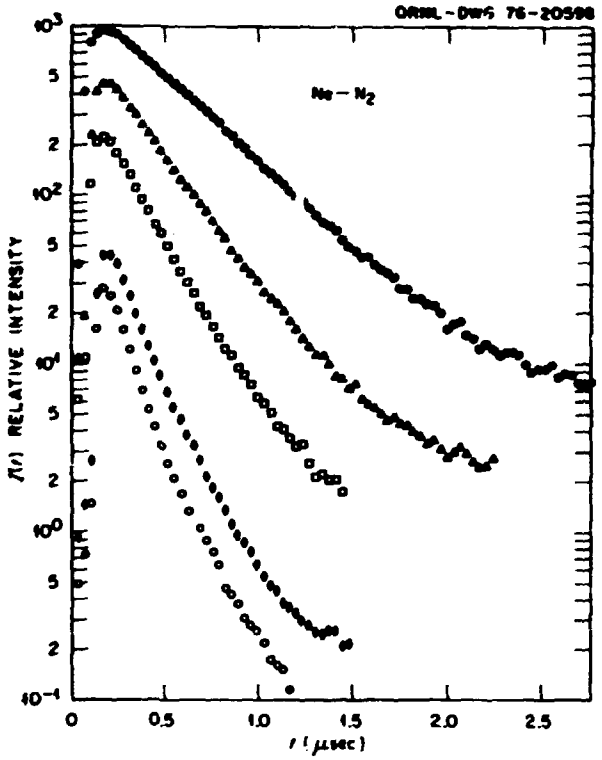

Fig. 12.24. Time-resolved emission of $N_2^+(B^2\Sigma_u)_{v=0} \rightarrow N_2^+(X^2\Sigma_g)_{v=0}$ for P_{Ne} = 600 torr. •, ▲, □, ◇, and ○ represent nitrogen partial pressures at 0.0192, 0.0458, 0.0915, 0.14, and 0.177 torr respectively.

Fig. 12.26. Emission spectrum of Ne-N_2 mixtures excited by a proton beam. The pressures of neon and N_2 are 600 and 0.183 torr respectively. The proton beam intensity is 0.8 μA, and the time interval between two pulses is 4 μsec.

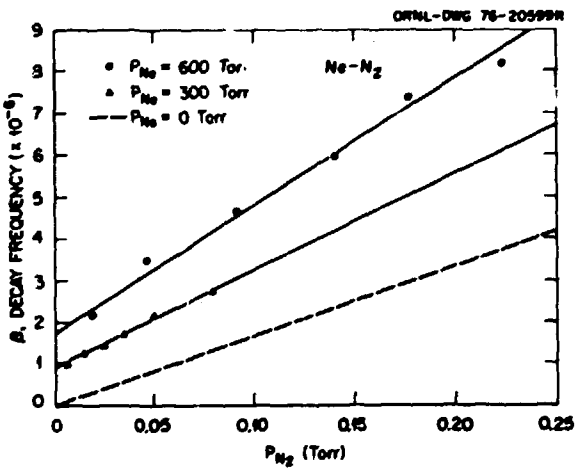

Fig. 12.25. Decay frequency of $N_2^+(B^2\Sigma_u)_{v=0}$ is plotted against various nitrogen pressures.

are found to be due to $N_2^+(B^2\Sigma_u)$, $N_2(C^3\Pi_u)$, and $N_2(E^3\Sigma_g^+)$. From time-resolved spectra of $N_2(E^3\Sigma_g^+)$, it is found that $N_2(E^3\Sigma_g^+)$ is populated by dissociative recombination of N_2^+ since the decay of $N_2(E^3\Sigma_g^+)$ is very slow. Willett and Litynski[57] added SF_6 to the nitrogen laser system and found that the 3371-Å output energy pulse corresponding to the $N_2(C^3\Pi_u)_{v'=0} \rightarrow N_2(B^3\Pi_g)_{v''=0}$ transition was increased by 50%. Chen et al.[58] pointed out that the addition of SF_6 can increase the population of $N_2(C^3\Pi_u)$. Since the energy level of $N_2(E^3\Sigma_g)_{v=0}$ is 11.87 eV, which is close to the energy level of $N_2(C^3\Pi_u)_{v=0}$, the population of $N_2(E^3\Sigma_g)$ is probably very significant compared with the population of $N_2(C^3\Pi_u)_{v=0}$. Thus, we consider the following mechanism to be the important process whereby $N_2(C^3\Pi_u)_{v=0}$ is populated:

$$N_2(E^3\Sigma_g) + SF_6 \rightarrow N_2(C^3\Pi_u) + SF_6^* .$$

In Fig. 12.27, we compare the fluorescence efficiency of He-H_2 and Ne-N_2 mixtures excited by a proton beam. The fluorescence efficiency of Ne-N_2 is only 70% of He-N_2. Since the energy deposition to neon is higher

57. C. S. Willett and D. M. Litynski, *Appl. Phys. Lett.* **26**, 118 (1973).

58. C. H. Chen et al., *J. Chem. Phys.* **65**, 3863 (1976).

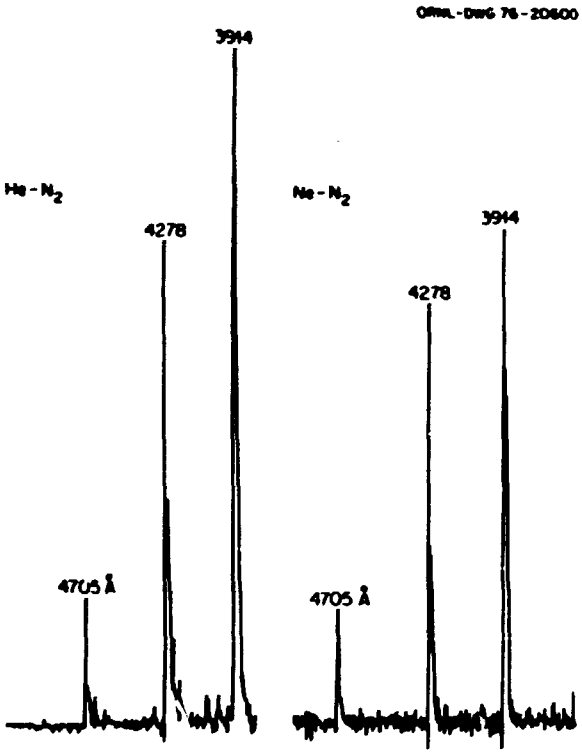

Fig. 12.27. Emission spectra of He-N_2 mixtures and Ne-N_2 mixtures excited by a proton beam. The proton beam intensity was kept the same for both mixtures. The pressures of helium and N_2 are 600 and 0.183 torr respectively.

than that to helium, the absolute fluorescence efficiency for Ne-N_2 mixtures is only 18% of the fluorescence efficiency of He-N_2 mixtures. Thus, it can be concluded that Ne-N_2 mixtures probably cannot lase more efficiently than He-N_2.

Energy Transfer Processes in Proton-Excited Argon-Xenon and Ar-F_2 Mixtures

Gendaken et al.[59] obtained the emission spectra of argon-xenon mixtures from the pulsed electric discharge method, and they suggested the possibility of heterogeneous rare-gas lasers. The detailed mechanism for the formation of heterogeneous dimers and for energy transfer processes has not been studied.

Since the reports by Golde[60] and Velazco and Setser[61] of emission from rare-gas–halide excimers (created by two-body reaction between metastable rare-gas atoms and halogen-containing molecules), rare-gas–halide lasers have been considered intensively for laser isotope separation and laser-induced fusion. By electron beam pumping, laser emission has been demonstrated for KrF*, KrCl*, XeBr*, XeF*, XeCl*, and ArF*. Laser oscillations have also been reported for some of the above systems following electric discharge excitation. Molecular bromine and iodine lasers have also been demonstrated.

Although an ionic model has been used to explain the emission spectra of rare-gas monohalides, there is no reported direct evidence for the energy precursors of rare-gas–monohalide excimers. Since the excitation of gases by low-intensity fast protons is similar to that by low-intensity fast electrons, the study of gas kinetics by proton beam excitation should supply information on electron-beam-pumped lasers. Here, time-resolved emission spectra are used to study the energy precursors of argon-xenon and Ar-F_2. Measurements of the rate constants for quenching $Ar(^3P_1)$, $Ar(^1P_1)$, and $Ar_2^*(1_u)$ with xenon and F_2 are also reported. The kinetics of Ar-F_2, Ar-Kr-F_2, and Ar-Xe-F_2 lasers are discussed.

Some energy levels of atomic argon, $Ar_2^*(1_u)$, and atomic xenon are tabulated in Table 12.2. Since a few energy levels of argon almost overlap certain excited states of xenon, the energy transfer cross sections for quenching such states are presumably larger. The fluorescence emission spectra of argon-xenon mixtures excited by proton beams, with argon partial pressures at 30 torr, are given in Fig. 12.28. The emission lines from $Xe[^2P_{3/2}(5d), J = 1]$ (1192 Å); $Xe[^2P_{3/2}(6s), J = 1]$, that is, $Xe(^3P_1)$ (1470 Å); and $Xe[^2P_{1/2}(6s), J = 1]$, that is, $Xe(^1P_1)$ (1296 Å) have been observed.

Time histories of emission line intensities for $Ar(^3P_1)$ and $Xe[^2P_{3/2}(5d), J = 1]$ for a 30-torr argon partial pressure and a 0.0211-torr xenon partial pressure are given in Fig. 12.29. There are fast- and slow-decay components for the time-resolved intensity of $Xe[^2P_{3/2}(5d), J = 1]$. By subtracting the slow-decay part from the

59. A. Gendaken et al., *J. Chem. Phys.* **57**, 3456 (1972).
60. M. F. Golde, *J. Mol. Spectrosc.* **58**, 261 (1975).
61. J. E. Velazco and D. W. Setser, *J. Chem. Phys.* **62**, 1990 (1975).

Table 12.2. Excited states of Ar, Xe, and Ar_2 (energy in cm^{-1})

Ar	Xe	Ar_2
95,399 ($^1P_1$)	95,499 [$^2P_{3/2}(9d), J = 1$]	
	95,287 [$^2P_{3/2}(10p), J = 0$]	
	95,274 [$^2P_{3/2}(9d), J = 2$]	
94,533 ($^3P_0$)	93,421 [$^2P_{3/2}(5f), J = 3$]	
93,750 ($^3P_1$)	93,423 [$^2P_{3/2}(9s), J = 1$]	93,750
93,143 ($^3P_2$)	85,440 [$^2P_{3/2}(7s), J = 1$]	
	83,890 [$^2P_{3/2}(5d), J = 1$]	
	77,186 ($^1P_1$)	
	76,197 ($^3P_0$)	
		68,550
	68,045 ($^3P_1$)	
	67,068 ($^3P_2$)	

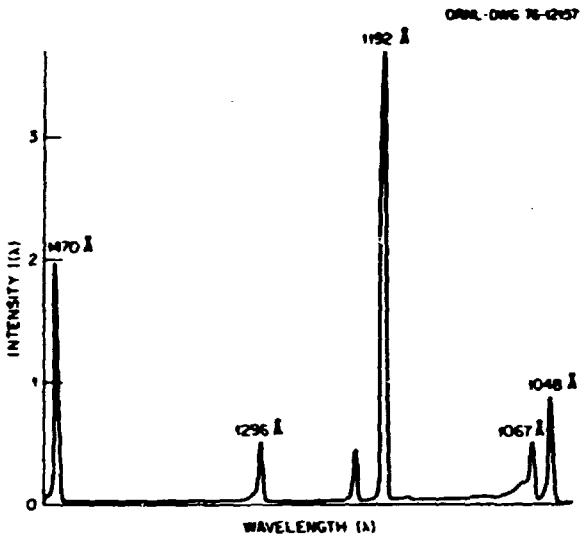

Fig. 12.28. Relative intensity vs wavelength for argon-xenon mixtures excited by a proton beam. P_{Ar} = 30 torr; P_{Xe} = 0.0276 torr.

fast-decay part, the resulting time history of $Xe(^2P_{3/2}(5d), J = 1]$ can be seen to almost follow the time history of $Ar(^3P_1)$. Thus the major precursor of $Xe[^2P_{3/2}(5d), J = 1]$ is $Ar(^3P_1)$. At low partial argon and xenon pressure, the decay of $Ar(^3P_2)$ is much slower than that of $Ar(^3P_1)$. Thus, $Ar(^3P_2)$ can be ruled out as a major precursor of $Xe[^2P_{3/2}(5d), J = 1]$.

Time histories of emission bands at 1100 Å due to $Ar_2^*(0_u)$, at 1250 Å due to $Ar_2^*(1_u)$, at 1296 Å due to $Xe(^1P_1)$, and at 1470 Å due to $Xe(^3P_1)$ are given in Fig. 12.30 for argon and xenon partial pressures of 398 and 0.0843 torr respectively. There are fast- and slow-decay parts for the emissions of $Xe(^1P_1)$ and $Xe(^3P_1)$. By subtracting the slow-decay part from the fast-decay part, the time histories of $Xe(^3P_1)$ and $Xe(^1P_1)$ are seen to closely follow the decay of $Ar_2^*(1_u)$, which gives the 1250-Å continuum. The energy precursors of both $Xe(^3P_1)$ and $Xe(^1P_1)$ should therefore be mainly $Ar_2^*(1_u)$. This conclusion agrees with the suggestion by Gendaken et al.[59]

The decay frequencies for the fast- and slow-decay parts of $Xe(^1P_1)$ were determined as before. The fast decay after subtraction of the slow-decay part at each pressure is similar to the decay of $Ar_2^*(1_u)$. The slow-decay part probably comes from the dissociative recombination process since the quenching rates of $Ar(^3P_2)$, $Ar(^3P_1)$, $Ar(^3P_0)$, and $Ar(^1P_1)$ are much faster than the slow-decay part of $Xe(^1P_1)$ and since the similar slow-decay part also occurs in $Xe(^3P_1)$ and $Xe[^2P_{3/2}(5d), J = 1]$. Bohme et al.[55] measured the rate at which krypton quenches Ar_2^+, and they found that the predominant product is $ArKr^+$. A similar procedure may occur for argon-xenon mixtures excited by fast charged particles. The proposed mechanism is

$$Ar_2^+ + Xe \begin{cases} \nearrow ArXe^+ + Ar \\ \searrow Xe^+ + 2Ar \end{cases} ,$$

$$ArXe^+ + e \rightarrow Xe^* + Ar ,$$

$$Xe^+ + Xe(Ar) + e \rightarrow Xe^* + Xe(Ar) .$$

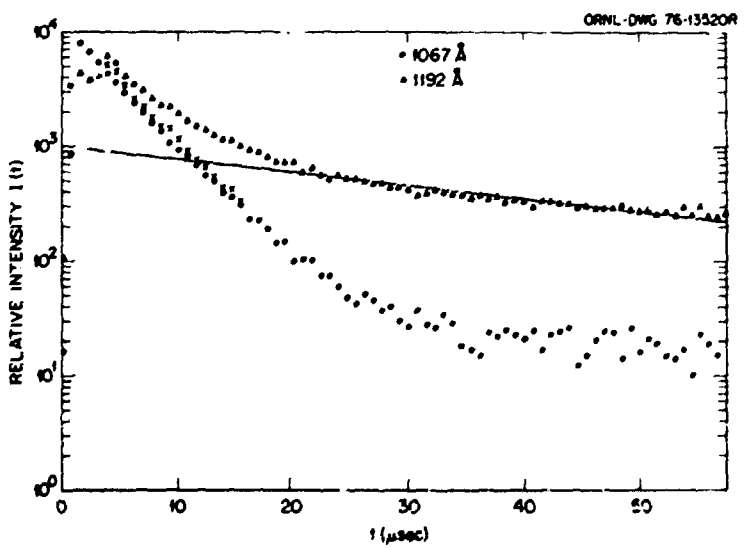

Fig. 12.29. Time decay of emission from $Ar(^3P_1)$ and $Xe[^2P_{3/2}(5d), J = 1]$ in argon-xenon mixtures excited by a proton beam. P_{Ar} = 30 torr; P_{Xe} = 0.0211 torr. • and ▲ represent $Ar(^3P_1)$ and $Xe[^2P_{3/2}(5d), J = 1]$ respectively. × represents the results of the subtraction of the fast-decay part from the slow-decay part.

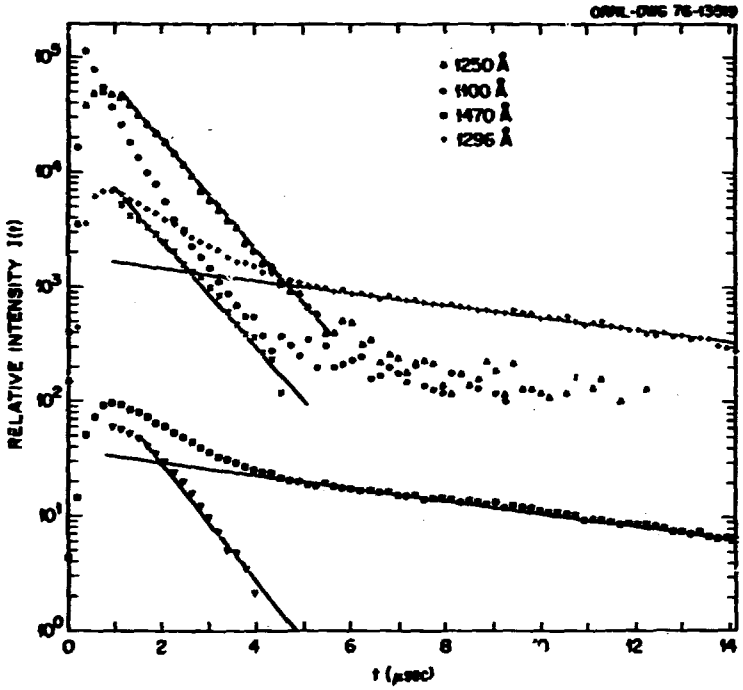

Fig. 12.30. Time decay of emission in line and band spectrum features at 1100, 1250, 1470, and 1296 Å in argon-xenon mixtures. The partial pressures for argon and xenon are 398 and 0.0843 torr respectively. ●, ▲, □, and + represent $Ar_2^*(0_u)$, $Ar_2^*(1_u)$, $Xe(^3P_1)$, and $Xe(^1P_1)$ respectively. × represents the results of the subtraction of the fast-decay part from the slow-decay part of the emission of $Xe(^1P_1)$, and ▼ represents the results of the subtraction of the fast-decay part from the slow-decay part of the emission of $Xe(^3P_1)$.

The overall quenching rate constant of Ar_2^* by xenon is obtained as 7.2×10^{-11} cm^3/sec from the slope of the slow-decay line.

The quenching rate constants obtained for $Ar(^1P_1)$, $Ar(^3P_1)$, $Ar_2^*(1_u)$, and $Ar_2^*(0_u)$ are 3.3×10^{-10}, 2.2×10^{-10}, 2.2×10^{-10}, and 2.4×10^{-10} cm^3/sec respectively. Since the lifetime of $Ar_2^*(0_u)$ is only a few nanoseconds, the quenching of $Ar_2^*(0_u)$ by xenon is the same as the quenching rate of the precursors of $Ar_2^*(0_u)$.

An emission spectrum from 1000 to 5000 Å for Ar-F_2 mixtures excited by a proton beam is shown in Fig. 12.31. The emission spectrum of ArF* with a peak at 1933 Å is very similar to the laser spectrum obtained by Hoffman, Hays, and Tisone[62] but differs from the emission spectrum at low pressure ($P_{Ar} \sim 1$ torr) obtained by Golde.[60] With the argon partial pressure at a few hundred torr, the vibrational levels of the upper electronic state of ArF* have relaxed into a Boltzmann distribution. A very intense broad continuum with the peak at 2840 Å is also observed. This broad continuum is probably due to the transition of ArF_2^* or Ar_2F^*.

Time-resolved spectra with wavelengths at 1933 Å (from ArF*), 2840 Å, 3805 Å [from $N_2(C^3\Pi_u)_{v=0} \rightarrow N_2(B^2\Pi_g)_{v=3}$], and 1270 Å [from $Ar_2^*(1_u)$] are shown in Fig. 12.32. Since there are always traces of N_2 (<2 ppm) in the cell, the emission of $N_2(C^3\Pi_u)_{v=0}$ can be observed. The decay spectra at early times (<5 μsec) for ArF* and 2840-Å band are similar.

Thus, for Ar-F_2 mixtures, ArF* and Ar_2F^* will have common precursors. Since it has been shown that the energy precursor for $N_2(C^3\Pi_u)_{v=0}$ is $Ar(^3P_2)$, the emission from the transition of $N_2(C^3\Pi_u)_{v=0} \rightarrow N_2(B^3\Pi_g)_{v=2}$ (3805 Å) can be monitored to study the time history of $Ar(^3P_2)$. The long-life excited argon dimer $Ar_2^*(1_u)$, which gives the 1270-Å continuum, can be formed from $Ar(^3P_2)$ with the rate of $\sim 10P^2$. It is found that the early time histories (<1 μsec) of ArF* and Ar_2F^* follow the time history of $Ar(^3P_2)$. The time history of ArF* from 1 to 5 μsec follows the time history of $Ar_2^*(1_u)$, and the late time (>1 μsec) decay of Ar_2F^* is about the same as that for $Ar_2^*(1_u)$. A large discrepancy exists between the time decay histories of ArF* and Ar_2F^* for times longer than 5 μsec after the proton pulse. We believed that ion-ion recombination between Ar_2^+ and F^- might contribute to the late emission of ArF* but not directly for the 2840-Å band since

62. J. M. Hoffman, A. K. Hays, and G. S. Tisone, *Appl. Phys. Lett.* 28, 538 (1976).

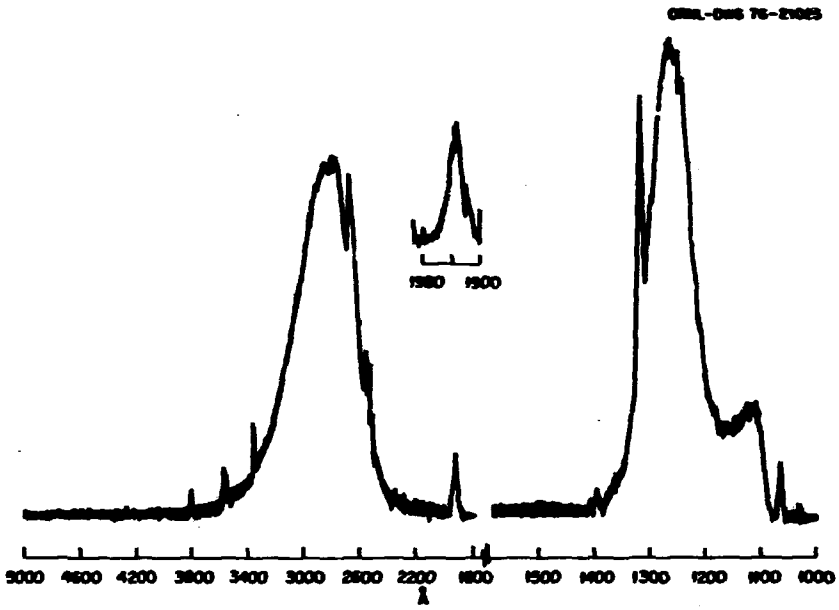

Fig. 12.31. Emission spectra of Ar-F_2 mixtures excited by a proton beam. Argon pressure is 413 torr and fluorine pressure is 0.055 torr. The proton beam current is 0.9 μA, and the time interval between two proton pulses is 4 μsec. The resolution of the monochromators is 1 A.

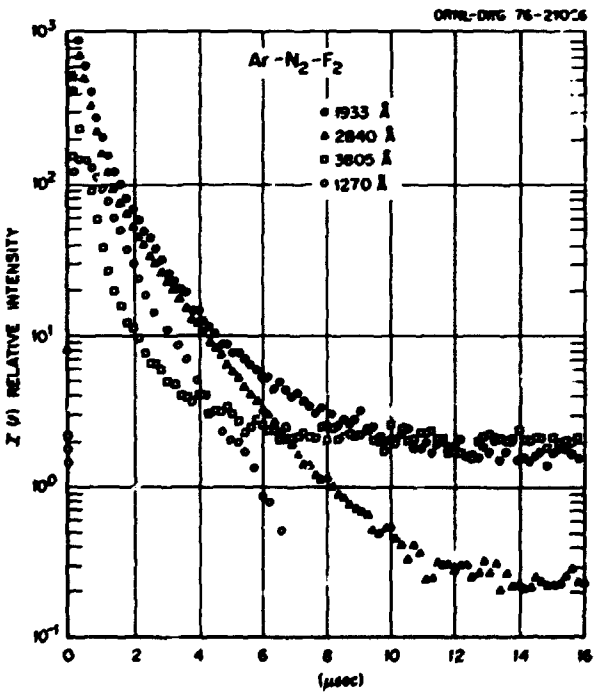

Fig. 12.32. Time histories of ArF^* (1933 A), F_2^* (2840 A), $N_2(C^3\Pi_u)_{v=0}$ (3805 A), and $Ar_2^*(1_u)$ (1270 A). P_{Ar} = 414 torr; P_{F_2} = 0.0551 torr. There is always a tiny amount of N_2 in the system, but the emission of $N_2(C^3\Pi_u)_{v=0}$ is strong enough to be measured (cf. Fig. 12.31).

the cross section for the formation of F^- due to the impact of electrons on F_2 is large. The contribution of ion-ion recombination to the present work is only about 10% ± 5% compared with the contribution by $Ar_2^*(1_u)$ and $Ar(^3P_2)$. For electron-beam-pumped lasers, the contribution of ion-ion recombination processes should be as important as excited argon neutrals, since the recombination rate is proportional to the square of electron beam intensity, whereas the population of excited argon neutrals is linearly proportional to electron beam intensity. The ratio of the contribution of ArF^* by $Ar(^3P_2)$ compared with $Ar_2^*(1_u)$ should be dependent on the partial pressure of argon and fluorine.

For real laser systems, the operating pressures range from one to a few atmospheres. In this pressure range, resonance-excited states such as $Ar(^3P_1)$ and $Ar(^1P_1)$ have longer lifetimes than metastable argon states. In the electron-beam-pumped laser, the radiation-trapped resonance states can rapidly convert to other resonance states or to metastable states by electron collision or by two-body collision processes. Chen and Payne[51] showed that $ArCl^*$ is populated mainly from $Ar(^3P_1)$ when Ar-Cl_2 mixtures are excited by proton beams. Thus the population and the quenching rates of both resonance and metastable states of argon are important for laser kinetic studies. The quenching rate constants for $Ar(^3P_1)$ and $Ar(^1P_1)$ by F_2 are obtained as 8.9 X

10^{-10} and 13×10^{-10} cm³/sec respectively. The ratio of the quenching rate of $Ar(^1P_1)$ by F_2 and xenon to the quenching rate of $Ar(^3P_1)$ by F_2 and xenon is 1.5, which is close to the theoretical prediction of 1.7, based on the ratio of the oscillator strength of $Ar(^1P_1)$ to $Ar(^3P_1)$. The quenching rate constant of $Ar_2^*(1_u)$ by F_2 was found to be 5.2×10^{-10} cm²/sec. In Fig. 12.33, the quenching rate constant of $Ar(^3P_2)$ by F_2 is obtained by monitoring the trace component emission of $N_2(C^3\Pi_u)_{v=0} \rightarrow N_2(B^3\Pi_g)_{v=2}$. The quenching rate constant for $Ar(^3P_2)$ by F_2 is obtained as 9.4×10^{-10} cm³/sec, which agrees with the results obtained by Velazco, Kolts, and Setser.[63] The decay frequency of ArF^* is also plotted in Fig. 12.33. It is obvious that the precursor of ArF^* at low argon pressure is $Ar(^3P_2)$. The accuracy of the quenching rate constants reported in this work is estimated to be within 25%. The quenching rate constants obtained in this work and those obtained by other groups for $Ar(^3P_1)$, $Ar(^3P_2)$, $Ar(^1P_1)$, and $Ar_2^*(1_u)$ by xenon, F_2, and krypton are tabulated in Table 12.3.

The emission line of 1192 Å from $Xe[^2P_{3/2}(5d), J = 1]$ when argon-xenon mixtures are excited by proton beams is very intense. This emission line was not observed by Gendaken et al.,[54] who used an electric discharge to excite fluorescence spectra. This may imply that the destruction cross section of $Xe[^2P_{3/2}(5d), J = 1]$ by slow electrons is quite significant, or that the ratios of the populations of excited states of argon depend on the method of excitation.

Gendaken et al.[59] used a long-range dipole-dipole interaction model to estimate the quenching cross section of the excited argon molecule by xenon and obtained 30 Å². The results obtained in this work disagree with these calculational results, since long-range dipole-dipole interaction is a good approximation (when

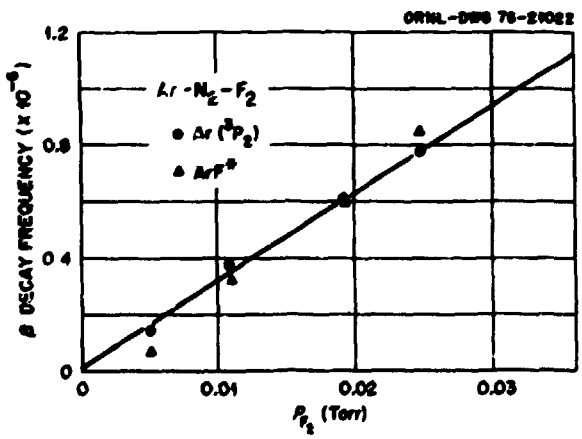

Fig. 12.33. Decay frequency of ArF^* and $Ar(^3P_2)$ for various F_2 pressures with argon pressure at 36 torr. The N_2 pressure is estimated to be <0.001 torr.

Table 12.3. Quenching rate constants and quenching cross sections of $Ar(^3P_1)$, $Ar(^1P_1)$, $Ar(^3P_2)$, and $Ar_2^*(1_u)$ by F_2, xenon, and krypton

	F_2	Xe	Kr
$Ar(^1P_1)$			
k^a	12.9[b]	3.3[b] (3.47)[c]	0.012[d]
σ^e	225[b]	73[b] (77)[c]	0.25[d]
$Ar(^3P_1)$			
k^a	8.9[b]	2.2[b] (1.92)[c]	
σ^e	156[b]	49[b] (43)[c]	
$Ar(^3P_2)$			
k^a	9.4[b] (7.5)[f]	1.8[g]	0.062[g]
σ^e	165[b] (131)[f]	40[g]	1.3[g]
$Ar_2^*(1_u)$			
k^a	5.2[b]	2.4[b] (1.92)[c]	0.091[d]
σ^e	105[b]	57[b] (46)[c]	1.9[d]

[a] k is in units of 10^{-10} cm³ sec⁻¹ molecule⁻¹.
[b] Present work.
[c] P. K. Leichner, E. H. Hall, and K. F. Palmer, to be published.
[d] Ref. 65.
[e] $\sigma = k/v = k/[8k'T/\pi\mu]^{1/2}$, where k' is Boltzmann's constant and μ is reduced mass; σ is in units of Å².
[f] Ref. 63.
[g] Ref. 43.

calculating quenching cross sections) only if the energy defect (ΔE) is less than 50 cm⁻¹. Thus the prediction of energy transfer cross sections requires very detailed information on interaction potentials.

Since the energy levels of $Ar_2^*(1_u)$ are higher than those of $Xe(^3P_1)$, one would not expect the energy transfer directly from $Ar_2^*(1_u)$ to $Xe(^3P_1)$ to proceed at a high rate. Gendaken et al.[59] proposed that $Xe(^1P_1)$ can be converted to $Xe(^3P_1)$ by a two-body collision. We found that the ratio of the emission intensity to $Xe(^3P_1)$ to that of $Xe(^1P_1)$ increases very significantly when the xenon partial pressure increases. Since the time histories of $Xe(^3P_1)$ and $Xe(^1P_1)$ are the same in this work, the destruction rate of $Xe(^1P_1)$ by xenon from the two-body collision process should be larger than the quenching rate of $Ar_2^*(1_u)$ by xenon (i.e., 2.4×10^{-10} cm³/sec).

Ewing and Brau[64] demonstrated laser action of KrF^* from mixtures of argon, krypton, and F_2 in the ratio of 98.9:1:0.1 (pressure range, 1 to 4 atm) excited by intense electron beams. They also achieved lasing of XeF^* with the mixtures of argon, xenon, and F_2 in the ratio of 99.6:0.3:0.1. The mechanism suggested was

63. J. E. Velazco, J. H. Kolts, and D. W. Setser, *J. Chem. Phys.* 65, 3468 (1976).

64. J. J. Ewing and C. A. Brau, *Phys. Rev. A* 12, 129 (1975).

that of rapid electron-ion recombination to produce excited states of argon which then transfer their energy to krypton or xenon. The excited rare-gas halides are then formed by the reaction of excited krypton or xenon with F_2. The quenching rate constants of $Ar(^3P_2)$ and $Ar(^3P_0)$ by krypton were measured by Piper, Velazco, and Setser[63] as 6.2×10^{-12} and 2.3×10^{-12} cm^3/sec respectively. Leichner[65] obtained the quenching rate constants of $Ar(^3P_1)$, $Ar(^1P_1)$, and $Ar_2^*(1_u)$ by krypton as 9.1×10^{-12}, 1.2×10^{-12}, and 9.4×10^{-12} cm^3/sec respectively. From the quenching rate constants of excited atomic and molecular argon by krypton, xenon, and F_2, the following mechanisms are proposed for the kinetics of KrF* lasers which were demonstrated by Ewing and Brau:[66]

$$Ar^* \text{ (or } Ar_2^*) + F_2 \begin{cases} F_2^* + Ar\ (2Ar) \\ ArF^* + F + (Ar) \end{cases},$$

$$ArF^* + Kr \rightarrow KrF^* + Ar\ .$$

For the XeF* laser, the following mechanisms should apply:

$$Ar^* \text{ (or } Ar_2^*) + F_2 \rightarrow F_2^* + Ar\ (2Ar)$$

$$\rightarrow ArF^* + F + (Ar)\ ,$$

$$Ar^* \text{ (or } Ar_2^*) + Xe \rightarrow Xe^* + Ar\ (2Ar)\ ,$$

$$Xe^* + F_2 \rightarrow XeF^* + F\ .$$

The ratio of the population of Ar_2F^* to the population of ArF* is estimated in the present work to be about 7.

For electron-beam-pumped lasers, the ion-ion recombination and dissociative recombination processes should also populate KrF* and XeF*, since the charge transfer rates of Ar_2^+ to krypton and xenon are only 7.5×10^{-10} (ref. 55) and 7.2×10^{-11} cm^3/sec respectively. The mechanism in which ion-ion recombination populates KrF* and XeF* probably involves ArF* as an intermediate state instead of recombination between Xe^+ or Kr^+ with F^-. Thus

$$e + F_2 \rightarrow F^- + F\ ,$$

$$Ar_2^+ + F^- \rightarrow ArF^* + Ar\ ,$$

$$ArF^* + Xe \rightarrow XeF^* + Ar\ ,$$

or

$$ArF^* + Kr \rightarrow KrF^* + Ar\ .$$

Energy Pathways for Pollutant Detection

In the past year we excited Ar-NO, Ar-NO_2, and Ar-N_2O mixtures; emission lines were observed from NO, NO_2, and N_2O. Since these emission lines are very narrow-band and are intense, we believe this type of pollutant can be detected with high efficiency by an energy transfer process from excited argon. We plan to use a laser-induced breakdown technique to replace the proton excitation, which we believe will greatly improve the sensitivity. Recently, we demonstrated ultrasensitive detection of D_2O for Ar-D_2O mixtures excited by the proton beam. A high resolution of rotational spectrum of OD(A) was obtained in the 2700-Å region. We expect that the same technique can be extended to detect THO.

Simple Geometry Experiment and Its Supporting Calibration Laboratory

An apparatus was built for measurement of the absolute fluorescence efficiency of gases excited by a proton beam (Fig. 12.34). The important feature of this apparatus is its simple geometry,[67] defined by the aperture and the slit. It is possible to calculate the number of photons emitted from a unit length of the excited gas volume in terms of the number of photons observed by the detector system.

65. P. K. Leichner, private communication.
66. J. J. Ewing and C. A. Brau, *Appl. Phys. Lett.* 27, 350 (1975).
67. T. E. Stewart et al., *J. Opt. Soc. Am.* 60, 1290 (1970).

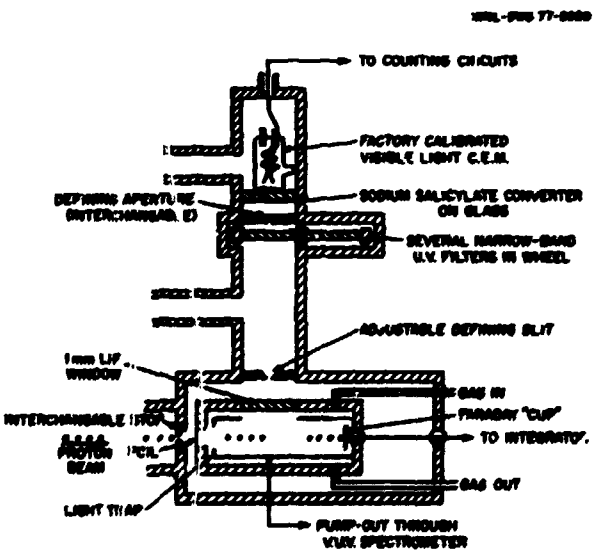

Fig. 12.34. Simple geometry experiment. Sodium salicylate is now coated directly on Channeltron envelope.

Calibrations of the Channeltron, the sodium salicylate convertor, the LiF window, and the filters are crucial to the success of the experiment. The first is provided by the manufacturer; the second is provided in a series of publications;[68–70] and the window and filter calibrations will be accomplished by an auxiliary system.

The calibration system is shown in Fig. 12.35. It is designed so that the transmittance of windows and filters can be obtained as needed.

Systematics of Compiled Intensity Constants for Diatomic Molecular Electronic Transitions

Progress has been made in a continuing effort[71] to compile wavelength-dependent oscillator strengths and transition moments at the 0,0 band for *A-X* and related transitions. Systematics for transition moments were reported previously;[72] systematics for wavelength-dependent oscillator strengths at 0,0 are also encouraging (Figs. 12.36 and 12.37).[73] In a few cases, lifetimes of low excited levels have been considered (Fig. 12.38).[73]

LASER BREAKDOWN AND LASER FLUORESCENCE FOR POLLUTION MEASUREMENTS

Ultrasensitive Pollutant Analysis by a Laser-Induced Rare-Gas Breakdown Technique

Last year, in experiments conducted in our group at ORNL,[52] it was demonstrated that there is a strong O-H emission band at 3100 Å when an Ar-H_2O mixture is irradiated by 3-MeV protons. More recently, a similar experiment (Fig. 12.39) showed an O-D band at 2700 Å when an Ar-D_2O mixture was used. It is expected that an Ar-THO mixture will yield similar results. Thus, it appears likely that this technique would be a quite sensitive detector of tritiated water, which is a possible pollutant from some nuclear processes. Furthermore, the fast energy transfer from excited rare-gas atoms or molecules to other pollutants such as Cl_2, NO_2, NO, and Cd, which results in strong characteristic fluorescence bands, could also serve as a sensitive method of detection for these substances. This method is, in principle, much simpler than other sensitive detection schemes such as gas chromatography and mass spectroscopy. In addition, background effects which would limit ultimate sensitivity would be of a different nature in each of these techniques. For example, measuring low concentrations of THO in the presence of naturally occurring amounts of D_2O is difficult using mass spectroscopy since they differ in mass by only about one part in ten thousand.[74] However, this difficulty does not occur in the rare-gas excitation technique since it separates isotopes on the basis of fluorescence rather than mass.

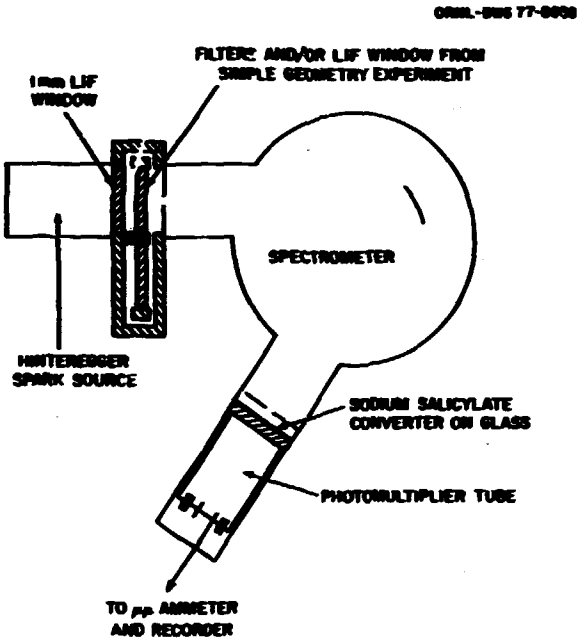

Fig. 12.35. Calibration system for simple geometry experiment windows and filters.

The main technological drawback to the rare-gas excitation method is the use of protons produced by a Van de Graaff accelerator as an excitation source. However, there exist other ways to excite the Ar_2 excimer, which is apparently the most efficient precursor of fluorescence. The most straightforward method is direct excitation of the excimer by light in its absorption band near 1250 Å. The purpose of the present experiment is to demonstrate that laser-induced rare-gas breakdown can be used to generate intense short pulses of vuv photons in this wavelength region. There currently do not appear to be any other sources that can produce the short, intense pulse required. Although there is some

68. R. Allison, J. Burns, and A. J. Tuzzolino, *J. Opt. Soc. Am.* 54, 747 (1964).
69. R. C. Bless, A. D. Code, and D. J. Schroeder, *Astrophys. J.* 153, 545 (1968).
70. E. C. Bruner, Jr., *J. Opt. Soc. Am.* 59, 204 (1969).
71. Ray Hefferlin et al., *J. Tenn. Acad. Sci.* 51, 100 (1976).
72. Ray Hefferlin, *J. Quant. Spectrosc. Radiat. Transfer* 16, 1101 (1976).
73. Ray Hefferlin, *Bull. Am. Phys. Soc.* 22, 77 (1977).
74. T. Sikes, private communication.

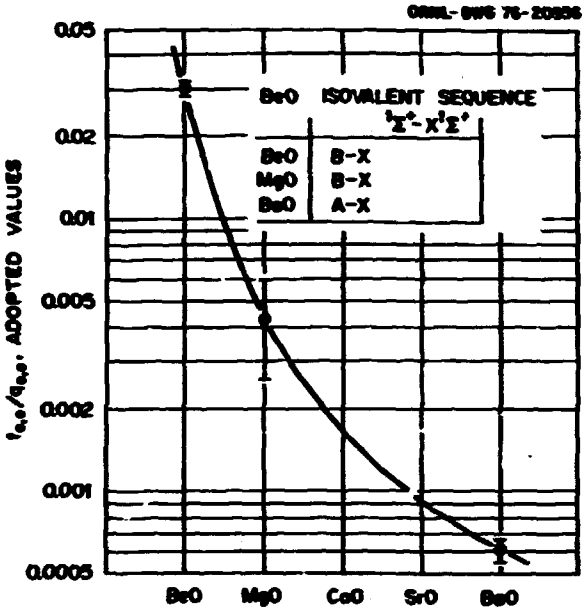

Fig. 12.36. Wavelength-dependent oscillator strength at the 0, 0 band of transition for the BeO isovalent sequence.

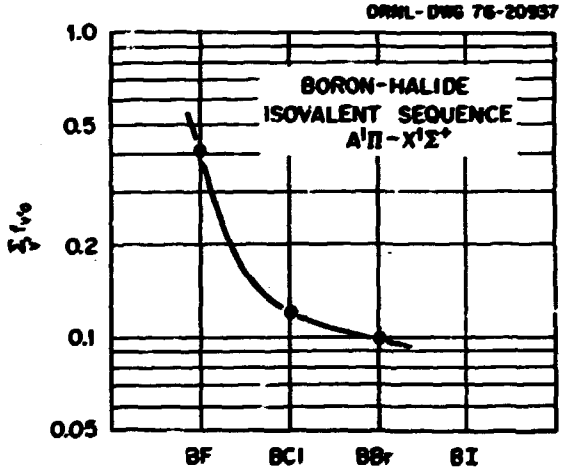

Fig. 12.37. Oscillator strengths summed over v′ for transition of the boron halide isovalent sequence.

information on the wavelength and temporal characteristics of the plasma caused by laser breakdown in the visible region of the spectrum,[75,76] there is almost no data in the vuv near 1200 Å (refs. 77 and 78) which is, of course, the region of interest in the present study.

Available information indicates that the plasma produces line radiation superimposed on a continuum black-body background of roughly equal amplitude. A black-body source with a peak emission at 1200 Å would have to have a temperature of about 5 eV. At this temperature, about 10% of the radiated light will be

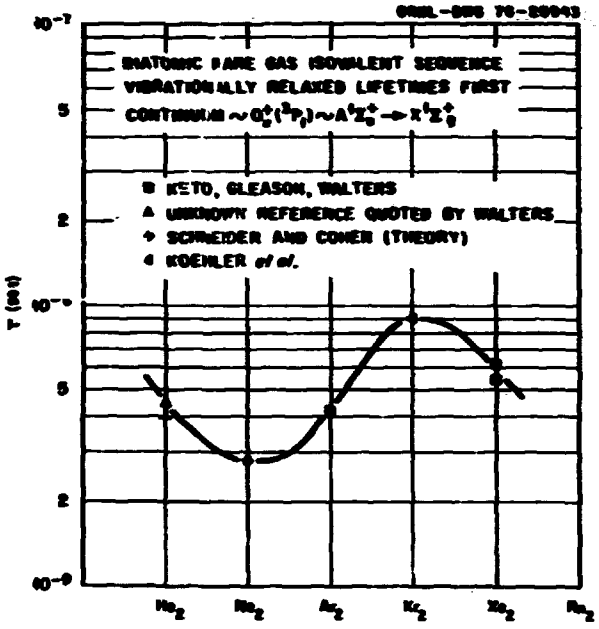

Fig. 12.38. Lifetimes for the 0_u^+ level of vibrationally relaxed rare gases. The references are ■, *Phys. Rev. Lett.* 33, 1365 (1976); ▲, personal communication; ◆, *J. Chem. Phys.* 61, 3240 (1974); and ◀, *Phys. Rev. A* 12, 968 (1975).

between 1100 and 1300 Å. Ruby laser pulses of 0.4 J total energy have already been used to produce plasmas with temperatures of 10 eV, so a plasma generated by laser breakdown should be a usable and convenient source.

The first phase of this experiment will be to test this prediction and to optimize the photon output from the plasma. To this end, the gas cell shown in Fig. 12.40 is currently under construction. A 1-J, *Q*-switched ruby or neodymium laser, both of which are currently in our laboratory, will be pulsed into the cell. The gas pressure in the cell and the focal length of the focusing lenses can both be varied to optimize the light output as measured by a nude electron multiplier. Transmission of the LiF window, coupled with the response of the nude electron multiplier, provides an effective filter for the wavelength range of interest. This choice of component

75. R. Papoular, pp. 79–96 in *Laser Interactions and Related Plasma Phenomena*, vol. 2, M. Schwarz and H. Nora, eds., Plenum Press, New York, 1972.

76. W. T. Silfvast and O. R. Wood II, *Appl. Phys. Lett.* 25, 275 (1974).

77. B. C. Fawcett et al., *Proc. Phys. Soc.* 88, 1051 (1966).

78. A. W. Ehler and G. L. Weissler, *Appl. Phys. Lett.* 8, 89 (1966).

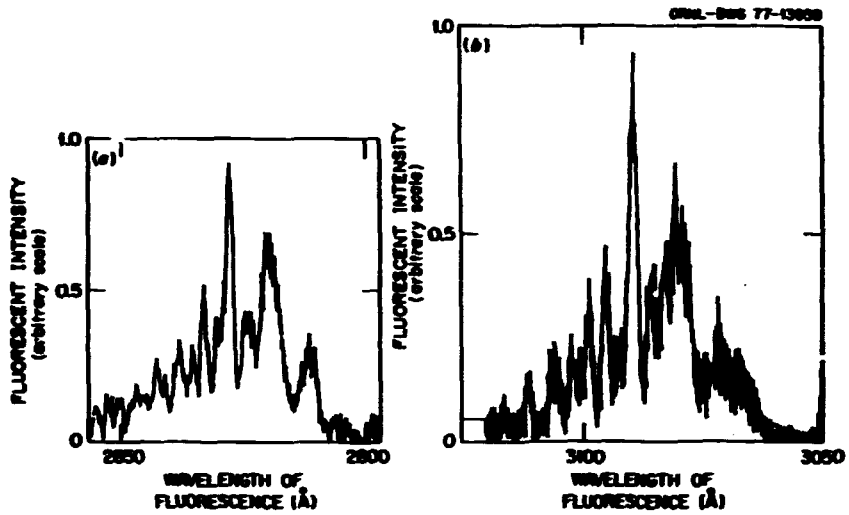

Fig. 12.39. Graphs (a) and (b) depict the fluorescent signals from the O-D and O-H bands, respectively, due to concentration differences of D_2O and H_2O in the two experiments. The relative amplitudes in the two graphs are not comparable.

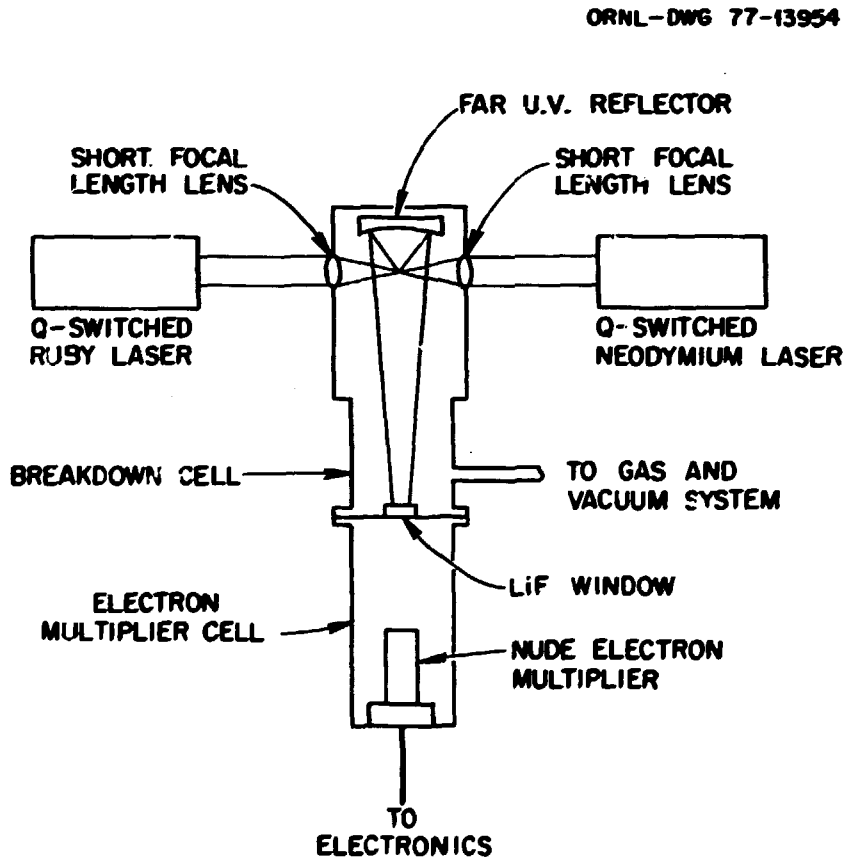

Fig. 12.40. Experimental configuration for the optimization of vuv light output produced by laser-induced breakdown. The two lasers are used independently.

eliminates the need for expensive vuv spectrometers. In addition, provision has been made to focus the laser onto various high-Z materials such as tantalum and titanium, since work by others indicates that these materials produce a dense plasma under laser irradiation.

Once maximization of the plasma output has been achieved, the cell providing the nude electron multiplier will be replaced by one containing a flowing gas mixture of Ar-H_2O or Ar-D_2O, as shown in Fig. 12.41. The O-H and O-D fluorescence from these mixtures will then be optimized and measurements made to determine the minimum concentrations that can be detected. In addition, other important pollutants such as Cl_2, NO_2, and NO will also be tested.

Laser-Induced Fluorescence Spectroscopy

It is well known that complicated molecules emit very complicated spectra. Smalley, Wharton, and Levy[79,80] used a seeded jet technique and obtained narrow-band spectra for I_2, NO_2, etc. We expect to use time-resolved laser-induced fluorescence spectroscopy to detect the even more complicated compounds, such as carcinogenic molecules, at low concentrations. The experiments by Smalley, Wharton, and Levy[79,80] are sensitive to 1 ppm of I_2 in helium; time-resolved techniques probably can improve the detection efficiency by a factor of 10 to 100. We already have the required narrow-band tunable dye laser. The nozzle jet, spectrometer, and required electronics will be obtained in the near future. We believe that this experimental facility will be a tool for detecting complicated pollutants, and it can be used to study chemical kinetics for weakly bound Van der Waals molecules.

THEORY OF LASER INTERACTION WITH MATTER

During the past year we have pursued a wide range of theories related to the use of lasers in RIS and to basic laser pulse–atom interactions. We present here a brief description of some of the basic studies concerning the interaction of narrow-bandwidth pulsed laser fields with both isolated and colliding atoms.

General Method for Near-Resonance Multiphoton Ionization with Narrow-Bandwidth Lasers

Resonance multiphoton ionization of atoms has received much attention in recent years (e.g., refs. 81–94). Much of the theoretical effort[81–88] has pro-

79. R. E. Smalley, L. Wharton, and D. H. Levy, *J. Chem. Phys.* 63, 4977 (1975).
80. R. E. Smalley, L. Wharton, and D. H. Levy, *J. Chem. Phys.* 64, 3266 (1976).
81. Y. Gontier and M. Trahin, *Phys. Rev. A* 7, 1899 (1973).
82. H. B. Bebb, *Phys. Rev.* 149, 25 (1966).
83. C. S. Chang and P. Stehle, *Phys. Rev. Lett.* 30, 1283 (1973).
84. P. Lambropoulas, *Phys. Rev. A* 9, 1992 (1974).
85. C. Cohen-Tannaudji et al., *Phys. Rev. A* 8, 2747 (1973).
86. A. DeCoster, *Phys. Rev. A* 9, 1446 (1974).
87. V. L. Jacobs, *J. Phys. B* 6, 1461 (1973).
88. L. Gersten and M. H. Mittleman, *Phys. Rev. A* 10, 24 (1974).
89. D. Popescu et al., *Phys. Rev. A* 9, 1182 (1974).
90. B. Held et al., *Phys. Rev. Lett.* 30, 423 (1973).
91. R. A. Fox, R. M. Kogan, and E. J. Robinson, *Phys. Rev. Lett.* 26, 1416 (1971).
92. G. A. Delone, N. B. Delone, and G. K. Piskova, *Zh. Eksp. Teor. Fiz.* 62, 1272 (1972) [*Sov. Phys. – JETP (Engl. Transl.)* 35, 672 (1972)].
93. M. Luvan et al., *Phys. Rev. A* 7, 91 (1973).
94. R. G. Evans and P. C. Thoneman, *Phys. Lett.* 39A, 133 (1972).

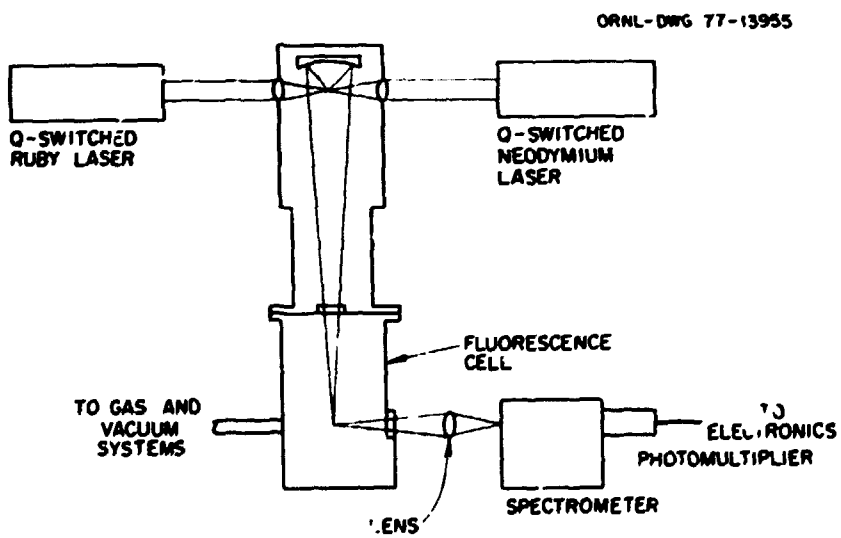

Fig. 12.41. Experimental configuration for the detection of fluorescence from H_2O, D_2O, and HDO.

ceeded along the lines of using perturbation theory to calculate an ionization rate which incorporates intensity-induced shifts and widths of the near-resonant intermediate states.[81-88] More recently, Beers and Armstrong,[95] Armstrong, Beers, and Feneville,[96] Payne and Choi,[97] and Choi[98] showed that, in some instances, the ionization rate approach is quite accurate, whereas in others it leads to erroneous results.

The method presented here is a generalization of one used in work by Payne and Choi[97] and Choi.[98] One proceeds as follows.

1. The Hamiltonian for the atom plus laser field is written as a sum of the isolated-atom Hamiltonian $\hat{H}_0$ and an interaction term $\hat{v}$:

$$\hat{H} = \hat{H}_0 + \hat{v}, \tag{25}$$

where the laser field is treated classically. We follow Power and Zienau[99] in writing a multipole expansion of $\hat{v}$ with $\hat{P}$ = dipole operator and $\hat{Q}_{ij}$ = quadrupole operator:

$$\hat{v} = -\hat{P} \cdot \mathbf{E}[\mathbf{R}(t), t] - \frac{1}{2}\sum_{i,j} \hat{Q}_{ij} \nabla_j \mathbf{E}_i[\mathbf{R}(t), t] + \cdots \tag{26}$$

In Eq. (26), $\mathbf{E}[\mathbf{R}(t), t]$ is the electric field evaluated at the position of the nucleus $\mathbf{R}(t)$, and the nuclear position vector $\mathbf{R}(t)$ is evaluated along the classical path followed by the atom. The classical treatment of the laser field is in anticipation of the high peak power typically used in ionization studies. The multipole expansion of the laser field assumes $\lambda \gg a_B$ = Bohr radius. Typically, the quadrupole terms are only important[100] if the laser is tuned near a quadrupole-allowed transition. Higher multipoles are seldom important.

2. The state vector of the perturbed atom is written as

$$|\psi(t)\rangle = \sum_i a_i(t) e^{-i\omega_i t} |i\rangle + \sum_\mu \int dE_c C_\mu(E_c, t) e^{-i\omega_c t} |E_c, \mu\rangle, \tag{27}$$

where $|i\rangle$ is a finite set of most-resonant discrete states and $|E_c, \mu\rangle$ are continuum states such that $\hat{H}_0 |i\rangle = \hbar\omega_i |i\rangle$ and $\hat{H}_0 |E_c, \mu\rangle = \hbar\omega_c |E_c, \mu\rangle$.

3. The limited basis of Eq. (27) is combined with the time-dependent Schrödinger equation to derive a set of coupled differential equations for $a_i(t)$ and $C_\mu(E_c, t)$. Typically, an approximation similar to the rotating wave approximation is made in keeping only the most-resonant interaction terms. Coupling between different $C_\mu(E_c, t)$ is neglected.

4. It is assumed that matrix elements $\langle i|\hat{v}|E_c, \mu\rangle$ evaluated near resonance vary slowly with E_c. In particular, a range of E_c exists such that we can choose $|\Delta E_c/\hbar| \gg |d/dt \ln a_i(t)|$ and $\langle i|\hat{v}|E_c + \Delta E_c, \mu\rangle \simeq \langle i|\hat{v}|E_c, \mu\rangle$. If the laser field amplitudes (there can be more than one laser field present) also vary very little in a time $\hbar/\Delta E_c$, one can express $C_\mu(E_c, t)$ in terms of $a_i(t)$, yielding a finite number of close coupled differential equations for the $a_i(t)$.[81-88] In the latter equations, photoionization effects now enter only in terms of level shifts and damping terms.

5. Standard asymptotic methods are used to express any far-off-resonance amplitudes as linear combinations of the amplitudes for the most-resonant states. A smaller number of close coupled equations then result which couple amplitudes for the most-resonant states. The equations for the amplitudes of the most-resonant states now contain damping terms and shifts due to the continuum, as well as dynamic Stark shifts due to the off-resonance discrete states. Without the coupling to the continuum, the latter equations would be equivalent to those used by many workers (e.g., refs. 101, 102) in describing multiphoton excitation.

6. The amplitudes for the most-resonant states are determined. From these one can find $C_\mu(E_c, t)$, and the ionization probability R can be determined by

$$R = \sum_\mu \int dE_c |C_\mu(E_c, \infty)|^2 . \tag{28}$$

---

95. B. L. Beers and L. Armstrong, Jr., *Phys. Rev. A* **12**, 2447 (1975).

96. L. Armstrong, Jr., B. L. Beers, and S. Feneville, *Phys. Rev. A* **12**, 1903 (1975).

97. M. G. Payne and C. W. Choi, "Multiphoton Ionization with Strong Pulsed Laser Fields. I: Two-Photon Ionization," submitted to *Physical Review A*.

98. C. W. Choi, "Two-State and Two-State Plus Continuum Problems Associated with the Interaction of Intense Laser Pulses with Atoms," Ph.D. dissertation, University of Kentucky, 1977 (unpublished).

99. E. A. Power and S. Zienau, *Philos. Trans. R. Soc. London A* **251**, 427 (1959).

100. P. Lambropoulos, G. Doolen, and S. P. Rountree, *Phys. Rev. Lett.* **34**, 636 (1975).

101. E. M. Belenov and I. A. Polvektov, *Zh. Eksp. Teor. Fiz.* **56**, 1407 (1969) [*Sov. Phys. – JETP (Engl. Transl.)* **29**, 754 (1969)].

102. M. Takatsuji, *Phys. Rev. A* **4**, 808 (1971).

In almost all cases where the resonant (or energy-conserving) continuum energy is well above any autoionizing levels, a sufficiently large $|\Delta E_c|$ can be found at power levels less than 10^{11} W/cm^2. An equivalent approximation (*i.e.*, to step 4) is usually made in work based on resolvent operator techniques (e.g., ref. 103). Such an approximation enters when the transform-variable dependence of the level shift is suppressed.

In contrast to the usual procedure,[81–88] the procedure described here enables one to calculate an ionization probability directly without reference to an ionization rate. It also includes various intensity-induced shifts and widths in a way that enables one to examine the effect of laser pulse shape for cases where the coupling between the discrete states is very strong. The way that the effect of ionization enters into the equations for the amplitudes of the near-resonant states leads, in many cases, to easy interpretation in terms of previous work on multiphoton excitation. One consequence is that many processes monitored previously by fluorescence can be studied by much more sensitive ionization measurements.[8,9,13] It is also obvious that many other types of processes involving laser-induced collisions (e.g., refs. 104–106) or far wing line broadening (e.g., refs. 107 and 108) could be studied with increased precision by choosing a situation where the excited state can be ionized and the ionization detected. In the latter problems, the elimination of the continuum states proceeds in exactly the same way, and ionization yields are calculated by an analogous prescription. It should also be noted that in a quantized treatment of the laser field the continuum could still be dealt with similarly.

Three-Photon Ionization Near a Two-Photon Resonance

In the particular multiphoton ionization problem to be considered in this report, we consider a moving atom subjected to counterpropagating laser beams of frequency ω_1' and ω_2'. The laser beams are pulsed with the counterpropagating pulses at ω_1' and ω_2', overlapping in both space and time. The atom in question has energy levels as shown in Fig. 12.42. Figure 12.42 shows only the most-resonant levels since we assume that (1) the atom is initially in the ground state which we call $|0\rangle$, (2) ω_1' is much closer to resonance between $|0\rangle$ and $|P, j\rangle$ than to any other one-photon resonance, and (3) $\hbar(\omega_1' + \omega_2')$ is very close to $\hbar(\omega_2 - \omega_0)$. Thus, there is a dominant intermediate state (or group of closely spaced intermediate states $|P, j\rangle$) for the two-photon excitation of $|2\rangle$. The case where the states $|P, j\rangle$ are within a few percent of being exactly halfway between $|0\rangle$ and $|2\rangle$ is of particular interest since if $|\delta| \ll |\omega_2' - \omega_1'|$ and the power level is not too high, the two-photon excitation of $|2\rangle$ will be dominated by processes where one photon is absorbed from each of the counterpropagating beams. In such a situation, the only Doppler shift for two-photon excitation is $|\omega_2' - \omega_1'|v_z/c$, which is usually very small if ω_2' and ω_1' differ

103. C. Cohen-Tannoudji, p. 437 in *Cargese Lectures in Physics*, vol. 2, M. Levy, ed., Gordon and Breach, New York, 1969.

104. L. I. Gudzenko and S. I. Yakovlenko, *Zh. Eksp. Teor. Fiz.* 62, 1686 (1972) [*Sov. Phys. – JETP (Engl. Transl.)* 35, 877 (1972)].

105. S. E. Harris and D. B. Lidow, *Phys. Rev. Lett.* 33, 644 (1974).

106. R. W. Falcone et al., "Observation of Laser-Induced Inelastic Collisions," submitted to *Physical Review Letters*.

107. S. Y. Ch'en and C. W. Fountain, *J. Quant. Spectrosc. Radiat. Transfer* 4, 323 (1964).

108. J. Pascale and J. Vandeplanque, *J. Chem. Phys.* 60, 2278 (1974).

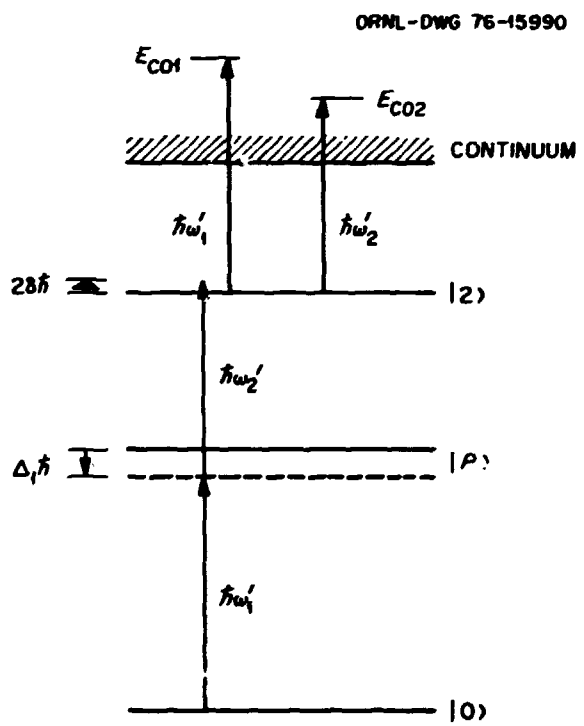

Fig. 12.42. Energy-level diagram for the atom under consideration. The laser with frequency ω_1' is tuned closely enough to resonance between $|0\rangle$ and $|P, j\rangle$ for $|P, j\rangle$ to be the dominant intermediate states for the two-photon excitation of $|2\rangle$. However, the power level is low enough and ω_1' is detuned from one-photon resonance sufficiently so that the states $|P, j\rangle$ are only weakly excited.

by only a few percent. Doppler-free two-photon excitation was first proposed by Vasilenko, Chebotaev, and Shishaev[109] and variations on it have been studied by many workers.[110–116]

In the present work, the emphasis is on high-power levels where the line widths for the two-photon process are much larger than the full Doppler width. At high power levels, either pulsed lasers or sharply focused beams are used, and in either case the ac Stark shifts are time-dependent in the rest frame of the atom. Thus, since power-induced shifts are usually larger than the two-photon coupling rate, one expects crossing phenomena to play a large role in determining the line shape. We find, in fact, that the line shape with smoothly varying laser pulses is extremely different from those resulting from discontinuous pulses such as the square pulse used by Beers and Armstrong[95] and Armstrong, Beers, and Feneville.[96] Typically, a square pulse leads to a shifted but symmetric line shape, whereas smooth pulses at high power levels usually lead to very asymmetric line shapes. With certain types of pulses, a sharp rise in the ionization probability occurs when $\omega_1' + \omega_2'$ is varied across the unperturbed two-photon resonance energy. The rise can be from near zero to near unity in a region of δ which is of the order of the residual Doppler width.

We believe that a closely related effect was seen in fluorescence following two-photon excitation by Liao and Bjorkholm.[117] In the latter work, the time-dependent level shifts occurred due to the atoms moving across a very tightly focused laser beam. Thus, when $\omega_1' + \omega_2'$ is on one side of the unperturbed two-photon resonance, the atom can momentarily cross through resonance while moving through the beam. On the other side, resonance is never achieved. If the laser fields are strong but the dynamic Stark shifts are large compared with the coupling rate, the situation is dominated by crossing effects and the very asymmetric line shapes occur. Some theoretical aspects of two-photon excitation under similar conditions have been discussed by Grischkowsky and Loy[118] and others.

We consider counterpropagating laser pulses which are plane-polarized parallel to the x axis and which propagate along the z axis. Thus the field seen by an atom with z component of velocity v_z is of the form

$$\mathbf{E}[\mathbf{R}(t),t] = \hat{i}[E_1(t)\cos(\omega_1' t - k_1 v_z t) + E_2(t)\cos(\omega_2' t + k_2 v_z t + \beta')] \,. \tag{29}$$

The functions $E_1(t)$ and $E_2(t)$ are nonoscillatory field amplitudes which are assumed to build up continuously from zero at $t = -\infty$ to a maximum at $t = 0$ before decreasing again to zero at $t = \infty$.

As described earlier, we assume that the atom has energy levels such that $\hbar\omega_1'$ is close to $\hbar(\omega_{Pj} - \omega_0)$ and $\hbar\omega_2'$ is close to $\hbar(\omega_2 - \omega_{Pj})$. Further, $\hbar(\omega_1' + \omega_2')$ is even closer to $\hbar(\omega_2 - \omega_0)$. An energy-level diagram showing the most-resonant states is shown in Fig. 12.42. We let

$$\hat{H} = \hat{H}_0 - \hat{P}_x[E_1(t)\cos(\omega_1' t - k_1 v_z t) + E_2(t) \times \cos(\omega_2' + k_2 v_z t + \beta)] - i\hbar\frac{\gamma_2}{2}|2\rangle\langle 2| \,, \tag{30}$$

and

$$|\psi(t)\rangle = a_0(t)e^{-i\omega_0 t}|0\rangle + a_2(t)e^{-i\omega_2 t}|2\rangle + \sum_j a_{P,j}(t)e^{-i\omega_{Pj} t}|P,j\rangle + \sum_k \int dE_c C_{P,k}(E_c,t)e^{-i\omega_c t}|E_c,k\rangle \,. \tag{31}$$

Use of the general method described earlier yields

$$\frac{dA_0}{dt} = i\Omega_4(t)A_2(t)\exp[i\phi(t)] \,,$$

109. L. S. Vasilenko, V. P. Chebotaev, and A. V. Shishaev, *JETP Lett.* 12, 113 (1970).
110. B. Cagnac, G. Grynberg, and F. Biraben, *Phys. Rev. Lett.* 32, 643 (1974).
111. M. D. Levenson and N. Bloembergen, *Phys. Rev. Lett.* 32, 645 (1974).
112. T. W. Hänsch et al., *Phys. Rev. Lett.* 34, 307 (1975).
113. T. W. Hänsch, *Opt. Commun.* 11, 50 (1974).
114. F. Biraben, B. Cagnac, and G. Grynberg, *C. R. Acad. Sci. (Paris)* 279, B51 (1974).
115. P. F. Liao and J. E. Bjorkholm, *Phys. Rev. Lett.* 34, 1 (1975).
116. J. E. Bjorkholm and P. F. Liao, *Phys. Rev. Lett.* 33, 128 (1974).
117. P. F. Liao and J. E. Bjorkholm, *Phys. Rev. Lett.* 34, 1 (1975).
118. D. Grischkowsky and M. M. T. Loy, *Phys. Rev. A* 12, 1117 (1975).

$$\frac{dA_2}{dt} = -\left(\frac{\gamma_2}{2} + P(t)\right) A_2 \tag{32}$$

$$+ i\Omega_4^*(t) A_0 \exp[-i\phi(t)] ,$$

where

$$\phi(t) = \int_{-\infty}^{t} [\Omega_2(t') - \Omega_3(t') + \Delta\omega(t') + 2\delta]\, dt' , \tag{33}$$

$$\Omega_1(t) = -\sum_j \frac{\langle 0|\hat{P}_x|P,j\rangle\langle P,j|\hat{P}_x|2\rangle}{4\hbar^2\Delta_{2j}} E_1(t)E_2(t)e^{i\beta'} ,$$

$$\Omega_2(t) = -\sum_j \frac{|\langle \hat{P},j|P_x|2\rangle|^2 E_2^2(t)}{4\hbar^2\Delta_{2j}} ,$$

$$\Omega_3(t) = -\sum_j \frac{|\langle 0|\hat{P}_x|F,j\rangle|^2 E_1^2(t)}{4\hbar^2\Delta_{1j}} , \tag{34}$$

$$P(t) = \sum_{l=1}^{2} \frac{\pi E_l^2(t)}{4\hbar} \sum_k |\langle 2|\hat{P}_x|E_{c0,l}, k\rangle|^2 ,$$

$$\Delta\omega(t) = \sum_{l=1}^{2} \frac{E_l^2(t)}{4\hbar} P\int \sum_k \frac{|\langle E_c, k|\hat{P}_x|2\rangle|^2\, dE_c}{\omega_c - \omega_2 - \omega_l'} ,$$

and $E_{c0,l} = \hbar(\omega_2 + \omega_l')$. A_0 and A_2 differ only by phase factors from a_0 and a_2. Also, $2\delta = \omega_1' + \omega_2' - \omega_2 + \omega_0 - (k_1 - k_2)v_z$. The quantity $2\hbar\delta$ is a measure of the excess energy available in the two-photon excitation process. The quantity $P(t)$ represents a damping of the populations of $|0\rangle$ and $|2\rangle$ due to photoionization, $\Delta\omega(t)$ is an ac Stark shift due to coupling with the ionization continuum, $\Omega_2(t)$ is the ac Stark shift of $|2\rangle$ due to the states $|P, j\rangle$, $\Omega_3(t)$ is the ac Stark shift of $|0\rangle$, and $\Omega_4(t)$ is the two-photon coupling coefficient. We can also show that

$$R = 2\int_{-\infty}^{\infty} P(t)|A_2(t)|^2\, dt . \tag{35}$$

Thus, one needs to solve Eqs. (32) for $A_2(t)$ and to determine R through Eq. (35).

If a third laser which is far off resonance for discrete transitions coupling $|0\rangle$ or $|2\rangle$ to any other states is used to assist in ionization, only $\Delta\omega(t)$ and $P(t)$ are modified. This modification is through the addition of a third term to both $\Delta\omega$ and $P(t)$. We assume, of course, that the third laser cannot ionize $|0\rangle$ by a single-photon process.

For mathematical simplicity we assume that

$$E_1^2(t) = E_{10}^2 g(t/\tau) ,$$
$$E_2^2(t) = E_{20}^2 g(t/\tau) . \tag{36}$$

Thus the pulse shapes of the two laser fields are identical. The function $g(x)$ has a value of unity at $x = 0$, and it decreases continuously and monotonically as $|x|$ increases. The quantity $g(x)$ is assumed to decrease considerably in a unit interval about $x = 0$. Useful examples of $g(x)$ are $g(x) = [1 + x^2]^{-n}$ $(n \geq 2)$ and $g(x) = \exp[-x^2]$. The parameter τ in Eqs. (36) is a measure of the pulse length. By varying the value of τ, we consider a family of problems involving the same pulse shape but different pulse lengths.

We note that Ω_4, Ω_2, Ω_3, $P(t)$, and $\Delta\omega$ are all proportional to $g(t/\tau)$ and

$$P(t) = P_0 g(t/\tau) ,$$
$$d\phi/dt = 2\delta - \mu g(t/\tau) , \tag{37}$$
$$\Omega_4(t) = \alpha g(t/\tau) .$$

Expressions for P_0, μ, and α are obtained by comparing Eqs. (34) and (37) while using Eqs. (36). Thus, with our assumptions about $E_1(t)$ and $E_2(t)$,

$$\frac{d\bar{A}_0}{dv} = i\beta\bar{A}_2 g(v) \exp\left[i\int_{-\infty}^{v} [\Delta - mg(v')]\, dv'\right] ,$$

and

$$\frac{d\bar{A}_2}{dv} = -[\sigma + \rho g(v)]\bar{A}_2 + i\beta^*\bar{A}_0 g(v)$$
$$\times \exp\left[-i\int_{-\infty}^{v} [\Delta - mg(v')]\, dv'\right] , \tag{38}$$

where $\beta = \alpha\tau$, $\Delta = 2\delta\tau$, $m = \mu\tau$, $v = t/\tau$, $\sigma = \gamma_2\tau/2$, $\rho = P_0\tau$, $\bar{A}_0(v) = A_0(t)$, and $\bar{A}_2(v) = A_2(t)$. The dimen-

sionless forms of Eqs. (38) are very useful if $\sigma \ll 1$. Here R cannot be affected by spontaneous decay because σ only affects A_2 appreciably after the laser pulses are gone, whereas the ionization occurs largely while $|v| \lesssim 1$. One important conclusion is that as long as one does not go outside the range of validity of the model (and $\sigma \ll 1$), β, m, and ρ can all be fixed by holding constant the energy per pulse for each laser. However, for fixed β, m, and ρ, one must change δ in order to keep Δ fixed. Thus, at different peak power levels, but with equal energy per pulse, one obtains line shapes for R that are identical except for the line width varying in direct proportion to the peak power or inversely with the pulse length. A corresponding argument can be given when the pulse shape for the two lasers is different but the pulse length is changed by the same factor, with the power being changed so that the energy per pulse for each remains fixed. Within the limits of validity of the model, the above scaling law for the line shape is exact.

When $|\beta| \gg 1$; $\Gamma^2/J \ll 1$; $\sigma \ll 1$; and $|\Delta| \gg |(d/dv) \ln g||m/\beta|^2$ is satisfied at all crossings, we find

$$R = 1 - \exp\left[-\rho H\left(\frac{\Delta}{m}, \left|\frac{\beta}{m}\right|\right)\right], \tag{39}$$

where

$$H\left(\frac{\Delta}{m}, \left|\frac{\beta}{m}\right|\right) = 2\int_{-\infty}^{\infty} g(v) F\left(v, \frac{\Delta}{m}, \left|\frac{\beta}{m}\right|\right) dv, \tag{40}$$

$$F\left(v, \frac{\Delta}{m}, \left|\frac{\beta}{m}\right|\right) = \frac{1}{2}\left[1 - \frac{\Sigma'\left[\frac{\Delta}{m} - g(v)\right]}{\sqrt{[\Delta/m - g(v)]^2 + 4|\beta/m|^2 g^2(v)}}\right], \tag{41}$$

and where $\Sigma' = m\Delta(|m\Delta|)^{-1}$. An extensive tabulation of $H(x, y)$ is given in a dissertation by Choi[98] for the case $g(v) = [1 + v^2]^{-3}$. Other continuous forms of $g(v)$ having the properties $g(0) = 1$, $\int_{-\infty}^{\infty} g(v)\,dv = 3\pi/8$, and $g(-v) = g(v)$ have been tested numerically: They yield very similar values of R.

Due to the failure of $|\Delta| \gg |(d/dv) \ln g||m/\beta|^2$, Eq. (39) fails at $\Delta = 0$. However, in this latter case, Eqs. (38) can be solved exactly. Choosing $g(v) = [1 + v^2]^{-3}$, we find ($|\beta| \gg 1$):

$$R(\delta = 0) = 1 - \exp\left[-\frac{3\pi}{2}\rho|\beta/m|^2(1 + 4|\beta/m|^2)^{-1}\right]. \tag{42}$$

It is also interesting to compare the smooth pulse results with those for a square pulse with comparable pulse length and the same energy per pulse. We choose $g(0) \neq 1$:

$$\begin{aligned} g(v) &= 0, & v &< 0; \\ &= \frac{3\pi}{8}, & 0 &< v < 1; \\ &= 0, & v &> 1. \end{aligned} \tag{43}$$

Letting $J \equiv \sqrt{(\Delta - mg)^2 + 4|\beta|^2 g^2} = \sqrt{\Delta'^2 + 4|\beta|^2 g^2}$ and $\Delta' = \Delta - mg$, we have for $|\beta| \gg 1$:

$$R = 1 - \frac{1}{2}\left[1 - \frac{|\Delta'|}{J}\right]\exp\left[-\rho\left(1 + \frac{|\Delta'|}{J}\right)\right] - \frac{1}{2}\left[1 + \frac{|\Delta'|}{J}\right]\exp\left[-\rho\left(1 - \frac{|\Delta'|}{J}\right)\right]. \tag{44}$$

Equation (44) is an exact solution to Eqs. (38) and (39).

In situations where $|m| \gg 1$ and $|\beta/m| \ll 1$, the quantity A_0 of Eqs. (38) only changes when v is such that $\Delta \approx mg(v)$. This is because $|dA_0/dv| \ll |\beta|$ and, except for v values such that $\Delta \simeq mg(v)$, the factor $\exp\{i\int_{-\infty}^{v}[\Delta - mg(v')]\,dv'\}$ oscillates many times in a time $1/|\beta|$. The result is that no net change in $\bar{A}_0$ occurs due to the dephasing effect on the coupling term. Conversely, large changes in $\bar{A}_0$ would occur if $|\beta|$ were larger than $\Delta - \mu g$ over a region Δv large enough so that $|\beta||\Delta v| \gtrsim 1$.

The above situation can be dealt with by using a method developed by Zener[119] for the classical path treatment of near-resonance energy transfer in atom-atom collisions. A detailed discussion of some applica-

119. C. Zener, *Proc. R. Soc. London A* 137, 696 (1932).

tions of the Zener method to multiphoton processes can be found in a dissertation by Choi.[98]

Since the Zener method is standard textbook material,[119] we will give an expression for R in cases where $|m| \gg 1$, $|\beta\Gamma/m| \ll 1$, and $|\beta/m| \ll 1$ without proof. The method is easily extended to cases where $E_1(t)$ and $E_2(t)$ have different profiles and $\sigma \neq 0$; but here we deal with $\sigma = 0$, $E_1^2(t) = E_{10}^2 g(t/\tau)$, and $E_2^2(t) = E_{20}^2 g(t/\tau)$. We do not assume that $E_{10} = E_{20}$. We find $R \approx 0$ for $\Delta/m < 0$ or $\Delta/m > 1$, and for $0 < \Delta/m < 1$,

$$R = T[1 - Q^2(v_+)] + T(1-T)[1 + Q^2(v_+)][1 - Q(\infty)/Q(v_+)] , \quad (45)$$

where

$$Q(v) = \exp[-2\rho m(v)] ,$$

$$m(v) = \int_0^v dv' g(v') ,$$

$$T = 1 - \exp(-2\pi |Z_1|^2) , \quad (46)$$

$$|Z_1|^2 = |\beta^2/m| g^2(v_+) |dg(v_+)/dv|^{-1} ,$$

where v_+ is a function of Δ/μ determined as the positive root of $\Delta = mg(v_+)$. We have assumed $g(v) = g(-v)$, but this restriction is easily removed.

We see that $R = R(\rho, |\beta^2/m|, \Delta/m)$. If we take $g(v) = [1 + v^2]^{-3}$, we find for $0 < \Delta/m < 1$

$$v_+ = [(m/\Delta)^{1/3} - 1]^{1/2} ,$$

$$|Z_1|^2 = |m|/6|\beta/m|^2 (\Delta/m)^{1/2} [1 - (\Delta/m)^{1/3}]^{-1/2} ,$$

$$m(v) = \frac{1}{8}\left[\frac{3v}{1+v^2} + \frac{2v}{(1+v^2)^2} + 3\tan^{-1} v\right] . \quad (47)$$

If one fixes $|\beta^2/m|$ and ρ and plots R vs Δ/m, it is found that the same universal curve is valid within the present model whenever $|m| \gg 1$, $|\beta/m| \ll 1$, and $|\beta\Gamma/m| \ll 1$. The more strictly these inequalities are satisfied, the closer Δ/m can approach 0 and 1 without having Eq. (45) become inaccurate. The line shapes calculated by this method fail near $\Delta = 0$ because sufficiently near this point there is insufficient dephasing at times before the first crossing and after the second. One should be suspicious when $|\Delta| \lesssim 2$. The line shapes calculated by the Zener method give $R \sim 0$ at $\Delta = 0$. However, the $\Delta = 0$ case can be solved exactly and when $g(v) = (1 + v^2)^{-2}$ and $|\beta| \gg 1$, we find Eq. (42). When $|\beta/m| \ll 1$ and $|\beta\rho/m| \ll 1$, but $|\beta| \gg 1$, we have $R(\Delta = 0) \approx + (3\pi/2)\rho|\beta/m|^2 \ll 1$. The latter value of R for $\Delta = 0$ is not zero, but it is very small compared with the peak value of R in any case where the Zener conditions are met. As implied previously, the Zener result again fails at points very near $\Delta = m$. In the latter case the two crossings are not well separated and the linear in v approximation to $g(v)$ fails. Again the exact $R(\Delta = 1)$ is not zero, but it is small compared with R at its maximum and it approaches zero rapidly for $\Delta > 1$. The region near $\Delta = 1$ over which the Zener method fails has a width of $\sim 3|\beta|$.

We have used two different methods to solve Eqs. (38). There is a region of overlap in the conditions for the validity of the two methods; this is when $|m| \gg 1$, $|\beta/m| \ll 1$, $|\Gamma\beta/m| \ll 1$, but $|\beta^2/m| \gg 1$. In the latter case, the method of calculating R given earlier is valid over most of the line shape, but so is that for calculating R when $|m| \gg 1$, $|\beta\Gamma/m| \ll 1$, and $|\beta/m| \ll 1$. In both cases, if photoionization were omitted, one would have a nearly complete population inversion[118] produced at the first crossing; at the second crossing the population would be converted back to $|0\rangle$. In this limiting case (i.e., $|\beta^2/m| \gg 1$), R becomes

$$R = 1 - \exp[-4m(v_+)] . \quad (48)$$

Due to the production of population inversions with smooth pulses, the peak value of R is often larger than would be found with equal peak power and pulse length with square pulses. The occurrence of a population inversion at the first crossing followed by a destruction of this inversion at the second crossing suggests that fluorescence out of $|2\rangle$ would have a very striking time behavior, with the time over which fluorescence was strong depending on the value of δ. Line shapes of fluorescence by atoms moving across tightly focused laser beams tuned near a two-photon resonance are discussed in the dissertation by Choi.[98]

Two-Photon Excitation and Three-Photon Ionization Due to a Narrow-Bandwidth Laser

We begin by considering a three-level atom experiencing a strong pulsed laser field of the form

$$\mathbf{E} = E_{10} g(t) \mathbf{k} \cos \omega_1' t + E_{20} g(t) \mathbf{k} \cos \omega_2' t . \quad (49)$$

In Eq. (49), $g(t)$ increases monotonically until it achieves the value unity at $t = 0$. Thereafter, it decreases in a monotonic way to zero. Thus, $g(t)$ is the pulse shape function, and its width in time is a measure of the laser pulse length. The angular frequency ω_1' is assumed

ORNL-DWG 77-13956

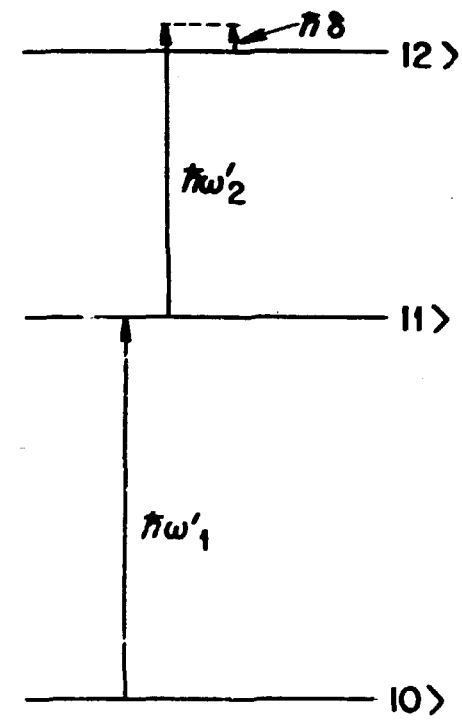

Fig. 12.43. Level diagram for a three-level atom in the presence of two laser fields at frequencies ω_1' and ω_2'.

to be in exact resonance for the transition $|0\rangle \rightleftarrows |1\rangle$ (as shown in Fig. 12.43) but well off resonance for the transition $|1\rangle \rightleftarrows |2\rangle$. The frequency ω_2' is close to or on resonance between $|1\rangle \rightleftarrows |2\rangle$ but not between $|0\rangle$ and $|1\rangle$. This situation is of particular interest due to the linear ac Stark shifts that should occur for the levels $|0\rangle$ and $|1\rangle$. We assume further that the laser pulse length is short compared with the spontaneous decay rate and that collisional effects are absent. We also neglect Doppler effects, assuming that the power broadening and ac Stark shifts are much larger than the Doppler width.

Using the finite basis $|0\rangle$, $|1\rangle$, and $|2\rangle$; the rotating wave approximation; and treating the laser field–atom interaction in the dipole approximation, we obtain

$$\frac{da_0}{dt} = i\frac{P_{01}E_1}{2\hbar}a_1 ,$$

$$\frac{da_1}{dt} = i\frac{P_{10}E_{10}}{2\hbar}a_0 g + i\frac{P_{12}E_{20}}{2\hbar}ge^{i\delta t}a_2 , \tag{50}$$

$$\frac{da_2}{dt} = i\frac{P_{21}E_{20}}{2\hbar}ge^{-i\delta t}a_1 .$$

In Eq. (50), a_0, a_1, and a_2 are probability amplitudes for being in states $|0\rangle$, $|1\rangle$, and $|2\rangle$, respectively, and the $P_{ij} = \langle i|P_z|j\rangle$ are dipole matrix elements; δ is defined in Fig. 12.43. We define the Rabi frequencies $W_{P1} = P_{10}E_{10}/2\hbar$, $W_{P2} = P_{12}E_{20}/2\hbar$ and let $\tau = |W_{P1}|t$, $\epsilon = |W_{P2}/W_{P1}|^2$, and $\beta_2 = \delta/|W_{P1}|$. Finally, letting $A_2 = e^{i\beta_2\tau}a_2$,

$$\frac{da_0}{d\tau} = ig(t)a_1 ,$$

$$\frac{da_1}{d\tau} = ig(t)\sqrt{\epsilon}A_2 + ig(t)a_0 , \tag{51}$$

$$\frac{dA_2}{d\tau} = i\sqrt{\epsilon}g(t)a_1 + i\beta_2 A_2 ,$$

with $a_0(-\infty) = 1$ and $a_1(-\infty) = A_2(-\infty) = 0$.

In what follows we will develop a theory suitable for using the laser at ω_2' as a probe for studying the ac Stark shifts of the state $|1\rangle$. For this purpose we are interested in the limit $\epsilon \ll 1$. The latter restriction does not imply that the second laser must be so weak that one can use perturbation theory in ϵ. In fact, there are a number of interesting saturation effects which will now be discussed.

We begin by reducing Eqs. (51) to a single third-order differential equation for A_2. We factor this equation into the form

$$\left(\frac{d}{dt}+g_1\right)\left(\frac{d}{dt}+g_2\right)\left(\frac{d}{dt}+g_3\right)A_2 = 0 , \tag{52}$$

where g_1, g_2, and g_3 must satisfy

$$g_1 + g_2 + g_3 = -i\beta_2 - 3\frac{d}{d\tau}\ln g ,$$

$$\frac{dg_2}{d\tau} + 2\frac{dg_3}{d\tau} + g_2g_3 + g_1g_2 + g_1g_3 = \frac{d^2}{d\tau^2}\ln g$$

$$+ 3i\beta_2\frac{d}{d\tau}\ln g + \left(\frac{d}{d\tau}\ln g\right)^2 + (1+\epsilon)g^2 , \tag{53}$$

$$\frac{d}{d\tau}(g_2 g_3) + \frac{d^2 g_3}{d\tau} + g_1 g_2 g_3 + g_1 \frac{dg_3}{d\tau} = i\beta_2 \frac{d^2}{d\tau^2} \ln g$$

$$- 2i\beta_2 \left(\frac{d}{d\tau} \ln g\right)^2 - i\beta_2 g^2 .$$

The procedure used here is valid either for the pulsed case where $g(t)$ varies continuously with time or for the cw case where the laser pulse function can be taken to be zero before $t = 0$ and unity thereafter. In the latter case, g is constant and for $\epsilon \ll 1$ we find g_1, g_2, and g_3 to be

$$g_1 \cong -i(u - J) ,$$

$$g_2 \cong i \left[1 + \frac{\epsilon}{2(1 + |\beta_2|)} \right] , \tag{54}$$

$$g_3 = -i(u + J) ,$$

where

$$u = \frac{1 + |\beta_2|}{2} ,$$

$$V = \frac{1 - |\beta_2|}{2} ,$$

and

$$J = \sqrt{v^2 + \frac{\epsilon}{4}\left(1 + \frac{2|\beta_2|}{1 + |\beta_2|}\right)} .$$

Applying initial conditions, we find in terms of the original parameters:

$$|A_2(t)|^2 = \frac{|W_{P2}|^2}{(|W_{P_1}| - |\delta|)^2 + 2|W_{P2}|^2}$$

$$\times \sin^2 \sqrt{\left(\frac{|W_{P1}| - |\delta|}{2}\right)^2 + \frac{|W_{P2}|^2}{2}}\, t . \tag{55}$$

Thus, $|A_2(t)|^2$ peaks when $\delta = \pm|W_{P1}|$ and at the exact resonance has a time average of ¼. On either side of $\delta = \pm|W_{P1}|$ its average value decreases, having a full width of $2\sqrt{2}|W_{P2}|$. When $|\delta| = 0$, we have for the time average of $|A_2|^2$ the very small value $|W_{P2}|^2/2|W_{P1}|^2 \approx \epsilon/2$. The interpretation of Eq. (55) is that the $|1\rangle$ level is split into two levels separated by an amount $2|W_{P1}|$, with the unperturbed level lying halfway between. Since the second laser is weak, by comparison, the $|2\rangle$ level is split by a much smaller amount. Thus, resonance is obtained roughly when the second laser is tuned so that $\delta = |W_{P1}|$. When δ is changed around these values there is a slight width of the line shape due to power broadening.

To some extent the pulsed case can be understood in the same way. In this case the ac Stark splitting of the $|1\rangle$ level is time-dependent with the separation between the adiabatic levels varying between zero at $t = +\infty$ up to a peak value of $2|W_{P1}|$ at $t = 0$. Correspondingly, if $0 < |\beta_2| < 1$, there will be some time at which $\delta = \pm|W_{P1}|g$ so that for a brief time there is exact resonance between one of the levels into which $|1\rangle$ is split and $|2\rangle$. In this situation we speak of a crossing having occurred. Obviously, one crossing occurs for $t < 0$ and one for $t > 0$. If one investigates the condition for a strong effect to occur at the crossing and yet for the two crossings to be well separated, it is found that one must have

$$1 > |\beta_2| \gg \epsilon^{-1/2}\, |W_{P2}\tau_0|^{-1} , \tag{56}$$

where τ_0 is a measure of the pulse length. Thus, since ϵ must be very small (i.e., $\ll 10^{-3}$), we must have $|W_{P2}\tau_0| \gg 1$. With restriction (56) on $|\beta_2|$ we can use an iterative scheme similar to that described in earlier work[120,121] in order to find g_1, g_2, and g_3. We find that, as t approaches the time at which the first crossing occurs, $|A_2|^2$ remains near zero until $|W_{P1}|g$ gets very close to δ. Then the following expression holds until one is well past the crossing:

$$|A_2|^2 \simeq \frac{1}{4}\left| 1 + \frac{g - |\beta_2|}{\sqrt{(g - |\beta_2|)^2 + 2\epsilon|\beta_2|^2}} \right| . \tag{57}$$

Thus, near the crossing, $|A_2|^2$ rises from zero to a value equal to ½. Figure 12.44 shows a comparison between Eq. (57) and a numerical solution of Eqs. (53) for the choices $\epsilon = 10^{-4}$, $|W_{P1}\tau_0| = 10^5$, $|\beta_2| = 0.8$, $\tau_0 = 10^{-6}$ sec, and $g = [1 + (t/\tau_0)^2]^{-3/2}$. It is clear that the approximation is excellent. The above crossing effects make possible a much broader set of double peaks than are predicted for the cw case.

In the event that a third photon can ionize the state $|2\rangle$, one has an excellent way of monitoring the excita-

120. M. G. Payne and M. H. Nayfeh, *Phys. Rev. A* 13, 595 (1976).

121. C. W. Choi, *Two-State and Two-State Plus Continuum Problems Associated with the Interaction of Intense Laser Pulses with Atoms*, ORNL/TM-5754 (February 1977).

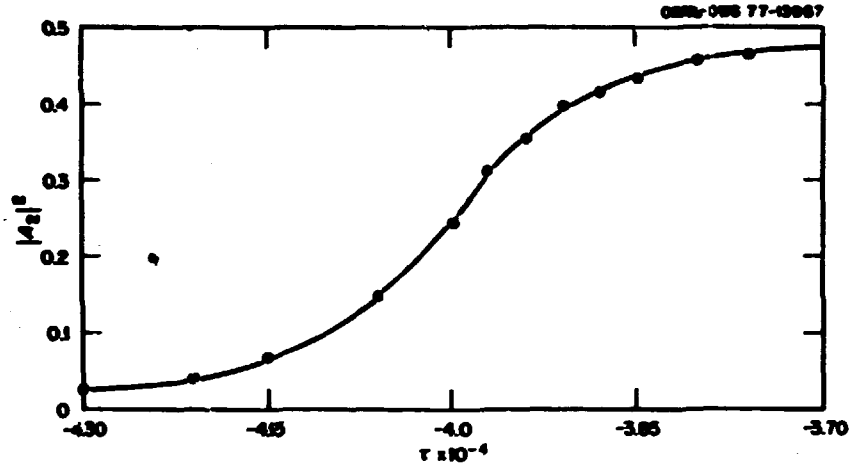

Fig. 12.44. Comparison of Eq. (57) (shown by the smooth line) with numerical calculations (•••) for $\epsilon = 10^{-4}$, $|\phi_2| = 0.8$, $\tau_0 = 10^{-4}$ sec, $W_{P1} = 10^{11}$/sec, and $g = [1 + (t/\tau_0)^2]^{-3/2}$.

tion. Since electrons can be detected with great sensitivity,[13] while the presence of ionization only introduces a damping and shift term into the third of Eqs. (53),[97] the effects of the crossing on the ionization are similar to those on fluorescence out of $|2\rangle$ and are much easier to measure.

The results derived here can be generalized to the case where the first laser is also off resonance if $\epsilon \ll 1$. Studies along these lines are being continued, as is the effort to generalize to cases where $\epsilon^{-1/2}|W_{P2}\epsilon_0|^{-1} \gtrsim 1$. The latter generalization is of particular interest due to the nonadiabatic behavior induced. We believe that the latter generalization can proceed along lines similar to the Landau-Zener method.

Collision-Induced Resonances in the Two-Photon Ionization of Excited-State Populations

We consider a collision between atoms A and B with atom A initally in the excited state $|1a\rangle$ and atom B in its ground state $|0b\rangle$. We wish to study the process[122–124]

$$\hbar\omega + A(1a) + B(0b) \rightarrow A(0a) + B(2b) \qquad (58)$$

for the case where $|0a\rangle$ is the ground state of A and $|2b\rangle$ is an excited state of B with the same parity as $|0b\rangle$. The very intense narrow-band laser that provides the photon of energy $\hbar\omega$ is at a frequency such that $\hbar\omega \simeq E_{2b} - E_{0b} - (E_{1a} - E_{0a})$. The process is enhanced greatly if atom B has a state $|1b\rangle$ whose excitation energy is relatively close to the excitation energy of the state $|1a\rangle$. Thus, we assume that the states of dominant importance are those shown in Fig. 12.45. Payne and Choi[97] showed that excitation processes that are near resonance so that a finite set of discrete states can be used can be monitored in a very sensitive way by ionization. In fact, in the latter type of theory, one obtains finally a finite set of close-coupled equations for amplitudes for being in various discrete states in which the laser

122. L. I. Gudzenko and S. I. Yakovlenko, *Zh. Eksp. Teor. Fiz.* 62, 1686 (1972) [*Sov. Phys. – JETP (Engl. Transl.)* 35, 877 (1972)].

123. V. S. Lisita and S. I. Yakovlenko, *Zh. Eksp. Teor. Fiz.* 66, 1550 (1974) [*Sov. Phys. – JETP (Engl. Transl.)* 39, 759 (1974)].

124. S. E. Harris and D. B. Lidow, *Phys. Rev. Lett.* 33, 644 (1974).

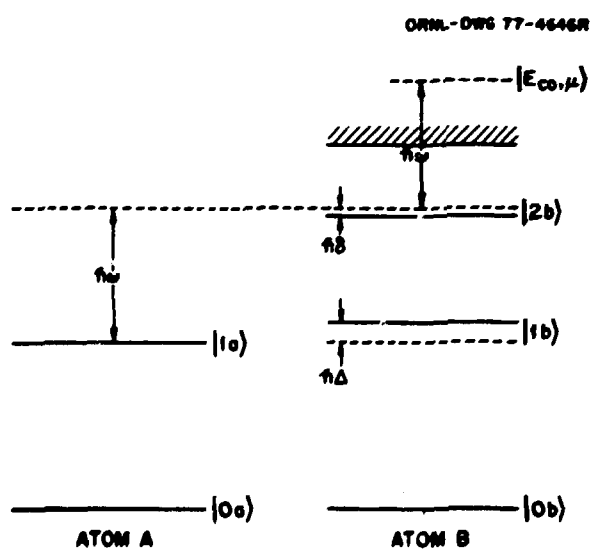

Fig. 12.45. Energy-level diagrams for atoms A and B.

field is incorporated to all orders and the ionization enters only as power-dependent damping shift terms in the equations for the amplitudes of states that can be ionized.

In our model we take

$$|\psi(t)\rangle = a_0(t)e^{-i(\omega_{1a}+\omega_{0b})t}|1a\rangle|0b\rangle + a_1(t)e^{-i(\omega_{0a}+\omega_{1b})t}|0a\rangle|1b\rangle + a_2(t)e^{-i(\omega_{0a}+\omega_{2b})t}|0a\rangle|2b\rangle + |0a\rangle\sum_{\mu}\int dE_0 C_\mu(E_0,t)e^{-i(\omega_{0a}+\omega_c)t}E_0,\mu\,, \tag{59}$$

and

$$\hat{H} = \hat{H}_{0a} + H_{0b} + \hat{V}_{ab}(t) - \hat{P}_{xb}E_1\cos\omega t\,, \tag{60}$$

where $\hat{H}_{0a}$ and $\hat{H}_{0b}$ are Hamiltonians for the isolated atoms and $\hat{V}_{ab}(t)$ is the atom-atom interaction evaluated along a straight-line classical path with impact parameter P. The laser is plane-polarized in the x direction, and the atom-field interaction is treated in the classical field-dipole approximation. The quantities ω_{1a}, ω_{0b}, etc., are defined so that their product with $\hbar$ gives the corresponding eigenenergy. In what follows we assume $|\omega_{1a} - \omega_{0a} - \omega| \gg |\Delta| \gg |\delta'|$, $\langle 1b|\hat{P}_{0x}|2b\rangle E_0 \ll \hbar|\Delta|$, $\hbar|\Delta| \gg \hbar|v/b|$, $P_a(0,1)E_0 \equiv \langle 0_a|\hat{P}_{ax}|1a\rangle E_0 \ll \hbar|\omega_{1a} - \omega_{0a} - \omega|$, and $P_b(0,1)E_0 \equiv \langle 0b|\hat{P}_{bx}|1b\rangle E_0 \ll \hbar|\omega_{1b} - \omega_{0b} - \omega|$ and that no other accessible one- or two-photon near resonances exist in either atom. The field amplitude is assumed to change very little in the time of collision.

With the above assumptions, we find[9,7]

$$\frac{dA_0}{dt} = -i\frac{V(t)\omega_p^0\hbar}{\Delta}A_2 \times \exp\left[i\delta' t - i\int_{-\infty}^{t}\frac{|V(t')|^2}{\Delta}dt'\right], \tag{61}$$

$$\frac{dA_2}{dt} = -P_0A_1 - i\frac{\omega_p V^*(t)\hbar}{\Delta}A_0 \times \exp\left[-i\delta' t + i\int_{-\infty}^{t}\frac{|V(t')|^2}{\Delta}dt'\right],$$

where A_0 and A_2 differ only by a phase factor from a_0 and a_2, $\omega_p = \langle 2b|\hat{P}_{bx}|1b\rangle E_0/2\hbar$, $V(t) = \langle 0a|\langle 1b|\hat{V}_{ab}|0b\rangle|1a\rangle/\hbar$, $\alpha_\mu(E_c) = E_0(2\hbar)^{-1}\langle E_c, \mu|\hat{P}_{bx}|2b\rangle$, $P_0 = \hbar\pi\Sigma_\mu|\alpha_\mu(E_{c0})|^2$, $\delta' = \delta + |\omega_p|^2\Delta^{-1} + \Delta\omega$, $\Delta\omega = \hbar P\int\Sigma_\mu|\alpha_\mu(E_c)|^2\,dE_c(E_c - E_{c0})^{-1}$; and if both $|1a\rangle$ and $|1b\rangle$ have allowed transitions to the ground state, $V(t) \equiv C_3R^{-3}(t)$. Magnetic sublevels have been ignored by using a rotating atom type ω approximation. Equations (61) are a special case of equations derived previously,[122–124] except for the existence of the damping term and the shift $\Delta\omega$. The probability of the process

$$2\hbar\omega + A(1a) + B(0b) \to A(0a) + B^+ + e \tag{62}$$

is given by

$$R(E_0,\delta,b,v) = \int\sum_{\mu}|C(E_c,\infty)|^2\,dE_c\,,$$

$$= 2\int_{-\infty}^{\infty}|A_2(t)|^2\,dt\,P_0\,.$$

We shall not elaborate on the solution of Eqs. (61); instead, we point out that even one photoelectron can be detected[8,9] and that for power levels $\lesssim 10^{10}$ W/cm^2, P_0 is a relatively small rate so that it has a nearly negligible effect during the collision. Thus, if t_0 is the time of collision, A_2 thereafter evolves as follows:

$$\frac{dA_2}{dt} \simeq -P_0A_2\,,$$

so that

$$A_2(t) \simeq 0\,,\quad t < t_0$$

$$\approx A_2(t_0^+)\exp\left(-\int_{t_0}^{t}P_0\,dt'\right),\quad t > t_0\,.$$

Correspondingly,

$$R(E_0,\delta,b,v) \simeq |A_2(t_0^+)|^2 \times\left[1 - \exp\left(-2\int_{t_0}^{t}P_0(t')\,dt'\right)\right].$$

At the power levels where $|A_2(t_0^+)|^2$ starts to become appreciable, one often has $2\int_{t_0}^{t}P_0(t')\,dt' \gg 1$, even when t_0 is relatively near the end of the pulse.

At the lower power levels and with long laser pulses, it is important to include accumulation of the population of $|2b\rangle$ in competition with the reverse reaction, spontaneous decay, collisional mixing of magnetic sublevels, and photoionization. This is easily done by incorporating a cross section for process (58) and its reverse reaction along with a decay rate and a photoionization rate into a set of rate equations. At power levels $\lesssim 10^9$ W/cm^2 and with pulses of $>10^{-6}$ sec length, saturation of the ionization will often occur before another collision in which the process could be reversed.

Laser-Induced Collisional Excitation Transfer

During the last four years, considerable theoretical effort[122–128] was devoted to describing absorption or stimulated emission resonances that are only present during collisions of excited atoms with ground-state atoms of another element. In the above collision process, the initially excited atom having excitation energy ϵ returns to its ground state and leaves the second atom in an excited state of excitation energy nearly equal to $\epsilon \pm \hbar\omega$. Large cross sections (i.e., several Å^2) are predicted at power levels $\sim 10^7$ W/cm^2 in many cases where no excitation transfer occurs in the absence of the laser field.[122,123] Such effects were suggested in 1972 by Gudzenko and Yakovlenko (GY),[122] and a rather thorough theoretical treatment was given, concentrating largely on the case where the laser is tuned to exact resonance. In 1974, the GY theory was extended further in the off-resonance situation by Lisita and Yakovlenko (LY).[123] The GY and LY theories are rather complete, but, because of the brevity of their discussions, they have not (in the opinion of the present authors) been properly appreciated. More recently (1974), Harris and Lidow (HL)[124] gave a more physical discussion of a simpler situation with the laser tuned to exact resonance and the laser field weak. Other work has generalized to multiphoton resonances and allowed for more general adiabatic potentials for the quasi molecule.[125–128] The effect has recently been studied experimentally by Falcone et al.[106]

In the present work, a model similar to that of GY is used and a tabulation of the thermally averaged cross section (i.e., a line shape for the process) is given for power levels $\lesssim 10^9$ W/cm^2 (we follow GY in calling this the weak-field limit). In cases where the atom-atom interaction is large enough to detune the laser for internuclear separations $\lesssim 10$ Å, we show that the thermally averaged cross section for the weak-field process can be represented as

$$\bar{\sigma}(E_0, \delta, T) = |\alpha|^2 E_0^2 \bar{K}_0^{-2/s} \left(\frac{2kT}{\mu}\right)^{-4/s} \times J\left[s|\bar{K}_0|^{1/s} \left(\frac{2kT}{\mu}\right)^{-2/s} \delta\right], \quad (63)$$

where $|\alpha|$ ($|\alpha|$ is equivalent to the $|B_2|$ defined by LY[123]) is an atom-atom parameter which measures the strength of the laser field-collisional coupling for the process, E_0 is the laser field amplitude, T is absolute temperature, s is the sign of $\bar{K}_0$, μ is the reduced mass, $\hbar\delta$ is the excess energy of the photons relative to exact resonance, $\hbar\bar{K}_0/R^6$ is the shift in resonant energy for the quasi molecule at internuclear separation R, and $J(x)$ is a function of one variable which is tabulated in the present work. In deriving Eq. (63), the dipole-dipole form of the atom-atom interaction was assumed to dominate at large R. Thus, in many cases, the line shape of $\bar{\sigma}$ is the same except for changes in width which depend on the magnitude of $\bar{K}_0$, μ, and T. The weak-field line shape based on Eq. (63) is shown in Fig. 12.46.

125. J. M. Yuan, T. F. George, and F. J. McLafferty, *Chem. Phys. Lett.* 40, 163 (1976).
126. T. F. George et al., *Discuss. Faraday Soc.* (in press).
127. N. M. Kroll and K. M. Watson, *Phys. Rev. A* 13, 1018 (1976).
128. A. M. F. Lau, *Phys. Rev. A* 13, 139 (1976).

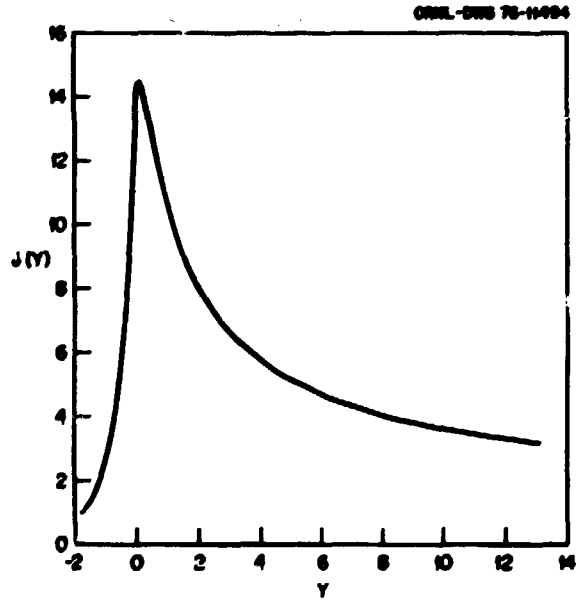

Fig. 12.46. Line shape function for laser-induced collisional excitation transfer in the weak-field limit.

Even though general features of the line shape were discussed by LY,[123] our work is the first to present a tabulation of the universal line shape in the region near $\delta = 0$ where the cross section is largest.

Adiabatic Following in Two-Photon Transition

More interest has been generated recently in coherent multiphoton transitions in many-level systems.[129–133] Coherent two-photon propagations in two-[129,130,132] and three-level[131] systems were considered theoretically and observed experimentally. An adiabatic following model was used to derive and explain parametric generation processes.[134] In this work, we consider the effect of relaxation on the response of a three-level system to smoothly varying, near-resonant two fields and calculate the relaxation-dependent contributions to the nonlinear refractive index. This system, when the intermediate state is sufficiently far from resonance, can be described by the following "two-photon Bloch equations" of Bloch vector components (u, v, w), which are analogous to those for a one-photon transition in a two-level system, except for the presence of a two-photon coupling and a frequency shift:[133]

$$\frac{du}{dt} + \gamma_2 u = -\Delta(t) v , \tag{64}$$

$$\frac{dv}{dt} + \gamma_2 v = \Delta(t) u + k\epsilon^2(t) w , \tag{65}$$

$$\frac{dw}{dt} + \gamma_1 w = -k\epsilon^2(t) v - \gamma_1 , \tag{66}$$

where $\Delta(t) = \Delta_0 + s_1 e_1^2 + s_2 e_2^2$; $\Delta_0 = \omega_1 + \omega_2 - \omega_{12}$; $s_1 = \mu_{01}^2/4\hbar^2\Delta\omega_0$; $s_2 = \mu_{12}^2/4\hbar^2\Delta\omega_0$; $k = \mu_{01}\mu_{12}/2\hbar^2\Delta\omega_0$; $\epsilon^2 = e_1(t)e_2(t)$; $\Delta\omega_0 = |\omega_1 - \omega_{01}| = |\omega_2 - \omega_{12}|$ is the off-resonant frequency; ω_{01} and ω_{12} and μ_{01} and μ_{12} are the eigenfrequencies and dipole moments, respectively, of the levels; $e_1(t)$ and $e_2(t)$ and ω_1 and ω_2 are the amplitudes and frequencies, respectively, of the electric-field modes. To determine an approximation to the general solutions of Eqs. (64) through (66), one first reduces these equations to three uncoupled third-order equations with time-dependent coefficients. The resulting equations are then easily reduced to quadratures by assuming the logarithmic time derivative of the field $d/dt(\ln \mu\epsilon)$, which is a measure of the pulse width, to be small compared with the Rabi frequency.[135,136] When $\gamma_1 = \gamma_2 = \gamma$ (which is a reasonable assumption for strong collisions) and for adiabatic fields and an atom that is initially in the ground state, the oscillatory solutions vanish and w takes the simple form

$$w = -\frac{\Delta}{\Omega} e^{-\gamma t} - \gamma \frac{\Delta}{\Omega} e^{-\gamma t} \times \left[\int_{-\infty}^{t} \frac{\Omega e^{\gamma\tau}(\gamma^2 + \Delta^2)}{\Delta(\gamma^2 + \Omega^2)} d\tau \right] . \tag{67}$$

When γ_1 and γ_2 are small but different, one can easily show that the population inversion for the case of adiabatic following is given by[135,136]

$$w = -\frac{\Delta(t)}{\Omega(t)} e^{-\gamma_1 t - q(t)} - \gamma_1 e^{-q(t)} \times \frac{\Delta(t)}{\Omega(t)} \int_{-\infty}^{t} \frac{\Delta(\tau)}{\Omega(\tau)} e^{\gamma_1(\tau - t) + q(\tau)} d\tau , \tag{68}$$

where

$$q(t) = (\gamma_2 - \gamma_1) \int_{-\infty}^{t} \frac{k^2\epsilon^4}{\Omega^2} dt . \tag{69}$$

The population inversion in Eq. (67) does not have any power-dependent decay. As $\gamma \to 0$, $w \to -\Delta/\Omega$. On the other hand, w in Eq. (68) has an induced damping $q(t)$. For weak fields, the lowest-order term in $q(t)$ depends on the integrated square of the intensity, which is an indication of the two-photon process. For sufficiently strong fields, $q(t)$ has no field dependence, and the inversion is damped by the phase relaxation γ_2 only.

In addition to the line shift, which is inherent in two-photon processes due to the involvement of virtual

129. E. M. Belenov and I. A. Poluektov, *Sov. Phys. – JETP (Engl. Transl.)* 29, 754 (1969).
130. M. Takatsuji, *Phys. Rev. A* 4, 808 (1971).
131. N. Tan-no, K. Yokoto, and H. Inaba, *Phys. Rev. Lett.* 29, 1211 (1972).
132. T. L. Gvardzhaladze, A. Z. Grasyuk, and V. A. Kovalenko, *Sov. Phys. – JETP (Engl. Transl.)* 37, 227 (1973).
133. N. Tan-no, K. Yokoto, and H. Inaba, *J. Phys. B* 8, 339 (1975).
134. D. Grischkowsky, M. M. T. Loy, and P. F. Liao, *Phys. Rev. A* 12, 2514 (1975).
135. M. H. Nayfeh, *Phys. Rev. A* 14, 1304 (1976).
136. M. H. Nayfeh and A. H. Nayfeh, *Phys. Rev. A* 15, 1169 (1977).

intermediate levels, there is a relaxation-dependent line asymmetry due to the buildup of the pulsed field. To see this, we derive an expression for the refractive index of three-level systems in the weak-field limit. One can easily show that[135,136]

$$u = \frac{k\epsilon^2}{\Omega} e^{-\gamma_1 t - q(t)} \times \left[1 + \gamma_1 \int_{-\infty}^{t} \frac{\Delta(\tau)}{\Omega(\tau)} e^{\gamma_1 \tau + q(\tau)} d\tau\right]. \quad (70)$$

Since the refractive index of the medium is related to u by $n = 1 + 2\pi N k\hbar u \epsilon^{-2}$, it is given for weak fields by

$$n - 1 = -\frac{2\pi N k^2 \hbar}{\Delta_0} \left\{ \left[1 - \frac{s_1\epsilon_1^2 + s_2\epsilon_2^2}{\Delta_0} + \frac{(s_1\epsilon_1^2 + s_2\epsilon_2^2)^2}{\Delta_0^2} - \frac{1}{2}\frac{k^2\epsilon^4}{\Delta_0^2}\right] \times (1 + e^{-\gamma_1 t}) - \frac{1}{2}(2\gamma_2 - \gamma_1) \times \int_{-\infty}^{t} \frac{k^2\epsilon^4(\tau)}{\Delta_0^2} e^{\gamma_1(t-\tau)} d\tau - (\gamma_2 - \gamma_1) e^{-\gamma_1 t} \int_{-\infty}^{t} \frac{k^2\epsilon^4(\tau)}{\Delta_0^2} d\tau \right\} + O(\epsilon^6). \quad (71)$$

We note that the lowest-order contribution to the induced refractive index is intensity dependent. It is equal to $2\pi N k^2 \hbar \Delta_0^{-2}(s_1\epsilon_1^2 + s_2\epsilon_2^2)[1 + \exp(-\gamma_1 t)]$, which is inversely proportional to the square of the frequency shift of the transition. The next order contribution is $\pi N k^2 \hbar \Delta_0^{-3}[k^2\epsilon^4 - 2(s_1\epsilon_1^2 + s_2\epsilon_2^2)^2][1 + \exp(-\gamma_1 t)]$; part of this contribution is due to the two-photon level shift. The last two contributions depend on the integrated square of the intensity. These contributions cause asymmetry in the refractive index at the long-wavelength wing of the transition due to the accumulation of the square of the intensity at later times. We note that for pulses of the same total energy, the asymmetry depends on the pulse length. For long pulses, the term proportional to $(\gamma_2 - \gamma_1)$ vanishes, whereas the term proportional to $(2\gamma_2 - \gamma_1)$ increases with increasing times. Thus, it is expected that there exists a pulse length for which the asymmetry is maximum.

All these contributions are dependent on the relaxation. In the absence of relaxation (i.e., $\gamma_1 = \gamma_2 = 0$), it follows from Eq. (71) that

$$n - 1 = -\frac{4\pi N k^2 \hbar}{\Delta_0}\left[1 - \frac{s_1\epsilon_1^2 + s_2\epsilon_2^2}{\Delta_0} + \frac{2(s_1\epsilon_1^2 + s_2\epsilon_2^2)^2 - k^2\epsilon^4}{2\Delta_0^2}\right]. \quad (72)$$

When the relaxation is due entirely to spontaneous emission (i.e., $2\gamma_2 = \gamma_1$), the last contribution in Eq. (71) vanishes. In this case, the two-photon level shifts contribute to the asymmetry of the line to $O(\epsilon^6)$ at early times only. At times larger than the relaxation time T_1, it follows from Eq. (71) that

$$n - 1 = -\frac{2\pi N k^2 \hbar}{\Delta_0}\left[1 - \frac{s_1\epsilon_1^2 + s_2\epsilon_2^2}{\Delta_0} + \frac{2(s_1\epsilon_1^2 + s_2\epsilon_2^2) - k^2\epsilon^4}{2\Delta_0^2} - \frac{1}{2}(2\gamma - \gamma_1) \times \int_{-\infty}^{t} \frac{k^2\epsilon^4(\tau)}{\Delta_0^2} e^{\gamma_1(\tau - t) + q(\tau)} d\tau\right]. \quad (73)$$

In conclusion, the leading contribution to the refractive index is intensity dependent caused by the level shifts inherent in multiphoton processes; it includes a relaxation-dependent part which is important at times shorter than γ_1^{-1}. The second-order contributions depend on the square of the intensity and the time-integrated square of the intensity. The latter contribution, which is relaxation dependent, causes line asymmetry at the long-wavelength wing; it consists of a term proportional to $(\gamma_2 - \gamma_1)$ and one important at early times and a term proportional to $(2\gamma_2 - \gamma_1)$.

Dynamic Stark Splittings in Two-Photon Processes

An analytical semiclassical expression is presented for two-photon transition in a three-level system under the influence of two pulsed fields and with phenomenological decay constants.[137]

137. M. H. Nayfeh and A. H. Nayfeh (to be published).

We consider a three-level atomic system with only one of the excited states optically connected to the ground state. The position of this level is arbitrarily taken between the ground state and the optically forbidden higher excited state.

The state of the atom ψ at any time satisfies the equation

$$i\hbar\frac{\partial\psi}{\partial t} = H\psi\,, \tag{74}$$

where the Hamiltonian H is written in the electric dipole approximation as

$$H = H_A - \hat{\mu}\cdot\mathbf{E} + H_D\,, \tag{75}$$

where $\hat{\mu}$ is the atomic dipole operator, $\mathbf{E}$ is the classical electric field vector evaluated at the center of the atom, H_A is the Hamiltonian of the atomic system in the absence of the external field, and H_D describes the radiative damping of the excited states. We assume that the matrix H_D is diagonal with the elements $-(1/2)i\hbar\gamma_1$ and $-(1/2)i\hbar\gamma_2$ for the excited states and zero for the ground state.

The state of the atom may be expressed as a superposition of three orthogonal time-independent states; that is,

$$\psi = a_0(t)|0\rangle + a_1(t)e^{-i\omega_{10}t}|1\rangle + a_2(t)e^{-i\omega_{20}t}|2\rangle\,. \tag{76}$$

Explicit forms for a_0, a_1, and a_2 are found by solving the equation of motion given the initial conditions and the electric field. We let

$$E = 2\mathbf{E}_1(t)\cos(\omega_1 t) + 2\mathbf{E}_2(t)\cos(\omega_2 t)\,. \tag{77}$$

In the rotating wave approximation and for ω_2 away from ω_1, Eqs. (74) through (77) give the following equations under the $\Delta_m = 0$ selection rule:

$$A_0' = i\mu_{01}E_1A_1\,, \tag{78}$$

$$A_1' + i\delta_1A_1 = i\mu_{10}E_1A_0 + i\mu_{12}E_2A_2\,, \tag{79}$$

$$A_2' + i\delta_2A_2 = i\mu_{21}E_2A_1\,, \tag{80}$$

where the μ_{ij} are the elements of the dipole operator matrix, E_1 and E_2 are the lengths of the vectors $\mathbf{E}_1$ and $\mathbf{E}_2$, primes denote differentiation with respect to t, and

$$A_0 = a_0,\ A_1 = a_1\exp(i\Delta_1 t),\ A_2 = a_2\exp(i\Delta_2 t)\,, \tag{81}$$

$$\delta_1 = -(\Delta_1 + \tfrac{1}{2}i\gamma_1),\ \delta_2 = -(\Delta_2 + \tfrac{1}{2}i\gamma_2)\,,$$

$$\Delta_1 = \omega_1 - \omega_{10},\ \Delta_2 = \omega_1 + \omega_2 - \omega_{20}\,. \tag{82}$$

We determine an approximate solution to Eqs. (78) through (80) when the amplitudes of the field, E_1 and E_2, are slowly varying functions of time. The magnitudes of the amplitudes are arbitrary; thus the solution is valid for both strong as well as weak fields. Eliminating A_0 and A_1 from Eqs. (78) through (80) and neglecting terms the order of $(\ln E_n)''$ and $[(\ln E_n)']^2$, we obtain

$$A_2''' + [i\delta - (\ln E_1E_2^2)']A_2'' + [\alpha^2 - i\delta_1(\ln E_1E_2)' - i\delta_2(\ln E_1E_2^2)']\,, \tag{83}$$

$$A_2' + \{i\delta_2E_1^2 - \alpha^2(\ln E_1E_2)' + 2\alpha\alpha' + E_1^2[\ln(E_2/E_1)]'\}A_2 = 0\,,$$

where

$$\delta = \delta_1 + \delta_2,\ \alpha^2 = E_1^2 + E_2^2 - \delta_1\delta_2,\ e_1 = \mu_{01}E_1,\ e_2 = \mu_{12}E_2\,. \tag{84}$$

A number of techniques, including the method of multiple scales, can be used to determine an approximate solution[138] to Eq. (83). In this paper, we represent Eq. (83) in the factored form[130,135,136]

$$\left(\frac{d}{dt} + g_3\right)\left(\frac{d}{dt} + g_2\right)\left(\frac{d}{dt} + g_1\right)A_2 = 0\,. \tag{85}$$

With Ω defined as $\Omega^2 = 4e_1^2 + 4e_2^2 + (\delta_1 - \delta_2)^2$ we solve for g_i by assuming that $|\delta_2e_1^2| \ll |\alpha^2\Omega|$. Using the definitions of α and Ω, this condition can be written as

$$|\delta_2e_1^2| \ll |(e_2^2 + e_2^2 - \delta_1\delta_2) \times [4e_1^2 + 4e_2^2 + (\delta_1 - \delta_2)^2]^{1/2}\,.$$

138. A. H. Nayfeh, Chap. 6 in *Perturbation Methods*, Wiley-Interscience, New York, 1973.

If we denote the larger of γ_1 and γ_2 by γ_m, the above condition is satisfied if one or more of the following conditions is satisfied:

$$e_1 < \gamma_m \,, e_1 > \gamma_m \,, e_2 > \gamma_m$$

$$e_2 > e_1, \; |\mathcal{E}_2| < |\mathcal{E}_1| \,, \text{when } e_1 < O(|\mathcal{E}_1|) \,.$$

Moreover, the above condition may be satisfied by some intermediate value of $e_1/|\mathcal{E}_1|$ and $|\mathcal{E}_2|/|\mathcal{E}_1|$. With this assumption, we write $g_i = G_i + e_i (i = 1, 2, 3)$ with $|e_i| < |G_i|$. Using an iterative procedure one can easily get a solution for g_i and then integrate Eq. (83).

This work extends the analyses on the two-photon process to the case of pulsed fields, both adiabatically and rapidly switched fields. The relaxation of the system is included in detail, with different states allowed to have different relaxation constants. The solution is valid in the limit of strong fields as well as in the limit of weak fields. More importantly, it is valid in the intermediate field regime; therefore, it bridges the gap in the previous analyses. In the limit of fields having constant amplitudes, the reduction from the pulsed solution is exact; therefore, the above range of parameters is still applicable. New predictions are obtained in the latter case which were not considered before.

We investigate the dependence of the ac Stark splittings on the detunings, the decays constants, and the amplitudes of the pulses. New shifts are calculated; they were not predicted in the previous ac Stark effect theory. Some of these shifts depend on the rate of change of the amplitudes of the pulses. For constant fields which are resonant with the second transition, the splittings are essentially linear in the amplitudes of the pulses, and the atomic oscillations exhibit resonance enhancement if the relaxation constants are either equal or negligible.

Induced decays are calculated for both the steady contribution and the atomic oscillations. It is found that, for some combinations of the relaxation constants, detunings, and field amplitudes, the atomic oscillations suffer induced enhancement which slows down their decay. Other dampings are calculated which are induced by the rate of change of the field amplitudes. The dependence of the broadenings on the detunings, relaxations, and field amplitudes and rates of change are also calculated.

Saturation of the two-photon transition is discussed for the case of metastable and nonmetastable final states. In the metastable case, saturation can be achieved regardless of the position of the intermediate state, whereas in the nonmetastable case, saturation can only be achieved if the saturation parameter is much greater than the detuning mismatch in the line widths of the intermediate state. When the product of the intermediate state detuning and the two-photon transition detuning is positive, population inversion can be achieved at moderate fields.

CONCLUSION

Other studies that are closely related to our experimental program included (1) the modeling of signal power dependence as a function of wavelength in our line-broadening studies; (2) studies of the effect on ionization or dissociation saturation curves of a laser flux depending on position like $F(\rho) = F_0 \exp[-(\rho/R)^2]$, where ρ is the distance from beam center, F_0 is the flux at beam center, and R is the beam waist; (3) theory related to our studies of diffusion; (4) theory related to concentration fluctuations under transport-limited conditions; and (5) further considerations of the conditions on bandwidth, peak power detuning from resonance, and pressure which permit the use of rate equations in describing the interaction of a pulsed laser field with a dilute vapor of atoms.

13. Chemical Physics

R. N. Compton

J. E. Bloor[1] P. W. Reinhardt
Ada Carter Burke Ritchie[1]
C. D. Cooper[1] H. C. Schweinler
W. F. Frey[1] J. A. D. Stockdale
W. R. Garrett R. J. Warmack[2]
C. E. Klots A. D. Williamson[2]
B. P. Pullen[1]

The Chemical Physics Group has pioneered research in two new areas of molecular physics: electron attachment to molecular clusters and multiphoton ionization of molecules. The former allows a unique new approach to the study of the liquid phase using precise measurement techniques used in gas-phase studies (i.e., mass analysis, monoenergetic electrons, etc.). The results reported for carbon dioxide and nitrous oxide offer a prelude to our studies of the "hydrated electron" in the gas phase. The multiphoton ionization studies of molecules offer possibilities for the development of sensitive and specific detectors of low-ionization-potential molecules (e.g., PAHs), in addition to being a sensitive new method for the detection of optically forbidden transitions in complex molecules. Both these new developments complement our continuing research in atmospheric chemistry and radiation physics.

STUDIES OF MOLECULAR CLUSTERS FROM SUPERSONIC JET EXPANSIONS

We have begun to study the properties of clusters of molecules made during the approximately isentropic expansion of a gas through a sonic nozzle. These studies have included measurements of ionization potentials and electron attachment to molecular clusters.

An important preliminary has been a study of the optimum experimental parameters for creating clusters of a given size. Figure 13.1 illustrates, for example, the intensity of the ions O^-, $O^-(N_2O)$, and $O^-(N_2O)_6$, which are believed to originate from electron attachment to one, two, and seven molecules, respectively, of N_2O, as a function of nozzle pressure. The optimum pressure for a given ion clearly depends on the parent cluster size. We have also studied how these intensities depend on nozzle temperature and diameter and on nozzle-skimmer separation. A theoretical description of these observations in terms of the rate constants for cluster development has been formulated. We deduce that the observable signal from a monomer should vary approximately with the nozzle pressure as

$$n \sim n_0[(3\gamma-4)/\gamma] ,$$

where γ is the usual heat-capacity ratio. This is in good agreement with the O^- signal in Fig. 13.1.

The concentration of dimers in a nozzle beam is predicted to increase with the square of the nozzle pressure, as Fig. 13.1 indicates. The nozzle pressure yielding the maximum dimer signal is predicted to scale with the nozzle diameter (d_0) and temperature (T_0) in accordance with

$$P_0 \sim d_0^{-0.5} T_0^{[(5\gamma-2)/4(\gamma-1)]} ,$$

which agrees rather well with data in the literature and our own observations.

We have been able to observe, in N_2O expansions, ions with the general formula $O^-(N_2O)_n$ for $0 \leq n \leq 30$. The attachment cross section for making several of these, as a function of electron energy, is illustrated in Fig. 13.2. The energy dependence of O^- is what is

1. Consultant.
2. Postdoctoral fellow.

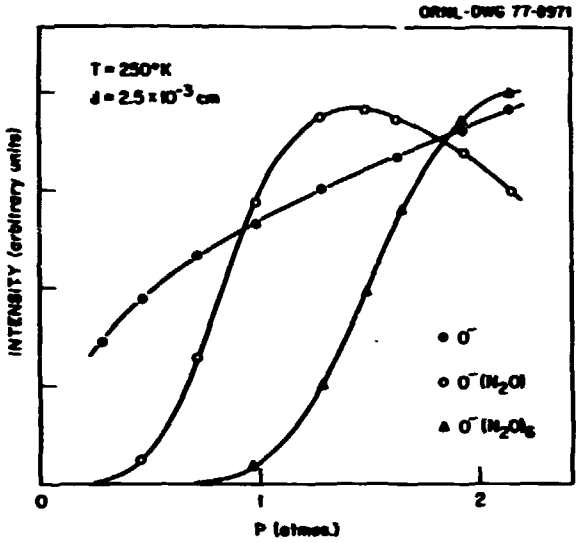

Fig. 13.1. Intensities of several negative ions from N_2O as a function of nozzle pressure.

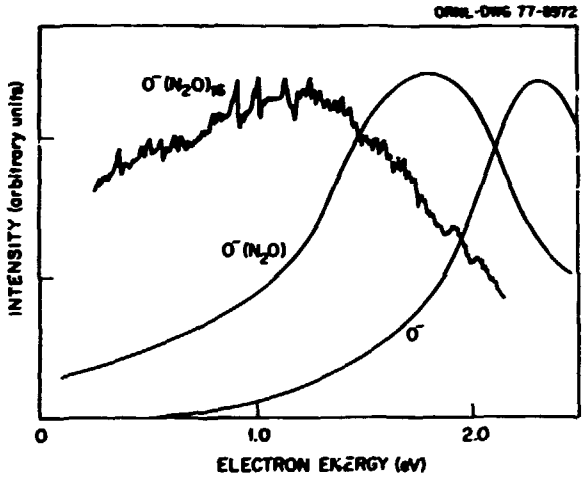

Fig. 13.2. Intensity of several negative ions from N_2O as a function of electron energy.

typically observed from N_2O, with one noteworthy exception: A low-energy shoulder, thought to originate from electron attachment to "hot" N_2O molecules, is absent in our experiments. This illustrates nicely the drastic cooling that the gas undergoes in the adiabatic expansion.

The cross section for $O^-(N_2O)$ peaks 0.5 eV below that of O^-. It is otherwise structureless and seems to extrapolate to a finite value at zero energy. This behavior is without precedent. The cross sections for the larger clusters continue these trends; the maxima shift progressively to lower energies with the cross section near zero energy becoming proportionately greater.

Observations of positive ions also are proving informative. We find that the ionization potential of the dimer of ethylene is well below that of the ethylene monomer and close to that corresponding to the heat of formation of the cyclobutane ion. This suggests that the structure of the neutral dimer is also cyclic. We further find that, with increasing energy, the dimer ion fragments much as the cyclobutane ion does.

A preliminary study of the electron attachment to clusters of carbon dioxide reveals that CO_3^- is the dominant ion. This result was anticipated from the studies described for N_2O. CO_2 and CO_3^- are isoelectronic with N_2O and $N_2O_2^-$, respectively. In addition, ions with charge-to-mass ratios corresponding to the formula $(CO_2)^-_{(n=2,3,4,5,6)}$ were detected. No metastable decay, either via autodetachment or dissociation, could be detected. Thus the adiabatic electron affinity of the CO_2 dimer may be positive.

Thermodynamic quantities derived from electron impact–induced reactions will be less affected by internal energy in the target because of the lower temperatures in the sonic nozzle beam. For example, the onset of O^- from N_2O gives the approximate bond dissociation energy of N_2O, whereas electron impact on room-temperature N_2O gives a considerably higher value. Also, the observed onset for O^- from CO_2 corresponds closely to the thermochemical threshold, which further illustrates how a lower onset due to hot bands in room-temperature CO_2 can be eliminated via the adiabatic cooling in the nozzle expansion.

A second, more versatile molecular cluster experiment has been constructed which is capable of handling all types of condensable and noncondensable gases. The apparatus is double differentially pumped (Fig. 13.3). The scattering chamber is equipped with a spherical sector electron gun for high-resolution (~0.05 eV) electron impact studies and a vuv tunable light source for photoionization studies. A quadrupole mass filter has been installed for mass analysis of the electron or photon impact products. This apparatus also will be used for the laser fluorescence and photoionization experiments described elsewhere in this report.

TWO-PHOTON IONIZATION OF CESIUM WITH TUNABLE DYE LASERS

The atomic multiphoton ionization work begun last year continued with further experiments involving atomic cesium. The experimental apparatus shown in Fig. 13.4 involves an ultrahigh vacuum system in which an atomic beam is intersected by the beam of a nitrogen laser–pumped tunable dye laser. Ions created by two-

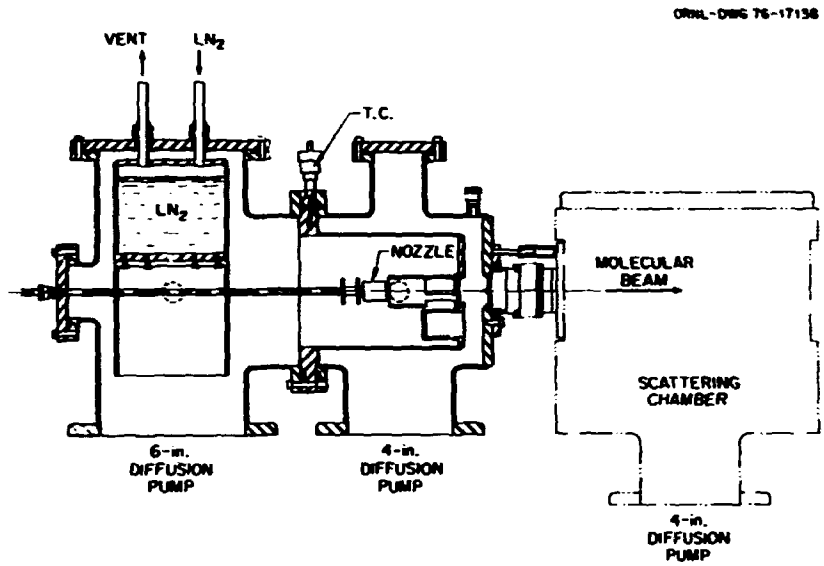

Fig. 13.3. Schematic diagram of molecular clustering apparatus. *The scattering chamber is equipped with a quadrupole mass spectrometer and a spherical sector electrostatic electron velocity analyzer. Ports are provided for laser beams and a vuv monochromator.*

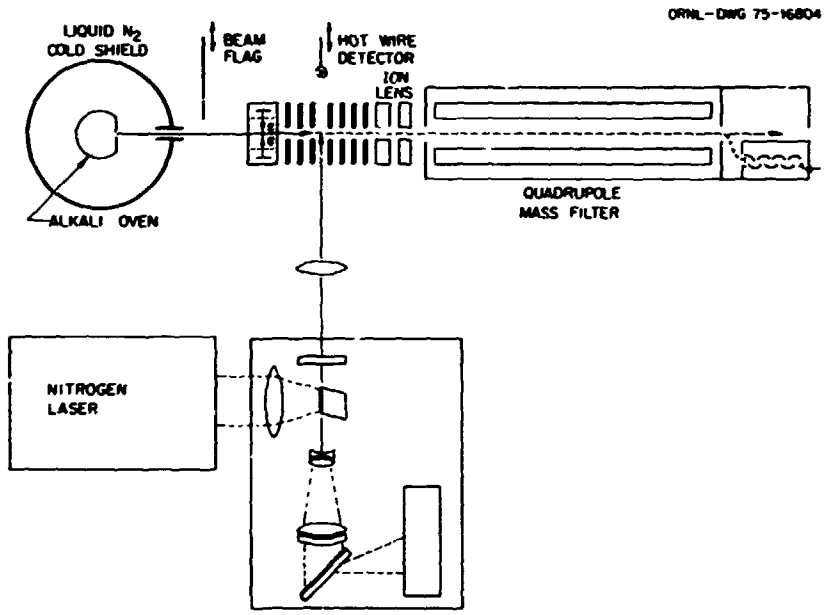

Fig. 13.4. Experimental apparatus for atomic multiphoton ionization experiment.

photon absorption are mass analyzed and detected by a quadrupole mass spectrometer. Alternately, cesium metal is placed in the vacuum chamber at its room-temperature vapor pressure (about 10^{-6} torr) and is irradiated with the laser. Resonance enhancements of the ionization were observed at laser energies corresponding to electric dipole transitions from the $6s^2S_{1/2}$ ground state to the $7p$, $8p$, and $9p^2P_{1/2,3/2}$ states. In addition, two-photon ionization was observed via the electric-quadrupole-allowed transition to the $6d^2D_{3/2,5/2}$ state as an intermediate resonance. Measurements of the relative two-photon ionization cross sections for these processes are in progress.

In addition, we have used the unfocused beam of the dye laser to study the laser power dependence of the ionization signal and the approach to saturation. Figure 13.5 shows a log-log plot of the cesium photoionization signal as a function of laser power for photon energies

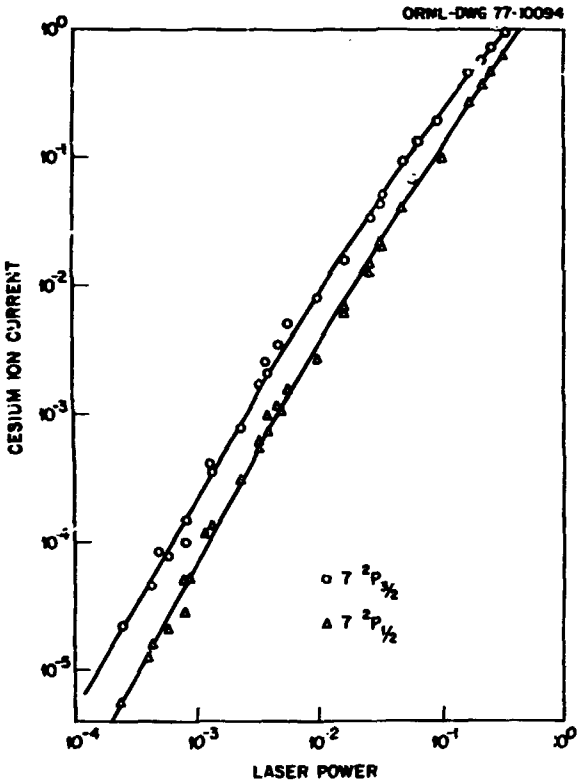

Fig. 13.5. Two-photon ion yield in cesium as a function of laser power, showing approach to saturation for $7p^2P_{1/2,3/2}$ resonances.

corresponding to the $7p^2P_{1/2,3/2}$ fine-structure levels. The ease of saturation is demonstrated by the fact that even at the lowest power density levels used (corresponding to about 200-W/cm^2 peak power) the curves depart from the expected quadratic dependence on laser power. It is also noteworthy that the two fine-structure resonances show different power dependences – the $^2P_{3/2}$ intermediate being "more saturated" at all accessible powers. The effect of this different power dependence is to make the ratio of the cross-section values at these two energies vary with incident power. At low energies in the near-quadratic power dependence region, the $^2P_{3/2}/^2P_{1/2}$ ratio approaches 4 to 1, the approximate ratio of the oscillator strengths of the corresponding single-photon transitions. At higher powers the ratio approaches 1.5 to 1, and with a focused beam the ratio tends toward unity, as it must for complete saturation in which the irradiated atoms are ionized with unit probability.

MULTIPHOTON IONIZATION OF MOLECULAR SPECIES

We are currently extending our multiphoton ionization studies to molecular species, combining the power of high-resolution laser spectroscopy with the sensitivity and specificity of mass spectrometry. Most of our pilot experiments have involved the well-studied iodine molecule.

One of the advantages of multiphoton spectroscopy is the relaxation of optical selection rules, allowing observation of transitions which, due to parity or angular momentum factors, are dipole-forbidden in single-photon absorption. An example of this effect in iodine is shown in Fig. 13.6. The vibrational progression is due to an uncharacterized state of gerade symmetry at an energy twice that of the exciting laser. Since this state is of even parity, it has apparently not been seen in previous single-photon studies of iodine and was discovered by Petty, Tai, and Dalby[3] using multiphoton techniques. We have extended our investigations to longer wavelengths and have seen strong signals even at 6000 Å. At these wavelengths, absorption of five photons is necessary for ionization. Since there exist a large number of states potentially resonant with a multiple of the photon energy, sizable enhancements of the ionization cross section are expected. As also might be expected, the resulting spectra are extremely complex, yet assignments may be attempted on the basis of known features in absorption spectra. For example, in Fig. 13.7 the dissociation limit of the $B^3\Pi^+_{0u}$ state is easily noted. Since four-photon ionization is occurring in this wavelength region, some of the structure may be due to two- or three-photon resonances as well as the single-photon resonances of the $B \leftarrow X$ transition. The high resolution possible in laser spectroscopy is an invaluable aid to assignment of complex spectra. This is especially true in cases such as our molecular iodine multiphoton ionization spectra, in which an inherently dense single-photon spectrum is superimposed on possible higher-order resonances due to two-, three-, or even four-photon absorption to higher electronic states. A

3. G. Petty, C. Tai, and F. W. Dalby, *Phys. Rev. Lett.* **34**, 1207 (1975).

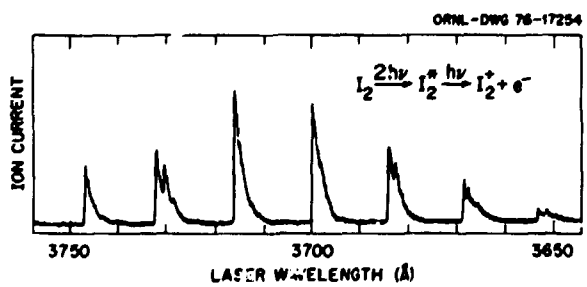

Fig. 13.6. Three-photon ionization of iodine via two-photon resonance with a state of even parity.

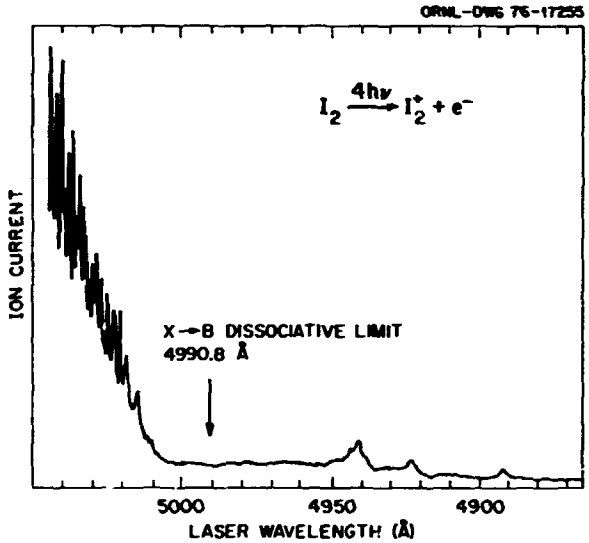

13.7. Four-photon ionization of iodine. The dissociation limit of the $B^3\Pi_{0u}^+$ state is shown.

sample of the resolution obtainable in the present experiment is shown in Fig. 13.8, a subset of the wavelength region in Fig. 13.7 examined at a photon bandwidth of about 0.01 Å.

Thus far, all of our molecular multiphoton ionization experiments have been conducted in static ionization chambers with high-sensitivity current amplifiers. We anticipate achieving a great increase in sensitivity and spectral simplification by irradiating the sample in a supersonic molecular beam. First, the molecular beam

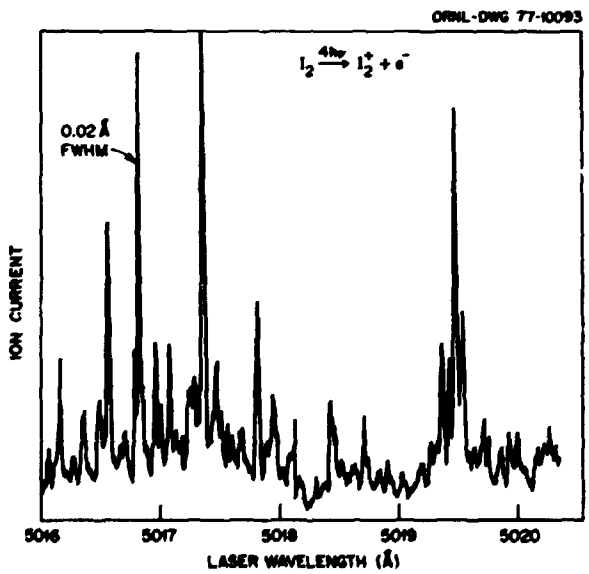

Fig. 13.8. Portion of data shown in Fig. 13.7 at 0.01-Å laser bandwidth.

gives high flux in a relatively low-pressure background, allowing mass analysis of products. This feature is of special importance in molecules such as iodine which have significant cross sections for ion-pair formation below the adiabatic ionization potential of the molecule. Mass analysis permits detection of multiphoton processes leading to ion-pair products. A second advantage is the adiabatic cooling induced by the molecular jet, which may be used to simplify the spectra of molecular species by eliminating rotational and vibrational hot bands. A third advantage of the molecular jet apparatus is the elimination of most Doppler and collisional effects, which hinder high-resolution spectroscopy. Finally, the new apparatus will be used to investigate multiphoton processes involving cluster species formed by condensation in the isentropic free jet expansion. The combination of multiphoton techniques and molecular free jets is potentially a powerful spectroscopic tool. We are pursuing these experiments under a seed-money grant from the ORNL Exploratory Studies Program.

COLLISIONAL IONIZATION BETWEEN GROUND-STATE REACTANTS

We previously have reported charge exchange between alkali atoms and certain hexafluoride molecules in their ground state, which produces separated ion pairs. The reaction can be represented as $A + MF_6 \rightarrow A^+ + MF_6^-$. These observations imply that the electron affinity of the hexafluoride is greater than the ionization potential of the alkali. The general behavior of the charge-exchange cross section with energy is basically the same for all collision partners. The cross section begins at a low value and rapidly increases to a rather large magnitude within a few electron volts of zero energy. It is well known from collision theory that the transition probability between electronic states with energy spacing E is small unless the nuclear velocity is high, that is, $V \gtrsim Ea/\hbar$, where a is the range of the interaction. Cross sections for electron transfer are small unless the neutral covalent surface crosses the ionic surface. Since the zeroth-order (ground state) ionic surface always lies below the covalent surface, such a crossing is impossible. Two questions are of basic interest: (1) How can charge transfer occur in the first place? and (2) Why does the cross section increase with collision energy? The possibility that the neutral channel $A + MF_6 \rightarrow AF + MF_5$ dominates the ionic channel at low collision energies has been presented[4] as an explanation for the

4. R. N. Compton, *J. Chem. Phys.* 66, 4478 (1977).

drop in the ion production cross section as the collision energy decreases. The assumption of a collision complex $A^+ \ldots MF_6^-$ which can decay either to $AF + MF_5$ or $A^+ + MF_6^-$ was invoked. Calculations were performed with the usual approximations of quasi-equilibrium theory. For the case of $Cs + UF_6$, the calculations strongly support the "competitive" model. The neutral channel dominates the ionic channel at low energies. However, for the reaction $Cs + WF_6$, the model fails miserably. Figure 13.9 shows that the ionic channel is expected to dominate at low energy. Hence the charge-exchange cross section should increase with decreasing energy. It is clear that the "competition" model is not correct in all cases.

Evidence suggests that many MF_6^- ions have low-lying excited states. UF_6^-, for example, exhibits two excited states ($^2T_{2u}$ and $^2T_{1u}$) in the region of 1 to 4 eV. The existence of excited states could permit the crossing of ionic and covalent surfaces and hence offer an explanation for the large cross sections observed and also account for the fact that the cross sections increase with increasing energy. This hypothesis is being examined by measuring the energy loss of the alkali after the collision. If the reaction proceeds as $A + MF_6 \rightarrow A^+ \ldots MF_6^{-*} \rightarrow A^+ + MF_6^{-*}$, then the A^+ kinetic energy will reflect the fact that MF_6^- is excited.

COLLISIONAL IONIZATION REACTIONS BETWEEN ALKALI ATOMS AND SOME METHANE DERIVATIVES

Collisions between thermal alkali atoms and methyl-halides which result in methyl radicals and alkali halides have been studied thoroughly in molecular beam experiments.[5] These reactions are believed to proceed via an "electron jump" mechanism from the covalent to the ionic potential energy surface. At sufficiently high collision energies, the ionic state can separate into ion pairs as well as neutrals. We have studied the negative ion products resulting from collisions between orthogonal beams of alkali atoms (sodium, potassium, and cesium) and the methane derivatives CH_3CN, CH_3NO_2, CF_3Br, and CF_3I. The reactions were studied in the region from threshold to about 40 eV (lab). Ions with masses corresponding to the parent molecules of the latter three species were detected, and the following electron affinities were derived from measurements of the energy threshold for the ion-pair production reactions: $EA(CH_3NO_2) = 0.4^{+0.1}_{-0.2}$ eV; $EA(CF_3Br) = 0.99 \pm 0.2$ eV; and $EA(CF_3I) = 1.5 \pm 0.2$ eV. From measurements of the difference in the energy threshold for the production of the various fragment ions and the parent ion, the following bond dissociation energies are deduced: $D(CH_3 - NO_2^-) = 0.56 \pm 0.2$ eV; $D(CF_3 - Br^-) = 0.54 \pm 0.2$ eV; and $D(CF_3 - I^-) = 0.32 \pm 0.2$ eV. Figure 13.10 shows the ion yields for sodium colliding with CF_3Br. The electron affinity derived for CF_3I is in excellent agreement with the value of 1.4 ± 0.2 eV reported by Tang et al.[6] but is in substantial disagree-

5. D. R. Herschbach, *Adv. Chem. Phys.* **10**, 319 (1966).
6. S. Y. Tang et al., *J. Chem. Phys.* **64**, 1270 (1976).

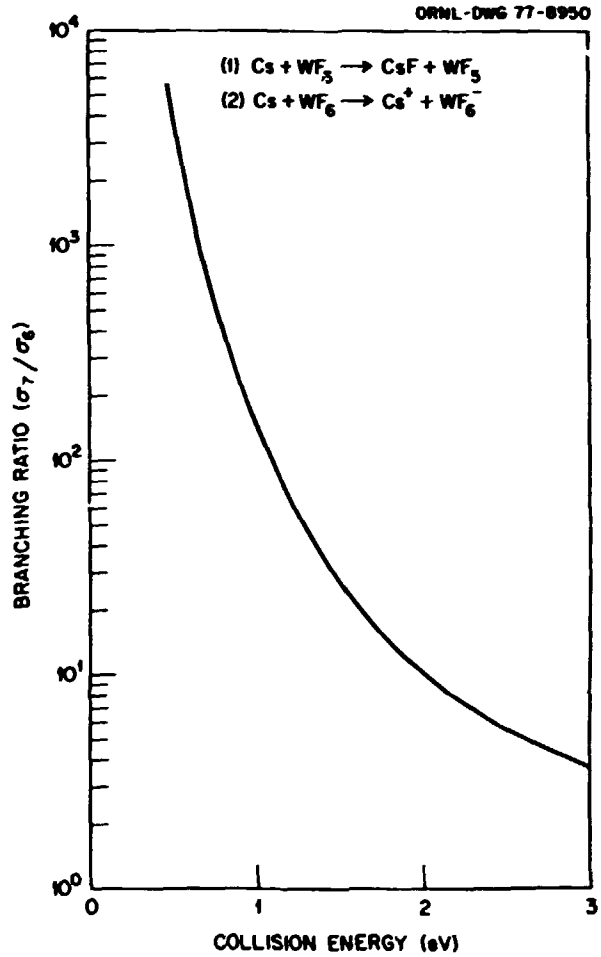

13.9. Calculation of the branching ratio $\sigma 2/\sigma 1$ for the decay of the complex $Cs^+ \ldots WF_6^-$ into $CsF + WF_5$ (1) and $Cs^+ + WF_6^-$ (2). The ratio is calculated from the expression of Klots, Mintz, and Baer:[29]

$$\frac{\sigma 2}{\sigma 1} = \frac{5}{6} \times \frac{6}{24} \left[\frac{\left(B_{CsF}\right)\left(B^{1/2}_{WF_6}\right)}{B^{1/2}_{WF_6^-}} \right] \times \left[\frac{\int_0^{E_2} \rho(x)(E-x)^{3/2}\,dx}{\int_0^{E_1} \rho(x)(E-x)^{3/2}\,dx} \right],$$

where B refers to the rotational constant of the subscript molecular species and E_1 and E_2 are the total energies available for reactions (1) and (2) respectively. The factor $6/24$ accounts for the statistical weights of the collision products.

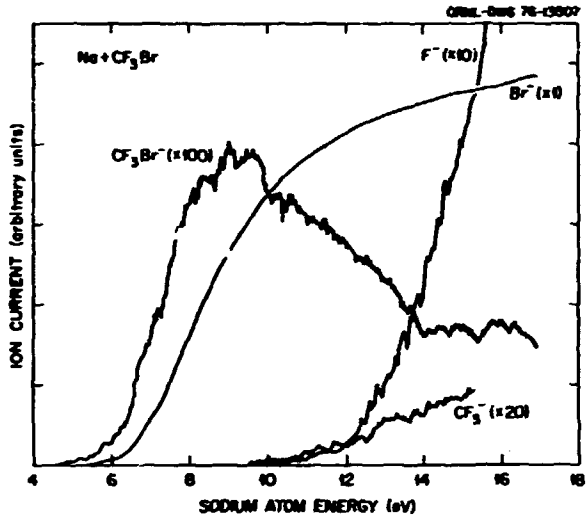

Fig. 13.10. Negative ions produced from collisions of fast sodium atoms with CF_3Br.

ment with the value of 2.2 ± 0.2 eV reported by McNamee, Lacmann, and Herschbach.[7]

The fact that CH_3CN^- ions are not produced in collisions of fast sodium, potassium, or cesium with CH_3CN is significant. CH_3CN does not attach thermal electrons in high-pressure electron-swarm experiments although collisional charge exchange between atoms in highly excited Rydberg states and CH_3CN occurs with a large probability.[8] The dipole moment of CH_3CN is 3.92 D and well exceeds the minimum moment required to bind an electron.[9] These experimental observations can be justified by assuming that electrons are bound primarily to the dipole field of CH_3CN. Electrons in a dipole field exist in large orbits and are described by very diffuse wave functions, much like those of an electron in a Rydberg orbital of large n. Thus, charge exchange in this case would be efficient because of favorable overlap between the two wave functions. Loosely stated, the electron gently changes centers of force in the collision. Free-electron attachment into the dipole field of a molecule to form a bound state would require radiative or collisional stabilization, which may be unlikely during the short lifetime of the temporary ion ($\tau \sim 10^{-15}$ sec). Also, because of the fragile nature of the ion, collisional detachment may be more probable than stabilization. The inability of the present experiment to produce measurable amounts of CH_3CN^- by collisions with fast alkali atoms may be related to the gross differences in the wave function representing an electron in the lowest s orbit of an alkali as compared to the very diffuse nature of an electron in the field of the molecular dipole.[9] The distance at which the covalent ($Cs + CH_3CN$) surface crosses with the ionic ($Cs^+ + CH_3CN^-$) surface is about 3 Å. Because the wave function describing a weakly bound electron in a dipole field is extremely diffuse, the probability that an electron would be transferred at this distance is probably small. Therefore, the inability to observe CH_3CN^- from alkali collisions may be related to the nature of the orbital into which the electron is attached and is apparently not due to the smallness of the electron affinity of CH_3CN. For example, the reaction of cesium with nitric oxide (EA = 0.024 eV) (ref. 10) produces copious signals of NO^-.[11] In summary, the interpretation of experimental observations presented here and earlier[8] supports earlier beliefs[12,13] that electron binding to CH_3CN occurs primarily through the dipole field. Further studies of energy and angular distributions of photodetached electrons from CH_3CN^- or studies of reactions of well-defined Rydberg states with CH_3CN may be more conclusive. Acetonitrile or HCN may be the best system, excluding the alkali halides, in which to study the electron-dipole interaction problem.

STUDIES OF ATOMIC POLARIZABILITY

At thermal energies, the atomic or molecular polarizability is the most important rate-determining parameter in ion-molecule, charge-exchange, and clustering reactions. A cooperative joint project, initiated between the Health Physics Division and the Atomic Beams and Plasma Physics Laboratory of New York University, has been aimed at extending the range of applicability of beam techniques for measuring polarizability. The project has resulted in the design and construction of a new high-temperature atomic beam source which is installed and operating on the 3-m, high-resolution, E-H gradient[14] atomic beam apparatus at New York University. As illustrated in Fig. 13.11, the critical section of the source is a heating element which consists of a resistivity heated, 1-mil-thick, double-walled tantalum cylinder suspended from water-cooled flanges which serve as electrodes. This tantalum cylinder surrounds and radiantly heats a centrally suspended, movable source container.[15,16] The beam passes through holes punched in the heating element and in the surrounding radiation shields. The system is capable of sustained operation at temperatures up to 2500°K. A temperature-current plot for the source is shown in Fig. 13.12. About 1 kW is dissipated at 1400°K.

7. P. E. McNamee, K. Lacmann, and D. R. Herschbach, *Faraday Discuss. Chem. Soc.* 55, 318 (1973).
8. J. A. D. Stockdale et al., *J. Chem. Phys.* 60, 4279 (1974).
9. W. R. Garrett, *Phys. Rev. A* 3, 961 (1971).
10. M. W. Seigel et al., *Phys. Rev.* 6, 607 (1972).
11. S. J. Nalley et al., *J. Chem. Phys.* 59, 4125 (1973).
12. M. A. Bonin et al., *Chem. Phys. Lett.* 2, 363 (1968).
13. K. D. Jordan and J. J. Wendoloski, *Chem. Phys.* 21, 145 (1977).
14. R. W. Molof et al., *Phys. Rev. A* 10, 1131 (1974).
15. D. M. Cox et al., *Phys. Rev. A* 10, 1409 (1974).
16. J. A. D. Stockdale et al., *Rev. Sci. Instrum.* 48, 938 (1977).

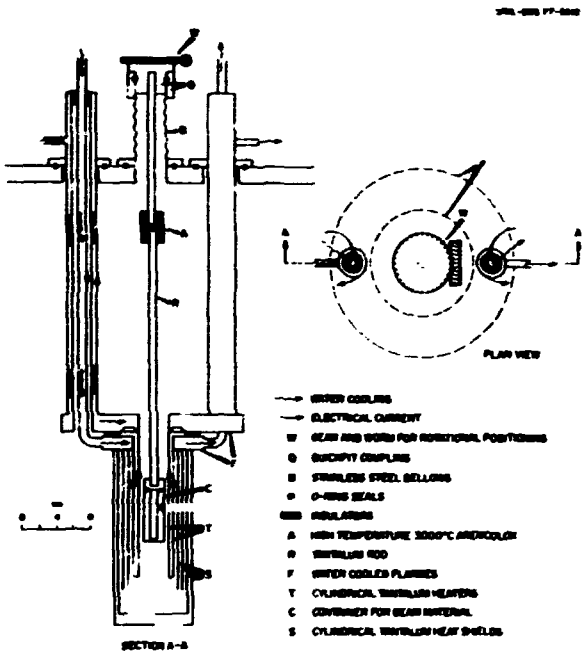

Fig. 13.11. High-temperature atomic beam source.

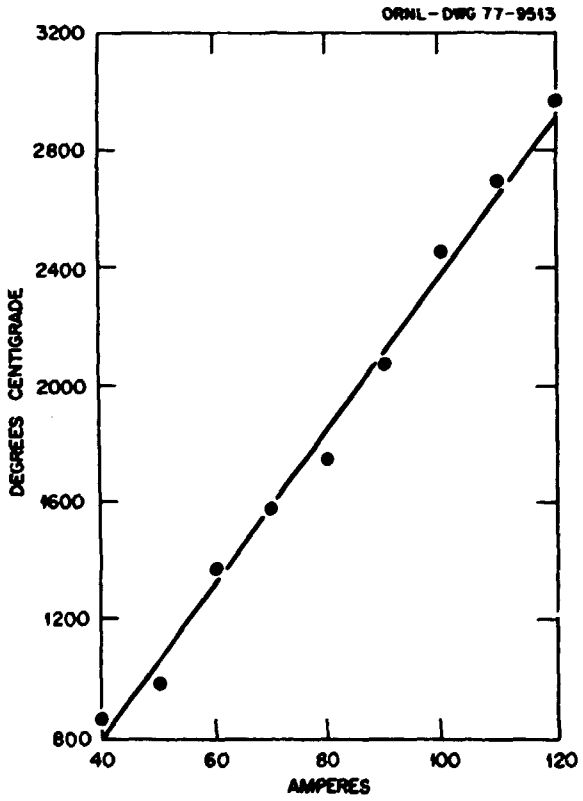

Fig. 13.12. Temperature as a function of input direct current (amperes) for high-temperature atomic beam source.

As part of a program to measure the static electric dipole polarizabilities of heavy elements, the E-H gradient balance method[14] was used to measure the polarizability of ground-state indium, $5s^2 5p(^2P_{1/2})$. A preliminary value of $5.4 \pm 1.1 \times 10^{-24}$ cm^3 was obtained by electric field refocusing of the $M_f = -1$ state at a magnetic field slightly above that corresponding to the first zero moment of indium. The work will be extended to measurements of the polarizabilities of other heavy atoms, including uranium. This is of particular interest in laser isotope separation because the polarizability of the neutral uranium atom determines the rate of charge exchange or excitation transfer between $^{235}U^+$ or $^{235}U^*$ and ^{238}U.

ENERGY AND ANGULAR DISTRIBUTIONS OF COLLISIONAL IONIZATION PRODUCTS

A major new apparatus, constructed for studies of collisional ionization processes and for measurement of molecular electron affinities, is shown schematically in Fig. 13.13. The apparatus consists in outline of two main vacuum chambers connected by a gate valve, V, which serves to isolate the source chamber on the left from the target and measurement area. The source consists of an alkali oven, O, with open slits on two sides so that effusing thermal neutral atoms can reach the filament, F, become ionized, and be repelled by an adjustable electric field of known strength back into the oven where they charge exchange in the high-density neutral cloud, emerging as fast neutrals. Any ions surviv-

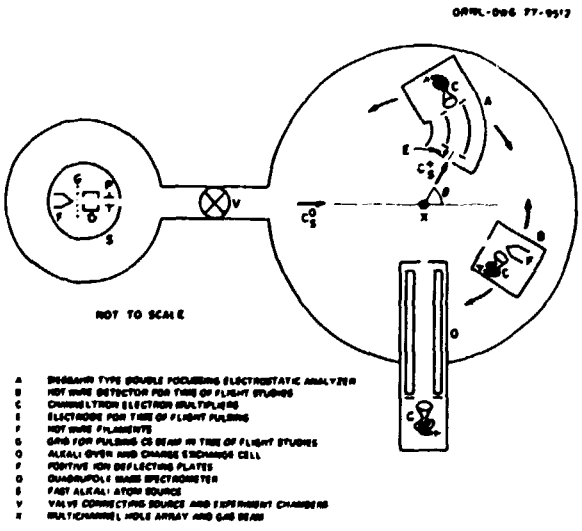

Fig. 13.13. Schematic plan view of collisional ionization apparatus (not to scale).

ing passage through the source can be removed by applying an electric field to the plates, *P*. The neutral beam enters the experimental region on the right where it collides with a target gas beam, *X*, produced by a multichannel hole array. Collision products can be detected and examined in several ways. Mass spectra of both positive and negative ions can be obtained with a quadrupole mass spectrometer, *Q*, located at 90° to the intersection of the two beams; energy spectra of positive or negative ions can be measured with the double-focusing electrostatic analyzer, *A*, and time-of-flight studies can be performed on the original neutral beam (or possibly in some instances on neutral products) with the hot-wire detector, *B*. Both the hot-wire detector and electrostatic analyzer can be rotated about the point of intersection of the beams in the horizontal plane so that angular distributions can be obtained. In addition, a small electrode, *E*, located inside the shielding box of the analyzer, *A*, but outside the region of the electrostatic deflecting plates, can be pulsed to permit energy-resolved time-of-flight measurements through the analyzer on positive or negative ions. The apparatus is interfaced with a PDP-11 computer, and data is stored on a magnetic diskette system.

Collisional Ionization of Cesium by Water

Charge exchange between fast (0 to 100 eV) cesium atoms and deuterated water (D_2O) has been investigated in the apparatus described above, and energy and angular distributions of both product positive and negative ions have been determined with the hemispherical-sector electrostatic analyzer. Figure 13.14 shows typical energy loss spectra, $E_{Cs^0} - E_{Cs^0}$, at an incident energy, E_{Cs^0}, of 100 eV (lab) for a range of laboratory scattering angles. A contact potential correction should be applied to correct the alkali atom energy. This will decrease the energy losses by about 2 to 3 eV. The two broad peaks at 0° (forward scattering in the lab) represent forward scattering (lower energy loss) and backward scattering (higher energy loss) of cesium in the center of mass (c.m.) frame. Note that as the scattering angle increases (approaching 90° scattering in the c.m.), the two peaks approach the same energy loss.

The mass filter, *Q*, was used to determine the masses of the negative ions produced by the charge transfer reaction; OD^- ions dominated. The onset for the OD^- ion signal occurred exactly at the energy corresponding to the thermodynamic threshold, that is, $IP(Cs) + D(D_2O) - EA(OD) = 3.28$ eV. The energies of these ions for various (lab) angles with an impact energy of

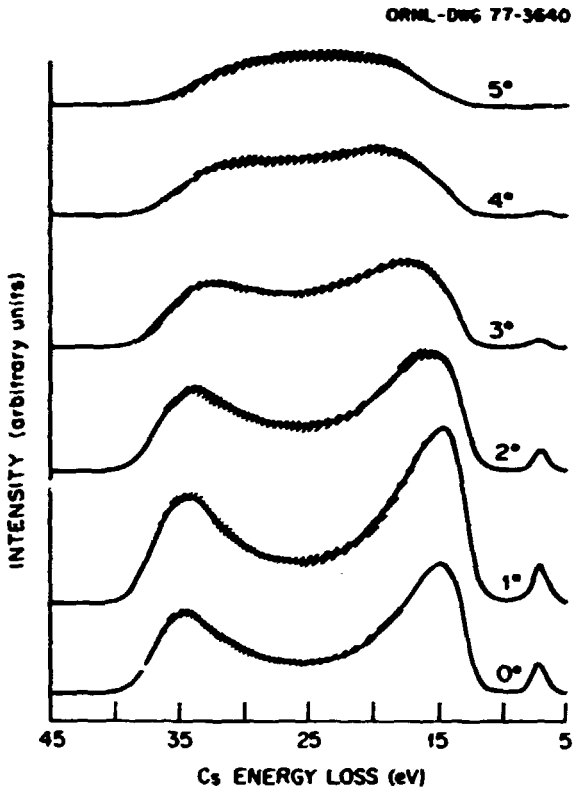

Fig. 13.14. Energy loss for 100-eV (lab) incident cesium beam on D_2O for various scattering angles (lab). The small peak on the right is due to an oxygen impurity.

100 eV (lab) are shown in Fig. 13.15. The lowest energy peak (~0.4 eV) seems to be due to electron ejection from the analyzer slits under impact of the unscattered fast alkali beam. The three higher energy peaks were shown to be OD^- by measuring the time-of-flight of the ions through the energy analyzer. The low- and high-energy peaks correspond, respectively, to forward and backward scattering of cesium in the c.m. frame. The central OD^- peak corresponds energetically to a completely inelastic Cs-D_2O collision (i.e., formation of a "pickup" complex) with subsequent release of an OD^- ion. Such a process might be expected to peak strongly in the forward direction. This is observed, in contrast to the other two OD^- peaks which remain strong at laboratory angles greater than 25°. The fact that OD^- is the dominant negative ion produced in cesium collisions is in sharp contrast to the case of electron impact on D_2O where D^- and O^- are the dominant ions observed. Apparently, in cesium impact, the lowest asymptotic dissociation limit ($OD^- + D$) is favored even though the transition involved may not be Franck-Condon in nature.

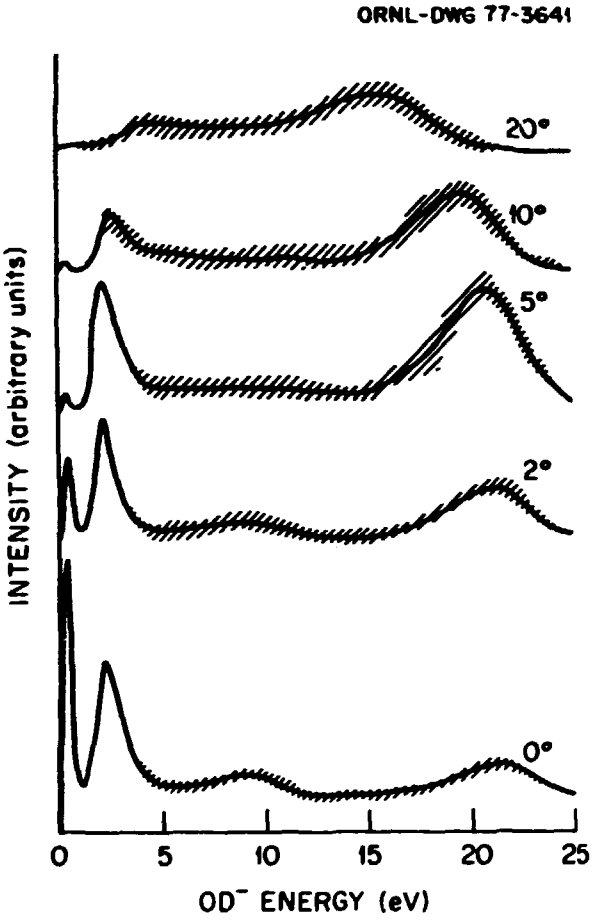

Fig. 13.15. OD^- ion energy resulting from 100-eV (lab) cesium collision with D_2O.

Collisional Ionization of Cesium by Oxygen

Collisional ionization of atomic cesium by impact on oxygen has been studied by a number of investigators. Lacmann and Herschbach,[17] using potassium impact, and Nalley and Compton,[18] using cesium as a projectile, examined thresholds for ion production as a function of c.m. energy and were the first to obtain lower limits to the electron affinity of oxygen by this method. More recently, Groszer and Meyer[19] and Mochizuki and Lacmann[20] have measured the energy loss of potassium in the collisional ionization process $K + O_2 \rightarrow K^+ + O_2^-$. The latter workers have also obtained detailed K^+ angular distributions. From these studies it appears that O_2^- is produced both in the ground state (with maximum excitation into the 4th to 6th vibrational levels) and in an excited O_2^- state, probably $^4\Sigma_u$ or $^2\Pi_u$.

With the apparatus shown in Fig. 13.13, we have investigated collisional ionization of cesium by oxygen. In addition to measuring Cs^+ energy and angular distributions, we have also recorded O_2^- negative ion spectra. The energy loss results are not inconsistent with the work described in refs. 19 and 20, but we also have observed a backward scattered (center of mass) Cs^+ peak corresponding to an energy loss of about 30 eV at a neutral cesium lab system energy of 60 eV. The reaction Q is the same as for the forward scattered peak, but further high-resolution data is needed to test whether these correspond to scattering with production of the O_2^- ground state, or an excited O_2^- state, or both. The O_2^- negative ion spectra show a broad peak with maximum at 2.5-eV O_2^- kinetic energy at a cesium lab energy of 20 eV. At 40-eV cesium energy this shifts upward to 5-eV kinetic energy.

DISSOCIATIVE IONIZATION BY ELECTRON IMPACT

High Kinetic Energy N^+ Ions from Decay of Doubly Ionized N_2

N^+ ions from the process $e + N_2 \rightarrow N_2^{2+} + 3e \rightarrow N^+ + N^+ + 3e$ have been sought by a coincidence method in which N^+ ions have been detected at 90° to crossed N_2 and pulsed electron beams. Figure 13.16 shows the apparatus schematically. The amplified Channeltron (CEM) outputs were connected through a coincidence circuit to the "stop" input of a time-to-pulse-height converter whose ramp was started by the electron beam pulse. The N^+ coincidence time-of-flight spectrum was accumulated and stored in a multichannel pulse-height analyzer. Separate N^+ time-of-flight distributions for the two Channeltrons were recorded at the beginning and end of each approximately 24-hr coincidence count. From the products of these, a linearly time-averaged spurious coincidence time-of-flight distribution was constructed for comparison with the measured distribution. The spurious coincidence distribution was due to accidental coincidences between the numerous N^+ ions from the process $e + N_2 \rightarrow N_2^+ + 2e \rightarrow N^+ + N + 2e$.

Figure 13.17 shows a typical comparison between measured and accidental coincidence distributions

17. K. Lacmann and D. R. Herschbach, *Chem. Phys. Lett.* 6, 106 (1970).

18. S. J. Nalley and R. N. Compton, *Chem. Phys. Lett.* 9, 529 (1971).

19. J. Groszer and G. Meyer, *Chem. Phys. Lett.* 37, 82 (1976).

20. T. Mochizuki and K. Lacmann, *J. Chem. Phys.* 65, 3257 (1976).

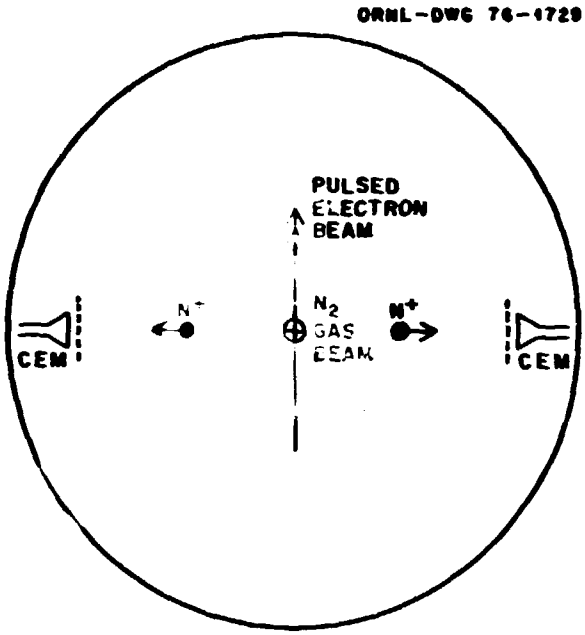

$$e + N_2 \rightarrow N_2^{++} + 3e \rightarrow N^+ + N^+ + 3e$$

Fig. 13.16. Schematic of apparatus for study of decay of doubly ionized N_2. ⊕ indicates N_2 gas beam traveling out of paper.

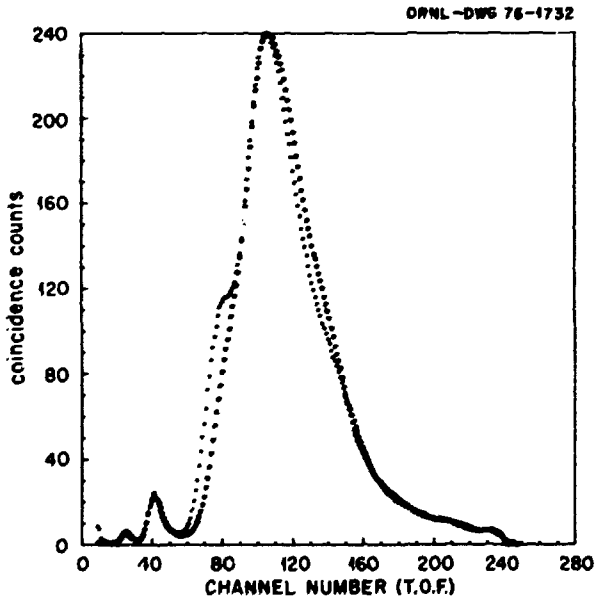

Fig. 13.17. Comparison between measured (▲) and accidental (⊙) coincidence distributions at an electron energy of 150 eV. Electron beam pulse length, 1.0 μsec; repetition rate, 10^4 Hz; coincidence resolving time, 1.15 μsec. Spectra are normalized to equal height at the main peak. The two small, early peaks near channels 30 and 40 are due to scattered electrons striking the shielding grids of the Channeltrons and producing ionization on these surfaces.

obtained at an electron beam energy of 150 eV.[8] The measured coincidence distribution between channels 55 and 85 (about 15 and 25 μsec time-of-flight) is seen to lie above the computed accidental distribution. The smaller percentage mismatch between the distributions from channels 105 to 150 (Fig. 13.17) was not consistently reproducible. If these particular curves were normalized to a better match in this region, the effect between channels 55 to 85 would be enhanced slightly. Similar results were obtained at 300-eV beam energy. No consistent differences were observed between the two distributions for data taken at 100-eV electron energy, and no other significant differences were found in 150- and 300-eV spectra. Figure 13.18, obtained by subtracting accidental from measured distributions in this region, illustrates these results and indicates the presence of peaks near 18 and 21 μsec time-of-flight. Figure 13.19 shows N^+ energy spectra computed from

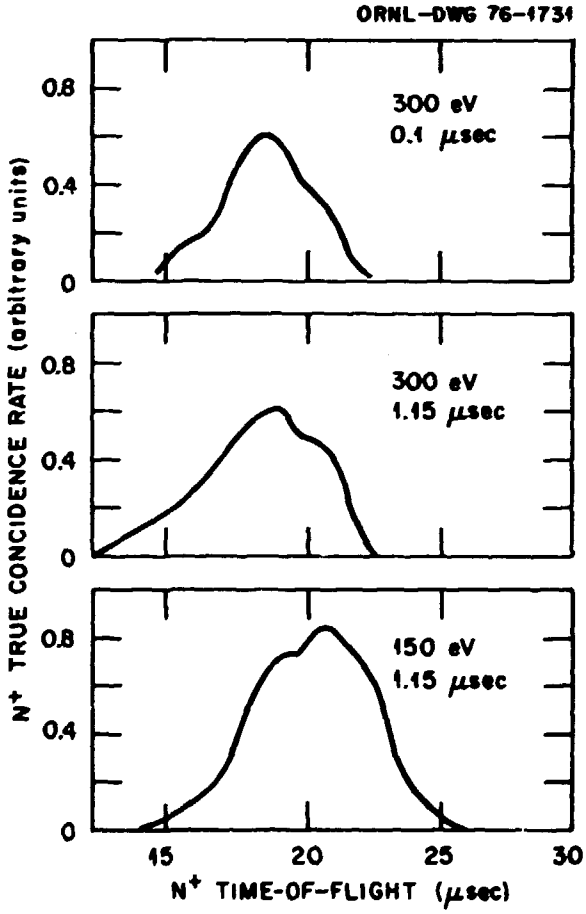

Fig. 13.18. Time-of-flight spectra of true N^+ coincidences from the process $e + N_2 \rightarrow N_2^{++} + 3e \rightarrow N^+ + N^+ + 3e$. Data are shown for coincidence resolving times of 1.15 and 0.1 μsec at 300-eV electron-impact energy and 1.15 μsec resolving time at 150 eV.

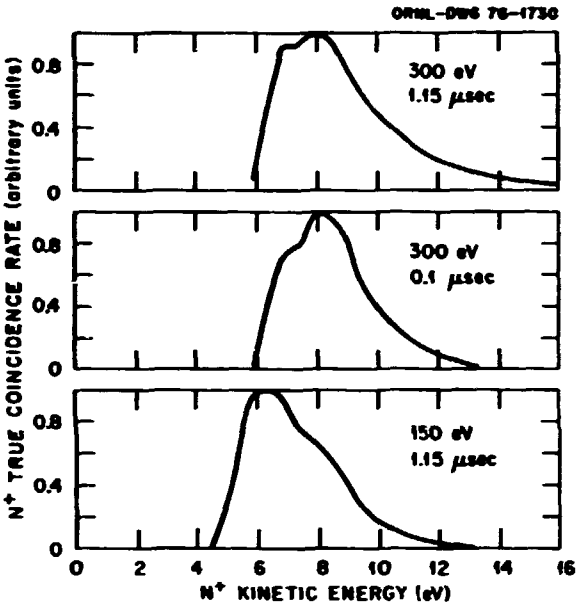

Fig. 13.19. N^+ energy spectra computed from data of Fig. 13.8. The energy scale gives the energy of individual N^+ ions produced in the process $e + N_2 \rightarrow N_2^{2+} + 3e \rightarrow N^+ + N^+ + 3e$.

the data of Fig. 13.18. Two possible peaks near 6.2- and 8-eV N^+ kinetic energy are seen, with a tail to higher N^+ kinetic energies.

Structure in the region from 5- to 8-eV kinetic energy has been observed in N^+ kinetic energy spectra in several studies of electron impact–induced dissociative ionization of N_2.[21–24] The electron energies at which it appeared lie between about 75 and 100 eV. An indication of two peaks near 6 and 8 eV is present in a 150-eV electron-impact N^+ kinetic energy spectrum obtained earlier with the present apparatus. Peaks in this kinetic energy region can also be seen in high-Rydberg electron-impact data at electron-impact energies above 85 eV. The N^+ coincidence ions detected in the present work certainly will contribute to these total peaks, but whether or not they are solely responsible remains in doubt for two reasons. First, accurate appearance potentials are not yet available from any of the experiments. Second, all of the kinetic energy distribution measurements discriminate against low-energy ions. Consequently, the fractional contribution of these high-energy peaks to the total ionization or dissociative-ionization cross sections is not known, and there is no accurate standard of comparison where intensities are concerned.

The present results clearly indicate that only a small fraction of the N_2^{2+} ions produced at about 150-eV electron energy are detected as real N^+-N^+ coincidences. From measurements by Märk[25] of the ratio of N_2^{2+} to N^+ and a comparison of our observed numbers of N^+ (real coincidence) and N^+ (total) in the present experiment, this fraction is estimated to be about 1 part in 700. Since preferential decay to the products $N^{2+} + N$ can hardly be favored to this extent, a likely explanation is that the lifetime against decay into two N^+ ions of most N_2^{2+} states is at least several microseconds. Further details of these measurements are available in ref. 26.

OSCILLATOR STRENGTH SUM RULE FOR ATOMIC ISOTOPE SHIFT

Consider an atom or atomic ion with nucleus of mass M and charge Ze at $r_0 = (x_0 y_0 z_0)$ and n electrons, each of mass m and charge $-e$ at $r_i = (x_i y_i z_i)$. We transform to the centroid frame $[r_c = (M/\mathcal{M}) r_0 + (m/\mathcal{M}) \Sigma_{i=1}^{n} r_i$, where $\mathcal{M} = M + nm]$ and introduce further the coordinates of each electron with respect to the nucleus ($r_j' = r_j - r_0$). The atomic Hamiltonian, when the nucleus has mass M, then takes the very simple form

$$H^{(M)} = T_c + H^{(\infty)} + \left(\sum_{j=1}^{n} p_j' \right)^2 / 2M ,$$

where T_c is the kinetic energy of centroid motion, $H^{(\infty)}$ is the Hamiltonian for an atom with fixed nucleus of infinite mass, and $(\Sigma_{j=1}^{n} p_j')^2/2M$ is the correction for nuclear motion. For an atom with nucleus of mass M, the atomic energy levels $E_I^{(M)}$ and many-electron wave functions $\psi_I^{(M)}$ satisfy the Schroedinger equation $H^{(M)}\psi_I^{(M)} = E_I^{(M)}\psi_I^{(M)}$. Applying first-order perturbation theory, based on infinite-mass energies and eigenfunctions, yields

$$E_I^{(M)} = E_I^{(\infty)} + \frac{1}{2M} \sum_J \sum_{\alpha=1}^{3} \times \left\langle I \middle| \sum_j p_{j\alpha}' \middle| J \right\rangle \left\langle J \middle| \sum_j p_{j\alpha}' \middle| I \right\rangle .$$

21. L. J. Kieffer and R. J. Van Brunt, *J. Chem. Phys.* **46**, 2728 (1967).
22. L. Deleanu and J. A. D. Stockdale, *J. Chem. Phys.* **63**, 3898 (1975).
23. R. Locht et al., *Chem. Phys.* **7**, 393 (1975).
24. K. Köllmann, *Int. J. Mass Spectrom. Ion Phys.* **17**, 261 (1975).
25. T. D. Märk, *J. Chem. Phys.* **63**, 3731 (1975).
26. J. A. D. Stockdale, *J. Chem. Phys.* **66**, 1792 (1977).

In terms of the infinite-mass, many-electron oscillator strength,

$$f_{JI}^{(\alpha\alpha)} = 2\left\langle I\left|\sum_{j=1}^{n} p_{j\alpha}\right|J\right\rangle \times \left\langle J\left|\sum_{j=1}^{n} p_{j\alpha}\right|I\right\rangle / m(E_J^{(\infty)} - E_I^{(\infty)}) ,$$

we find

$$E_I^{(M)} - E_I^{(\infty)} = (1/4)\frac{m}{M} \times \sum_J (E_J^{(\infty)} - E_I^{(\infty)}) \sum_{\alpha=1}^{3} f_{JI}^{(\alpha\alpha)} .$$

We consider this to be our basic identity, but other versions, such as the one that results from subtracting $E^{(M)}$ from $E^{(M')}$, may be useful.

Finally, we define an oscillator-strength-weighted excitation energy based on level I as

$$\bar{E}_{\mathrm{exc}\,I}^{(\infty)} = \sum_J (E_J^{(\infty)} - E_I^{(\infty)}) \times \sum_{\alpha=1}^{3} f_{JI}^{(\alpha\alpha)} \div \sum_J \sum_{\alpha=1}^{3} f_{JI}^{(\alpha\alpha)} ,$$

and evaluate the denominator ($3n$) by the Thomas-Reiche-Kuhn sum rule to get

$$E_I^{(M)} - E_I^{(\infty)} = (3nm/4M)\bar{E}_{\mathrm{exc}\,I}^{(\infty)} .$$

NEWTON'S DIVIDED DIFFERENCE FORM OF THE SCHROEDINGER EQUATION

Investigators who have numerically integrated the radial Schroedinger equation for an atom know that, given the same initial conditions at the origin, the $2s$ wave function almost coincides with the $1s$ until the vicinity of its outermost node; the $3s$ closely follows the $2s$ until the vicinity of the outermost node of the $3s$, and so on. Similar statements hold for other angular momenta. We have exploited this observation by formulating an equation for the function which is added to a linear combination of the previously obtained functions to give the next function; the equation is an inhomogeneous (not a homogeneous) eigenvalue equation, and the functions are technically Newtonian divided differences in energy space of a uniform function of energy and radial coordinate.

Let us start from the usual Schroedinger equation in the form $(H - E_i)\psi_i(E_i; r) = 0$, where H is the Hamiltonian operator, E_i is the ith energy eigenvalue, and $\psi_i(E_i; r)$ is the ith wave function. Our function of interest is $\psi(E; r)$; its value at the eigenvalue $E = E_i$ is $\psi_i(E_i; r)$. It will be convenient to start enumerating from $i = 0$. $\psi_0(E_0; r)$ is the first of a series of functions; we shall call it $D_0(r)$. The next equation (for $i = 1$) can be thrown into the form $(H - E_1)(\psi_1 - \psi_0) \div (E_1 - E_0) = \psi_0(E_0; r) = D_0(r)$. Let $D_1(E_1, E_0; r) = [\psi_1(E_1; r) - \psi_0(E_0; r)] \div (E_1 - E_0)$; thus $(H - E_1)D_1 = D_0$. For the next equation ($i = 2$), we have after a few minutes of algebraic manipulation, $(H - E_2)[(\psi_2 - \psi_1) \div (E_2 - E_1) - (\psi_1 - \psi_0) \div (E_1 - E_0)] \div (E_2 - E_0) = D_1$. The function on which $(H - E_2)$ acts is Newton's second divided difference coefficient, $D_2(E_2, E_1, E_0; r)$, of $\psi(E; r)$. The equations presented here illustrate the general case (verified by mathematical induction) $(H - E_i)D_i(E_i \ldots E_0; r) = D_{i-1}(E_{i-1} \ldots E_0; r)$, $i = 1, 2 \ldots$, with $(H - E_0)D_0 = 0$ (or $D_{-1} \equiv 0$). The wave function is given by $\psi(E; r) = D_0 + (E - E_0)D_1 + (E - E_0)(E - E_1)D_2 + (E - E_0)(E - E_1)(E - E_2)D_3 + \ldots$ Separate investigation shows that the D_n for $n > 0$ are functions with a single maximum or minimum which vanish at the origin as r^{l+2n} (for angular momentum l) and vanish exponentially at infinity.

For the one-dimensional harmonic oscillator with Hamiltonian $H = (-1/2)\partial^2/\partial\xi^2 + (1/2)\xi^2$ (in terms of the scaled length ξ) and scaled energy eigenvalue ϵ_n, the solutions fall into even (g) and odd (u) symmetry classes. The even eigenfunctions $\psi_{ng}(\epsilon_{ng}; \xi)$ with unit value and zero slope at $\xi = 0$ have divided differences $D_{ng} = [(-2)^n/(2n)!]\xi^{2n} \exp[(-1/2)\xi^2]$ and $\epsilon_{ng} = 2n + 1/2$; the odd eigenfunctions $\psi_{nu}(\epsilon_{nu}; \xi)$ with zero value and unit slope at $\xi = 0$ have divided differences $D_{nu} = [(-2)^n/(2n + 1)!]\ \xi^{2n+1} \exp[(-1/2)\xi^2]$ and $\epsilon_{nu} = 2n + 3/2$. These functions all satisfy $(H - \epsilon_{n\cdot})\ D_{n\cdot} = D_{(n-1)\cdot}$ (with $\cdot = g$ or u), and their unimodal property is evident.

ANGULAR MOMENTUM IN UNIMOLECULAR KINETICS

Our previous work has led to theoretical characterizations of the rate constants for unimolecular decomposition and for the kinetic energies of the resulting frag-

ments. The best experimental data available for comparison have hitherto been for a given reaction at selected energies. Recently, data have been obtained for the reaction

$$C_4H_6^+ \rightarrow C_3H_3^+ + CH_3$$

at different angular momenta. Figure 13.20 shows the kinetic energy distribution of the fragments from $C_4H_6^+$ made by electron impact[27] and hence with low angular momentum. Figure 13.21 illustrates the distribution obtained when the $C_4H_6^+$ is made by reacting $C_2H_2^+$ and C_2H_4 (ref. 28) and hence with large angular momentum. The widely different distributions are reproduced in each case by theory.[29]

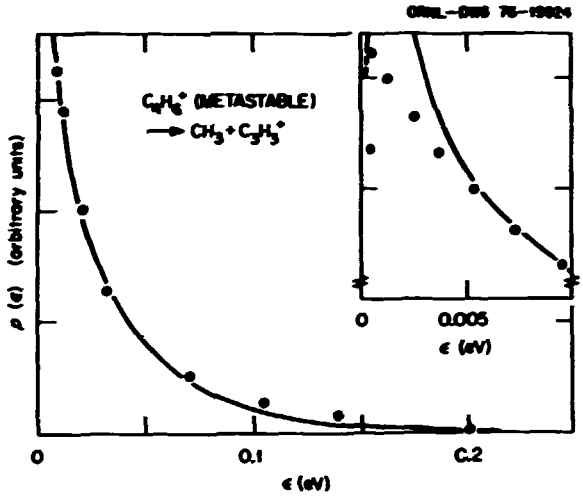

Fig. 13.20. Kinetic energy distribution of fragments from a metastable ion. Circles represent data from ref. 27; solid line is theory from ref. 28.

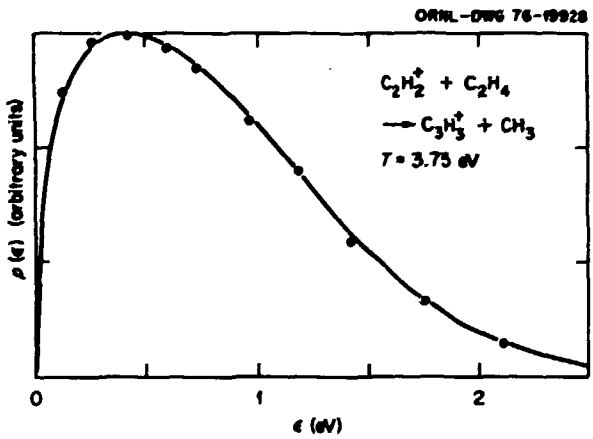

Fig. 13.21. Kinetic energy distribution of fragments from a collision complex. Circles represent data from ref. 29; solid line is theory from ref. 28.

THEORETICAL ELECTRON AFFINITIES OF POLAR MOLECULES

The electron binding properties of polar molecules have recently been a topic of considerable theoretical and experimental attention. This interest has been sparked by a number of effects that result from the very long range nature of the interaction potential for molecules that possess a permanent electric dipole moment. It has been shown that the electric dipole field is capable of supporting an infinite number of bound states for an electron if the dipole moment, μ, is greater than 1.625 D,[30] or none at all if μ is less than this critical value, μ_c.[31] On the basis of this result, it has been shown[32] that the conventional Born-Oppenheimer treatment of the electronic structure of molecules, wherein the nuclei are considered fixed in space, leads without further approximation to an infinite discrete spectrum of negative-ion states for polar molecules whose dipole moment exceeds μ_c, independent of any other properties of the molecules.[33] Furthermore, an exact *ab initio* Hartree-Fock treatment of a polar molecule with $\mu > \mu_c$ would yield an infinite number of unoccupied canonical molecular orbitals of negative energy.[34]

However, if a molecular system is treated dynamically to include the rotational degrees of freedom of the nuclei, the infinite number of bound states for a charged particle in the dipolar molecular field is reduced to a finite number.[35,36] The minimum dipole moment necessary to sustain at least one bound state for a finite dipolar system with non–Born-Oppenheimer rotational degrees of freedom is greater than that for the fixed dipolar systems by some 10% to 30%, depending on the dipole length, the rotational state, and the moments of inertia of the molecule.[36]

---

27. J. F. Elder, J. H. Beynon, and R. G. Cooks, private communication.
28. Z. Herman and K. Birkinshaw, *Ber. Bunsenges. Phys. Chem.* 77, 566 (1973).
29. C. E. Klots, D. Mintz, and T. Baer, *J. Chem. Phys.* 66, 5100 (1977).
30. μ_c = 1.625 debyes = 1.625 D = $0.639ea_0$, where 1 D = 10^{-18} esu-cm, $-e$ is the electronic charge, and a_0 is the Bohr radius.
31. E. Fermi and E. Teller, *Phys. Rev.* 72, 406 (1947).
32. O. H. Crawford, *Mol. Phys.* 20, 585 (1971).
33. $\mu > \mu_c$ is a sufficient condition for the binding of an electron in the Born-Oppenheimer approximation but is clearly not a necessary condition for real molecules. See, for example, H. S. W. Massey, *Negative Ions*, 3rd ed., Cambridge University Press, Cambridge, 1976, chap. 6.
34. O. H. Crawford, *Mol. Phys.* 26, 139 (1973).
35. W. R. Garrett, *Chem. Phys. Lett.* 5, 393 (1970); *Mol. Phys.* 20, 751 (1971).
36. W. R. Garrett, *Phys. Rev. A* 3, 961 (1971).

Recently, ab initio calculations of electron affinities have been published for a number of polar molecules whose dipole moments exceed the critical value for a stationary dipole.[37–39] Since the Born-Oppenheimer approximation was invoked in these calculations, stable negative ions should have resulted for every case in which μ is greater than 1.625 D. However, the authors reported that a critical moment greater than about 3.5 to 5 D is required to yield negative eigenvalues, ϵ(LUMO), for the lowest unoccupied molecular orbital of lithium compounds.[38] These conclusions are incorrect because any *ab initio* calculation within the Born-Oppenheimer approximation should yield a negative ϵ(LUMO) of the neutral molecule (and a positive electron affinity for the negative ion)[32] when $\mu > \mu_c$, as discussed above. The contrary conclusions reached in refs. 37–39 simply reflect incomplete convergence, or other inaccuracies, in the computations for these very weakly bound states.

In view of the incorrect conclusions that have been drawn on the basis of conventional Hartree-Fock molecular orbital calculations, it is quite instructive to ask what binding energy would be required in an accurate Born-Oppenheimer calculation to ensure a stable negative ion if non–Born-Oppenheimer terms were included in the molecular Hamiltonian.

We have determined the magnitudes of Born-Oppenheimer electron affinities which are required to ensure stable binding in the non–Born-Oppenheimer treatment, in the case of an electron interacting with a rigid rotor consisting of two point charges, $\pm q$, separated a distance R from each other, and having a moment of inertia I. This was accomplished by taking the critical dipole moments, μ_c', for the rigid rotor system from ref. 36 for various values of R, I, and rotational states, K, and determining the binding energy of electrons in the corresponding stationary fields. These binding energies, $-E_c$, were obtained by interpolating between values given by Turner, Anderson, and Fox.[40] The results are displayed in Table 13.1, in which the

37. K. D. Jordan et al., *J. Chem. Phys.* 64, 4730 (1976).
38. K. D. Jordan and W. Luken, *J. Chem. Phys.* 64, 2760 (1976).
39. K. D. Jordan, *J. Chem. Phys.* 65, 1214 (1976).
40. J. E. Turner, V. E. Anderson, and K. Fox, *Phys. Rev.* 174, 81 (1968).

Table 13.1. Fixed nuclei binding energies required for electron binding to nonstationary dipole

K	$I(ma_0^2)$	$R(a_0)$	$\mu'_c(D)$	$-E_c(e^2/a_0)$	$-E_c/B$
0	2×10^6	0.6672	1.792	1.3×10^{-10}	5.2×10^{-2}
		1.0284	1.802	1.3×10^{-10}	5.0×10^{-2}
0	2×10^6	0.6672	1.863	1.6×10^{-8}	6.5×10^{-2}
		1.0284	1.881	1.7×10^{-8}	6.8×10^{-2}
0	4×10^6	0.6672	1.970	1.1×10^{-6}	9.0×10^{-2}
		1.0284	2.000	1.1×10^{-6}	8.5×10^{-2}
0	1×10^6	0.6672	2.023	4.2×10^{-6}	8.5×10^{-2}
		1.0284	2.064	4.2×10^{-6}	8.4×10^{-2}
1	2×10^5	0.6672	2.038	6.1×10^{-6}	2.4
		1.0284	2.082	6.1×10^{-6}	2.4
1	4×10^6	0.6672	2.120	2.9×10^{-5}	2.3
		1.0284	2.176	2.9×10^{-5}	2.3
1	1×10^6	0.6672	2.211	1.2×10^{-4}	2.3
		1.0284	2.293	1.2×10^{-4}	2.4
2	2×10^5	0.6672	2.089[a]	1.7×10^{-4}	6.9
		1.0284	2.140	1.7×10^{-4}	6.9
2	4×10^6	0.6672	2.191	8.5×10^{-5}	6.8
		1.0284	2.265	9.2×10^{-5}	7.3
2	1×10^6	0.6672	2.305	3.4×10^{-4}	6.8
		1.0284	2.399	3.3×10^{-4}	6.7
3	2×10^5	0.6672	2.127	3.3×10^{-5}	13.0
		1.0284	2.186	3.3×10^{-5}	13.2
3	4×10^6	0.6672	2.242	1.6×10^{-4}	12.9
		1.0284	2.323	1.6×10^{-4}	13.1
3	1×10^6	0.6672	2.377	6.5×10^{-4}	13.0
		1.0284	2.486	6.5×10^{-4}	13.0

[a] Corrected value.

critical Born-Oppenheimer electron affinities, $-E_c$, are given along with $-E_c/B$, where $B = \hbar^2/2I$ is the conventional rotational constant of the rotor.

Although the finite dipole model used in this work is a simple one, we submit that the results, E_c, are valid approximations for real molecules with dipole moments greater than 1.625 D. There are three points to consider. First, within the fixed-nucleus, or Born-Oppenheimer approximation, the finite dipole has been shown to give an accurate portrayal of the behavior of real molecules, as far as the values of, and consequences of, the critical dipole moments are concerned.[32] Second, since the only issue is the effect of the B_j^2 term in the Hamiltonian, simplifications in the model which do not bear directly on rotation may well be inconsequential. Finally, and most important, Table 13.1 shows that the E_c values are insensitive to R, the dipole extension, there being no R dependence discernible outside the 5% interpolation errors, which shows that the short-range behavior (i.e., close to the molecule) of the Hamiltonian and the wave function are not important to the effect being studied (clearly due to the diffuse nature[41] of the wave function when the binding energy is small).

In conclusion, barring exoergic dissociative attachment, all electronically nondegenerate polar molecules ($\mu > 1.625$ D) are predicted to have positive electron affinities if their Born-Oppenheimer electron affinities exceed roughly one-twentieth to one-tenth the values of their rotational constants, B. Analogous criteria are presented above for the occurrence of rotationally excited negative ions. The critical dipole moments computed previously[35,36] for rigid rotors furnish a guide as to when these conditions are expected to be fulfilled.

---

41. W. R. Garrett, J. E. Turner, and V. E. Anderson, *Phys. Rev.* 188, 513 (1969).

Part IV. Emergency Technology

C. V. Chester

14. Consequences of Dispersal of a Radioactive Source

R. O. Chester C. V. Chester

As an outgrowth of previous work on the consequences of successful terrorist attack on nuclear facilities,[1] we are, at the request of the U.S. Nuclear Regulatory Commission (NRC), examining the consequences of dispersal of radioactive sources and other materials not requiring physical protection.

From the statement of work by the NRC, "The purpose of this study is to examine the question of whether the risk and consequences of theft or sabotage of facilities or vehicles containing small quantities of SNM, source, and by-product materials are such that licensees should be required to adopt further measures to safeguard them. In the course of the study an assessment will be made of the potential consequences of malevolent use of the referenced materials. To provide perspective, these will be compared with the corresponding characteristics of non-nuclear materials such as chemical or biological agents."

Previous work[1] showed that loss of life from radioactive dispersal would be very low under most circumstances. The principal effect of dispersal would be economic: cost of cleanup or condemnation. This cost would depend as much on the standards for cleanup as on the initial level of contamination. Preliminary estimates of cleanup to peacetime maximum permissible concentration levels indicate the costs from even a relatively small source could equal or exceed those of the destruction from a major dam failure.

Another large unknown is the effectiveness of various methods of removing radioactive metal oxide aerosols deposited on representative surfaces in an urban environment. The work being done under subcontract at the Georgia Institute of Technology (reported in a following chapter) is intended to shed some light on this. Cleanup costs reported officially for accidents in the past were minimized for obvious political reasons.

Another important area of ignorance is the degree to which radioactive aerosols penetrate buildings and the degree to which they can be excluded by improvised measures on the part of the occupants. The work reported in the following chapter on aerosol experiments is directed toward reducing this ignorance.

It is hoped that this work, in addition to providing a rationale for extending or not extending safeguards to smaller amounts of radioactive materials, will also put the whole subject of cleanup costs on a much firmer footing than it is now.

1. C. V. Chester, "Estimates of Threats to the Public from Terrorist Acts Against Nuclear Facilities," *Nucl. Saf.* 17, 659 (1976).

15. Aerosol Studies

G. A. Cristy M. E. Fish

Previous work[1-4] on economic and environmental recovery from severe reactor accidents showed that, although it is highly improbable, it is at least possible for a well-disciplined terrorist group to cause a light-water reactor to suffer a meltdown under conditions which could allow large amounts of fission products to be released to the atmosphere in the form of aerosols. We also showed that relatively simple and inexpensive measures would prevent loss of life or serious injury from the radioactive particles.

Expedient measures developed to protect people from inhaling radioactive aerosols generated by a meltdown of a light-water reactor should also be effective in protecting people from a clandestine biological attack. The aerodynamic properties of the radioactive aerosols closely resemble those of the type of biological agent a terrorist might use.

The purpose of this year's effort was to develop, test, and improve simple, effective, and inexpensive methods by which the average citizen, using materials at hand, can protect his residence, himself, and his family from injury from toxic aerosols.

CHOICE OF A SIMULANT

To develop and test methods of protecting people and the living spaces within buildings from radioactive particles without the experimental difficulties of working with radioisotopes, it was decided to experiment with aerosols of *Bacillus globegii* (BG) spores. BG are nonpathogenic organisms which grow readily in nutrient agar and form very hardy spores which can be handled quite safely.

A supply of BG spores was on hand from previous experiments, but preliminary tests indicated that the number of viable spores was much lower than when they had been obtained. Therefore, a new batch of BG spores was prepared by the Biology Division. The concentrated mass of spores (commonly called "mud" by bacteriologists) was analyzed at 2×10^{11} spores/g.

DEVELOPMENT OF AEROSOL GENERATOR

Preliminary experiments were performed to develop a modified Lauterbach generator that could produce large quantities of aerosols containing viable BG spores. The generator that was developed can produce aerosol at the rate of from 10^9 to 10^{10} spores/min from a suspension of the "mud" in denatured alcohol. The aerosol consists of particles with an average diameter of about 2 μ and shows a deposition velocity of about 3×10^{-4} m/sec.

The aerosol generator is shown in Fig. 15.1. The 3-liter, 3-neck flask holds the suspension of BG in alcohol, which is maintained at a constant level by a supply line at the bottom and an overflow line on the side. The 1-liter flask is used as a supply reservoir to which the overflow is pumped by an airlift. The two ½-in. stainless steel tubes each have eight 0.0135-in. (No. 80 drill) holes equally spaced around the circumference. The aerosol is generated by discharging compressed air at 30 psig through the 16 holes across the surface of the liquid.

SAMPLING TECHNIQUES

Several sampling techniques were tested and evaluated. In the primary method, the aerosol particles from a measured volume of air (actually a known constant flow rate and a measured time) were collected by drawing the air through two all-glass dust impingers in series. The first impinger contains water, but the second is

1. *Health Physics Div. Annu. Prog. Rep. June 30, 1975*, ORNL-5046 (September 1975), pp. 14–15.
2. *Health Physics Div. Annu. Prog. Rep. June 30, 1976*, ORNL-5071 (October 1976), pp. 329–59.
3. C. V. Chester, "Estimation of Threats to the Public from Terrorist Acts Against Nuclear Facilities," *Nucl. Saf.* 17, 659 (1976).
4. Nuclear Fuel Cycle Program Staff, "Safety and Security of Nuclear Power Reactors to Acts of Sabotage," *Nucl. Saf.* 17, 665 (1976).

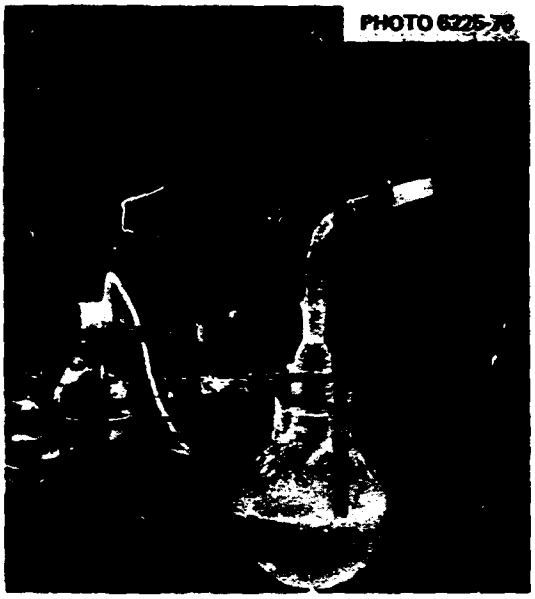

Fig. 15.1. Aerosol generator.

kept dry to protect the vacuum pump from spillover. This technique gave reproducible results. Tests showed that the loss of spores from such a sampler was about 3%. When especially accurate recovery was desired, two sets of impingers (of two each) were used in series, giving a leakage rate of less than 1 in 1000.

It was found that BG spores could remain viable when kept for several days in the demineralized water in which they were collected.

In another sampling method, a known amount of air was drawn through a sampling device which held a special type of filter paper. The filter papers were then transferred (using sterile tongs) to an 8-oz bottle containing 100 ml of water. Vigorous shaking of the bottle served both to break up the paper and to get the BG spores into suspension.

Aliquot samples of the water suspensions (or of serial dilutions of the suspensions) were cultured on nutrient agar surfaces to determine the number of spores collected.

A third sampling method used slit samplers, which have a clock mechanism that slowly rotates an agar plate under a slit in the lid. A vacuum pump draws air through the slit at a constant rate (measured at 9.4 liters/min). Any spores in the air will impact on the agar and be retained. The agar plates were then incubated for 12 hr to develop the colonies for counting.

A fourth sampling method, used on only the first two outdoor tests, employed the PART analyzer being developed by Edgewood Arsenal. The development is not complete yet, so the analyzer was operated at ORNL by Edgewood Arsenal personnel. The PART analyzer gave results generally comparable with the other sampling methods. However, it was somewhat difficult to use because it detects other airborne organic materials in the particle size range of 0.5 to 10 μ. In the outdoor tests, the background of other organic materials was often of the same order of magnitude as the BG samples. However, it does have one tremendous advantage over the other methods: The results are available within minutes rather than within a day or two.

AVERAGE SIZE OF AEROSOL PARTICLES

The average size of the aerosol particles was determined by two different methods. In the first method, the spores were allowed to settle on microscope slides on the bottom of a 1-m^2 plastic box and were examined under a microscope equipped with a measured grating. The average size was estimated to be 1.75 μ. The other method, based on a modified Stokes law calculation developed at Fort Detrick,[5] requires measuring the rate of decrease of the aerosol concentration in an enclosed space. The mathematical development is as follows.

From Stokes law,

$$f_v = 6\pi r n u \,, \tag{1}$$

where f_v = force applied to cause a particle of radius r to move with a constant velocity u through a medium with viscosity n (viscous flow). From gravitational considerations,

$$f_g = \frac{4}{3} g\pi r^3 (p - p') \,, \tag{2}$$

where f_g = force due to gravity on a particle of radius r and a density p falling through a medium of density p'. If $f_v = f_g$, then combining Eqs. (1) and (2) gives

$$u = \frac{(4/3)g\pi r^3 (p - p')}{6\pi r n} = \frac{gD^2 (p - p')}{18n} \,. \tag{3}$$

On the assumption that tranquil settling does not occur due to convection currents, the decrease in concentration C can be expressed by

$$\frac{dC}{dt} = \frac{-C}{T} = \frac{-uC}{H} \,, \tag{4}$$

5. *Special Report No. 36*, Camp Detrick, Md., Nov. 15, 1945.

where t = the variable time, T = the total time, and H = the height the spores have to fall to be removed. Rearrange Eq. (4), integrate, and solve for u:

$$u = \frac{H}{T} \ln\left(\frac{C_0}{C_t}\right) . \tag{5}$$

Combine Eqs. (4) and (5) and solve for D:

$$D = \left(\frac{18nH(C_0/C_t)}{Tg(p - p')}\right)^{1/2} \tag{6}$$

In our tests, H = 100 cm, n = 0.018 cP = 1.8×10^{-4} g sec^{-1} cm^{-1}, g = 980.7 cm/sec^2, p' = 1.29×10^{-3} g/cm^3 (negligible), and p = 1.2 g/cm^3. The experimental data on concentration reduction and the calculated values of D are shown in Table 15.1.

Table 15.1. Calculation of average particle diameter

T (hr)	C (spores/ml)	C_0/C_t	$\ln(C_0/C_t)$	D (μ)
0	6700			
1	4000	1.68	0.519	1.99
2	2250	2.98	1.092	2.04
5	420	15.95	2.769	2.06
24	19	352.6	5.865	0.50

CALCULATION OF DEPOSITION VELOCITY

The deposition velocity was calculated from the rate of settling of spores in a plastic glove box. Petri dishes containing nutrient agar were placed uncovered in the bottom of the glove box. Aerosol containing BG spores was discharged into the box for 1 min. One petri dish was covered at the end of each minute for the first 15 min, then one additional dish was covered each 15 min up to 2 hr. All dishes were incubated overnight. The data for the first 15 min from one such experiment are plotted in Fig. 15.2. The straight line shown on Fig. 15.2 was obtained by the least-squares method.

To calculate the deposition velocity,

$$V = R/C ,$$

where V = deposition velocity in cm/sec, R = rate of deposition in spores cm^{-2} sec^{-1}, C = initial concentration in spores/cm^3 (in this experiment C was 23 spores/cm^3).

The slope of the graph in Fig. 15.2 is 33 spores cm^{-1} min^{-1}. Therefore, R = 33/60 = 0.55 spore cm^{-2} sec^{-1}, and V = 0.55/23 = 0.0239 cm/sec = 2.4×10^{-4} m/sec.

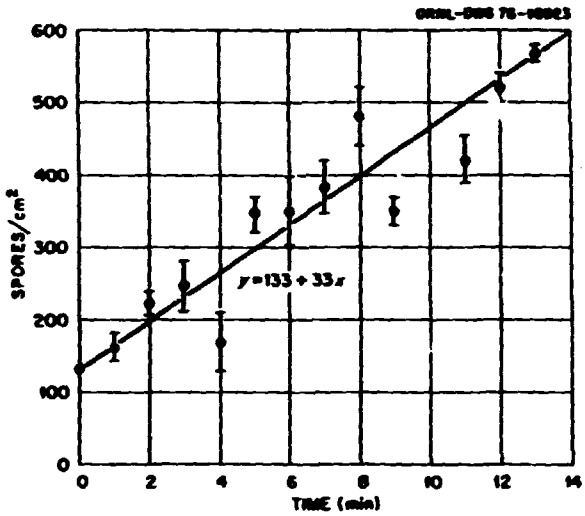

Fig. 15.2. Rate of deposition of spores.

TEST OF PROTECTION FACTORS USING VACUUM CLEANER

Experiments were performed to evaluate an ordinary home vacuum cleaner as a mechanism for removing aerosol particles to protect living spaces from intrusion of radioactive particles. Specifically, it was considered that an occupied house could be closed up before a radioactive cloud arrived and that the home vacuum cleaner would be rigged up to filter outside air and discharge it into the house to maintain a very small positive pressure which would reduce the infiltration of radioactive particles. Duplicate tests were performed on five different methods of providing the filtration:

1. one clean bag in the vacuum cleaner,
2. a double bag in the vacuum cleaner (one clean bag was opened at the bottom and another clean bag placed inside; the first bag was resealed with duct tape),
3. flour in a clean bag (the first test used 5 lb of flour, and the second test used only 1 cup of flour),
4. a clean bag in the sweeper canister with another clean bag on the exhaust, and
5. a dirty bag in the sweeper (bags were loaded with a normal three-month accumulation for ordinary households).

The tests were performed by generating aerosol for 10 min into a collapsible plastic box which contained 2 m^3 of air (see box on the left in Fig. 15.3), then using the sweeper to transfer and filter 1 m^3 of the contaminated air into a second expandable plastic box which already contained 1 m^3 of essentially clean air (see box on the right in Fig. 15.3). Figure 15.4 shows the two boxes

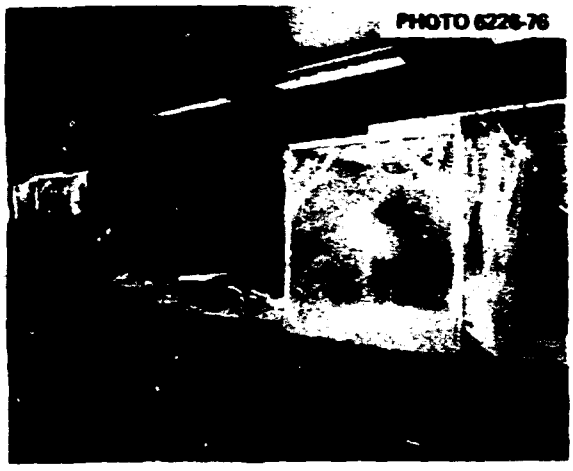

Fig. 15.3. Expandable plastic boxes before experiment.

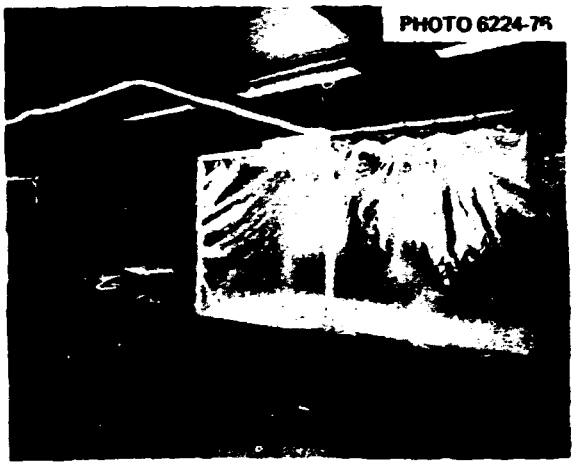

Fig. 15.4. Expandable plastic boxes after experiment.

after the transfer. By analyzing the BG content of both boxes before and after the transfer, the protection factor (*PF*) could be calculated as follows:

$$PF = \frac{\text{number of spores in 1 ft}^3 \text{ of air in box 1}}{\text{increase in spores in box 2}} .$$

The *PF* is defined as

$$PF = \frac{\text{concentration in air before filtration}}{\text{concentration in air after filtration}} .$$

The results are shown in Table 15.2.

PRELIMINARY FIELD TEST

To check experimental techniques and to compare actual results with expected values, a preliminary field test was run. The generator was set up and operated for 10 min, discharging into a closed plastic box. Samples were taken to determine the rate of generation of aerosol. The generator was then operated for 30 min, discharging into the air at a height of 1 m aboveground. Open petri dishes had been placed downwind of the generator at intervals of 3 m with one dish as close to the direction the wind was blowing as possible and with one dish on either side at a distance of 1 m. An impinger sample was taken continuously at a point 15 m downwind at a height of 1 m aboveground. The wind velocity was measured every 5 min with a Hastings air meter. The wind velocity varied from 1 to 2.5 m/sec with some gusting to 5 m/sec. The average wind velocity was estimated to be 2.0 m/sec.

The expected fallout and the expected concentration 15 m downwind of a point source were calculated using published correlations.[6] Comparisons between calculated and observed values are shown in Table 15.3.

The fallout was based on a deposition velocity of 3×10^{-4} m/sec. The fact that the values observed for fallout are low by a factor of 10 suggests that the deposition velocity may be about 3×10^{-5} m/sec.

Table 15.2. Protection factors (*PF*)

Filtration method	First experiment	Second experiment
One clean bag	67	117
Double clean bag	97	500
Flour in one clean bag	280	400
Clean bag in sweeper and clean bag on the exhaust	100	286
Dirty bag in sweeper	1400	1700

METHOD OF CALCULATING PROTECTION FACTOR OF CLOSED HOUSES

Definitions

The protection afforded by a building is postulated to consist of two parts. The first is time-dependent and occurs because a closed building delays the entrance of outside air. The second is not time-dependent and will occur only if the passage through the walls removes some of the contaminant. If the radioactive cloud passes rather quickly compared with the time it takes for equilibrium to be established between outside and inside air, the total inhaled dose received by persons

6. U.S. Atomic Energy Commission, *Meteorology and Atomic Energy 1968*, July 1968, pp. 99–103.

Table 15.3. Comparison of calculated and experimental values of fallout and downwind concentration

Distance from generator (m)	Fallout (spores/cm²)		Average concentration (spores/liter)	
	Calculated	Observed	Calculated	Observed
3	83.7	6.9		
6	58.2	3.6		
9	36.8	2.9		
12	24.8	3.2		
15			172	123

inside the house will be reduced. The amount of reduction is strongly dependent on the rate of inleakage and on the length of time the cloud of radioactive particles takes to pass.

Protection factors (*PF*s) are normally defined as the ratio of the dose one would receive on the outside to the dose one would receive inside. In our case we will consider the *PF* as the product of the two protection factors – one due to diffusion, which we know exists, and one, if it does exist, due to removal of the contaminant as the air passes through the wall. Let

$$PF = P_D \cdot P_F ,$$

where PF = total protection factor, P_D = protection factor provided by diffusion, and P_F = protection factor provided by filtration.

In the case of radioactive aerosols, the dose rate will be proportional in some complex manner to the concentration of radioactive particles in the air if it is assumed that the dose from fallout on the ground is negligible compared with the inhaled dose from airborne particles. It is also assumed that the rate of decay of the radioactive particles is small during the period of exposure to the radioactive cloud. In experiments that simulate the exposure to radioactive clouds, it is reasonable to assume that the dose rate is proportional to the concentration of the simulant.

Calculation of the Diffusion Protection Factor (P_D)

The diffusion protection factor can be estimated by using carbon dioxide (CO_2) to measure the infiltration rate into the house. A measured amount of CO_2 is released into the closed house, and the air inside is analyzed for CO_2 at periodic intervals (e.g., every ½ hr for 4 hr).

The first step in calculation of the diffusion protection factor is to calculate the rate of diffusion of air into the house, which should be essentially the same as the rate of diffusion of CO_2 out.

Let C = concentration of CO_2 inside house (m³ of CO_2 per m³ of air), $C_i = C$ at time zero, $C_T = C$ at time T, v = rate of influx of air into the house (m³ of air per hr), V = volume of the house (m³ of air), and $R = v/V$ = rate of change of air in the house (change per hour). The material balance equation is rate of increase = rate of influx – rate of outflow,

$$V\frac{dC}{dt} = 0 - Cv . \tag{7}$$

This can be solved for the infiltration rate R.

$$R = -\frac{1}{T}\ln\frac{C_T}{C_i} . \tag{8}$$

The value of R depends on the wind velocity around the house and the design of the house. With steady wind velocity the value of R should be a constant.

The diffusion protection factor can then be calculated by letting D_o = inhaled dose (either thyroid or whole body) a person would receive outside (roentgens), D_i = inhaled dose a person would receive inside (if there were no loss of particles because of walls), $P_D = D_o/D_i$, k = proportionality factor between particles and dose[7] (roentgens/min per particles/liter), T = time the cloud takes to pass (minutes), E = concentration of the contaminant particles inside the house at time t (particles/liter), E_o = concentration of the contaminant particles outside the house (assumed constant from $t = 0$ to $t = T$) (particles/liter). Then

$$D_o = k\int_0^T E_o\,dt = kE_oT , \tag{9}$$

7. This proportionality factor is assumed to be constant for any one cloud although its value may vary.

and

$$\frac{D_i}{k} = \int_0^\infty E\,dt = \int_0^T E\,dt + \int_T^\infty E\,dt\,. \tag{10}$$

Let

$$A = \int_0^T E\,dt \tag{11}$$

and

$$B = \int_T^\infty E\,dt\,, \tag{12}$$

where A is proportional to the dose accumulated during cloud passage and B is proportional to the dose accumulated after cloud passage. The material balance during cloud passage is

$$V\frac{dE}{dt} = E_o \mathrm{v} - E \cdot \mathrm{v}\,, \tag{13}$$

from which

$$\frac{d(E_o - E)}{E_o - E} = -R\,dt\,. \tag{14}$$

Therefore, at any time t

$$\ln\left(\frac{E_o - E_t}{E_o - E_i}\right) = -Rt\,, \tag{15}$$

where E_i is the initial concentration of the contaminant inside the house. Since $E_i = 0$, we can write

$$E_t = E_o[1 - e^{-RT}]\,. \tag{16}$$

Combining Eqs. (16) and (11) and integrating gives

$$\frac{A}{E_o} = T - \frac{1}{R} + \frac{e^{-RT}}{R}\,. \tag{17}$$

Examples are shown in Table 15.A, based on an assumed value of $R = 1$ (i.e., one air change per hour). Comparison of the last two columns in Table 15.A indicates how the inside dose approaches the outside dose as T increases.

Table 15.A. Calculated dose inside house during cloud passage

T	$T - 1/R$	e^{-RT}/R	A	$D_o/k = E_oT$
0.5	−0.5	0.61	$0.11E_o$	$0.5E_o$
1.0	0	0.37	$0.37E_o$	$1.0E_o$
2.0	1	0.14	$1.14E_o$	$2.0E_o$
4.0	3	0.02	$3.02E_o$	$4.0E_o$
10.0	9	0.000	$9.000E_o$	$10.0E_o$

If the occupants of a house could know when the cloud has passed and open up the house immediately, the accumulated dose inside would be less than what would have been received outside. When the length of time that it takes for the cloud to pass is long compared with the time for one air change, the dose inside would be very nearly the same as the dose outside.

The material balance after cloud passage (starting at time T and ending at time t when concentration inside the house becomes negligible) is

$$V\frac{dE}{dt} = -E\mathrm{v}\,. \tag{18}$$

As before, $R = \mathrm{v}/V$ is substituted, and the solution for the concentration of contaminant particles at time $t > T$ is given by

$$E_t = E_T e^{-R(t-T)}\,, \tag{19}$$

where E_T is the concentration at time T. Combining Eqs. (19) and (12) gives

$$B = \frac{E_T}{R}\,. \tag{20}$$

This indicates that the maximum dose received inside the house after the cloud passed would be equal to the dose one would get by being exposed to the maximum concentration for the length of time it takes for one air change.

From Eq. (16) at time $t = T$, Eq. (20) becomes

$$B = E_o\frac{1 - e^{-RT}}{R}\,. \tag{21}$$

From Eq. (10)

$$\frac{D_i}{k} = A + B = E_o T - \frac{E_o}{R} + \frac{E_o e^{-RT}}{R} + \frac{E_o (1 - e^{-RT})}{R} = E_o t \,. \quad (22)$$

Therefore,

$$P_D = \frac{D_o}{D_i} = \frac{kE_o T}{kE_o T} = 1 \,. \quad (23)$$

That is, if a person stays in the closed-up house long after the radioactive cloud has passed, the house will have given him no protection from diffusion only.

Calculation of the Contamination Protection Factor Due to Filtration

This contamination protection factor due to filtration will be estimated by subjecting the house to a cloud of BG aerosol of known concentration (F_o) for a specific time (T). The infiltration rate (R) will be determined at the same time to ensure identical wind conditions for both calculations.

Let G = concentration of BG spores in the house (spores/m^3), G_o = concentration of BG spores outside the house (spores/m^3), P_F = protection factor provided by the house, $R = v/V$ = rate of change of air in the house, G_o/P_F = concentration of BG spores actually entering the house. The material balance is

$$V\frac{dG}{dt} = \frac{G_o}{P_F} v - Gv \,, \quad (24)$$

$$\frac{dG}{dt} = \frac{R}{P_F}(G_o - G \cdot P_F) \,, \quad (25)$$

$$\frac{d(G_o - G \cdot P_F)}{(G_o - G \cdot P_F)} = -RT \,, \quad (26)$$

$$\ln\left(\frac{G_o - G_T \cdot P_F}{G_o - G_i \cdot P_F}\right) = -RT \,. \quad (27)$$

But $G_i = 0$; therefore,

$$R = -\frac{1}{T}\ln\left(\frac{G_o - G_T \cdot P_F}{G_o}\right). \quad (28)$$

Combining Eqs. (8) and (28),

$$\frac{G_o - G_T \cdot P_F}{G_o} = \frac{C_T}{C_i} \,; \quad (29)$$

to solve for P_F:

$$P_F = (G_o/G_T)(1 - C_T/C_i) \,. \quad (30)$$

This equation can be used to calculate the contamination protection factor afforded by the house using the measurements of CO_2 concentrations and BG concentrations at each time T.

Examples are shown in Table 15.5 based on the assumption that R = 1 (i.e., one change per hour). This table shows that G_T will have increased to 98% of its equilibrium value in the time it takes to make four air changes.

Table 15.5. Contamination protection factors afforded by filtration

T (hr)	P_F
1	0.632 (G_o/G_T)
4	0.9817 (G_o/G_T)

Tests on Closed Houses

Four separate experiments were conducted on three houses. One house was tested only for leakage rate. In each of the other cases, the aerosol generator was set up and operated for several hours on the windward side of the house being tested. At the beginning of the test, CO_2 from a fire extinguisher was released into the closed house. A Wilks MIRAN-101 portable specific-vapor analyzer was used to record the concentration of CO_2 during the experiment. A set of impingers was used to collect a continuous sample of air just outside the house. Various methods of analysis were used to measure the buildup of BG concentration inside the house. A sensitive anemometer and a recording wind-direction instrument were erected on a 2-m pole outside the building. The data of the four tests are summarized in Table 15.6.

During test 4, 30-min samples were taken inside the building to determine the rate of BG buildup. Figure 15.5 shows the results for these samples compared with the rate of buildup calculated on the basis of the measured leakage rate.

Figure 15.6 shows the results of similar samples taken during test 5. The sample times were 5 min during the first ½ hr and 10 min thereafter.

Table 15.6. Tests on closed houses

Test variables	Test No. 1	2	5	4	3
	Building				
	Tool shed			Trailer home	Private home
Leakage rate (R), changes per hour	0.20	0.25	0.44	0.163	0.130
Average wind velocity, m/sec	2.1	1.3	1.5	0.7	1.3
Average concentration outside building (from impinger sample), spores/liter	150	165	540	514	
Calculated concentration outside building, spores/liter			560	376	
Duration of experiment, min	150	120	180	180	250
Concentration inside house at end of experiment, spores/liter	105		470	111	

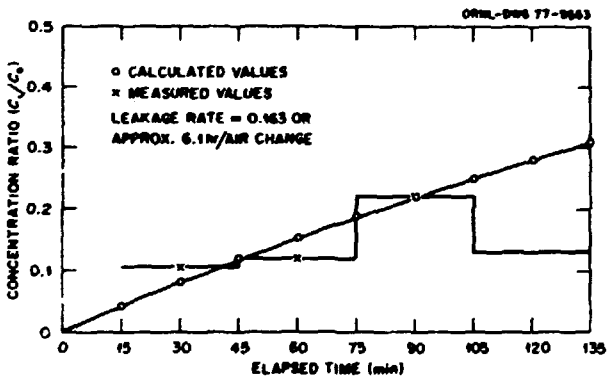

Fig. 15.5. Buildup of concentration vs time (test 4).

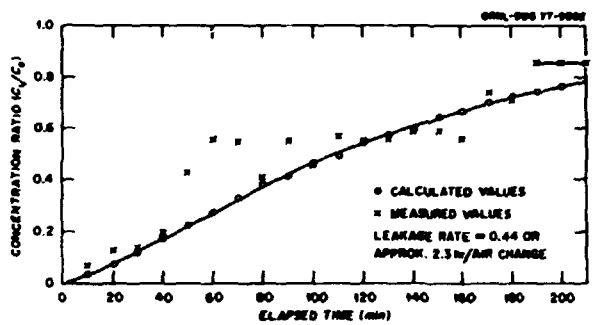

Fig. 15.6. Buildup of concentration vs time (test 5).

DISCUSSION

The results of tests thus far do not give any assurance that there is any filtration of the aerosol during passage of the air through the walls of a building. More sophisticated tests will be run to try to ascertain whether it does or does not occur.

If there is no improvement in protection factor due to filtration, a building will provide significant protection from inhaled dose only for about the time for one air change. For example, from Table 15.4 it can be seen that the protection factor is reduced to less than 3 when $T = 1/R$. The buildings tested are believed to be at least as tight as most residences. With no defense other than the closed building against intrusion of contamination, people in such houses will have protection only for 3 to 5 hr. Therefore, it is important to find better protection. Various means of introducing filtered makeup air for the closed buildings will be tested, including but not limited to using vacuum cleaners with dirty bags.

16. Decontamination Studies

G. A. Cristy

These studies are part of a program to develop guidance for civilian authorities for recovery from a very severe reactor accident caused by willful malevolent acts, which result in release of radioactivity. The ultimate goal of the program is to complete the research before questions concerning such accidents are raised by intervenors during congressional hearings.

To accomplish these goals, realistic accidents involving reactor types now in use and new types that may be deployed in the near future were studied.[1,2] Careful appraisal[3,4] of these accidents showed that it is improbable, but nevertheless possible, that a well-disciplined terrorist group could cause a light-water reactor meltdown. The containment could be breached sufficiently to allow the release of large amounts of radioactivity into the atmosphere in the form of particles (about 1 μ in diameter) of the oxides of uranium and the major fission products. The quantities and proportions of the various fission products would be similar to those reported in the Parsly-Fontana model given in Appendix VII of ref. 5.

Our studies of such accidents showed that relatively simple and inexpensive measures can prevent loss of life or serious injury from radiation. However, the potential economic impact could be immense, amounting to tens of billions of dollars. Unfortunately, the accuracy of estimations of the economic consequences is impossible to ascertain because there is virtually no reliable information on the cost of the decontamination of structures and the environment from aerosols of finely divided oxides. Therefore, this study was undertaken to provide reliable cost information for large-scale decontamination.

Small samples of a number of building materials are being subjected to fallout in the Chemistry Division's Reactor Safety Test Facility. The fallout consists of depleted UO_2 particles in the 1- to 2-μ size range. The building materials include painted wood, asphalt shingles, galvanized sheet metal, painted concrete block, concrete, aluminum plates, brick, asphalt paving, glass, sandstone, and aluminum siding coated with three different materials [4-mil polyvinyl chloride (PVC), 1-mil enamel, and 1-mil acrylic].

It was determined by measuring ^{239}Np activity that activation of the UO_2 fallout particles in the Georgia Institute of Technology reactor will give adequate sensitivity down to about 10 $\mu g/cm^2$ of material. An irradiation framework was installed in front of the neutron beam in the Georgia Institute of Technology biomedical facility. The beam profile was mapped, and several methods of obtaining direct comparison data by simultaneous irradiation of contaminated and clean areas of a given sample were tested.

Uncontaminated specimens of cement brick, red brick, aluminum siding with baked enamel, and aluminum siding with Tedlar were activated to test for background uranium. After overnight cooling to reduce alu-

1. *Health Phys. Div. Annu. Prog. Rep. June 30, 1975*, ORNL-5046 (September 1975), pp. 14–15.

2. *Health Phys. Div. Annu. Prog. Rep. June 30, 1976*, ORNL-5071 (October 1976), pp. 329–59.

3. C. V. Chester, "Estimation of Threats to the Public from Terrorist Acts Against Nuclear Facilities," *Nucl. Saf.* 17(6), 659 (1976).

4. Nuclear Fuel Cycle Program Staff, "Safety and Security of Nuclear Power Reactors to Acts of Sabotage," *Nucl. Saf.* 17(6), 665 (1976).

5. U.S. Nuclear Regulatory Commission, *Reactor Safety Study – An Assessment of Accident Risk in U.S. Commercial Nuclear Power Plants*, Appendix G to Appendix VII, WASH-1400 (NUREG-75/014), October 1975, pp. VII-143–VII-150.

minum and sodium radiation fields, no neptunium peaks were obtained.

Using activation analysis, the quantity of UO_2 fallout on each sample will be determined. Various methods of decontamination will then be tried to determine the best and most economical methods of removal. When the best methods of decontamination are determined, larger samples of each material will be contaminated, and the methods of decontamination will be evaluated on an economic basis. The ultimate goal is to produce sufficient data on the cost of decontaminating large land areas to estimate cleanup costs in the case of a severe reactor accident (or as a consequence of sabotage).

17. Elements of a War-Survival Policy for the United States

C. V. Chester

It is widely believed in intellectual circles in the West that a world in which nuclear war is not possible is infinitely preferable to any world in which nuclear war is possible. To achieve such a world, the strategic policy of the United States has been directed almost exclusively to deterring nuclear war. Stable deterrence has been sought by designing strategic offensive forces in such a way that after absorbing the largest attack the enemy could launch, the surviving forces could retaliate and deliver "unacceptable damage" to the enemy's population and industry. Unacceptable damage has been variously defined as destruction of 20% of the population and 50% of the industry, destruction of the enemy as a twentieth century society, and destruction so vast that recovery time would not be significantly shorter than that for the United States.

Implicit in this approach is that no effective action would be taken to protect any significant fraction of either side's population or industry from the other's retaliatory forces. In effect, each side leaves its population as hostage for its peaceful behavior. The combination of invulnerable offensive forces and vulnerable population is the essence of the strategic doctrine of Mutual Assured Destruction, or MAD.

It is beginning to become clear to even the most ardent Western proponents of MAD that the Soviet Union has never accepted this strategic doctrine. Soviet acceptance of the treaty limiting antiballistic missiles, which contains in its preamble the phrase "Proceeding from the premise that nuclear war would have devastating consequences for all mankind . . . ," had for a time been cited as evidence of Soviet acceptance of MAD. However, the interpretation of that phrase depends very much on how severe one considers "devastating consequences."

Soviet historical experience and perspective are very different from those of the West. For example, most Americans believe that the United States played the predominant role in Europe during World War II. Very few Americans are aware that 80% of Germany's losses were inflicted on the Russian front. The United States has not been invaded by a foreign power for 163 years, and even then by what was then probably the most civilized military force in the world. Most Soviet leaders today are veterans of World War II, in which the Soviet Union was invaded by a power bent on genocide. From that experience, and accounts from the Mongol invasion of the thirteenth century, the Soviet leadership is well aware that there are circumstances far worse than nuclear war. Being overrun by infantry can be much more destructive than present concepts of bombardment. Carthage is the historical example most famous in the West.

Since 1968, the Soviet Union has made a very serious effort to protect its population and industry from the effects of nuclear war. Its program has included widespread shelter construction for essential cadre, military, and essential production workers, dispersal of new industrial construction, accumulation of hardened and dispersed food reserves, comprehensive planning for evacuation of civilians in target areas in a crisis, and a universal education program in civil defense for all citizens.[1-3] Soviet officials have recently admitted to an annual civil defense budget of one billion rubles ($1.3 billion) to U.S. visitors.[4]

Estimates of the effectiveness of this program vary, depending principally on the prejudices of the estimators and their selection of assumptions. In terms of population losses, estimates vary from one-half to one-

1. L. Gouré, *War Survival in Soviet Strategy Soviet Civil Defense*, Center for Advanced International Studies, University of Miami, Coral Gables, Fla., 1976.

2. L. Gouré, *The Soviet Civil Defense Shelter Program*, Center for Advanced International Studies, University of Miami, Coral Gables, Fla., May 1977.

3. G. Kolt, "The Soviet Civil Defense Program," *Strategic Rev.* 5, 52 (1977).

4. J. H. Proctor, "Five Days in Russia," *J. Civ. Def.* 10, 2 (1977).

thirtieth of U.S. losses in comparable circumstances, with the broad consensus being around one-tenth. Typically, 5% Soviet losses are estimated – compared with 50% U.S. losses – in an all-out war.[5]

Perception of this disparity is widespread and becoming more so. Authoritative statements and congressional testimony by Gen. George J. Keegan, Jr., former Director of Air Force Intelligence, and T. K. Jones of Boeing Aerospace Co. describing the situation have received wide coverage in print.[6,7] Keegan and Jones have put special emphasis on the measures the Soviets have taken to protect their government and party officials, communications, and industry. Jones estimates the time to recover Soviet pre-war gross national product at four years or less. The corresponding recovery time for the United States is twelve years or more.

It is the stated policy of the United States to retain at least rough strategic parity with the Soviet Union. It is arguable whether parity exists when the Soviets have a tenfold advantage in vulnerability and a corresponding advantage in estimates of recovery time. Increasing perception of this situation, especially among the American people, would make the bargaining position of a U.S. president very difficult in some future confrontation with the Soviet Union. Perception of the U.S. disadvantage by allies and third-world countries would tend to undermine confidence in the U.S. deterrent and the likelihood of U.S. assistance in difficulties they might have with the Soviet Union or Soviet-sponsored forces. It is difficult to see how this situation, or a series of severe diplomatic reverses which could result from it, would enhance the role of the United States as the champion of Western values, particularly human rights.

It seems clear that parity in offensive forces is meaningless if there is not at least rough parity in vulnerability. Arguments that no meaningful recovery from nuclear war is possible simply do not face up to the measures the Soviets have taken and are not supported by any defensible calculations of their effectiveness in the face of the probable circumstances of an attack.

Vulnerability reduction, or a war survival policy, should be regarded as an adjunct to the U.S. strategic deterrent. Like the strategic offensive forces, it is extremely unlikely that such a policy would ever be called into action. However, if the policy is to act as a deterrent, it must be completely credible. But because there is such a low probability of use, it should have the lowest possible impact on the social and economic fabric of the nation under "normal" peacetime conditions. During a crisis, it would make maximum use of available resources.

A policy to restore some semblance of parity in vulnerability must take into account a wide range of constraints, including especially those that are economic and political. It cannot be based only on what is technologically feasible.

For example, a tenfold expansion of U.S. strategic offensive forces is prohibited by the Strategic Arms Limitation Treaty (SALT), as well as by the political difficulty of obtaining the tens to hundreds of billions of dollars it would cost. As another example, a large capital investment in urban blast shelters, besides being of questionable political feasibility, would consume $20 to $50 billion – capital acutely needed for expansion of energy production. The protection of areas with population densities above 5000 or 10,000 people per square mile is very difficult if less is to be spent than by the enemy to overcome the protection. The Chinese have been able to provide a cost-effective protection program by using "volunteer" after-hours labor to retrofit urban blast shelters into all their cities. In the United States, costs of constructing underground systems in existing cities are nearly prohibitive because of a combination of the clutter of utilities and the work rules of urban construction unions. The Washington, D.C. Metro, the city's new subway system, is a good example. This observation does not apply to modifying new construction in appropriate areas to provide enhanced protection from nuclear weapons effects. This modification, called "slanting," can provide substantial protection at a very modest cost, typically 5 to 10% of the cost of single-purpose shelters. Most urban blast shelter in the Soviet Union has been achieved this way; the Moscow Subway is the most famous example.

New construction in U.S. cities should be slanted where necessary to provide fallout protection and modest blast protection – but against *n*th nation and terrorist threats, not a full-scale Soviet attack. The protection method of choice for population densities over 5000 to 10,000 per square mile (75 to 40 × 10^6 U.S. population) against a full-scale attack must remain evacuation and dispersal. This method is dictated by eco-

5. J. M. Collins, *United States and Soviet City Defense Considerations for Congress*, 94th Congress Senate Document 94-268, August 1976.

6. T. K. Jones, *Industrial Survival and Recovery after Nuclear Attack*, Report to the Joint Committee on Defense Production, U.S. Congress, Boeing Aerospace Co., Seattle, Wash., Nov. 18, 1976.

7. G. J. Keegan, Jr., "New Assessment Put on Soviet Threat," address reprinted in *Aviat. Week Space Technol.* 160, 38 (1977).

nomics. In addition, according to an analysis by Kupperman,[8] it can promote stability in arms competition.

A program of vulnerability reduction for the United States should exploit where possible the strategic advantages the country enjoys by virtue of geography and institutions. The most salient of these are an unparalleled automotive transportation system and a relatively mild climate. These are critically important to crisis evacuation – the cheapest and most effective means of protecting population – and the only means available to the United States in the near future.

The U.S. automotive transportation system consists of over 108 million vehicles and a vast, highly redundant road network. There are about 2.5 passenger spaces for each person of the entire population. This combination of automobiles and road network can evacuate most of the population from target areas within three days. New York and other large cities in the Northeast Corridor,[9] as well as Los Angeles, may take four or five days.

The climate of the United States is much milder than that of the Soviet Union, the United States lying largely below the 45th parallel and the Soviet Union above the 50th. Moscow is approximately lat. 55°N. The roads in even the northern United States are passable a surprisingly large fraction of the time in the winter. It is news when an area is immobilized by snow, and sensational news when a city is immobilized for five days, as Buffalo, New York, was last winter.

The interstate highway system is one of the most important civil defense assets in the United States. It was originally designed in the 1950s partly to serve as an evacuation system, although it is woefully inadequate for this purpose by itself with today's automobile population. However, it is a major stimulus for the movement of industry and population out of urban centers. In the long term this movement, properly encouraged, could result in major reductions in vulnerability of U.S. population and industry.

Another major strategic advantage enjoyed by the United States is its very productive agriculture. The nation raises about 2.5 times as much grain as would be required to sustain the population on an all-grain diet. The vast majority of this grain is used to feed livestock and remains in rural areas. Because of the staggering of harvests with crop and location, at any time – even the low point in June – there usually remains enough grain on farms to feed the entire population for a year.[10] At present levels of nuclear armament, it has been shown that surviving transportation resources would be adequate to supply the population in the postattack environment in a timely manner.[10] The excess productivity of U.S. agriculture ensures that there will be adequate production to feed the U.S. population in the postwar environment, even allowing for some shortages of fertilizer, pesticides, herbicides, fuel, and abandonment of some land use due to contamination by fallout.

The United States suffers from two major, though correctable, disadvantages that affect its vulnerability with respect to the Soviet Union. These can be summarized as psychology and petroleum – the widespread belief of the myth of nuclear holocaust and extensive dependence of the U.S. economy on refined petroleum. These disadvantages must be vigorously redressed by any plan to reduce vulnerability.

By far the most serious problem is the psychological. The belief prevalent among academic, intellectual, and to a suprising extent, government leaders, is that nuclear war means "the end of mankind" or "the end of civilization," at least in the countries involved. There are two components to this belief, the overkill myth and the "On the Beach" scenario.

The overkill myth refers to the assertion that the nuclear arsenals of the world are sufficient to kill everyone "10 times over" or "17 times over" or whatever. These numbers were obtained by taking the number of deaths per kiloton from the nuclear bomb detonated at Hiroshima, multiplying by the estimated yield of the world inventory of nuclear weapons, and dividing by the world population. This misleading calculation is based on the implicit assumption that the world population could be gathered to the density of Hiroshima and kept in a correspondingly unwarned vulnerable posture for the exercise. For such a bovinely cooperative population, it would be equally valid to say the world's inventory of small arms ammunition, or for that matter, kitchen knives, could kill them 10 or more times over.

The "On the Beach" scenario refers to the belief, based on a novel and movie of that title, that worldwide fallout from a nuclear war would ultimately kill everyone in the world from radiation. The problem of the effects of worldwide fallout was treated in the National Academy of Sciences report.[11] It was estimated that

8. R. H. Kupperman and H. A. Smith, "The Role of Population Defense in Mutual Deterrence," *SIAM Rev.* 19, 297 (1977).

9. W. E. Strope, C. D. Henderson, and C. T. Rainey, *The Feasibility of Crisis Relocation in the Northeast Corridor*, Stanford Research Institute, Arlington, Va., December 1976.

10. C. M. Haaland, C. V. Chester, and E. P. Wigner, *Survival of the Relocated Population in the U.S. after a Nuclear Attack*, ORNL-5041 (June 1976).

11. A. O. C. Nier, chairman, Committee to Study the Long-Term Worldwide Effects of Multiple Nuclear Weapons Detonations, *Long-Term Worldwide Effects of Multiple Nuclear Weapons Detonations*, National Academy of Sciences, Washington, D.C., August 1975.

the net long-term effect of radiation would be a 2% increase in cancer rate 15 years after the war. We estimated the long-term radiation effects from a 5000-megaton attack on the United States and found a 30% increase in cancer 15 years after the war due principally to increased ^{90}Sr in the diet.[12] This increase would be almost exactly canceled if the nation decided to refrain from rebuilding the cigarette industry after the war. If, in addition, much of the meat and refined carbohydrate in the American diet were replaced with whole grain after the war, the net long-term effect of the war could be a 30% decrease in cancer rate.

A puzzling aspect of the psychological problem is the persistence of certain high government officials in the "end of civilization" rhetoric despite their access to classified government studies, such as PONAST II,[13] every one of which supports the contention that nuclear war is survivable. It strains credulity to believe that the real state of affairs has been concealed from them by their subordinates, and that they are forced to base their policies on the arm-waving arguments of the academics rather than the careful quantitative analyses of their professional staffs. One can only speculate that they are practicing a form of unilateral psychological disarmament in the hope of inducing the Soviets to abandon nuclear war as a feasible option for "continuation of policy by military means."

The Achilles heel of the U.S. economy is its dependence on petroleum. Figure 17.1 shows the reduction in petroleum production with refinery destruction. A relatively tiny fraction of the Soviet strategic force can severely cripple present production capacity. However, production is so large that only a relatively tiny fraction of capacity need survive for national survival. Only 3% of present production is required to keep farms operating. Hzaland[10] has shown that an additional 3% is required to move enough food for survival from the farms to the population. Furthermore, more than enough fuel in wholesale and retail storage would survive to provide critical transportation needs for a year.

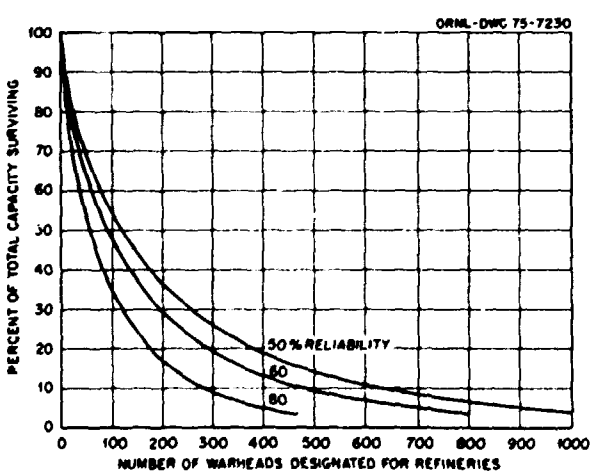

Fig. 17.1. Survival of North American refineries (266 in 1973) as a function of number of warheads and reliability.

Given the above constraints, we believe it is possible to devise a war survival policy that can function within them. The most important elements as we see them are listed below.

1. *Official Sanction for Civil Defense.* There must be recognition at the highest levels of government that in the event of nuclear war, survival of the United States and most of its population is possible and desirable and is the policy of the U.S. government. There must be an end to demoralizing and misleading clichés by high officials about nuclear war being "the end of mankind" or "the end of civilization." This rhetoric, besides misinforming the public, can render ineffective programs to educate the public on the real nature of nuclear war and realistic measures to survive it.

2. *Counter Evacuation Plans.* Crisis Relocation Planning (CRP) for all potential target areas should be developed as expeditiously as possible. A more vigorous effort must be made to make these plans deal realistically with the anticipated threat. The plans must include provisions for preparation of fallout shelter with a higher protection factor in host areas, especially in the Northeast, than is currently the practice. Plans must also be made for the accumulation of food reserves in the host areas early in the crisis. More emphasis than now given must be put on water storage, shelter ventilation, and other vital survival details.

The plans must be exercised by the officials involved. Experience with hurricanes has demonstrated that smooth evacuations are possible with untrained civilians if the responsible official organizations are well trained.

3. *Public Education.* The American people must eventually be exposed to the facts about nuclear war and its survival rather than to demoralizing clichés. A good vehicle for this education process may be a high school course using as a text an American version of a Soviet civil defense manual.

4. *Damage-Limiting Roles for Bombers and Minuteman.* General Keegan,[7] among others, has pointed out that the possibility exists that the Soviets could in a few days reload their "cold-boost" or "pop-up" launchers for the SS-17, -18, and -19 missiles. This refire capa-

12. C. V. Chester and R. O. Chester, "Civil Defense Implications of the U.S. Nuclear Power Industry During a Large Nuclear War in the Year 2,000," *Nucl. Technol.* 31, 326 (1976).

13. "PONAST II's Survival Blueprint," *Survive* 8, 8 (1975).

bility would enable the Soviets to continue strategic bombardment long after American missile-delivered capacity for retaliation is exhausted. If the practice by the Soviet Union with some of its older systems of providing four reloads per launcher is followed, significant casualties could be produced from weapon effects even in a population that is dispersed and dug in. However, the most severe threat would be to efforts to resupply the Northeast's population with food. One or two hundred large-yield weapons ground-burst every few days to renew fallout would terribly complicate this effort. In four to six weeks, tens of millions of additional fatalities could be produced by starvation.

The B-1 bomber would have had the necessary payload and accuracy to destroy Soviet silos. It was designed to continue operations during a nuclear war. About 100 second sorties by surviving aircraft could, in theory, have carried enough weapons to attack all Soviet silos. The number required for destruction would have depended on, among other things, the degree to which air defenses have been suppressed by the attack. Presumably, the Cruise missile will be able to carry out this mission.

Inexorable increases in accuracy will eventually permit the silo destruction mission to be assigned to Minuteman. This action might be appropriate if corresponding increases in Soviet accuracy require that a launch-on-warning doctrine be adopted for Minuteman. Launch-on-warning tends to destabilize crises, but not as much if only counterforce targets are assigned to these forces.

If both sides develop forces with a high silo-kill probability, and adopt launch-on-warning firing doctrines and exclusively counter-silo targeting, the two forces effectively cancel each other. It may then be possible logically to dispose of them with arms control agreements.

5. *Air Defense.* To limit the payload which can be delivered by bomber, an air defense system should be reinstituted if the Soviets continue to deploy the Backfire bomber. The reasoning is the same as for the destruction of cold-launch silos discussed above. The principal characteristics of such defense, in addition to effectiveness, should be mobility and concealability to prevent its destruction by intercontinental ballistic missiles.

6. *Demilitarize Cities.* Present policies encouraging population and industry to relocate outside cities should be continued. New industrial plants that manufacture items or material used by the military or that are essential to national survival should be especially strongly encouraged to build away from cities.

7. *Disperse Industry.* Where possible, new or relocating industry should be encouraged to build away from other targets, including cities and other industrial concentrations. Special attention should be given to development of the synthetic fuel industry. Every effort should be made to keep the production plants and refineries as small as practicable and widely dispersed over the coal and oil shale mining areas. This policy will minimize transportation costs of the raw materials at some increase in cost of the transportation of the product. The objective should be to have several hundred separate plants capable of producing automotive fuel when this industry is fully developed.

8. *"Slanted" New Construction.* Government funded, financed, or insured new construction should be "slanted" or slightly modified to provide fallout protection and, where appropriate, blast protection. Although much good research work has been done in slanting, the development of new building materials and techniques and the new incentives for energy conservation will require that much additional research and development be done in this area. In particular, the growth in popularity for energy conservation of berned, semiburied, hillside, or "Terraset" construction is particularly congenial to protective construction. The development of an inventory of this type of shelter should be regarded as a very long range program to last 50 years or more.

CONCLUSION

The elements of the war-survival policy presented above cannot in themselves ensure national survival in nuclear war. The indispensable element, and the one that cannot be created by legislation or administrative fiat, is morale. Morale for the will to survive is necessary on the part of both the citizens and the national leadership. However, historical experience has shown that crises usually bring forth natural leaders if the existing leadership is inadequate. The measures listed above should help counter the present demoralizing myths about nuclear war. The pervasiveness of these myths in the West, and their absence in the Soviet Union, provide temptation on the part of our adversaries to use the threat of nuclear war to gain their aims of foreign policy. This temptation could lead, to use General Keegan's words, to "a scenario of *inadvertence* and *miscalculation* – the basic mode of entry into all our previous wars."[14]

14. G. J. Keegan, Jr., "An Editorial in the Form of a Letter," *Strategic Rev.* 5, 10 (1977).

18. Foreign Civil Defense Studies

R. N. Thurmer

For many years, we have continually reported civil defense preparations in foreign countries, only to have our observations passed over lightly as "possibly so – but probably only paper plans." Now, it would seem, the Soviet Union's civil defense program has finally been "discovered," and, as a result, civil defense for the United States is being discussed openly. The sheltering facilities in Soviet cities, rural areas, and industrial sites have been recognized to be just exactly what the Soviets have been telling us they were. The training of school children and the nonworking public has been carried on, the organization of civil defense units at national economic enterprises has advanced, and specialization has improved gradually. Dispersal of industry and new residential areas is being adhered to as was ordered years ago. Storage facilities for 20 million tons of grain were built during the ninth 5-year-plan period, and the tenth 5-year plan calls for the construction of additional "elevators and other grain storage facilities with the overall capacity of 30 million tons."[1] Many knowledgeable people in the U.S. military and intelligence fields have, in recent months, publicized the very real accomplishments achieved by the years of "paper planning" in the U.S.S.R.

The Soviets have reacted typically to the U.S. awakening. Their first approach was to treat the possibility of protection for Americans as a joke. An oversight hearing on civil defense which was held in Washington, D.C., in mid-1976 was described in the Soviet press as a meeting of "moles on Capitol Hill."[2] These "unpopular pests" were described as wanting to put Americans "underground," or "on a train to evacuation areas" – neither of which appealed to the American people who "love to live under the clear blue sky." Members of our section participated in this particular hearing, which was also attended by Soviet representatives.

The Soviet media moved from the joking, fun-making tactic to a more determined attitude which took the stand that Soviet civil defense was no "big deal" militarily. It was a humanitarian gesture and posed no "threat" to anyone. Of course, the fact that the United States still was (and is) adhering to the "mutual assured destruction" (*MAD*) doctrine (*the idea of unprotected* civilians on both sides serving as a mutual deterrent) was never mentioned. It was natural for the Soviet people, but foolish for Americans, to be protected.

As more and more information about Soviet shelter construction, evacuation, residential and industrial dispersal into less populated areas, and construction of huge grain storage facilities has been confirmed, the reaction of the Soviets has taken an even more serious turn.

Their attitude changed again to one of trying to discredit anyone who advocates equal protection for the U.S. population. Such persons are called pseudo-scientists, hawks, dilettantes, tools of the military-industrial complex, or any other unflattering title that would cast doubt on the validity of their statements.[3]

The Soviets are continuing along the path of perfecting their own civil defense and, as usual, they tell the world about it. A. Altunin, head of U.S.S.R. civil defense, stated in his annual report[4] on the program prior to the beginning of the 1977 Soviet training year:

". . . Civil Defense of the USSR, in pursuing the only human goal – the organization of the defense of our Soviet people and the national economy against contemporary weapons despite the hostile voices of international reaction and while aggressive military blocs of

1. Moscow Domestic Service in Russian, 1910 GMT, Jan. 7, 1977, as reported in *Daily Report, Soviet Union*, FBIS-SOV-77-9, Jan. 13, 1977, vol. III, No. 9, pp. T1–3.

2. S. Vishnevskiy, "Trouble with Moles," Moscow *PRAVDA* in Russian, July 11, 1976, p. 5.

3. V. Petrov, "Who Needs the Provocative Hullabaloo?" Moscow *KRASNAYA ZVEZDA* in Russian, Jan. 21, 1977, p. 3, as reported in *Daily Report, Soviet Union*, FBIS-SOV-77-21, vol. III, No. 15, pp. B11–14.

4. A. Altunin, "Main Direction," Moscow *VOYENNYYE ZNANIYA* in Russian, No. 10, October 1976, pp. 4–5.

imperialism exist – will become even stronger in the future in the name of this noble goal."

Following this firm promise by the head of U.S.S.R. civil defense, a broadcast[5] from Radio Moscow reported that the huge Soviet civil defense program does not even exist.

"Even Secretary of Defense–designate Harold Brown, when interviewed on this subject (Soviet civil defense), said there was little reason to believe such a program, *if it indeed existed* [emphasis added], would in fact confer a significant advantage in the event of a nuclear war. The future defense secretary is understandably cautious in his assessment, for he says 'if such a program indeed exists,' *in reality he knows it doesn't*" [emphasis added].

Possibly the most unusual development in the continuing saga is reported in a recent article[6] by J. Howard Proctor, former president of the U.S. Civil Defense Council. Much to the surprise of his group which visited the Soviet Union for the express purpose of checking Soviet civil defense, the group was told that the activity was indeed very real. The government officials informed the visitors quite candidly that the U.S.S.R. civil defense budget is "around one billion rubles." As far as we can determine, that was the first time anyone had been given actual figures on the level of Soviet spending for civil defense. The Soviets readily admitted the existence of their shelters: "Why not? Shelters *protect* people, *protect* resources. Civil defense is basic and natural – a humane necessity. Why don't Americans understand this? Puzzling, these Americans." The Soviets who were contacted by Proctor's group stated, "We want peace because we know first-hand the utter tragedy of war."

Perhaps this attitude of the Soviet people is the reason behind the constant emphasis placed on detente by the Soviet leaders; however, here again, when talking to their fellow communists, they "tell it like it is."[7]

"It was once again declared . . . that detente by no means signifies the social and political status quo. It creates more favorable conditions for the success of movements for democratic and socialist transformation in capitalist countries. . . ."

The Soviets have indeed led the way in preparing their country for civil defense, but they are not alone in the effort. The Chinese, we know, have excellent tunnel networks under their cities. They devote a vast amount of time and care to the training of their children. Both aspects have been observed by many people over the years, but U.S. Congressman G. W. Whitehurst[8] visited China in 1976 and described them in shockingly vivid detail – especially the fact that a little 12-year-old Chinese girl conducted the briefing for his group, and that an 8-year-old girl participated in an exercise, shouldering an SKS semiautomatic rifle. Just this past spring (Mar. 5–10, 1977), the Kweichow Province held a conference on civil defense,[9] at which the participants pledged increased efforts.

". . . They discussed and studied professional issues such as planning and management of civil defense projects, made arrangements and worked out this year's tasks for civil defense preparedness against war.

"Conference participants unanimously pledged: In the excellent situation at home and abroad, we must heighten our vigilance a hundredfold and must absolutely not forget that tigers and wolves lie in our path."

Switzerland, which has already attained protection for four-fifths of its population, continues its civil defense program at an annual cost of $72,680,000. This spending rate amounts to 1.4% of the total Swiss budget[10] and will make realization of Switzerland's final objectives possible "sometime between 1990 and 2000." According to ref. 10, this small European country's excellent civil defense situation has been accomplished by an investment of $11.18 per capita per year, whereas the United States spends less than 50¢ per capita per year.

It is reported that Yugoslavia is devoting a great deal of attention to civil defense.[11]

"According to Colonel Ivan Dolnicar, assistant secretary for national defense, 500,000 Yugoslav women are now members of the civil defense corps . . . Yugoslav women and girls in particular not only have worked hard in civil defense but are well prepared for armed struggle."

---

5. V. Pozner's Radio Moscow broadcast in English to North America, Jan. 6, 1977, as reported in *Daily Report, Soviet Union*, FBIS-SOV-77-5, Jan. 7, 1977, vol. III, No. 5, p. B4.

6. J. H. Proctor, "Five Days in Russia," *J. Civ. Def.* 10(3), 2 (1977).

7. Yu. Solodukhin, "Community of Aims, Unity of Action," Moscow *MEZHDUNARODNAYA ZHIZN* in Russian, No. 2, signed to press Jan. 19, 1977, pp. 3–13.

8. G. W. Whitehurst, "Impressions of China," *J. Civ. Def.* 10(1), 2 (1977).

9. Kweiyang Kweichow Provincial Service in Mandarin 1100 GMT, Mar. 12, 1977, as reported in *Daily Report, People's Republic of China*, FBIS-SOV-77-49, Mar. 14, 1977, vol. I, No. 49, p. J1.

10. "Where are We? – A Swiss Appraisal," *J. Civ. Def.* 10(3), 7 (1977).

11. Peking *NCNA* in English 1602 GMT, Mar. 7, 1977, dateline Belgrade, as reported in *Daily Report, People's Republic of China*, FBIS-CHI-77-46, Mar. 9, 1977, vol. I, No. 46, p. A8–9.

The reason for Yugoslavia's concern for civil defense preparations is given by the Chairman of the Committee of All-People Defense and Social Self-Defense, Gen. Ivan Kuboc, in an interview with the Yugoslav *Weekly News:*[12]

"General Kuboc . . . dwelt on the bearing which the Soviet invasion of Czechoslovakia in 1968 had on the formation of the Yugoslav concept of all-people defense. He said: It is exactly the military and political reality at that time which prompted the contemplation of, search for, and emergence of such a concept. . . . We rule out surrender in any case."

The countries discussed above are not the only ones that have begun to face the problem of providing civil defense for their population and industry. Our section members have contributed to the effort to bring these worldwide activities to the attention of the public as well as our nation's decision makers and government and military leaders. Field testing and improvement of various shelter concepts and the perfecting of many survival techniques have resulted from research of foreign civil defense activities. Many reports, open literature publications, briefings, television presentations, etc. have emanated from our group, and it is hoped that they have contributed to the present awareness of the need to look seriously at what other nations are doing in the civil defense field.

Much remains to be done, but the increased amount of publicity now being given U.S. civil defense (or the lack of it) will bring about at least some hope for America's people being offered a program fairly comparable to those of other nations of the world.

---

12. Peking *NCNA* in English 1751 GMT, Mar. 16, 1977, dateline Belgrade, as reported in *Daily Report, People's Republic of China,* FBIS-CHI-77-52, Mar. 17, 1977, vol. I, No. 52, p. A6.

19. Blast Tests of Expedient Shelters in the DICE THROW Event

C. H. Kearny

In 1973, the Oak Ridge National Laboratory (ORNL) participated in Defense Nuclear Agency's (DNA's) MIXED COMPANY event. This test subjected expedient shelters of various designs to the blast from an explosion of 500 tons of TNT. All the ORNL expedient shelters incurred little or no damage.[1] As a result, it was decided that the most promising designs should be subjected to blast effects severe enough to indicate the worst blasts that these shelters are capable of withstanding. Therefore, ORNL participated in the main event of DNA's recent DICE THROW series, a 630-ton ANFO (ammonium nitrate–fuel oil) explosion, producing airblast effects about equivalent to a 1-kiloton nuclear surface burst. This shot was detonated on October 6, 1976, at White Sands Missile Range, New Mexico. Eighteen expedient shelters (including four half-scale models) were subjected to the blast effects at overpressures ranging from 53 to 5.8 psi, and expedient life-support equipment (mostly placed inside shelters) was exposed to overpressures of 53 to 1 psi. Several one-tenth-scale models of shelters were also tested, at overpressures of up to 180 psi.

PRINCIPAL OBJECTIVES

The principal objectives of ORNL's participation in DICE THROW were (1) to obtain field data useful in making more reliable estimates about the ability of promising expedient shelters and expedient life-support equipment to withstand all blast effects from large explosions, and (2) to observe the relative effectiveness of several different ways of using earth arching and trench-wall shoring to increase the blast protection afforded by lightly constructed shelters, in order to develop improved shelter designs.

INSTRUMENTATION USED AND TEST DATA RECOVERED

Blast overpressures were measured by yielding foil membrane blast gauges.[2] These passive gauges, developed at ORNL, performed well at the lower overpressures (less than 7 psi). However, the ORNL gauges that were installed adjacent to principal shelters to measure overpressures above 7 psi all recorded overpressures 28% to 60% higher than those recorded by the transducers at the same radial distances from ground zero on DNA's adjacent gauge line 1. Therefore, we used DNA's measurements for all the aboveground overpressures to which the ORNL shelters were subjected.

The ORNL pressure gauges inside the shelters recorded low overpressures. All these gauges functioned well, except those inside the shelters at the 31-psi overpressure. All were recovered, and the data are used in this report.

Elastic and permanent deformations of the roofs and some other parts of the shelters were measured by passive mechanical devices. Over 90% of these functioned effectively. Linear measurements of distances between parts of a shelter were taken before and after the blast.

Blast-wind scouring of the earth mounded over shelters and around entryways was determined by driving 12-in. steel spikes into the earth until their heads were flush with the ground and measuring their exposures after the blast. (The duration of blast winds is proportional to the cube root of weapon yield;[3] thus the depth of scouring by larger weapons can be estimated.) Preblast and postblast depths of earth over and around shelters were also recorded.

Blast damage to all structural parts of shelters and to the earth walls of unshored shelters and of water-storage pits was determined primarily by observation. Numerous photographs were taken, both before and after the

1. C. H. Kearny and C. V. Chester, *Blast Tests of Expedient Shelters*, ORNL-4905 (January 1974).

2. R. W. Manweiler, C. V. Chester, and C. H. Kearny, *Measurement of Shock Overpressure in Air by a Yielding Foil Membrane Blast Gauge*, ORNL-4868 (September 1973).

3. U.S. Atomic Energy Commission, *The Effects of Nuclear Weapons*, Samuel Glasstone, ed., U.S. Government Printing Office, Washington, D.C., April 1962.

blast, to record blast damage – the most important part of the test data.

SUMMARIES OF THE MOST SIGNIFICANT TESTS

Small-Pole Shelter at 53 psi

The main room and the horizontal part of the entryway at the east end were of unmodified Russian design,[4,5] except that the excavation in the hard caliche was made 2 ft deeper than the final level of the shelter floor. Then this bottom 2 ft was backfilled with dry, sandy earth. This soft earth under the wall poles permitted them to be pushed down sufficiently under blast loading to throw most of the loading onto the resultant earth arch that blast overpressure sets up over a yielding structure.

A previous ORNL analysis[6] of the survivability of this shelter indicated that without the protection of earth arching it would withstand an overpressure from a 200-kiloton weapon of about 15 psi with blast doors closed. The analysis assumed the use of green hardwood poles, the strengths of which were determined in the ORNL materials laboratory. The roof poles and wall poles of all the ORNL pole shelters in DICE THROW were ponderosa pine. In this shelter, the poles averaged about 5 in. in diameter, including their bark. The shelter room was 10½ ft long (Fig. 19.1).

The horizontal part of the entryway at the south end was only 4½ ft in height, with its floor 2½ ft above the floor of the main room and the east entryway.[4,5] This height proved adequate, and the stoop-in entryway required significantly less material and labor to build than did the Russian-type horizontal entryway with 6 ft of headroom. The Russian small-pole shelter has only a small chimney-like air duct at one end; ORNL tests had proved that this small air duct would provide such inadequate ventilation that fatalities could result from excessive heat and humidity in warm or hot weather after a day of full occupancy. The vertical entryways were of ORNL design,[5] as shown in Fig. 19.1, except that they extended 5 ft above the ceilings of the horizontal entryways. The Russian inclined stairway entrance had been found to be weak and not suitable for the installation of a blast door.

The roof poles of this boxlike shelter were at ground level. To provide adequate shielding against the initial

4. P. T. Egorov, I. A. Shyakhov, and N. I. Alabin, *Civil Defense, Moscow, 1970*, ORNL/TR-2793 (December 1973).

5. G. A. Cristy and C. H. Kearny, *Expedient Shelter Handbook*, ORNL-4941 (August 1974).

6. C. V. Chester and R. O. Chester, "Analysis of Effects of Nuclear Weapons Overpressures on Hasty Pole Shelters," *Civil Defense Research Project Annu. Prog. Rep., March 1971–March 1972*, ORNL-4784 (December 1972).

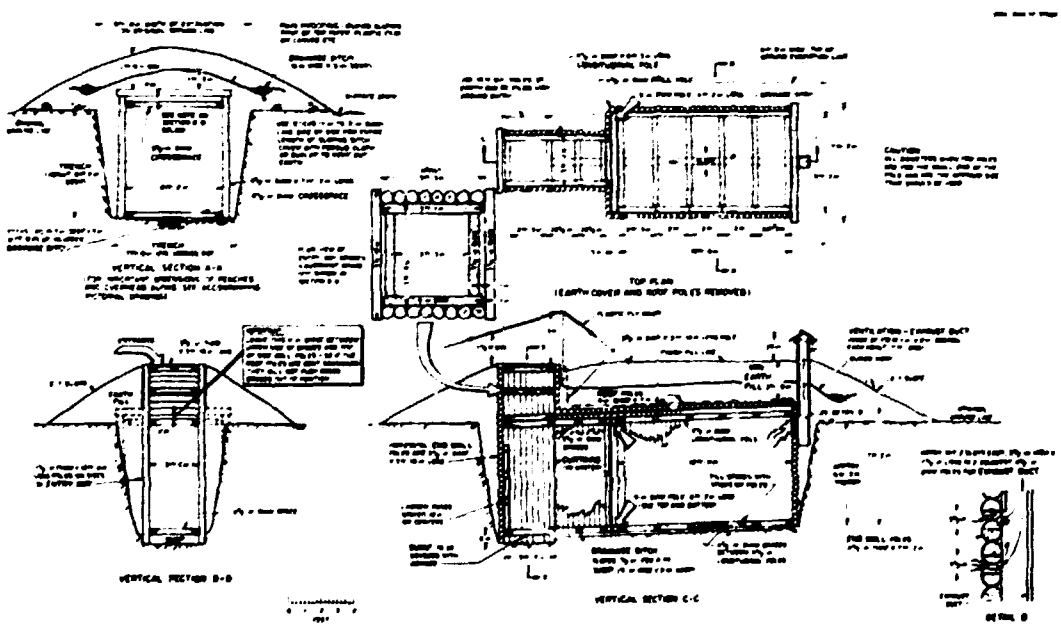

Fig. 19.1. Small-pole shelter.

nuclear radiation to be expected at the approximately 50-psi overpressure from smaller nuclear weapons, the roofs of the shelter room and its entryways were covered with 5 ft of mounded earth.

The need for blast doors on family shelters has long been recognized.[7,8] ORNL blast tests[1] had demonstrated the effectiveness of expedient blast doors at overpressures of up to 29 psi; and since the present Soviet nuclear arsenal could subject over half of all Americans, if in their normal areas, to serious blast dangers, we included three new designs of expedient blast doors in our DICE THROW tests.

Both entrances of the small-pole shelter were protected by expedient blast doors, each measuring 48 by 42 in. and each made of five thicknesses of ¾-in. exterior plywood. The plywood sheets were glued with waterproof resin and nailed from both sides. Expedient hinges made of strips cut from the worn treads of automobile tires were nailed to the door and to vertical poles of the entry (Fig. 19.2).

After seeing the bright light from a nuclear explosion, an alert shelter occupant can close and secure this type of door within 4 sec – shorter than the time of arrival of the airblast shock wave from an 8-megaton or larger weapon at 20 psi or less overpressure, but not fast enough at 53 psi. Therefore, this shelter should have been equipped with expedient blast valves of the tire-strip type previously blast-tested without being damaged at 65 psi.[1]

Each blast door was surrounded with blast-protector logs which were notched and spiked together. These logs (about 8 in. in diameter and 8 ft long) were placed with their upper sides about 2 in. higher than the top of the closed blast door. Figure 19.3 shows the four blast-protector logs around the north door after the blast. This explosion produced a peak overpressure of about 53 psi and a peak blast-wind velocity of about 1000 mph at this range of 540 ft from ground zero.

Fig. 19.2. Nailing tire-strip hinges to expedient blast door tested at 53 psi overpressure.

Fig. 19.3. Blast-protector logs around blast door after being moved by blast effects at 53 psi overpressure.

Figure 19.3 shows the door after the blast winds had blown away most of the dry earth previously piled around the blast-protector logs and after the force of the shock wave and the dynamic drag effects had shifted these four connected logs from their original positions. In its pictured final position, the log nearest ground zero was so close to the hinges that the door could be opened from the inside only to an inclination of about 60°.

If this door and its protector logs had been subjected to the same overpressure from a large surface burst, dynamic drag and blast-wind effects of much longer duration would have been produced, and the door would have been jammed closed by the shifted logs. If long, strong stakes had been driven prior to the blast to secure the logs, their movement would have been re-

7. Archie P. Flynn, *Operation Buster*, WT-359, Federal Civil Defense Administration, Washington, D.C., March 1952.

8. Joseph B. Byrnes, *Effects of an Atomic Explosion on Underground and Basement Types of Home Shelters*, WT-801, Federal Civil Defense Administration, Washington, D.C., October 1953.

duced. However, for blast protection against nuclear weapons this whole shelter should have been positioned deep enough in the earth so that its blast doors would have been only a few inches above ground level, with the earth surrounding the blast-protector logs sloped up around them at an angle of less than 10°.

About 12 in. of the mounded dry earth was blown away from around the protector logs of the small-pole shelter at 53 psi. Blast-wind scouring was serious at much lower overpressures. For example, at 15 psi the blast winds scoured away up to 7 in. of dry shielding soil which was placed in a narrow-topped mound over the ridge-pole shelter built entirely above ground. This shelter was built at a right angle to the direction of the blast winds. Scouring was up to 17 in. deep around some rigid obstructions (such as the inadequately protected vertical entryway of the covered-trench shelter at 31 psi), due to the formation of violent turbulence where the direction of airflow changes abruptly. Similar disastrous blast-wind erosion (as regards the postblast fallout protection afforded by shelters) was observed in nuclear blast tests of small family shelters covered with dry desert soil in Nevada.[7,8] In contrast, negligible blast-wind scouring of steeply mounded wet, sandy earth over shelters resulted from the 500-ton MIXED COMPANY explosion, at overpressures of up to 29 psi.

The small-pole shelter was essentially undamaged by the blast effects at 53 psi overpressure (Fig. 19.4). However, occupants would have been injured if they had been standing with their heads close to the ceiling, which was rapidly depressed when pressure on the roof poles caused the wall poles to be punched down into the soft, backfilled earth supporting them. This downward movement of the roof and walls varied from a minimum of 2 in. in the southwest corner to a maximum of 6¼ in. in the northeast corner. Figure 19.5 shows the movement at the center of the room, where the upper part of the shelter was moved 4½ in. away from ground zero and 4½ in. downward, relative to the "fixed" vertical post to which the lower part of the damaged deflection gauge was attached. Furthermore, about 15% of the floor area "puffed up" from 2 to 8 in. above its original elevation, due to rapid earth flow.

Figure 19.6 shows how the floor puffed up about 6 in. in the northeast corner of the shelter and in the east entryway; earth pressure had caused some earth to "flow" up into the closed room. The floor in front of the man's hand resting on the cross-brace was not disturbed. Neither the blast gauge resting on the brace pole in the corner nor the small expedient fallout meter on top of it was moved.

If a person had been standing on the floor when it was puffed up, his legs could have been injured. To prevent

Fig. 19.4. Small-pole shelter after being tested at 53 psi overpressure with blast doors closed. Note the slightly damaged expedient shelter-ventilating pump in the stoop-in doorway. Two men worked about 5 min to replace the four blown-loose flaps, the only damage.

Fig. 19.5. Movement of upper part of small-pole shelter due to blast effects at 53 psi overpressure.

Fig. 19.6. "Puffed-up" part of the floor of small-pole shelter at 53 psi overpressure.

possible injuries due to an intact ceiling moving very rapidly downward and/or the floor moving upward, occupants could recline in expedient sheet hammocks[9] slung from the upper horizontal brace poles of the main shelter room (Fig. 19.7).

The whole roof, the upper horizontal braces, and the upper ends of the wall poles were all displaced about 4¼ in. to the west (away from ground zero) by the blast effects on the 5-ft-high mound of shielding earth over this shelter. The sides of this mound sloped about 36°; its width on top averaged about 10 ft. (If the mound had been subjected to the blast effects of a large nuclear weapon at the same 53 psi overpressure, the much greater impulse probably would have caused the earth mound to be displaced so far as to wreck the underlying pole shelter. Even wet earth, which is less vulnerable to long-duration blast-wind scouring, probably would have been displaced so far as to cause disastrous structural damage.)

The maximum overpressure measured inside the shelter was 1.5 psi – not enough to be harmful. Less than half this pressure increase was due to the sudden reduction in the volume of the shelter room described above. The rest was caused by blast wind that blew through cracks between the poles near the top of the vertical entryways. These cracks appeared after the initial blast wind had scoured away the covering earth and torn away the polyethylene film which, with the essential help of small-scale earth arching, had kept earth from being forced between the cracks by the peak overpressure.

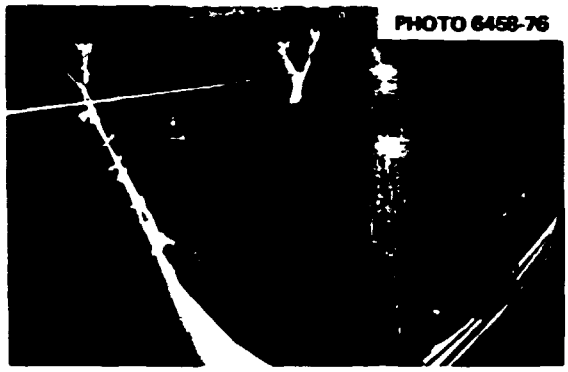

Fig. 19.7. Expedient sheet hammock, useful to avoid severe shock effects in a shelter at high overpressures. The man is operating an expedient shelter-ventilating pump via an expedient pulley-equivalent, a forked stick suspended on strings.

There was no damage to any of the life-support equipment in this shelter, except for the expedient shelter-ventilating pump pictured in Fig. 19.4. The damaged ventilating pump was the Kearny air pump (KAP).[10] The expedient water storage was unaffected by the blast. (The shock-resistant water-storage container consisted of two 30-gal polyethylene trash bags used as a waterproof liner inside a smaller burlap potato bag. After about 10 gal of water was placed inside, both bags were closed with a ¼-in. rope tied around the burlap bag near its mouth. One end of this rope was then tied to a large nail driven into a wall post to keep the water bags in an upright position.)

Unmodified Russian Pole-Covered Trench Shelters

To make a more accurate estimate of the blast protection afforded occupants of a common type of Russian expedient shelter ("dugout") designed to be built in stable earth, two identical Russian pole-covered trench

9. C. H. Kearny, *Expedient Shelter Construction and Occupancy Experiments*, ORNL-5039 (March 1976).

10. C. H. Kearny, *How to Make and Use a Homemade, Large-Volume, Efficient Shelter-Ventilating Pump, the Kearny Air Pump*, ORNL/TM-3916 (August 1972).

shelters were tested at 6.7 and 20 psi overpressures. The unmodified shelters were of the design detailed in the 1969 Soviet civil defense handbook,[11] except that the entrance stairways were at right angles to their lengths, a modification recommended in both the 1972[12] and a 1976 Russian shelter building manual.[13] Figure 19.8 gives the details of this simple fallout shelter. Figure 19.9 shows most of the roof poles in position before the shelter was covered with 4-mil polyethylene and earth mounded 30 in. deep. A total of 62 lodgepole pine poles, each 7 ft long, were laid across the 31-ft trench (not including the right-angle entry stairway shown in the foreground of Fig. 19.9).

A Soviet civil defense handbook[4] states that within "the zone of complete destruction" the overpressure exceeds 0.5 kg/cm^2 (~7 psi) and that all residential and industrial buildings and all fallout shelters will be destroyed. Therefore, one of these shelters was built at the forecast 7 psi overpressure (6.7 psi was measured). Because of the almost rocklike caliche earth, an identical shelter was built at 20 psi overpressure to see if occupants might survive more severe blast effects than those at 7 psi. Neither shelter had a blast door. In the shelter at 20 psi, two anthropomorphic dummies (supplied by the Lovelace Foundation) were seated side by side just inside the inner curtain (Figs. 19.8 and 19.10). A movie camera was installed by Denver Research Institute for the U.S. Army's Ballistic Research Laboratory. This camera was farther inside the shelter, mounted on a post concreted in the ground. The camera took 400 frames/sec; the four photographs in Fig. 19.10 were taken in $^1/_{100}$ sec. The first photograph shows only a slight movement of the inner blanket curtain. The second shows the earth walls beginning to crumble under the forces of a ground shock wave, before the airborne shock wave reached the walls or the dummies. The third and fourth photographs show the inner blanket curtain being torn, revealing the torn outer, darker curtain being blown behind and against the

Fig. 19.9. Poles covering Russian pole-covered trench shelter at 20 psi overpressure.

11. N. I. Akimovetal et al., *Civil Defense, Moscow 1969*, ORNL/TR-2306, J. S. Gailar and C. H. Kearny, eds. (April 1971).

12. V. I. Molodykhetal et al., *Antiradiation Shelters in Rural Areas, Moscow 1972*, ORNL/TR-2745, C. H. Kearny and J. S. Gailar, eds. (October 1973).

13. G. K. Kotlukov et al., *Civil Defense, Moscow 1976*, translated by Defense Civil Preparedness Agency, 1977 (unpublished).

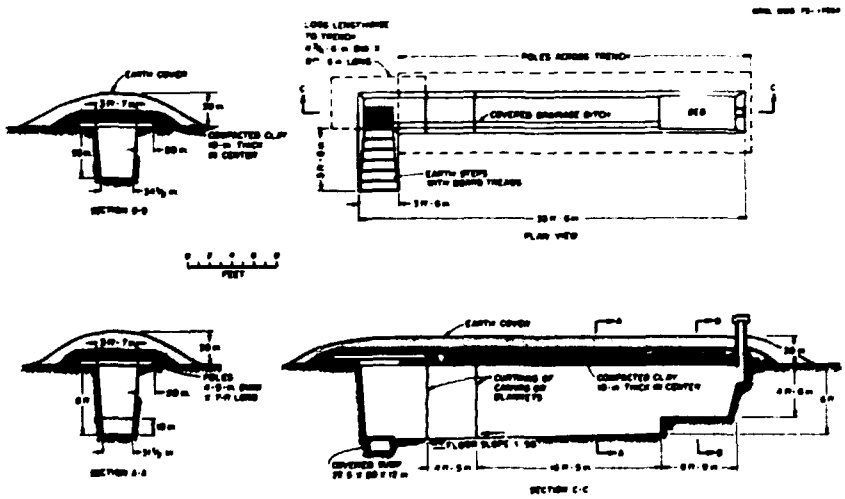

Fig. 19.8. Russian pole-covered trench shelter in stable earth.

Fig. 19.10. Dummies being struck by airblast and curtains traveling about 180 mph. Note the walls collapsing under ground-shock stresses before the arrival of the airborne shock wave.

inner. The collapsing walls trapped the two dummies before the entering blast wind, which had a calculated velocity of about 180 mph, could blow them over. (A blast wind peaking at about 470 mph blew outside this shelter.)

Figure 19.11 shows the dummies trapped by the collapsed walls. Because of the way in which their strong steel joints were constructed, the collapsing walls did not bend them forward, knock them down, and bury them, as would have been the fate of two men. Note the unbroken roof poles.

The peak overpressure inside this shelter was 7 psi – high enough to burst eardrums. (If this shelter had been subjected to the blast effects of a megaton weapon at 20 psi, the maximum overpressure inside the shelter would have been almost 20 psi.)

The entry was wrecked, and much of its covering earth was blown away (Fig. 19.12). The ventilation duct was broken off.

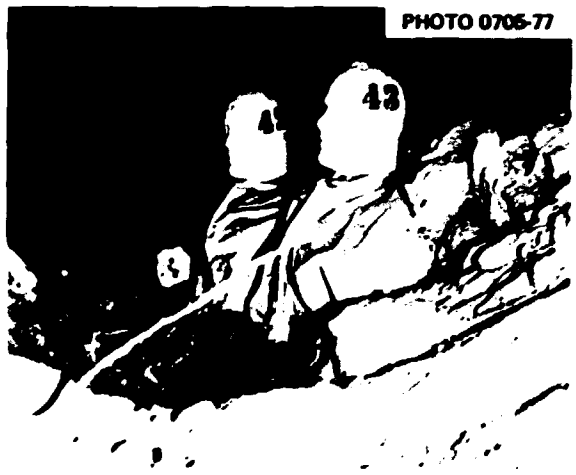

Fig. 19.11. Dummies at 20 psi overpressure after ground-shock collapsed earth walls of shelter. Their steel "bones" prevented them from being knocked down and buried.

Fig. 19.12. Wrecked entry of Russian pole-covered trench shelter at 20 psi.

At 6.7 psi, an identical shelter suffered serious damage. Chunks of hard caliche weighing up to about 100 lb were broken off the stable earth walls and would have injured shelter occupants. A dummy seated on a fixed bench next to the blanket curtains was knocked off the bench by the shock wave and the entering blast winds (Fig. 19.13). In soils typical of most inhabited areas, if a shelter of this design were subjected (at 7 psi overpressure) to the blast effects of a much larger explosion, the Russian estimate of "total destruction" would probably be proved realistic.

Fig. 19.13. Dummy knocked off bench in Russian pole-covered trench shelter at 6.7 psi overpressure.

Log-Covered Trench Shelters

Full-scale log-covered trench shelter at 53 psi. This shelter was built with half its 12-ft-long room having roof poles positioned at ground level in the Russian manner (Figs. 19.8, 19.9, and 19.14). The other half of the room had roof poles positioned in a recommended Chinese manner[14] (i.e., 28 in. below ground level). Figure 19.14 shows the vertical cross sections of these two halves as modified from the original designs to permit a better comparison between the merits of the two different ways of positioning roof poles. (The room of the Russian half was made 16 in. less in height than in the original design, and the Chinese half was made 4 in. less in width than specified in the Chinese handbook.[14])

The Chinese half (Fig. 19.14) was built with the roof poles resting on earth shelves 28 in. below ground level, cut into the hard caliche. The ponderosa pine poles averaged about 5 in. in diameter, not including their bark. All were cut 7 ft long. Earth was mounded about 5 ft above ground level over the whole shelter. This resulted in about 4½ ft of earth covering the roof logs of the Russian half and about 6 ft covering the roof logs of the Chinese half. Blast-wind scouring removed about 1 ft of the mounded earth.

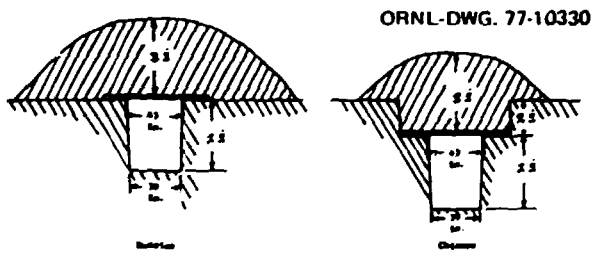

Fig. 19.14. Comparison of Russian and Chinese ways of positioning poles to roof a trench shelter.

The vertical parts of the two entries to the shelter were of a newly developed design with triangular cross sections. The expedient blast doors were of a new triangular type. This design (Fig. 19.15) was developed to (1) use green poles cut from ordinary trees to make a tight-closing expedient blast door which takes advantage of the fact that three intersecting straight lines deter-

14. C. V. Chester and C. H. Kearny, eds., *Chinese Civil Defense*, ORNL/TR-4171 (to be published).

Fig. 19.15. Expedient triangular blast door made of pine poles. The automobile-tire flap valves over the 1½-in.-wide spaces between the poles were undamaged by the blast effects at 53 psi overpressure.

mine a plane, (2) require only widely available hand tools and common materials (e.g., auto tires, nails, and some wire or rope, in addition to poles), and (3) make practical the use of a triangular vertical shelter entry, which has a smaller cross-sectional area than does a rectangular vertical entry big enough for the same-sized person to use and shows promise of requiring less materials to meet a given level of blast protection.

Figure 19.15 shows the triangular blast door on the south end of the shelter, undamaged after the blast. Its hinges were made of 18-in.-long strips of worn auto tires, cut and nailed as were the hinges of the plywood blast door of the small-pole shelter. Note that one of the 13 blast-protector logs (the log in the lower left corner of the photograph) was pushed by the blast up against the hinge pole of the blast door. The door was undamaged, but the movement of the earth mound broke the door-seat log on which the man's foot rests.

Under the longer-duration blast effects of a large nuclear explosion, these entries would probably have been wrecked by the combined effects of blast-wind scouring and dynamic drag on the earth mounded over the shelter. The blast doors should have been positioned only a few inches above ground level. Unfortunately, such deeper excavation, even in softer earth, might make construction within 48 hr impractical for builders having only hand tools.

Both the triangular blast doors were undamaged. Their expedient blast valves were closed by the blast and about 80% opened after the blast, permitting adequate ventilation with the KAP. The overpressure inside the Chinese half was 1.5 psi, and the overpressure directly under the north door was 3 psi. Results of this test indicate that the use of expedient blast valves over the 1½-in.-wide cracks of this blast door is impractical. The valves opened before the strong blast afterwinds subsided. These winds, plus the natural desert winds, blew so much dirt and sand through the valves that a serious fallout entry problem would exist after a nuclear blast.

Although not one roof pole of any part of this shelter or any other shelter was broken or cracked, the ground-shock effects collapsed the walls of the Russian half of this shelter so badly (Fig. 19.16) that all occupants would have been killed. Damage to the Chinese half was much less serious, although chunks of caliche weighing up to 20 lb were broken off the edges of the shelves supporting the roof logs. The roof-deflection gauge in the Chinese half recorded a maximum transient downward deflection of 1½ in. and a permanent deflection of ⅞ in.

Half-scale log-covered trench shelter at 53 psi. This shelter was much less damaged than was its full-scale counterpart at the same 53 psi overpressure. Serious wall caving resulted in the Russian half, with roof poles permanently depressed 3¾ in. at the center and sloped. In the Chinese half, the unshored walls were only slightly damaged, although the roof poles were permanently depressed a measured maximum of 2¼ in.

Full-scale log-covered trench shelter at 31 psi. This shelter was constructed the same as the Russian half of

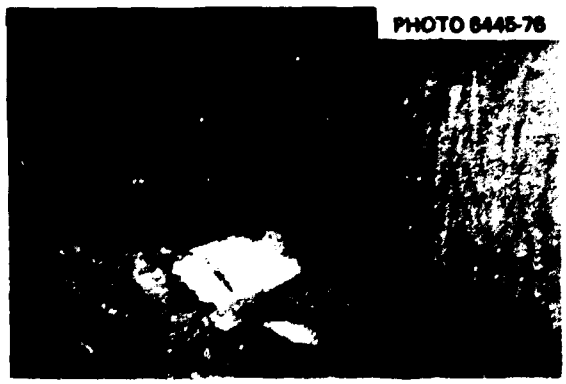

Fig. 19.16. Postshot view of the caved-in caliche walls of the "Russian" half of the log-covered trench shelter at 53 psi.

the log-covered trench shelter at 53 psi, except that it had an expedient blast door made from a 30-gal steel oil drum. Rubber-tire hinges and rubber-tire seals made a snug closure between the door and the upper part of the vertical entry into which it closed. The vertical entry was built of two thicknesses of 2-in. boards nailed together.

Although the blast effects loosened some of the bolts of the steel door, tore the metal in several places, and produced other damage indicating that it was on the verge of failure, it did not fail. The door was made by a part-time welder and requires more time, materials, tools, and skills than do the other two types of expedient blast doors, which were much less damaged under more severe blast conditions. Therefore, this expedient door was judged unsatisfactory and not deserving of further development.

Figure 19.17 shows the shelter interior after the blast. Some occupants would have survived inside this shelter. If built in less stable ground or subjected to the more severe ground-shock effects of a large weapon at this same overpressure (31 psi), this shelter would have been a total loss.

Door-Covered Earth-Roll Shelters

Two of these aboveground, small fallout shelters,[5] made of interior hollow-core doors, sheets, and other materials available in tens of millions of American homes, were tested at 5.8 and 15 psi overpressures.

Figure 19.18 gives details of their construction. Both these shelters were built with their lengths on radii from ground zero. Figure 19.19 shows the interior of the shelter at 15 psi before the explosion. The vertical stick touching a roofing door is a roof-deflection gauge, with its upper end consisting of a thin cylinder of household aluminum foil.

Fig. 19.17. **Serious wall caving.** The beam deflection gauge on top of the post showed a 2½-in. lowering of the center roof log.

Figure 19.20 is a posttest picture of the northward-facing entry of the shelter at 15 psi overpressure. This photograph also shows part of the northward-facing side of the shelter. Blast winds scoured only about 1 in. of earth from the top of this shelter, apparently because its long, flat top extended in the same direction that the blast winds blew. Note the proof of the toughness of polyester-cotton pillowcases used to make 100-lb sandbags. The sandbag in the foreground was blown about 7 ft by the approximately 370-mph blast wind without being broken.

To the surprise of most observers, earth arching above the roof doors prevented them from being broken in by the blast effects. The doors were not broken in, even though the inner ⅛-in. plywood veneers of all the doors (except those over the two entryways) were broken. Figure 19.21 shows the interior of the shelter at 15 psi overpressure after the blast effects outside had caused the sandy soil inside the sheet "earth rolls" to "flow" inward rapidly. The width of the shelter was reduced from 36 in. to a minimum of 14 in. No additional earth movements were observed during the two weeks following this test.

Pressure-time measurements on the adjacent DNA gauge line 1 showed that only about 40 msec elapsed between the peak overpressure of 14.9 psi recorded at the same distance (820 ft) from ground zero and its reduction to 6 psi, the maximum overpressure recorded inside this shelter by the ORNL pressure gauge shown in the foreground of Fig. 19.21. The gauge that had been installed to measure roof deflection was blown away by the entering shock wave and blast wind. The reduction in ceiling height appeared to be less than 1 in. in this part of the shelter, but up to about 4 in. in other parts.

A door-covered earth-roll shelter obviously is impractical for use as a blast-protective shelter against blast effects considerably less than those at 15 psi overpressure from even a very small nuclear weapon.

At 5.8 psi overpressure, the door-covered earth-roll shelter was still habitable for weeks after the test. Figure 19.22 shows that the walls were not forced inward by the blast effects. The bottom ⅛-in. veneer plies held as flexible membranes, and earth arching was set up in time to prevent the roof from being collapsed either as a result of the initial earth loading or of the 5.8-psi blast effects.

The peak overpressure measured inside this shelter was 3 psi, about half the 5.8 psi measured outside on DNA's adjacent gauge line 1. The blast winds, which peaked outside at about 175 mph, scoured away only a fraction of an inch of the shielding earth.

If this fallout shelter with a protection factor of at least 200 had been built in a typical suburb and had

ORNL-DWG. 74-8132

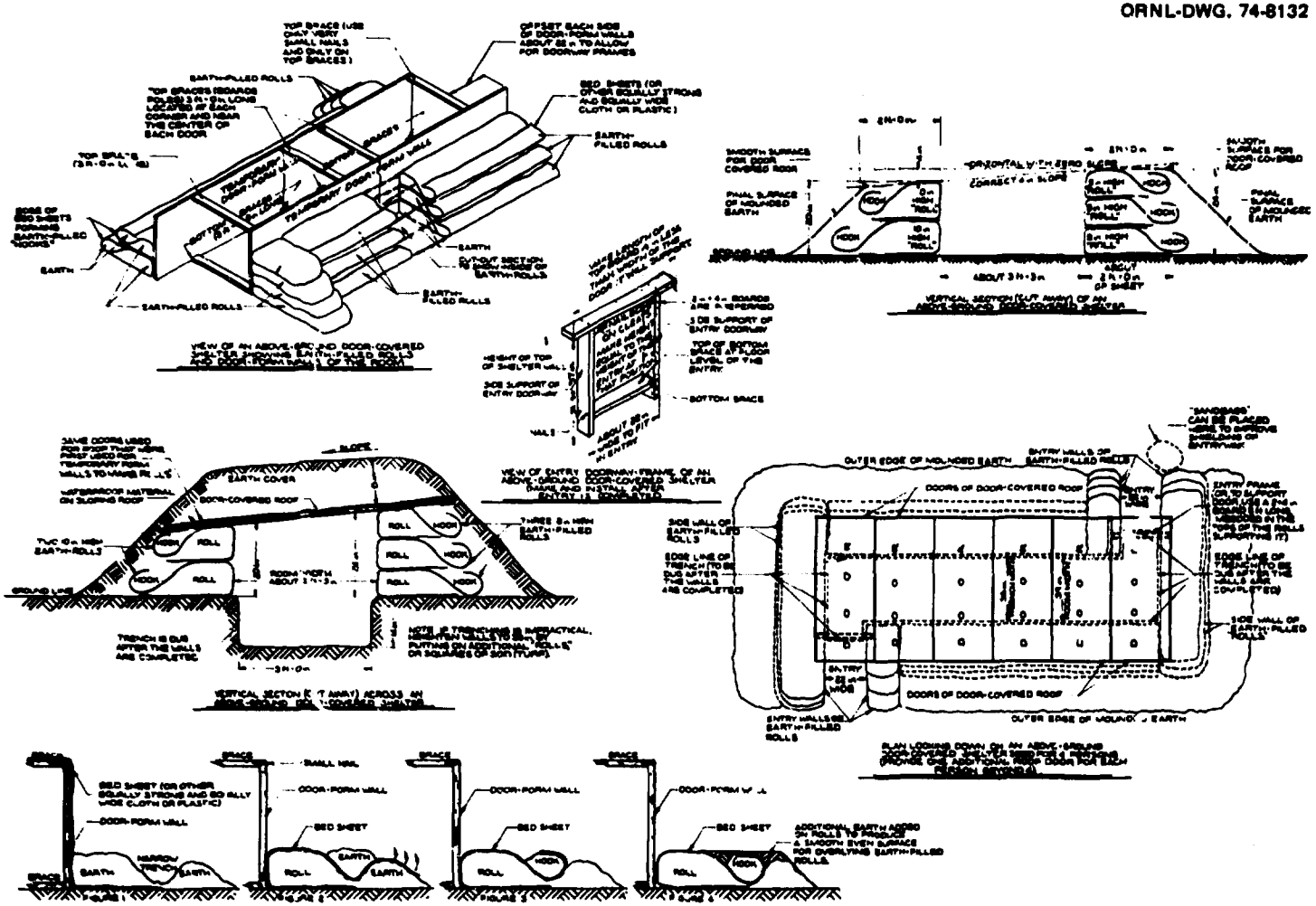

Fig. 19.18. Door-covered earth-roll shelter.

Fig. 19.19. Sheet "earth-roll" walls were 36 in. apart before the test.

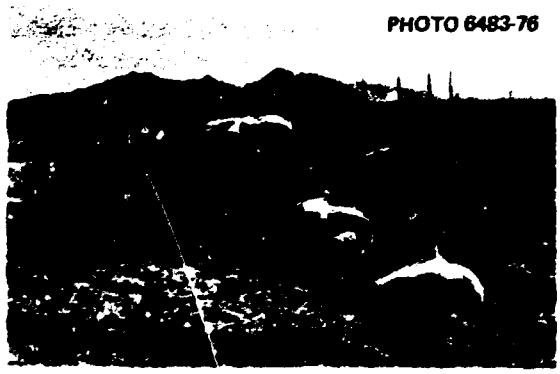

Fig. 19.20. Posttest photograph of northward-facing entry (at right angle to the direction to ground zero) of door-covered earth-roll shelter at 15 psi overpressure.

been subjected to the blast winds from a megaton weapon at the same 5.8 psi overpressure, it probably would have been badly damaged or destroyed by blast-hurled pieces of houses and trees. However, in spite of these hazards, the occupants of this simple shelter would have a decidedly better chance of surviving than

Fig. 19.21. Interior of door-covered earth-roll shelter after 15-psi blast effects had reduced width of the shelter to a minimum of 14 in.

Fig. 19.22. Posttest interior of the door-covered earth-roll shelter at 5.8 psi overpressure. The lower ¼-in. veneer of the doors was broken before the test.

would people inside typical residences, which would be demolished by the blast effects at 5.8 psi.

TEST LIMITATIONS

Caution should be used in extrapolating from the results of these DICE THROW tests to estimate the survivability of expedient shelters built in typical inhabited areas and subjected to the blast effects of a large nuclear weapon, for the following reasons.

1. This blast was small, with airblast effects roughly equivalent to a 1-kiloton nuclear explosion. At locations receiving the same peak overpressures from a multimegaton surface burst, much more severe blast effects would result because:

a. The duration of the overpressures and the dynamic overpressures would be much longer (20 times as long from an 8-megaton explosion),[3] and the energy transmitted to structures on and below the surface would be many times greater. At the same maximum overpres-

sures, the resulting destructive effects from an 8-megaton explosion on deeply buried parts of shelters and the unshored earth walls of shelters would be much greater. Also, the earth-flow phenomena observed (to a relatively minor extent in some of these DICE THROW tests) would certainly increase.

b. Damages from ground shock would be more extensive due to the greater amplitude of the ground wave and (in the case of an 8-megaton burst) to the 20-fold greater distances from ground zero to a given overpressure. These greater distances would permit the ground shock to arrive at the overpressure of interest up to hundreds of milliseconds in advance of the air shock wave; this difference between arrival times would cause the shelter roof supports to be accelerated upward before any downward forces from the airborne shock wave could cause downward movement of the earth covering a shelter. The vertical amplitude of such initial ground-shock (ground-wave) effects can be several inches, and the inertial mass of the earth covering a shelter roof would thus cause the roof members to be bowed downward to an extent not observable in high-explosive tests of similar shelters at similar overpressures.

c. Earth scouring by the blast winds (those from an 8-megaton explosion would blow about 20 times longer than those from this "1-kiloton" DICE THROW shot) could be up to 20 times as deep. Especially if the shielding earth were dry, such long-duration blast winds could blow away most of the shielding earth mounded above ground level over a shelter, thus drastically reducing its usefulness as a fallout shelter.

d. Blast-hurled large projectiles, such as steel girders and the trunks of large trees, can be accelerated by a 1-kiloton explosion to velocities only a small fraction of those to which the same objects, if at the same overpressure, would be propelled by a multimegaton explosion. Persons estimating blast damage should remember that the kinetic energy varies as the square of its velocity. Furthermore, a hurled object ten times as large as a small object having the same velocity, density, and relative proportions, and impacting in the same relative position on a fixed object, delivers ten times the amount of energy per square inch of impact area. Therefore, the impact damage to be expected from large objects accelerated by a multimegaton blast cannot be accurately estimated from the results of experiments like those at DICE THROW nor from the damage caused by blast-displaced heavy objects at Hiroshima and Nagasaki.

e. Blast tests of scale-model shelters can give misleading results regarding the survivability of full-scale shelters subjected to the same blast effects. In the DICE THROW tests, all the reduced-scale models of shelters withstood blast effects better than the corresponding full-scale shelters. For example, the half-scale rug-covered trench shelters tested at 15 and 5.8 psi were undamaged, whereas the full-scale models both failed at the same overpressures. Figure 19.23 illustrates the construction of a full-scale model.

2. The earth, a firm caliche deposit, was extremely stable in the DICE THROW test area. At almost all the DICE THROW shelter sites, at depths of only a few inches the sandy desert soil changes to very firm caliche. At 53 and 31 psi overpressure, the hardness of this caliche earth approached that of a very soft limestone rock. Thus, if shelters were built in typical inhabited areas – which have much less stable soils – and were subjected to blast effects similar in magnitude to those at DICE THROW, the collapse of the unshored walls of trench shelters, the pressures exerted on deeply buried parts of shelters, and the earth-flow effects would all have been more pronounced and damaging.

PRINCIPAL CONCLUSIONS AND RECOMMENDATIONS

1. Expedient shelters of the types tested – especially if the ones with shored walls are equipped with blast doors – would afford better protection against the blast and fire effects of nuclear weapons and much better fallout protection.

2. Failures of expedient shelters caused by a nuclear blast would be primarily due to ground-shock effects.

3. Even in very stable ground, unshored trench shelters would be unsafe if subjected to the blast effects of large nuclear explosions at overpressures of more than about 7 psi.

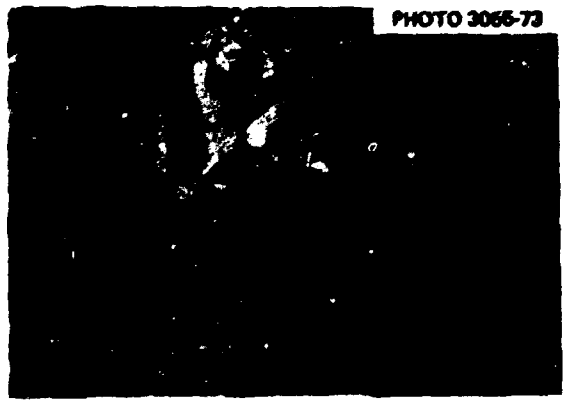

Fig. 19.23. Construction of rug- or tarpaulin-covered trench shelter.

4. Earth arching over a flexible shelter roof with an earth cover equal in thickness to at least half the roof span is so effective that flexible poles considerably smaller in diameter than those used to roof the ORNL unshored shelters should prove adequately strong.

5. Shelters likely to be subjected to blast effects should be built, whenever practical, with their roofs far enough below ground so that the tops of their entrances are only a few inches above ground level. This positioning would greatly reduce blast damage and the removal of shielding earth by blast winds.

6. Expedient blast doors – especially doors made of poles and of triangular design – can be readily built strong enough to withstand blast effects as severe as those survived by the strongest expedient shelters tested to date.

7. Since the ground-shock and earth-flow effects from large nuclear weapons were not well simulated by the DICE THROW blast, expedient shelters and their life-support equipment should be tested under conditions producing much more severe blast effects on below-ground structures – such as those conditions in the Air Force Weapon Laboratory's 125-kiloton Dynamic Air Blast Simulation (DABS) test planned for April 1978.

20. Manual Estimation of Casualties Due to Fallout from a Nuclear Attack

K. S. Gant C. M. Haaland

Suppose the United States is in the midst of a nuclear attack. Reports of weapon detonations are arriving at regional, state, and national operations centers. Civil and military authorities need immediate estimates of casualties, not only for strategic decisions, but also for planning and allocating resources to aid the impacted areas. Because of disruptions in civil communication systems, accurate reports may be days or weeks in arriving. The decision process, however, must begin immediately.

A blast and fallout casualty estimation system can provide first approximations to the needed information. It should require minimal input – location, size, class, and type of detonation. For fallout casualty estimation, the effective fallout wind speed and direction are also required. Those authorities with limited training and no computer facilities should find these systems simple to use. It is our responsibility to develop such a fallout casualty estimation system compatible with existing manual estimation systems for blast damage.

Casualty estimations on a county basis might proceed in the following manner. Locations of the reported detonations would be marked on a regional map; only the surface detonations would be considered a fallout threat. The distance from the detonation to the county population centroid would be measured along and perpendicular to the wind vector. The seven-day exposure attributable to that weapon would be read from charts or tables; these values would be summed for all weapons.

This external exposure would be reduced by the shielding capabilities (protection factors) of the shelters in use. Tables of casualty or fatality probabilities for given exposures would enable the emergency operation centers to estimate casualties and deaths from the county population data.

Development of each step of this system presents difficulties. The principal problem is to replace the involved calculations with tables and approximations and still maintain sufficient accuracy for good estimates. This process is complicated further by the limited data and assumptions on which fallout models and casualty probabilities are based. Results are not available at this time, but work on this project is continuing.

21. Instrumentation Requirements for Population Protection from Fallout from a Nuclear War

C. M. Haaland K. S. Gant

Current planning by the Defense Civil Preparedness Agency (DCPA) includes two major plans for protecting the civilian population in the event of a nuclear war. One involves the use of shelters "in-place," that is, shelters available within a mile or two of the citizen's home. The second involves relocation of people from high-risk areas to low-risk areas during the crisis period preceding the attack. This program is designed to evaluate the numbers and types of dosimeters and radiation survey meters required for the in-place mode of shelter.

For either protection plan, two types of shelters are being considered – public shelters listed under the National Shelter Survey (NSS) and home basements. A third type of shelter, the expedient shelter, may come under consideration later when estimates are obtained on how many people do not have access to either the NSS shelters or to home basements.

Present requirements for federally supplied radiological instruments for the population in the in-place shelter mode will be based on estimates of the number of people who will use public shelters. Future policy may enable radiological instruments to be supplied to homeowners who indicate a willingness to share their basement with others.

Our evaluation of population numbers, instruments, and shelter availability will be made with the 1960 Standard Location Areas (SLAs) as the basic unit of area. The use of the 42,000 SLAs in the United States instead of the 3300 county-type areas will provide increased detail, primarily in the urban areas.

In previous analysis of NSS shelter space availability, the total number of spaces in a county was compared with the total population of that county. Urban areas usually showed an excess number of shelter spaces because large high-rise buildings in the Central Business Districts (CBDs) were considered to provide excellent fallout protection not only throughout their extensive basement areas but also in their high-rise portions. Unfortunately, these buildings in the CBDs are not readily accessible to residents in outlying areas, and the high-rise portions may be unusable for fallout protection because of blast damage.

In our analysis, only underground NSS spaces accessible to residents of that SLA are accepted. These include spaces in the home SLA as well as excess spaces in neighboring SLAs with geographical centroids within a mile of the centroid of the home SLA. These restrictions, which are considered to be realistic for the in-place mode, will considerably reduce the total number of NSS spaces nationwide. This loss of available NSS space increases the importance of home-basement shelters in the in-place shelter mode.

Results are not available at this time because the project has not been completed.

22. Clinch River Breeder Reactor Plant Safety Design and Electromagnetic Pulse

P. R. Barnes

The liquid-metal fast breeder reactor (LMFBR) is the most technically advanced of the long-term energy sources that can be available to the nation by the end of the century. The LMFBR uses ^{238}U and plutonium as fuel. Enough ^{238}U will be available as a waste product from uranium enrichment operations to provide LMFBR fuel for several centuries. Plutonium will be produced from ^{238}U during the LMFBR power operation to generate thermoelectrical energy. A commercial breeder will "breed" enough plutonium to refuel itself and another reactor every 10 to 15 years. The uranium used in LMFBRs could provide 90% of our economically recoverable energy resource and could increase our total energy resources tenfold.

The LMFBR development program consists of four parts: (1) the Fast-Flux Test Facility (FFTF), (2) the Clinch River Breeder Reactor Plant (CRBRP), (3) the Prototype Large Breeder Reactor (PLBR), and (4) the Base Technology Program. The FFTF is scheduled for completion in 1978 at Hanford, Washington. The CRBRP was scheduled for completion around 1983 at Oak Ridge, Tennessee.[1] The purpose of the CRBRP is to demonstrate that the LMFBR can be licensed and can operate safely and reliably within a utility system.

SAFETY CONSIDERATIONS

The LMFBR program emphasizes a high level of safety to ensure protection of the public. Safety measures include strict air emission standards, plutonium safeguards, planned permanent waste disposal, and safety levels engineered into the plants.[2] The CRBRP has three levels of design: (1) quality of design, (2) protection against the consequences of malfunctions, and (3) design features to protect against unlikely events. The first level of protection includes quality assurance, redundancy, testability, and fail-safe features. A component or system is fail-safe if the plant automatically shifts to a safe condition when the component or system fails. The second level of safety includes redundant plant protection systems to protect the reactor and ensure safe shutdown.

The third level of protection is accomplished by designing all systems, components, and structures necessary for a safe shutdown to withstand or be protected from the effects of extremely unlikely environmental conditions such as severe earthquakes, tornadoes, maximum floods, etc. The electromagnetic pulse (EMP), which is produced by a high-altitude nuclear detonation, is an electromagnetic environmental condition which is considered at this time to have a relatively low probability of occurrence. Thus, EMP protection should be provided by the third level of CRBRP protection. In this report, we examine the design features of the CRBRP to determine if a high level of EMP protection is provided.

EMP ENVIRONMENT

The electromagnetic pulse (EMP) produced by a high-altitude nuclear detonation consists of very intense, short-duration electric and magnetic fields. The generation of the EMP has been described in several references.[3-6] The amplitude of the electric field is on the

1. The U.S. LMFBR program may be canceled or delayed due to concerns about plutonium safeguards.

2. Westinghouse Electric Corporation, *Clinch River Breeder Reactor Plant Project 1975 Technical Progress Report, CRBRP-ARD-0134, 1975.* (Available from ERDA Technical Information Center, P.O. Box 62, Oak Ridge, Tenn.)

3. L. W. Ricketts, J. E. Bridges, and J. Miletta, *EMP Radiation and Protective Techniques*, John Wiley and Sons, Inc., New York, 1976.

4. C. R. Fisher, D. B. Nelson, and P. R. Barnes, "EMP and the Radio Amateur," *QST* LIX, 40 (1975).

5. P. R. Barnes, "EMP and Nuclear Plant Safety," *Nucl. Saf.* 18, III-B (1977).

6. P. R. Barnes, R. W. Manweiler, and R. R. Davis, *The Effects of Nuclear Electromagnetic Pulse (EMP) on Nuclear Power Plants*, ORNL-5029 (to be published).

order of 50 kV/m. The time history of an EMP is characterized by a very short rise time of about 10 nsec and by an exponential-type decay with a time constant on the order of 200 nsec. A double exponential is often used to describe the EMP waveform. An example of a double exponential EMP time history is shown in Fig. 22.1. The fast rise time implies a wide excitation bandwidth, and the high intensity implies significant energy content in a broad range of the electromagnetic spectrum. A portion of this energy will couple to any electrical conductor exposed to the fields.

A single high-altitude nuclear detonation with a 400-km height of burst (HOB) over the central portion of the United States could subject most of the nation to an intense EMP. Typical areas of coverage for a megaton-range weapon detonated at 100- and 400-km HOB are shown in Fig. 22.2. Nuclear power plants throughout the country could be subjected to an

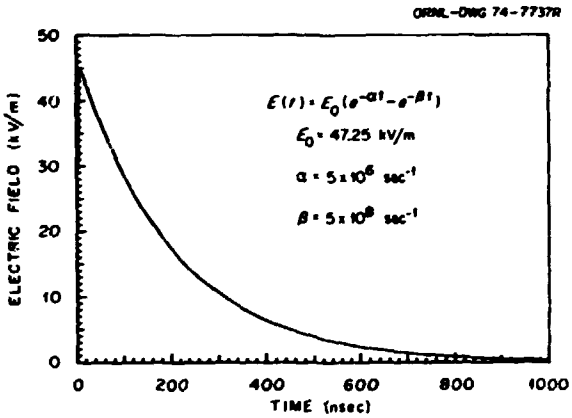

Fig. 22.1. Double-exponential EMP time history.

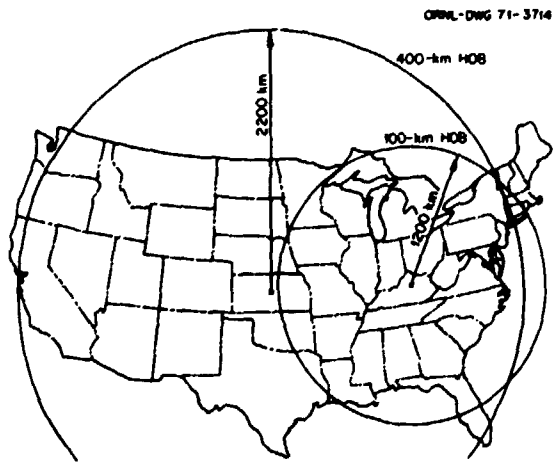

Fig. 22.2. Area of coverage of EMP from high-altitude detonations.

intense EMP environment produced by one or more high-altitude detonations. A previous study showed that EMP is not a serious problem to light-water reactor (LWR) plants.[5,6] To determine the EMP effects on the safety of the CRBRP, we shall examine the Plant Protection System (PPS) and the Steam Generator Auxiliary Heat Removal System (SGAHRS). The PPS is responsible for a safe plant shutdown in the event that important plant parameters become abnormal; the SGAHRS will remove both sensible and decay heat from the reactor once it is shut down.

CRBRP DESIGN FEATURES

Many systems in the CRBRP are designed to operate correctly in an environment of electrical and electromagnetic transients. These transients are due to the many motors and circuit switches in the plant. To ensure the operation of instrumentation and control and safety equipment, a relatively high level of noise and transient protection is employed. Much of this protection provides for a high level of inherent impermeability against an EMP environment.

All the PPS wires will be run in conduits; wiring for redundant channels will be run in separate conduits.[7] Instrument and control cables required for a safe shutdown and maintenance of a safe shutdown condition will be routed in separate enclosed raceways. Power circuits for the PPS will be routed in conduit.[8] All transformers connected to important safety-related equipment will have electrostatic shielding.[8]

Buffers will provide isolation of the PPS from other plant systems and circuits.[7] The buffers will prevent the effects of failures on the non-PPS side from affecting PPS performance. The PPS uses two shutdown systems – a primary and a secondary system. Light-emitting diodes (LEDs) and phototransistors are used to provide complete electrical isolation for the primary shutdown system logic. The secondary system will use buffers for isolation. The buffers used throughout the PPS will likely use LED-phototransistor pairs.[8] Grounded cabinets used to house the PPS equipment will provide protection against electromagnetic transients.

7. Project Management Corporation, *Clinch River Breeder Reactor Plant Preliminary Safety Analysis Report (1975), Overall Plant Design Description*, rev. 2, July 26, 1976. (Available from ERDA Technical Information Center, P.O. Box 62, Oak Ridge, Tenn.)

8. R. J. Rosecky, CRBRP Project Office, Oak Ridge, Tenn., Apr. 21, 1977, private communication.

The SGAHRS consists of two subsystems – a short- and a long-term heat removal system. The short-term system removes sensible heat from the reactor by dumping steam directly to the atmosphere. After about 1 hr, the long-term system is used. The long-term system uses three protected, air-cooled condensers located on the roof. Cooling water is provided by the auxiliary feedwater system consisting of three feedwater pumps. There are two electric motor pumps, each rated at 50% of design flow, and one steam-driven pump rated at 100% design flow.

EMP ANALYSIS

The primary means of coupling EMP energy to the plant protection system are the instrumentation, control, and power cables. All PPS cables will be run in conduits. The open-circuit voltage transient induced by EMP between a long (160-m) conduit and an internal cable is shown in Fig. 22.3. An electromagnetically tight conduit has been assumed, and a 20-dB building attenuation was used to compute the voltage. The actual CRBRP building attenuation will probably range between 20 dB near the exterior wall subjected to the incident EMP and at least 40 dB at the center of the building. Thus the induced EMP voltage in the PPS cables should not exceed several millivolts in amplitude. This EMP noise should cause no problems for the PPS.

To estimate the EMP transients induced on the plant cables located in cable trays, we shall assume conservative EMP attenuation values. The building attenuation for cables run along the exterior wall subjected to the incident EMP is about 20 dB.[9] However, most cables will not run along the exterior wall. For cables that are run from an area near the exterior wall to an area deep within the plant, the average attenuation probably will be at least 30 dB. Also, most cables are run in bundles in cable trays or conduits. The bundle attenuation for a bundle of 50 cables is about 22 dB.[9] The grounded, solid cable trays with solid covers will provide an EMP attenuation of at least 20 dB. (Note: Open cable trays will provide an EMP attenuation of about 3 dB.)

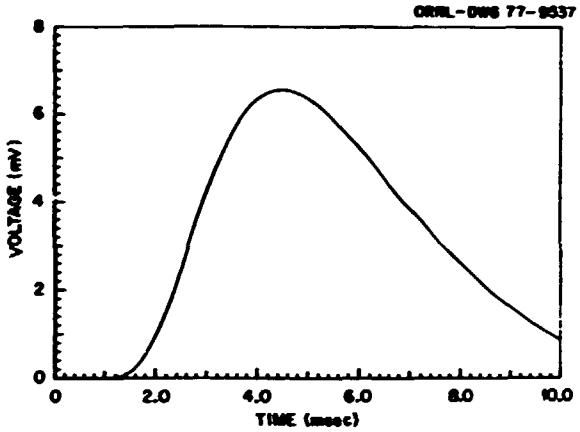

Fig. 22.3. Open-circuit EMP voltage transient between an internal cable and a conduit 160 m long.

The total attenuation provided by the building, cable bundles, and solid cable trays is at least 55 dB. The EMP open-circuit voltage transient between the power or control wires and the plant ground for a 160-m line is shown in Fig. 22.4. Peak voltage is limited to about 1000 V due to the 55-dB EMP attenuation. The voltage transient shown in Fig. 22.4 was calculated by assuming a straight 160-m-long wire located 10 m above the earth

9. P. R. Barnes and J. H. Marable, *Transient Response of Nuclear Power Plant Cables to High-Altitude Nuclear Electromagnetic Pulse (EMP)*, ORNL-5152 (May 1976).

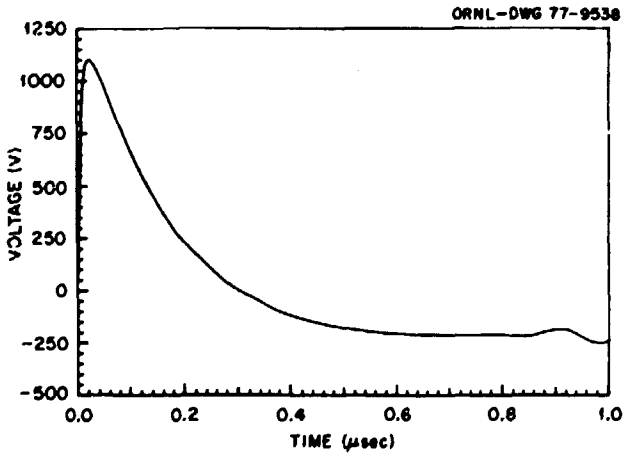

Fig. 22.4. Open-circuit voltage transient induced by EMP on insulated-wire power or control cables.

and subjected to a representative EMP attenuated by 55 dB. This calculation, however, does not account for the probable lengthening of the pulse rise time by the effects of the cable tray shield. The EMP transients induced on the offsite power lines are assumed to be suppressed by the combination of the station transformer and the lightning protection.

The PPS power supplies use electrostatically shielded transformers for transient protection. The 1000-V EMP transients on the 120-V PPS power cables will cause no problems. Instrumentation and control systems that interface with the PPS could have transients on the order of 1000 V for any unshielded cables. Shielded cables will have transients on the order of a few volts. Since the PPS is isolated from other systems by buffers, these transients will cause no damage to the plant protection system. However, if the buffers are damaged, a reactor trip (shutdown) could result. In any case, the PPS will not be prevented from performing its task.

One question remains: Can the EMP prevent the removal of the reactor decay heat? The SGAHRS requires electrical power for motors and 125-V dc power for controls. In addition to the large motors, smaller battery-powered motors are also specified to drive sodium pumps in both the primary and intermediate heat transport systems. These pumps have two backup power sources – diesel generators and very large banks of batteries. The third loop of SGAHRS, the steam generator loop, requires auxiliary feedwater, which can be provided by either a steam- or motor-driven pump. Control power is obtained from batteries.

The EMP voltage transient induced between the 4.16-kV generator output cables and the plant ground will be similar to that shown in Fig. 22.4. The inductances of the transformers, generator, and motors are high impedances to the relatively fast rising transient; thus the open-circuit calculation is applicable. A transient of about 1000 V will not cause any problems on the 4.16-kV diesel generator output circuits. The 125-V dc diesel generator control cables will experience similar transients. These cables control electromechanical relays which are relatively insensitive to electrical transients. A short 1000-V transient may harm a 125-V relay. However, these control relays should be fail-safe. Thus, it is unlikely that the standby ac power source will be damaged by the EMP.

In the event of a total loss of ac power, the SGAHRS can operate with power from batteries and, to some extent, from natural circulation. Auxiliary feedwater would be provided by the steam-driven pump. Batteries have high capacitance valves which will pass the fast transients induced in the dc cable to the plant ground. The battery chargers will be powered by 480-V ac. The EMP transients on the 480-V cables should not damage the chargers, providing they do not capacitively couple to the charger's control circuitry.

CONCLUSIONS AND RECOMMENDATIONS

The CRBRP design provides a high degree of electromagnetic shielding which is obtained by the double-course reinforced concrete building walls, metal conduit, and solid steel cable trays. The EMP shielding effectiveness for the PPS and other safety-related cables ranges from about 55 dB to well over 100 dB. Also, circuits with low signal levels normally use shielded cables. In addition to shielding, transient protection is provided by electrostatically shielded transformers, and transient isolation is provided by buffers. Due to the shielding and transient isolation, it is unlikely that EMP could prevent the PPS or the SGAHRS from performing safety-related tasks. Thus, EMP is not considered a serious threat to plant safety. However, as a precautionary measure, fast-responding EMP transient suppressors are recommended for the important battery power systems, diesel generator control circuits, and both the control and power circuits associated with SGAHRS.

23. Solar Energy Development Program

H. D. Guberman

Oak Ridge National Laboratory's involvement in solar energy development and utilization stems naturally from two different but not unrelated interests. The first is concerned directly with activities that attempt to help the United States achieve greater independence in matters of energy supply and the second is to conserve nonrenewable fossil fuels to the greatest extent possible. Increased use of solar energy to replace fossil fuels is an important aspect of this program.

Within the scope of the activities of the Emergency Technology Section, this work has relevancy insofar as it will reduce the vulnerability of the American people to catastrophes such as nuclear war, reactor accidents, or terrorist use of weapons of mass destruction. This goal will be furthered in two ways. First, in the event of a possible catastrophe, solar energy may be the only energy available to many people; thus, we should be prepared to make use of this energy source if necessary. Second, greater reliance on solar energy in the general populace prior to any catastrophic event will reduce their dependency on central power stations and, to some extent, make them less vulnerable to threats.

Among the important subcategories of energy users are those in the agricultural and industrial sectors of the economy. Recent shortages and rapidly rising fuel prices have potentially profound effects on these users and thus have become reasons for promoting the substitution of solar energy where possible. ERDA sponsors considerable effort in these and many other fields. It is the purpose of this group's program to provide technical management assistance to the Agricultural and Industrial Process Heat Branch of the ERDA Solar Energy Division in the monitoring and management of these research and development efforts.

For FY 1977, this aspect of ERDA-supported projects is represented by 29 contracts in 18 states. The work is summarized in Table 23.1 and Fig. 23.1.

Much of the present work is concerned with demonstrating technical and economic feasibility. Computer simulation and modeling is a rather widely used tool which forms an integral part of many of the research efforts. Another general trend is to seek opportunities for multiple use of solar collectors and solar systems to increase the load factor and thus reduce the unit cost of energy supplied by the solar system. A number of different thermal storage systems are also being investigated (from water to rock beds to eutectics), as well as a substantial range of collector designs (from flat-plate collectors to solar ponds) and concentrating types for higher-temperature applications. Although many of the endeavors may be considered "low technology," there is ample room for development of ideas and devices that rest firmly on basic engineering and scientific principles.

Although this aspect of involvement with solar energy is a small one, it is increasing in magnitude and importance within the general programs aimed at increasing the nation's energy supply and reducing consumption of nonrenewable fossil fuels.

Table 23.1. Summary of research and development projects supported by ERDA-USDA in FY 1977

Institution	Location	Principal investigator	Remarks
		Grain drying	
Colorado State University	Fort Collins, CO	R. W. Hansen	Development of multiple-use solar collector and storage system for drying corn
University of Florida	Gainesville, FL	C. D. Baird	Determining methods of drying corn and soybeans in hot, humid areas. Mathematical modeling to evaluate drying systems, management schemes, and economic feasibility
University of Illinois	Urbana, IL	G. C. Shove	Solar heat and heat pump for drying corn. Collectors also incorporated into roofs and walls of large storage buildings
Iowa State University of Science and Technology	Ames, IA	C. J. Bern	Comparison of solar, electric, and solar-assisted heat pump for drying corn
Kansas State University of Agriculture and Applied Science	Manhattan, KS	R. Lipper	Comparison of solar grain-drying bag, flat storage collector, and wraparound collector
University of Kentucky	Lexington, KY	B. F. Parker	Focusing solar collector and rock-bin storage for high-temperature drying in the Southeast
University of Missouri	Columbia, MO	D. B. Brooker	Salt-hydrate eutectics melting at 55°F for heat storage for use in grain drying and environmental control of animal shelters
University of Nebraska	Lincoln, NB	T. L. Thompson	Simulation studies of fan operation schedules, levels of solar and continuous supplemental heat for Iowa and Indiana
Ohio Agricultural Research and Development Center	Wooster, OH	H. M. Keener	Simulation modeling of solar air heating systems. Also, solar and natural air drying of shelled corn
Purdue University	West Lafayette, IN	R. M. Peart	Drying tests using solar collectors and stirring augers. Eutectic salt thermal storage to be tested. Simulation studies
Agricultural Research Station, U.S. Dept. of Agriculture	Beaumont, TX	D. L. Calderwood	Drying rice using stored solar energy during periods of high humidity. Both hot-water and pebble-bed storage systems are studied
Agricultural Research Station, U.S. Dept. of Agriculture	Ames, IA	G. L. Kline	Studying solar collectors of various designs, materials, and configurations for efficiency and durability
Agricultural Research Station, U.S. Dept. of Agriculture	Manhattan, KS	H. H. Converse	Drying corn and sorghum with different solar collectors and evaluating use of heat storage
South Dakota State University	Brookings, SD	M. A. Hellickson	Solar energy-intensifier system for drying shelled corn. Thermal storage being added for agricultural space heating

Table 23.1 (continued)

Institution	Location	Principal investigator	Remarks
Agricultural Research Station, U.S. Dept. of Agriculture	West Lafayette, IN	J. R. Barrett, Jr.	Simulation studies of wheat drying
		Peanut, tobacco, and forage drying	
Agricultural Research Station, U.S. Dept. of Agriculture	Tifton, GA	J. L. Butler	Heat storage in rocks and in water as well as direct heating by sun for drying and curing. Computer simulation
Oklahoma State University of Agriculture and Applied Science	Stillwater, OK	B. L. Clary	Large hot-water storage pond to store heat collected over extended period, then transferred to drying air stream during drying season for peanuts. Computer simulation
Agricultural Research Station U.S. Dept. of Agriculture	Lexington, KY	L. R. Walton	Two-stage solar-energy tobacco curing system. Rock-bed storage
North Carolina State University	Raleigh, NC	B. K. Huang	Combination greenhouse–bulk curing system for tobacco
University of Georgia	Tifton, GA	J. S. Cundiff	Developing system using solar energy and rock-bed storage; also a heat pump for curing tobacco
The University of Tennessee	Knoxville, TN	B. L. Bledsoe	Final drying of hay using different types of solar collectors
Georgia Institute of Technology	Atlanta, GA	A. P. Sheppard	Design, fabricate, and furnish plans of improved solar collectors for agricultural driers
Colorado State University	Fort Collins, CO	R. W. Hansen	Comparing solar-energy-system dried forage with forage dried by other means
		Food processing	
Michigan State University	East Lansing, MI	F. W. Bakker-Arkema	Survey of meat, milk, and fruit-vegetable industry to determine economics and fuel-savings potential of introducing solar water heaters in processing plants
University of Wisconsin	Madison, WI	F. H. Buelow and D. B. Lund	Investigate compatibility of solar systems with food processing industries. Computer modeling
Colorado State University	Fort Collins, CO	C. C. Smith	Design, fabrication, and operation of drier for potato products to determine efficiency of operation and quality of product
Oklahoma State University of Agriculture and Applied Science	Stillwater, OK	G. H. Brusewitz	Pilot solar still used to determine potential energy savings for drying beef packing plant paunch
University of Hawaii	Honolulu, HI	J. H. Moy	Drying of fruit and vegetables; concentration of fruit juices. Drying tropical root crops and tropical fruit for possible new products
U.S. Citrus and Subtropical Products Laboratory	Winter Haven, FL	R. E. Berry and W. L. Bryan	Development of solar process for drying southeastern fruits and vegetables

Part V. Medical Physics and Internal Dosimetry

K. E. Cowser

24. Internal Dosimetry

W. S. Snyder[1] K. E. Cowser L. C. Henley[3]
S. R. Bernard S. B. Watson[2] W. W. Parkinson[2]
M. R. Ford L. T. Dillman[1] G. G. Warner[2]
C. W. Nestor, Jr.[2]

DOSE FROM ^{40}K FOR THE ORGANS OF REFERENCE MAN

The naturally occurring isotope of potassium, ^{40}K, is a principal contributor to the natural background dose. Dose rates to body organs from ^{40}K, however, are available from the literature in only very approximate terms. In the report on dose from ^{40}K for the organs of Reference Man, data of Tipton (ICRP Publication 23) on the content of potassium in the organs and tissues of 150 "normal" adults are analyzed to provide a detailed metabolic model for potassium. A single exponential half-time of 30 days, being consistent with the daily intake of Reference Man, is adopted for all tissues. Using this model and the mathematical phantom of Reference Man, total doses and dose rates which indicate variations to body tissues by a factor of about 10 have been computed. The total doses tabulated for the inhalation case assume intake of a class D aerosol of AMAD = 1 μm, but methods of adjustments for other aerosols are indicated. Adjustments of the doses due to age are discussed also.

Although ^{40}K is one of the commonly measured radionuclides, a reference that elaborates and discusses a well-considered metabolic model for it is not easy to find. This paper gives such a model for the 70-kg ICRP Reference Man and discusses the sources of data used and the effect on the dose estimate of various conditions such as age.

Distribution in the Body

Potassium and its naturally occurring radioactive isotope ^{40}K, which has a half-life of 1.27×10^9 years, can be considered to be mixed uniformly in biological and in most environmental materials. It has been extensively measured in the human.[4-6] The results can be summarized by the graphs shown in Fig. 24.1 which indicate (1) a substantial difference of the two sexes, (2) the relative stability of the measurements at different times, and (3) the possible association of potassium with the lean body mass or other related parameters. For example, data on the concentration of potassium in skeletal muscle show much less variation with age than do data on the average concentration in the total body.[7]

Tipton[7] has given the average potassium concentrations found in the organs and tissues of 150 supposedly "normal" adults, and some of these are shown in Table 24.1. This concentration is much like that given by

1. Deceased.
2. Computer Sciences Division.
3. Radiation Monitoring Section.
4. E. C. Anderson, *Ann. NY Acad. Sci.* 110, 189 (1963).
5. L. A. Pertsov, *The Natural Radioactivity of the Biosphere*. Clearinghouse for Federal Scientific and Technical Information, U.S. Department of Commerce, 1967.
6. P. Burch and F. Spiers, *Science* 120, 719 (1954).
7. International Commission on Radiological Protection, *ICRP Task Group Report on Reference Man*, ICRP Report 23, Pergamon Press, New York, 1975.

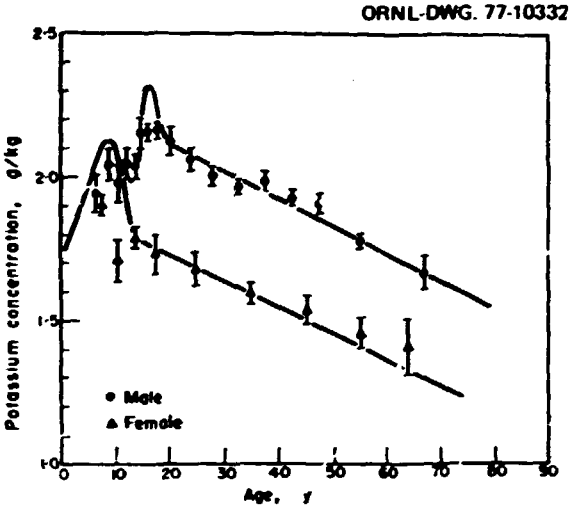

Fig. 24.1. Potassium concentration (g/kg) in the human body as a function of age for two large population samples. The solid curves are drawn for the 1956–1958 sample, displaced downward by 2%, and the points are the 1959–1960 repetition. Source: ref. 18.

Table 24.1. Concentrations of potassium in various tissues of Reference Man

Tissues	Concentration (g/kg)
Adipose tissue (separable)	0.32
Adrenals	1.0
Aorta	1.2
Blood	1.6
Brain	3.0
Gastrointestinal tract	
Stomach	1.4
Small intestine	1.4
Upper large intestine	1.0
Lower large intestine	1.2
Heart	2.2
Kidneys	1.9
Larynx	1.4
Liver	2.5
Lung	1.9
Muscle	3.0
Pancreas	2.3
Prostate	1.9
Skeleton	1.5
Skin	0.85
Spleen	3.1
Testes	2.0
Thyroid	1.2
Tongue	2.9
Urinary bladder	1.4
Total body	(average) ∿2.0

Pertsov[5] and other authors. More specifically, a high concentration in muscle and in brain is indicated, together with a low concentration in adipose tissue and in bone. The value for the skeleton given in Table 24.1 is a composite of the values for bone, red marrow, yellow marrow, and for other organic components of bone. In particular, it is known that the potassium concentration in erythrocytes is high, and thus, if the concentration in red marrow is considered to be of the same order, then a 4.5-g concentration of potassium is obtained for the red marrow. This assumes an average concentration in red marrow of ∿3 g of potassium per kilogram of tissue. If the concentration in yellow marrow is to be equal to that in adipose tissue, then a 0.5-g concentration of potassium is obtained for yellow marrow. For bone, a value of ∿10 g of potassium would be reasonably consistent with the total value given by Tipton.[8] This is in reasonable agreement with the range of 61 to 110 mg % (mg/100 g) cited by Pertsov.[9]

If the concentrations given in Table 24.1 are converted to amounts of stable potassium and if allowances are made for other tissues, then a representative body burden of ∿140 g of potassium is obtained for Reference Man.

Calculation of Dose Rate

Two calculations have been programmed for the computer. In the first, which is termed the "uniform model," the concentration of potassium is uniform in all the tissues – 2 g of potassium (containing 1.18×10^{-4} g of ^{40}K per gram of potassium) per kilogram of tissue.[10] In the second model, termed the "heterogeneous model," the average concentration in body tissues is the same, but the concentrations in the various organs are proportional to the values given in Table 24.1. There are a number of special situations in which the procedure for specifying the source is not straightforward, and these will now be discussed.

Blood is one of the tissues present in nearly all organs and is assumed to be present in the amount estimated for the living person. Thus, no separate source for blood should be indicated. That is, the mass of the organ is assumed to include the blood normally present in the living person. However, when these measured values are used an allowance for loss of blood from these organs at the time of measurement should probably be made. This has prompted us to indicate a value for blood distributed in the total body. This total-body value may be too large, but values for some tissues are missing, and the mathematical phantom of Reference Man used in the computations includes no representation for some organs. This situation may partially offset the use of the somewhat larger value for blood. The mass of "blood"

8. Ref. 7, Table 108.
9. Ref. 5, p. 211.
10. R. D. Beckinsale and M. H. Gale, *Earth Planet. Sci. Lett.* 6, 289 (1969).

is indicated as the difference of the mass of the total body and of the specified compartments or tissues.

In a number of other cases, the organ is missing from the phantom and these include the aorta, all portions of the gastrointestinal tract, the larynx, the prostate, and the tongue; all of these, except the gastrointestinal tract and its contents and the bladder wall, are a part of the compartment of "other tissues" that remain after the organs constructed in the phantom are removed. Fortunately, none of these organs is among the highest or lowest in potassium concentration. Here, the gastrointestinal tract and its contents and the bladder wall have been assumed to have an average concentration of ∿1.5 g of potassium per kilogram, which is well in line with the measured values. However, the contents do not seem to have been measured. Adipose tissue is low in concentration and is partitioned into two types: "separable adipose tissue," which consists of the larger masses of fat, and "other adipose tissue," which includes lipids and fat not readily dissected. The separable fat, consisting of 12.5 kg of "localized" adipose tissue, is considered to be located in the "other tissue" compartment. It is considered that beta energy emitted in the separable fat will be completely absorbed in this tissue. In addition, the adipose tissue will receive a higher level of gamma irradiation due to its proximity to muscle. The dose received by fat is taken as the same as the dose received by muscle. Since muscle also belongs to the "other tissues," this compartment has the two extremes of concentration intermixed, separable fat being low and muscle being high.

The brain also has a high concentration but has not been made a part of the regular system of organs. However, absorbed fractions are available, with the brain listed as the source tissue in MIRD pamphlet 5.[11] A dose rate for the brain is obtained by using the dose from electron irradiation, as in muscle, but without changing the dose in muscle from photons, which is only a small part of that dose. Finally, the "skeleton" is represented by ∿4.5 g in red marrow and 0.5 g in yellow marrow; bone is split into 8 g in cortical bone and 2 g in cancellous bone, as is mentioned earlier. The source intensities (μCi) used in the heterogeneous model are presented in Table 24.2 and correspond to a body burden of 140 g of potassium in the body. The dose rates to the various organs of Reference Man from the heterogeneous model are presented in Table 24.3. Note that the dose rate varies by about a factor of 10. In contrast, the uniform model gives a nearly constant dose rate of 4.7×10^{-5} to all the organs.

11. W. S. Snyder et al., *J. Nucl. Med.*, Suppl. 3, 10, 5 (1969).

Table 24.2. Sources of K and ^{40}K in the heterogeneous model for Reference Man

Source organs	Reference Man weight (g)	Amount[a] (g of K)
Adrenals	0.014	0.014
Kidneys	310	0.589
Liver	1800	4.5
Lungs	1000	1.9
Pancreas	100	0.23
Skeleton	10,000	15
Cancellous bone	1000	2
Cortical bone	4000	8
Red marrow	1500	4.5
Yellow marrow	1500	0.5
Skin	2600	2.2
Spleen	180	0.558
Testes	35	0.07
Thyroid	20	0.024
Other tissue compartments	48,000	103
Muscle	28,000	84
Adipose tissue (separable)	12,500	4
Remaining tissue	7,500	15
Total body (GI tract, contents of GI tract, body fluids, and bladder)	5,955	8.8

[a]The corresponding organ burdens of ^{40}K are obtained by multiplying by 8.31×10^{-4} (μCi of ^{40}K per g of K).

Table 24.3. Dose rate at equilibrium[a] and dose per unit intake of ^{40}K – heterogeneous model

Body organs	Dose rate (rem/day)	Dose (rem/μCi intake)	
		Oral	Inhalation
Adrenals	2.9×10^{-5}	1.1×10^{-2}	6.7×10^{-3}
Bladder wall	7.0×10^{-6}	2.5×10^{-3}	1.6×10^{-3}
Stomach wall	1.3×10^{-5}	4.6×10^{-3}	1.9×10^{-3}
Small intestinal wall	6.8×10^{-6}	2.5×10^{-3}	1.6×10^{-3}
Upper large intestinal wall	7.0×10^{-6}	2.6×10^{-3}	1.6×10^{-3}
Lower large intestinal wall	7.3×10^{-6}	2.7×10^{-3}	1.6×10^{-3}
Kidneys	4.8×10^{-5}	1.8×10^{-2}	1.1×10^{-2}
Liver	6.1×10^{-5}	2.2×10^{-2}	1.4×10^{-2}
Lungs	4.7×10^{-5}	1.7×10^{-2}	1.6×10^{-2}
Muscle	8.4×10^{-5}	3.1×10^{-2}	1.9×10^{-2}
Ovaries	7.7×10^{-6}	2.8×10^{-3}	1.8×10^{-3}
Pancreas	5.7×10^{-5}	2.1×10^{-2}	1.3×10^{-2}
Bone	5.0×10^{-5}	1.8×10^{-2}	1.2×10^{-2}
Red marrow	6.4×10^{-5}	2.3×10^{-2}	1.5×10^{-2}
Yellow marrow	1.3×10^{-5}	4.8×10^{-3}	3.0×10^{-3}
Cortical endosteal cells	5.1×10^{-5}	1.9×10^{-2}	1.2×10^{-2}
Cancellous endosteal cells	6.4×10^{-5}	2.3×10^{-2}	1.5×10^{-2}
Total endosteal cells	5.7×10^{-5}	2.1×10^{-2}	1.3×10^{-2}
Skin	2.0×10^{-5}	7.5×10^{-3}	4.7×10^{-3}
Spleen	7.3×10^{-5}	2.7×10^{-2}	1.7×10^{-2}
Testes	4.9×10^{-5}	1.8×10^{-2}	1.1×10^{-2}
Thymus	8.1×10^{-6}	2.9×10^{-3}	1.9×10^{-3}
Thyroid	3.2×10^{-5}	1.2×10^{-2}	7.3×10^{-3}
Uterus	7.1×10^{-5}	2.6×10^{-2}	1.6×10^{-3}
Total body	4.6×10^{-5}	1.7×10^{-2}	1.1×10^{-2}
By adjustment:			
Brain	8.4×10^{-5}	3.1×10^{-2}	1.9×10^{-2}
Adipose tissue	2.7×10^{-5}	1.0×10^{-2}	6.3×10^{-3}

[a]Based on 140 g of potassium in the total body.

Calculation of Dose Conversion Factor

Table 24.3 includes a total dose (rem/μCi of intake) by a specified route. However, this entry is subject to several additional considerations. A daily 3.3-g potassium intake (as given in the ICRP report on Reference Man[12]) is assumed to produce the measured body burden; this is consistent with a biological half-time of ∿30 days, which is close to the value of ∿25 days given by Pendleton et al.[13] They indicate variations from this biological half-time by a factor of 2 or more which is also the approximate variability one would expect among different tissues and individuals.[14] We know of no study that provides estimates of biological half-times for various tissues, but the fact that the body exerts some homeostatic control may exclude extremes typical of pathological cases among "normal" individuals. Only an inhalation of a class D aerosol with an activity median aerodynamic diameter (AMAD) equal to 1 μm is given.

Discussion

It should be emphasized that potassium, being an essential element, is subject to homeostatic control and thus does not have a true biological half-time. However, for the average individual who is assumed to be eating a diet neither unduly rich nor poor in potassium, there is an apparent half-time. Individuals will differ in tissue concentration due to a variety of factors – variations in intake of potassium, age, sex, degree of exercise, etc. Pertsov[14] indicates variability of a factor of 2 to be typical of many animals and even for some readily obtainable human samples. The single exponential half-time of 30 days is adopted for all tissues of the adult body (although we know of no experimental data on this point), but it is consistent with the body burden of

12. Ref. 7, p. 403.
13. R. C. Pendleton et al., *Health Phys.* 11, 1503 (1965).
14. Ref. 5, pp. 210–11.

potassium in the body and in the diet of Reference Man [i.e., 140 g of potassium ≅ 3.3 (grams of potassium per day) × 30/0.693 (days)]. Partly because of this uncertainty and also because the concentration is not grossly different among the tissues (being at most a factor of about 10), a model that assumes a uniform body concentration has often been assumed. This neglects variations by about a factor of 3, but it may be of some interest to point out that ^{40}K is primarily a beta emitter, and thus the total doses received by the various organs will more nearly reflect the average concentration of activity in the organ. In short, one would expect the total doses as well as the dose rates to indicate a variation by about a factor of 10. The doses by inhalation are for an aerosol of AMAD = 1 μm. It is easily adjusted for other aerosols. Three fractions represent dose received as a result of lung deposition in the regions of the nasal passages (N-P), the trachea and bronchial tree (T-B), and the pulmonary (P). These fractions can be used to adjust for any desired depositions. A typical set of such fractions is 47%, 13%, and 40%, which indicates that the dose to the muscle, for example, is partitioned so that 47%, 13%, and 40% of the dose is due to deposition in the N-P, T-B, and P regions respectively. Since the deposition fraction D for the N-P region is only 0.30 of that inhaled for an aerosol of an AMAD equaling 1 μm, this means that if another aerosol deposits an activity fraction, A (measured in microcuries) in the N-P region, the dose to the muscle from the N-P deposition will be

$$D_{muscle} \times \frac{A\ 0.47}{0.30}\ \text{rem}/\mu\text{Ci}\ ,$$

and similarly for the other regions of the respiratory tract. Because all the organs have a common biological half-time, the fractions are the same for all organs obtaining their activity through blood. The only exceptions are the lungs at 31%, 9%, and 60% and the stomach wall at 56%, 11%, and 33%.

Conceptually, adjustments for individual differences of adults are possible but difficult to implement. One might attempt to estimate the amount of lean body mass, fat, and total body water. The partitioning of the body burden among these, or other components, presents difficulties because the deposition in these various tissues is also affected by many other factors, for example, exercise.[9]

Adjustments due to age appear to be possible, at least in an average sense. Pendleton et al.[15] have indicated the variation of the biological half-time, T_b, with age; and although the number of individuals sampled is not large, the data indicate a gradual decrease in T_b as age decreases. The five infants (17 to 143 days old) indicate values of T_b of ten days or slightly less; the three individuals of 5 to 9 years of age indicate ∿20 days; and the adults indicate a value of ∿25 days with values ranging from ∿10 to 40 days. Thus, there seems to be a gradual decline as age decreases to ∿10 days, although none of these values represent the newborn. Using these values and the average masses of the organs, the dose from electrons is fairly straightforward. No absorbed fractions for photons are available for these ages, although some preliminary estimates have been given.[16,17] However, the problem is not of great importance since the dose from photons always appears to be a relatively small part of the total. Although one uses approximate values of the relevant absorbed fractions, it does not appear to be a major contributor to the total dose.

The fact that ^{40}K emits primarily electron irradiation means that the dose per μCi of intake at these younger ages probably exceeds the dose received by the adult. This is because the doses are inversely proportional to the masses of the organs. Of course, the dose at equilibrium is also proportional to the body burden, and this reflects the individual's diet. Although there have been some measurements of infants and children,[11] the measurements have not been so extensive as to exclude all uncertainty. It may be best to make some direct measurements if a situation involving exposure of infants or children arises.

REVISED EFFECTIVE ENERGIES FOR USE IN INTERNAL DOSE ESTIMATIONS

Revised radioactive decay data together with revised fractions of energy absorbed in body organs, have been used to reevaluate the effective energy values appearing in ICRP Publication 2. The effective energy values of Publication 2 are the basis for the body burden and maximum permissible concentration (MPC) values presently used as guidelines for controlling dose to persons exposed occupationally, and there has been no general revision of these guidelines since 1959. Thus, an indica-

15. Ref. 13, Fig. 2.

16. W. S. Snyder, pp. 625–30 in *Proceedings of the Third International Congress of the International Radiation Protection Association, Washington, D.C., Sept. 9–14, 1973*, CONF-730907-P1, U.S. AEC, 1973

17. M. J. Hilyer, G. S. Hill, and G. G. Warner, pp. 631–36 in *Proceedings of the Third International Congress of the International Radiation Protection Association, Washington, D.C., Sept. 9–14, 1973*, CONF-730907-P1, U.S. AEC, 1973.

tion of the discrepancies to be expected in using the older energy values is of importance. This study indicates that about 80% of the new values are within a factor of 2 of the older values and that 88% to 90% are within a factor of 3 although a few differ by greater than a factor of 10.

The energy values computed 15 to 20 years ago for ICRP Publication 2 are still widely used in estimating dose from internal emitters.[18] These weighted energies, termed effective energies, are also incorporated in the maximum permissible concentration (MPC) values presently in force in the federal regulatory guide (10 CFR 20) for controlling dose to persons occupationally exposed. In the present study, the effective energies listed in ICRP 2 were reevaluated, taking into account improved computational methods and revised decay data which had accrued during the years since that publication was issued; we compare the updated energies with the previous values.

Since dose is the product of absorbed energy and the time integral of activity accumulated in body organs, both parameters are of fundamental and equal importance. In estimating metabolic factors, it is not uncommon for much disagreement to arise and, consequently, for much time and effort to be expended in determining, for example, whether the fraction of a particular radionuclide crossing the gastrointestinal tract into blood is 0.2 or 0.3. That is, a difference of 50% in a biological factor is of concern. Thus, we conclude that the energy terms should be correct within somewhat the same limits, and to effect this they should be reevaluated periodically to incorporate revised decay data and other updated parameters or assumptions that may have become available.

The new computations take into account (1) updated decay schemes, (2) a revised method of computing the energy emitted, (3) revised photon absorbed fractions, (4) a change in the quality factor for low-energy electrons from 1.7 to 1, and (5) revised weights of body organs based on the ICRP Reference Man.[7] Item 4, recommended by the National Council on Radiation Protection and Measurements (NCRP) in 1971,[19] is of little importance except in the case of values for ^{3}H which are lowered by a factor of 1.7, because ^{3}H is the only radionuclide considered which decays significantly by emission of low-energy electrons; item 5 is responsible for several small changes in absorbed fractions of photon energy. It is the first three items that account for most of the changes, and each will be discussed in turn. It should be pointed out also that in the present study each radionuclide is treated separately – that is, in the ^{226}Ra decay chain, for example, the energy of radium as computed now is compared with the energy of radium as computed in ICRP 2,[18] and the energy of each daughter is compared by the new and the old methods. We have not attempted to compare the total energy of the chain (radium plus daughter) which, of course, would involve not only energies but also metabolic models for the entire chain.

To illustrate the effect of updated decay schemes, the ^{187}Re decay scheme of ICRP 2[18] versus the revised decay scheme[20] is shown in Fig. 24.2. Rhenium-187 decays 100% by beta emission with an end-point energy of 0.0025 MeV by current measurements compared with 0.043 MeV reported previously. Thus the previous value is about 20 times greater. The change in the decay scheme is reflected in the effective energies as shown in the table beneath the decay schemes. Two body organs of reference appear in the first column with the corresponding effective energies of ICRP 2[18] in column 2 and the new values in column 3. The last column contains the ratios of the new to the old values, showing, in this case, the new energy terms to be about $^{1}/_{20}$ of the old.

Data in Table 24.4 illustrate the revised method of computing the energy emitted. Nickel-59, used in the

18. International Commission on Radiological Protection, *Report of Committee 2 on Permissible Doses for Internal Radiation*, ICRP Publication 2, Pergamon Press, New York, 1959.

19. National Council on Radiation Protection and Measurements, *Basic Radiation Protection Criteria*, NCRP Report 39, NCRP, Washington, D.C., 1971.

20. K. Way, ed., *Nuclear Data B1-2-24*, Academic Press, New York, 1966.

ORNL DWG. 76-9709

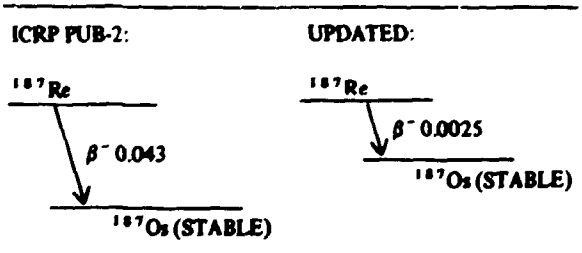

BODY ORGAN	EFFECTIVE ENERGY		NEW/PUB-2
	PUB-2	NEW	
BONE	0.062	0.0031	0.052
OTHER ORGANS	0.012	0.00063	0.052

Fig. 24.2. Effect of revised decay data.

Table 24.4. Comparison of energy emitted by ^{59}Ni: Dillman's method vs ICRP publication 2 method

Radiation	Mean number per disintegration	Mean energy per particle
	ICRP publication 2[a]	
K x ray	1	0.0077
	Dillman[b]	
K_α x ray	0.28	0.0069
K_β x ray	0.03	0.0077
KLL Auger	0.48	0.0061
KLX Auger	0.12	0.0068
LMN Auger	1.43	0.0007
MXY Auger	3.03	0.0001

Body organ	Effective energy		New/ICRP publication 2
	ICRP publication 2	New	
Bone	0.0077	0.027	3.5

[a]Ref. 18.
[b]Ref. 21.

example, decays 100% by electron capture, and this has not changed over the years; but in ICRP 2,[18] for simplicity, all the energy emitted following electron capture was assigned to the K-shell x ray. More recently, Dillman[21] designed a computer code that accepts information from decay schemes and produces quite a detailed breakdown of the energy emitted following rearrangements in the electron shells due, in this case, to electron capture.

In the simple case shown here, his code provided the intensity and energy of the different x rays and Auger electrons emitted. Because much of the energy is really due to electron emission instead of being all photon emission, as assumed previously, the updated effective energy for bone, as seen in the last line of Table 24.4, is about a factor of 3.5 higher because electron energies are assigned a relative damage factor of 5 compared with a factor of 1 for photons. In all cases, data from Dillman's code were used to produce the new effective energies.

Differences in absorbed fractions of photon energy as taken from ICRP 2 and as computed presently by Monte Carlo methods in a mathematical anthropomorphic phantom[22] are shown in Fig. 24.3. Absorbed fractions by the Monte Carlo method are generally lower (as shown in Fig. 24.3 for the lungs), and this is reflected in the new energy values given in Table 24.5 for ^{24}Na. Sodium-24 decays by beta-gamma emission. The decay scheme has remained essentially the same since ICRP 2, and the energy emitted, whether computed by Dillman's code or by ICRP 2 methods, is the same because there is no internal conversion of the gammas. Thus the differences in the effective energies as seen in column 4 are due to differences in the absorbed fractions.

Other examples of updated vs ICRP 2 values are given in Table 24.6. For ^{210}Pb, the new values range from 1 to about 4 times greater than the previous values. In

21. L. T. Dillman and F. C. Von der Lage, *Radionuclide Decay Schemes and Nuclear Parameters for Use in Radiation Dose Estimation*, MIRD pamphlet 10, Society of Nuclear Medicine, New York, 1975.

22. W. S. Snyder et al., *Estimates of Absorbed Fractions for Monoenergetic Photon Sources Uniformly Distributed in Various Organs of a Heterogeneous Phantom*, MIRD pamphlet 5, *J. Nucl. Med., Suppl. 3*, 10 (August 1969).

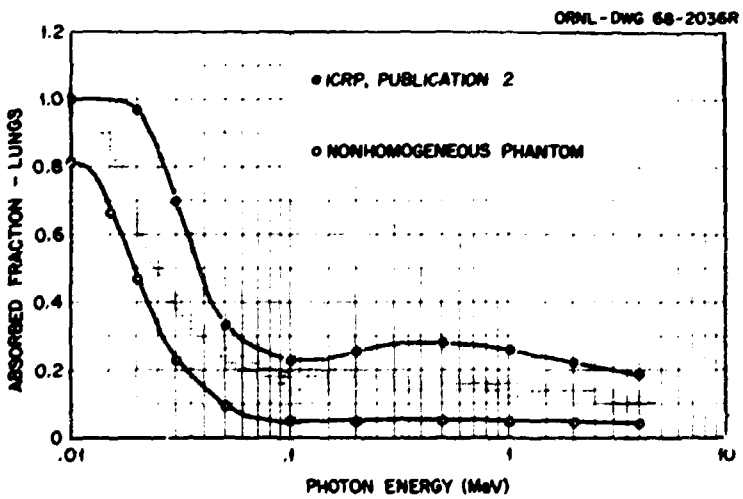

Fig. 24.3. Estimates by various methods of absorbed fractions of photon energy in the lungs – source uniform in the lungs.

Table 24.5. Effect of Monte Carlo absorbed fractions vs ICRP publication 2[a] values for ^{24}Na

Body organs	Effective energy		New/ICRP publication 2[a]
	ICRP publication 2[a]	New	
Total body	2.7	1.7	0.64
Lungs	1.5	0.71	0.48
GI (S)	1.5	0.64	0.43
GI (SI)	2.7	0.91	0.34
GI (LI)	1.0	0.65	0.65

[a]Ref. 18.

Table 24.6. Effective energies: new vs ICRP publication 2[a]

Radionuclide	Organ of reference	Effective energy		New/ICRP publication 2[a]
		ICRP publication 2[a]	New	
^{210}Pb	Total body	0.045	0.043	0.95
	Lungs	0.027	0.041	1.52
	GI (LLI)	0.019	0.039	2.07
	Kidneys	0.023	0.042	1.81
	Bone	0.051	0.20	3.88
	Liver	0.027	0.042	1.56
^{191}Pt	Total body	0.70	0.13	0.18
	GI (LLI)	0.16	0.054	0.34
^{90}Y	Total body	0.89	0.93	1.04
	Bone	4.4	4.7	1.05

[a]Ref. 18.

other cases the reverse is true (i.e., the new values are considerably lower). Such is the case for ^{191}Pt, for which the previous values are 3 to 5 times higher. In many other instances the values are very nearly equal. Yttrium-90 is such an example, with the new values being only about 5% greater.

The question then arises as to what fraction of the new values are high, low, or the same as ICRP 2 values and by what factor. Figure 24.4 was designed to provide the answer. Figure 24.4 is a plot of the ratio of new values to those of ICRP 2 for all organs of reference and all radionuclides listed in ICRP 2 except the noble gases, which are not included in the study. Thus, this graph includes data for over 2000 cases, that is, for over 200 radionuclides, each with an average of 10 organs of reference. On the abscissa, the numeral 1 marks the point at which the values are equal; to the left, the height of the bars indicates the number of cases in each interval of 0.1 which are in the indicated range. Bars to the right pertain to cases for which the ratios are greater than 1. As shown at the bottom of the graph, 67% of the new values are lower than the previous values, and 33% are higher; all are concentrated around 1 so that about half the new values are no more than 20% greater or less than the previous values. About 80% of the new values are within a factor of 2 of the ICRP 2 values, and 88% to 90% are within a factor of 3.

Concerning the use of the new values, perhaps the obvious thought is that the MPCs should be altered by the ratios of the new versus the ICRP 2 values. In some cases this would be appropriate; however, in other cases it would not. Along with revisions of the energy values, there have been revisions in dose computation. We are able now, for example, to provide estimates of the energy absorbed in an organ from a radionuclide residing in a nearby organ, and this cross-irradiation sometimes makes a significant contribution to dose. For example, referring back to the values for ^{24}Na in Table 24.5, if one uses the updated effective energies shown there plus cross-irradiation from nearby organs, the

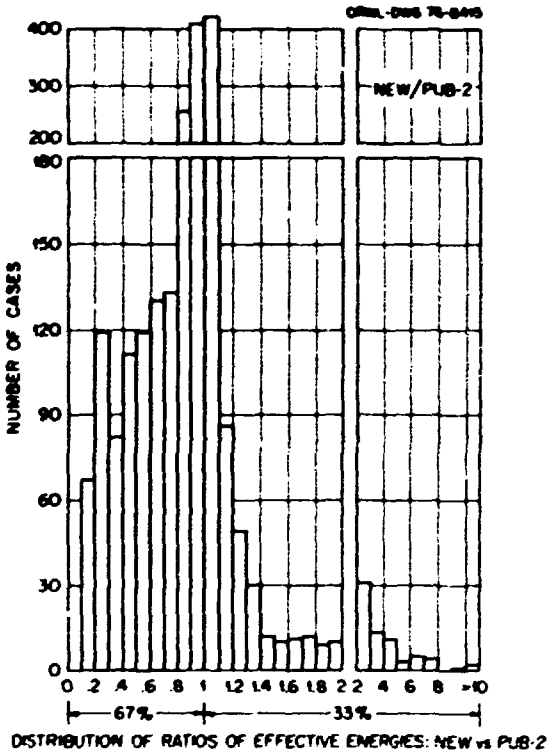

Fig. 24.4. Distribution of ratios of effective energies: new vs ICRP Publication 2.

resultant MPC value, which is based on dose to the small intestine, would be the same or nearly the same as the ICRP 2 MPC values (i.e., it would not be a third lower as the new energies shown in Table 24.5 and used as in ICRP 2 without considering cross-irradiation would indicate). This is the case if the metabolic model is unchanged. Actually, as indicated earlier, to recompute MPCs one should consider not only changes in the absorbed energy including cross-irradiation, but also changes in the metabolic models.

For updating the energy component, we are making available, as time permits, in the ORNL-5000 series,[23] values that provide for cross-irradiation and take full account of all the revisions in the absorbed energies mentioned here, such as revised decay schemes, Monte Carlo absorbed fractions, etc. Thus, in addition to the ORNL-5000 data,[23] one will need only the metabolic models, whether from ICRP 2 or updated models, to revise the MPC values of ICRP 2 or 10 CFR 20.

RADIOACTIVE DECAY SCHEME DATA

The computer code developed previously to provide radioactive decay data in the form needed for estimating internal dose has been used over the years to generate data for more than 550 radionuclides. Data for certain radionuclides of interest in nuclear medicine have been published by the MIRD Committee (MIRD pamphlet 10). Plans are now under way to publish a comprehensive list as a data base for the forthcoming revision of the ICRP Report of Committee 2 on Internal Dose. Before publication, the data will be updated using a revised computer code (see ORNL-5171) and more recent decay scheme data and presented in a format illustrated in this report. Publication will be in several installments, the first to contain data for the 250 to 300 radionuclides of greatest interest in radiation protection work.

The Medical Physics and Internal Dosimetry Section of ORNL has collected and analyzed decay scheme data for a number of years. These data are available for more than 550 radionuclides of interest in medical and health physics applications. Although this broad data base has been provided on request, it has never been published. In connection with the work of committee 2 of the ICRP, the section plans to publish these decay scheme data in several installments. The first publication will contain data on about 250 radionuclides associated with about 20 of the most important elements involved in radiation protection work. Data on all members of a radioactive decay chain will be provided.

Since several sources of radioactive decay scheme data are already available,[24,25] the rationale for publication of our data needs to be explained. In medical and health physics dosimetry calculations it is necessary to know the mean energies and absolute intensities of all radiations emitted in the radioactive decay process. This includes intensities and energies of x rays and Auger electrons which arise due to atomic readjustments following a nuclear decay. It is also necessary to know the average energy of β^+ or β^- transitions, the energies and intensities of internal conversion electrons, and the energies and intensities of radiations concomitant with spontaneous fission. These data often are not available directly from *Nuclear Data Sheets*[24] or *Table of Isotopes*[25] or the original literature. A computer program was developed which uses the data available in *Nuclear Data Sheets*[24] and *Table of Isotopes*[25] to calculate the additional parameters indicated above, a requirement in making radiation dose estimates. This computer code has been described elsewhere.[21] Some

23. W. S. Snyder et al., *A Tabulation of Dose Equivalent per Microcurie-Day for Source and Target Organs of an Adult for Various Radionuclides*, ORNL-5000, Parts I and II (1974).

24. *Nuclear Data Sheets*, ed. by Nuclear Data Group, Oak Ridge National Laboratory, Oak Ridge, Tenn.

25. C. M. Lederer et al., *Table of Isotopes*, 6th ed., John Wiley and Sons, New York, 1967.

recent improvements in the computer code have been described by Dillman.[26]

The output of the computer program for a given nuclide is conveniently divided into four parts: (1) the decay scheme drawing, (2) a tabulation of input data used, (3) a tabulation of the basic output decay scheme data, and (4) a tabulation of special data related to decay schemes, which is useful in specialized dosimetry calculations. We shall discuss each of these four parts using ^{144}Ce as a sample case. The computer-generated data for the case of ^{144}Ce is shown in Fig. 24.5 and in Tables 24.7 through 24.10.

The decay scheme drawing is intended to provide the viewer with a concise overview of the main decay properties. In the ^{144}Ce sample case note that there are gamma transitions ending on a 0.0590-MeV level in the daughter nuclide ^{144}Pr; however, there are no gamma transitions depopulating this level. This occurs because the level at 0.0590 MeV is an isomeric level with a half-life of 7.2 min. The decays of all isomeric levels are treated separately with separate decay scheme drawings.

The tabulation of the input data gives, in addition to the energies and intensities of the primary radiations emitted in the decay, information on the values of other nuclear parameters used by the computer code in various ways. For example, it is necessary to know the multipolarity of a gamma-ray transition to evaluate theoretical internal conversion coefficients. Values of internal conversion coefficients are, in turn, required to obtain intensities of internal conversion electrons, x rays, and Auger electrons. The references used to obtain the input data are always listed at the conclusion of the tabulation of input data.

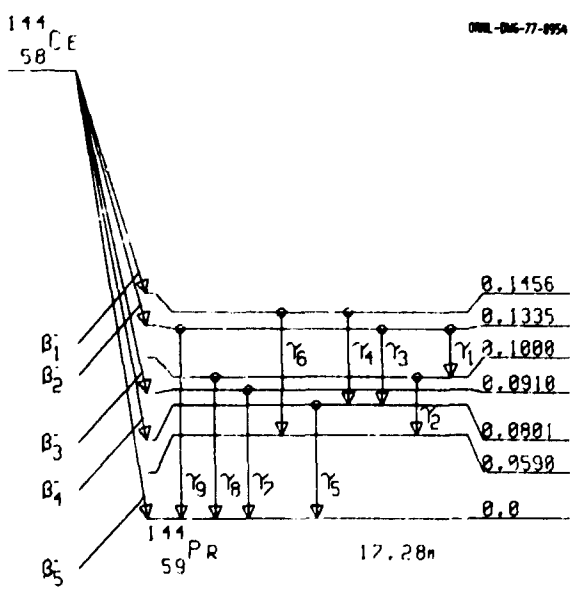

Fig. 24.5. Radiological decay of ^{144}Ce.

The tabulation of output data gives all radiations of a particular category which contribute more than a specified cutoff percentage to that category. The cutoff percentage value is an input parameter and is typically set at 0.010%. The three major categories to which the cutoff percentage is separately applied are (1) x rays, gamma rays, and annihilation radiation; (2) β^+ and β^- particles, internal conversion, and Auger electrons; and (3) alpha particles and recoil nuclei from alpha emission or spontaneous fission. The reason for applying the cutoff separately to these categories is associated with the widely differing ways the categories of radiation interact with matter. For example, a nuclide may be an almost pure beta emitter with a very weak gamma ray. Because only the gamma radiation is penetrating, it may contribute the entire dose to many tissues and, therefore, should not be neglected.

Also, in the tabulation of output data there are groupings of radiations with very similar properties. The presence of a grouping is indicated by the word "total" preceding the radiation type in the output. In the sample case of ^{144}Ce, there are eight radiations that begin with "total," each representing a grouping of several radiation types. The total L_α x-ray entry consists of $L_{\alpha 1}$ and $L_{\alpha 2}$ x rays which have energies differing only slightly from one another. The listed energy value is a weighted mean of the two energy values. The total KLL Auger electron consists of KL_1L_1, KL_1L_2, KL_1L_3, KL_2L_2, KL_2L_3, and KL_3L_3 transitions of slightly differing energies. Indeed, the KL_1L_2, KL_1L_3, and KL_3L_3 transitions each have an additional satellite associated with them. The mean number per decay value listed for total KLL Auger electron is the sum over all these KLL-type transitions. The listed energy is a weighted mean energy for all these KLL-type transitions. Similar remarks apply to all the other radiations that are grouped together.

Important remarks are listed at the conclusion of the tabulation of output data. If the daughter nuclides are radioactive, this is noted. The branching fractions to isomeric levels in the daughter nuclide are noted so that the user can correctly take into account the contribution to dose due to radiations arising from the decay of any such isomeric levels.

Finally, the computer program tabulates data related to decay schemes that are useful in specialized dosim-

26. L. T. Dillman, *Health Phys. Div. Annu. Prog. Rep. June 30, 1976*, ORNL-5171 (October 1976), pp. 55–58.

Table 24.7. Computer-generated input data for $^{144}Ce_{58}$ β^- decay

Half-life = 2.843E2 days

Type of transition	Mean No. per decay	Transition energy (MeV)	Other nuclear parameters
β_1^-	6.00E−3	1.699E−1[a]	Unique first forbidden
β_2^-	1.94E−1	1.820E−1[a]	First forbidden
β_3^-	3.50E−3	2.245E−1[a]	Unique first forbidden
β_4^-	4.20E−2	2.354E−1[a]	First forbidden
β_5^-	7.58E−1	3.155E−1[a]	First forbidden
γ_1	1.32E−2	3.357E−2	M_1: AK = 0.00E−1, AM = 7.88E−1T,[b] AN^+ = 2.15E−1T, AL = 3.76T, $L_{1/2}$ = 1.17E1T, $L_{1/3}$ = 5.63E1T
γ_2	1.39E−2	4.093E−2	M_1: AK = 0.00E−1, AM = 4.39E−1T, AN^+ = 1.20E−1T, AL = 2.09T, $L_{1/2}$ = 1.18E1T, $L_{1/3}$ = 5.76E1T
γ_3	1.05E−2	5.341E−2	M_1: AK = 6.88T, AM = 2.00E−1T, AN^+ = 5.49E−2T, AL = 9.57E−1T, $L_{1/2}$ = 1.21E1T, $L_{1/3}$ = 5.95E1T
γ_4	1.80E−3	6.600E−2	
γ_5	5.52E−2	8.012E−2	M_1: K/L = 7.50, $L_{1/2}$ = 1.23E1, $L_{1/3}$ = 5.88E1, AK = 2.12T, AM = 6.13E−2T, AN^+ = 1.68E−2T
γ_6	3.80E−3	8.650E−2	
γ_7	3.50E−3	9.100E−2	
γ_8	1.20E−3	9.995E−2	E_2: AK = 1.23ET, AM = 1.60E−1T, AN^+ = 4.17E−2T, AL = 7.16E−1T, $L_{1/2}$ = 3.78E−1T, $L_{1/3}$ = 3.48E−1T
γ_9	1.70E−1	1.335E−1	M_1: AK = 4.90E−1, AL = 6.85E−2, $L_{1/2}$ = 1.35E1, $L_{1/3}$ = 5.57E1, AM = 1.42E−2T, AN^+ = 3.89E−3T

[a]End-point energy, MeV.

[b]T = evaluated from theory.

Source: *Nucl. Data Sheets* **16**(2), 234, 244, 250, and 251 (1975), Academic Press, New York.

Table 24.8. Computer-generated output data for $^{144}Ce_{58}$ β^- decay

Half-life = 2.843E2 days

Type of radiation	Mean No. per decay	Energy (MeV)[a]	Gram-rad per microcurie-hour
β_1^-	6.00E−3	5.474E−2	7.00E−4
β_2^-	1.94E−1	4.939E−2	2.04E−2
β_3^-	3.50E−3	7.337E−2	5.47E−4
β_4^-	4.20E−2	6.530E−2	5.84E−3
β_5^-	7.58E−1	9.026E−2	1.46E−1
γ_1	2.29E−3	3.357E−2	1.64E−4
L_1 shell conversion electron	7.80E−3	2.674E−2	4.44E−4
L_2 shell conversion electron	6.69E−4	2.713E−2	3.87E−5
M shell conversion electron	1.81E−3	3.233E−2	1.24E−4
N^+ shell conversion electron	4.92E−4	3.357E−2	3.52E−5
γ_2	3.80E−3	4.093E−2	3.32E−4
L_1 shell conversion electron	7.23E−3	3.410E−2	5.25E−4
L_2 shell conversion electron	6.11E−4	3.449E−2	4.49E−5

Table 24.8 (continued)

Type of radiation	Mean No. per decay	Energy (MeV)[a]	Gram-rad per microcurie-hour
M shell conversion electron	1.67E-3	3.969E-2	1.81E-4
N^+ shell conversion electron	4.56E-4	4.093E-2	3.98E-5
γ_3	1.15E-3	5.341E-2	1.31E-4
K shell conversion electron	7.95E-3	1.142E-2	1.93E-4
L_1 shell conversion electron	1.00E-3	4.658E-2	9.97E-5
M shell conversion electron	2.31E-4	5.217E-2	2.57E-5
γ_4	1.80E-3	6.600E-2	2.53E-4
γ_5	1.59E-2	8.012E-2	2.71E-3
K shell conversion electron	3.36E-2	3.813E-2	2.73E-3
L_1 shell conversion electron	4.08E-3	7.329E-2	6.37E-4
L_2 shell conversion electron	3.31E-4	7.368E-2	5.19E-5
M shell conversion electron	9.74E-4	7.888E-2	1.64E-4
N^+ shell conversion electron	2.67E-4	8.012E-2	4.56E-5
γ_6	3.80E-3	8.650E-2	7.00E-4
γ_7	3.50E-3	9.100E-2	6.78E-4
γ_8	3.82E-4	9.995E-2	8.12E-5
K shell conversion electron	4.68E-4	5.796E-2	5.78E-5
L_2 shell conversion electron	1.11E-4	9.351E-2	2.21E-5
L_3 shell conversion electron	1.20E-4	9.399E-2	2.41E-5
γ_9	1.08E-1	1.335E-1	3.07E-2
K shell conversion electron	5.28E-2	9.154E-2	1.03E-2
L_1 shell conversion electron	6.77E-3	1.267E-1	1.83E-3
L_2 shell conversion electron	5.02E-4	1.271E-1	1.36E-4
L_3 shell conversion electron	1.22E-4	1.276E-1	3.30E-5
M shell conversion electron	1.53E-3	1.323E-1	4.31E-4
N^+ shell conversion electron	4.19E-4	1.335E-1	1.19E-4
$K\alpha_1$ x ray	4.50E-2	3.603E-2	3.45E-3
$K\alpha_2$ x ray	2.46E-2	3.555E-2	1.86E-3
$K\beta_1$ x ray	8.90E-3	4.075E-2	7.73E-4
$K\beta_2$ x ray	3.58E-3	4.179E-2	3.18E-4
$K\beta_3$ x ray	4.59E-3	4.065E-2	3.97E-4
$K\beta_5$ x ray	1.28E-4	4.105E-2	1.12E-5
KXY Auger electron	3.56E-4	3.946E-2	3.00E-5
MXY Augur electron	1.86E-1	1.092E-3	4.34E-4
Residual low energy	1.00	5.968E-4	1.27E-3
Total L_α x ray	6.27E-3	5.031E-3	6.72E-5
Total L_β x ray	6.56E-3	5.575E-3	7.79E-5
Total L_γ x ray	1.00E-3	6.451E-3	1.38E-5
Total KLL Auger electron	5.18E-3	2.914E-2	3.21E-4
Total KLX Auger electron	2.53E-3	3.434E-2	1.85E-4
Total LMM Auger electron	5.86E-2	4.043E-3	5.05E-4
Total LMX Auger electron	3.44E-2	5.157E-3	3.78E-4
Total LXY Auger electron	5.37E-3	5.974E-3	6.83E-5
All listed x rays, gamma rays, and annihilation radiation			4.27E-2
All neglected x rays, gamma rays, and annihilation radiation[b]			1.35E-6
All listed betas, internal conversion, and Auger electrons			1.95E-1
All neglected betas, internal conversion, and Auger electrons[b]			7.02E-5
All listed radiations			2.37E-1
All neglected radiations[b]			7.16E-5

[a]Average energy for β^+ or β^-.

[b]Each neglected transition contributes less than 0.010% to the total equilibrium dose constant for this category.

Remarks: Daughter nuclides, ^{144m}Pr and ^{144}Pr, are radioactive and may contribute to the dose. Branching to the 0.05903-MeV, 7.2-min half-life, isomeric level in ^{144}Pr is 0.0177 per disintegration of ^{144}Ce.

Table 24.9. Computer-generated β spectrum data for all decay branches for $^{144}Ce_{58}$

Half-life = 2.843E2 days

Energy[a] (MeV)	Betas per MeV per decay[b]	Energy[a] (MeV)	Betas per MeV per decay[b]
0.00000	8.994	0.00650	8.644
0.00010	8.989	0.00700	8.617
0.00011	8.988	0.00750	8.590
0.00012	8.988	0.00800	8.563
0.00013	8.987	0.00850	8.536
0.00014	8.987	0.00900	8.509
0.00015	8.986	0.01000	8.455
0.00016	8.986	0.01100	8.417
0.00018	8.985	0.01200	8.376
0.00020	8.984	0.01300	8.334
0.00022	8.982	0.01400	8.292
0.00024	8.981	0.01500	8.250
0.00026	8.980	0.01600	8.207
0.00028	8.979	0.01800	8.123
0.00030	8.978	0.02000	8.038
0.00032	8.977	0.02200	7.952
0.00036	8.975	0.02400	7.866
0.00040	8.973	0.02600	7.780
0.00045	8.970	0.02800	7.694
0.00050	8.967	0.03000	7.607
0.00055	8.965	0.03200	7.520
0.00060	8.962	0.03600	7.345
0.00065	8.959	0.04000	7.170
0.00070	8.956	0.04500	6.950
0.00075	8.954	0.05000	6.729
0.00080	8.951	0.05500	6.508
0.00085	8.948	0.06000	6.286
0.00090	8.946	0.06500	6.065
0.00100	8.940	0.07000	5.845
0.00110	8.935	0.07500	5.625
0.00120	8.929	0.08000	5.407
0.00130	8.924	0.08500	5.189
0.00140	8.919	0.09000	4.974
0.00150	8.913	0.10000	4.549
0.00160	8.908	0.11000	4.134
0.00180	8.897	0.12000	3.733
0.00200	8.886	0.13000	3.348
0.00220	8.875	0.14000	2.983
0.00240	8.865	0.15000	2.641
0.00260	8.854	0.16000	2.327
0.00280	8.843	0.18000	1.792
0.00300	8.832	0.20000	1.355
0.00320	8.821	0.22000	9.936E−1
0.00360	8.800	0.24000	6.301E−1
0.00400	8.778	0.26000	3.572E−1
0.00450	8.751	0.28000	1.531E−1
0.00500	8.724	0.30000	3.054E−2
0.00550	8.697	0.31550	0.000E−1
0.00600	8.671		

[a]Average beta energy = 8.104E−2.
[b]Total betas per decay for all branches = 1.003.

Table 24.10. Bremsstrahlung photons per disintegration for $^{144}Ce_{38}$

Half-life = 2.843E2 days

Energy interval (MeV)		Internal	Air[a]	Tissue[a]	Bone[a]	Fat[a]
From	To					
0.0045	0.0055	8.4233E-5	4.4335E-4	4.1954E-4	5.2044E-4	3.7478E-4
0.0055	0.0065	6.8927E-5	3.5032E-4	3.3167E-4	4.1115E-4	2.9647E-4
0.0065	0.0075	5.8019E-5	2.8615E-4	2.7103E-4	3.3579E-4	2.4240E-4
0.0075	0.0085	4.9857E-5	2.3949E-4	2.2693E-4	2.8102E-4	2.0306E-4
0.0085	0.0095	4.3527E-5	2.0421E-4	1.9357E-4	2.3962E-4	1.7328E-4
0.0095	0.0105	3.8477E-5	1.7671E-4	1.6756E-4	2.0736E-4	1.5006E-4
0.0105	0.0115	3.4358E-5	1.5475E-4	1.4678E-4	1.8160E-4	1.3150E-4
0.0115	0.0125	3.0938E-5	1.3687E-4	1.2985E-4	1.6062E-4	1.1638E-4
0.0125	0.0135	2.8053E-5	1.2206E-4	1.1583E-4	1.4325E-4	1.0385E-4
0.0135	0.0145	2.5590E-5	1.0962E-4	1.0406E-4	1.2866E-4	9.3319E-5
0.0145	0.0155	2.3464E-5	9.9057E-5	9.4055E-5	1.1627E-4	8.4371E-5
0.0155	0.0165	2.1611E-5	8.9988E-5	8.5464E-5	1.0564E-4	7.6686E-5
0.0165	0.0175	1.9983E-5	8.2133E-5	7.8021E-5	9.6425E-5	7.0026E-5
0.0175	0.0185	1.8543E-5	7.5274E-5	7.1521E-5	8.8382E-5	6.4209E-5
0.0185	0.0195	1.7260E-5	6.9244E-5	6.5806E-5	8.1310E-5	5.9093E-5
0.0195	0.0210	2.4165E-5	9.5864E-5	9.1122E-5	1.1258E-4	8.1846E-5
0.0210	0.0230	2.8278E-5	1.0983E-4	1.0444E-4	1.2901E-4	9.3852E-5
0.0230	0.0250	2.5027E-5	9.5320E-5	9.0673E-5	1.1198E-4	8.1516E-5
0.0250	0.0270	2.2305E-5	8.3417E-5	7.9378E-5	9.8017E-5	7.1391E-5
0.0270	0.0290	1.9999E-5	7.3520E-5	6.9983E-5	8.6403E-5	6.2967E-5
0.0290	0.0320	2.7034E-5	9.7791E-5	9.3116E-5	1.1495E-4	8.3813E-5
0.0320	0.0360	2.9654E-5	1.0410E-4	9.9187E-5	1.2240E-4	8.9345E-5
0.0360	0.0400	2.4738E-5	8.4503E-5	8.0557E-5	9.9381E-5	7.2615E-5
0.0400	0.0440	2.0867E-5	6.9498E-5	6.6287E-5	8.1750E-5	5.9794E-5
0.0440	0.0480	1.7761E-5	5.7768E-5	5.5128E-5	6.7963E-5	4.9761E-5
0.0480	0.0550	2.6652E-5	8.4771E-5	8.0936E-5	9.9743E-5	7.3106E-5
0.0550	0.0650	2.6585E-5	8.0315E-5	7.6772E-5	9.4508E-5	6.9460E-5
0.0650	0.0750	1.9058E-5	5.4931E-5	5.2566E-5	6.4627E-5	4.7639E-5
0.0750	0.0850	1.3913E-5	3.8374E-5	3.6762E-5	4.5128E-5	3.3372E-5
0.0850	0.0950	1.0287E-5	2.7206E-5	2.6092E-5	3.1973E-5	2.3727E-5
0.0950	0.1100	1.1511E-5	2.9230E-5	2.8063E-5	3.4320E-5	2.5567E-5
0.1100	0.1300	8.6688E-6	2.0345E-5	1.9577E-5	2.3829E-5	1.7905E-5
0.1300	0.1500	4.9197E-6	1.0687E-5	1.0308E-5	1.2475E-5	9.4681E-6
0.1500	0.1700	2.7595E-6	5.5487E-6	5.3655E-6	6.4481E-6	4.9518E-6
0.1700	0.1900	1.5016E-6	2.7923E-6	2.7076E-6	3.2266E-6	2.5122E-6
0.1900	0.2300	1.5468E-6	2.6580E-6	2.5852E-6	3.0497E-6	2.4130E-6
0.2300	0.2900	1.4432E-7	1.9495E-7	1.9165E-7	2.1629E-7	1.8299E-7

[a]Air, tissue, bone, and fat columns include internal bremsstrahlung.

etry applications. For example, there are circumstances in which knowledge of the spectral distribution of beta particles may be important. This would be true, for example, where beta depth doses are calculated. Also, bremsstrahlung radiation accompanying beta decay can represent a significant contribution to dose under special conditions.

ADJUSTMENTS OF INHALATION DOSES TO TAKE ACCOUNT OF PARTICLE SIZES

The computer code reported in ORNL-4506 and in ORNL/CSD/TM-17 is programmed to compute the time integral of activities using metabolic models for the lungs, gastrointestinal tract, and other organs of the body. The lung model incorporated in the code is that of the ICRP Task Group on Lung Dynamics which provides data for aerosols having a wide range of particle sizes. The code, however, until the recent modification described in this report, could provide doses only for one particle size. With the new scheme, three fractions are produced which indicate the percentages of the dose applicable to the three major regions of the lungs. Thus the dose estimates for one particle size can be adjusted with these fractions to produce dose estimates for aerosols of different particle sizes. These fractions for many

radionuclides are expected to form a part of the forthcoming ICRP and NCRP reports on internal emitters.

In *Deposition and Retention Models for Internal Dosimetry of the Human Respiratory Tract*[27] the ICRP Task Group on Lung Dynamics has given a particularly simple model for deposition of an aerosol in the air passages of the human. Although the model only applies for a particulate aerosol and is only to be used when the distribution of AMAD is log-normally distributed, it has proven useful in predicting the fraction of the inhaled activity which is deposited in the various regions of the tract. Generally, the log-normal distribution of activities seems to be a characteristic of the samples encountered in most working situations, and thus the amounts deposited have been reduced to the determination of a single parameter, the AMAD. The activity deposited in the nasopharyngeal region (N-P), in the tracheobronchial region (T-B), and in the pulmonary region (P) vary widely as the AMAD changes from, say, 0.2 to 10 μm.

These amounts deposited are reflected by the doses to the various organs. Thus, if a particulate aerosol of AMAD = 10 μm is inhaled, it will be deposited largely in the N-P region; for class Y the clearance is largely by way of the gastrointestinal (GI) tract. However, if the AMAD is, say, 0.2 μm, deposition in the pulmonary region will predominate, and although a considerable portion may clear by way of the GI tract, there may still be a considerable portion that clears to the blood. For a fairly recent summary of the deposition and clearance half-times and fractions of activity following each pathway, one may consult Fig. 24.6 for the deposition and Fig. 24.7 for the clearance data. It will be noted that not only is there a wide spectrum of possibilities for clearance from the respiratory tract, but also the independent parameter representing the fraction of activity absorbed to the blood from the GI tract is another consideration that affects the pathways the radionuclide will follow.

Nevertheless, it is possible to define by a single calculation the entire spectrum of doses if they reflect only the dependence on particle size. Thus, assuming (1) absorption to the blood from the GI tract and (2) that other biological parameters involved in the model do not change and (3) that only the AMAD of the aerosol change (or, equivalently, that the fractions of activity deposited in the N-P, T-B, and P regions change), one can define the dose for an aerosol of any given AMAD by a simple calculation of the portion of the organ dose caused by deposition in the various regions of the lung. To see this we note that dose to an organ X is a sum of doses emitted in various source organs, Y, that is,

$$D(X) = \sum_{Y} U(Y) \times S(X \leftarrow Y) , \qquad (1)$$

where U denotes the number of nuclear transformations occurring in source organ Y (perhaps in units of μCi-days), and S represents the dose received by organ X due to 1 μCi-day in source organ Y. In the present simplified and idealized models for calculation of internal dosimetry, the distribution of the radionuclide in organ Y is not accurately represented. In fact, few

27. ICRP Task Group on Lung Dynamics, *Health Phys.* 12, 173 (1966).

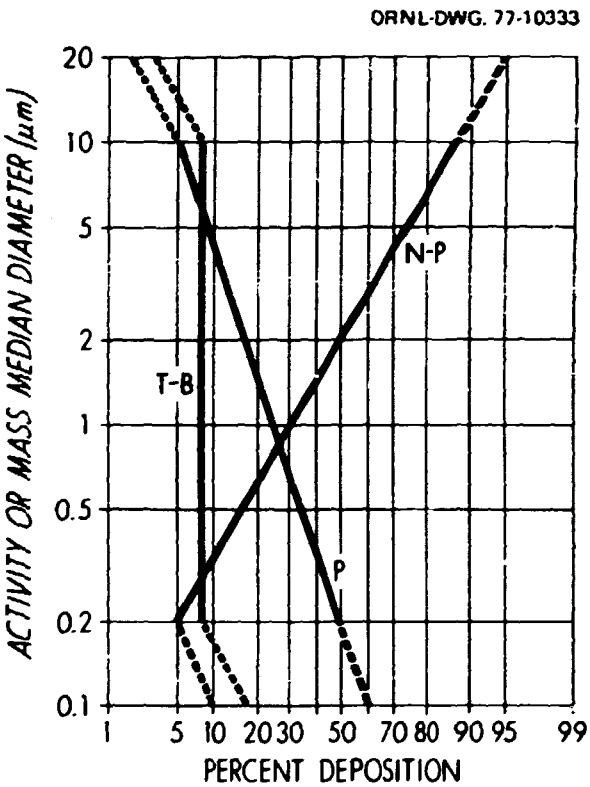

Fig. 24.6. Deposition model: The radioactive or mass fraction of an aerosol which is deposited in the N-P, T-B, and P regions is given in relation to the activity or mass median aerodynamic diameter (AMAD or MMAD) of the aerosol distribution. The model is intended for use with aerosol distributions having an AMAD or MMAD between 0.2 and 10 μm and whose geometric standard deviations are less than 4.5. Provisional deposition estimates further extending the size range are given by the dashed lines. For the unusual distribution having an AMAD or MMAD greater than 20 μm, complete N-P deposition can be assumed. The model does not apply to aerosols with AMADs or MMADs below 0.1 μm (e.g., radionuclei and fumes).

ORNL-DWG 73-7250

CLEARANCE MODEL

COMPARTMENT		CLASS D T	CLASS D F	CLASS W T	CLASS W F	CLASS Y T	CLASS Y F
N-P	a	0.01	0.5	0.01	0.1	0.01	0.01
(D_{N-P}=0.30)	b	0.01	0.5	0.40	0.9	0.40	0.99
T-B	c	0.01	0.95	0.01	0.5	0.01	0.01
(D_{T-B}=0.08)	d	0.2	0.05	0.2	0.5	0.2	0.99
	e	0.5	0.8	50	0.15	500	0.05
P	f	n.a.	n.a.	1.0	0.4	1.0	0.4
(D_P=0.25)	g	n.a.	n.a.	50	0.4	500	0.4
	h	0.5	0.2	50	0.05	500	0.15
L	i	0.5	1.0	50	1.0	1000	0.9

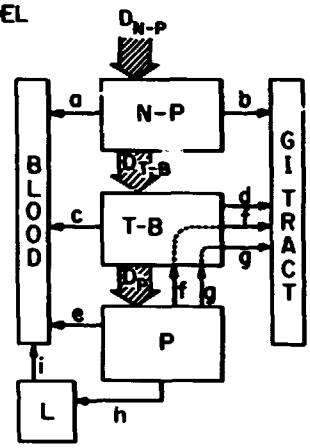

Fig. 24.7. Values for the removal half-times, T_{a-i}, and regional fractions, F_{a-i}, are given in the tabular portion of the figure for each of the three classes of retained materials. The values given for D_{N-P}, D_{T-B}, and D_P (left column) are the regional depositions based on an aerosol with a 1-μm AMAD. The schematic drawing identified the various clearance pathways in the model, *a-i*, in relation to the depositions D_{N-P}, D_{T-B}, and D_P and the three respiratory regions, N-P, T-B, and P.

details are available; thus the tendency has been to assume it is uniform even though one could calculate differently if data were available. Thus, $S(X \leftarrow Y)$ will not normally involve much biological information and, in particular, is assumed to be independent of whether the activity distributed in Y came from the N-P, T-B, or P region. This approximation is the one normally used in computing the doses received by an organ.

The calculation of $U(Y)$, the μCi-days in the various source regions, can be done in a variety of ways, but here it specifically relates to the TIMED computer program described by Watson, Snyder, and Ford.[28] This computer code has already programmed the ICRP lung model, as revised by the Task Group on Plutonium and Other Actinides,[29] and the code for the GI-tract model described in ORNL-5171.[30] Other organs must be inserted in the form of a sum of exponentials for running. The code does not record automatically for each bit of activity entering an organ whether it originated in the N-P, T-B, or P region. The same effect is achieved in another way. The program is run for the N-P region receiving a prescribed deposition, for example, D_3, but with the depositions in the T-B and P regions equal to 0. Then the code is rerun to obtain the doses from deposition of D_4 in the T-B region but with the other two regions having zero deposition. Finally, the code is run for the case of D_3 deposition in the N-P region, D_4 deposition in the T-B region, and D_5 deposition in the P from, for example, a standard aerosol of 1 μm in diameter. The portion of the doses from these three regions are obtained by subtraction. Thus, if D_{N-P}, D_{T-B}, and D_P are the doses to an organ from material deposited in the N-P, T-B, and P regions, one can form the fractions D_{N-P}/D, D_{T-B}/D, and D_P/D, where $D = D_{N-P} + D_{T-B} + D_P$ for organ X. These indicate what portion of the dose originated from each of the three depositions.

The results for an aerosol of a different AMAD are obtained by simply consulting Fig. 24.6 to determine the depositions, say, D_3^*, D_4^*, D_5^*. Assuming that all other features of the dosimetry model are the same, one determines that doses to the organ X from activity in the N-P, T-B, and P regions are given by

$$D_{N-P}^* = \frac{D_{N-P}}{D_3} \times D_3^* \; ; \; D_{T-B}^* = \frac{D_{N-P}}{D_4} \times D_4^* \; ; \qquad (2)$$

$$D_P^* = \frac{D_P}{D_5} \times D_5^* \; .$$

28. S. B. Watson, W. S. Snyder, and M. R. Ford, *TIMED: A Computer Program for Calculating Cumulated Activity of a Radionuclide in the Organs of the Human Body at a Given Time, t, after Deposition*, ORNL/CSD/TM-17 (1976).

29. International Commission on Radiological Protection, *The Metabolism of Compounds of Plutonium and Other Actinides*, ICRP Publication 19, Pergamon Press, New York, 1972.

30. S. F. Deus, V. Provenzano, and W. S. Snyder, *Health Phys. Div. Annu. Prog. Rep. June 30, 1976*, ORNL-5171 (October 1976), p. 12.

Equation (2) simply expresses the fact that the μCi-days are additive, and thus $D_{N\text{-}P}/D_3$ is the dose to organ X for unit deposition in the N-P region. The equations used are all linear, and thus the doses, $D^*_{N\text{-}P}$, etc., are all proportional to the activity deposited. Hence the sum of these doses is the total dose D^* to organ X and can be expressed in the convenient form

$$D^* = \frac{D_{N\text{-}P}(1)}{D_3(1)} \times D_3^* + \frac{D_{T\text{-}B}(1)}{D_4(1)} \times D_4^* + \frac{D_P(1)}{D_5(1)} \times D_5^* , \quad (3)$$

where D^* is the total dose to organ X resulting from depositions of D_3^*, D_4^*, and D_5^* in the N-P, T-B, and P regions, respectively, and $D_{N\text{-}P}(1)$, $D_{T\text{-}B}(1)$, and $D_P(1)$ represent the doses resulting from the deposition of activities $D_3(1)$, $D_4(1)$, and $D_5(1)$ in these respective regions. The use of $D_{N\text{-}P}(1)$, etc., indicates that these doses are for an aerosol of 1-μm AMAD, but there is nothing special about this as long as none of the depositions [$D_3(1)$, etc.] are equal to 0. These fractions for a number of radionuclides are expected to form a part of the forthcoming ICRP and NCRP reports on internal emitters.

CURVE FITTING OF CURIUM EXCRETION DATA

The curve-fitting study of an employee's excretion of curium illustrates one technique that can be used to determine the body burden from an unknown intake of radioactive material. In this case, the body burden was estimated at about $1/10$ to $1/20$ of the maximum permissible body burden, indicating minimal hazard to the employee; however, more data would be required to give a more exact estimate of the hazard. This technique has wide applicability in other cases.

In the past year several employees were accidentally exposed by inhalation or by skin absorption to ^{244}Cm. We report here on curve fitting of the excretion data on one of the employees. The urinary excretion data appear in Table 24.11. The employee inhaled airborne compounds when his plastic airsuit was punctured by burning as he was using electric arc techniques to cut piping that had contained $CmCl_3$ or $Cm(NO_3)_3$ some years earlier. (The heat involved in the cutting would probably convert $Cm(NO_3)_3$ to Cm_2O_3.) To fit this data with a sum of exponentials the curve-fitting procedure ORDEAL[31] was used. This procedure uses least squares to minimize

Table 24.11. Urinary excretion data on one employee

Time (days)	Dis min^{-1} day^{-1}
1	21
5	1.4
10	0.7
17	0.62
23	0.28
30	0.3
44	0.26
51	0.29
65	0.36
86	0.24
99	0.01
131	0.19
168	0.4
380	0.18

$$\phi = \sum_{i=1}^{N} W_i(Y_i - y_i)^2 \qquad i = 1, 2, \ldots . N ,$$

where Y_i is the observed excretion and

$$y_i = \sum_{j=1}^{n} a_j e^{-\alpha_j t_i}$$

is the function fitted to the data and the a_j and α_j (parameters) have to be determined such that ϕ is a minimum and N is the number of data points to be fitted. In the sum of exponentials, n is the total number of terms (usually we did not fit more than three) and t_i is the time of measurement after the accidental intake of ^{244}Cm. Mention needs to be made that W_i is a weighting factor. Usually it is taken as unity. The method of minimization is to expand the y_i in Taylor series about initial estimates for the a_j and α_j and drop the second- and higher-order terms. Then the partial deviations of ϕ with respect to the parameters are taken and set equal to 0. This gives a set of linear equations in small correction factors for the a_j and α_j, and these can be computed in iterative fashion to get a minimum in ϕ.

31. M. Feliciano et al., *ORDEAL, Oak Ridge Data Evaluation and Analysis Language*, ORNL-4506 (March 1970).

When this was done using a two-exponential model, one of the α_js became negative, and the best fit was a parabolic type of exponential sum. This was due to the one low point at 99 days. It was found that this could be removed by taking the best-fitting sum of exponentials in the form

$$y_i = \sum_j a_j e^{-\alpha_j^2 t_i} ;$$

that is, by merely squaring the α_j it could take on negative values and α_j^2 would always be a positive number so that the sum of exponentials would decline. When this was done the best-fitting equation became

$$y_i = 41e^{-0.723t} + 1.08e^{-0.0841t} + 0.24e^{-0.000267t} \text{ dis min}^{-1} \text{ day}^{-1} .$$

The graph of this appears in Fig. 24.8.

To obtain an estimate of the hazard to the man involved, we integrated the above equation from 0 to infinity and found the total area to be about 0.4 nCi. Now, in studies by Wrenn, Cohen, and Eisenbud[32] on baboons injected with curium, a plot of the excretion in urine could be fitted with a power function, and when we integrated it to infinity, 0.1 of the injected dose was excreted in urine. So, by applying this factor the body burden is estimated to be 4 nCi. This is small compared to the 40 to 80 nCi required to irradiate bone at the permissible level of 30 rems per year for bone and 15 rems per year for lungs. Even so, it would be comforting to have more data so that more confidence could be placed in the extrapolation to infinity.

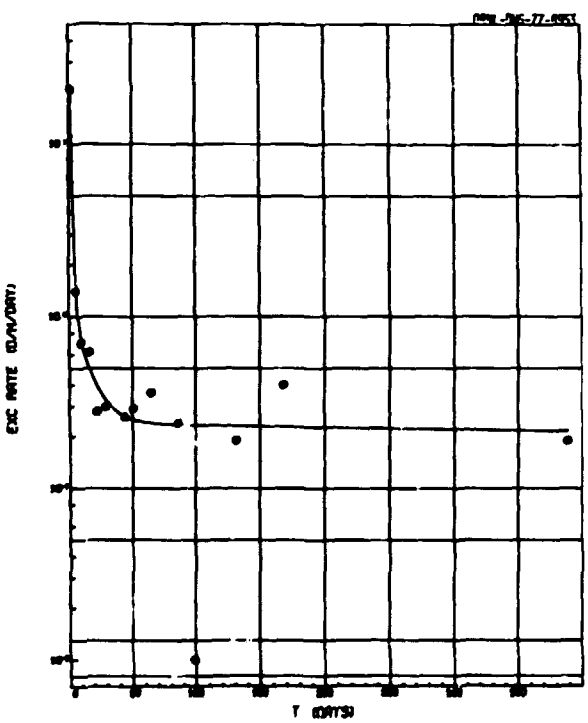

Fig. 24.8. Excretion data for one ORNL employee, $w = 1$, three-exponential fit (with 168-day point).

DISTRIBUTION OF DOSE WITHIN THE BODY FROM A PHOTON EMITTER PRESENT IN AN ORGAN

When a source of photons is located in a particular organ of the body, nearby organs and tissues receive doses that decrease markedly with distance from the source. Thus the dose to "other tissues," being averaged over an extensive region, generally will give only a poor approximation to the dose received by tissues close to the organ. In this study the mean doses are estimated in a set of enveloping "shells" for lungs, liver, and kidneys at distances from 0 to 1 and 1 to 2 cm from the source organs. Preliminary Monte Carlo estimates indicate that the average dose in tissues close to the source may be as much as 60% to 70% of the average dose within the source organs. Further exploration will be made of the effect of mass and shape of the source organ as well as the position of the maximum dose when there are several source organs.

A dosimetric system that provides estimates of mean dose to organs from sources distributed uniformly in one or more organs has been developed.[23,33] Although the sources of photons in the system are assumed to be distributed uniformly, it is not true that dose from these photons is uniformly distributed. In particular, when a source of photons is located in a particular organ, nearby tissues will be irradiated at doses that decrease markedly with distance from the source. The mean dose may give a poor approximation to the actual dose if the tissues over which the dose is averaged are extensive (e.g., the remainder of the body). In this section, we have devised a set of "enveloping organs"

32. M. E. Wrenn, Norman Cohen, and M. Eisenbud, *Progress Report – Radioactivity Studies*, COO-3382-15, New York University Medical Center, Institute of Environmental Medicine, New York, Apr. 1, 1976.

33. W. S. Snyder et al., *"S", Absorbed Dose per Unit Cumulated Activity for Selected Radionuclides and Organs*, MIRD pamphlet 11, Society of Nuclear Medicine, New York, 1975.

for liver, lungs, etc., which gives mean dose at distances from the source organ of 0 to 1 cm, from 1 to 2 cm, etc. These can be used to yield estimates of the extent of inhomogeneity of the dose distribution from a source of photons located in the source organ. We are also exploring the inhomogeneity due to several such source organs.

Assume that a certain amount of activity of a radionuclide is distributed in a source organ and produces an average absorbed dose, D, in the organ. If the radionuclide emits photons, the surrounding tissue also will be irradiated to some extent. Published dose tables usually give only average doses for an organ, and this tends to obscure the dose from the nearby tissue since these doses are averaged over a much greater mass of tissue. For example, if a photon emitter is present in the liver, some of the tissues near the liver will get a fairly high dose, but when this is averaged over the other tissues of the body the average dose is small. Of course, the same problem exists for beta rays and alpha particles, but the tissue in which the peak dose outside the source organ is reached would lie very close to the source organ and be of a limited and somewhat uncertain mass. For photons, however, the extent of tissue receiving substantially the maximum level outside the source organ is much greater, and those attempting to estimate risk to these tissues may wish to have this information. In this section, we only consider the photon emitter.

Many calculations of dose with the source uniformly distributed in a single organ of the body have been estimated by Monte Carlo techniques, which allow for estimation of dose to neighboring organs and tissues (reported in ORNL-5000,[2,3] Parts 1 and 2). The doses received by these neighboring tissues are only reported on an average basis for an organ. These calculations use an anthropomorphic phantom with a total mass of ~70 kg, consisting of three tissue compositions, namely, bone at a density of ~1.5 g/cm^3, lung tissue at a density of ~0.3 g/cm^3, and general soft tissues at a density of ~1 g/cm^3. Each of these has an appropriate average elemental composition (see Part 1, ORNL-5000).[2,3] These estimates have been made for 12 photon energies ranging from 0.01 to 4 MeV.

In this section we try to assess the extent of the maximum photon dose outside the source organ and the mass of tissue receiving this larger dose. The problem is complicated by the variety of shapes for the organs (ellipsoidal, truncated ellipsoids, etc.), the various energies used (12 energies from 0.01 to 4 MeV), and the fact that some organs occur in pairs (kidneys, lungs, etc.). No complete solution can be offered at this time but preliminary Monte Carlo calculations indicate the following general trends.

1. For source organs occurring in pairs, but separated (kidneys, ovaries, etc.), the maximum exposure apart from the source organ seems to occur near the organ rather than at intermediate positions, and this seems to hold for all energies tested.

2. The mass of tissue irradiated outside the source organ varies with energy, as would be expected, but the ratio of the peak dose in this tissue to the average dose in the source tissue shows a remarkable stability.

3. Detailed tables of these doses will be published when the Monte Carlo calculations are completed, but the influence of multiple source organs on the position of the maximum requires further consideration.

The ratio of the doses in the tissues at distances of up to 1 cm or at a distance of 1 to 2 cm is shown in Figs. 24.9 through 24.11 for shells around the kidneys and

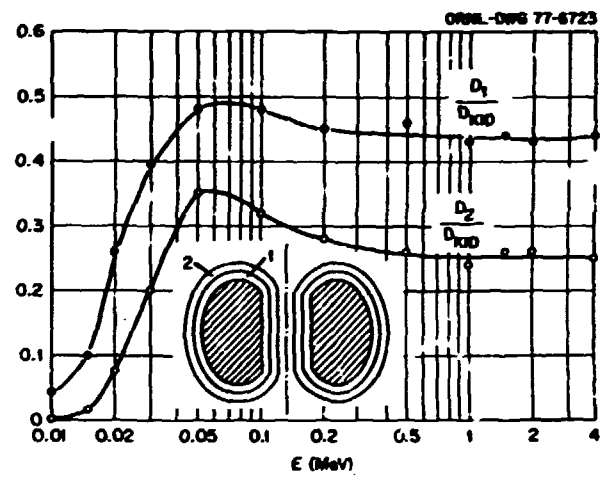

Fig. 24.9. Ratio of doses in shells to dose in kidneys.

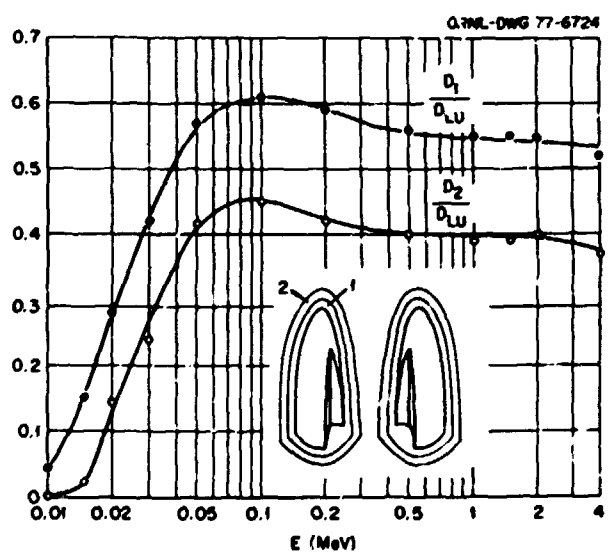

Fig. 24.10. Ratio of doses in shells to dose in lungs.

the lungs and for a portion of a shell in the case of the liver. Not only are the curves similar in shape, but they are similar to the curves published by Snyder.[34] They indicate that the average dose in the tissues close to the source organ may be as much as 60% to 70% of the dose within the source organ.

We intend to explore more fully the effect of this dose on (1) the mass and shape of the organ and (2) the position of the maximum dose when there are several source organs.

34. W. S. Snyder, "Estimation of Absorbed Fraction of Energy from Photon Sources in Body Organs," in *Medical Radionuclides: Radiation Dose and Effects*, Oak Ridge Associated Universities, Division of Technical Information, Oak Ridge, Tenn., 1970.

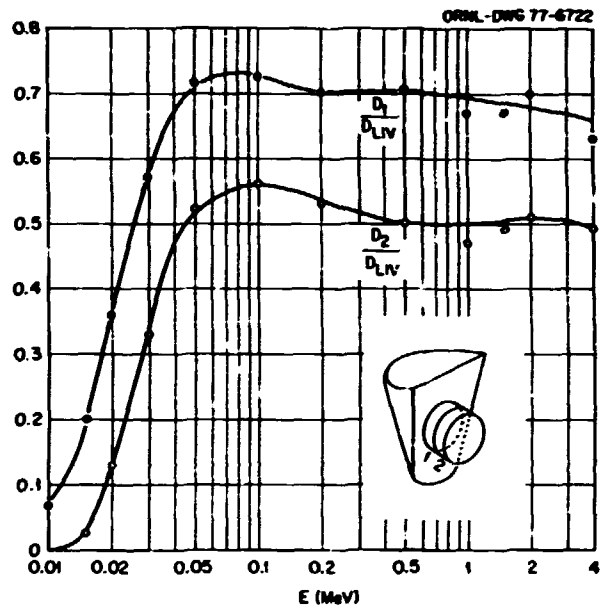

Fig. 24.11. Ratios of doses in tissue 1 and tissue 2 to dose in liver.

25. External Dosimetry

G. G. Warner[1] J. W. Poston[2]

Experiments on absorbed doses caused by various external x-ray exposure situations were made using Monte Carlo transport computer codes with mathematical representations of an adult human. Especial interest was centered on doses absorbed in the female breasts, caused by some radiological procedures, such as breast therapies, diagnostic radiologies, and pneumothoracic fluoroscopies. Variables studied were breast size, sizes and energies of beams, and the incident locations of beams. Also of interest were doses absorbed by other body organs, those not necessarily in the direct beam of x rays.

Work was also expanded on prior investigations of the relationship of absorbed dose as a function of depth for broad, parallel beams of monoenergetic photons, unilaterally incident on the trunk of the adult phantom. These efforts extended the range of energies downward from 50 to 15 keV and added a new depth-dose region in the form of an elliptical cylindrical annulus between 1.0 and 1.2 cm deep in the trunk of the phantom. Average depth-dose values are now available for depths in the trunk of the phantom of 0.1 (skin), 1.0, 1.1, 3.0, 5.0, and 7.0 cm over a range of energies from 15 keV to 10 MeV.

ABSORBED DOSE TO MAMMARY GLANDS

Through an interagency agreement with the Food and Drug Administration (FDA), the doses absorbed in the female breast due to various x-ray exposures typical of diagnostic radiologies and pneumothoracic fluoroscopies were computed.[3] The 70-kg phantom in the computer program BRHGAM[4] was modified to allow for mathematical descriptions of female breasts. Specifications for the breasts, which are parts of prolate spheroids on the trunk of the phantom, and for the exposure situations were provided by the FDA, Bureau of Radiological Health.[5,6] Data presented in Tables 25.1 and 25.2 are for one breast and for other critical organs and represent computed estimates of absorbed dose per unit of surface radiation exposure. A variety of breast sizes, breast composition, projections, and x-ray beams was investigated.

In Table 25.2, the source-to-skin distance has little meaning because the x-ray beams in the calculations were assumed to be parallel rather than divergent. In addition, for the calculations simulating pneumothoracic fluoroscopies, the x-ray source was assumed to be a spectrum generated by an accelerating potential of 75 kVp. Thus, the half-value layer and the average energy are listed in the table to specify the x-ray beam quality.

Since the ribs and the trunk skin of the phantom extend around the trunk, the dose to them is an average dose for a part directly in the beam and a part not directly in the beam. Blank spaces in the tables indicate where inadequate data were obtained. Data for the breast nearer the beam of x rays are presented. Generally, data for the breast nearer the x-ray beam are presented in the tables. For example, in Table 25.1, the heading indicates that the data are for the left breast. However, for the right lateral exposures (Table 25.1), data are given for the right breast. In some cases, the higher dose was not deposited in the breast closer to the beam (see the data for the right lateral, upper GI series),

1. Computer Sciences Division.
2. School of Nuclear Engineering, Georgia Institute of Technology, Atlanta.
3. G. G. Warner and J. W. Poston, *Health Phys. Div. Annu. Prog. Rep. June 30, 1976*, ORNL-5171 (October 1976).
4. G. G. Warner, *BRHGAM, A Medical X-Ray Dose Estimation Program*, ORNL/TM-4393 (October 1973).
5. Personal correspondence, Dr. M. Rosenstein to J. W. Poston, Apr. 30, 1976.
6. Personal correspondence, Dr. M. Rosenstein to J. W. Poston, Nov. 16, 1976.

Table 25.1. Absorbed dose per unit exposure from diagnostic radiology[a]

View (projection)	Field size [width × height (cm)]	SSD[b] (cm)	Energy (MeV)	Absorbed dose (rads/R)			
				Left breast	Red marrow (ribs)	Trunk skin	Thyroid
Anterior-posterior, chest	29.2 × 35.4	150	0.020	0.297	0.363	0.126	0.007
			0.030	0.640	1.03	0.159	0.058
			0.040	0.920	1.63	0.209	0.132
			0.055	1.14	1.99	0.260	0.244
			0.080	1.19	1.66	0.312	0.312
Anterior-posterior, ribs	24.1 × 29.2	69	0.020	0.302	0.290	0.078	0.003
			0.030	0.645	0.734	0.102	0.032
			0.040	0.913	1.13	0.136	0.103
			0.055	1.11	1.34	0.172	0.189
			0.080	1.16	1.12	0.205	0.246
Anterior-posterior, shoulder (one)	17.2 × 20.6	69	0.020	0.154	0.043	0.031	c
			0.030	0.311	0.156	0.043	0.003
			0.040	0.436	0.276	0.052	0.011
			0.055	0.516	0.333	0.068	0.024
			0.080	0.567	0.291	0.075	0.026
Anterior-posterior, thoracic spine	24.1 × 29.2	69	0.020	0.297	0.309	0.076	c
			0.030	0.664	0.768	0.097	0.015
			0.040	0.907	1.16	0.131	0.053
			0.055	1.10	1.37	0.169	0.138
			0.080	1.19	1.16	0.195	0.116
Anterior-posterior, upper GI tract	24.1 × 29.2	69	0.020	0.001	0.200	0.094	
			0.030	0.013	0.500	0.113	
			0.040	0.036	0.769	0.144	c
			0.055	0.067	0.930	0.184	c
			0.080	0.084	0.786	0.204	c
Posterior-anterior, chest	29.2 × 35.4	150	0.025	0.002	0.750	0.149	c
			0.035	0.030	1.38	0.182	c
			0.055	0.149	1.98	0.257	0.009
			0.080	0.249	1.66	0.293	0.121
Posterior-anteri , ribs	24.1 × 29.2	69	0.025	0.001	0.596	0.103	c
			0.035	0.020	1.03	0.123	c
			0.055	0.111	1.40	0.173	0.113
			0.080	0.176	1.17	0.200	0.064
Posterior-anterior, upper GI tract	24.1 × 29.2	69	0.025	0.001	0.347	0.107	
			0.035	0.008	0.637	0.126	
			0.055	0.047	0.922	0.171	c
			0.080	0.071	0.763	0.200	c
Right lateral, chest	27.4 × 33.2	140.8	0.025	0.265[d]	0.316	0.162	c
			0.035	0.388[d]	0.659	0.193	0.007
			0.055	0.643[d]	0.962	0.258	0.053
			0.080	0.764[d]	0.791	0.284	0.103
Right lateral, thoracic spine	20.9 × 25.3	59.8	0.025	0.001[d]	0.202	0.081	c
			0.035	0.007[d]	0.398	0.097	c
			0.055	0.047[d]	0.597	0.130	0.016
			0.080	0.063[d]	0.503	0.151	0.052

Table 25.1 (continued)

View (projection)	Field size [width × height (cm)]	SSD[b] (cm)	Energy (MeV)	Absorbed dose (rads/R)			
				Left breast	Red marrow (ribs)	Trunk skin	Thyroid
Right lateral, upper GI tract	20.9 × 25.3	59.8	0.025	0.010	0.148	0.106	
			0.035	0.017	0.302	0.126	
			0.055	0.025[e]	0.460	0.170	c
			0.080	0.043	0.393	0.187	0.023

[a]Breast size – 10-cm diam at chest wall; 8 cm chest-wall-to-nipple distance. Breast composition – adipose tissue: 23.2% O, 64% C, 12% H, 0.8% N; density = 0.92 g/cm³. Divergent beam – field size is at appropriate skin surface (for anterior-posterior views, the anterior surface of the breast).

[b]Source-to-skin distance.

[c]Statistically unreliable, coefficient of variation greater than 50%.

[d]Right breast.

[e]Right breast; left breast = 0.024.

Table 25.2. Absorbed dose per unit exposure from pneumothoracic fluoroscopy

HVL[c] (mm Al)	Field size [width × height (cm)]	SSD[a]	Average energy (MeV)	Absorbed dose (rads/R)			
				Right breast	Red marrow (ribs)	Trunk skin	Thyroid
			Anterior-posterior (75 kVp)[b]				
0.88	12.4 × 17.0	N/A[d]	0.0342	0.490	0.258	0.036	e
1.6	12.4 × 17.0		0.0376	0.545	0.302	0.038	0.002
0.88	24.8 × 17.0		0.0342	0.556	0.610	0.068	0.006
1.6	24.8 × 17.0		0.0376	0.683	0.580	0.074	0.005
1.6	24.8 × 14.7		0.0376	0.016	0.510	0.065	0.004
			Anterior-posterior (75 kVp)[f]				
0.88	12.5 × 17.2	N/A	0.0342	0.763	0.276	0.039	e
1.6	12.5 × 17.2		0.0376	0.868	0.321	0.040	e
0.88	25.0 × 17.2		0.0342	0.841	0.538	0.075	0.004
1.6	25.0 × 17.2		0.0376	0.871	0.635	0.078	0.010
			Posterior-anterior (75 kVp)[b]				
0.88	19.3 × 26.5	N/A	0.0342	0.044	0.554	0.095	0.003
1.6	19.3 × 26.5		0.0376	0.064	0.640	0.102	0.008
0.88	38.5 × 26.5		0.0342	0.047	1.11	0.182	0.017
1.6	38.5 × 26.5		0.0376	0.075	1.30	0.194	0.009
0.88	35.0 × 42.5		0.0342	0.057	1.35	0.256	0.033
1.6	35.0 × 42.5		0.0376	0.069	1.60	0.274	0.058
1.6	38.5 × 22.9		0.0376	0.015	0.988	0.170	e

Table 25.2 (continued)

View (beam quality)	Field size [width × height (cm)]	SSD[a]	Average energy (MeV)	Absorbed dose (rads/R)			
				Right breast	Red marrow (ribs)	Trunk skin	Thyroid
			Anterior-posterior (75 kVp)[g]				
HVL[c] (mm Al)							
1.6	12.4 × 17.0	33	0.0376	0.573	0.285	0.040	0.005
1.6	24.8 × 17.0	33	0.0376	0.631	0.604	0.078	0.007
1.6	24.8 × 14.7	33	0.0376	0.016	0.541	0.073	

[a]Source-to-skin distance.

[b]Breast size – 7.5-cm diam at chest wall; 6-cm chest-to-wall-to-nipple distance. Breast composition – average total body elemental composition and density. Parallel beam – field normal to phantom vertical midplane (for anterior-posterior views, the anterior surface of the breast).

[c]Half-value layer.

[d]Not applicable.

[e]Statistically unreliable, coefficient of variation greater than 50%.

[f]Breast size – 3.75-cm diam at chest wall; 3- chest-to-wall-to-nipple distance. Breast composition – average total body elemental composition and density. Parallel field normal to phantom vertical midplane (for anterior-posterior views, the anterior surface of the breast).

[g]Breast size – 7.5-cm diam at chest wall; 6-cm chest-wall-to-nipple distance. Breast composition – average total body elemental composition and density. Divergent beam – field size is at vertical plane 3 cm deep in breast.

and such situations are indicated. In the upper GI tract series, this situation was probably due to secondary interactions in the left breast because the right breast was not directly in the beam.

ABSORBED DOSE DURING BREAST ^{60}Co THERAPY

Studies of induced cancer in women treated with radiation therapy have been limited by several problems, one of which has been discussed in this study. Radiation dosimetry for organs outside the treatment field generally has not been available. We have attempted to throw some light on this problem by carrying out computer-calculated dosimetry on organs of women treated for breast cancer with radiotherapy.

The computations used the computer code BRHGAM,[4] which contains a more recent mathematical version of the Snyder-Fisher phantom.[7] The code was modified to include a mathematical description of female breasts, which were each assumed to be a portion of a prolate spheroid located on the chest of the phantom. The diameters were 10 cm and the surface-to-nipple distances were 6.8 cm.

Three situations were considered in these computations. A set of data was obtained for the phantom having both breasts. A second set of data was obtained for the phantom having only a right breast. It was assumed that the left breast had been removed in response to the medical need for a mastectomy. A third set of data had been obtained for the phantom having no breasts.[8] Each situation comprised four separate exposures, two anterior-posterior and two lateral-oblique. These exposure situations are shown schematically in Fig. 25.1. The source nuclide was ^{60}Co, and it was at a point 70 cm from the surface of the phantom. Each beam was rectangular in cross section.

New target regions were placed into the phantom in front of each radiotherapy beam – one region for each of the anterior-posterior exposures and one for the lateral-oblique exposures. Each region had a finite thickness, closely matched the beam dimensions, and was placed from 2.9 to 4 cm inside the surface of the phantom. Absorbed dose was computed in these regions for each of the exposure situations, enabling us to express the data as absorbed dose in an organ per unit absorbed dose in the useful beam. Results of the calculations are presented in Tables 25.3, 25.4, and 25.5.

7. H. L. Fisher and W. S. Snyder, *Health Phys. Div. Annu. Prog. Rep. July 31, 1967*, ORNL-4168 (October 1967), pp. 245–56.

8. G. G. Warner and J. W. Poston, *Health Phys. Div. Annu. Prog. Rep. June 30, 1975*, ORNL-5046 (October 1975), p. 283.

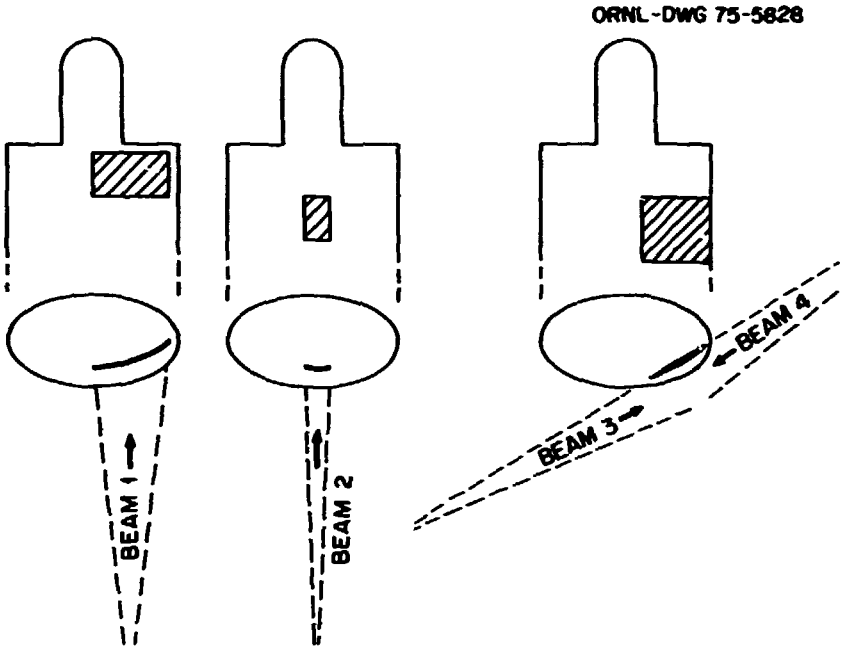

Fig. 25.1. Four exposures for breast x-ray therapy.

Table 25.3. Absorbed dose (in rads/rad) during breast therapy using ^{60}Co at 70 cm with both breasts present

Organ	Beam			
	1[a]	2[b]	3[c]	4[d]
Heart	0.015	0.572	0.003	0.013
Left lung	0.143	0.020	0.022	0.016
Pancreas	0.003	0.004	0.004	0.002
Left arm bone	0.238	0.002	0.061	0.108
Clavicles	0.442	0.002	0.001	0.003
Ribs	0.148	0.047	0.085	0.055
Scapulae	0.134	0.006	0.004	0.001
Spine	0.109	0.097	0.001	0.002
Skin	0.038	0.009	0.026	0.023
Spleen	0.003	0.003	0.005	0.002
Thyroid	0.021	0.001	0.001	e
Left breast	0.733	0.129	0.592	0.466
Right breast	0.006	0.020	0.001	0.018
Red bone marrow	0.063	0.028	0.010	0.007
Total body	0.047	0.019	0.011	0.010

[a]Exposure, anterior-posterior; size, 10 by 18 cm; depth, 4.0 cm.

[b]Exposure, anterior-posterior; size, 6 by 10 cm; depth, 3.0 cm.

[c]Exposure, right lateral/31.5°; size, 10 by 15 cm; depth, 2.9 cm.

[d]Exposure, left lateral/31.5°; size, 10 by 15 cm; depth, 2.9 cm.

[e]<0.001 rad/rad.

ABSORBED DOSES TO THE SKIN AND TO A 1.1-CM-DEEP ANNULUS FROM BROAD, PARALLEL, MONOENERGETIC X-RAY BEAMS INCIDENT ON THE TRUNK OF THE ADULT PHANTOM

In response to a request from Working Group 15 of the Health Physics Society Standards Committee, we have undertaken to extend the work of Jones et al.[9] For certain broad, parallel, monoenergetic x-ray beams incident on the front and on the back of the trunk of the adult phantom, we computed absorbed doses per flux density in (1) the trunk skin, which is 0.2 cm thick on the outside of the phantom, and (2) in an elliptical annulus between 1.0 and 1.2 cm deep in the trunk of the phantom. The horizontal cross section of the trunk is elliptical and the 0.2-cm "thicknesses" were measured along the semi-axes.

The trunk was "exposed" to full-trunk, broad, parallel beams of monoenergetic x rays (40 cm wide by 70 cm high). Interactions of the radiation with the tissues of the skin and the annulus were noted, energy deposition was computed, and dose was computed for 50,000 incident x rays. The trunk had been horizontally sectioned into five tiers and vertically sectioned by two planes (Fig. 25.2). For the skin and for the annulus,

9. T. D. Jones et al., *Health Phys.* 24, 241 (1973).

Table 25.4. Absorbed dose (in rads/rad) during breast therapy using ^{60}Co at 70 cm with left breast removed

Organ	Beam			
	1[a]	2[b]	3[c]	4[d]
Heart	0.009	0.585	0.003	0.012
Left lung	0.145	0.020	0.021	0.015
Pancreas	0.002	0.005	0.003	0.002
Left arm bone	0.133	0.002	0.069	0.116
Clavicles	0.239	0.002	0.001	0.003
Ribs	0.133	0.050	0.100	0.054
Scapula	0.171	0.007	0.004	0.001
Spine	0.042	0.099	0.001	0.001
Skin	0.028	0.010	0.032	0.022
Spleen	0.003	0.004	0.004	0.001
Thyroid	0.008	0.001	e	e
Left breast				
Right breast	0.003	0.021	e	0.015
Red bone marrow	0.051	0.028	0.011	0.007
Total body	0.040	0.020	0.012	0.010

[a]Exposure, anterior-posterior; size, 10 by 18 cm; depth, 4.0 cm.
[b]Exposure, anterior-posterior; size, 6 by 10 cm; depth, 3.0 cm.
[c]Exposure, right lateral/31.5°; size, 10 by 15 cm; depth, 2.9 cm.
[d]Exposure, left lateral/31.5°; size, 10 by 15 cm; depth, 2.9 cm.
[e]<0.001 rad/rad.

Table 25.5. Absorbed dose (in rads/rad) during breast therapy using ^{60}Co at 70 cm with both breasts removed

Organ	Beam			
	1[a]	2[b]	3[c]	4[d]
Heart	0.010	0.498	0.003	0.011
Left lung	0.214	0.021	0.035	0.022
Pancreas	0.003	0.004	0.002	0.003
Left arm bone	0.130	0.001	0.073	0.108
Clavicles	0.251	0.002		0.002
Ribs	0.140	0.037	0.102	0.053
Scapula	0.176	0.005	0.004	0.001
Spine	0.095	0.088	0.001	0.001
Skin	0.057	0.016	0.059	0.044
Spleen	0.003	0.003	0.004	0.002
Thyroid	0.012	0.002	e	0.002
Left breast				
Right breast				
Red bone marrow	0.052	0.024	0.012	0.008
Total body	0.041	0.016	0.012	0.010

[a]Exposure, anterior-posterior; size, 10 by 18 cm; depth, 4.0 cm.
[b]Exposure, anterior-posterior; size, 6 by 10 cm; depth, 3.0 cm.
[c]Exposure, right lateral/31.5°; size, 10 by 15 cm; depth, 2.9 cm.
[d]Exposure, left lateral/31.5°; size, 10 by 15 cm; depth, 2.9 cm.
[e]<0.001 rad/rad.

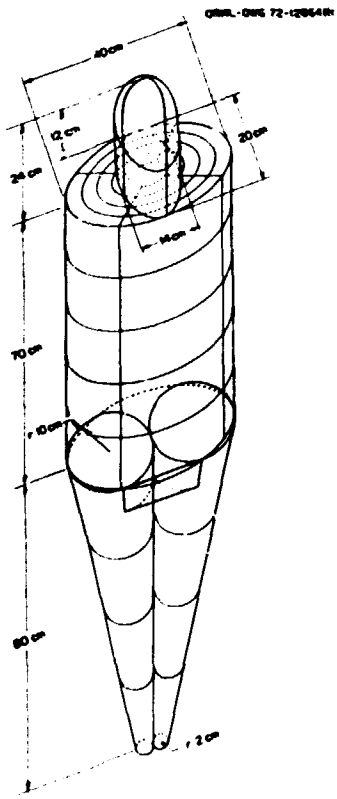

Fig. 25.2. The adult human phantom.

doses were computed at the front and at the back of each tier at each of eight energies. Reported in Tables 25.6 and 25.7 are the averages of the ten computations for each energy. The averaging of the doses for the skin was a straightforward mathematical manipulation since the tier sections of the skin were the same with respect to size and mass. However, for the internal annulus all the sections were the same size, but the masses differed due to the occasional presence of bone in an otherwise all normal tissue section. The average doses for the sections of the annulus are weighted averages, and a range of coefficients of variation is given. The statistics are considered to be from excellent to good at all energies for all sections.

Table 25.6. Dose to skin from broad, parallel, monoenergetic x-ray beams incident on trunk of adult phantom

Energy (MeV)	Average dose (rads photon^{-1} cm^{-2})	Coefficient of variation (%)
0.015	2.8E−10[a]	2.9
0.020	1.6E−10	4.0
0.030	8.5E−11	5.2
0.050	5.2E−11	6.0
0.100	6.0E−11	7.5
0.250	1.5E−10	9.8
0.670	3.6E−10	13.0
1.25	6.5E−10	14.0
3.00	1.1E−09	18.0
6.00	2.0E−09	20.0
10.0	2.8E−09	22.0

[a]Read as 2.8×10^{-10}.

Table 25.7. Dose to annulus from broad, parallel, monoenergetic x-ray beams incident on trunk of adult phantom

Energy (MeV)	Average dose (rads photon^{-1} cm^{-2})	Range of coefficients of variation (%)
0.015	5.8E−11[a]	5.1–8.0
0.020	8.6E−11	4.6–6.6
0.030	7.7E−11	5.2–6.2
0.050	5.5E−11	5.9–6.6
0.100	6.6E−11	6.7–8.0
0.670	3.7E−10	12.0–14.0
1.25	5.7E−10	15.0–17.0
3.00	1.1E−09	18.0–23.0

[a]Read as 5.8×10^{-11}.

26. Experimental Studies

K. E. Cowser
P. S. Stansbury[1]
J. W. Poston[2]
S. F. Deus[3]
W. L. Chen[2]
R. L. Roswell[4]
R. E. Goans[5]
J. H. Cantrell, Jr.[6]

ABSORBED DOSE FROM DIAGNOSTIC X RAYS

Studies of the absorbed-dose contributions in phantoms continued using x-ray beams in a manner typical of diagnostic medical examinations. We describe in this report spectral fluence measurements in an adult phantom. A NaI(Tl) probe was used in various locations within the phantom and pulse-height spectra were obtained for seven beam configurations and three generating potentials. Some typical spectra results are presented.

A comparison of calculated dose to experimental measurements is presented. Two heterogeneous phantoms representing a 1-year-old and a 5-year-old child were fabricated to match mathematical models used in calculations of absorbed dose. Thermoluminescent dosimeters placed strategically in the phantoms measured the absorbed dose for a variety of radiographic examinations. Calculated and measured values for most organs were found to agree within twice the coefficient of variation, and absorbed dose in children may be less than in an adult when proper procedures are used in the examinations. Similar considerations for a third pediatric phantom are discussed.

HIGH-RESOLUTION ULTRASONIC ANALYSIS OF BURN DAMAGE

Development of high-frequency ultrasound for investigations of burn injury illustrates one application of physics in medicine. In an effort to enhance analyses of burns and thereby their subsequent treatment, a high-resolution ($\sim$0.2 mm) ultrasonic pulse-echo system was assembled to determine burn depth. In experimental tests using Yorkshire pigs, because of the histological similarity between human and porcine skin, burn depths were found to be immediately postburn-identifiable. Also investigated were the tissue characteristics, density and acoustic attenuation, which affect the impedance mismatch at the burn–viable tissue interface.

IN-PHANTOM SPECTROMETRY OF DIAGNOSTIC MEDICAL X RAYS

The program of measurements to determine the spectral fluence distributions at locations of interest inside the MR. ADAM (Mockup of a Realistic Analytical Description of an Adult Male) phantom exposed to x-ray beams in a manner simulating diagnostic medical examinations was completed. The measurements were made with a specially constructed NaI(Tl) scintillation detector.[7] The detector has a spherically shaped active volume 0.6 cm in diameter. Although the resolution of this detector was fivefold less effective than that of a more conventional NaI(Tl) spectrometer, its size, construction, and angular dependence were suitable for use in this project. Resolution broadening and other distor-

1. ORAU Graduate Laboratory Participation Grant, School of Nuclear Engineering, Georgia Institute of Technology, Atlanta. Presently employed at the University of North Carolina at Chapel Hill, Department of Environmental Sciences and Engineering.
2. School of Nuclear Engineering, Georgia Institute of Technology, Atlanta.
3. Employee, Instituto de Energia Atomica, Sao Paulo, Brazil. Assigned as a student to the Health Physics Division.
4. Graduate student, Rensselaer Polytechnic Institute, Troy, N.Y.
5. Radiation Monitoring Section.
6. Consultant, Langley Research Center, NASA.
7. P. S. Stansbury and J. W. Poston, *Health Phys. Div. Annu. Prog. Rep. June 30, 1976*, ORNL-5171 (October 1976), pp. 81–82.

tions were removed from the observed pulse-height spectra with a computer-coded, iterative unfolding technique developed by McCorkle, Christophorou, and Anderson.[8]

The performance of the spectrometer and the unfolding scheme was assessed by comparing, in a few cases, the unfolded Na(Tl) spectra with spectra determined with a high-resolution Ge(Li) spectrometer. Figure 26.1 shows such a comparison. The histogram in Fig. 26.1 is the output spectrum of an x-ray machine as determined with a Ge(Li) high-resolution spectrometer. [The Ge(Li) data were grouped into "bins" 2 keV wide to facilitate comparison.] The spherical NaI(Tl) raw data (pulse-height spectrum) and the spectrum unfolded from this raw data are presented also. It was necessary to truncate or extrapolate the unfolded spectrum to remove a spurious high-energy tail.

The NaI(Tl) probe was positioned at seven different locations within or on the surface of the MR. ADAM phantom.[9] At each probe location, pulse-height spectra were acquired for twenty-one combinations of seven beam configurations and three generating potentials. The seven probe locations were chosen to be at the center of or near seven regions of radiological significance: testes, right ovary, thyroid, eyes, heart, fifth lumbar vertebra, and thoracic region of the spine. The triangles in Fig. 26.2 show the probe locations. Also shown are the x and z axes of a reference coordinate system and the configuration of one of the seven x-ray beams. The source of x rays was the x-ray facility in Building 2008.[10]

8. D. L. McCorkle, L. G. Christophorou, and V. E. Anderson, *J. Phys. B: Molec. Phys.* 5, 1211 (1972).

9. P. S. Stansbury and J. W. Poston, *Health Phys. Div. Annu. Prog. Rep. July 31, 1974*, ORNL-4979 (1974), pp. 73–76.

10. P. S. Stansbury and J. W. Poston, *Health Phys. Div. Annu. Prog. Rep. June 30, 1976*, ORNL-5171 (October 1976), p. 80.

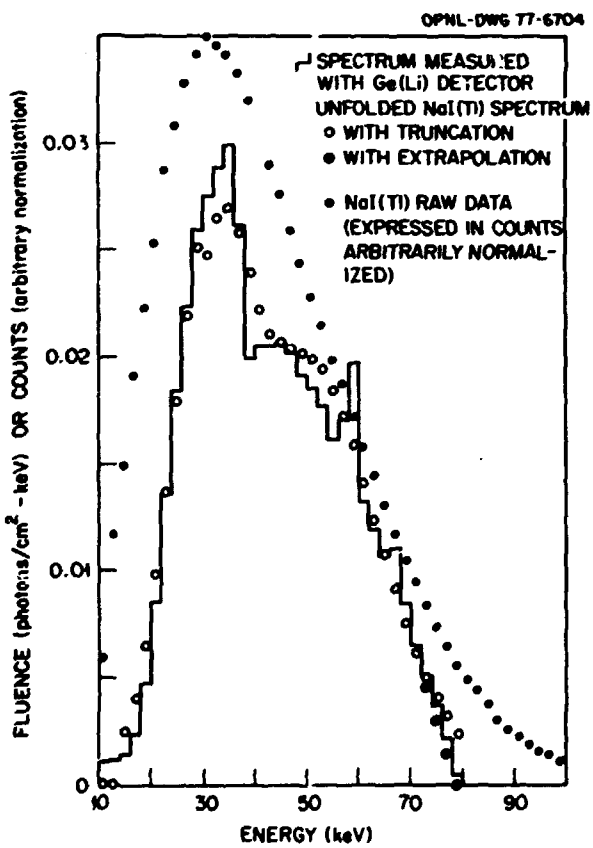

Fig. 26.1. Comparison of unfolded NaI(Tl) spectrum measured with a Ge(Li) detector–80 kVcp x-ray machine output spectrum at 3 m.

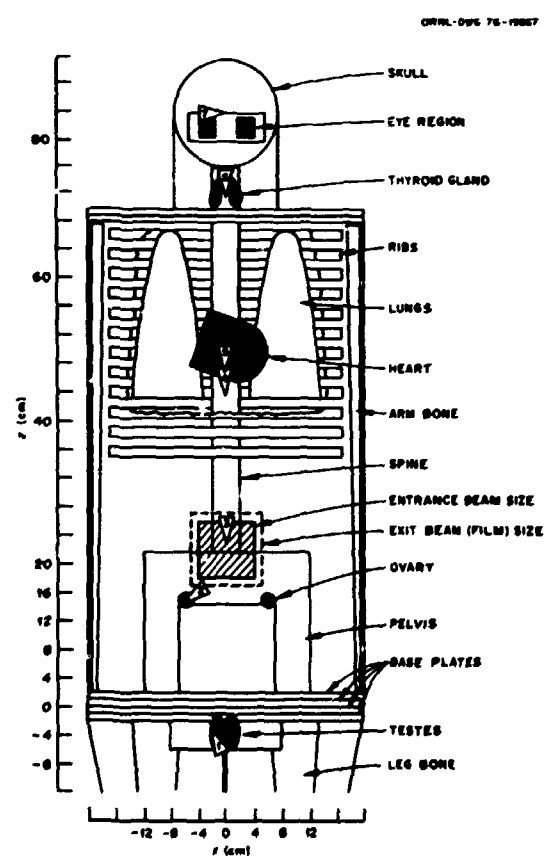

Fig. 26.2. Probe locations and lower-spine beam configuration.

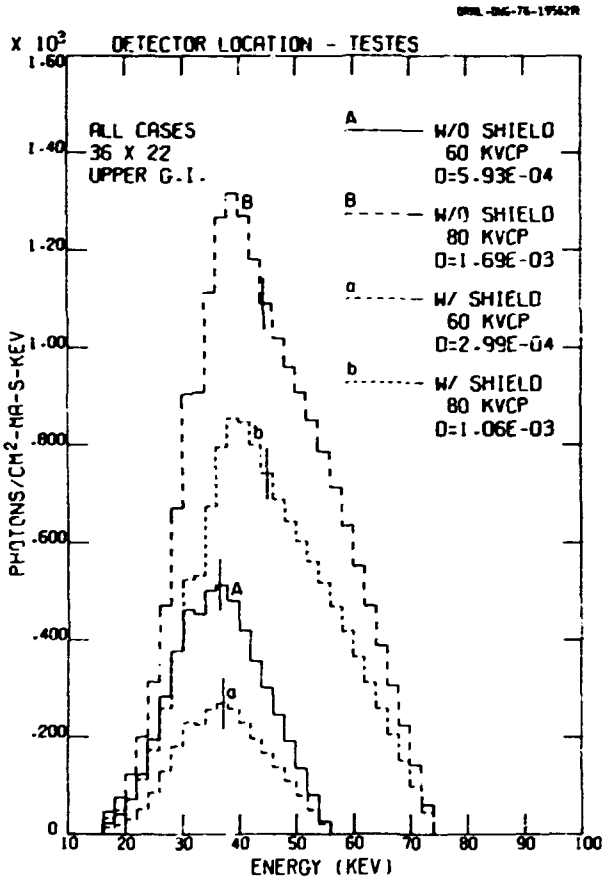

Fig. 26.3. Effect of gonad shield on the spectrum at the testes – uppe. GI (testes far from the beam). Vertical ticks indicate mean energy. Field size is in centimeters. *D* is the absorbed dose per unit current per unit time (mrad mA^{-1} sec^{-1}).

Figure 26.3 shows some results typical of those found in this study. Illustrated are the spectra at the testes resulting from a simulated upper gastrointestinal examination. Spectra were measured for 60 and 80 kV, with and without the testes region covered with a 0.16-cm-thick lead shield. The calculated absorbed dose to the testes per unit tube current is given in the figure legend. Note the ability of shielding to reduce absorbed dose to a region, even when that region is outside the useful beam.

Full specifications of the beam configurations and probe locations are presented in ORNL/TM-5873.[11] Other data determined by experiment to verify the results of this study and a comparison of the results of this study with absorbed doses calculated by the Bureau of Radiological Health (BRH) are presented also in this technical memorandum. The results of this study agree reasonably well with the calculated absorbed doses presented in a recent BRH publication.[12]

DEVELOPMENT OF A MATHEMATICAL PHANTOM REPRESENTING A TEN-YEAR-OLD CHILD FOR USE IN INTERNAL DOSE CALCULATIONS

The main purpose of this research was to design a mathematical phantom representing, as closely as practicable, a 10-year-old child.

The phantom is similar in shape to the adult phantom (MR. ADAM) of Snyder and Fisher, but several changes were made in the design to make the phantom more realistic.[13–15] These changes included adding a neck, placing the arms outside the trunk section, changing the shape of the trunk region, and redesigning the male genitalia region. Several modifications were made to the idealized skeleton. For example, the skull, ribs, pelvis, spine, scapulae, clavicles, and arm and leg bones were redesigned to approximate more closely the true anatomical shapes. Some internal organs were modified as a result of the above changes. These organs included the brain, lungs, liver, and large and small intestines. In all cases an attempt was made to modify the shapes and locations in a manner such that they were more representative of those of a 10-year-old child.

Due to the different values for the masses of the red marrow, yellow marrow, and of the individual bones,[16] the parameters of the equations representing each bone of the skeleton had to be recalculated. The previous values of the parameters were determined using the volume of each bone according to the proportionality between the volume of the bones in the child to the volume of the bones in the adult.

Additional changes were made in the trunk and head to make them more like the anatomical shape of a 10-year-old child (Fig. 26.4).[13–15] The cuts in the lower front and back are planes with suitable inclinations to diminish the thickness of soft tissue in front and back of the uterus, ovaries, and bladder and to decrease the shielding of the testes. Another modifica-

11. P. S. Stansbury, *In-Phantom Spectrometry of Medical Diagnostic X Rays*, ORNL/TM-5873 (1977).

12. M. Rosenstein, *Handbook of Selected Organ Doses for Projections Common in Diagnostic Radiology*, HEW Publication (FDA) 76-8031, 1976.

13. R. Warwick and P. C. Williams, *Gray's Anatomy*, 35th British ed., W. B. Saunders Co., Philadelphia, 1973.

14. B. J. Anson, *Morris' Human Anatomy, A Complete Systematic Treatise*, The Blakiston Division, McGraw-Hill Book Co., New York, 1966.

15. International Commission on Radiological Protection, *ICRP Task Group Report on Reference Man*, ICRP Publication 23, Pergamon Press, Oxford, 1975.

16. *Health Phys. Div. Annu. Prog. Rep. June 30, 1976*, ORNL-5171 (October 1976).

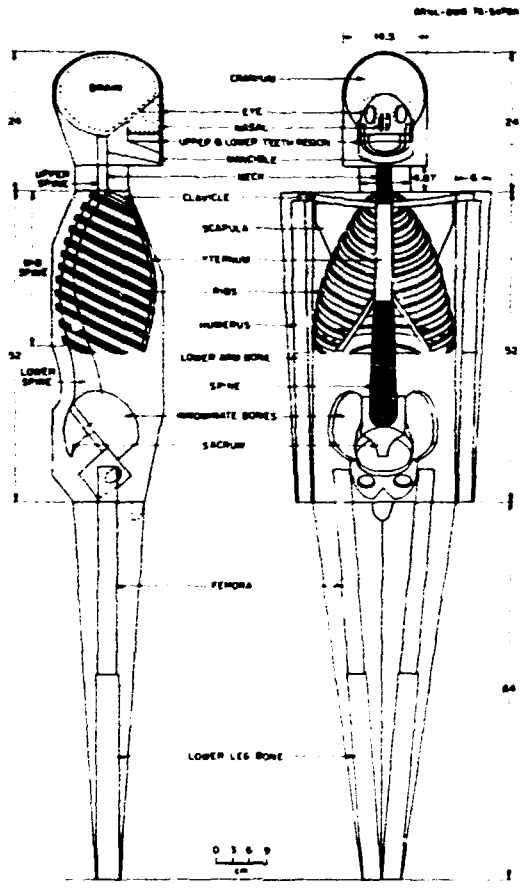

Fig. 26.4. Idealized 10-year-old human phantom.

tion was the elimination of the "belly" to decrease computer time. The positions of the spine and ribs were also changed so that the ribs meet the spine (Fig. 26.4).

Since the feet would add negligible contributions to the values of the doses to the organs of the body, and yet would significantly increase computer time, it was decided to include their mass in the lower leg region for design simplicity. The feet would have applicability in case of beta radiation in contaminated areas but, due to the wearing of shoes, the dose would be drastically reduced. Doses from neutrons and photons generally are not restricted to the feet, and critical organs such as genitalia and bone marrow would be of significantly greater interest.

Thermoluminescent dosimeters were used to measure exposures to x rays in an adult phantom to permit comparison of the calculated doses (for an adult) with the measured ones.[15,17–20] These measurements are now being analyzed. Also, comparison is in progress of dose calculations obtained using the 10-year-old pediatric phantom with those obtained using the similitude phantom of the 10-year-old child. The 10-year-old similitude phantom was obtained by shrinking the reference man phantom by factors that vary in the x, y, and z directions according to their respective sizes.

EVALUATION OF THE DISTRIBUTION OF ABSORBED DOSE IN PEDIATRIC PHANTOMS EXPOSED TO DIAGNOSTIC MEDICAL X RAYS

The purpose of this study was to determine, by theoretical calculation and experimental measurement, the absorbed dose distribution in two heterogeneous phantoms of 1- and 5-year-old children from radiographic examinations typical for those ages.

Theoretical work included the modification of an existing internal dose code which uses Monte Carlo methods to determine doses within the Snyder-Fisher mathematical phantom.[21] A Ge(Li) detector and a pinhole collimator were used to measure x-ray spectra which serve as input (i.e., the source routine) to the modified Monte Carlo codes that were used to calculate organ doses in children.

Experimental work included the fabrication of child-sized phantoms to match the existing mathematical models.[22] The phantoms were constructed of molded Lucite shells filled with different materials to simulate lung, skeletal, and soft-tissue regions. A specially designed detector-holder and the skeletal regions of the phantoms allowed meaningful measurements to be made of absorbed dose to bone marrow and the bone. A Victoreen model 550 Radocon III integrating rate electrometer system and ion chamber were used as the primary dosimetry reference for radiation measurement and thermoluminescent dosimeter (TLD) calibration. Thermoluminescent dosimetry techniques were used extensively in this study. The TLD calibration was focused on the diagnostic x-ray region. The steps of TLD calibration included a grading or selection, a fading test, an angular dependence test, a sensitivity and linearity test, and an energy response test. The TLD, LiF:Mn

17. Z. Spurny, J. Novotny, and L. Hedvicakova, *Phys. Med. Biol.* 16(2), 295 (1971).

18. C. J. Karzmark, J. White, and J. F. Fowler, *Phys. Med. Biol.* 9(3), 273 (1964).

19. J. R. Cameron, N. Suntharalingam, and G. N. Kenney, *Thermoluminescent Dosimetry*, University of Wisconsin Press, Madison, 1968.

20. T. E. Blackman et al., *Brit. J. Radiol.* 47, 361 (1974).

21. G. G. Warner and A. M. Craig, Jr., *ALGAM, A Computer Program for Estimating Internal Dose from Gamma-Ray Sources in a Man Phantom*, ORNL/TM-2250 (1968).

22. M. L. Hwang et al., *Mathematical Descriptions of a One- and Five-Year Old Child for Use in Dosimetric Calculations*, ORNL/TM-5293 (1976).

and Ca_2F_2:Mn, "in-tandem technique" was used to determine the effective energy at various locations inside the phantoms.[23-25] Thirteen to fourteen sites in bones of the skeleton were chosen for placement of TLDs to represent the important regions in which active bone marrow is located.

Sixteen representative radiographic examinations were performed for comparison with the common pediatric diagnostic procedures described by McClure.[26] The multiple-exposure method was used to give a good TLD reading both for in-beam and out-of-beam locations during the exposure processes. The maximum exposure used per field was 6000 mA-sec regardless of tube voltage. Uncertainty associated with the measured doses was estimated to be 7%.

The calculated and measured tissue-air values were compared for a number of organs (see ref. 27). For most organs, the results of the calculated absorbed doses agreed with the measured absorbed doses within twice the coefficient of variation[28] of the calculated value. The absorbed doses to specific organs for several of the selected radiological examinations of patients with ages representing one-year-old and five-year-old children and an adult are shown in Figs. 26.5 through 26.8.

The data on the adult were obtained from the work of Rosenstein.[29] In Figs. 26.7 and 26.8, the data for lateral exposures follows closely that of the anterior-posterior (AP) exposure; therefore, the lateral data were not plotted.

As might be expected, the absorbed doses in the adult are higher than the absorbed doses in the children. The reduced absorbed dose in children can be attributed to the procedures used in the radiographic examinations as well as to the differences in physical size.

23. S. G. Gorbics and F. H. Attix, *Int. J. Appl. Radiol. Isotopes* 19, 81 (1968).

24. Z. Spurny, C. Milu, and N. Racoreanu, *Phys. Med. Biol.* 18, 276 (1973).

25. M. J. Rossiter, *Phys. Med. Biol.* 20, 735 (1975).

26. P. L. McClure, *A Handbook of Pediatric Radiographic Technology*, Department of Radiology, Henrietta Egleston Hospital for Children, Atlanta, Ga., 1976.

27. W. L. Chen, J. W. Poston, and G. G. Warner, *An Evaluation of the Distribution of Absorbed Dose in Pediatric Phantoms Exposed to Diagnostic Medical X Rays*, ORNL/TM-5933 (1977).

28. Coefficient of variation = $\frac{\text{standard deviation}}{\text{average energy deposited}} \times 100$.

29. M. Rosenstein, *Organ Doses in Diagnostic Radiology*, HEW Publication (FDA) 76-8030, 1976.

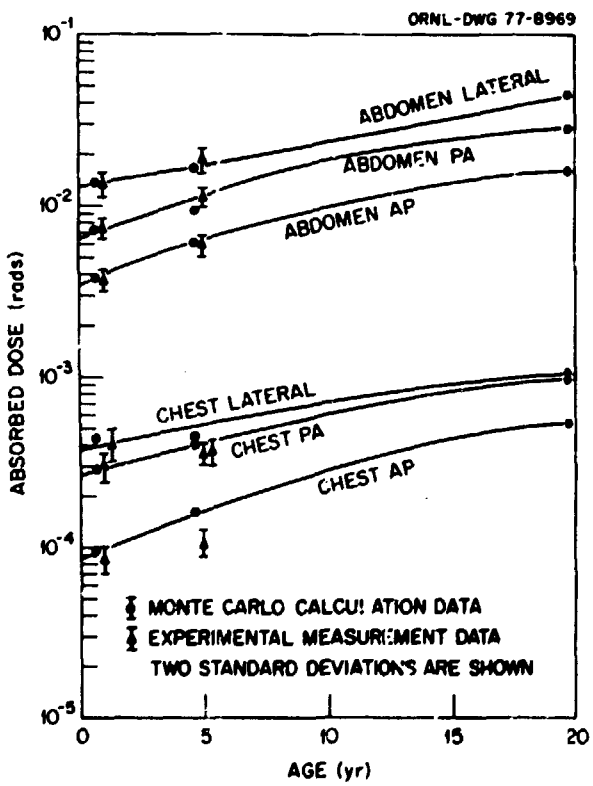

Fig. 26.5. Mean active bone marrow dose as a function of age for selected roentgenography.

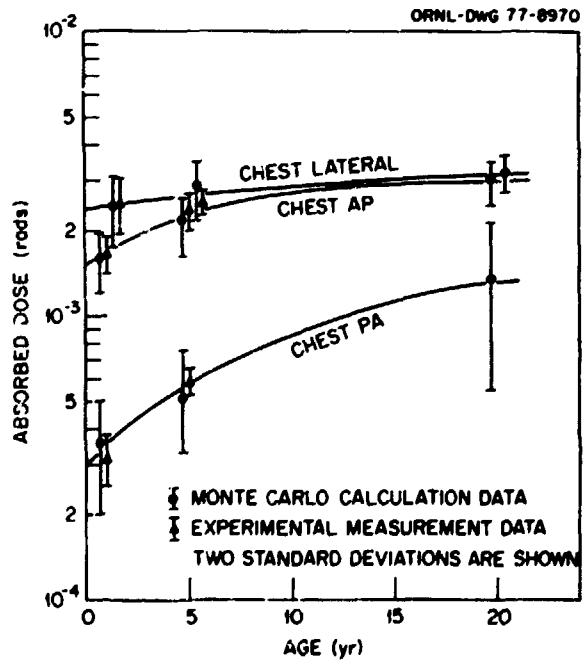

Fig. 26.6. Absorbed dose to the thyroid as a function of age for selected roentgenography.

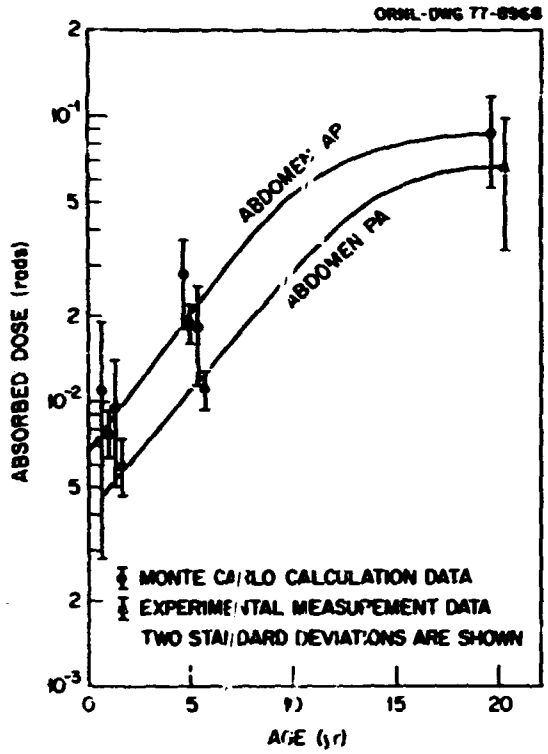

Fig. 26.7. Absorbed dose to the ovaries as a function of age for selected roentgenography.

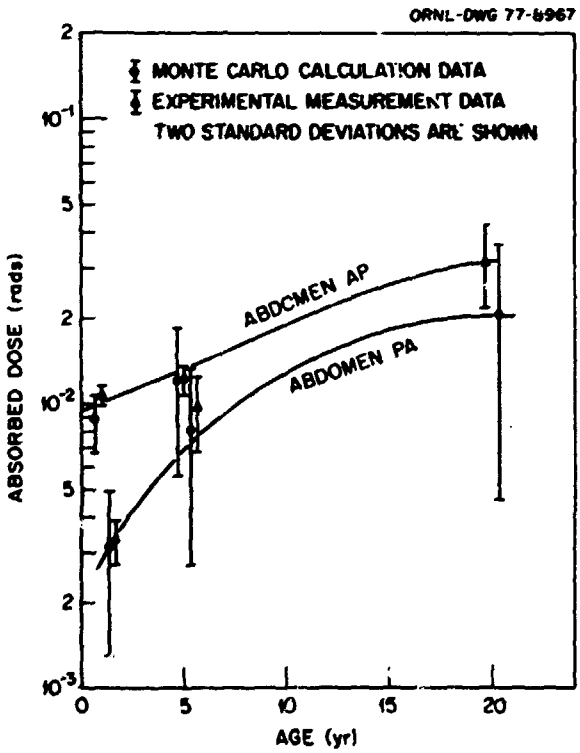

Fig. 26.8. Absorbed dose to the testes as a function of age for selected roentgenography.

The organ size in children is less than in the adult; thus the energy absorbed should be less. The body of the child is not as thick as an adult and, therefore, lower generating potentials can be used while still obtaining the same detail on the film. In addition, beam size can be reduced due to the small area to be irradiated in children compared with an adult. For example, more than one-third of the total red bone marrow is contained in the lower spine and pelvis. For exposures in which these two regions are in the direct x-ray beam, the dose to the red bone marrow will be significantly higher than the dose due to other exposures. An examination of Fig. 26.5 makes this clear. For an abdominal examination (lower spine and pelvis in the beam), the absorbed dose is more than a factor of 10 higher than for a typical chest examination.

A similar argument can be made for small organs and their locations relative to the incident beam. That is, the closer the organ is to the direct radiation beam the higher the absorbed dose in the organ. Another effect on the absorbed dose to small organs is the direction of incidence of the beam [i.e., AP, posterior-anterior (PA), or lateral]. This is illustrated in Fig. 26.6 in the dose to the ovaries for AP and PA incidence. These figures indicate that the absorbed dose in children may be less by a factor of 2 to more than 10 if the proper procedures are used in the radiographic examinations.

HIGH-RESOLUTION ULTRASONIC ANALYSIS OF BURN DAMAGE

Surgeons have long recognized the value of early excision of a burn wound and many major burn treatment centers are now following this regimen. It would be of significant benefit for the burn clinician to have available an objective method for evaluating the depth of thermal injury during these early hours. Various techniques such as dye differentiation,[30] use of radioactive tracers,[31] thermography,[32] and infrared spectral methods[33] have been used to determine the depth of necrosis; but none has come into widespread clinical use. On the basis of the data presented here, ultrasonic techniques appear to offer promise for a completely quantitative determination of burn depth.

---

30. Dieran Goulian, Jr., and Herbert Conway, *Surg. Gynec. and Obst.* 121, [illegible] (1965).

31. James E. Bennett and Reed O. Dingman, *Plast. Reconst. Surg.* 20, 261 (1957).

32. F. Mlandick and Nicholas Georgiade, *Plast. Reconst. Surg.* 38, 512 (1966).

33. National Aeronautics and Space Administration, *Computer Aided Diagnosis of Thermal Burns*, Technology Utilization Program Report, NASA Sp-5120, 1974.

Instrument System Development

To measure the depth of necrotic tissue resulting from severe burns, a conventional ultrasonic pulse-echo (A-mode) system was assembled and modified electronically so that small distances in soft tissue could be easily resolved. A description of the experimental equipment and the results of preliminary applications in animal systems have been reported elsewhere.[34-36] Diagnostic A-mode and B-scan units currently in use operate with transducers in the frequency range of 1 to 5 MHz and, consequently, have an axial depth resolution of ∿0.5 to 1 cm. The ORNL system uses very highly damped, broad-band transducers in the 5 to 25 MHz frequency range, thereby having an ultrasonic pulse width of ∿200 nsec. With appropriate wide-band instrumentation, a resolution of ≤0.2 mm is possible in soft tissue. This resolution is at least a factor of 3 to 4 better than any value reported in the literature for diagnostic purposes.

Data Analysis of Experimental Burns

During the course of preliminary investigation,[34-36] model burns of various degrees were made on anesthetized Yorkshire pigs because of the histological similarity of porcine skin to human skin. Figure 26.9*a* presents a typical time-dependent pulse-echo study for one such experiment. The reflection spectra were taken at various time intervals postburn to ascertain the depth of thermal damage at that time. There are several features to be noted. First, separate reflections result from both the near and far sides of the epidermis. These reflections are virtually always present in in vivo and in vitro experiments. In both investigations a careful microscopic study showed that the epidermis was the only structure that could cause these reflections. The dermis-subcutaneous fat interface is also observable at 3.5 mm. This reflection serves as a natural anatomic landmark and greatly facilitates diagnosis of whether the burn is partial thickness or full thickness.

The most significant feature of Fig. 26.9*a* is the reflection at ∿1.4 mm which we ascribe (Fig. 26.9*b*) to a distinct acoustical interface between necrotic tissue and viable tissue. Reflections from this interface are visible immediately postburn and are very distinct by the third day postburn. It was evident from these data and from histological study that the burn described here was second degree with significant thermal damage extending down to the middermal region. The middermal damage, furthermore, was irreversible since the burn interface reflection remained a prominent feature of the spectra throughout the remaining portion of the experiment.

In Fig. 26.9*b* we present a histology section taken immediately postburn (at about the same time as the second spectrum in Fig. 26.9*a*). The most significant feature to be noted here is the distinct staining interface between viable tissue and necrotic tissue and the observation that there is a one-to-one correspondence between the necrosis interface and the prominent ultrasonic reflection at ∿1.4 mm in Fig. 26.9*a*. Careful measurements with a stage micrometer indicated that the average thickness of necrotic tissue during the early postburn period was 1.35 ± 0.009 mm, consistent with the data in Fig. 26.9*a*. By the end of the second week postburn, the necrotic tissue thickness had deepened to ∿2 mm, most probably through infection. Table 26.1 shows a typical comparison between the pulse-echo measurements and microscopic measurements for burns of varying severity.

Linear Scanning Unit

A prototype linear scanning system (Fig. 26.10) was constructed at ORNL to provide design data for a clinical scanning unit to be built later. The ORNL linear scanner uses the A-mode system to generate ultrasonic pulses and to receive the signals reflected from the various layers of the skin. The received signals are rf oscillations which are rectified and shaped in a low-noise research amplifier with time-gain compensation to provide exponential tail pulses having a fast rise time. The first pulse in each pulse train (the main "bang" resulting from the high-voltage input to the transducer) is used to gate a linear delayed-time base generator which provides a depth calibration for the *x-y* display unit. The ramp is routed to the linear input of a fast linear gate (30 MHz) which allows a narrow slice ($\Delta t \sim 50$ nsec) of the ramp through, only when an echo pulse is present at the gate input of the linear gate. In this manner, a train of monotonically increasing pulses is generated, with the height of each one proportional to the transit time of the corresponding echo pulse. This pulse train provides the *y* coordinate (depth) on a high-resolution *x-y* display unit. The *x* coordinate is generated from a linear potentiometer connected to the transducer. The transducer is operable either in an immersion mode using a normal saline solution as the propagation medium or in a con-

34. R. E. Goans et al., *Health Phys. Div. Annu. Prog. Rep. June 30, 1976*, ORNL-5171 (October 1976), p. 80.

35. R. L. Roswell, R. E. Goans, and J. H. Cantrell, Jr., *High Resolution Ultrasonic Scanning of Animal and Human Tissue In-Vivo*, ORNL/TM-5934 (in press).

36. Ronald E. Goans, John H. Cantrell, Jr., and F. Bradford Meyers, *Med. Phys.* 4 (1977).

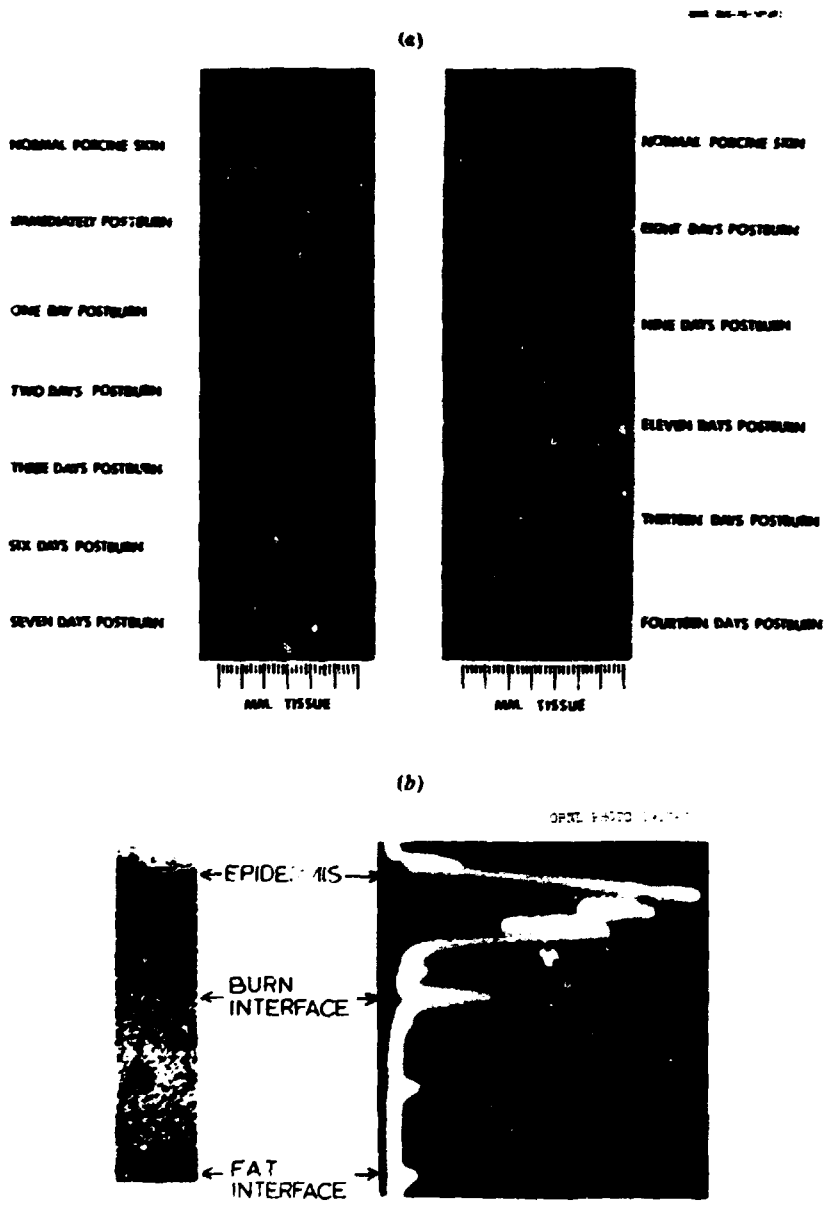

Fig. 26.9. Burn reflection spectra. (*a*) Burn reflection spectra taken various days postburn. (*b*) Comparison of the spectrum taken immediately postburn with the corresponding histology sample (see text for details).

Table 26.1. *Representative comparison between pulse-echo and microscopic measurements of burns*

Conditions – contact @ 100°C (sec)	Microscopic measurement (mm)	Ultrasound measurement (mm)
10	0.7 ± 0.07	0.83 ± 0.1
20	0.82 ± 0.11	0.77 ± 0.1
30	1.07 ± 0.06	1.08 ± 0.1

tact mode using a liquid-filled delay line. Some propagation delay is always needed so that real skin reflections can be separated from "main bang" artifacts. The ORNL prototype scanner is reasonably simple in construction and will be able to scan only over linear surfaces. Nevertheless, it is expected to give us important design information through cooperative animal studies at The University of Tennessee Comparative Animal Research Laboratory.

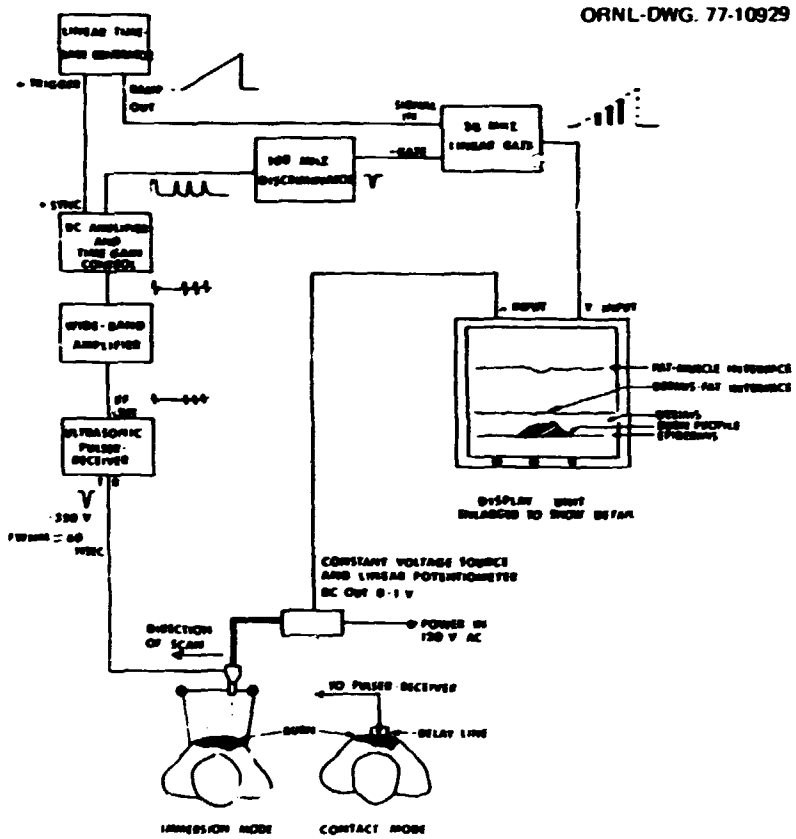

Fig. 26.10. Block diagram of the ORNL ultrasonic linear scanner.

Density Studies on Burned Tissue

One of the objectives of recent research was to determine why an impedance mismatch occurs at the interface between viable and nonviable tissue in a burn wound. The minimum detectable mismatch between the impedances appears to be about 1%. Previously unpublished work showed that the velocity of sound in both normal and necrotic porcine tissue was about equal (±5%) at a value of ∿1720 ± 45 m/sec. Initial experiments on human eschar gave a value of ∿1540 m/sec, which is the currently accepted value for the velocity of sound in soft tissue. The acoustic impedance, Z, is dependent on the wave velocity, c, the medium density, ρ, and the attenuation of the wave in the medium by

$$Z = \rho c(1 - i\alpha/k) , \qquad (1)$$

where $\alpha = R/2\rho c$ is the attenuation coefficient, R is a damping term, and $k = \omega/c$ is the wave number. Because the velocities of the two types of tissue being considered were assumed to be equal, it was apparent that the impedance mismatch must be caused by a density change or an attenuation change from the burned layer to the viable layer, or possibly both.

In attempting to measure the density of burned pigskin, two methods were developed. Both experiments used burned and normal plugs of skin (½ in. in diameter and about ½ in. in depth) taken from the pig. The burned portions were removed from the center of each burn made on the back of the pig. The normal sections were removed from unburned areas of skin adjacent to the burns. All burning times were 45 sec at 100°C.

The first method of density determination used the principle of fluid displacement. The mass of a small piece of skin was determined (to 4 significant figures, i.e., ±1 μg) on a metric balance. The sample was then placed in a tuberculin syringe containing a known amount of water. The volume displacement was measured and the density was calculated from

$$\rho = m/v , \qquad (2)$$

where m is the mass of the sample and v is the sample volume.

The second method for determining the densities of the viable and necrotic tissue used copper sulfate solutions of differing specific gravities. The solutions, made from $CuSO_4 \cdot 5H_2O$, were prepared yielding specific gravities varying from 1.0032 to 1.1020 in increments of ~0.005. The specific gravity, and therefore the density, was bracketed by a float–no-float test in the sample solutions. The bracket was obtained when the sample sank in one solution but floated in the next.

Both methods for density determination yielded similar results. From the mass and volume displacement method, the density for burn tissue was found to be 1.082 g/ml ± 0.14. Normal tissue yielded a density value of 0.998 g/ml ± 0.196, which agrees reasonably well with the accepted value of about 1 g/cm^3 for soft tissue. Published values for burned skin density are not available.

The copper sulfate method yielded the following specific gravities: normal, 1.0981 ± 0.006; viable, 1.0828 ± 0.001; burned, 1.0901 ± 0.008. Using 0.99823 g/ml for the density of water at 20°C, the average densities for normal, viable, and burned tissue were calculated to be 1.0961, 1.0808, and 1.0802 g/cm^3 respectively (Table 26.2). The characteristic impedances were calculated; the mismatch between viable and burned tissue was less than 1%, whereas the mismatch for normal vs burned tissue was 1%. Based on these results, it was concluded that the density variation between the burned and viable tissue was not significant enough to produce the boundary interface between the tissue layers. The change in acoustical impedance must therefore arise from attenuation differences as shown below.

Fourier Spectral Analysis of Attenuation Characteristics

In recent years, many investigators have begun to realize that significant information content is available in the Fourier transform spectra of time-domain ultrasound. A complete spectrum analyzer system was recently purchased at ORNL for use in various aspects of the ultrasound studies. We are currently undertaking a comprehensive effort to develop a burn-wound damage signature, using frequency-domain techniques. The techniques again are noninvasive and harmless to the patient.

Table 26.2. Density of viable and necrotic tissue

Tissue	Specific gravity	Density	Density by fluid displacement
Normal	1.0981 ± 0.006	1.0961	0.998 ± 0.196
Viable	1.0828 ± 0.011	1.0808	
Burned	1.0901 ± 0.008	1.0882	1.082 ± 0.14

Generally, in pulse-echo work, the received signal is an rf oscillation having a time-domain functional form $f(t)$. The Fourier transform (frequency-domain analysis) of $f(t)$ is given by

$$F(\omega) = \frac{1}{2\pi} \int_{-\infty}^{\infty} f(t) e^{-j\omega t}\, dt \,. \tag{3}$$

where ω = angular frequency, $J = \sqrt{-1}$, and t is the time variable. Typical Fourier transform spectra of ultrasound transducers used in this work are illustrated in Fig. 26.11.

Figure 26.12 shows, in block form, the apparatus used for these experiments. A Panametrics pulser-receiver (model 5052 PR) provided the "main bang" signal for the transducer, causing an ultrasonic pulse to be generated and transmitted into the sample. The reflected pulse, or echo, was received by the transducer and hence the pulser-receiver. The reflected echo was then sent into a Panametrics stepless gate (model 5052 G) so that a selectable portion of the wave could be gated for analysis. The Hewlett-Packard spectrum analyzer (model HP 8557A) received the gated signal and displayed the Fourier spectrum of the pulse. An oscilloscope was connected to the pulser-receiver and gate to simultaneously view the unregulated echo pattern from the sample and also the gated portion of the pattern. Once a suitable spectrum appeared on the analyzer, a hard copy of the spectrum was drawn by an X-Y recorder.

To obtain the attenuation measurements on burned tissue, the usual exponential attenuation expression was used in another form. Suppose $E_1(\omega)$ is the Fourier spectrum of the echo from the front surface of a burn:

$$E_1(\omega) = \rho_1 P(\omega) \,, \tag{4}$$

where ρ_1 is the pressure reflection coefficient, and $P(\omega)$ is the spectrum of the pulse if it were totally reflected from the front surface. For small values of ρ_1, the back surface echo spectrum is

$$E_2(\omega) = \rho_2 P(\omega) e^{-2\alpha(\omega)x - i2kx} \,, \tag{5}$$

where x is the sample thickness, α is the attenuation coefficient, $k = \omega/c$ is the wave number, and ρ_2 is the

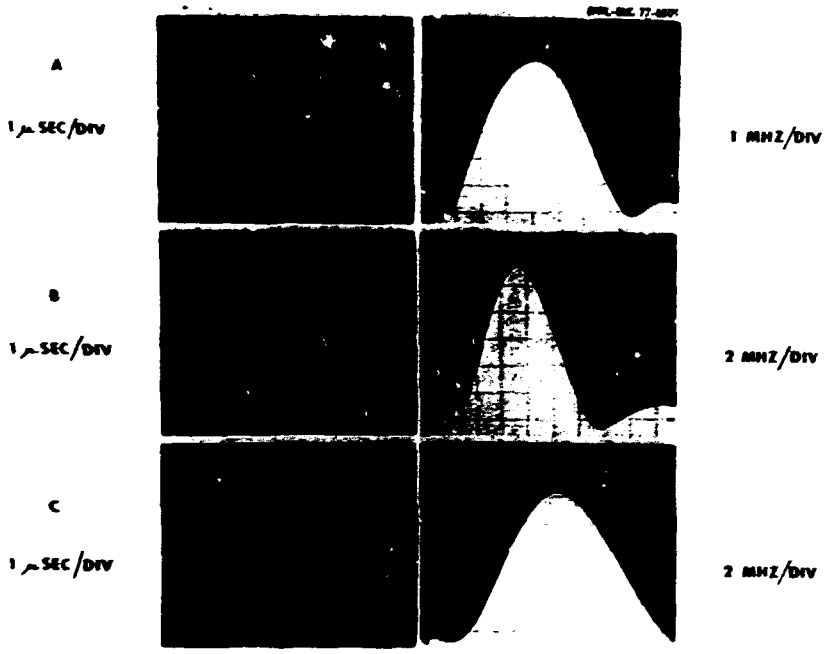

Fig. 26.11. Time- and frequency-domain representations for ultrasonic rf pulse.

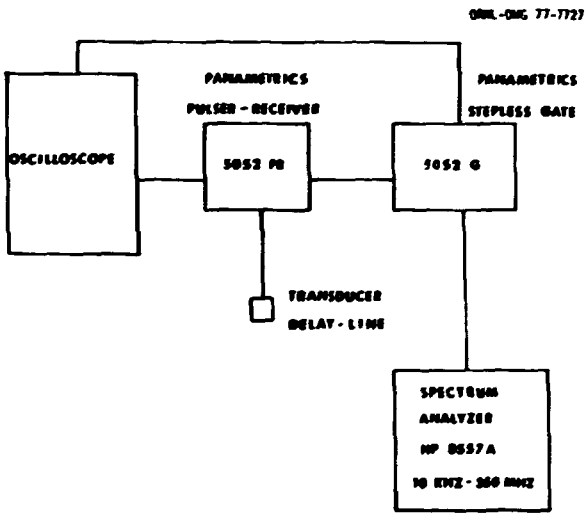

Fig. 26.12. Block diagram of the spectrum analysis system.

pressure reflection coefficient for the near surface. The ratio of $E_1(\omega)$ and $E_2(\omega)$ eliminates $P(\omega)$ from consideration and gives

$$R(\omega) = \frac{E_2(\omega)}{E_1(\omega)} = \frac{\rho_2}{\rho_1} e^{-2\alpha(\omega)x - i2kx} . \tag{6}$$

The magnitude of the ratio $R(\omega)$, expressed in decibels, gives

$$20 \log R(\omega) = 20 \log \frac{\rho_2}{\rho_1} - 17.4\alpha(\omega)x . \tag{7}$$

With some manipulation, the attenuation coefficient $\alpha(\omega)$ can be obtained as

$$\alpha(\omega) = [\log E_1(\omega) - \log E_2(\omega)] \left(\frac{20}{17.4x}\right) . \tag{8}$$

Figures 26.13 to 26.15 show the spectra of normal, viable, and burned porcine tissues respectively. The accepted value for soft-tissue attenuation in humans is about 0.8 dB cm^{-1} MHz^{-1}. From the graphs in Fig. 26.13, the experimental value for attenuation in pigskin was calculated to be 0.73 dB cm^{-1} MHz^{-1} over the 9 to 15 MHz range, which is in general agreement with the human skin attenuation value. The experimental values for viable tissue and burned tissue were 0.30 and 0.59 dB/cm respectively. These experimental values establish a significant difference in the attenuation of sound passing through samples of skin tissue exhibiting various conditions of viability.

From Figs. 26.13, 26.14, and 26.15, it can be concluded that the attenuation does differ significantly from burned to viable tissue layers, thereby causing an impedance mismatch. The spectral shape for each layer (burned to viable) changes, and the calculated attenuations are significantly different in going from the first

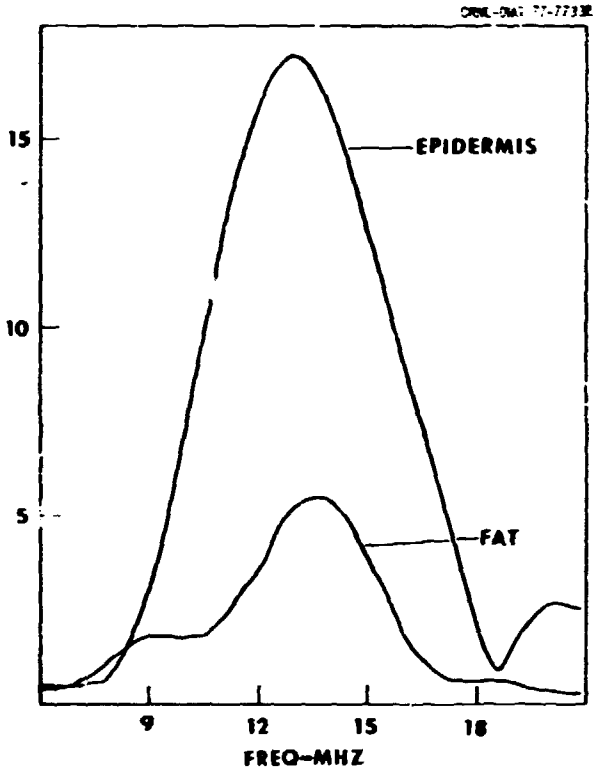

Fig. 26.13. Frequency spectra of normal tissue. Labels refer to reflecting structure.

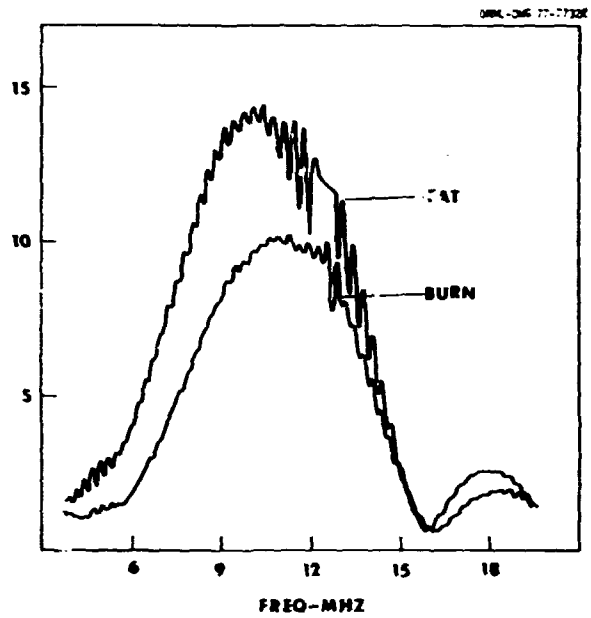

Fig. 26.14. Frequency spectra of thermally injured but viable tissue. Labels refer to reflecting structure.

layer to the deeper tissue below. Moreover, it is interesting to note that the normal and viable spectra differ from each other significantly. The unburned skin layer below the burn is not left undamaged by thermal injury to the skin. The experimental data collection of the spectrum analysis measurements could be improved significantly if signal averaging were incorporated into the system. If several spectra (30 to 40) for each interface were to be obtained and averaged together, much of the uncertainty could be removed. For this to occur, a link to a minicomputer is necessary. The data presented in Figs. 26.13 to 26.15 should be considered to be preliminary since there are many burn-wound parameters that can affect the spectral characteristics of the reflection pulses. The minicomputer link is being implemented at present, and better data should be available in the near future.

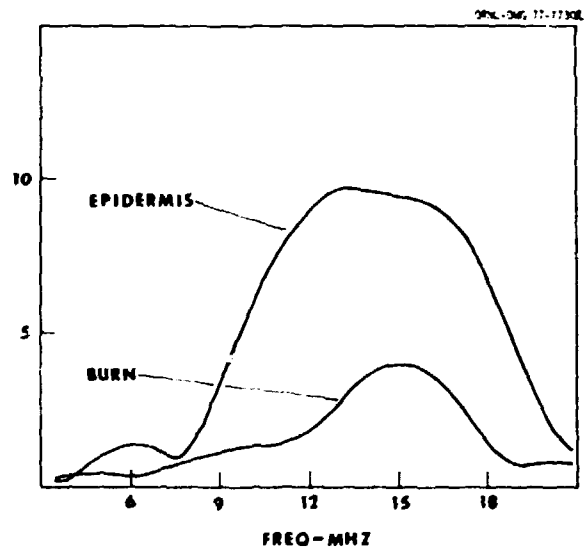

Fig. 26.15. Frequency spectra of necrotic tissue. Labels refer to reflecting structure.

27. Nuclear Medicine Imaging and Data Processing

P. R. Bell R. S. Dillon[1]

The nuclear medicine physician today is presented with images of poor resolution and inadequate statistical accuracy as a result of dose limitation, short imaging time, and instrument design. Because diagnosis depends on these images, considerable effort is justified in exploring techniques to improve their clinical usefulness. The most promising efforts involve using a digital computer for image access, storage, display, and processing.

The Oak Ridge Imaging System (ORIS) is a software operating system structured around the Digital Equipment Corporation's PDP-8 minicomputer which provides a complete range of image manipulation procedures. Through its modular design it remains open-ended for easy expansion to meet future needs. Already included in the system are image access routines for use with the rectilinear scanner or gamma camera (both static and flow studies); display hardware design and corresponding software; archival storage provisions; and, most important, many image processing techniques. The image processing capabilities include image defect removal, smoothing, nonlinear bounding, preparation of functional images, and transaxial emission tomography reconstruction from a limited number of views.

ORIS was designed with the physician's needs in mind and with the cooperation of several nuclear medicine clinics. Our clinical experience to date appears promising, and as we adapt the programming into different computer lines, we expect even broader dissemination of our image processing techniques.

Gamma-ray imaging for nuclear medicine produces images of poor resolution and inadequate statistical accuracy as a result of dose limitation, imaging time, and instrument design. The images also contain a considerable amount of false information due to gamma-ray scattering within the patient, oblique collimator penetration, and electrical interference. Thus, the nuclear medicine clinician is confronted with serious problems in interpreting an image and rendering a diagnosis. In addition, he is simply prevented from attempting more complex imaging procedures (such as heart imaging) when his gamma camera is equipped only with a Polaroid or 35-mm camera for direct recording of image data from the gamma camera display. These problems have led to the use of computers for image access, storage, display, and processing.

The ORIS provides a reliable and comprehensive clinical operating system to enable the incorporation of a minicomputer into the nuclear medicine clinic. The system is coded in assembler language for the Digital Equipment Corporation's (DEC) PDP-8 computer and is currently being reprogrammed for the DEC PDP-11 system. The command structure is such that an imaging protocol can be executed by a technician with little or no need for making independent judgments. The system is designed to relieve some of the need for better-trained personnel and to reduce the cost and disruption to a clinic by permitting gradual introduction of small, single-instrument computers into the clinic rather than an all-inclusive large-scale computer that attempts to service the entire clinic.

ORIS supplies all of the basic services required of a nuclear medicine computer – acquisition, storage, display, and processing of images – yet is open-ended to allow new applications to be added as necessary. Several nuclear medicine clinics have cooperated in the development and improvement of ORIS over the past years. These include Oak Ridge Associated Universities (ORAU), the Veterans Administration Hospital (Gainesville, Fla.), the University of Florida at Gainesville, the University of Kentucky at Lexington, and Vanderbilt University. This clinical evaluation has resulted in both a rather fail-proof operating system design and a highly relevant and useful set of program units to meet the needs of today's nuclear medicine clinics.

---

1. Computer Sciences Division.

ORIS COMPONENTS

ORIS has been structured to operate under either the OS/8 operating system or the older Disk/DECtape monitor.[2] The operating system is generally invisible to the user because chaining and program calls are performed from ORIS with standard commands. The services performed by ORIS can be divided into the four categories listed above — data acquisition, storage, display, and processing. A brief description of some of the highlights of these categories follows.

Data Acquisition

The purpose of this task is to record the actual disintegration events by way of gamma-ray emissions as the radionuclide decays. The position of the gamma ray is determined by the gamma camera or rectilinear scanner, and this information is provided to the computer. The computer then accumulates a great number of these events which ultimately constitute the "image." The important thing to note here is that the image is in the form of digital data (i.e., numbers), not a photographic representation of the data. The numbers are thus available for any type of display or mathematical manipulation desired. The two general types of imaging instruments provided for are the rectilinear scanner and the Anger gamma camera.

Rectilinear scanner. This device is used when high resolution or large areas are to be imaged. It is also more suitable for the higher energy gamma-ray-emitting radionuclides.

Anger gamma camera Although the gamma camera is restricted to a smaller imaging area than the rectilinear scanner, it can collect images much more quickly. The camera remains aimed at a given region of the patient, whereas the scanner is constantly in motion traversing the patient's body. Thus, for motion picture type imaging (dynamic sequences), in which the time variation (as well as the spatial distribution) of radionuclide tracer is of interest, the camera is used.

ORIS provides three basic modes of data collection from the gamma camera: static, dynamic, and gated-dynamic.

The static access is used to collect data when the tracer variation with time is not significant. Examples of this type of collection are ^{67}Ga imaging, delayed brain imaging, and thyroid imaging. Dynamic access techniques are used when the time variation of tracer concentration is vital. Examples of this type of collection are brain perfusion studies, kidney flow studies, and heart bolus studies. The third type is the dynamic gated study. It involves dynamic imaging in which the images are not taken strictly sequentially but rather on cue from some physiological trigger. The gated heart study is the best example of this type of data access. Briefly, the heart is continually contracting (systole) and relaxing (diastole), fulfilling its job of pumping blood. The sequence of systole/diastole is known as the heart cycle and occurs about 70 to 80 times a minute in the normal adult. However, this pumping motion makes it extremely difficult to get an image of the heart. Thus, we resort to a technique in which we divide the cycle into twelve parts and record the data from each of these parts separately, for many heart beats (cycles), thereby deriving an averaged picture of the heart at various stages of contraction. To know when to start taking pictures, we rely on an electrocardiograph (ECG) signal indicating a particular position in the heart cycle (systole). The signal turns on the data access; hence the term "gate."

Data Storage

Once we have the image in hand, it is necessary to provide proper lodging for it. The magnetic disk is adequate for short-term storage, but, because its capacity is limited, we chose to record the data on magnetic tape (specifically, DECtape). This permits several sequential studies to be performed without the need to process each study in the interim and also preserves the data for future reference. A program is included to compress the rather dilute image tapes (image files), especially dynamic sequences, to conserve magnetic tape.

Image Display

Of course, all effort expended thus far would be wasted if the images could not be seen. Hence, a means of displaying the image data, both with regard to spatial location and intensity, is required. Our display translates the computer data into a plot of intensity vs position, in two dimensions, on a cathode ray tube (CRT). The naked eye, however, is able to perceive rather few distinct intensity levels; although our computer data varies from zero to several thousand, the naked eye can distinguish perhaps sixteen levels. The display electronics can generate only thirty-two intensity levels. One solution we have used to combat this contrast limitation is to display the data so that when the 32-level limit is saturated, the display returns to

2. Monitors of the Digital Equipment Corporation.

level zero and begins again. We have thus extended our contrast range by allowing the display to cycle. This cycle is called Multicycle Contrast Enhancement (MCCE) and is illustrated in Fig. 27.1. The image on the left in Fig. 27.1 displays data compressed to be within the 32-level limit. The middle image, however, allows full display of the data, with each saturation level indicated by a return to darkness. Starting from the periphery, each cycle (or "contour") crossed indicates an additional jump of 32 counts in the image data. Thus, in Fig. 27.1 four cycles are noted; hence, in the hottest area (in the center of the right lobe of the liver phantom), the counting rate was about 4 X 32 (128 counts). Although this number of cycles is perceived fairly easily, many more than this is not. Hence, we have included the ability to scale the data by various factors of 2 until a reasonable number of cycles is displayed. Background subtraction is also available, as well as image addition and subtraction.

All the displays discussed are interpolated, that is, the original image data matrix is expanded by a factor of 4 by interpolating neighboring points by simple averaging. We have found it much easier to comprehend interpolated images than noninterpolated ones, especially the 64 X 64 matrix size images, which are the ones normally accessed by our computer from the gamma camera.

Finally, an essential ingredient of every image is a collection of text describing the image. ORIS provides space for 127 characters of descriptive comments to accompany each image. These are displayed with the image, as shown in Fig. 27.1. Additionally, each processing modality that is applied to the image inserts a short tag to the comments indicating just what manipulation has been used on the data.

Fig. 27.1. Liver phantom image incorporating a small (17 ml) void near the right and left lobe boundary. (*Left*) Bounded and smoothed image displayed in nonmulticycle mode; (*middle*) same as left, but displayed in multicycle mode; (*right*) image is further smoothed with 0.9 of the linear 7 X 7 matrix subtracted from the 5 X 5 quadratic smoother.

Image Processing

Our principal motivation for collecting the gamma-ray image data in digital form is to allow quantitative manipulation of that data via computer. This is referred to as image processing. It is undertaken to enhance the clinical, diagnostic value of the images, either by increasing their apparent information content or by permitting certain technically difficult procedures to be carried out. It could be argued that techniques no more complicated than background subtraction are true image processing schemes. And, indeed, they do require a computer system to function. However, in this section we will deal only with the more sophisticated, more computationally demanding procedures.

A number of our processing algorithms are implemental through the use of a matrix weighting technique.[3,4] In its simplest form, it resembles the familiar nine-point averager. The nine-point averager consists of a set of nine weights which, when applied to nine data points in a two-dimensional image, yield a simple smoothing. For instance, when all the weights are equal, the result is a simple arithmetic mean of nine contiguous data elements. This averaging is done for each data element in the image with the result being a smoothed image. Our matrix method uses a 49-point smoothing matrix taking advantage of certain symmetries of the matrix to reduce the number of weights that need be saved. Special techniques are needed for processing points near the image edges, and an efficient weighting algorithm is used to effect the actual matrix multiplication. The matrix method thus serves as a basis for our antiscatter-antipenetration correction, smoothing, nonlinear bounding, and edge-detection algorithms. These and other processing modalities are discussed below.

Linear matrix-method processing. These techniques use the matrix method for each data element regardless of its value. Later we shall see how the nonlinear techniques produce different actions depending on the value of the data elements.

Antiscatter and antipenetration correction. As we attempt to locate radioactivity within the patient through the external detection of gamma rays released by radioactive decay, the gamma rays ideally should follow a direct path from their source to the detector. However, two factors work to the detriment of this goal. Compton scattering of gamma rays, especially of those gamma rays higher in energy than those for which

3. P. R. Bell et al., *ORSS-72: A Computer-Based Dual-Data Rectilinear Scanning System*, ORNL/TM-4045 (August 1973).
4. P. R. Bell et al., *A Computer Based Scanning System*, ORNL-4038 (January 1973).

the imaging device is adjusted, results in anomalous location of activity by the scintillation detector. Also troubling are those gamma rays that penetrate the septa of the collimator, and thus are counted as emanating from a location removed from their actual point of origin. By collecting an image of a point source of the radioisotope of interest immersed in a scattering medium (usually water) and deleting from this image the estimated optical response (the desired portion) of the imaging instrument, we can form an error matrix to correct other images for these defects. This is accomplished through a one-pass deconvolution process using the matrix method to apply the point-source data to the image, thus generating a correction.

Two-dimensional least-squares polynomial smoothing. The recently developed least-squares weighting matrices[5] yield a least-squares fit to a two-dimensional polynomial up to degree four. These matrices result in image smoothing that yields superior detail relief as compared to the nine-point or Gaussian method as well as an acceptable degree of smoothing. The least-squares matrices are linear; they can be added or subtracted from one another in any combination, with the result being identical to that obtained by separate processing with individual matrices. An example of this linear combination of matrices is presented in the liver phantom images of Fig. 27.1. The phantom contains a small (17 ml) void near the division of the left and right liver lobes which can be demonstrated by use of least-squares processing. The image on the left results from a bounding (to be described later) and smoothing process and is displayed in nonmulticycle format. The middle image is a multicycle representation that allows some guess to be made of the lesion location and size. The image on the right results from a further smoothing done in one pass with 0.9 of the linear 7 X 7 matrix subtracted from the 5 X 5 quadratic smoother. In essence, this removes much of the low-frequency portion of the spectrum and demonstrates the lesion quite well.

Least-squares fits to second-derivative functions are also available and have proved useful in delimiting organ boundaries. For example, second derivations can help determine left ventricular size during various stages in the cardiac cycle.

Nonlinear matrix method processing. This technique is similar to the linear least-squares smoothing previously described except that a data element is altered only if it is arbitrarily far removed from the calculated smoothed value. The image elements are therefore restricted as to their variation relative to their neighbors, thus removing statistically unlikely points. Hence, this bounding action is fundamentally nonlinear in nature: A value-dependent decision is made at each point, resulting in some smoothed ("bounded") points and some unmodified points.

Other nonlinear techniques. *Two-dimensional median smoothing.* This method replaces each point with the median of the points surrounding it. The result is smoothing with exceptional rejection of erroneous data points and retention of fast transitions in the data.

Fast Fourier transform (FFT). We are studying the possibilities of applying nonlinear filtering techniques in the frequency domain. However, our progress to date has been limited to linear smoothing (filtering) and instrument characterization (error detecting) using frequency domain images.

Functional images. It is often convenient to summarize or extract some physiologic variable from either a sequence of dynamic images or some related grouping of static images. An example of the latter is the ventilation/perfusion (V/Q) ratio images relating respiratory airflow to blood flow within the lungs. Under normal circumstances, one would expect a rather constant balance of these two quantities throughout the lungs. Any disturbance of this balance is readily demonstrated in this functional image. We have developed a set of functional images that extract both the arrival time of blood to cerebral tissue and the maximum perfusion enjoyed by that tissue independent of time. These NTMAX functional images are calculated from a standard dynamic flow study of brain circulation. Figure 27.2 illustrates the TMAX (left) and NMAX (right) images from a representative dynamic brain study. In the TMAX image, areas receiving blood early in the study are lighter; those receiving blood later are darker. In this patient, an obvious perfusion deficit is observed in the right hemisphere in the distribution of the middle and anterior cerebral arteries. However, the NMAX image displays a fairly uniform pattern, indicating effective collateral flow and a promising prognosis.

CURRENT PROJECTS

The modular, open-ended design of ORIS permits great flexibility in extending its scope to new areas. Several representative tasks from our present developmental studies will now be described. When completed, these procedures will be incorporated into ORIS.

5. M. R. Bell, *A One- and Two-Dimensional Least-Squares Smoothing and Edge Sharpening Method for Image Processing*, ORNL/TM-5222 (January 1976).

PHOTO 0601-77

Fig. 27.2. NTMAX functional images of dynamic brain perfusion study. TMAX (*left*) displays time at which an image element reached its maximum, with earliest being brightest; NMAX (*right*) displays maximum level of brain perfusion without regard to time.

Bone Imaging

Several radionuclides produce gamma rays of energies useful in transmission imaging of bones. In its simplest form, a bone to be imaged is interposed between an external gamma-ray source (^{125}I in our case) and a gamma camera. A certain fraction of the gamma radiation will be absorbed by the bone and thus not counted by the camera. The resulting image can then be analyzed and bone mineral content estimated. Together with Dr. Robert Bright (Department of Orthopedics, University of Florida), we hope to refine this technique and introduce it into the clinic as an aid to following bone graft patency.

Comparison of Nonlinear Image Processing Techniques

The use of the least-squares data bounding procedure produced unexpectedly good effect in revealing detail and reducing image mottling when used on moderately noisy nuclear medicine images. It is currently being studied and compared with other methods. In this method, a two-dimensional least-squares fit is made at every point of an image for the 5 X 5 or 7 X 7 element area surrounding the point. The fitted value is compared with the data point, and the point is replaced by the fitted value if it departs from the fit by more than the assigned number of standard deviations. This process is then followed by one or more passes of the same or different least-squares-fitted smoothers in which the points are always replaced by the fit. The processes (1) produce a marked improvement in smoothness and freedom from image mottling when compared with standard methods at the same relief of true image detail above the surroundings or (2) show much better relief of image detail above the surroundings and less mottling when compared at the same smoothness.

The performance of the nonlinear bounding is illustrated by comparison with two other methods: (1) the Gaussian weighting method, the best of the standard methods, and (2) a new two-dimensional version of the median method of Tukey.[6,7] In the Gaussian weighting method, a matrix of 5 X 5 or 7 X 7 weight factors with a Gaussian shape is multiplied by the corresponding data values at a point, and the sum of the products replaces the data point. The Tukey method arranges the data in a 5 X 5 area in increasing order, then selects the median point to replace the data point. The resulting image is then smoothed and saved. This image is subtracted from the original image, the difference image is again processed as above, and the smoothed difference image is added to the once-processed image as a correction. Figure 27.3 shows a comparison of a portion of a ^{67}Ga scan of a patient processed by these three methods. This image, as in all gallium images, has poor statistical strength due to dose limitation. The better sharpness and relief of detail for the nonlinear bounding can be seen.

6. L. R. Rabiner, M. R. Sambur, and C. E. Schmidt, *IEEE Trans. Acoust. Speech Signal Process.* **ASSP-23** (1975).
7. A. E. Beaton and J. W. Tukey, *Technometrics* **16**, 147 (1974).

Fig. 27.3. Comparison of smoothing methods. The left image was smoothed by two passes of a Gaussian with a sharpness of 1.5 standard deviations per element spacing. The center image was smoothed by a two-dimensional modification of the Tukey median method using a 5 × 5 element area and smoothing with a 5 × 5 element least-squares quadratic. The right image was smoothed by a nonlinear bounding to a 5 × 5 element least-squares quadratic, then smoothed by two passes of this same matrix as a smoother. The amplitude intensity profiles were made at the line shown in the image. Note the superior smoothness and detail relief in the nonlinear method.

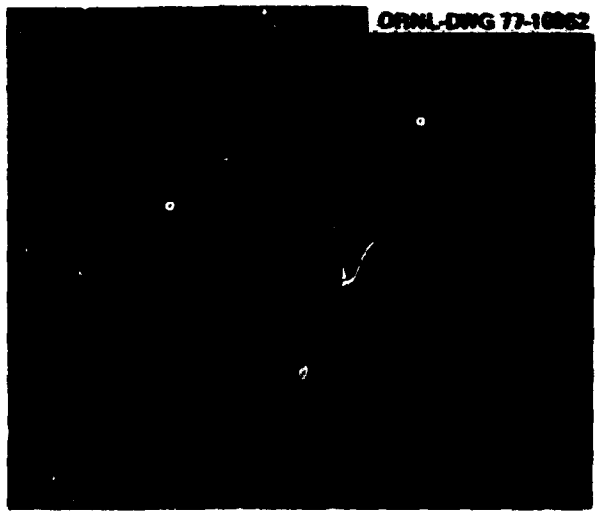

Fig. 27.4. A line from a Poisson noise field (N = 5) corresponding to 45 counts/cm² with a 1 × 7 cm (3 × 21 element) signal bar with N = 8 corresponding to 72 counts/cm². The line is perpendicular to the length of the signal bar. *Left column* shows raw data at top followed by successive passes of smoothing with a broad Gaussian except for the last line which has eight passes. The center *column results from a sharper Gaussian* smoother. The right column is produced by a pass of the nonlinear least-squares bounder (line 2), followed by a pass of the least-squares smoother, then followed by successive passes of the smoother except for the last line, which has eight passes.

Those who have used the nine-point or the Gaussian weighting smoothers are familiar with the rapid flattening of detail that occurs with successive resmoothing of an image. The least-squares quadratic or quartic smoothers do not produce this rapid flattening of detail. Figure 27.4 shows one line of a Poisson noise field containing a signal bar. The noise field corresponds to a level activity region with 45 counts/cm², whereas the signal bar represents a 1 × 7 cm area at 72 counts/cm². The line is taken perpendicular to the long axis of the signal bar representing a 1-cm-wide detail. The left set shows the application of a 7 × 7 Gaussian with one standard deviation per element spacing; the center shows a sharper Gaussian with 1.5 standard deviations between elements; and the right column shows the application of a 7 × 7 element quartic bounder, bounding at 0.7 standard deviation, followed by the same fit as a smoother. The signal is hardly evident in the raw data line at the top but becomes more evident with smoothing. The signal has been greatly reduced in amplitude and broadened by eight passes of the broader Gaussian smoother. The sharper Gaussian smoother does not produce such a rapid decrease in amplitude, but, of course, neither does it produce as much smoothing. The nonlinear bounding and least-squares smoothing produce the least flattening of the signal. It is constructive to note the widening of the signal bar after two operations of each method because this is a practical number of passes. The data width is three elements. The broad, medium, and least-squares smoothers give a width of nine elements, six elements, and four elements respectively.

Emission Tomography with Small Numbers of Images

Conventional computer-assisted transaxial emission tomography requires the acquisition of 60 to 180 images of 1 or more lines around the patient for reconstruction. This large number of images can be obtained only by the use of large, special-purpose imaging devices and requires long imaging time or rather large internal source strength for adequate statistical strength.

Four or five images taken with a gamma camera around a patient using ^{99m}Tc show by inspection, however, that enough information is available for some form of transaxial image reconstruction. We are attempting to develop an acceptable method of reconstruction using only a few images made by a standard gamma camera. The essential fact that makes the reconstruction possible is the attenuation of the gamma rays from an emitting source by the substance of the patient. When back-projection embodying this attenuation is used, some

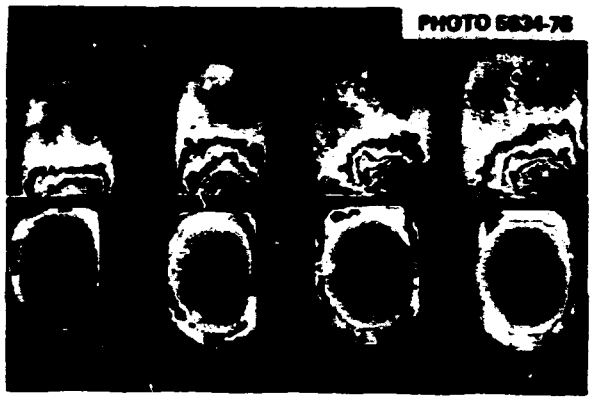

Fig. 27.5. Transaxial emission tomography using five images. The top line shows the four transverse views used showing the computer-simulated hot spot. The images from left to right are: anterior, posterior (as though seen from an anterior location), right lateral, left lateral (as seen from the right side). The fifth original image not shown is a vertex (top) view. It is used only for the outline boundary. The top slice is at the left. The reconstructed image of the hot spot appears in the third slice.

degree of reconstruction is practical. Figure 27.5 shows the results of reconstruction of four slices of a brain image. The patient images in the top line include a computer-simulated hot spot. This spot appears in the third slice image below. The image on the left is the top slice. Reconstruction is fairly good although the boundary outline is not as well reconstructed as desired due to the small number of images. For torso reconstruction, eight images would produce better results due to better definition of the patient outline.

Part VI. Analytic Dosimetry and Education

J. E. Turner

28. Analytic Dosimetry

J. E. Turner C. F. Holoway A. S. Loebl[1]

The Analytic Dosimetry Program was established to gather information for review of critical areas of the Division's research and to serve as a base to which technical questions can be directed to assist researchers in the Division as well as outside. This program also provides the link between programs of the Health Physics Division and the local Information Center Complex (ICC). Reports, bibliographies, and files developed by the Analytic Dosimetry Group are abstracted and added to the Health Physics Information System (HPIS) as one of the ICC data bases available for local or remote computer search. The design and structuring of the HPIS data base has been extended to provide specific support to the critical areas addressed. Although the group continues to conduct searches and respond to specific questions on request, this function does not now consume a large fraction of the total effort. During the current year, emphasis was placed on specific studies in selected areas as detailed below.

The Analytic Dosimetry Program interacts with other programs in the Division, in the Energy Division, and at Oak Ridge Associated Universities (ORAU). A close liaison is maintained with the Information Division's ICC and with the Nuclear Safety Information Center.

During the year, a near-final draft of *Guide to Radioactive Waste Management Literature* was completed and circulated for review and comment. The guide includes a bibliography with the categorization, listing, and abstracts of 1000 selected documents that cover various aspects of waste management. In addition, it contains analyses and summaries written by the Analytic Dosimetry Group to assist users in finding definitive documents with specific information. The contents of the guide are in the HPIS file and are available for computer searches by key word, subject, author, etc.

A workshop on the dosimetry of radon and radon daughters was held at ORNL on April 12 and 13, 1977. The workshop was planned and organized under the Analytic Dosimetry Program. Twelve scientists from outside ORNL attended, representing various specialties in problems associated with radon daughters. The workshop, which was conducted informally around a structured agenda, concentrated on problems in the conversion of measured values of inhaled air concentrations into dose estimates and risk assessment. The workshop identified the areas and degrees of scientific uncertainty and their possible bearing on health-protection practices, on regulations, and needed research. A state-of-the-art summary of the workshop findings and recommendations is being prepared. As a supplement to the workshop, *Select Bibliography on the Dosimetry, Metabolism, Pathology, Epidemiology and Environmental Aspects of Radon and Its Daughters* is being prepared.

Work on health standards for energy production continued. This project is closely related to health-effects studies in the Health Physics Division, the Energy Division, and at ORAU. This program is beginning now to address the questions and areas that limit health standards research to date. Specifically, we seek to address factors that relate human epidemiological studies and laboratory experiments. Knowledge based on limited data from human studies can be extended by

1. Energy Division.

integrating findings from such studies with results from laboratory research.

Some preliminary work was begun to study various approaches to formulation of dosimetric concepts for exposure to nonradioactive environmental pollutants. This activity will tie in both with the Division's basic physical studies in microdosimetry and the studies on health effects.

An investigation was also begun to ascertain the inherent physical limitations of various concepts used frequently in biological effects modeling. For example, absorbed dose is often treated as a point function, even in small volumes. The average radial distribution of dose around a particle track is also frequently used, without incorporating any influences of the physical fluctuations that occur. Criteria to delineate the applicability of macroscopic quantities, such as absorbed dose, and microscopic ones – and the transition between the two – apparently have not been formulated. These concepts will be critically reviewed and their limitations expressed quantitatively.

The group continued to respond to inquiries in a number of areas. Written or verbal information was provided for about 50 requests from both in and outside ORNL.

29. Education and Vocational Training

M. F. Fair J. E. Turner

The Faculty Institute in Applied Health Physics was started in the summer of 1974 in response to the nation's need for persons trained at the bachelor's level in health physics technology. A number of surveys[1-4] as well as our own forecasts[5] indicate that between 3300 and 5000 new trained technologists will be needed by 1985. They will be required for nuclear power reactors, fuel-cycle operations, nuclear medicine, regulatory activities, and as replacements for currently employed workers. The Faculty Institute program provides support for contacting college officials to make them aware of these forecasts and to interest them in introducing undergraduate health physics course work at their institutions. In addition, the program provides support for ten faculty participants from different universities to spend ten weeks during the summer in the Health Physics Division. These participants have access to the staff and the diverse research and field facilities of the Division. They also utilize the facilities of the Special Training Division at Oak Ridge Associated Universities (ORAU).

Instructors from ten colleges participated in the Institute program during the summer of 1976. These schools were the University of North Carolina (Greensboro), The University of Tennessee (Martin), Milligan College, West Virginia State College, District of Columbia Teacher's College, Texas College, Carson-Newman College, Kentucky Wesleyan College, Union College, and East Central University. These schools have indicated an interest in having suitable undergraduate courses for health physics technologists. Several have already been involved in graduate training programs in health physics. Our experience indicates that the Faculty Institute program is successful – 21 of the 25 schools represented either now have or expect to have ongoing courses by September 1977.

The Health Physics Division provided assistance to The University of Tennessee, where five staff members taught courses in the Department of Physics. Approximately ten graduate students used Division facilities to work on their theses for advanced degrees under the supervision of Division staff members.

Major assistance was given to ORAU in the presentation of ten-week courses in health physics. Twelve student trainees from ORAU spent the summer of 1976 in the Division as research participants. Three student trainees from the Southern College University Union and one student trainee from the Great Lakes Colleges Association spent a semester in the Division.

An in-house course in health physics was presented to new members in the Applied Health Physics sections.

Tours were provided for various college groups visiting Division facilities.

---

1. *The Nation's Energy Future*, WASH-1281, Stock No. 5210-00363, U.S. Government Printing Office, Washington, D.C., 1973.
2. K. Becker, *Health Phys.* 32, 429 (1977).
3. R. L. Kathren, *Health Phys.* 31, 489 (1976).
4. D. W. Moeller and R. Eliassen, *Health Phys.* 31, 1 (1976).
5. M. F. Fair and J. E. Turner, "Faculty Institute in Applied Health Physics – A Program to Help Meet Future Requirements for Health Physics Technologists," to be published in *Health Physics*.

Theses, Papers, Publications, and Lectures

Theses

Javaid Ashraf

Optimization of Electrochemical Etching Parameters for Alpha Particle Registration in Polymers and Application to Radon Monitoring (The University of Tennessee) (December 1976)

W. L. Chen

"An Evaluation of the Distribution of Absorbed Dose in Child Phantoms Exposed to Diagnostic Medical X Rays" (Georgia Institute of Technology) (in preparation)

C. W. Choi

Two-State and Two-State-Plus Continuum Problems Associated with the Interaction of Intense Laser Pulses with Atoms, ORNL/TM-5754 (University of Kentucky) (December 1976)

S. F. Deus

"The Development of a Mathematical Phantom Representing the Reference 10-Year-Old Child for Use in Dose Calculations" (University of São Paulo) (in preparation)

Pedro M. Echenique

"Aspectos do Estela en la Interaccion de Particulas Caragadas con Medios Materiales" (Universidad Autonoma de Barcelona, Spain) (1977)

K. S. Gant

Electron Capture and Drift in Polyatomic Gases (The University of Tennessee) (August 1976)

L. W. Grossman

"Studies of Single Atoms of Lithium Using Resonance Ionization Techniques" (University of Kentucky) (in preparation)

J. P. Johnson

A Mass Spectrometric Study of Dissociative and Nondissociative Electron Attachment to Organic Molecules (The University of Tennessee) (February 1977)

R. L. Roswell

High Resolution Ultrasonic Scanning of Animal and Human Tissue In-Vivo (Rensselaer Polytechnic Institute) (May 1977)

J. J. Shonka

"Fast Neutron Dose Distribution in a Heterogeneous Phantom" (Georgia Institute of Technology) (in preparation)

P. S. Stansbury

In Phantom Spectrometry of Medical Diagnostic X-Rays (Georgia Institute of Technology) (May 1977)

Papers

J. C. Ashley and T. L. Ferrell
"Excitation of Surface Plasmons on Spherical Voids in a Metal by Fast Electrons," American Physical Society, Quebec, Canada, June 14–17, 1976

J. C. Ashley and R. H. Ritchie
"Influence of Plasmon Damping on the Mean Free Path of Electrons for Plasmon Excitation," American Physical Society, Southeastern Section, Virginia Beach, Va., Nov. 11–13, 1976

J. C. Ashley, C. J. Tung, and R. H. Ritchie
"Calculations of Mean Free Paths and Stopping Powers of Low Energy Electrons (≤10 keV) in Solids Using a Statistical Model," IEEE Annual Conference on Nuclear and Space Radiation Effects, San Diego, Calif., July 27–30, 1976

J. K. Baird
"Kinetics of Electron Capture by SF_6 in Solution," International Conference on Electrons in Fluids, Banff, Alberta, Canada, Sept. 5–11, 1976

G. Basbas, W. Brandt, and R. H. Ritchie
"Z_1-Dependence of Swift Heavy Charged Particles Stopping in Matter," American Physical Society, Southeastern Section, Virginia Beach, Va., Nov. 11–13, 1976

P. R. Bell and R. S. Dillon
"Comparison of Some Non-Linear Smoothing Methods," Fifth International Conference on Information Processing in Medical Imaging, Nashville, Tenn., June 27–July 1, 1977

"The Use of Computers in Nuclear Medicine," Nuclear Science Symposium, New Orleans, La., Oct. 19–22, 1976

"Five and Eight Image Tomography," Society of Nuclear Medicine Computer Council Meeting. "The Symposium on Computer Assisted Data Processing in Nuclear Medicine," Atlanta, Ga., Jan. 16–17, 1977

P. A. Berardo, M. A. Paciotti, H. A. Amols, M. E. Schiliaci, J. Bradbury, C. A. Kelsey, A. R. Smith, R. Lane, I. Rosen, K. Hogstrom, H. A. Wright, R. Hamm, and J. E. Turner
"The Effect of Inhomogeneities on Static Pion Beam Dose Distributions," RSNA/AAPM Meeting, Chicago, Ill., Nov. 22, 1976

S. R. Bernard
"An Urn Model Study of Variability Within a Compartment," Annual Meeting of the Society of Mathematical Biology, University of Pennsylvania, Pittsburgh, Pa., Aug. 19, 1976

S. R. Bernard, L. C. Henley, and W. W. Parkinson
"Dose Commitment Estimates for Employees Accidentally Inhaling ^{244}Cm," 22nd Bioassay, Environmental and Analytical Conference, Philadelphia, Pa., Oct. 6–7, 1976

R. D. Birkhoff
"Collective Electronic Oscillations in H_2O and Other Liquids," Gordon Conference on Water and Aqueous Solutions, Plymouth, N.H., Aug. 2–6, 1976

R. D. Birkoff, R. N. Hamm, M. W. Williams, E. T. Arakawa, R. J. Colchin, and R. V. Neidigh
"A Laser Reflection Technique for Studying Contamination Buildup on a Fusion Reactor Liner," International Conference on Surface Effects in Controlled Fusion Devices, San Francisco, Calif., Feb. 16–20, 1976

T. A. Callcott and E. T. Arakawa
"Soft X-ray Emission From Li and Na," American Physical Society Meeting, San Diego, Calif., March 1977

C. H. Chen
"Energy Pathways of Pure Gases and Gas Mixtures by Proton Excitation," IEEE International Conference on Plasma Science, Troy, N.Y., May 23–25, 1977

C. H. Chen, J. P. Judish, M. G. Payne, and G. S. Hurst

"Energy Pathways Studies of Gaseous Laser Candidates," 29th Annual Gaseous Electronics Conference, Cleveland, Ohio, Oct. 19–22, 1976

"Kinetics of Pure Gases and Gas Mixtures by Proton Excitation," LASL's Information Exchange on Lasers for Isotope Separation, Albuquerque, N.M., May 17–19, 1977

C. H. Chen and Y. T. Lee

"Scattering of Metastable Rare Gas Atoms with Small Molecules," Fifth International Conference on Atomic Physics, Berkeley, Calif., July 26–30, 1976

C. H. Chen and M. G. Payne

"Kinetic Studies of Potential Laser Systems," Fifth International Conference on Atomic Physics, Berkeley, Calif., July 26–30, 1976

C. H. Chen, M. G. Payne, G. S. Hurst, and J. P. Judish

"Kinetics Following Proton Excitation of Ar-N_2 Mixtures and N_2-SF_6 Mixtures," Fifth International Conference on Atomic Physics, Berkeley, Calif., July 26–30, 1976

C. W. Choi and M. G. Payne

"Three-Photon Ionization of Atoms by Strong Pulsed Laser Fields," 29th Annual Gaseous Electronics Conference, Cleveland, Ohio, Oct. 19–22, 1976

L. G. Christophorou

"Electron Attachment to Molecules in Dense Gases," Gordon Research Conferences, Boston, Mass., Aug. 23–27, 1976

"Electron Attachment to Molecules in Low- and High-Pressure Gases and in Liquids," International Conference on Electrons in Fluids, Banff, Alberta, Canada, Sept. 5–11, 1976

"Metastable Negative Ions, Their Lifetimes and Implications for Physical and Biological Science," Radiation Research Society, San Juan, Puerto Rico, May 8–12, 1977

L. G. Christophorou and D. L. McCorkle

"Experimental Evidence for the Existence of a Ramsauer-Townsend Minimum in Liquid CH_4 and Ar (Kr and Xe) and in Gaseous C_2H_4 and C_3H_8," International Conference on Electrons in Fluids, Banff, Alberta, Canada, Sept. 5–11, 1976

R. N. Compton

"On the Formation of Positive and Negative Ions in Gaseous UF_6," U.S.-Canadian American Physical Society Meeting, Quebec, Canada, June 14–17, 1976

"Reactions of Fast Alkali Atoms and Highly Excited Rydberg States with Molecules," Gordon Research Conferences, Boston, Mass., Aug. 23–27, 1976

James J. Cowan

"Holography with Optical Guided Waves," 1976 Annual Meeting, Optical Society of America, Tucson, Ariz., Oct. 18–22, 1976

"Blazed and High Line Density Holographic Gratings Produced by Use of Optical Guided Waves," 1976 Annual Meeting, Optical Society of America, Tucson, Ariz., Oct. 18–22, 1976

H. W. Dickson and W. D. Cottrell

"Radiological Assessment of Decommissioned Nuclear Facilities," Tenth Midyear Topical Symposium of the Health Physics Society, Saratoga Springs, N.Y., Oct. 10–13, 1976

J. S. Eldridge, T. W. Oakes, and M. E. Pruitt

"Radioactive Pollutant Determination Using Gamma-Ray Spectroscopy," American Industrial Hygiene Conference, New Orleans, La., May 22–27, 1977

"Environmental Surveillance for Radionuclide Contamination Utilizing High-Resolution Gamma-Ray Spectroscopy," 11th Annual Conference on Trace Substances in Environmental Health, Columbia, Mo., June 7–9, 1977

T. L. Ferrell and R. H. Ritchie

"Energy Losses by Slow Ions and Atoms to Electronic Excitations in Solids," American Physical Society, Southeastern Section, Virginia Beach, Va., Nov. 11–13, 1976

W. R. Garrett

"Rotational Dipole States of Polar Molecules," 29th Annual Gaseous Electronics Conference, Cleveland, Ohio, Oct. 18–22, 1976

"Effects of Long Range Interactions on Molecular Scattering of Charged Particles," University of Alabama Physics Department, Nov. 22, 1976

"Mathematical Models of Radiobiological Effects from Low LET Radiation," Berkeley, Calif, Dec. 8, 1976

M. W. Grant and L. G. Christophorou

"On the Applications of Molecular Orbital Theory to Shape Resonances of Organic Molecules," Southeastern Section of the American Chemical Society, Gatlinburg, Tenn., October 1976

R. N. Hamm, J. Neufeld, R. H. Ritchie, J. E. Turner, and H. A. Wright

"Calculation of Statistical Distribution of Energy Deposition Along Electron Tracks in Water," Radiation Research Society, San Juan, Puerto Rico, May 7–12, 1977

A. R. Hawthorne

"Preliminary Results from Second-Derivative Absorption Spectroscopy Applied to Monitoring of PNA," Workshop on Exposure to Polynuclear Aromatic Hydrocarbons in Coal Conversion Processes, Oak Ridge, Tenn., Mar. 9–11, 1977

A. Hawthorne, T. Vo-Dinh, J. Thorngate, and R. Gammage

"Spectroscopic Methods for Monitoring Occupational Exposure to Synfuel Pollutants," American Industrial Hygiene Conference, New Orleans, La., May 22–27, 1977

G. S. Hurst

"Use of Lasers for Photoionization," Gordon Research Conference on Electron Spectroscopy, Wolfeboro, N.H., July 19–23, 1976

"One Atom Detection with Resonance Ionization Spectroscopy," Southeastern Section of American Physical Society, Virginia Beach, Va., Nov. 11–13, 1976

T. D. Jones

"CHORD Operators for Insult Assessment and the Application to Stem-Cell Survival," Annual Meeting of the Radiation Research Society, San Juan, Puerto Rico, May 7–12, 1976

T. D. Jones, W. A. Goldsmith, and F. F. Haywood

"CHORD Distribution Functions from a Monte Carlo Simulation of the Tracheobronchial Tree," 21st Annual Meeting of the Health Physics Society, San Francisco, Calif., June 27–July 2, 1976

T. D. Jones, G. D. Kerr, and W. A. Goldsmith

"Insult Assessment to the Basal Cells of the Bronchial Epithelium from CHORD Distributions," 21st Annual Meeting of the Radiation Research Society, San Francisco, Calif., June 27–July 2, 1976

R. H. Kennedy, L. Joe Deal, W. A. Goldsmith, and F. F. Haywood

"Management and Control of Radioactive Wastes from Uranium-Milling Operations," to appear in *Proceedings of the IAEA International Conference on Nuclear Power and Its Fuel Cycle, Salzburg, Austria, May 2–13, 1977*

C. E. Klots

"Role of Angular Momentum in Unimolecular Kinetics," 25th Annual Conference on Mass Spectrometry and Allied Topics, Washington, D.C., May 30–June 4, 1977

"Studies of Rydberg State Reactions," National Bureau of Standards, Washington, D.C., Apr. 14, 1977

S. D. Kramer

"Third Order Nonlinear Optical Spectroscopy in CuCl," Optical Society of America, Tucson, Ariz., Oct. 18–23, 1976

W. J. McDowell, F. G. Seeley, and M. T. Ryan
"Penetration of HEPA Filters by Alpha Recoil Aerosols," 14th ERDA Air Cleaning Conference, August 1976

T. G. Miller
"Nuclear Laser Optimization Experiments," IEEE International Conference on Plasma Science, Troy, N.Y., May 23–25, 1977

M. H. Nayfeh, G. S. Hurst, and J. P. Young
"Collisional Broadening of Cs Resonance Lines Using Two-Photon Ionization," International Conference on Multiphoton Processes, Rochester, N.Y., June 6–9, 1977

M. H. Nayfeh and A. H. Nayfeh
"Adiabatic Following in Two-Photon Transition," Fourth Rochester Conference on Coherence and Quantum Optics, Rochester, N.Y., June 8–9, 1977

T. W. Oakes, C. E. Easterly, and K. E. Shank
"Radionuclide Accumulations in Clinch River Fish," Tenth Midyear Topical Symposium of the Health Physics Society, Saratoga Springs, N.Y., Oct. 11–13, 1976

T. W. Oakes and A. K. Furr
"The Distribution and Accumulation of Traceable Elements in Roadside Plants and Soils," 1977 American Association for the Advancement of Science Meeting, Denver, Colo., Feb. 20–25, 1977

T. W. Oakes, A. K. Furr, D. J. Adair, and T. F. Parkinson
"Neutron Activation Analysis of Automobile Exhaust Pollutants," 1976 International Conference on Modern Trends in Activation Analysis, Munich, Germany, Sept. 13–17, 1976

T. W. Oakes, E. D. Gupton, and K. E. Shank
"A Stream Monitor Control System for Widely Varying Flows," American Industrial Hygiene Conference, New Orleans, La., May 22–27, 1977

T. W. Oakes, K. E. Shank, and J. L. Danek
"Quality Assurance Applied to an Environmental Radiological Surveillance Program," 105th APHA Annual Meeting, Washington, D.C., Oct. 30–Nov. 3, 1977

T. W. Oakes, K. E. Shank, and C. E. Easterly
"Natural and Man-Man Radionuclide Concentrations in Tennessee Soils," Tenth Midyear Topical Symposium of the Health Physics Society, Saratoga Springs, N.Y., Oct. 11–13, 1976

"Iodine-131 Air Concentrations: A Comparison of Calculated Versus Measured Values," 1976 American Nuclear Society International Meeting, Washington, D.C., Nov. 14–19, 1976

"Concentrations of Radionuclides and Selected Trace Metals in Fruits and Vegetables," 11th Annual Conference on Trace Substances in Environmental Health, Columbia, Mo., June 7–9, 1977

R. Y. Pai, L. G. Christophorou, D. R. James, and M. O. Pace
"Dependence of Breakdown Strengths of Gaseous Dielectrics on Electron Attachment Cross Sections and Inelastic Scattering," 29th Annual Gaseous Electronics Conference, Cleveland, Ohio, Oct. 19–22, 1976

C. H. Patrick
"The Need for Epidemiological Research in Energy," Epidemiology Department Seminar, The Johns Hopkins University School of Hygiene and Public Health, Baltimore, Md., Apr. 11, 1977

"Trace Substances and Electric Power Generation: The Need for Epidemiological Studies to Determine Health Risks," to appear in *Proceedings of the Eleventh Annual Conference on Trace Substances in Environmental Health, Columbia, Mo., June 7, 1977*

"Human Health Effects Studies: Shortcomings and Needs," SIAM Annual Meeting, Philadelphia, Pa., June 15, 1977

M. G. Payne and C. W. Choi
"Collisional Induced Resonances in the Two-Photon Ionization of Excited State Atoms by Strong Laser Fields," International Conference on Multiphoton Processes, Rochester, N.Y., June 6–9, 1977

"Three-Photon Ionization of Atoms Near a Two-Photon Resonance," International Conference on Multiphoton Processes, Rochester, N.Y., June 6–9, 1977

M. G. Payne, C. Y. Choi, and M. H. Nayfeh
"Laser-Induced Collisional Excitation Transfer," International Conference on Multiphoton Processes, Rochester, N.Y., June 6–9, 1977

A. B. Ritchie
"Calculation of Resonance Cross Sections for Multiphoton Ionization Under Single-Mode Conditions," Rochester, N.Y., June 6–9, 1977

A. B. Ritchie, W. R. Garrett, and V. E. Anderson
"Calculation of Nonresonant Multiphoton Ionization Cross Section for Complex Atoms," Rochester, N.Y., June 6–9, 1977

R. H. Ritchie
"Surface Plasmons in Solids," invited paper at the American Physical Society, Southeastern Section, Virginia Beach, Va., Nov. 11–13, 1976

R. H. Ritchie and G. Basbas
"Scaling Law for the Z_1-Dependence of Charged Particles Stopping in Matter," American Physical Society, Washington, D.C., Apr. 25–28, 1977

R. H. Ritchie and Werner Brandt
"Electron Capture and Loss by a Swift Ion in an Electron Gas," American Physical Society, San Diego, Calif., Mar. 21–24, 1977

R. H. Ritchie, R. N. Hamm, H. A. Wright, J. E. Turner, W. R. Garrett, and F. W. Hecker, Jr.
"Transport Parameters of Swift Electrons in Liquid Water," Radiation Research Society, San Juan, Puerto Rico, May 7–12, 1977

V. C. Rogers, W. A. Goldsmith, F. F. Haywood, and G. K. Gantner
"Alternative Management Techniques for the Uranium Mill Tailings Site at Salt Lake City, Utah," Tenth Midyear Topical Symposium of the Health Physics Society, Northeastern New York Chapter, Saratoga Springs, N.Y., Oct. 11–13, 1976

K. E. Shank, R. J. Vetter, and P. L. Ziemer
"Zinc-Cadmium Interrelationships and the Kinetics of Cadmium Transport in a Biological System," Tenth Annual Conference on Trace Substances in Environmental Health, Columbia, Mo., June 8–10, 1976

W. S. Snyder, M. R. Ford, and G. G. Warner
"Distribution of Dose Within the Body from a Photon Emitter Present in an Organ," IRPA Fourth International Congress, Paris, France, April 1977

W. S. Snyder and J. E. Turner
"Review and Assessment of Problems in the Dosimetry of Rn and Rn Daughters," Radiation Research Society Annual Meeting, San Juan, Puerto Rico, May 8–12, 1977

J. A. D. Stockdale, I. Efremov, K. Rubin, and B. Bederson
"Measurement of the Electric Dipole Polarizibility of Indium," Fifth International Conference on Atomic Physics, Berkeley, Calif., July 26–30, 1976

J. H. Thorngate
"Measurements of the Additivity of Stopping Cross Sections for 50 to 150 keV Protons in Nine Hydrocarbon Gases," Radiation Research Society Meeting, San Francisco, Calif., June 27–July 2, 1976

"Measurements of Distribution of Energy Loss and Additivity of Energy Losses for 50 to 150 keV Protons in Hydrogen and Nine Hydrocarbon Gases," Scientific and Industrial Applications of Small Accelerators, Fourth Conference, Denton, Tex., Oct. 27–29, 1976

J. H. Thorngate and D. J. Christian
"Recent Developments in the Detector and the Electronic System Used for the High-Resolution Liquid-Scintillation Spectroscopy of Alpha Particles," *Health Physics Society Annual Meeting, San Francisco, Calif.*, June 27–July 2, 1976

R. N. Thurmer
"Current American Press Reactions to U.S. Civil Defense," 10th Annual Conference for the Journal of Civil Defense, Starke, Fla., Nov. 13, 1976

C. J. Tung, R. H. Ritchie, V. E. Anderson, and J. C. Ashley
"Inelastic Interactions of Energetic Electrons in Semiconductors and Insulators," American Physical Society, Chicago, Ill., Feb. 7–10, 1977

C. J. Tung, R. H. Ritchie, and J. C. Ashley
"Electron Slowing-Down Spectra in Al and Al_2O_3," American Physical Society, Southeastern Section, Virginia Beach, Va., Nov. 11–13, 1976

T. Vo-Dinh
"Recent Progress in Room Temperature Phosphorimetry for Analysis of PNA," 2nd ORNL Workshop on Polynuclear Aromatic Hydrocarbons, Mar. 9–11, 1977

H.-t. Wang and L. G. Christophorou
"Systematics of Negative Ion States of Atoms and Small Molecules," American Physical Society, San Diego, Calif., Mar. 21–24, 1977

S. B. Watson
"Applying Matrix Techniques to Health Physics Problems," Oak Ridge–University of Tennessee Seminar on Matrix Methods in Numerical Analysis, Feb. 4, 1976

M. W. Williams, T. Inagaki, R. N. Hamm, and E. T. Arakawa
"Optical Properties of Polystyrene and Optical Sum Rules," Southeastern Section of the American Physical Society, Virginia Beach, Va., Nov. 11–13, 1976

A. D. Williamson and R. N. Compton
"Resonant Two-Photon Ionization of Atomic Cesium," Rochester, N.Y., June 6–9, 1977

H. A. Wright, R. N. Hamm, J. E. Turner, R. H. Ritchie, and R. Katz
"Slowing Down Spectra from Electrons in Liquid Water," Radiation Research Society, San Juan, Puerto Rico, May 7–12, 1977

J. P. Young, G. S. Hurst, and M. H. Nayfeh
"Specific Detection of Single Atoms by Resonance Ionization Spectroscopy," 173rd American Chemical Society National Meeting, New Orleans, La., Mar. 20–25, 1977

"Laser Spectroscopy and the Specific Detection of Single Atoms," Annual Conference, Cleveland area of American Chemical Society, Cleveland, Ohio, May 25, 1977

Publications

J. D. Allen, Jr., J. D. Durham, George K. Schweitzer, and W. E. Deeds
"A New Electron Spectrometer Design: II," *J. Electron Spectrosc. Relat. Phenom.* 8, 395 (1976)

M. Anderson, S. Nir, J. M. Heller, Jr., and L. R. Painter
"Optical Constants and Dispersion Equations of Chloroform, Lecithin, Cholesterol and Fucose. Measurements in Vacuum Ultraviolet to Visible Wavelength Region," submitted to *Journal of Chemical Physics*

B. R. Appleton, R. H. Ritchie, J. A. Biggerstaff, T. S. Noggle, S. Datz, C. D. Moak, and H. Verbeek
"Investigations of Radiative Electron Capture by Ion Channeling Techniques," in *Proceedings of the International Conference on Surface Effects in Controlled Fusion Devices, San Francisco, Calif., February 1976;* also, to be published in *Journal of Nuclear Materials*

E. T. Arakawa, M. S. Chung, and M. W. Williams
"Self-Supporting Thin Films – Parting Agent," *Rev. Sci. Instrum.* 48, 707 (1977)

E. T. Arakawa, M. W. Williams, and T. Inagaki
"Optical Properties of Arc-Evaporated Carbon Films Between 0.6 and 3.8 eV," *J. Appl. Phys.* **48**, 3176 (1977)

D. Arora, J. E. Turner, and P. G. Khubchandani
"Alkali-Metal-Halogen Charge-Exchange Collisions," *Phys. Rev. A* **14**, 2089 (1976)

J. C. Ashley and T. L. Ferrell
"Excitation by Fast Electrons of Surface Plasmons on Spherical Voids in a Metal," *Phys. Rev. B* **14**, 3277 (1976)

J. C. Ashley and R. H. Ritchie
"The Influence of Damping on the Mean Free Path of Low Energy Electrons in an Electron Gas," to be published in *Physica Status Solidi B*

J. C. Ashley, C. J. Tung, R. H. Ritchie, and V. E. Anderson
Inverse Mean Free Path, Stopping Power, CSDA Range, and Straggling in Ge and GaAs for Electrons of Energy ≤10 keV, RADC-TR-76-350, November 1976

"Calculations of Mean Free Paths and Stopping Powers of Low Energy Electrons (≤10 keV) in Solids Using a Statistical Model," *IEEE Trans. Nucl. Sci.* **NS-23**, 1833 (1976)

Inverse Mean Free Path, Stopping Power, CSDA Range, and Straggling in Ni, Cu, Ag, and Au for Electrons of Energy ≤10 keV Calculated from a Statistical Model, RADC-TR-76-220, June 1976

J. C. Ashley and M. W. Williams
Studies of Electron Interactions with Communications Materials, RADC-TR-77-74, February 1977

J. K. Baird
"Kinetics of Electron Capture by SF_6 in Solution," *Canadian Journal of Chemistry* (in press)

James K. Baird, Verner E. Anderson, and Stephen A. Rice
"Comment on Probability of Escaping Neutralization When the Mobility is Field Dependent," submitted to *Journal of Chemical Physics*

P. R. Barnes
"EMP and Nuclear Plant Safety," *Nucl. Saf.* **18**(2) (1977)

C. J. Barton, F. F. Haywood, W. D. Cottrell, M. T. Ryan, R. W. Leggett, P. T. Perdue, H. W. Dickson, J. L. Danek, J. Burden, D. L. Anderson, R. W. Doane, B. S. Ellis, R. E. Hamilton, and W. S. Shinpaugh
Radiological Survey of the Mallinckrodt Chemical Works, St. Louis, Missouri (to be published as an ERDA report)

G. Basbas and R. H. Ritchie
"Comparison of Vicinage Effects in the Penetration of Ion Clusters in Gases and in Condensed Matter," to be submitted to *Physical Review*

P. R. Bell and R. S. Dillon
"Five and Eight Image Tomography," *Proceedings of the Symposium on Computer Assisted Data Processing in Nuclear Medicine, Atlanta, Ga., Jan. 16–17, 1977* (in press)

"The Use of Computers in Nuclear Medicine," *Proceedings of Nuclear Science Symposium, New Orleans, La., Oct. 19–22, 1976* (in press)

ORIS – The Oak Ridge Imaging System, Operations Manual, ORNL/TM-5875 (to be published)

S. R. Bernard
"An Urn Model Study of Variability Within a Compartment," *Bull. Math. Biol.* **39**, 463 (1977)

"Dosimetric Data and Metabolic Model for Lead," *Health Phys.* **32**, 44 (1977)

"Metabolic Model and Dosimetric Data for Copper," *Bulletin of Mathematical Biology* (in press)

R. D. Birkhoff, J. C. Ashley, H. H. Hubbell, Jr., and L. C. Emerson
"Light Scattering from Micron-Size Fibers," *J. Opt. Soc. Am.* **67**, 564 (1977)

R. D. Birkhoff, R. N. Hamm, M. W. Williams, E. T. Arakawa, R. J. Colchin, and R. V. Neidigh
"A Laser Reflection Technique for Studying Contamination Buildup on a Fusion Reactor Liner," *J. Nucl. Mater.* **63**, 501 (1976)

R. D. Birkhoff, H. H. Hubbell, Jr., D. B. Smathers, and H. L. Barnawell
"Electron Gun Filament Supply," to be published in *Journal of Electron Spectroscopy and Related Phenomena*

R. D. Birkhoff, L. R. Painter, and J. M. Heller, Jr.
"Measurement of Reflectance by Gas Ionization," to be published in *Applied Optics*

J. B. Birks, C. E. Easterly, and L. G. Christophorou
"Stokes and Anti-Stokes Fluorescence of 1:12-Benzoperylene in Solution," *J. Chem. Phys.* **66**, 4231 (1977)

Werner Brandt and R. H. Ritchie
"Penetration of Swift Ion Clusters through Solids," *Nucl. Instrum. Methods* **132**, 43 (1976)

W. S. Brey, B. W. Martin, B. H. Davis, and R. B. Gammage
"Magnetic Resources Studies of Thorium Oxide Catalysts," pp. 216–32 in *Magnetic Resonance in Colloid and Interface Science*, ACS Symposium Series 34, American Chemical Society, New York, 1976

T. A. Callcott and E. T. Arakawa
"Temperature Dependence of the K x-ray Emission Edge of Li," *Phys. Rev. Lett.* **38**, 442 (1977)

T. A. Callcott, E. T. Arakawa, and D. L. Ederer
"The Emission and Absorption X-ray Edges of Li," submitted to *Physical Review*

C. H. Chen, J. P. Judish, and M. G. Payne
"Charge Transfer and Penning Ionization of N_2, CO, CO_2, and H_2S," *J. Chem. Phys.* **67**, 3376 (1977)

"Charge Transfer Studies of Ne-N_2 by Proton Excitation," submitted to *J. Chem. Phys.* **67**, 2713 (1977)

"Energy Transfer Processes in Proton-Excited Ar-Xe and Ar-F_2 Mixtures," submitted to *Journal of Chemical Physics*

"Quenching Rates for Electronic Energy Transfer from Excited Argon Atoms and Argon Dimers," submitted to *Journal of Chemical Physics*

C. H. Chen and M. G. Payne
"Kinetic Studies of Potential Laser Systems," *Opt. Commun.* **18**, 118 (1976)

"A Potential Hydroxyl Ultraviolet Laser," *Opt. Commun.* **18**, 476 (1976)

"A Potential High Efficiency Cl_2 Ultraviolet Laser," *Appl. Phys. Lett.* **28**, 219 (1976)

C. H. Chen, M. G. Payne, G. S. Hurst, and J. P. Judish
"Kinetic Studies of N_2 and N_2-SF_6 Following Proton Excitation," *J. Chem. Phys.* **65**, 3863 (1976)

"Kinetic Studies of Ar-N_2-SF_6 Mixtures Following Proton Excitation," *J. Chem. Phys.* **65**, 4028 (1976)

W. L. Chen, J. W. Poston, and G. G. Warner
An Evaluation of the Distribution of Absorbed Dose in Child Phantoms Exposed to Diagnostic Medical X Rays, ORNL/TM-5933 (to be published)

C. V. Chester
"Estimates of Threat to the Public from Terrorist Acts Against Nuclear Facilities," *Nucl. Saf.* **17**, 659 (1976)

C. V. Chester and R. O. Chester
"Civil Defense Implications of the U.S. Nuclear Power Industry During a Large Nuclear War in the Year 2000," *Nucl. Technol.* **31**, 326 (1976)

C. W. Choi and M. G. Payne
Two-State and Two-State-Plus Continuum Problems Associated with the Interaction of Intense Laser Pulses with Atoms, ORNL/TM-5754, February 1977

"Multiphoton Ionization with Strong Pulsed Laser Fields. I. Two-Photon Ionization," submitted to *Physical Review A*

L. G. Christophorou
"Electron Attachment to Molecules in Low- and High-Pressure Gases and in Liquids," *Canadian Journal of Chemistry* (in press)

"The Lifetimes of Metastable Negative Ions," *Advances in Electronics and Electron Physics* (in press)

L. G. Christophorou, K. S. Gant, and V. E. Anderson
"Long-Lived Parent Negative Ions Formed Via Nuclear-Excited Feshbach Resonances. Part 5 – Effective Number of Degrees of Freedom Participating in the Sharing of the Ion's Excess Energy," *J. Chem. Soc., Faraday Trans. II* **73**, 804 (1977)

L. G. Christophorou, M. W. Grant, and D. L. McCorkle
"Interactions of Slow Electrons with Benzene and Benzene Derivatives," *Adv. Chem. Phys.* **36**, 413 (1977)

L. G. Christophorou and D. L. McCorkle
"Experimental Evidence for the Existence of a Ramsauer-Townsend Minimum in Liquid CH_4 and Liquid Ar (Kr and Xe)," *Chem. Phys. Lett.* **42**, 533 (1976)

"Experimental Evidence for the Existence of a Ramsauer-Townsend Minimum in Liquid CH_4 and Ar (Kr and Xe) and Gaseous C_2H_6 and C_3H_8," *Canadian Journal of Chemistry* (in press)

R. N. Compton
"On the Formation of Positive and Negative Ions in Gaseous UF_6," *J. Chem. Phys.* **66**, 4478 (1977)

R. N. Compton and C. D. Cooper
"Negative Ion Properties of Tetracyanoquinodimethan: Electron Affinity and Compound States," *J. Chem. Phys.* **66**, 4325 (1977)

R. N. Compton, P. W. Reinhardt, and W. R. Garrett
"Uranium Hexafluoride Negative Ions from Surface Reactions Involving Uranium and Fluorine," to be published in *Journal of Chemical Physics*

J. J. Cowan and B. Aničin
"Longitudinal and Transverse Displacements of a Bounded Microwave Beam at Total Internal Reflection," to be published in *Journal of the Optical Society of America*

J. J. Cowan and E. T. Arakawa
"Artificial Polarization Anomalies from Holographic Gratings," *Opt. Commun.* **21**, 428 (1977)

O. H. Crawford and W. R. Garrett
"Electron Affinities of Polar Molecules," to be published in *Journal of Chemical Physics*

S. F. Deus, V. Provenzano, and W. S. Snyder
"Specific Absorbed Fractions for Photons Emitted in the Walls of the GI Tract," submitted to *Health Physics*

H. W. Dickson, W. F. Fox, and F. F. Haywood
"Intercomparison of Personnel Dosimeters," pp. 225–32 in *Measurements for the Safe Use of Radiation*, NBS Special Publication 456, Washington, D.C., November 1976

H. W. Dickson, L. W. Gilley, and D. R. Ward
Thirteenth Dosimetry Intercomparison Study, August 16–20, 1976, ORNL/TM (in preparation)

H. W. Dickson, G. D. Kerr, P. T. Perdue, and S. A. Abdullah
"Environmental Gamma-Ray Measurements Using *In-Situ* and Core Sampling Techniques," *Health Phys.* **30**, 221 (1976)

H. W. Dickson, W. F. Fox, and F. F. Haywood
"Intercomparison of Personnel Dosimeters," pp. 225–32 in *Measurements for the Safe Use of Radiation*, NBS Special Publication 456, Washington, D.C., November 1976

H. W. Dickson, L. W. Gilley, and D. R. Ward
Thirteenth Dosimetry Intercomparison Study, August 16–20, 1976, ORNL/TM (in preparation)

H. W. Dickson, G. D. Kerr, P. T. Perdue, and S. A. Abdullah
"Environmental Gamma-Ray Measurements Using *In-Situ* and Core Sampling Techniques," *Health Phys.* **30**, 221 (1976)

H. W. Dickson, R. W. Leggett, F. F. Haywood, W. A. Goldsmith, W. D. Cottrell, and W. F. Fox
Radiological Survey of the Middlesex Sampling Plant, December 1976 (to be published as an ERDA report)

H. W. Dickson, T. W. Oakes, and K. E. Shank
"Occupational Radiation Exposure Control at Operating Nuclear Power Stations," *Nucl. Saf.* **18**(4), 492 (1977)

H. W. Dickson, M. T. Ryan, R. W. Doane, W. H. Shinpaugh, and W. M. Johnson
Radiological Survey of the Former Kellex Corporation, July 1977 (to be published as an ERDA report)

C. E. Easterly and D. G. Jacobs
"Tritium Release Strategy for a Global System," p. III-58 in *Proceedings of the International Conference on Radiation Effects and Tritium Technology for Fusion Reactors, Gatlinburg, Tenn. Oct. 1–3, 1975*, CONF-750989, March 1976

C. E. Easterly and K. E. Shank
Metabolic and Environmental Aspects of CTR Activation Products: Niobium, ORNL/TM-5496 (in press)

C. E. Easterly, K. E. Shank, and R. L. Shoup
Health Physics Aspects of Fusion Power, ORNL/TM-5461, October 1976

"Radiological Aspects of Fusion Power," *Nucl. Saf.* **18**(2), 203 (1977)

P. M. Echenique and R. H. Ritchie
"Energy Loss by a Slow Ion Moving in the Vicinity of a Solid Surface," to be submitted for publication

J. S. Eldridge and T. W. Oakes
"Environmental Surveillance for Radionuclide Contamination Utilizing High-Resolution Gamma-Ray Spectroscopy," to appear in *Proceedings of the Eleventh Annual Conference on Trace Substances in Environmental Health, Columbia, Mo., 1977*

J. S. Eldridge, T. W. Oakes, and M. E. Pruitt
"Radioactive Pollutant Determination Using Gamma-Ray Spectroscopy," *Journal of the American Industrial Hygiene Association* (in press)

L. C. Emerson, J. T. Cox, G. L. Ostrom, L. R. Painter, and G. H. Cunningham
"Automatic Concentric Shaft Reflectometer for Use in the Vacuum UV," *Rev. Sci. Instrum.* **47**, 1065 (1976)

L. C. Emerson, S.-I. Juan, M. W. Williams, and E. T. Arakawa
"Optical and Dielectric Properties of Adenine Below 80 eV," submitted to *Radiation Research*

M. F. Fair and J. E. Turner
"Faculty Institute in Applied Health Physics – A Program to Help Meet Future Requirements for Health Physics Technologists," submitted to *Health Physics*

T. L. Ferrell, J. C. Ashley, and R. W. Hendricks
"X-ray Excitation of Surface Plasmons on Spherical Voids in Metals," *Philos. Mag.* **34**, 929 (1976)

T. L. Ferrell and R. H. Ritchie
"Energy Losses by Slow Ions and Atoms to Electronic Excitations in Solids," *Phys. Rev. B* **16**, 115 (1977)

M. R. Ford, W. S. Snyder, L. T. Dillman, and S. B. Watson
"Maximum Permissible Concentration (MPC) Values for Spontaneously Fissioning Radionuclides," *Health Phys.* **33**, 35 (1977)

R. B. Gammage
Abstracts of the 1st ORNL Workshop on Polycyclic Aromatic Hydrocarbons: Characterization and Measurement with a View Towards Personnel Protection, ORNL/TM-5598, November 1976

"The Present Situation and Outlook for Exoelectron Dosimeters," pp. 117–21 in *Proceedings of the 5th International Symposium on Exoelectron Emission and Dosimeters*, A. Bohun and A. Scharmann, eds., Zvikov, CSSR, 1976

R. B. Gammage and J. S. Cheka
"Further Characteristics Important in the Operation of Ceramic BeO TLD," *Health Phys.* **32**, 189 (1977)

"Operational Difficulties with Ceramic BeO TLD," pp. 68–74 in *Proceedings of the 5th International Conference on Luminescence Dosimetry, São Paulo, Brazil, February 1977*

"The Importance of Hydration in Exoelectron Emission from BeO," pp. 73–81 in *Proceedings of the 5th International Symposium on Exoelectron Emission and Dosimetry*, A. Bohun and A. Scharmann, eds., Zvikov, CSSR, 1976

"Bank of Calibrated BeO Ceramic Dosimeters for TSEE and TL," *Health Phys.* **30**, 311 (1976)

R. B. Gammage, J. S. Cheka, and T. E. Gesell
"A Passive Environmental Radon Monitor Based on the Exoelectron Dosimeter," submitted to *Nuclear Instruments and Methods*

R. B. Gammage and D. R. Glasson
"Recovery of Crystallinity in Ground Calcite," pp. 437–52 in *Proceedings of the International Conference on Colloids and Surfaces, San Juan, Puerto Rico, June 21–25, 1976*

"Recovery of Crystallinity in Ground Calcite," pp. 437–52 in *Colloid and Interface Science, Vol. V. Biocolloids, Polymers, Monolayers, Membranes, and General Papers*, Academic Press, New York, 1976

R. B. Gammage and F. F. Haywood
"Experiences in Environmental Monitoring with BeO Ceramic Dosimeters," pp. 324–29 in *Proceedings of the Ninth Midyear Topical Symposium of the Health Physics Society, Denver, Colo., Feb. 9–12, 1976*

R. B. Gammage and H. F. Holmes
"Effect of Surface Water on the Adsorption of Inert Gases," pp. 73–81 in *Colloid and Interface Science, Vol. III. Adsorption Catalysis, Solid Surfaces, Wetting, Surface Tension, and Water*, Academic Press, New York, 1976

"Effect of Annealing Temperature on the Reactivity of Lunar Foils Toward Absorbed Water," *Earth Planet. Sci. Lett.* **34**, 445 (1977)

R. B. Gammage, G. D. Kerr, and L. Huskey
"Exploratory Study of the Use of TSEE Dosimeters in Radon Monitoring," *Health Phys.* **30**, 145 (1976)

R. B. Gammage and D. J. Simpkin
"Assessment of Dosimetry Requirements and Techniques for Measuring Polycyclic Aromatic Hydrocarbons," *Proceedings of the 20th Conference on Analytical Chemistry in Energy and Environmental Technology, Gatlinburg, Tenn., Oct. 12–14, 1976*

R. B. Gammage, D. J. Simpkin, and A. K. Garrison
"Dependence of Thermoluminescence and Exoelectron Emission on the Ceramic Character of BeO," *Radiat. Eff.* **29**, 171 (1976)

R. B. Gammage and J. H. Thorngate
"Depth of the Exoelectron Layer in Ceramic BeO Thermalox 995," pp. 107–21 in *Proceedings of 5th International Symposium on Exoelectron Emission and Dosimetry*, A. Bohun and A. Scharmann, eds., Zvikov, CSSR, 1976

K. S. Gant and L. G. Christophorou
"Attachment of Slow Electrons to Hexafluorobenzene," *J. Chem. Phys.* **65**, 2977 (1976)

W. R. Garrett and M. G. Payne
"Applications of Models for Cell Survival: The Fixation Time Picture," to be published in *Radiation Research*

L. W. Gilley, H. W. Dickson, and D. J. Christian
1976 Intercomparison of Personnel Dosimeters, ORNL/TM-5672, December 1976

F. M. Glass and R. D. Birkhoff
"A Simple Electrometer-Ratiometer of High Sensitivity and Precision," submitted to *Health Physics*

R. E. Goans, J. H. Cantrell, Jr., and F. Bradford Meyers
"Ultrasonic Pulse-Echo Determination of Thermal Injury in Deep Dermal Burns," *Med. Phys.* **4** (1977)

M. W. Grant and L. G. Christophorou
"On the Application of Molecular Orbital Theory to Shape Resonances in Organic Molecules," submitted to *Chemical Physics*

L. W. Grossman, G. S. Hurst, S. D. Kramer, M. G. Payne, and J. P. Young
"A Sensitive, Absolute, and Time-Resolved Method for the Study of Reactive Atoms," *Chem. Phys. Lett.* **50**, 207 (1977)

L. W. Grossman, G. S. Hurst, M. G. Payne, and S. L. Allman
"Saturated Photodissociation of CsI," *Chem. Phys. Lett.* **50**, 70 (1977)

C. M. Haaland
"Availability and Shipment of Grain for Survival of the Relocated Population of the United States After a Nuclear Attack," *Am. J. Agric. Econ.* **59**(2) (1977)

"Why So Many Reactor Designs? Reactor Anatomy, Part III," *J. Civ. Def.* **9**(5) (1976)

C. M. Haaland and K. S. Gant
First Quarterly Report on the Development of Procedures for Manual Estimation of Casualties Due to Fallout from a Nuclear Attack, ORNL/CF-77/29, January 1977

Project Work Plan for Studying U.S. Requirements for Radiological Defense Against Fallout from a Hypothetical Nuclear War, ORNL/CF-76/372, October 1976

Project Work Plan for Development of Procedures for Manual Estimation of Casualties Due to Fallout from a Nuclear Attack, ORNL/CF-76/435, December 1976

C. M. Haaland and E. P. Wigner
"Defense of Cities by Anti-Ballistic Missiles," *SIAM Rev.* (May 1977)

"Surviving a Nuclear War," *Nat. Rev.* (Sept. 16, 1976)

R. N. Hamm, H. A. Wright, R. H. Ritchie, J. E. Turner, and W. R. Garrett
"Calculation of Spatial Distribution of Primary Products Around an Ion Track in Liquid Water" (manuscript in review)

R. N. Hamm, H. A. Wright, and J. E. Turner
"Effects of Tissue Inhomogeneities on Dose Patterns in Cylinders Irradiated by Negative Pion Beams," *Phys. Med. Biol.* **21**, 982 (1976)

"Influence of Beam Characteristics and Detector Size in Negative-Pion Dose Studies," submitted to *Physics in Medicine and Biology*

A. R. Hawthorne
"Preliminary Results from Second-Derivative Absorption Spectroscopy Applied to Monitoring of PNA," to appear in *Workshop on Exposure to Polynuclear Aromatic Hydrocarbons in Coal Conversion Processes, Oak Ridge, Tenn., Mar. 9–11, 1977*, to be published as an ORNL technical memorandum

A. R. Hawthorne, R. B. Gammage, and D. J. Simpkin
"Assessment of Dosimetry Requirements and Techniques for Measuring Polycyclic Aromatic Hydrocarbons," pp. 684–89 in *Proceedings of Symposium on Analytical Chemistry of Tar Sands and Oil Shale, New Orleans, La., Mar. 20–25, 1977*, American Chemical Society, Division of Petroleum Chemistry

A. R. Hawthorne and R. P. Gardner
"Fundamental Parameters Solution to the X-Ray Fluorescence Analysis of Nickel-Iron-Chromium Alloys Including Tertiary Corrections," *Analyt. Chem.* **48**, 2130 (1976)

"Monte Carlo Applications to the X-Ray Fluorescence Analysis of Aerosol Samples," pp. 209–20 in *X-Ray Fluorescence Analysis of Environmental Samples*, Thomas G. Dzubay, ed., Ann Arbor Science Publishers Inc., Ann Arbor, Mich., 1977

A. R. Hawthorne and J. H. Thorngate
"Improved Analysis from Second-Derivative UV-Absorption Spectrometry," *Applied Optics* (in press)

"Application of Second-Derivative UV-Absorption Spectrometry to PNA Analysis," submitted to *Environmental Science and Technology*

F. F. Haywood, J. E. Burden, D. R. Stone, and H. W. Dickson
Radiological Survey of the Former Bridgeport Brass Company Special Metals Extrusion Plant, March 1977 (to be published as an ERDA report)

F. F. Haywood, W. A. Goldsmith, P. T. Perdue, W. F. Fox, and W. H. Shinpaugh
Assessment of Radiological Impact of the Inactive Uranium Mill Tailing Pile at Salt Lake City, Utah, ORNL/TM-5251, April 1977

F. F. Haywood, G. D. Kerr, W. A. Goldsmith, P. T. Perdue, and J. H. Thorngate
"Measurements of Radon Daughter Concentrations in Structures Built On or Near Uranium Mill Tailings," *Proceedings of Specialist Meeting on Personal Dosimetry and Area Monitoring Suitable for Radon and Daughter Products, Elliot Lake, Canada, Oct. 4–8, 1976*, Organization for Economic Cooperation and Development, Paris, 1977

F. F. Haywood, R. W. Leggett, P. T. Perdue, B. S. Ellis, and D. L. Anderson
Radiological Survey of the Former Vitro Rare Plant, Canonsburg, Pennsylvania (Phase I) (to be published as an ERDA report)

J. M. Heller, R. D. Birkhoff, and L. R. Painter
"Isotopic Effects in the Optical and Dielectric Functions of H_2O and D_2O in the Vacuum UV," to be published in *Journal of Chemical Physics*

H. F. Holmes and R. B. Gammage
"Surface Properties of a North Ray Crater Soil (Apollo 16)," *Earth Planet. Sci. Lett.* **36**, 14 (1977)

C. F. Holoway, J. E. Turner, and A. S. Loebl
Select Bibliography on the Dosimetry, Metabolism, Pathology, Epidemiology and Environmental Aspects of Radon and Its Daughters, ORNL-5284 (in preparation)

B. L. Houser, C. F. Holoway, and D. G. Madewell
Guide to Radioactive Waste Management Literature, ORNL-5226, 1977

H. H. Hubbell, Jr., R. D. Birkhoff, and J. D. Allen
"Rutherford Revisited: The Deflection of an Electron in Inverse First, Second and Third Power Central Fields," to be published in *American Journal of Physics*

G. S. Hurst and C. E. Klots
"Elementary Processes in Irradiated Noble Gases," pp. 1–96 in *Advances in Radiation Chemistry*, vol. 5, M. Burton and J. L. Magee, eds., Wiley-Interscience, New York, 1976

G. S. Hurst, M. H. Nayfeh, and J. P. Young
"A Demonstration of One-Atom Detection," *Appl. Phys. Lett.* **30**, 229 (1977)

"One-Atom Detection Using Resonance Ionization Spectroscopy," *Physical Review A* (in press)

T. Inagaki, E. T. Arakawa, R. D. Birkhoff, and M. W. Williams
"Optical Properties of Liquid Na Between 0.6 and 3.8 eV," *Phys. Rev. B* **13**, 5610 (1976)

T. Inagaki, E. T. Arakawa, R. N. Hamm, and M. W. Williams
"Optical Properties of Polystyrene from the Near-Infrared to the X-Ray Region and Convergence of Optical Sum Rules," *Phys. Rev. B* **15**, 3243 (1977)

M. Inokuti, Y. Itikawa, and J. E. Turner
"Addenda: Inelastic Collisions of Fast Charged Particles with Atoms and Molecules – The Bethe Theory Revisited," to be published in *Review of Modern Physics*

D. G. Jacobs and J. E. Turner
"Letter to the Editor on Cohen's Analysis of Deep Geological Disposal of Radioactive Wastes," *Phys. Today* **29**(11), 15 (1976)

J. P. Johnson, L. G. Christophorou, and J. G. Carter
"Fragmentation of Aliphatic Chlorocarbons Under Low-Energy ($\lesssim$10 eV) Electron Impact," submitted to *Journal of Chemical Physics*

R. M. Jones, J. W. Poston, J. L. Hwang, T. D. Jones, and G. G. Warner
The Development and Use of a Fifteen-Year-Old Equivalent Mathematical Phantom for Internal Dose Calculations, ORNL/TM-5278, June 1976

T. D. Jones
A CHORD Simulation for Insult Assessment to the Red Bone Marrow, ORNL-5191, September 1976

"CHORD Operators for Cell-Survival Models and Insult Assessment to Active Bone Marrow," *Radiat. Res.* **71**, 269 (1977)

T. D. Jones and L. T. Dillman
"Monte Carlo Simulated Irradiation in a Spatially Dependent Field," *Health Phys.* **30**, 167 (1976)

T. D. Jones and J. W. Poston
"Isotropic and Cloud Source Irradiation by Monoenergetic Neutrons and Photons," *Health Physics* (in press)

G. D. Kerr, J. M. L. Hwang, and R. M. Jones
"A Mathematical Model of a Phantom Developed for Use in Calculations of Radiation Dose to the Body and Major Internal Organs of a Japanese Adult," *Radiat. Res.* **17**, 211 (1976)

G. D. Kerr, T. D. Jones, J. M. L. Hwang, F. L. Miller, and J. A. Auxier
"An Analysis of Leukemia Data from Studies of Atomic-Bomb Survivors Based on Estimates of Absorbed Dose to Active Bone Marrow," to appear in *Proceedings of the Fourth International Congress of the International Radiation Protection Association, Paris, Apr. 24–30, 1977*

G. D. Kerr, P. T. Perdue, and J. H. Thorngate
"A GeLi Detector System for Laboratory Counting of Natural Radioactivity in Environmental Samples," *Proceedings of the Tenth Midyear Topical Symposium of the Health Physics Society, Saratoga Springs, N.Y., Oct. 11–13, 1976*

G. D. Kerr, H. Yamada, and S. Marks
"A Survey of Radiation Doses Received by Atomic-Bomb Survivors Residing in the U.S.," *Health Phys.* **31**, 305 (1976)

C. E. Klots
"Role of Angular Momentum in Unimolecular Kinetics: Kinetic Energy Release in Fragmentation of $C_4H_6^+$," *J. Chem. Phys.* **66**, 5100 (1977)

"Studies of Rydberg State Reactions," *J. Chem. Phys.* **66**, 5240 (1977)

S. D. Kramer
"Letter to the Editor on Bence-Jones Proteins," *Sci. Am.* **236**, 8 (1977)

S. D. Kramer and N. Bloembergen
"Third-Order Nonlinear Optical Spectroscopy in CuCl," *Phys. Rev. B* **14**, 4654 (1976)

R. W. Leggett, J. E. Burden, M. T. Ryan, D. L. Anderson, B. S. Ellis, and D. J. Christian
Radiological Survey of the Simonds Saw and Steel Company, February 1977 (to be published as an ERDA report)

R. W. Leggett, W. D. Cottrell, and H. W. Dickson
Radiological Survey of the Seaway Industrial Park, January 1977 (to be published as an ERDA report)

R. W. Leggett, W. D. Cottrell, H. W. Dickson, D. L. Anderson, C. A. Golden, and W. F. Fox
Radiological Survey of the Former Haist Property, January 1977 (to be published as an ERDA report)

R. W. Leggett, W. D. Cottrell, R. W. Doane, and D. J. Christian
Radiological Survey of the Seneca Army Depot, February 1977 (to be published as an ERDA report)

R. W. Leggett, W. D. Cottrell, F. F. Haywood, W. H. Shinpaugh, R. W. Doane, and W. M. Johnson
Radiological Survey of the Former Horizons Inc., Thorium Metal Production Plant, May 1977 (to be published as an ERDA report)

R. W. Leggett, M. T. Ryan, W. D. Cottrell, J. Burden, D. J. Christian, R. W. Doane, B. S. Ellis, D. L. Anderson, and W. M. Johnson

Radiological Survey of the Tonawanda, New York Plant of Linde Division of Union Carbide Corporation, March 1977 (to be published as an ERDA report)

R. W. Leggett, M. T. Ryan, F. F. Haywood, P. T. Perdue, E. B. Wagner, and C. J. Barton

Radiological Survey of the Property at 9200 Latty Avenue, Hazelwood, Missouri (in preparation) (to be published as an NRC report)

R. W. Leggett and L. R. Williams

"On Multiple Solutions of Nonlinear Hammerstein Integral Equations," submitted to *Journal of Mathematical Analysis of the Society for Industrial and Applied Mathematics*

"On the Multiplicity of Fixed Points of Nonlinear Operators," to be submitted to *Journal of Mathematical Analysis and Applications*

R. A. MacRae, E. T. Arakawa, and M. W. Williams

"Refractive Indices of Transparent Solvents," submitted to *Journal of Chemical and Engineering Data*

J. B. Mailhes, A. F. McFee, and J. W. Poston

"Chromosomal Aberrations in Swine Leukocytes After In-Vivo or In-Vitro Exposure to Fission Neutrons," submitted to *Radiation Research*

W. J. McDowell, F. G. Seeley, and M. T. Ryan

"Penetration of HEPA Filters by Alpha Recoil Aerosols," pp. 662–74 in *Proceedings of the 14th ERDA Air Cleaning Conference, Sun Valley, Idaho, Aug. 2–4, 1976*, NTIS, Springfield, Va., February 1977

M. H. Nayfeh

"Effect of Relaxation on Adiabatic Following," *Phys. Rev. A* **14**, 1304 (1976)

"Two-Photon Ionization of Colliding Atoms," submitted to *Physical Review A*

M. H. Nayfeh, C. H. Chen, and M. G. Payne

"Kinetic Studies of Energy Transfer from He (n = 2,3) to Ne, Ar, Kr, and Xe," *Phys. Rev. A* **14**, 1739 (1976)

M. H. Nayfeh and A. H. Nayfeh

"Adiabatic Following in Two-Photon Transition," *Phys. Rev. A* **15**, 1169 (1977)

"Adiabatic Following in Two-Photon Transition," to appear in *Proceedings of the Fourth Rochester Conference on Coherence and Quantum Optics, Rochester, N.Y., June 8–10, 1977*

"Optical Resonance of a Two-Level Atomic System," *J. Appl. Phys.* **47**, 2528 (1976)

"Dynamic Stark Splittings in Two-Photon Processes," submitted to *Physical Review A*

V. N. Neelavathi, R. H. Ritchie, and W. Brandt

"Theory of Plasmon Energy Gain by Auger Electrons," to be submitted to *Physical Review B*

T. W. Oakes

"Environmental Monitoring," p. 18 in *Applied Health Physics and Safety Annual Report – 1976*, ORNL-5310, 1977

T. W. Oakes, J. L. Danek, and K. E. Shank

Methods and Procedures Used in Environmental Surveillance at ORNL, ORNL-5185 (in preparation)

T. W. Oakes, C. E. Easterly, and K. E. Shank

"Radionuclide Accumulations in Clinch River Fish," pp. 231–38 in *Proceedings of the Tenth Midyear Topical Symposium of the Health Physics Society, Saratoga Springs, N.Y., Oct. 11–13, 1976*

T. W. Oakes, A. K. Furr, D. J. Adair, and T. F. Parkinson

"Neutron Activation Analysis of Automobile Exhaust Pollutants," pp. 560–65 in *Proceedings of the International Conference on Modern Trends in Activation Analysis, Munich, Germany, Sept. 13–17, 1976*; also, *J. Radioanal. Chem.* **37**, 881 (1977)

T. W. Oakes and K. E. Shank
"ORNL Environmental Monitoring Section," *Environmental Monitoring Report – CY-1976*, Y-UB-6, 1977

T. W. Oakes, K. E. Shank, and C. E. Easterly
"Natural and Man-Made Radionuclide Concentrations in Tennessee Soils," pp. 322–33 in *Proceedings of the Tenth Midyear Topical Symposium of the Health Physics Society, Saratoga Springs, N.Y., Oct. 11–13, 1976*

"Verification of an Air-Transport Code Using Iodine-131 as a Tracer," *Health Physics* (in press)

"Iodine-131 Air Concentrations: A Comparison of Calculated Versus Measured Values," *Trans. Am. Nucl. Soc.* 24, 109 (1976)

T. W. Oakes, K. E. Shank, C. E. Easterly, and L. R. Quintana
"Concentrations of Radionuclides and Selected Stable Elements in Fruits and Vegetables," to appear in *Proceedings of the Eleventh Annual Conference on Trace Substances in Environmental Health, Columbia, Mo., 1977*

P. Otaduy, C. E. Easterly, R. S. Booth, and D. G. Jacobs
"Factors Affecting Calculations of Dose Resulting from a Tritium Release into the Atmosphere," p. 1425 in *Proceedings of the Second Topical Meeting on the Technology of Controlled Nuclear Fusion, Richland, Wash., Sept. 21–23, 1976*, CONF-760935

M. O. Pace, L. G. Christophorou, D. R. James, R. Y. Pai, R. A. Mathis, and D. W. Bouldin
"Improved Unitary and Multicomponent Gaseous Insulators," to be published in *IEEE Transactions on Insulation Group 32*

P. J. Papagiannakopoulos and C. E. Easterly
Conversion of Tritium Gas to Tritiated Water, ORNL/TM-5686 (to be published)

C. H. Patrick
"Trends in Public Health in the Population Near Nuclear Facilities: A Critical Assessment," *Nucl. Saf.* 18(5) (1977)

"Mortality Trends in Counties Surrounding the Oak Ridge Nuclear Facilities: A Time Series Analysis," to appear in *Proceedings of the Social Statistics Section, 1977 Meeting of the American Statistical Association*

"Human Health Effects Studies: Shortcomings and Needs," p. 17 in *Abstracts of the SIAM 1977 National Meeting, Society for Industrial and Applied Mathematics*

"Trace Substances and Electric Power Generation: The Need for Epidemiological Studies to Determine Health Risks," to appear in *Proceedings of the Eleventh Annual Conference on Trace Substances in Environmental Health, Columbia, Mo., 1977*

M. G. Payne and C. W. Choi
"Multiphoton Ionization with Strong Pulsed Laser Fields. I. Two-Photon Ionization," submitted to *Physical Review A*

M. G. Payne and M. H. Nayfeh
"Energy Transfer Between Slowly Moving Atoms – The Case of No Crossing Point," *Phys. Rev. A* 13, 595 (1976)

L-G. Petersson, R. Melander, D. P. Spears, and S. B. M. Hogström
"Density of States of Ferro- and Paramagnetic Ni and Fe Studied by Photoelectron Spectroscopy," to be published in *Physical Review Letters*

H. R. Petty, E. T. Arakawa, and J. K. Baird
"Methods to Determine the Temperature Dependence of the Pre-Exponential Factor of the Arrhenius Equation from Thermogravimetric Data," *Journal of Thermal Analysis* (in press)

H. R. Petty, J. A. Crumb, V. E. Anderson, E. T. Arakawa, and J. K. Baird
"New Differential Bottcher-Onsager Method Used To Determine the Polarizability and Apparent Radius of $SiO_4(WO_3)_{12}^{4-}$," *J. Phys. Chem.* 81, 696 (1977)

J. E. Phillips and C. E. Easterly
"Sources of Tritium," submitted to *Nuclear Safety*

J. W. Poston, W. S. Snyder, and L. A. Owen
"The Dosimetry of ^{241}Pu Reconsidered," submitted to *Health Physics*

M. M. Abd-El Razek and J. H. Thorngate
"Studies of a Tetralin-Based Scintillator with Possible Applications in Neutron Spectrometry," *Nucl. Instrum. Methods* **141**, 477 (1977)

R. H. Ritchie, G. Basbas, and V. E. Anderson
"The Impact Parameter Representation of Charged Particle Energy Losses to Condensed Media," to be submitted to *Journal of Physics F*

R. H. Ritchie, Werner Brandt, and P. M. Echenique
"Wake Potential of Swift Ions in Solids," *Phys. Rev. B* **14**, 4808 (1976)

R. H. Ritchie, R. N. Hamm, M. W. Williams, and E. T. Arakawa
"Dispersion Relations of Elementary Excitations When Damping Is Present," to be published in *Physica Status Solidi*

R. H. Ritchie and A. Howie
"The Effect of Electronic Excitation on the Optical Potential in Electron Diffraction," *Philos. Mag.* **36**, 463 (1977)

V. C. Rogers, W. A. Goldsmith, F. F. Haywood, and G. K. Gantner
"Alternative Management Techniques for the Uranium Mill Tailings Site at Salt Lake City, Utah," p. 81:11 in *Proceedings of Tenth Midyear Topical Symposium of the Health Physics Society, Saratoga Springs, N.Y., Oct. 11–13, 1976*

R. L. Roswell, R. E. Goans, and J. H. Cantrell, Jr.
High Resolution Ultrasonic Scanning of Animal and Human Tissue In-Vivo, ORNL/TM-5934 (to be published)

M. T. Ryan, R. W. Leggett, J. E. Burden, D. J. Christian, B. S. Ellis, and D. L. Anderson
Radiological Survey of the Hooker Chemical Company, February 1977 (to be published as an ERDA report)

M. T. Ryan, R. W. Leggett, R. W. Doane, W. H. Shinpaugh, F. F. Haywood, and W. M. Johnson
Radiological Survey of E. I. du Pont Chemical Company, July 1977 (to be published as an ERDA report)

M. T. Ryan and W. J. McDowell
Observations of the Distribution and the Nature of Alpha-Active Particulate Material in a HEPA Filter Used for Plutonium-Containing Dust, ORNL/TM-5765, February 1977

M. T. Ryan, W. H. Shinpaugh, W. M. Johnson, R. W. Doane, F. F. Haywood, and R. W. Leggett
Radiological Survey of the AEC St. Louis Airport Storage Site, April 1977 (to be published as an ERDA report)

L. J. Saethre, D. P. Spears, L. Johonsson, and S. B. M. Hogström
"ESCA Studies of Some Three Coordinated Complexes of Divalent Tellurium," to be published in *Journal of Electron Spectroscopy and Related Phenomena*

"On ESCA Study of Phosphorus 2*p* Electron Binding Energies in 5,5-dimethyl-2-oxy-1,3,2-dioxaphosphlorinones," to be submitted to *Journal of Electron Spectroscopy and Related Phenomena*

G. K. Schweitzer, A. C. McMurtrie, J. D. Allen, Jr., L. C. Cusachs, D. O. Vick, and G. Finkelstein
"The Photoelectron Spectra of Some Gaseous Thallium(I) Oxyanion Salts," *J. Electron Spectrosc. Relat. Phenom.* **10**, 155 (1977)

L. M. Scott, G. G. Warner, and J. W. Poston
"Theoretical Evaluation of Optimum Detector Size and Positioning for Low-Energy In Vivo Gamma Spectrometry," submitted to *Health Physics*

M. U. Shaikh, H. W. Dickson, and J. Ashraf
Dose Calculations for Dosimetry Intercomparison Studies with a Heavy Concrete Shield Around the HPRR Core, ORNL/TM-5562 (in preparation)

K. E. Shank and C. E. Easterly
Tritium Instrumentation for a Fusion Reactor Power Plant, ORNL/TM-5344, September 1976

K. E. Shank, T. W. Oakes, and C. E. Easterly
"Critical Assessment of Radiological Releases from a Fusion Reactor," to be published as an ORNL technical memorandum

K. E. Shank, R. J. Vetter, and P. L. Ziemer
"Zinc-Cadmium Interrelationships and the Kinetics of Cadmium Transport in a Biological System," p. 395 in *Proceedings of the Tenth Annual Conference on Trace Substances in Environmental Health, Columbia, Mo., June 8–10, 1976*, 1977

"Uptake and Distribution of Cadmium in Mice Following Repeated Administrations," *Arch. Environ. Contam. Toxicol.* **6**, 63 (1977)

"A Mathematical Model of Cadmium Transport in a Biological System," *J. Environ. Res.* **13** 209 (1977)

R. L. Shoup
"International Waste Management Symposium," submitted to *Nuclear Safety*

W. S. Snyder
"Basic Concepts in the Assessment of Human Exposures and Risks," *Proceedings of Third International Summer School of Radiation Protection, Herceg-Novi, Yugoslavia, Aug. 24–Sept. 3, 1976* (in press)

"Pathways from Reactors to Food Chains," *Proceedings of Third International Summer School of Radiation Protection, Herceg-Novi, Yugoslavia, Aug. 24–Sept. 3, 1976* (in press)

W. S. Snyder, M. R. Ford, and G. G. Warner
Estimates of Specific Absorbed Fractions for Radiation Sources Uniformly Distributed in Various Organs of a Heterogeneous Phantom, NM/MIRD Pamphlet No. 5, rev., Society of Nuclear Medicine, New York (in press)

"Distribution of Dose Within the Body from a Photon Emitter Present in the Organ," *Proceedings of the Fourth International Congress of IRPA, Paris, France, Apr. 24–30, 1977* (in press)

D. Spears, H. H. Hubbell, Jr., J. D. Allen, and R. D. Birkhoff
"A Highly Collimated Pinhole Electron Gun," to be submitted to *Review of Scientific Instruments*

D. P. Spears, R. Melander, L-G. Petersson, S-E. Karlson, and S. B. M. Hogström
"Angular Dependent Photoemission Studies of Ag (111) and Ag (110); $h\omega$ = 16.8, 21.2, and 26.9 eV," to be submitted to *Physical Review Letters*

P. S. Stansbury
"A 'Chirper Checker' – An Adjunct to the Use of Personal Radiation Monitors," submitted to *Health Physics*

P. S. Stansbury, J. W. Poston, and G. G. Warner
In Phantom Spectrometry of Medical Diagnostic X-Rays, ORNL/TM-5873 (in press)

J. A. Stockdale
"High Kinetic Energy N^+ Ions from Decay of Doubly Ionized N_2," *J. Chem. Phys.* **66**, 1792 (1977)

J. A. Stockdale, L. Schumann, H. H. Brown, and B. Bederson
"High Temperature Atomic Beam Source," *Rev. Sci. Instrum.* **48**, 938 (1977)

J. H. Thorngate
"Measurements of Distributions of Energy Loss and Additivity of Energy Losses for 50 to 150 keV Protons in Hydrogen and Nine Hydrocarbon Gases," *Proceedings of Small Accelerator Conference, Denton, Tex., Oct. 25–27, 1976*

"Measurements of Distributions of Energy Loss for 51, 102 and 153 keV Protons in Nine Hydrocarbon Gases," *Nucl. Instrum. Methods* **137**, 569 (1976)

"Measurements of the Additivity of Stopping Cross-Sections for 50–150 keV Protons in Nine Hydrocarbon Gases," *Health Phys.* **32**, 541 (1977)

"A Simplified Pulse-Shape Discrimination Circuit for Use in Liquid-Scintillation Spectroscopy of Alpha Particles," *Health Physics* (in press)

"Letter to the Editor of Health Physics: Comments on the Note: 'Liquid Scintillation Alpha Particle Assay with Energy and Pulse Shape Discrimination' by P. Cross and G. W. McBeth," *Health Phys.* **32**, 119 (1977)

J. H. Thorngate and D. J. Christian
"Optimization of the Detector and Association Electronics Used for High-Resolution Liquid-Scintillation Alpha Spectroscopy," *Health Physics* (in press)

J. H. Thorngate, D. J. Christian, and C. P. Littleton
"An Apparatus for Electrochemical Etching of Recoil Particle Tracks in Plastic Foils," *Nucl. Instrum. Methods* **138**, 561 (1976)

J. H. Thorngate and M. M. Abu-El Razek
"Limits to the Applicability of Commonly Used Pulse-Shape Figures of Merit and Possible Alternative Measures of Performance," *Nucl. Instrum. Methods* **144**, 209 (1977)

R. N. Thurmer
"Over the Iron Curtain," *J. Civ. Def.* **9**(5) (1976); **9**(6) (1976); **10**(1) (1977); **10**(2) (1977)

C. J. Tung, J. C. Ashley, and R. H. Ritchie
"Electron Inelastic Mean Free Paths in Solids I: Aluminum Metal," to be submitted to *Physical Review*

"Electron Inelastic Mean Free Paths in Solids II: Electron Gas Statistical Model," to be submitted to *Physical Review*

C. J. Tung and R. H. Ritchie
"Electron Slowing-Down Spectra in Al," to be published in *Physical Review B*

C. J. Tung, J. C. Ashley, R. D. Birkhoff, R. H. Ritchie, L. C. Emerson, and V. E. Anderson
"Electron Slowing-Down Flux Spectrum in Al_2O_3," *Phys. Rev. B* **16**, 3049 (1977)

J. E. Turner
"Minimum Dipole Moment Required to Bind an Electron – Rediscovery of 1947 Fermi-Teller Result," *Am. J. Phys.* **45**, 758 (1977)

J. E. Turner, R. N. Hamm, and H. A. Wright
"Calculations for Cancer Radiotherapy with Pion Beams," *Nature* **263**, 195 (1976)

T. Vo-Dinh
"A Methodology for Multicomponent Analysis Based on Synchronous Luminescence," submitted to *Analytical Chemistry*

T. Vo-Dinh, R. B. Gammage, A. R. Hawthorne, and J. H. Thorngate
"Synchronous Spectroscopy for the Analysis of Polynuclear Aromatic Compounds," submitted to *Environmental Science and Technology*

T. Vo-Dinh, K. P. Li, and J. D. Winefordner
"Fluorescence Studies of Benzo(a)Pyrene in Liposome Membrane Systems," *Biochem. Biophys. Res. Commun.* **73**, 187 (1976)

T. Vo-Dinh, U. P. Wild, M. Lamotte, and A. M. Merle
"Quasilinear Fluorescence of Pyrene in a Monocrystalline Matrix of n-Heptane," *Chem. Phys. Lett.* **39**, 118 (1976)

T. Vo-Dinh and J. D. Winefordner
"Room-Temperature Phosphorimetry as a New Spectrochemical Method of Analysis," *Applied Spectroscopy Review* (in press)

T. Vo-Dinh, E. Lue Yen, and J. D. Winefordner
"Heavy Atom Effect on Room-Temperature Phosphorimetry," *Analyt. Chem.* **48**, 1186 (1976)

"Room-Temperature Phosphorescence of Several Polyaromatic Hydrocarbons," *Talanta* **24**, 146 (1977)

H.-t. Wang and L. G. Christophorou
"Systematics of Negative Ion States of Atoms and Small Molecules," submitted to *Journal of Physics B*

D. R. Ward

An Operational Method for Demonstrating Fuel Loading Integrity in a Reactor Having Accessible ^{235}U Fuel, ORNL/TM-4898, July 1976

R. J. Warmack, J. A. D. Stockdale, and R. N. Compton

"Apparatus for Energy, Angle, and Mass Analysis of Products from Alkali-Molecule Reactions," *International Journal of Mass Spectrometry and Ion Physics* (in press)

"Ionizing Collisions of Potassium Atoms with D_2O," *Chemical Physics Letters* (in press)

"Ionizing Collisions of Cesium and Potassium Atoms with Water," *Journal of Chemical Physics* (in press)

G. G. Warner and J. M. L. Hwang

"Absorbed Doses in Pediatric Phantoms from Simulated External X-Ray Exposures," *Journal of Applied Radiology* (in press)

S. B. Watson, W. S. Snyder, and M. R. Ford

TIMED: A Computer Program for Calculating Cumulated Activity of a Radionuclide in the Organs of the Human Body at a Given Time, t, After Deposition, ORNL/CSD/TM-17, December 1976

Lectures

J. A. Auxier

"Nuclear Power and Public Concern," The University of Tennessee Center for Health Sciences, Memphis, Tenn., Sept. 13, 1976

"Nuclear Power and Public Concern," Central Rocky Mountain Chapter, Health Physics Society, Denver, Colo., Oct. 21, 1976

"Nuclear Power and Public Concern," Western Pennsylvania Chapter, Health Physics Society, Pittsburgh, Pa., Oct. 27, 1976

"Low Level Effects of Radiation," North Central Chapter, Health Physics Society, Rochester, Minn., Oct. 29, 1976

"Laboratory Assessment of Internal Exposure," Oak Ridge Associated Universities, Oak Ridge, Tenn., Nov. 10, 1976

"Nuclear Power and Public Concern," New England Chapter, Health Physics Society, Waltham, Mass., Nov. 18 1976

"Radiation Measurements Technology," Harvard Medical School, Boston, Mass., Nov. 19, 1976

"Radiation Measurements Technology," Delaware Chapter, Health Physics Society, West Conshohocken, Pa., Dec. 2, 1976

"The Effects of Radiation on Humans," Mid-America Chapter, Health Physics Society, Columbia, Mo., Dec. 10, 1976

"Radiation Measurements Technology," Deep South Chapter, Health Physics Society; Louisiana State University; and Louisiana Nuclear Society, Baton Rouge, La., Jan. 15, 1977

"Effects of Radiation on Humans," Columbia Chapter, Health Physics Society, Richland, Wash., Jan. 18, 1977

"Radiation Measurements Technology," Cascade Chapter, Health Physics Society, Portland, Ore., Jan. 19, 1977

"Cleaning Up Old Sites Associated with the Uranium Fuel Cycle," Northern California Chapter, Health Physics Society, Berkeley, Calif., Jan. 20, 1977

"Planning for Radiation Emergencies," Oak Ridge Associated Universities, Oak Ridge, Tenn., Jan. 24, 1977

"Cleaning Up Old Sites Associated with the Uranium Fuel Cycle," Baltimore-Washington Chapter, Health Physics Society, Bethesda, Md., Feb. 16, 1977

"Cleaning Up Old Sites Associated with the Uranium Fuel Cycle," Argonne National Laboratory, Argonne, Ill., Feb. 17, 1977

"Radiation Measurements Technology," Midwest Chapter, Health Physics Society, Chicago, Ill., Feb. 17, 1977

"Effects of Radiation on Humans" and "Nuclear Power and Public Concern," University of South Carolina, Spartanburg, S.C., Feb. 23, 1977

"Health Physics: Past, Present, Future," Oak Ridge Associated Universities, Oak Ridge, Tenn., Feb. 28, 1977

"Radiation Measurements Technology," Texas A&M University, College Station, Tex., Mar. 4, 1977

"Nuclear Power and Public Concern," North and South Texas Chapters, Health Physics Society, College Station, Tex., Mar. 4, 1977

"Low Level Effects of Radiation," Seminar on National Waste Terminal Storage Program, Atlantic Beach, N.C., Mar. 11, 1977

"Cleaning Up Old Sites Associated with the Uranium Fuel Cycle," University of Florida, Gainesville, Fla., Mar. 17, 1977

"Effects of Radiation on Humans," Florida Chapter, Health Physics Society, Tallahassee, Fla., Mar. 18, 1977

"Nuclear Power and Public Concern," Great Lakes Chapter, Health Physics Society, Lansing, Mich., Mar. 24, 1977

"Cleaning Up Old Sites Associated with the Uranium Fuel Cycle," Rio Grande Chapter, Health Physics Society, Sante Fe, N.M., Apr. 15, 1977

"Radiation Protection: How Is It Accomplished," 5th International Conference on Reactor Shielding, Knoxville, Tenn., Apr. 20, 1977

"Low Level Effects of Radiation," Meeting on Biological Effects and Control of Low Level Radiation, Richmond, Va., May 13, 1977

"Nuclear Power and Public Concern," Rutgers University, New Brunswick, N.J., May 24, 1977

"Effects of Radiation on Hamans," North East New York Chapter, Health Physics Society, Schenectady, N.Y., May 25, 1977

"Effects of Radiation on Humans," Greater New York Chapter, Health Physics Society, New York, N.Y., May 26, 1977

"Cleaning Up Old Sites Associated with the Uranium Fuel Cycle," Savannah River Chapter, Health Physics Society, Augusta, Ga., May 31, 1977

"Cleaning Up Old Sites Associated with the Uranium Fuel Cycle," Southern California Chapter, Health Physics Society, Los Angeles, Calif., June 9, 1977

"Effects of Radiation on Humans," Hawaii Chapter, Health Physics Society and Nuclear Medicine Society, Honolulu, Hawaii, June 14, 1977

J. K. Baird

"Measurement of Molecular Properties in Liquids," Society of Physics Students, Western Kentucky University, Bowling Green, Ky., Oct. 7, 1976

"Laser Fusion," Department of Physics, Appalachian State University, Boone, N.C., Dec. 8, 1976

"Laser Fusion," Department of Physics, East Carolina University, Greenville, N.C., Dec. 10, 1976

"Laser Fusion," Department of Physics, North Texas State University, Denton, Tex., Jan. 20, 1977

"Physics and Chemistry of Electrons in Fluids," Department of Chemistry, Wayne State University, Detroit, Mich., Mar. 16, 1977

"Laser Fusion," Department of Chemistry, Wayne State University, Detroit, Mich., Mar. 18, 1977

"Irving Langmuir's Rules for Scientific Discovery," ORION, Oak Ridge, Tenn., Mar. 24, 1977

"Laser Fusion," Department of Chemistry, College of William and Mary, Williamsburg, Va., Apr. 1, 1977

"Physics and Chemistry of Electrons in Fluids," Department of Chemistry, University of Florida, Gainesville, Fla., May 6, 1977

P. R. Barnes

"Nuclear War Survival," 228th Combat Communications Squadron, Knoxville, Tenn., Jan. 15, 1977

P. R. Bell

"The Origin of the Solar System," Wright-Patterson Air Force Base, Oct. 7–9, 1976

R. D. Birkhoff

"Collective Effects in Biophysics," Georgia State University, Atlanta, Jan. 19, 1976

J. S. Carver

"Radiation Exposure and the Woman Worker," 10-Week Health Physics and Radiation Protection Course, Oak Ridge Associated Universities, Oak Ridge, Tenn., Mar. 30, 1977

C. V. Chester and R. O. Chester

"Testimony Before the California Energy Resources Conservation and Development Commission," San Francisco, Calif., June 17, 1977

L. G. Christophorou

"The Formation and the Lifetimes of Metastable Negative Ions," California Institute of Technology, Pasadena, Calif., Dec. 7, 1976

"The Lifetimes of Metastable Negative Ions," Bell Laboratories, Murray Hill, N.J., Dec. 23, 1976

H. W. Dickson

"Potential Health Hazards at Light-Water Reactors," Medical Planning and Care in Radiation Accidents Seminar, Oak Ridge Associated Universities, Oak Ridge, Tenn., Nov. 11, 1976

"Design and Operation of Commercial Reactors," Medical Planning and Care in Radiation Accidents Seminar, Oak Ridge Associated Universities, Oak Ridge, Tenn., Mar. 30, 1977

"Elements of Organization," Roane State Community College Course in Management and Supervision, Campbell County Comprehensive High School, Mar. 28, 1977

Ray Hefferlin

"Intensity Constants for Diatomic Molecular Electronic Transitions – Are We Getting Anywhere," Centre for Research in Experimental Space Science, York University, Toronto, Canada, Feb. 2, 1977

"Intensity Constants for Diatomic Molecular Electronic Transitions – Status Report," seminar presented at Sandia Laboratory, Albuquerque, N.M., May 12, 1977

G. S. Hurst

"Resonance Ionization Spectroscopy and Its Applications," Department of Physics and Astronomy, Western Kentucky University, Bowling Green, Ky., Sept. 30, 1976

"Resonance Ionization Spectroscopy and Its Applications," Argonne National Laboratory, Argonne, Ill., Oct. 15, 1976

"A Laser Technique for the Detection of Single Atoms," EG&G, Inc., Santa Barbara, Calif., Apr. 11, 1977

"A Laser Technique for the Detection of Single Atoms," Lawrence Berkeley Laboratory, Berkeley, Calif., Apr. 13, 1977

"A Laser Technique for the Detection of Single Atoms," Los Alamos Scientific Laboratory, Los Alamos, N.M., Apr. 20, 1977

C. H. Kearny

"Blast Tests of Expedient Shelter in the DICE THROW Blast Test of Defense Nuclear," Washington, D.C., June 24, 1977

"The DICE THROW Blast Test," ORNL Project Officers Briefing at the Symposium of Defense Nuclear Agency, Aberdeen, Md., June 21–23, 1977

"Expedient Blast Shelter and Expedient Life Support Equipment," Annual Meeting of the Alabama Civil Defense Association, Gulf Shores, Ala., June 29–30, 1977

M. H. Nayfeh

"Photoionization of Atoms," Department of Physics, Yale University, New Haven, Conn., Jan. 12, 1977

"Photoionization of Atoms," Department of Physics, University of Arizona, Tucson, Ariz., Jan. 17, 1977

"Photoionization of Atoms," Kansas State University, Manhattan, Kan., Mar. 28, 1977

T. W. Oakes

"Technical Fundamentals of Nuclear Reactors," Technical Fundamentals for New Technicians, Oak Ridge National Laboratory, Oak Ridge, Tenn., June 7, 1976

"Technical Fundamentals of the Nuclear Fuel Cycle," Technical Fundamentals for New Technicians, Oak Ridge National Laboratory, Oak Ridge, Tenn., June 9, 1976

"Dispersion Calculation Methods," Union Carbide Corporation Nuclear Division and Chemical and Plastic Division Joint Environmental Protection Meeting, Oak Ridge, Tenn., June 16, 1976

"Introduction to Reactor System Theory," ORNL Health Physics Faculty Institute, Oak Ridge, Tenn., June 29, 1976

"Reactor Types and the Nuclear Fuel Cycle," ORNL Health Physics Faculty Institute, Oak Ridge, Tenn., June 30, 1976

"Methods of Environmental Surveillance," ORNL Health Physics Faculty Institute, Oak Ridge, Tenn., June 30, 1976

"Environmental Surveillance and the Nuclear Fuel Cycle," ORNL Health Physics Faculty Institute, Oak Ridge, Tenn., July 1, 1976

"Environmental Monitoring in Emergency Situation," ORNL Health Physics Faculty Institute, Oak Ridge, Tenn., July 2, 1976

"Fundamentals of Nuclear Reactors, Part I," Health Physics Technicians Program, Oak Ridge National Laboratory, Oak Ridge, Tenn., Dec. 6, 1976

"Fundamentals of Nuclear Reactors, Part II," Health Physics Technicians Program, Oak Ridge National Laboratory, Oak Ridge, Tenn., Dec. 8, 1976

"Environmental Monitoring at ORNL," Visiting Group from West Virginia Wesleyan College, Oak Ridge National Laboratory, Oak Ridge, Tenn., Jan. 6, 1977

"Energy and the Environment," Science Classes, Knox Doss Junior High School, Hendersonville, Tenn., Feb. 14, 1977

"Nuclear Power and the Environment," Science Classes, Knox Doss Junior High School, Hendersonville, Tenn., Feb. 15, 1977

"Environmental Monitoring During Normal Operations," Health Physics Technicians Program, Oak Ridge National Laboratory, Oak Ridge, Tenn., Mar. 14, 1977

"Environmental Monitoring Under Emergency Conditions," Health Physics Technicians Program, Oak Ridge National Laboratory, Oak Ridge, Tenn., Mar. 16, 1977

"Upgrading Liquid and Gaseous Monitoring Systems," Union Carbide Environmental Division Staff Seminar, Oak Ridge National Laboratory, Oak Ridge, Tenn., Apr. 15, 1977

"Environmental Surveillance and Evaluation Programs Around Nuclear Facilities," Ten-Week Health Physics and Radiation Protection Course, Oak Ridge Associated Universities, Oak Ridge, Tenn., Apr. 18, 1977

"Environmental Monitoring Under Emergency Conditions," Ten-Week Health Physics and Radiation Protection Course, Oak Ridge Associated Universities, Oak Ridge, Tenn., Apr. 20, 1977

"Environmental Surveillance at the Oak Ridge National Laboratory," Ten-Week Health Physics and Radiation Protection Course, Oak Ridge Associated Universities, Oak Ridge, Tenn., Apr. 20, 1977

M. G. Payne

"Weak Field Limit of Laser-Induced Collisional Excitation Transfer," Department of Physics, University of Kentucky, Lexington, Ky., Nov. 12, 1976

R. H. Ritchie

"Ion Cluster Penetration and Wake Phenomena in Condensed Matter," Gordon Research Conference on Particle-Solid Interactions, Proctor Academy, Andover, N.H., Aug. 5, 1976

"Cluster-Wake Interactions; Theory," Informal Workshop on Wake Phenomena, New York University, New York, N.Y., Jan. 6, 1977

"Speculations About Wake-Bound Electrons," Informal Workshop on Wake Phenomena, New York University, New York, N.Y., Jan. 7, 1977

"The Penetration of Swift Ion Clusters in Matter," Department of Physics, University of Wisconsin, Madison, Wis., Apr. 1, 1977

"The Penetration of Swift Charged Particles in Matter," Department of Physics, University of Alabama in Huntsville, Huntsville, Ala., Apr. 12, 1977

"Collective Effects in Charged Particle Track Formation," Department of Physics, University of Delaware, Newark, Del., Apr. 20, 1977

"Ion Cluster Penetration Phenomena," Department of Physics, University of Sussex, Sussex, England, June 14, 1977

K. E. Shank

"Health Physics Aspects of Fusion Power Development," ORNL Health Physics Faculty Institute, Oak Ridge, Tenn., June 16, 1977

"Environmental Monitoring at Oak Ridge National Laboratory," ORNL Health Physics Faculty Institute, Oak Ridge, Tenn., June 29, 1977

W. S. Snyder

"Historical Summary of Dosimetry for Rn and Rn Daughters – Concepts and Problems," Workshop on Dosimetry for Rn and Rn Daughters, Oak Ridge National Laboratory, Oak Ridge, Tenn., Apr. 12–13, 1977

R. N. Thurmer

"Current American Press Reactions to U.S. Civil Defense," 10th Annual Conference for the Journal of Civil Defense, Starke, Fla., Nov. 13, 1976

J. P. Young

"Resonance Ionization Spectroscopy and the Specific Detection of Single Atoms," Analytical Chemistry Division Seminar, Oak Ridge National Laboratory, Oak Ridge, Tenn., Feb. 24, 1977

Miscellaneous Staff Activities

Academic Appointments

J. K. Baird
Adjunct Professor of Physics, University of Kansas

R. D. Birkhoff
Professor of Physics, The University of Tennessee

L. G. Christophorou
Professor of Physics, The University of Tennessee

R. H. Ritchie
Professor of Physics, The University of Tennessee

POSTDOCTORAL FELLOW APPOINTMENTS

M. W. Grant
The University of Tennessee

C. H. Patrick
The Johns Hopkins University

D. P. Spears
The University of Tennessee

Chaun J. Tung
The University of Tennessee

H.-t. Wang
The University of Tennessee

R. J. Warmack
The University of Tennessee

A. D. Williamson
University of Kentucky

Awards

R. D. Birkhoff
American Physical Society Fellowship

L. G. Christophorou
AAAS Fellowship

Alan R. Hawthorne
Phi Kappa Phi's Most Outstanding Ph.D. Candidate Award at North Carolina State University

K. E. Shank
Recipient of the Glenn L. Jenkins Recognition Award for Excellence in Research, Purdue University, 1976

R. H. Ritchie
Recipient of NATO Research Grant

Service in Professional Organizations

E. T. Arakawa
International Advisory Committee, 5th Conference on Vacuum Ultraviolet Radiation Physics

J. A. Auxier
President-elect of the Health Physics Society; National Council on Radiation Protection and Measurements; National Academy of Sciences Advisory Committee on Civil Defense; National Academy of Sciences Subcommittee on Radiation Shielding; ICRU Task Group on Neutron Instrumentation; U.S. American National Standards Institute Subcommittee N13.8; NCRP Scientific Committee 23; NCRP Scientific Committee 34; IAEA Panel on Nuclear Accident Dosimetry Systems; AEC-DBER CF-252 Biomedical Advisory Panel; ICRP Task Group on Emergency and Accidental Exposures; Joint SNS/BER Biomedical Working Group; Managing Editor, *Health Physics*; Special Consultant to the Radiation Effects Research Foundation, Hiroshima, Japan

P. R. Bell
Society of Nuclear Medicine Computer Council, Task Group on Image Processing Methods

S. R. Bernard
ICRP Task Group on Dose Calculations for the Report of Committee 2

J. S. Carver
Member, Affirmative Action Committee, Health Physics Society; News Editor, *Health Physics*

L. G. Christophorou
Organizing International Symposium on Gaseous Dielectrics

K. E. Cowser
NCRP Scientific Committee 41: Public Radiation Exposure Resulting from Nuclear Power Generation; IAEA Panel on Principles for Establishing Limits for Release of Radioactive Material into the Environment

J. M. Davis
Scientists and Engineers for Appalachia, member of Planning Committee for Inventors Fair

H. W. Dickson
President, East Tennessee Chapter of the Health Physics Society (1976)

C. E. Easterly
Review Committee for Government Grant to St. Mary's College, Winona, Minn

M. R. Ford
ICRP Task Group on Dose Calculations for the Report of Committee 2; NCRP Scientific Committee 32: Administered Radioactivity; NCRP Scientific Committee 33: Dose Calculations

R. B. Gammage
Coprincipal Investigator of the NSF International Spring School on the Development and Applications of Solid State Nuclear Track Detectors, Rawalpindi, Pakistan, March 1978; Member of ORNL Life Science Committee for Synthetic Fuels; Divisional Coal Conversion Liaison Representative

C. F. Holoway
Vice President, Scientists and Engineers for Appalachia

G. D. Kerr
Editor, *Health Physics*; Consultant, Radiation Effects Research Foundation, Japan

W. S. Nichols
Editorial Secretary, *Health Physics*

T. W. Oakes
Oak Ridge Chapter of the American Nuclear Society, Chairman, Public Information and Education Committee, 1976–1977; East Tennessee Chapter, Health Physics Society, Chairman, Public Information and Certification Committee, 1976, and Member, Public Information and Education Committee, 1977

J. W. Poston
ICRP Task Group on Dose Calculations for the Report of Committee 2; NCRP Committee 55: Experimental Verification of Internal Dosimetry Calculations; Society of Nuclear Medicine, Medical Internal Radiation Dose (MIRD) Committee; MIRD Task Group on Pediatric Phantoms; MIRD Task Group on a Cardiac Model; ANSI Committee on the Internal Dosimetry of Fission Products and Corrosion Products; NCRP Scientific Committee 51B: Radiation Protection in Nuclear Medicine Applied to Children; Advisory Committee for the Transuranium Registry; Cochairman, Health Physics Society Ad Hoc Committee on SI Units in Radiation Protection; Cochairman, Health Physics Society Local Arrangements Committee for Annual Meeting in Atlanta

R. H. Ritchie
Member, Organizing Committee for Workshop on Wake Phenomena, New York University, January 1977

K. E. Shank
East Tennessee Chapter of the Health Physics Society, Member of Audio-Visual and Education and Certification Committees, 1976; Chairman of Public Information and Education Committee, 1977

J. E. Turner
Editor, *Health Physics*; President-Elect, East Tennessee Chapter, Health Physics Society; Member, ICRU Stopping Power Committee

Guests and Trainees

FACULTY INSTITUTE PARTICIPANTS

Frank A. Butler, Department of Physical Sciences, Northern Kentucky University, Highland Heights, Ky.

Donald Lee Davenport, Department of Biological Sciences, Kentucky Wesleyan College, Owensboro, Ky.

Kyle Lee Hathcox, Department of Physics, Union University, Jackson, Tenn.

Granvil C. Kyker, Jr., Department of Physics, Rose-Hulman Institute of Technology, Terre Haute, Ind.

FACULTY RESEARCH PARTICIPANT

T. F. Gesell, School of Public Health, University of Texas, Houston, Tex.

STUDENTS

Graduate Students

C. C. Chan, The University of Tennessee

Myung S. Chung, The University of Tennessee

S. J. Cotter, Purdue University

P. M. Echenique, Universidad Autonoma de Barcelona, Spain

J. R. Frazier, The University of Tennessee

K. S. Gant, The University of Tennessee

J. P. Johnson, The University of Tennessee

P. Otaduy, University of Florida

P. J. Papagiannakopoulos, The University of Tennessee

J. E. Phillips, University of North Carolina

R. L. Roswell, Rensselaer Polytechnic Institute

J. J. Shonka, Georgia Institute of Technology

F. J. Slagle, The University of Tennessee

P. S. Stansbury, Georgia Institute of Technology

D. E. Tittle, The University of Tennessee

K. L. Webster, The University of Tennessee

ORAU Student Trainees

D. K. Lorenzo, Georgia Institute of Technology, Atlanta

I. Pyron, Clark College, Atlanta

D. J. Simpkin, University of Wisconsin – Madison

Robert Zauper, Pennsylvania State University

NSF Students

Cathy Hesemann, Centenary College of Louisiana

Thomas L. Haltom, Millsaps College

Southern College and University Union Participants

Thomas L. Haltom, Millsaps College

Frank W. Hecker, Centre College of Kentucky

Cathy S. Hesemann, Centenary College of Louisiana

FOREIGN GUESTS

J. Ashraf, *University of Baluchistan, Quetta, Pakistan*

W. L. Chen, *Chinese Atomic Energy Council, Taiwan, Republic of China*

Kei-Den Chou, *Taiwan, Republic of China*

Myung Chung, *South Korea*

S. F. Deus, *Instituto de Energia Atomica, São Paulo, Brazil*

P. M. Echenique, *Universidad Autonoma de Barcelona, Spain*

Werner Hett, *SIN, Zurich, Switzerland*

J. M. L. Hwang, *Taiwan, Republic of China*

M. M. Rahman, *Atomic Energy Center, Dacca, Bangladesh*

M. U. Shaikh, *Pakistan Atomic Energy Commission, Reactor School, PINSTECH, Rawalpindi, Pakistan*

Cheng-May Tung, *Taiwan, Republic of China*

C. J. Tung, *Taiwan, Republic of China*

H.-t. Wang, *Taiwan, Republic of China*

HEALTH AND SAFETY RESEARCH DIVISION

MAY 1, 1978

S. V. KAYE, DIRECTOR
E. C. JONES, SEC.

ENGINEERING MAINTENANCE
E. T. LOY
J. T. COX
D. S. HIBBEN

FINANCE OFFICER
D. J. BOOK FM

EDITOR
J. L. VINSON I

BIOLOGICAL AND RADIATION PHYSICS SECTION
H. A. WRIGHT**
R. N. HAMM**
W. J. ADKISSON, SEC.

ANALYTIC DOSIMETRY
J. E. TURNER**
S. S. STOCKSTILL, SEC.
K. B. JACOBSON B
S. MITRA B
S. K. MIYOGI B
H. P. WITSCH B
W. W. WILLIAMS**

ATOMIC, MOLECULAR AND HIGH VOLTAGE PHYSICS
L. G. CHRISTOPHOROU
C. D. SAVIN, SEC.
J. K. BAIRD
D. W. BOULDIN[1]
J. G. CARTER
A. A. CHRISTODOULIDES[2]
D. R. JAMES
R. Y. PAI
I. SAUERS[1]
K. SORROS
C. C. CHAN[3]
D. L. McCORKLE[3]
C. METCALFE[3]
W. PACE[4]
R. A. MATHIS
D. V. MAXEY

PHYSICS OF SOLIDS AND MACROMOLECULES
E. T. ARAKAWA
T. A. CALLCOTT[1]
W. S. CHUNG[3]
R. N. HAMM**
L. R. PAINTER**
W. W. WILLIAMS**

SUBMICRON PHYSICS
R. D. BIRKHOFF***
J. D. ALLEN[5]
D. P. SPEARS[1]

TRANSPORT AND SURFACE PHYSICS
R. H. RITCHIE
V. E. ANDERSON CS
J. C. ASHLEY
R. N. HAMM**
E. KRETSCHMANN[1]
J. E. TURNER**
H. A. WRIGHT**

CONSULTANTS
J. B. BIRKS
W. BRANDT
A. J. BRAUNDWEIER
J. M. ELSON
T. L. FERRELL
M. W. GRANT
A. HOWIE
H. H. HUBBELL
R. A. McRAE
J. MEUFELD
F. W. TODD
H. YANG

BIOMEDICAL EFFECTS AND INSTRUMENTATION SECTION
J. K. POGGENBURG
B. H. ESTES, SEC.

NUCLEAR MEDICINE TECHNOLOGY
F. F. KNAPP
K. R. AMBROSE**
T. A. BUTLER
J. W. DOUGHERTY CS
J. D. HOESCHELE
D. V. WOO
A. P. CALLAHAN
L. A. FRENCH
C. E. GUYER
J. A. ROBERTS

MONITORING TECHNOLOGY AND INSTRUMENTATION
R. B. GAMMAGE
B. V. PALMER, SEC.
A. CHOWDHURY[1]
A. R. HAWTHORNE
T. VO-DINH

HEALTH EFFECTS AND EPIDEMIOLOGY
P. J. WALSH
F. E. STOCKSBURY, SEC.
L. G. BERRY[1] E
C. E. EASTERLY
G. D. GRIFFIN
T. D. JONES
G. D. KERR
J. E. PHILLIPS

METABOLISM AND DOSIMETRY
M. R. FORD (ACTING)
S. R. BERNARD
M. T. CRISTY
G. G. WARNER CS
S. B. WATSON CS

CONSULTANTS
J. W. BECKER[2]
L. T. DILLMAN
A. F. RUPP

CHEMICAL PHYSICS SECTION
W. R. GARRETT**
B. F. THOMAS, SEC.

MOLECULAR PHYSICS
R. N. COMPTON[6]
W. R. GARRETT**
C. E. KLOTS
P. W. REINHARDT
H. C. SCHWEINLER
J. A. STOCKDALE
R. J. WARMACK AC
A. D. WILLIAMSON
A. E. CARTER
H. L. BARNAWELL IC

PHOTOPHYSICS
G. S. HURST
N. D. BRASHER, SEC.
C. E. BEMIS C
C. H. CHEN
J. P. JUDISH
S. D. KRAMER
T. G. MILLER[2]
W. G. PAYNE
J. P. YOUNG AC
S. L. ALLMAN

CONSULTANTS
J. E. BLOOR
C. D. COOPER
R. HEFFERLIN
J. E. PARKS
B. RITCHIE

TECHNOLOGY ASSESSMENTS SECTION
P. S. ROMPHER
B. S. VARNADORE, S.C.

METHODOLOGY DEVELOPMENT AND EVALUATIONS
D. C. PARZYCK
K. L. WARREN, SEC.
R. O. CHESTER
D. E. DUNNING, JR.
F. O. HOFFMAN ES
G. G. KILLOUGH
D. C. KOCHER
C. W. MILLER
R. E. MOORE
E. W. RUPP[1]
D. L. SHAEFFER ES
R. W. SHOR[1]
C. C. TRAVIS

ASSESSMENTS APPLICATIONS
J. P. WITHERSPOON
A. R. WEBB, SEC.
S. J. COTTER
E. L. ETNIER[1]
G. S. HILL
C. A. LITTLE
L. W. McDOWELL
H. R. MEYER
F. R. O'DONNELL
W. L. RANDOLPH
A. P. WATSON
W. G. YALCINTAS

OFF-SITE POLLUTANT MEASUREMENTS
F. F. HAYWOOD
R. L. O'HATNICK, SEC.
W. D. COTTRELL
D. J. CRAWFORD
W. A. GOLDSMITH
P. W. LANTZ
R. W. LEGGETT
P. T. PERDUE
W. T. RYAN[1]
E. B. WAGNER
D. L. ANDERSON
D. J. CHRISTIAN
R. W. DOANE
B. S. ELLIS
R. S. HAMILTON
W. H. SHINPAUGH

DOSIMETRY APPLICATIONS RESEARCH
H. W. DICKSON
W. R. DAVIS, SEC.
L. W. GILLEY
C. F. HOLOWAY
L. W. HOLLAND O
C. S. SIMS
J. S. EPLER[1]

CONSULTANTS
J. E. YILL

*DUAL CAPACITY
**AFFIRMATIVE ACTION REPRESENTATIVE
***SAFETY AND RADIATION CONTROL OFFICER
[1] PART TIME
[2] POST DOCTORAL FELLOW
[3] GUEST ASSIGNMENT
[4] STUDENT
[5] LEAVE OF ABSENCE
[6] SUBCONTRACT
[6] ON ASSIGNMENT TO FOM INSTITUTE, AMSTERDAM, THE NETHERLANDS

FM FINANCE AND MATERIALS DIVISION
I INFORMATION DIVISION
B BIOLOGY DIVISION
CS COMPUTER SCIENCES DIVISION
E ENERGY DIVISION
AC ANALYTICAL CHEMISTRY DIVISION
C CHEMISTRY DIVISION
ES ENVIRONMENTAL SCIENCES
O OPERATIONS DIVISION

INDUSTRIAL SAFETY AND APPLIED HEALTH PHYSICS DIVISION

JANUARY 1, 1976

J. A. AUXIER, DIRECTOR
W. S. NICHOLS,[6] SECRETARY
D. M. DAVIS, ASSOCIATE DIRECTOR
S. A. WIEMAN, SECRETARY

ADMINISTRATIVE AIDE
J. L. MALONE
FINANCE OFFICER
T. J. BURNETT
ASSISTANT FINANCE OFFICER
D. W. GADDIS

ENVIRONMENTAL SURVEILLANCE AND EVALUATION
T. W. OAKES*

SECRETARIAL STAFF
L. J. BROWN

ATMOSPHERIC AND AQUATIC SURVEILLANCE
J. M. DAVIS*
D. W. PARSONS*
W. S. TOWNS*

BIOLOGICAL AND TERRESTRIAL SURVEILLANCE
J. M. DAVIS*
H. M. HUBBARD*
D. W. PARSONS*
L. R. QUINTANA*

DATA EVALUATION AND SPECIAL PROJECTS
T. W. OAKES*
K. E. SHANK[6]
J. S. ELDRIDGE[6]
C. E. EASTERLY
H. M. HUBBARD*
L. R. QUINTANA*
H. SUTANTO[6]
W. S. TOWNS*

RADIATION MONITORING
E. D. GUPTON

SECRETARIAL STAFF
D. W. GADDIS

INSTRUMENTATION
E. D. GUPTON
D. R. CLARK
I. T. FANN
J. E. JACKSON
S. W. NICHOLS

DOSE DATA
J. R. MUIR
R. W. LANE
D. M. SOARD
J. H. MILLER

INTERNAL DOSE
W. W. PARKINSON
R. E. GOANS
W. M. GOOD

PERSONNEL METERS
D. R. CLARK
S. S. HERREL
M. L. LEE
M. R. MATTHEWS
R. C. KUHLO

RADIOASSAYS
L. C. HENLEY
J. C. ANDERSON
M. W. JOHNSON
A. J. SOARD*

INDUSTRIAL SAFETY AND SPECIAL PROJECTS
A. D. WARDEN*

SECRETARIAL STAFF
M. R. DUNSMORE

SAFETY
D. C. GARY[2]
J. L. DANEK
R. E. MILLSPAUGH*
E. M. ROBINSON[5]

ORIENTATION AND TRAINING
R. E. MILLSPAUGH*

PROGRAM AND FACILITIES REVIEW
T. J. BURNETT*

BALANCE AREA REPRESENTATIVE
T. J. BURNETT*

STANDARDS AND PROCEDURES
A. D. WARDEN*
M. F. FAIR

RADIATION AND SAFETY SURVEYS
ROY L. CLARK

SECRETARIAL STAFF
S. A. CAMPBELL

BUILDING SURVEYS GROUP 1
H. M. BUTLER[1]

CENTRAL
W. T. MARTIN
S. C. BURRELL
R. D. PARTEN
D. K. THOMAS

EAST
W. F. OHNESORGE
J. F. ALEXANDER
S. A. HAMLEY
W. M. JOHNSON

SOUTH CENTRAL
A. J. SMITH
T. G. CLARK
A. B. ELDRIDGE
R. E. KENY
R. S. MALCOLM
S. A. POWERS

SOUTH EAST
C. E. HAYNES
W. D. CARDEN
T. L. COLLINS
C. F. JACKSON

SOUTH WEST
D. G. NOE
A. C. BUTLER
J. V. HILYER
J. H. SPENCE

BUILDING SURVEYS GROUP 2
L. C. JOHNSON

NORTHWEST
C. H. MILLER
M. L. CONNER
W. A. McLOUD
G. R. PATTERSON
J. R. SLATEN
C. F. ZAMZOW

NORTH CENTRAL
J. A. WORTH
J. H. PEMBERTON

MELTON VALLEY
R. S. COLEMAN
W. F. FOX
J. C. RICHTER
R. L. WALKER

Y-12 OPERATIONS
J. C. DAVIS
A. CARDWELL
P. E. COX
R. E. HALLIBURTON
R. S. HOWELL[3]

SHIFTS AND AREA SURVEYS
C. R. QUINN

SHIFTS SUPERVISORS
J. S. ADDISON
W. A. ALEXANDER
R. C. COOPER
R. L. JEFFERS

AREA SURVEYS
C. CLARK
C. F. SMITH
I. H. WIGGINS

*DUAL CAPACITY
[1] RADIATION CONTROL OFFICER
[2] DIVISION SAFETY OFFICER
[3] LEAVE OF ABSENCE
[4] AFFIRMATIVE ACTION REPRESENTATIVE
[5] QUALITY ASSURANCE COORDINATOR
[6] ENERGY CONSERVATION OFFICER
[7] HEALTH AND SAFETY RESEARCH DIVISION
[8] IAEA FELLOW

HEALTH PHYSICS DIVISION

JANUARY 1, 1977

J. A. AUXIER,* DIRECTOR
W. S. NICHOLS,* SECRETARY
D. W. DAVIS, ASSOCIATE DIRECTOR
B. A. PARKER, SECRETARY

ADMINISTRATIVE ASSISTANT
J. S. CARVER*[1]
D. S. HIBBEN,* SECRETARY

FINANCE OFFICER
D. J. HOOK
D. S. HIBBEN,* SECRETARY

ENGINEERING MAINTENANCE
E. T. LOY
J. T. COX
J. P. MICKEY
S. R. LANDONE[2]
J. L. MALONE

SENIOR RESEARCH ADVISORS
K. Z. MORGAN
E. P. WIGNER*

ENVIRONMENTAL HEALTH PHYSICS COORDINATOR
K. E. COWGER

ASSESSMENT AND TECHNOLOGY
R. W. DICKSON*

SECRETARIAL STAFF
L. J. BROWN
B. W. DAVIS
W. R. DAVIS
S. S. STECKSTILL
A. R. WEBB

TECHNICAL SUPPORT
C. E. FRITZ[2]
L. A. LEE[3]
C. P. LITTLETON[3]

EVALUATION OF HEALTH EFFECTS
G. D. KERR
C. E. EASTERLY
T. D. JONES*
C. H. PATRICK[3]
K. E. SHARK*

HEALTH PHYSICS RESEARCH REACTOR
H. W. DICKSON*
D. J. CHRISTIAN*
W. F. FOX*
L. W. GALLEY
L. B. HOLLAND[13]
D. R. WARD[13]

OFF-SITE MEASUREMENTS
F. F. HAYWOOD
D. L. ANDERSON
W. D. COTTRELL
J. L. DAMER[14]
R. W. DOANE
B. S. ELLIS[15]
R. E. HAMILTON
F. M. LANTZ
R. W. LEGGETT
F. T. PEARCE
M. T. RYAN
W. H. SHRIPAUGH
E. B. WAGNER

ON-SITE MEASUREMENTS
T. W. OAKES
J. M. DAVIS
H. W. HUBBARD
L. R. QUINTANA
K. E. SHARK*
J. P. SPRAIN
W. B. TOMPS

TECHNOLOGY AND DEVELOPMENT
R. B. GAMMAGE
A. R. HAWTHORNE
D. J. CHRISTIAN*
S. J. COTTER[6]
J. H. THORNGATE

CONSULTANTS
J. BURDEN
J. S. CHENA
C. E. WHEELER

BIOLOGICAL AND RADIATION PHYSICS
W. A. WRIGHT*
D. N. [illegible]*

SECRETARIAL STAFF
W. J. ADKISSON
L. K. WELTON

TECHNICAL SUPPORT
H. L. BARNWELL*[1]

ATOMIC AND MOLECULAR PHYSICS
L. G. CHRISTOPHOROU
J. L. BAIRD
J. G. CARTER
J. R. FRAZIER[6]
D. R. JAMES
J. P. JOHNSON[6]
R. A. MATHIS
D. V. MAKEY
C. METCALFE[6]
R. V. PAI
R. SIGMON
K. L. WEBSTER[6]

PHYSICS OF SOLIDS AND MACROMOLECULES
E. T. ARAKAWA
T. A. CALLCOTT[17]
M. CHUNG[6]
R. H. HARRY*
M. W. WILLIAMS

LIQUID AND SURFACE PHYSICS
R. D. BIRKHOFF
R. H. HARRY*
D. P. SPEARS[7]

GENERAL PHYSICS
R. H. RITCHIE
J. C. ASHLEY
R. H. HARRY*
C. J. TUNG[7]
J. E. TURNER*
W. A. WRIGHT*

MATHEMATICAL ANALYSIS
V. E. ANDERSON[6]

CONSULTANTS
J. D. ALLEN
G. BASBAS
J. B. BIRKS
D. W. BOULDIN
A. J. BRAUNDREIER
J. M. ELSON
T. L. FERRELL
M. GRANT
J. M. HELLER, JR.
H. H. HUBBELL, JR.
R. A. MacRAE
D. L. McCORKLE
J. REUFELD
M. D. PACE
L. R. PAINTER
H. PETTY
M. SILVER
G. M. L. SOMMERMAN
P. W. TODD

EMERGENCY TECHNOLOGY
C. V. CHESTER*

SECRETARIAL STAFF
M. A. CHRISSON
K. P. MULLINS

LIBRARIAN
R. N. THURNER*

STRATEGIC DEFENSE
C. V. CHESTER*
P. R. BARNES*
G. A. CRISTY*
K. F. GART
C. M. HALL AND
C. H. KEARNY
A. N. THURNER*

ENERGY SYSTEMS VULNERABILITY
G. A. CRISTY*
P. R. BARNES*
C. V. CHESTER*
R. O. CHESTER
M. E. FISH

CONSULTANT
E. P. WIGNER*

INDUSTRIAL SAFETY AND SPECIAL PROJECTS
A. D. WARDEN*

SECRETARIAL STAFF
M. R. DUNBORE

BALANCE AREA REPRESENTATIVE
T. J. BURNETT*

SAFETY
D. C. CARY[11]
R. E. MILLSPAUGH*
E. M. ROBINSON[6]

ORIENTATION AND TRAINING
R. E. MILLSPAUGH*

PROGRAMS AND FACILITIES REVIEW
T. J. BURNETT*

X-RAY AND MICROWAVE REVIEW
W. F. CHRESONGE*

STANDARDS AND PROCEDURES
A. D. WARDEN*

TRANSURANIUM HEALTH PHYSICS AND SAFETY PROCEDURES
C. E. HAYNES*

MEDICAL PHYSICS AND INTERNAL DOSIMETRY
J. W. POSTON
P. R. BELL
S. R. BERNARD
W. L. CHEN[6,8]
S. F. DELUCA[6,8]
R. S. DILLON[6]
M. R. FORD
T. D. JONES*
R. L. ROBINELL[16]
J. J. SHONKA[6]
P. S. STANSBURY[6]
G. G. WARNER[6]
S. B. WATSON[6]

SECRETARIAL STAFF
N. L. BARRINGER
K. M. BRANAM

CONSULTANTS
J. H. CANTRELL
L. T. DILLMAN
E. M. SMITH
W. S. SNYDER
F. C. VON DER LAGE

CHEMICAL PHYSICS AND SPECTROSCOPY
W. R. GARRETT*

SECRETARIAL STAFF
R. E. BRADFIER
J. S. BUTTS

TECHNICAL SUPPORT
H. L. BARNWELL*[1]
A. E. CARTER

CHEMICAL PHYSICS
R. N. COMPTON
W. R. GARRETT*
C. E. KLOTS
P. W. REINHARDT
H. C. SCHWEINLER
J. A. STOCKDALE
R. J. WARMACK[7]
A. D. WILLIAMSON[7]
J. M. YOURKIN[6]

ATOMIC PHYSICS AND LASER RESEARCH
G. S. HURST
S. L. ALLMAN
C. H. CHEN
C. W. CHOU[6]
L. W. GROSSMAN[6]
J. P. JUDISH
S. D. KRAMER
T. G. MILLER[17]
M. H. NAYFEH
W. G. PAYNE
J. P. YOUNG[16]

MATHEMATICAL ANALYSIS
V. E. ANDERSON[6]*

CONSULTANTS
J. E. BLOOM
C. D. COOPER
W. F. FREY
R. HEFFERLIN
J. E. PARKS
B. P. PULLEN
R. RITCHIE
P. W. TODD

RADIATION MONITOR
E. D. GUPTON*

SECRETARIAL STAF
D. W. CADDIS

INSTRUMENTATION
E. D. GUPTON*
D. R. CLARK*
G. L. ARTHUR
I. T. FARR
J. E. JACKSON
S. W. NICHOLS

DOSE DATA
J. R. MUNN
R. W. LANE
D. W. BOARD
J. H. WILLIAMS

INTERNAL DOSE
W. S. PARKINSON
R. [illegible]
W. W. GOOD

PERSONNEL METERS
D. R. CLARK*
B. B. HERRELL
W. L. LEE
W. R. MATTHEWS
R. C. WOOD

RADIOCHEMISTRY
L. C. HENLEY
J. C. ANDERSON
W. J. SMITH
A. J. BOARD

CONSULTANT
L. B. FARABEE

*DUAL CAPACITY
[1]RADIATION CONTROL OFFICER
[11]DIVISION SAFETY OFFICER
[2]ALTERNATE FINANCE OFFICER
[3]PLANT AND EQUIPMENT DIVISION
[4]LEAVE OF ABSENCE
[5]INSTRUMENTATION AND CONTROLS DIVISION
[6]ALIEN GUEST
[7]STUDENT
[8]POSTDOCTORAL FELLOW
[9]COMPUTER SCIENCES DIVISION
[10]QUALITY ASSURANCE COORDINATOR
[11]ANALYTICAL CHEMISTRY DIVISION
[12]ENERGY DIVISION
[13]SABBATICAL FROM U.T.
[14]OPERATIONS DIVISION
[15]RADIATION AND SAFETY SURVEYS SECTION
[16]BIOLOGY DIVISION
[17]ORAU GRADUATE RESEARCH PARTICIPANT
[18]VISITING SCIENTIST

OFFICE OF EDUCATION AND INFORMATION
J. E. TURNER*
A. S. LOGBI[11]
M. F. FAIR
C. F. HOLOWAY

HEALTH PHYSICS JOURNAL EDITORIAL OFFICE
J. A. AUXIER*
J. S. CARVER*
G. D. KERR*
W. S. NICHOLS*
J. E. TURNER*

HEALTH PHYSICS DIVISION LONG RANGE PLANNING COMMITT
J. W. POSTON,* CHAIRPERSON
J. A. AUXIER,* EX OFFICIO
G. A. CRISTY*
C. E. EASTERLY*
R. R. HARRY*
C. H. MILLER*
R. E. MILLSPAUGH*
T. W. OAKES*
H. C. SCHWEINLER*
D. W. BOARD*
J. H. THORNGATE*
J. E. TURNER, EX OFFICIO*

HEALTH PHYSICS DIVISION

JANUARY 1, 1977

J. A. AUXIER,* DIRECTOR
W. S. NICHOLS,* SECRETARY
D. W. DAVIS, ASSOCIATE DIRECTOR
R. A. PARKER, SECRETARY

ADMINISTRATIVE ASSISTANT
J. S. CARVER*[1]
D. S. HIBBEN,* SECRETARY

ENGINEERING MAINTENANCE
E. T. LOY
J. T. COX
J. P. HICKEY
S. R. LARRIMORE[2]
J. L. MALONE

FINANCE OFFICER
D. J. ROOK
D. S. HIBBEN,* SECRETARY

SENIOR RESEARCH ADVISORS
R. J. MORGAN
E. P. WIGNER*

ENVIRONMENTAL HEALTH PHYSICS COORDINATOR
R. E. CONSER

EMERGENCY TECHNOLOGY
C. V. CHESTER*

SECRETARIAL STAFF
M. A. CHENOWITH
K. P. MULLINS

LIBRARIAN
R. R. THURMER*

STRATEGIC DEFENSE
C. V. CHESTER*
P. L. BARNES*
G. A. CRISTY*
K. F. GANT
C. M. HAALAND
C. H. KEARNY
R. R. THURMER*

ENERGY SYSTEMS VULNERABILITY
G. A. CRISTY*
P. R. BARNES*
C. V. CHESTER*
R. G. CHESTER
M. E. FISH

CONSULTANT
E. P. WIGNER*

INDUSTRIAL SAFETY AND SPECIAL PROJECTS
A. D. WARDEN*

SECRETARIAL STAFF
M. R. DUNSMORE

BALANCE AREA REPRESENTATIVE
T. J. BURNETT*

SAFETY
D. C. GARY*[1]
R. E. MILLSPAUGH*
E. M. ROBINSON[3]

ORIENTATION AND TRAINING
R. E. MILLSPAUGH*

PROGRAMS AND FACILITIES REVIEW
T. J. BURNETT*

X-RAY AND MICROWAVE REVIEW
W. F. OHNESORGE*

STANDARDS AND PROCEDURES
A. D. WARDEN*

TRANSURANIUM HEALTH PHYSICS AND SAFETY PROCEDURES
C. E. HAYNES*

MEDICAL PHYSICS AND INTERNAL DOSIMETRY
J. W. POSTON
P. R. BELL
S. R. BERNARD
W. L. CHEN[4,5]
S. F. DEUS[5,6]
R. S. DILLON[5]
M. R. FORD
T. D. JONES*
R. L. POSNELL[7,8]
J. J. SHONKA[5]
P. S. STANSBURY[4]
G. G. WARNER[4]
S. R. WATSON[5]

SECRETARIAL STAFF
N. L. BARRINGER
K. W. BRANAN

CONSULTANTS
J. . CANTRELL
L. T. DILLMAN
E. M. SMITH
W. S. SNYDER
F. C. VON DER LAGE

CHEMICAL PHYSICS AND SPECTROSCOPY
W. R. GARRETT*

SECRETARIAL STAFF
M. E. BRASHEER
J. S. BUTTS

TECHNICAL SUPPORT
H. L. BARNABELL[10]
A. E. CARTER

CHEMICAL PHYSICS
R. N. COMPTON
W. R. GARRETT*
C. E. KLOTS
P. W. REINHARDT
H. C. SCHREINER
J. A. STOCKDALE
R. J. BARNACK[11]
A. D. WILLIAMSON[7]
J. W. YORKINS[6]

ATOMIC PHYSICS AND LASER RESEARCH
G. S. HURST
S. L. ALLMAN
C. H. CHEN
C. W. CHOU[6]
L. W. GROSSMAN[6]
J. P. JUDISH
S. D. KRAMER
T. G. MILLER[11]
M. H. RAYFIELD
W. G. PAYNE
J. P. YOUNG[12]

MATHEMATICAL ANALYSIS
V. E. ANDERSON[6]*

CONSULTANTS
J. E. BLOOR
C. D. COOPER
W. F. FREY
R. HEFFERLIN
J. E. PARKS
B. P. PULLEN
B. RITCHIE
P. W. TODD

RADIATION MONITORING
E. D. GUPTON*

SECRETARIAL STAFF
D. W. GADDIS

INSTRUMENTATION
E. D. GUPTON*
D. R. CLARK*
G. L. ARTHUR
I. T. FARR
J. E. JACKSON
S. W. NICHOLS

DOSE DATA
J. R. MUIR
R. W. LANE
D. W. SOARD
J. H. WILLIAMS

INTERNAL DOSE
W. W. PARKINSON
R. E. GOANS
W. M. GOOD

PERSONNEL METERS
D. R. CLARK*
B. B. MERRELL
M. L. LEE
M. R. MATTHEWS
R. C. WOOD

RADIOCHEMISTRY
L. C. HENLEY
J. C. ANDERSON
M. J. SMITH
A. J. SOARD

CONSULTANT
L. B. FARABEE

RADIATION AND SAFETY SURVEYS
R. L. CLARK

SECRETARIAL STAFF
C. M. SEXTON

BLDG. SURVEYS GP. 1
B. T. WALTERS

CENTRAL
W. T. MARTIN
B. C. BURRELL
R. D. PARTEE
J. R. SLATER
D. K. THOMAS

SOUTH CENTRAL
C. A. GOLDEN
A. C. BUTLER
J. V. MILVER
C. E. LITTLE
J. H. SPENCE

EAST
H. M. BUTLER*
J. S. ADDISON
J. F. ALEXANDER
W. D. CARDER
T. L. COLLINS
A. B. ELDRIDGE
C. E. HAYNES*
C. F. JACKSON
W. M. JOHNSON
R. E. KENY
S. B. LUPICA
W. F. OHNESORGE*

SOUTH EAST
A. J. SMITH
W. A. ALEXANDER
T. G. CLARK
R. B. MALCOLM

BLDG. SURVEYS GP. 2
L. C. JOHNSON

NORTH WEST
C. H. MILLER
M. L. CORNER
W. A. MILLOUD
G. R. PATTERSON
C. F. ZANZON

NORTH CENTRAL
J. A. NORTH
J. H. PEBBERTON

MELTON VALLEY
R. E. COLEMAN
W. F. FOX*
J. C. RICHTER
R. L. WALKER

Y-12 OPERATIONS
J. C. DAVIS
A. CARDWELL
R. E. HALLIBURTON
R. P. WARD

SHIFT AND AREA SURVEYS
C. R. GUNN

SHIFT SUPERVISORS
J. S. ADDISON
R. C. COOPER
R. L. JEFFERS
D. G. ROE

SHIFT SURVEYS
C. CLARK

AREA SURVEYS
C. F. SMITH
I. H. WIGGINS

*DUAL CAPACITY
[1]RADIATION CONTROL OFFICER
[2]DIVISION SAFETY OFFICER
[3]ALTERNATE FINANCE OFFICER
[4]PLANT AND EQUIPMENT DIVISION
[5]LEAVE OF ABSENCE
[6]INSTRUMENTATION AND CONTROLS DIVISION
[7]ALIEN GUEST
[8]STUDENT
[9]POSTDOCTORAL FELLOW
[10]COMPUTER SCIENCES DIVISION
[11]QUALITY ASSURANCE COORDINATOR
[12]ANALYTICAL CHEMISTRY DIVISION
[13]ENERGY DIVISION
[14]SABBATICAL FROM U.T.
[15]OPERATIONS DIVISION
[16]RADIATION AND SAFETY SURVEYS SECTION
[17]BIOLOGY DIVISION
[18]ORAU GRADUATE RESEARCH PARTICIPANT
[19]VISITING SCIENTIST

OFFICE OF EDUCATION AND INFORMATION
J. B. TURNER*
A. S. LOEBL[11]
M. F. FAIR
C. F. HOLLOWAY

HEALTH PHYSICS JOURNAL EDITORIAL OFFICE
J. A. AUXIER*
J. S. CARVER*
G. D. KERR*
W. S. NICHOLS*
J. E. TURNER*

HEALTH PHYSICS DIVISION LONG RANGE PLANNING COMMITTEE
J. W. POSTON,* CHAIRPERSON
J. A. AUXIER,* EX OFFICIO
G. A. CRISTY*
C. S. EASTERLY*
R. R. HAMM*
C. H. MILLER*
R. E. MILLSPAUGH*
T. W. OAKES*
H. C. SCHREINER*
D. W. SOARD*
J. H. THORNGATE*
J. B. TURNER, EX OFFICIO*

HEALTH PHYSICS DIVISION ADVISORY COMMITTEE
G. F. BIRG
LAWRENCE LIVERMORE LABORATORY
LIVERMORE, CALIFORNIA

WERNER BRANDT
NEW YORK UNIVERSITY
NEW YORK CITY, NEW YORK

E. D. TROUT
OREGON STATE UNIVERSITY
CORVALLIS, OREGON

M. E. WRENN
NEW YORK UNIVERSITY MEDICAL CENTER
TUXEDO, NEW YORK

ORNL-5308
Distribution Category UC-41

INTERNAL DISTRIBUTIOI.

1. E. T. Arakawa
2. J. C. Ashley
3. S. I. Auerbach
4–13. J. A. Auxier
14. J. K. Baird
15. J. A. Barker
16. S. R. Bernard
17. L. A. Berry
18. R. D. Birkhoff
19. F. R. Bruce
20. W. D. Burch
21. T. J. Burnett
22. H. M. Butler
23. J. G. Carter
24. C. H. Chen
25. C. V. Chester
26. L. G. Christophorou
27. R. L. Clark
28. R. N. Compton
29. W. B. Cottrell
30. W. D. Cottrell
31. K. E. Cowser
32. J. A. Cox
33. G. A. Cristy
34. D. M. Davis
35. H. W. Dickson
36. C. E. Easterly
37. D. E. Ferguson
38. M. R. Ford
39. W. Fulkerson
40. R. B. Gammage
41. A. S. Garrett, Jr.
42. W. R. Garrett
43. J. H. Gillette
44. E. D. Gupton
45. C. M. Haaland
46. R. N. Hamm
47. W. O. Harms
48. F. F. Haywood
49. H. N. Hill
50. G. S. Hurst
51. D. G. Jacobs
52. D. W. Jared
53. T. D. Jones
54. J. P. Judish
55. P. R. Kasten
56–75. S. V. Kaye
76. O. L. Keller
77. G. D. Kerr
78. C. E. Klots
79. S. D. Kramer
80. R. S. Livingston
81. B. K. Lyon
82. F. C. Maienschein
83. L. E. McNeese
84. O. B. Morgan
85. F. R. Mynatt
86. T. W. Oakes
87. M. G. Payne
88. J. K. Poggenburg
89. H. Postma
90. M. E. Ramsey
91. M. L. Randolph
92. P. W. Reinhardt
93. C. R. Richmond
94. R. H. Ritchie
95. G. D. Robbins
96. P. S. Rohwer
97. M. W. Rosenthal
98. H. C. Schweinler
99. H. E. Seagren
100. W. D. Shults
101. P. H. Stelson
102. J. A. Stockdale
103. J. B. Storer
104. H. E. Trammell
105. D. B. Trauger
106. J. E. Turner
107. J. R. Weir
108. M. K. Wilkinson
109. M. W. Williams
110. H. A. Wright
111. A. Zucker
112–113. Central Research Library
114. Document Reference
115–116. Laboratory Records
117. Laboratory Records RC
118. Patent Office

EXTERNAL DISTRIBUTION

119. F. Abeles, Institut D'Optique, 3 Blvd. Pasteur, Paris, France
120. N. F. Barr, Division of Biomedical and Environmental Research, U.S. Department of Energy, Washington, DC 20545
121. H. W. Berk, Department of Nuclear Engineering, Reactor Facility, University of Virginia, Charlottesville, VA 22901
122. J. B. Birks, Atomic, Molecular Physics Group, Schuster Laboratory, University of Manchester, Manchester 13, England
123. R. P. Blaunstein, Division of Biomedical and Environmental Research, U.S. Department of Energy, Washington, DC 20545
124. M. A. Bond, Jr., Chief, Resources Development Section, NBS Library, Washington, DC 20234
125. J. Bradford, RADC/ETSR, Hanscom AFB, MA 01731
126. W. Brandt, Physics Department, New York University, New York, NY 10003
127. A. J. Braundmeier, Faculty of Physics, Southern Illinois University, Edwardsville, IL 62025
128. A. B. Brill, Vanderbilt University Medical School, Nashville, TN 37235
129. A. Brodsky, U.S. Nuclear Regulatory Commission, Washington, DC 20555
130. P.R.J. Burch, Department of Medical Physics, University of Leeds, General Infirmary, Leeds I, England
131. R. L. Butenhoff, Division of Biomedical and Environmental Research, U.S. Department of Energy, Washington, DC 20545
132. J. R. Cameron, University of Wisconsin Medical Center, Department of Radiology, 1300 University Avenue, Madison, WI 53706
133. C. E. Carter, Division of Biomedical and Environmental Research, U.S. Department of Energy, Washington, DC 20545
134. M. W. Carter, School of Nuclear Engineering, Georgia Institute of Technology, Atlanta, GA 30332
135. R. J. Cloutier, Special Training Division, Oak Ridge Associated Universities, Oak Ridge, TN 37830
136. F. E. Coffman, DCTR, U.S. Department of Energy, Washington, DC 20545
137. Commander, U S. Army Environmental Hygiene Agency, Regional Division-South (Bldg. 180), ATTN: LT Lee, Fort McPherson, GA 30330
138. G. Cowper, Radiation Dosimetry Branch, Atomic Energy of Canada Limited, Chalk River, Ontario, Canada
139. F. L. Coller, Office of the President, Electric Power Research Institute, P.O. Box 10412, 3412 Hillview Avenue, Palo Alto, CA 94303
140. D. R. Davy, AAEA Research Establishment, Private Mail Bag, Sutherland, NSW, Australia
141. L. J. Deal, Associate Director for Health Protection, Division of Safety, Standards, and Compliance, U.S. Department of Energy, Washington, DC 20545
142. J. Dennis, Head, Health Physics Department, National Radiological Protection Board, Harwell, Didcot Berks, England
143. S. F. Deus, Instituto de Emergia Atomico, Cidade Universitaria, c.p. 11049, Pehheiros, Sao Paulo S. 9., Brazil
144. G. W. Dolphin, National Radiological Protection Board, Bldg. 566, Harwell, Didcot, Oxfordshire, OX111 ORQ, England
145. C. W. Eddington, Division of Biomedical and Environmental Research, U.S. Department of Energy, Washington, DC 20545
146. G. G. Eichholz, School of Nuclear Engineering, Georgia Institute of Technology, Atlanta, GA 30332
147. Environmental Radioactivity Section, Radiation Protection Bureau, Brookfield Road, Ottawa, Ontario K1A1Ck, Canada
148. F. Gabbard, Department of Physics, University of Kentucky, Lexington, KY 40506
149. J. H. Harley, Director, Environmental Measurements Laboratory, U.S. Department of Energy, 376 Hudson Avenue, New York, NY 10014

150 W. R. Hendee, University of Colorado Medical Center, 4200 East Ninth Avenue, Denver, CO 80220
151. J. I. Hopkins, Department of Physics, Davidson College, Davidson, NC 28036
152. A. Howie, Cavendish Laboratory, Madingley Road, Cambridge CB30HE, England
153. J. H. Hubbell, National Bureau of Standards, Washington, DC 20234
154. T. Inagaki, Department of Physics, Osaka Kyolky University, Tennoji, Osaka, Japan
155. International Atomic Energy Agency, Wien A-1001, Austria
156. Emilio Iranzo, Jefe de Proteccion y Medicina, Ministerio de Industria, Juota de Energia Nuclear, Avenida Complutense, Madrid 3, Spain
157. R. E. Johnston, Department of Radiology, Division of Nuclear Medicine, University of North Carolina, Chapel Hill, NC 27514
158. R. Katz, University of Nebraska, Department of Physics, Lincoln, NE 68588
159. Library, University of Tennessee, Knoxville, TN 37916
160. Bo Lindell, National Institute of Radiation Protection, Stockholm 60, Sweden
161. Jens Lindhard, Institute of Physics, Aarhus University, Aarhus, Denmark
162. J. L. Liverman, Assistant Administrator for Environment and Safety, U.S. Department of Energy, Washington, DC 20545
163. R. Loevinger, Radiation Physics Division, National Bureau of Standards, Washington, DC 20235
164. R. P. Madden, National Bureau of Standards, Gaithersburg, MD 20760
165. J. L. Magee, University of California, Berkeley, CA
166. Sigismond Makra, Department of Health Physics, Central Research Institute for Physics, Hungarian Academy of Sciences, P.O.B. 49, Budapest 114, Hungary
167. A. M. Marko, Director, Biology and Health Physics Division, Atomic Energy of Canada Limited, Chalk River, Ontario, Canada
168. C. A. Mawson, Atomic Energy of Canada Limited, Chalk River, Ontario, Canada
169. C. W. Mays, Jr., Radiobiology Laboratory, University of Utah, Salt Lake City, UT 84112
170. T. T. Mercer, University of Rochester, School of Medicine and Dentistry, Rochester, NY 14620
171. W. A. Mills, EPA, Rm. 635, Waterside Mall East, 401 M. Street, SW, Washington, DC 29460
172. K. Z. Morgan, School of Nuclear Engineering, Georgia Institute of Technology, Atlanta, GA 30332
173. R. H. Morgan, Johns Hopkins School, Hygiene and Public Health, 615 N. Wolfe Street, Baltimore, MD 21205
174. P. E. Morrow, The University of Rochester School of Medicine and Dentistry, Rochester, NY 14620
175. W. R. Ney, Executive Director, National Council on Radiation Protection and Measurements, 7910 Woodmont Avenue (Suite 1016), Washington, DC 20014
176. M. Oberhofer, Health Physics Division, EURATOM, Ispra, Italy
177. L. R. Painter, Physics Department, University of Tennessee, Knoxville, TN 37916
178. C. C. Palmiter, Radiation Office, Environmental Protection Agency, 5600 Fishers Lane, Rockville, MD 20852
179. P. Parks, Bureau of Radiological Health, Food and Drug Administration, 5600 Fishers Lane HEX300, Rockville, MD 20852
180. E.K.A. Piesch, Radiation Protection and Safety Department, Karlsruhe Nuclear Research Center, Postfach 3640, 75 Karlsruhe 1, Federal Republic of Germany
181. E. E. Pochin, Department of Clinical Research, University College Hospital Medical School, London, W.C.1, England
182. Carlo Polvani, C/O Chen, Viale Regina Margherita 125, 00198 Rome, Italy
183. J. W. Poston, School of Nuclear Engineering, Institute of Technology, Atlanta, GA 30332
184. C. J. Powell, Electron Physics Section, National Bureau of Standards, Washington, DC 20234
185. Serge B. Pretre, Head, Section for Protection of Persons and Environment, Safety Inspectiorate of Nuclear Installations, CH-5305 Wurenlingen, Switzerland
186. H. Raether, Institute for Applied Physics, University of Hamburg, Hamburg, West Germany
187. Research and Technical Support Division, U.S. Department of Energy, Oak Ridge Operations, P.O. Box E, Oak Ridge, TN 37830

188. S. Robin, Spectroscopy Laboratory, University of Rennes, Rennes, France
189. C. E. Roessler, 525 N.E. 4th Street, Gainesville, FL 32601
190. M. Rosenstein, Bureau of Radiological Health, Food and Drug Administration, 12720 Twinbrook Parkway, Rockville, MD 20852
191. H. H. Rossi, Radiological Research Laboratory, Columbia University, 630 West 168th Street, New York, NY 10032
192. A. Scharmann, I. Physikalisches Institut, Universitat Giessen, Giessen, Germany BDR
193. R. Schenider, Bureau of Radiological Health, Food and Drug Administration, 12720 Twinbrook Parkway, Rockville, MD 20852
194. G. B. Schofield, Chief Medical Officer, British Nuclear Fuels, Ltd., Windscale and Calder Works, Sellafield, Seascale, Cumbria, England
195. Ryszard G. Siwicki, Health Physics division, Institute for Nuclear Research, Swierk K/Otwocka, Poland
196. S. Somasondaram, Low Level Counting Laboratory, BARC Hospital, Bombay 400 094, India
197. Gian-Marie Sordi, Instituto De Energia Atomica, Cidade Universitaria, Caisa Postal 11049-Pinheiros, Sao Paulo 9, Brazil
198. W. Steinmann, II Physikalisches Inst. Der University Munchen, Munchen 13, Germany
199. C. Gordon Stewart, Director, Medical Division, Atomic Energy of Canada Limited, Chalk River, Ontario, Canada
200. B. J. Stover, Department of Pharmacology, School of Medicine, University of North Carolina, Swing Building 217 H, Chapel Hill, NC 27514
201. J. B. Swan, University of Western Australia, Nedlands, Western Australia
202. Jacob Tadmor, Director, Nuclear Safety, Israel Atomic Energy Commission, Soreq Nuclear Research Center, Yavne, Israel
203. L. Taylor, National Council on Radiation Protection and Measurements, 7910 Woodmont Avenue, Washington, DC 20014
204. C. Tobias, University of California, Lawrence Radiation Laboratory, Berkeley, CA 94720
205. Chuan-Jong Tung, Health Physics Section, National Tsing Hua University, Hsin Chu, Taiwan 300, Republic of China
206. J. Villforth, Bureau of Radiological Health, U.S. Public Health Service, 5600 Fisher Lane, Parklawn Building, Rockville, MD 20852
207. H. E. Walburg, Jr., UT-CARL, 1299 Bethel Valley Road, Oak Ridge, TN 37830
208. N. Wald, University of Pittsburgh, Graduate School of Public Health, Pittsburgh, PA 15213
209. W. Weyzen, Division of Biomedical and Environmental Research, U.S. Department of Energy, Washington, DC 20545
210. R. R. Winters, Director, Oak Ridge Science Semester, GLCA, Denison University, Main Street, Granville, OH 43023
211. E. P. Wigner, 8 Ober Road, Princeton, NJ 08540
212. R. W. Wood, Division of Biomedical and Environmental Research, U.S. Department of Energy, Washington, DC 20545
213. World Health Organization, Palais Des Nations, Geneva, Switzerland
214. H. O. Wyckoff, 4108 Montpelier Road, Rockville, MD 20853
215. P. L. Ziemer, Bionucleonics Department, Purdue University, West LaFayette, IN 47907

216–466 Given distribution as shown in TID-4500 under Dist. Category UC-41 (25 copies--NTIS)

☆U.S. GOVERNMENT PRINTING OFFICE: 1978-740-190/135